

Transactions of the ASME®

HEAT TRANSFER DIVISION

Chair, L. C. WITTE
Vice Chair, J. H. KIM
Past Chair, R. A. NELSON
Secretary, Y. BAYAZITOGU
Treasurer, R. D. SKOCYPEC
Editor, V. DHIR (2005)

Associate Editors,
C. T. AVEDISIAN (2002)
H. H. BAU (2003)
C. BECKERMANN (2001)
A. BEJAN (2003)
V. P. CAREY (2003)
F. B. CHEUNG (2002)
T. Y. CHU (2002)
B. T. F. CHUNG (2001)
M. FAGHRI (2003)
J. G. GEORGIADIS (2003)
J. P. GORE (2002)
M. HUNT (2002)
D. A. KAMINSKI (2001)
R. L. MAHAJAN (2001)
A. MAJUMDAR (2001)
G. P. PETERSON (2003)
D. POULIKAKOS (2002)
S. S. SADHAL (2002)
R. D. SKOCYPEC (2003)
D. A. ZUMBRUNNEN (2001)

BOARD ON COMMUNICATIONS

Chair and Vice President
OZDEN OCHOA

OFFICERS OF THE ASME

President, W. A. WEIBLEN
Executive Director,
D. L. BELDEN
Treasurer,
R. E. NICKELL

PUBLISHING STAFF

Managing Director, Engineering
CHARLES W. BEARDSLEY
Director, Technical Publishing
PHILIP DI VIETRO
Managing Editor, Technical Publishing
CYNTHIA B. CLARK
Managing Editor, Transactions
CORNELIA MONAHAN
Production Coordinator
COLIN McATEER
Production Assistant
MARISOL ANDINO

Transactions of the ASME, Journal of Heat Transfer (ISSN 0022-1481) is published bi-monthly (Feb., Apr., June, Aug., Oct., Dec.) by The American Society of Mechanical Engineers, Three Park Avenue, New York, NY 10016. Periodicals postage paid at New York, NY and additional mailing offices. POSTMASTER: Send address changes to Transactions of the ASME, Journal of Heat Transfer, c/o THE AMERICAN SOCIETY OF MECHANICAL ENGINEERS, 22 Law Drive, Box 2300, Fairfield, NJ 07007-2300.

CHANGES OF ADDRESS must be received at Society headquarters seven weeks before they are to be effective. Please send old label and new address.

STATEMENT from By-Laws. The Society shall not be responsible for statements or opinions advanced in papers or ... printed in its publications (B7.1, Para. 3). COPYRIGHT © 2001 by The American Society of Mechanical Engineers. For authorization to photocopy material for internal or personal use under those circumstances not falling within the fair use provisions of the Copyright Act, contact the Copyright Clearance Center (CCC), 222 Rosewood Drive, Danvers, MA 01923, tel: 978-750-8400, www.copyright.com. Request for special permission or bulk copying should be addressed to Reprints/Permission Department. INDEXED by Applied Mechanics Reviews and Engineering Information, Inc. Canadian Goods & Services Tax Registration #126148048.

Journal of Heat Transfer

Published Bimonthly by The American Society of Mechanical Engineers

VOLUME 123 • NUMBER 4 • AUGUST 2001

HEAT TRANSFER PHOTOGALLERY

- 617 Heat Transfer Photogallery
K. D. Kihm
- 618 Evaporating Capillary Pore Flows Ranging From 10-mm to 10- μ m Diameter
H. J. Kim and K. D. Kihm
- 619 Visualization of Atomic Force Microscopy From Molecular Dynamics Simulations
Tai-Hsi Fan and Andrei Fedorov
- 620 Subcooled Pool Boiling Heat Transfer in Microgravity and Hi-g
Jungho Kim, John Benton, John McQuillen, and Mary Vickerman
- 621 Shear Layer Instability and Mixing in Micro Heat Spreaders
C. Sert and A. Beskok
- 622 Oscillatory Entrained Droplet EHD Two-Phase Flow
J. S. Cotton, M. Shoukri, and J. S. Chang
- 623 Local Fin-Surface Heat Transfer for Flow Around a Circular Cylinder With and Without Vortex-Generating Winglets
J. E. O'Brien and Manohar S. Sohal

TECHNICAL PAPERS

Conduction Heat Transfer

- 624 Thermal Resistance Models for Non-Circular Moving Heat Sources on a Half Space
Y. S. Muzychka and M. M. Yovanovich
- 633 The Steady Inverse Heat Conduction Problem: A Comparison of Methods With Parameter Selection
Robert Throne and Lorraine Olson

Forced Convection

- 645 Film Cooling of a Cylindrical Leading Edge With Injection Through Rows of Compound-Angle Holes
Y.-L. Lin and T. I.-P. Shih
- 655 Time-Resolved Thermal Boundary-Layer Structure in a Pulsatile Reversing Channel Flow
Sean P. Kearney, Anthony M. Jacobi, and Robert P. Lucht
- 665 Effect of Turbulence With Different Vortical Structures on Stagnation Region Heat Transfer
Aung N. Oo and Chan Y. Ching
- 675 Effects of Rib Arrangements on Heat Transfer and Flow Behavior in a Rectangular Rib-Roughened Passage: Application to Cooling of Gas Turbine Blade Trailing Edge
Robert Kiml, Sadanari Mochizuki, and Akira Murata
- 682 Energy Separation and Acoustic Interaction in Flow Across a Circular Cylinder
R. J. Goldstein and Boyong He

(Contents continued on inside back cover)

This journal is printed on acid-free paper, which exceeds the ANSI Z39.48-1992 specification for permanence of paper and library materials. ©™
♻️ 85% recycled content, including 10% post-consumer fibers.

Natural and Mixed Convection

- 688 Experimental and Numerical Study of Conjugate Heat Transfer in a Horizontal Channel Heated From Below
Wilson K. S. Chiu, Cristy J. Richards, and Yogesh Jaluria
- 698 Conjugate Mixed Convection With Surface Radiation From a Vertical Plate With a Discrete Heat Source
C. Gururaja Rao, C. Balaji, and S. P. Venkateshan

Evaporation, Boiling, and Condensation

- 703 Heat Transfer in Direct Contact Condensation of Steam to Subcooled Water Spray
Minoru Takahashi, Arun Kumar Nayak, Shin-ichi Kitagawa, and Hiroyuki Murakoso
- 711 Experimental and Theoretical Study of Heating/Drying of Moist Paper Sheet With a Gas-Fired Infrared Emitter
J. Seyed-Yagoobi and A. N. Husain
- 719 The Effect of Dissolving Gases or Solids in Water Droplets Boiling on a Hot Surface
Qiang Cui, Sanjeev Chandra, and Susan McCahan

Manufacturing Processes

- 729 Interface Shape and Thermally-Driven Convection in Vertical Bridgman Growth of Gallium Selenide: A Semiconductor With Anisotropic Solid-Phase Thermal Conductivity
Hanjie Lee and Arne J. Pearlstein

Microscale Heat Transfer

- 741 Molecular Dynamics Simulation of Nanodroplet Evaporation
J. H. Walther and P. Koumoutsakos
- 749 Monte Carlo Study of Phonon Transport in Solid Thin Films Including Dispersion and Polarization
Sandip Mazumder and Arunava Majumdar

Heat Exchangers

- 760 Integrative Thermodynamic Optimization of the Crossflow Heat Exchanger for an Aircraft Environmental Control System
Jose V. C. Vargas, Adrian Bejan, and David L. Siems
- 770 An Improved Design and Rating Analyses of Counter Flow Wet Cooling Towers
Jameel-ur-Rehman Khan and Syed M. Zubair

Heat Transfer Enhancement

- 779 Heat Transfer Enhancement to the Drag-Reducing Flow of Surfactant Solution in Two-Dimensional Channel With Mesh-Screen Inserts at the Inlet
Peiwen Li, Yasuo Kawaguchi, Hisashi Daisaka, Akira Yabe, Koichi Hishida, and Masanobu Maeda
- 790 Using Porous Fins for Heat Transfer Enhancement
S. Kiwan and M. A. Al-Nimr

Thermal Systems

- 796 Precision Temperature Control of High-Throughput Fluid Flows: Theoretical and Experimental Analysis
Kevin M. Lawton, Steven R. Patterson, and Russell G. Keanini

TECHNICAL NOTES

- 803 Detailed Heat Transfer Coefficient Distributions on a Large-Scale Gas Turbine Blade Tip
Shuye Teng, Je-Chin Han, and G. M. S. Azad
- 810 Transport Phenomena of Developing Laminar Mixed Convection in Inclined Rectangular Ducts With Wall Transpiration
Wei-Mon Yan and Pei-Yuan Tzeng
- 814 Clouds Over Soot Evaporation: Errors in Modeling Laser-Induced Incandescence of Soot
G. J. Smallwood, D. R. Snelling, F. Liu, and Ö. L. Gülder

ANNOUNCEMENTS

- 819 Call for Papers: Microgravity Transport Processes in Fluid, Thermal, Materials, and Biological Sciences
- 820 Call for Photographs: 2001 International Mechanical Engineering Congress and Exposition (IMECE)

Heat Transfer Photogallery

The fifth "Heat Transfer Photogallery" was held at the 2000 International Mechanical Engineering Congress and Exhibition in Orlando last November. The Heat Transfer Visualization Committee sponsored the session and attracted 13 photo displays that illustrate phenomena that occur in the presence of a temperature gradient. Six entries were selected for publication in this special section of the ASME JOURNAL OF HEAT TRANSFER.

The purpose of publishing these photographs is to draw attention to the innovative features of optical diagnostics and aesthetic qualities of thermal processes. To focus on the visualization, the text is kept to a minimum and further details should be found through the listed references or directly from the authors. The photographs include visualizations of the following: (1) the effect of the pore diameter, ranging from 10-mm to 10- μ m, on the capillary thermal and flow fields; (2) molecular dynamics simulations for atomic force microscope visualization; (3) comparison of boiling bubble characteristics between 1-g and reduced gravity at 0.05-g; (4) oscillatory flow forced convection and mixing inside a micro heat spreader; (5) entrained drop formation from electrohydrodynamically driven oscillatory annular flow; and (6) mapping of local surface heat transfer coefficients with and without vortex-generating winglets. It is now proposed that the journal readers enjoy viewing these collections, acquire knowledge of the state-of-the-art features potentially applicable for their own research,

and promote their participation in 2001-IMECE Photogallery session presentation (refer to the Call for Photogallery for 2001-IMECE announced in this volume) [1–5].

References

- [1] Bae, S., Kim, M. H., and Kim, J., 1999, "Improved Technique to Measure Time and Space Resolved Heat Transfer under Single Bubbles during Saturated Pool Boiling of FC-72," *Exp. Heat Transfer*, **12**, No. 3, pp. 265–278.
- [2] Fedorov, A., and Viskanta, R., 1998, "Heat/Mass Transfer and Adsorption Dynamics in a Honeycomb Adsorbent: Application of the Simplified Local Density Model," *Therm. Sci. Eng.*, **6**, No. 1, pp. 1–10.
- [3] Kim, H. J., and Kihm, K. D., 2001, "Thermal and Flow Characteristics of Evaporating Capillary Pore Ranging from 10-mm to 10- μ m Diameter," *3rd Pacific Symposium on Flow Visualization and Image Processing (PSFVIP-3)*, Paper No. F3202, Maui.
- [4] O'Brien, J. E., and Sohal, M. S., 2000, "Heat Transfer Enhancement for Finned-Tube Heat Exchangers with Winglets," *Proceedings, 2000-ASME International Congress and Exposition, Orlando, HTD-Vol. 365*, pp. 137–146.
- [5] Sert, C., and Beskok, A., 2000, "Time Periodic Forced Convection Cooling in Micro Heat Spreaders," *Proceedings, 2000-ASME International Congress and Exposition, Orlando, MEMS-Vol. 2*, pp. 571–580.

K. D. Kihm

Department of Mechanical Engineering,
Texas A&M University,
College Station, TX 77843-3123

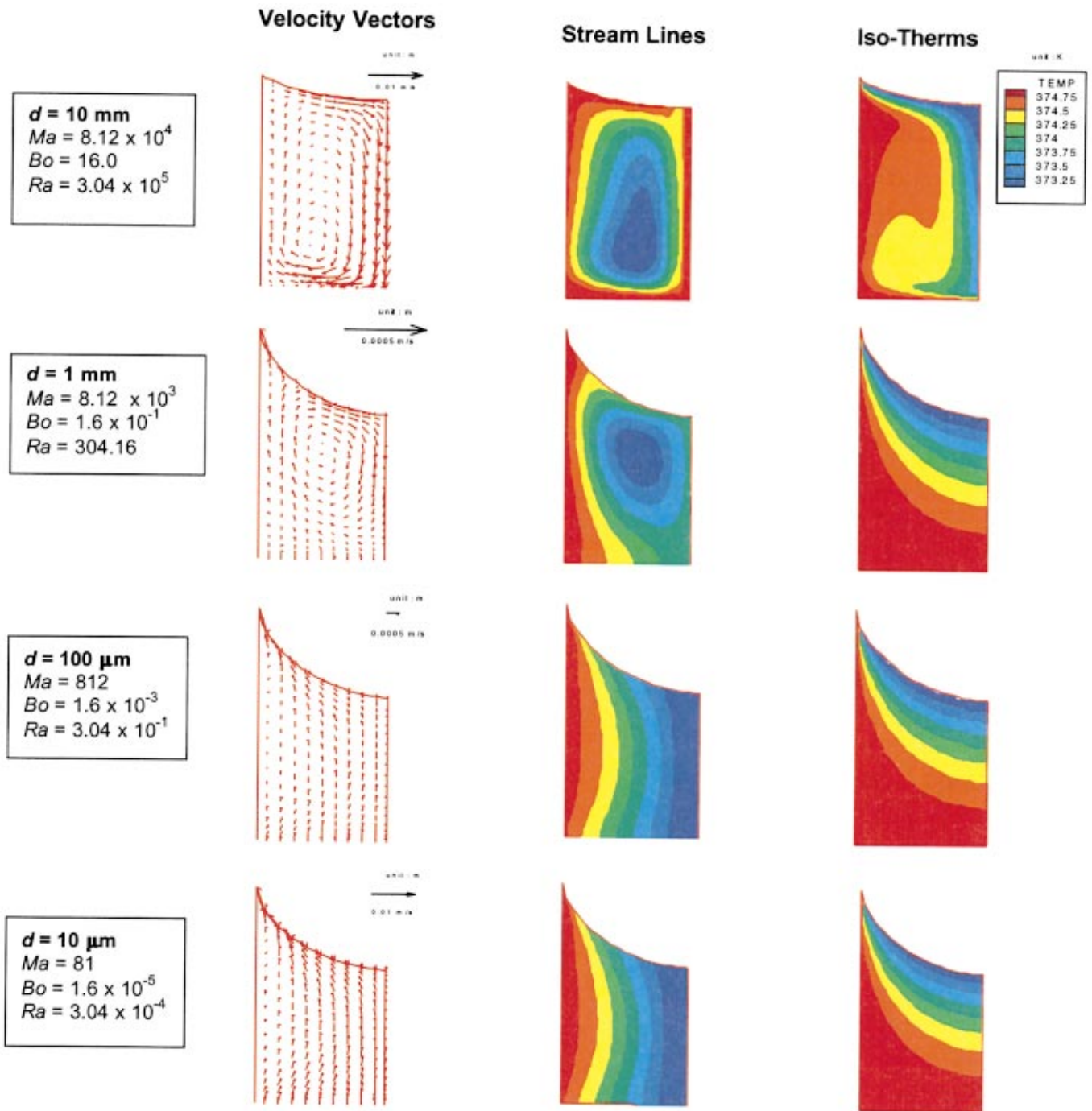


Fig. 1 Calculated flow and temperature distributions inside sidewall-heated capillary pores of different diameters

EVAPORATING CAPILLARY PORE FLOWS RANGING FROM 10-mm TO 10-μm DIAMETER

H. J. Kim and K. D. Kihm
Texas A&M University, College Station, Texas

Temperature and velocity profiles are numerically predicted for evaporating capillary pore flows that are driven by both thermo-capillary interfacial phoresis and buoyant convection of the pore bulk driven by the superheated (2°C) pore side wall. A finite volume method (FVM) is used with a generalized boundary-fitted coordinate (BFC) system to handle the concave meniscus surface geometry. The interfacial boundary conditions, the meniscus shape and the rate of evaporation, had to be simultaneously deter-

mined as part of the iterative solutions. The pore diameters are ranged from 10-mm to 10-μm for water at 1 atm. With decreasing pore diameter, the convection-driven circulating flows diminish and vertically migrating flows, driven by the interfacial evaporation, dominate. Note that the magnitudes of the velocity vectors are decreasing and then increasing with decreasing pore diameter. Nearly stratified temperature distribution prevails the pores smaller than 1-mm diameter indicating negligible convection (Fig. 1).

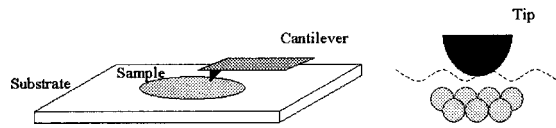


Fig. 1 Schematic of the AFM action

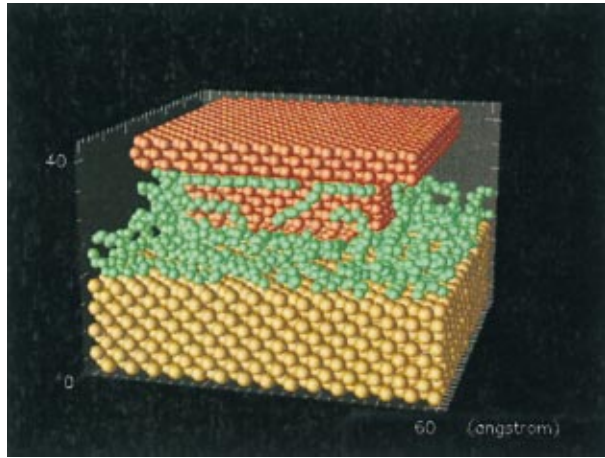


Fig. 2 Instantaneous snapshot of polymer molecular motion

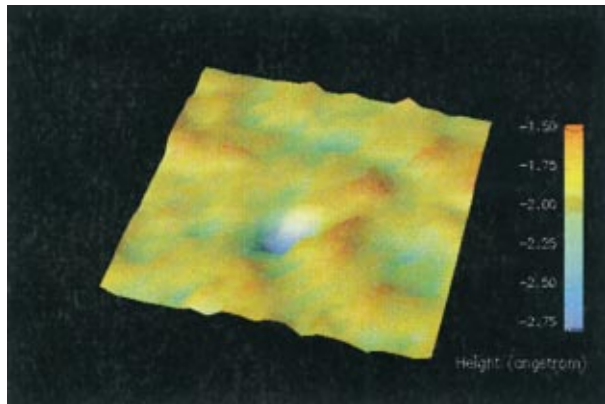


Fig. 3 Topology of the sample surface atomic structure

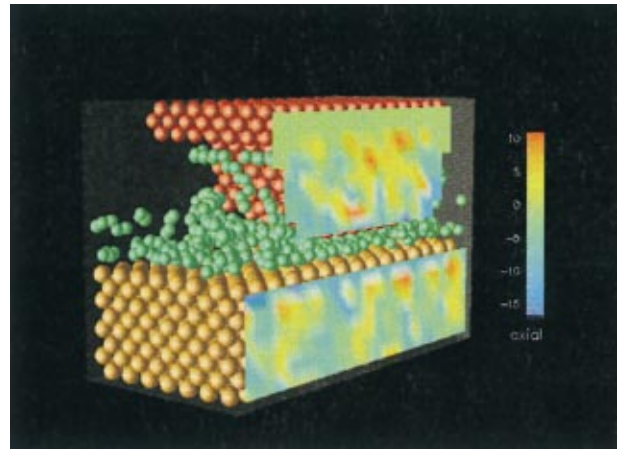


Fig. 4 Image of the atomic normal stress (axial) forces

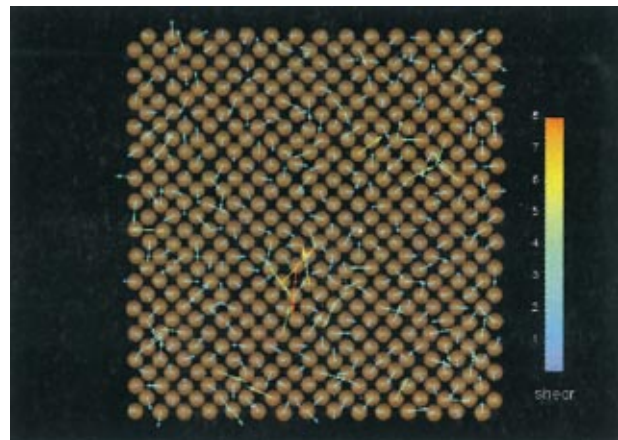


Fig. 5 Image of the atomic shear stress (friction) forces

VISUALIZATION OF ATOMIC FORCE MICROSCOPY FROM MOLECULAR DYNAMICS SIMULATIONS

Tai-Hsi Fan and Andrei Fedorov

School of Mechanical Engineering, Georgia Institute of Technology, Atlanta, Georgia

A computer visualization method is used to present the details of the imaging action by the surface scanning equipment—Atomic Force Microscope (AFM) from the Molecular Dynamics (MD) simulations. The purpose of the scanning process is to resolve (image) the surface details, to observe the tip-substrate interactions, and to record the dynamics of transport processes in the film down to the atomic or molecular level. The device uses a nondestructive tip to probe the interatomic and intermolecular forces and is schematically shown in Fig. 1. Figures 2 through 5 show results of MD simulations of an AFM cantilever tip that probes a sample covered with the lubricant film. The cantilever tip is made of nickel (Ni, shown in red color), the sample is gold (Au, shown in gold color), and the lubricant film consists of several long chain molecules of the polymer (shown in green color). Figure 2 presents an instantaneous snapshot of the polymer molecular motion around the AFM tip induced by intermolecular interactions between the molecules of the substrate, film, and the cantilever tip. In Fig. 3, we show the topology of the surface atomic structure of

the substrate via mapping the local height field by the color image to generate the rubbersheet-like surface. This is virtual representation of the instantaneous topographic image of the surface generated by AFM. Figure 4 presents computer imaging of the short range axial intermolecular forces (i.e., atomic normal stresses) induced by atoms located nearby to the cutting plane, while the atomic level friction forces induced by the tip and polymer molecules on the sample surface are demonstrated in Fig. 5. For the purpose of visualization of the unstructured data irregularly located in space, the mapping surfaces are created to interpolate the scattering data points into correct field values on the mapping surface (Fig. 4).

Acknowledgments

The authors would like to thank Dr. David Luedtke, Professor Uzi Landman from GIT School of Physics, and Dr. William Ribarsky from GIT College of Computing for providing the MD dataset.

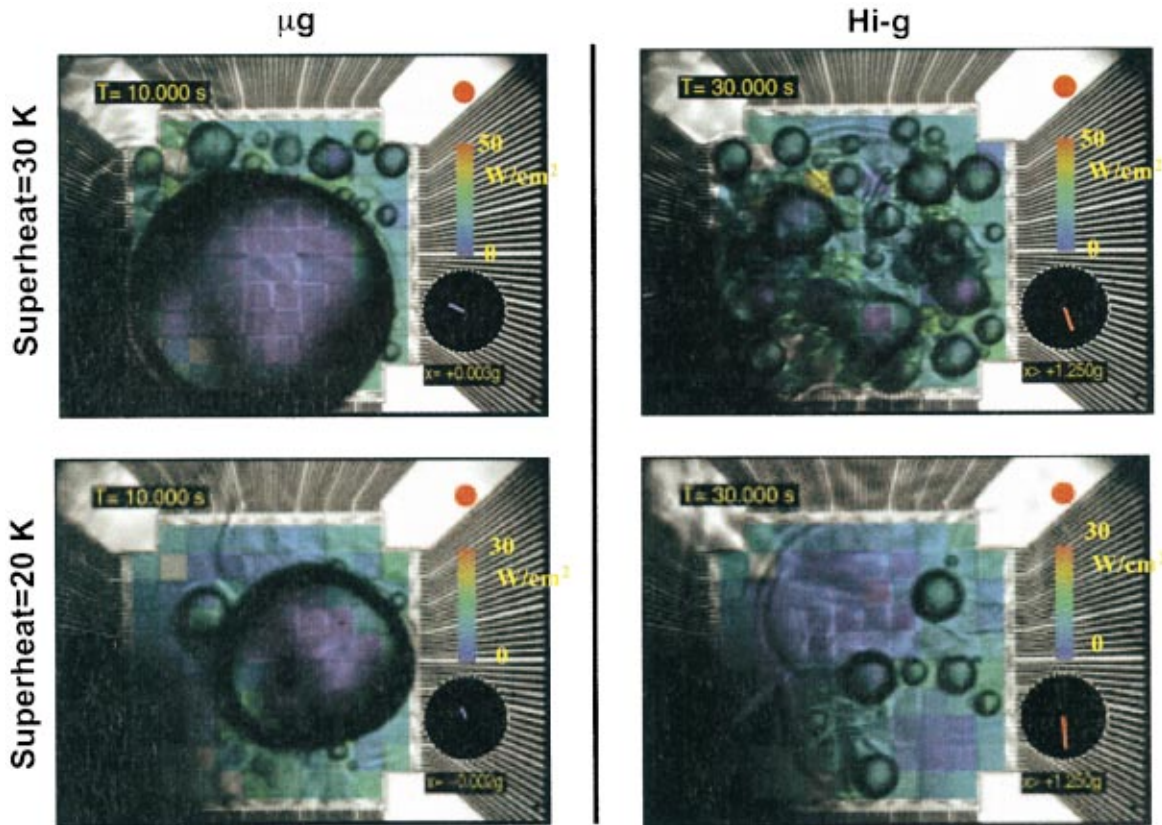


Fig. 1 False color images of boiling heat transfer in microgravity and Hi-g

SUBCOOLED POOL BOILING HEAT TRANSFER IN MICROGRAVITY AND Hi-g

Jungho Kim and John Benton
University of Maryland

John McQuillen and Mary Vickerman
NASA Glen Research Center

An array of microscale heaters each $0.27 \text{ mm} \times 0.27 \text{ mm}$ in size were held at constant temperature using electronic feedback loops, enabling the heat transfer from each heater to be determined. The above images were obtained by combining video images of boiling taken from below and adding false color according to the heat transfer from each heater in the array. The boiling behavior in microgravity and high-g (about 1.8 g) is shown on Fig. 1 at two wall superheats. The microgravity environment was provided by a KC-135. The bulk fluid (FC-72) was at 1 atm and subcooled by 35 K. The circle at the bottom right of each image shows the direction of the

acceleration vector within the plane of the image (the circle corresponds to 0.05 g). The x-direction is perpendicular to the image.

In microgravity, a large “primary” bubble surrounded by numerous smaller bubbles was observed. The primary bubble moved in a circular pattern on the heater array as it coalesced with the smaller bubbles. A dry spot formed underneath this primary bubble, as indicated by the low heat transfer. The size of the primary bubble increased with wall superheat. In high-g, numerous small bubbles that nucleate, grow, and detach very rapidly were observed.

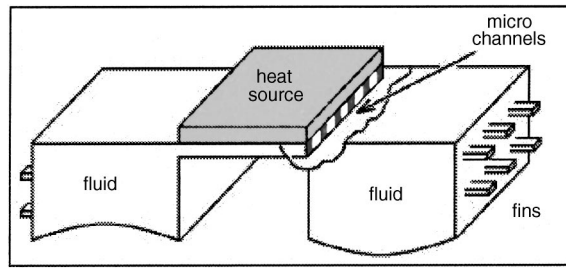


Fig. 1 A schematic view of the MHS

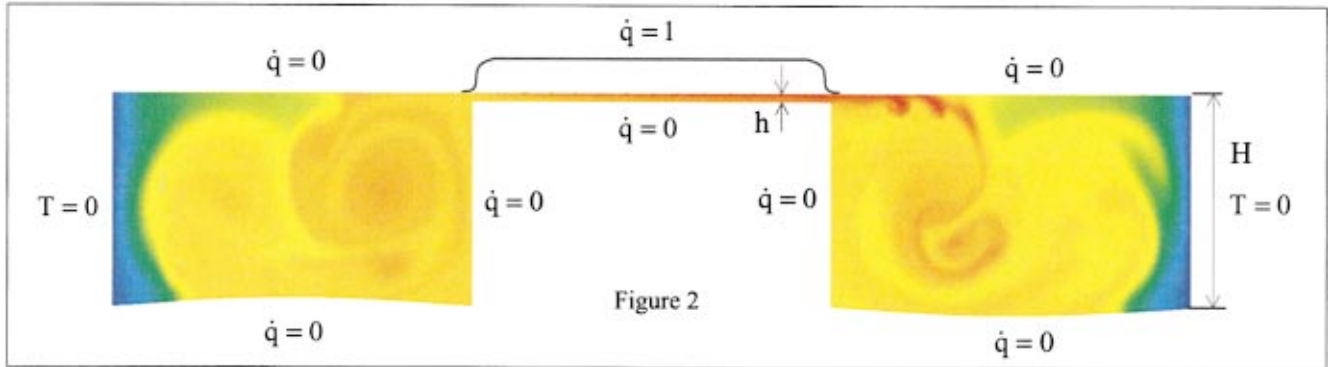


Fig. 2 Boundary conditions used in numerical modeling of MHS devices (insulated $q=0$, constant heat flux $\dot{q}=1$ and constant temperature $T=0$)

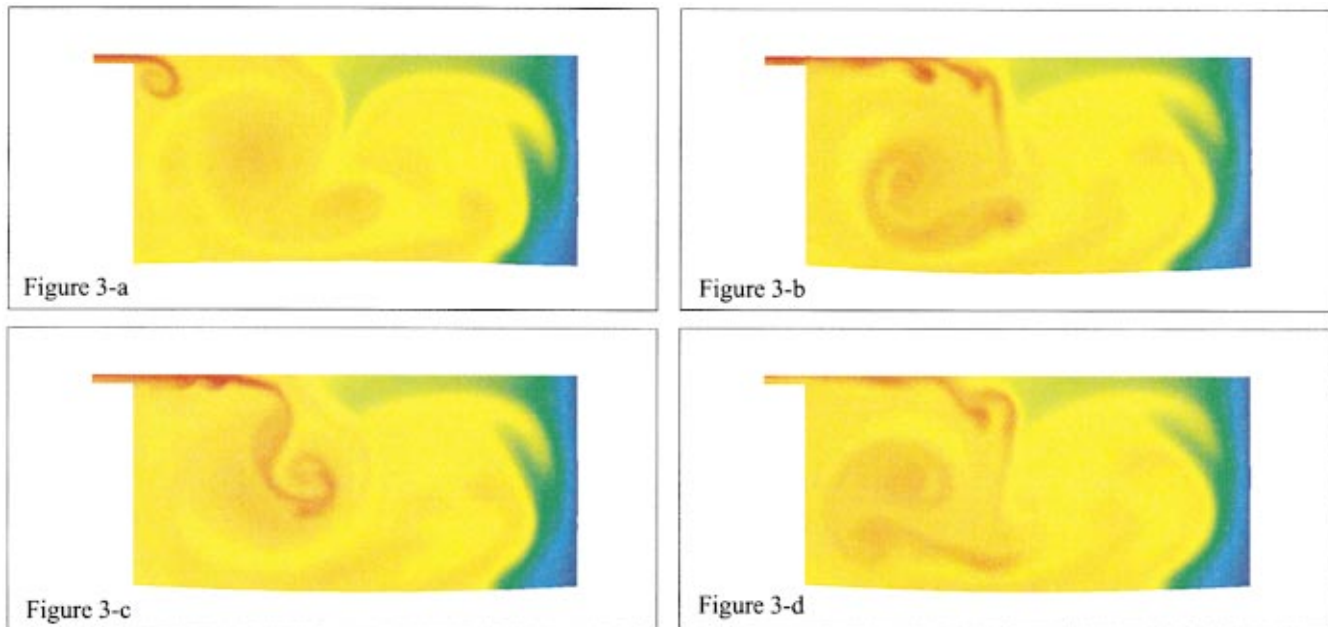


Fig. 3 Snapshots of temperature contours during ejection to the right reservoir. Red and blue show high and low temperatures, respectively.

SHEAR LAYER INSTABILITY AND MIXING IN MICRO HEAT SPREADERS

C. Sert and A. Beskok

Texas A&M University, Micro-Fluidics Laboratory, College Station, Texas

The micro heat spreader (MHS) is a micro-fluidic device designed for thermal management of microelectronic components. It connects two reservoirs by a set of micro-channels (Fig. 1). The bottom surfaces of the reservoirs are membranes that are driven with a phase difference of π , either by electrostatic or piezoelectric actuation. The idea is to minimize the chip surface temperature by *oscillatory flow forced convection and mixing*. Numerical simulations are performed for an MHS device with channel to reservoir expansion ratio $H/h=25$. The boundary conditions and the MHS geometry are shown in Fig. 2. Both the flow and temperature fields are time-periodic, and Womersley and Prandtl numbers are

$\alpha=5.6$. and $Pr=1$, respectively. Since $Pr=1$, the temperature field closely follows the flow. Figs. 3(a–d) show snapshots of temperature contours during ejection to the right reservoir, where shear layer instability at the channel expansion is observed. The vortex rolls due to the shear layer instability are visible in the temperature contours of Figs. 3 (b, c). The flow rapidly turns towards the oscillating membrane due to the influence of the end wall and the membrane motion. The temperature contours show two primary counter-rotating zones with various smaller rotating structures, which promote further mixing in the MHS system.

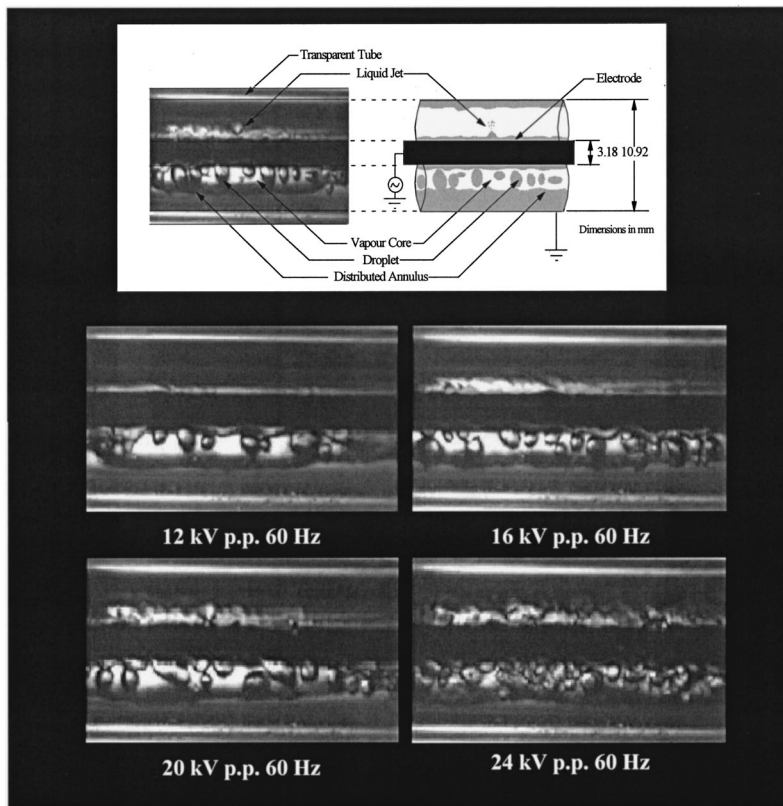


Fig. 1 High speed video images of oscillatory entrained droplet EHD two-phase flow

OSCILLATORY ENTRAINED DROPLET EHD TWO-PHASE FLOW

J. S. Cotton, Ph.D.^{†,*} and M. Shoukri, Ph.D.*

[†]Long Manufacturing, Dana Corp., Oakville, Ontario, Canada

J. S. Chang, Ph.D.*

*McMaster University, Engineering, Hamilton, Ontario, Canada

In an experimental investigation of electrohydrodynamic two-phase flow, the application of a 60 Hz AC voltage potential to convective boiling and condensation systems has led to a regime unique to any flow pattern previously observed [1–3]. It is an oscillatory flow, where droplets as large as 2 mm in diameter are entrained in a vapor core that is surrounded by an annular liquid film around the circumference of the tube and electrode, resembling a multi-layered annular flow. The droplets oscillate radially in the lower portion of the annulus at a frequency of approximately 120 Hz, twice the frequency of the applied field, occasionally being entrained by the inner or outer annular film. In addition to the droplet formation, small spouts or jets of liquid were observed on the upper half of the annular film surrounding the electrode. These spouts seemed to form randomly on the crest of a wave created by interfacial instabilities present in the film and would spray a fine mist into the upper portion of the vapor core, as shown in the upper figure. The size of the droplets, intensity of motion, rate of deposition and the occurrence of spouts were highly dependent on the amplitude of the 60 Hz applied voltage.

The interaction between the phases and the extremely high interfacial area, when coupled with the increased turbulent mixing created by the oscillatory motion of the flow, led to significant enhancement of the overall Nusselt number (~300 percent) and overall pressure drop in both condensation and evaporation when applied under the appropriate conditions [1–3]. The frequency of

the oscillations suggests that the fluctuations in the flow pattern are actually the continuous transition between flow regimes due to the approximate “on/off” electric field applied to the electrode. It is postulated that the resultant flow regime is the continuous construction and destruction of two separate flow regimes. For example, at $Re=3500$ the flow pattern in the absence of the electric field is dominantly stratified flow and intermittent annular or entrained droplet flow at high applied DC voltage levels [1,4]. Hence, the oscillatory-entrained droplet flow pattern is believed to be a result of the continuous flow pattern transition between these two regimes (Fig. 1).

References

- [1] Cotton, J. S., 2000, “Mechanisms of Electrohydrodynamic (EHD) Flow and Heat Transfer in Horizontal Convective Boiling Channels,” Ph.D. thesis, McMaster University, Hamilton, Ont., Canada.
- [2] Cotton, J. S., Chang, J. S., and Shoukri, M., 2001, “Numerical Simulation of Electric Field Distributions in Electrohydrodynamic Two-Phase Flow Regimes,” *IEEE/DEIS Transactions on Dielectric and Electrical Insulation*, submitted for review.
- [3] Cotton, J. S., Chang, J. S., and Shoukri, M., 2001, “Mechanisms of AC Electrohydrodynamic Flow and Convective Boiling Heat Transfer in Horizontal Annular Channels,” *ASME J. of Heat Transfer*, to be submitted.
- [4] Cotton, J. S., Shoukri, M. M., Chang, J. S., and Smith-Pollard, T., 2000, “Electrohydrodynamic (EHD) Flow and Convective Boiling Augmentation in Single-Component Horizontal Annular Channels,” *Proceedings of the ASME Heat Transfer Division, Heat Transfer Enhancement of Multi-Phase Flow*, HTD-366, pp. 177–184.

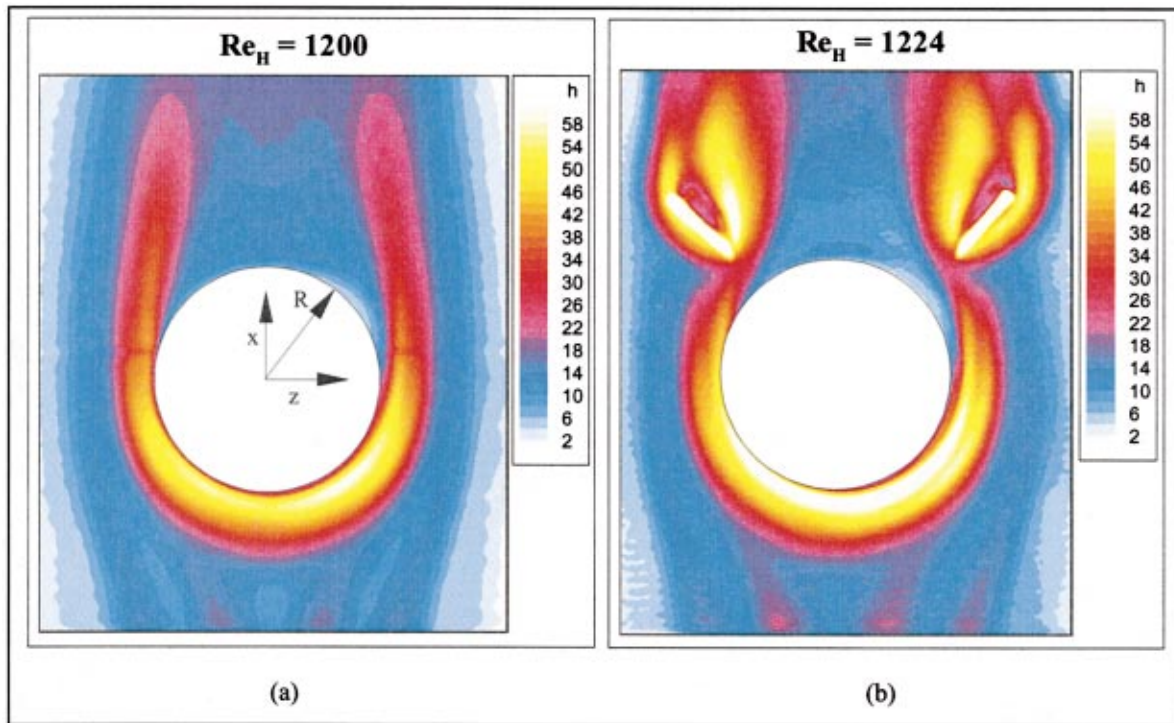


Fig. 1 Direct comparison of local fin-surface heat transfer distributions for flow around circular cylinder without (a) and with (b) vortex-generating winglets at $Re_H \sim 1200$

LOCAL FIN-SURFACE HEAT TRANSFER FOR FLOW AROUND A CIRCULAR CYLINDER WITH AND WITHOUT VORTEX-GENERATING WINGLETS

J. E. O'Brien and Manohar S. Sohal

Idaho National Engineering and Environmental Laboratory (INEEL), Idaho Falls, ID 83415

A direct comparison of local fin-surface heat transfer coefficients for flow around a circular tube without (a) and with (b) winglets at $Re_H \sim 1200$ is presented in Fig. 1. The comparison reveals that, for this winglet location, the horseshoe vortex produced by the interaction of the flow with the circular cylinder is disrupted by the winglets. There is a reduction in the width of the low-heat-transfer wake region, but heat transfer coefficients directly downstream of the cylinder are actually slightly reduced for the winglet case compared to the no-winglet case. Stagnation-region heat transfer coefficients are slightly higher for the winglet case compared to the no-winglet case. The experiments were performed in a narrow rectangular duct designed to simulate a single passage of a fin-tube heat exchanger. A transient heat transfer measurement technique was employed for obtaining detailed local heat transfer measurements on the model fin surface. Using this technique, the room-temperature fin/tube model is suddenly exposed to a uniformly heated airflow, initiating a heat conduction

transient in a lexan substrate. The transient localized heating is quantitatively recorded using an imaging infrared camera. Values of local heat transfer coefficient are then determined from a one-dimensional inverse heat conduction analysis. The winglets had a 1:2 height/length aspect ratio and were oriented at a 45 degree angle to the flow. The height of the winglets was 90 percent of the channel height. The quantitative thermal visualization images are obtained using a precision imaging infrared camera (FLIR PRISM DS). The camera detector has a 12-bit digital dynamic range and a minimum discernible temperature difference (MDT) of 0.1°C at 30°C . It is equipped with a 25-mm standard lens, which provides a $17\text{ deg} \times 13\text{ deg}$ field of view. Infra-red thermography has several advantages over thermochromic liquid crystals for surface temperature mapping, including wide available temperature range, high spatial resolution, excellent thermal resolution, and full-field direct digital data acquisition and processing.

Thermal Resistance Models for Non-Circular Moving Heat Sources on a Half Space

Y. S. Muzychka

Assistant Professor
Faculty of Engineering and Applied Science,
Memorial University of Newfoundland,
St. John's, NF, Canada, A1B 3X5
e-mail: yuri@engr.mun.ca

M. M. Yovanovich

Distinguished Professor Emeritus
Fellow ASME
Department of Mechanical Engineering
University of Waterloo
Waterloo, ON, Canada, N2L 3G1
e-mail: mmyov@mhtl.uwaterloo.ca

Solutions to stationary and moving heat sources on a half space are reviewed for rectangular and elliptic contacts. The effects of shape, heat flux distribution, and orientation with respect to the direction of motion are examined. The dimensionless thermal resistance is shown to be a weak function of heat source shape if the square root of contact area is used as a characteristic length scale. Simple expressions are developed for calculating total thermal resistances of non-circular moving heat sources by combining asymptotic solutions for large and small values of the Peclet number. Both uniform and parabolic heat flux distributions are examined. A model is developed for predicting average or maximum flash temperatures of real sliding contacts. Comparisons of the proposed model are made with numerical solutions for two cases involving non-circular contacts. [DOI: 10.1115/1.1370516]

Keywords: Conduction, Contact Resistance, Heat Transfer, Modeling, Tribology

Introduction

The analysis of heat transfer from sliding and rolling contacts is important in many tribological applications such as ball bearing and gear design. In these applications heavily loaded contacts are typical and knowledge of the contact temperatures which result from frictional heat generation is required for minimizing thermal related problems such as scoring, lubricant breakdown, and adhesive wear due to flash welding.

A review of typical tribology books such as the texts by Halling [1] and Williams [2], and Handbook sections by Winer and Cheng [3] and Cowan and Winer [4] shows that the analysis of heat transfer from sliding or rolling contacts has not been extensively modelled. These reviews generally present equations and results for only one configuration, the circular contact. Although this contact geometry arises quite frequently in tribology applications, others such as the elliptic contact are also quite common in ball bearing and gear applications where non-conforming contacts prevail [5–7].

The analysis for moving heat sources which is presented in a number of tribology references [1–4], is based upon the assumption that one of the contacts can be modelled as a stationary heat source and the other as a fast moving heat source. In many problems the assumption of a fast moving heat source may not be valid and the analysis will incorrectly predict the average or maximum contact temperature. With this in mind, Tian and Kennedy [8] developed accurate correlations for the circular and square heat source which predict the temperature for any speed. These correlations were then used to formulate models for predicting flash temperatures in sliding asperities.

In a recent paper [9], a hybrid computational method for non-circular heat sources was developed. For this method, a numerical approach based upon the superposition of point heat sources was employed for the stationary portion and a transient finite element method was employed for the moving portion. This new approach was then used to predict temperatures in a steel/bronze sliding contact problem, with sliding motion normal and parallel to the grinding direction. The primary motivation for the work of Neder

et al. [9] was that the conventional approach adopted in most tribology references was not applicable to non-circular heat sources.

The present work discusses various aspects of heat transfer in tribological applications involving stationary and sliding contacts. In all cases heat is either supplied to the contact or is generated through contact friction. This paper has four objectives. These are (i) provide a comprehensive review of the literature related to stationary and moving heat sources on half space, (ii) examine the effect that heat source shape and heat flux distribution have on the thermal resistance, (iii) develop a model which is applicable to a heat source of arbitrary shape and flux distribution, and (iv) use the proposed model to predict the flash temperature in a non-circular contact for real surfaces. In addressing these issues, a number of gaps in the literature have been filled. In addition, a clear and consistent approach to modeling arbitrary contacts has been developed. Presently, the field of tribology has only adopted a simplified approach in the prediction of contact temperatures due to sliding. The present approach does not allow for the effect of shape, aspect ratio, and flux distribution to be modelled easily. This was the primary motivation of the development of a hybrid numerical scheme by Neder et al. [9]. The expressions and method developed in the present work have been validated against a small set of numerical data for real and ideal contacts. The results of Neder et al. [9] are readily computed using the present approach with significantly less effort.

Governing Equations

A review of the literature [3,4,8,10–15], reveals that extensive analysis of the problem has been undertaken for various contact spot shapes and thermal boundary conditions for both stationary and moving heat sources.

The governing equation for a moving heat source may be obtained from the transient heat conduction equation with a transformation of variables [13]. The resulting equation for steady state conditions, is

$$\frac{\partial^2 T}{\partial x^2} + \frac{\partial^2 T}{\partial y^2} + \frac{\partial^2 T}{\partial z^2} = \frac{V}{\alpha} \frac{\partial T}{\partial x}, \quad (1)$$

where the coordinate system is fixed to the heat source and the half space moves beneath it with velocity V , see Figs. 1 and 2.

Contributed by the Heat Transfer Division for publication in the JOURNAL OF HEAT TRANSFER. Manuscript received by the Heat Transfer Division April 24, 2000; revision received January 8, 2001. Associate Editor: A. Bejan.

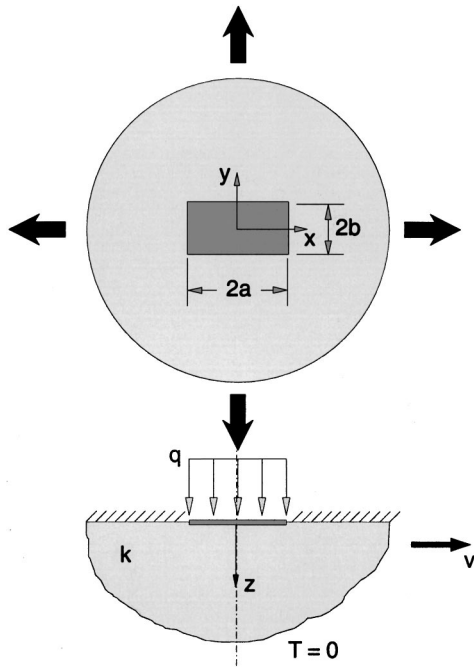


Fig. 1 Rectangular heat source

The thermal boundary conditions are constant or zero temperature in regions remote from the source, i.e., $r = \sqrt{x^2 + y^2 + z^2} \rightarrow \infty$, $T \rightarrow T_b$, or $T(x \rightarrow \pm \infty, y \rightarrow \pm \infty, z \rightarrow \infty) = T_b = 0$ and prescribed heat flux q over the source area $\partial T / \partial z|_{z=0} = -q(x, y) / k$ while the region outside of the source area is assumed to be adiabatic $\partial T / \partial z|_{z=0} = 0$.

Solution to Eq. (1) is usually obtained by superposition of the point heat source [11]

$$T - T_b = \left(\frac{Q}{2\pi kr} \right) e^{-V/2\alpha(r-x)} \quad (2)$$

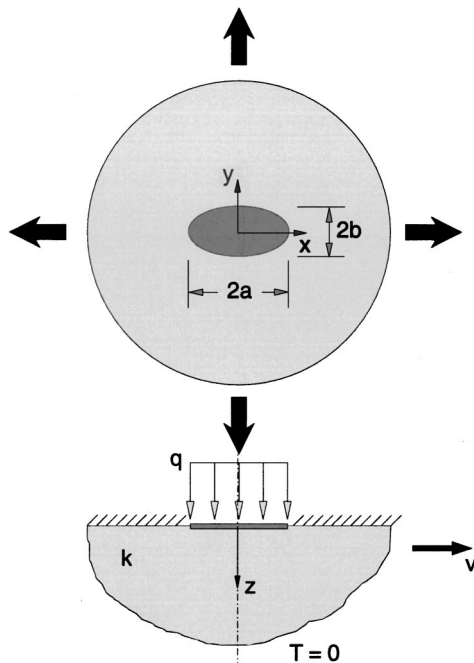


Fig. 2 Elliptic heat source

over the region of contact, where $r = \sqrt{x^2 + y^2 + z^2}$. Solution of the moving heat source by means of Eq. (2) is rather involved, requiring numerical integration. Solutions for the square and circular contact are tabulated in Tian and Kennedy [8]. A simpler approach based upon the combination of asymptotic solutions is presented in a later section for the arbitrarily shaped heat source.

Asymptotic Solutions

Stationary Heat Sources. If the velocity of the heat source is small ($V/\alpha \rightarrow 0$), the governing equation reduces to Laplace's equation

$$\frac{\partial^2 T}{\partial x^2} + \frac{\partial^2 T}{\partial y^2} + \frac{\partial^2 T}{\partial z^2} = 0 \quad (3)$$

with the same boundary conditions prescribed earlier.

Many solutions for stationary heat source problems have been obtained by superposition of the point heat source [11] on a half space

$$T - T_b = \frac{Q}{2\pi kr}, \quad (4)$$

where $r = \sqrt{x^2 + y^2 + z^2}$. Solutions for various heat flux distributions and source shapes have been found [14–16]. Of particular interest are the solutions for the rectangular and elliptical heat sources which contain the limiting cases for the square and circular contacts.

Moving Heat Sources. If the velocity of the heat source is large ($V/\alpha \rightarrow \infty$), Eq. (1) simplifies to give

$$\frac{\partial^2 T}{\partial z^2} = \frac{V}{\alpha} \frac{\partial T}{\partial x}. \quad (5)$$

Equation (5) is essentially the one dimensional diffusion equation for a half-space with $t = x/V$. This equation assumes that heat conduction into the half space is one-dimensional and the solution may be approximated by the equation for heat flow at the surface of a half space with flux specified boundary conditions [11,12]

$$T - T_b = \frac{2q}{k\sqrt{\pi}} \sqrt{\alpha t}, \quad (6)$$

where t must be replaced by the effective traverse time $t = 2x'/V$, and x' is the distance from an arbitrary point within the source to the leading edge of the source.

This approach was applied by Jaeger [12] for the strip and square heat sources, by Archard [17] for the circular source for the uniform heat flux distribution, and by Francis [18] for the circular heat source having a parabolic heat flux distribution. Later, it will be applied to obtain a solution for an elliptical heat source and comparisons will be made with the solution of Jaeger [12] for a rectangular source.

No solution was found for the equivalent isothermal moving heat source for a circular contact. A solution for this boundary condition may be obtained by extending the work of Francis [18] or Tian and Kennedy [8] for the parabolic heat flux distribution. The solution for a moving elliptic heat source with uniform and parabolic heat flux distribution will be obtained in a later section.

The analysis based on Eq. (6) is only valid for large values of the dimensionless group $Pe = Va/\alpha$, or Peclet number. This group may be interpreted as a measure of the relative thermal penetration depth, δ/a , of heat into the half space. Beginning with the definition, $\delta = \sqrt{\pi\alpha t}$, which is the thermal penetration depth for heat flow into a half space, the relative penetration depth for a circular contact is

$$\frac{\delta}{a} \sim \frac{\sqrt{\pi\alpha t}}{a}. \quad (7)$$

If the traverse time for a moving circular heat source is taken to be $t = 2a/V$, then Eq. (7) may be written as

$$\frac{\delta}{a} \sim \sqrt{\frac{2\pi\alpha}{Va}} \sim \frac{\sqrt{2\pi}}{\sqrt{Pe}} \quad (8)$$

Thus if $Pe \rightarrow \infty$, the penetration δ is small, and may be taken to be one-dimensional since the spreading of heat into the half-space is negligible. On the other hand, if $Pe \rightarrow 0$, the spreading of heat into the substrate will be significant. A solution for all values of Peclet number can only be obtained numerically.

Review and Solution of Stationary and Moving Heat Sources

A discussion of a number of important solutions for sliding heat sources is now presented. In many cases, gaps existed in the literature, and the present authors have developed new solutions for a number of problems. These are discussed throughout the sections that follow.

Stationary Heat Sources ($Pe \rightarrow 0$). Extensive analysis of heat conduction from isolated heat sources on a half space has been performed by a number of researchers [11,14–16,19]. The simplest contact geometry is the circular contact. The analysis has been performed for three heat flux distributions: the uniform heat flux, parabolic heat flux, and the inverse parabolic heat flux. The inverse parabolic heat flux represents a uniform temperature distribution over the contact area. The solutions for the dimensionless thermal resistance for these three cases are summarized in Table 1.

The thermal resistance may be defined with respect to the average surface temperature such that

$$\bar{R} = \frac{\bar{T}_c - T_b}{Q} \quad (9)$$

or with respect to the maximum surface temperature such that

$$\hat{R} = \frac{\hat{T}_c - T_b}{Q} \quad (10)$$

A dimensionless thermal resistance may be defined as

$$R^* = Rk\mathcal{L} \quad (11)$$

where \mathcal{L} is an appropriate characteristic length related to the heat source area [5,6,14–16]. This thermal resistance is a spreading resistance due to the transfer of heat through a finite discrete point of contact. Spreading resistance concepts appear in any analysis of stationary or sliding contact problems in heat transfer and tribology, and form the basis for the field of thermal contact conductance.

In most tribological applications involving frictional heat generation, the average heat flux $\bar{q} = Q/A$ is known. What may not be known precisely, is the distribution of heat flux $q(x,y)$ over the contact. If the contact is Hertzian, the distribution of frictional

Table 1 Effect of boundary conditions on stationary circular heat source [15]

Case	Flux Distribution	$\bar{R}ka$	$\hat{R}ka$
A - Isothermal	$\frac{1}{2}\bar{q} \frac{1}{\sqrt{1-(r/a)^2}}$	$\frac{1}{4} = 0.250$	$\frac{1}{4} = 0.250$
B - Isoflux	\bar{q}	$\frac{8}{3\pi^2} \approx 0.270$	$\frac{1}{\pi} \approx 0.318$
C - Parabolic Flux	$\frac{3}{2}\bar{q} \sqrt{1-(r/a)^2}$	$\frac{9}{32} \approx 0.281$	$\frac{3}{8} \approx 0.375$

Table 2 Effect of shape on isoflux stationary heat sources [11]

R^*	Circular	Square
$\bar{R}ka$	0.270	0.237
$\hat{R}ka$	0.318	0.282

heat generation may be represented by Case C in Table 1 [15]. In most analyses the assumption of a uniform heat flux distribution is often made. The effect of heat flux distribution on the thermal resistance based upon the average contact temperature is small. The variation from the uniform flux distribution is -7.4 percent for the isothermal heat source and $+4.1$ percent for the parabolic heat source. Thus the uniform heat flux distribution may be taken as representative of the mean value if the exact flux distribution is not known. If the resistance is based upon the maximum source temperature, the variation from the uniform flux distribution is -21.4 percent for the isothermal heat source and $+17.9$ percent for the parabolic heat source. In both cases the maximum and minimum values for the average or maximum source temperature are bounded by the solutions for Case A and Case C.

Table 2 presents a comparison of the dimensionless thermal resistance for a circular and square heat source with uniformly distributed heat flux [11]. In both cases, the dimensionless thermal resistance is greater for the circular heat source than for the square source. The relative differences are 12.2 percent for the resistance based upon the average source temperature and 11.3 percent for the resistance based upon the maximum source temperature. Later, it will be shown that if $\mathcal{L} = \sqrt{A}$, the effects of source shape and aspect ratio are minimized. This will eventually lead to a simplified model for an arbitrarily shaped moving heat source.

If the shape of the heat source shown in Figs. 1 and 2 is allowed to vary with aspect ratio $\epsilon = b/a$, then the solutions are somewhat more complex than those given in Table 2. The solution for the dimensionless thermal resistance of a stationary rectangular uniform heat source [11] is

$$\bar{R}ka = \frac{1}{2\pi} \left\{ \frac{\sinh^{-1}(\epsilon)}{\epsilon} + \sinh^{-1}(1/\epsilon) + \frac{1}{3} \left[\frac{1}{\epsilon^2 + \epsilon} - \frac{(1 + \epsilon^2)^{3/2}}{\epsilon^2} \right] \right\} \quad (12)$$

for the average contact temperature, and

$$\hat{R}ka = \frac{1}{2\pi} \left\{ \frac{\sinh^{-1}(\epsilon)}{\epsilon} + \sinh^{-1}(1/\epsilon) \right\} \quad (13)$$

for the maximum contact temperature.

The solution for the elliptic heat source was obtained by Yovanovich [5,14–16] and is given by

$$\hat{R}ka = \frac{1}{2\pi} \mathbf{K}(\epsilon') \quad (14)$$

for the isothermal contact, and

$$\bar{R}ka = \frac{16}{3\pi^3} \mathbf{K}(\epsilon') \quad (15)$$

and

$$\hat{R}ka = \frac{2}{\pi^2} \mathbf{K}(\epsilon') \quad (16)$$

for the isoflux contact, where $\epsilon' = \sqrt{1 - \epsilon^2}$, and $\mathbf{K}(\epsilon')$ is the complete elliptic integral of the first kind of complementary modulus ϵ' . Equations (15) and (16) were obtained by comparing the limiting case of the circular contact from Table 1 with the result for the isothermal contact. Equations (15) and (16) accurately predict the numerical results presented in [16] for the elliptic contact which were obtained using the method of superposition of point heat sources. No solution was available for the parabolic flux distribution. A solution for this configuration is easily obtained by analogy with the elastic contact problem [20], or by comparison with the solutions presented above. The effect of aspect ratio on a stationary elliptic heat source is

$$f(\epsilon) = \frac{2}{\pi} \mathbf{K}(\epsilon') \quad (17)$$

Thus the solution for the parabolic heat flux distribution is the function $f(\epsilon)$ multiplied by the values for the resistance for Case C in Table 1:

$$\bar{R}ka = \frac{9}{16\pi} \mathbf{K}(\epsilon') \quad (18)$$

and

$$\hat{R}ka = \frac{3}{4\pi} \mathbf{K}(\epsilon'). \quad (19)$$

Equation (19) may also be derived from the analogous elastic contact problem discussed in [20], for the Hertzian pressure distribution.

Moving Heat Sources ($Pe \rightarrow \infty$). Solutions for moving heat sources have been obtained for a number of configurations and boundary conditions. All of the moving source solutions are written in terms of the Peclet number. The Peclet number is defined as

$$Pe = \frac{V\mathcal{L}}{\alpha}, \quad (20)$$

where \mathcal{L} is a characteristic length scale representative of the contact geometry. If the contact geometry is circular or square then $\mathcal{L} = a$, the radius of the contact or the half side length of the square. Later, it will be shown that if $\mathcal{L} = \sqrt{A}$, the area of the heat source, the effect of shape and aspect ratio on the dimensionless resistance is small.

The effect of heat flux distribution (uniform or parabolic) on the thermal resistance for a moving circular heat source is given in Table 3. The solution for the uniform heat flux distribution was obtained by Archard [17] and the solution for the parabolic heat flux distribution was obtained by Francis [18]. These solutions are only valid for large values of the Peclet number. The effect of flux distribution on the thermal resistance based upon the average contact temperature is small. The relative difference being only 1.6 percent. The relative difference increases to 15.9 percent for the thermal resistance based upon the maximum source temperature.

Table 3 Effect of boundary condition on a moving circular heat source [17,18]

R^*	Uniform Flux	Parabolic Flux
$\bar{R}ka$	$\frac{0.318}{\sqrt{Pe}}$	$\frac{0.323}{\sqrt{Pe}}$
$\hat{R}ka$	$\frac{0.508}{\sqrt{Pe}}$	$\frac{0.589}{\sqrt{Pe}}$

Table 4 Effect of shape on isoflux moving heat sources [12,17]

R^*	Circular	Square
$\bar{R}ka$	$\frac{0.318}{\sqrt{Pe}}$	$\frac{0.266}{\sqrt{Pe}}$
$\hat{R}ka$	$\frac{0.508}{\sqrt{Pe}}$	$\frac{0.399}{\sqrt{Pe}}$

Finally, Table 4 presents a comparison of the asymptotic solutions for the fast moving heat source for the circular and square heat sources. The results are 16.4 percent and 21.5 percent higher for the circular heat source for the thermal resistance based upon the average and maximum source temperatures, respectively.

If the contact is rectangular the thermal resistance will vary with aspect ratio $\epsilon = b/a$, where $0 < \epsilon < \infty$. The solution obtained by Jaeger [12] for the strip source is applicable to a rectangular heat source since the solution assumes one dimensional heat flow into the half space, i.e., the penetration depth is small compared with the characteristic dimension of the contact zone. The solution for the finite rectangular source [12] is

$$\bar{R}ka = \frac{\sqrt{2}}{3\sqrt{\pi}} \left(\frac{a}{b}\right) \frac{1}{\sqrt{Pe}} \quad (21)$$

for the average contact temperature, and

$$\hat{R}ka = \frac{\sqrt{2}}{2\sqrt{\pi}} \left(\frac{a}{b}\right) \frac{1}{\sqrt{Pe}} \quad (22)$$

for the maximum contact temperature, where $Pe = Va/\alpha$, is based upon the half width of the rectangle in the direction of motion, see Fig. 1.

No solution was found for the fast moving elliptical contact. In order to obtain a solution for the elliptical contact, the approach developed by Jaeger [12] for the square source and by Archard [17] for the circular contact was applied. In this case the effective contact time is

$$t = \frac{2x'}{V} = \frac{2\sqrt{a^2\left(1 - \frac{y^2}{b^2}\right)}}{V}. \quad (23)$$

Applying the approach of Jaeger [12] and Archard [17] gives

$$\bar{R}ka = \frac{1}{\pi} \left(\frac{a}{b}\right) \frac{1}{\sqrt{Pe}} \quad (24)$$

for the dimensionless thermal resistance based upon the average contact temperature, and

$$\hat{R}ka = \frac{2\sqrt{2}}{\pi^{3/2}} \left(\frac{a}{b}\right) \frac{1}{\sqrt{Pe}} \quad (25)$$

for the dimensionless thermal resistance based upon the maximum contact temperature. In both cases, $Pe = Va/\alpha$ is based upon the half width of the heat source in the direction of motion, see Fig. 2.

Comparison of Eqs. (21) and (22) and Eqs. (24) and (25) with the solutions for the square and circular heat source provided in Table 4, shows that the solutions are identical except for the term (a/b) . This factor accounts for the effect of heat source aspect ratio with respect to the direction of motion. These results may be applied to infer the following solutions for a fast moving elliptic heat source with parabolic heat flux distribution:

$$\bar{R}ka = 0.323 \left(\frac{a}{b}\right) \frac{1}{\sqrt{Pe}} \quad (26)$$

and

$$\hat{R}ka = 0.589 \left(\frac{a}{b}\right) \frac{1}{\sqrt{Pe}}. \quad (27)$$

In the next section, the results will be applied to develop new models applicable to a real contact of non-circular shape.

Analysis of Real Contacts

In this section, application of the theory of moving heat sources to real contacts is discussed. A simple approach to modelling the effects of shape, aspect ratio, orientation, and heat flux distribution is presented. It will be assumed that the shape of a real contact is elliptic, and that classic Hertzian analysis for elastic contact of non-conforming surfaces may be used to predict the contact zone dimensions [21].

Effect of Contact Shape. Hertzian theory may be used to predict the contact size for elastic contact. However, this assumes the shape of the contact is elliptic. Depending on the surface topography, this assumption may not be valid. Thus, it is desirable to examine the effect that shape and aspect ratio have on the overall resistance of moving heat sources.

Yovanovich et al. [16] examined the effect of the shape and aspect ratio of an isolated stationary contact having a uniform flux distribution. The geometry examined by Yovanovich et al. [16] was the hyperellipse, defined as

$$\left(\frac{x}{a}\right)^\gamma + \left(\frac{y}{b}\right)^\gamma = 1, \quad (28)$$

where a and b are the semi-major and semi-minor axis lengths, respectively. The parameter γ determines the shape of the contact. The values of the parameter γ which were examined by Yovanovich et al. [16] were $\gamma = 1/2$, $\gamma = 1$, and $\gamma = 2$. If $\gamma \rightarrow \infty$ the hyperellipse becomes a rectangular contact. Yovanovich et al. [16] showed that if the thermal resistance is non-dimensionalized using the square root of the contact area, the solutions are weak functions of shape and aspect ratio.

Table 5 presents the dimensionless resistance based upon the average and centroidal values of temperature for different values of the parameter γ , Yovanovich et al. [16]. It is clearly seen that the dimensionless resistance varies very little with aspect ratio $\epsilon = b/a$ and shape parameter γ . The solutions for the isoflux stationary elliptic heat source become

$$\bar{R}_s k \sqrt{A} = \frac{16}{3\pi^3} \sqrt{\pi \epsilon_s} \mathbf{K}(\epsilon'_s) \quad (29)$$

for the average contact temperature, and

$$\hat{R}_s k \sqrt{A} = \frac{2}{\pi^2} \sqrt{\pi \epsilon_s} \mathbf{K}(\epsilon'_s) \quad (30)$$

for the maximum contact temperature. If the flux distribution is parabolic, then the solutions presented earlier become

$$\bar{R}_s k \sqrt{A} = \frac{9}{16\pi} \sqrt{\pi \epsilon_s} \mathbf{K}(\epsilon'_s) \quad (31)$$

and

$$\hat{R}_s k \sqrt{A} = \frac{3}{4\pi} \sqrt{\pi \epsilon_s} \mathbf{K}(\epsilon'_s). \quad (32)$$

If the heat source is rectangular, then the dimensionless thermal resistance, Eqs. (12, 13) become

Table 5 Dimensionless resistance for stationary isoflux hyperelliptic contacts [16]

ϵ	$\gamma = 1/2$		$\gamma = 1$	
	$\bar{R}k\sqrt{A}$	$\hat{R}k\sqrt{A}$	$\bar{R}k\sqrt{A}$	$\hat{R}k\sqrt{A}$
1.0	0.4440	0.5468	0.4728	0.5611
0.8	0.4428	0.5458	0.4713	0.5597
0.6	0.4376	0.5420	0.4651	0.5540
0.4	0.4237	0.5310	0.4487	0.5385
0.2	0.3860	0.5005	0.4052	0.4957

ϵ	$\gamma = 2$		$\gamma = \infty$	
	$\bar{R}k\sqrt{A}$	$\hat{R}k\sqrt{A}$	$\bar{R}k\sqrt{A}$	$\hat{R}k\sqrt{A}$
1.0	0.4787	0.5642	0.4732	0.5611
0.8	0.4772	0.5624	0.4718	0.5590
0.6	0.4711	0.5551	0.4658	0.5503
0.4	0.4548	0.5360	0.4502	0.5279
0.2	0.4112	0.4845	0.4082	0.4706

$$\bar{R}_s k \sqrt{A} = \frac{\sqrt{\epsilon_s}}{\pi} \left\{ \frac{\sinh^{-1}(\epsilon_s)}{\epsilon_s} + \sinh^{-1}(1/\epsilon_s) + \frac{1}{3} \left[\frac{1}{\epsilon_s^2} + \epsilon_s - \frac{(1 + \epsilon_s^2)^{3/2}}{\epsilon_s^2} \right] \right\} \quad (33)$$

for the average contact temperature, and

$$\hat{R}_s k \sqrt{A} = \frac{\sqrt{\epsilon_s}}{\pi} \left\{ \frac{\sinh^{-1}(\epsilon_s)}{\epsilon_s} + \sinh^{-1}(1/\epsilon_s) \right\} \quad (34)$$

for the maximum contact temperature. Since the effect of aspect ratio is small, average values of the dimensionless resistance given in Table 5 may be used to approximate the resistance for a heat source with variable aspect ratio.

In the case of the moving heat source the Peclet number should also be based upon the square root of the contact area, i.e., $\mathcal{L} = \sqrt{A}$ in Eq. (20). Table 6 summarizes the results for the rectangular and elliptic heat sources for different heat flux distributions, when the resistance is non-dimensionalized using the square root

Table 6 Dimensionless resistance of moving heat sources on a half-space

Shape (Boundary condition)	$\bar{R}k\sqrt{A}$	$\hat{R}k\sqrt{A}$
Rectangular (Isoflux)	$\frac{0.752}{\sqrt{Pe^* \sqrt{A}}}$	$\frac{1.130}{\sqrt{Pe^* \sqrt{A}}}$
Elliptic (Isoflux)	$\frac{0.750}{\sqrt{Pe^* \sqrt{A}}}$	$\frac{1.200}{\sqrt{Pe^* \sqrt{A}}}$
Elliptic (Parabolic Flux)	$\frac{0.762}{\sqrt{Pe^* \sqrt{A}}}$	$\frac{1.390}{\sqrt{Pe^* \sqrt{A}}}$

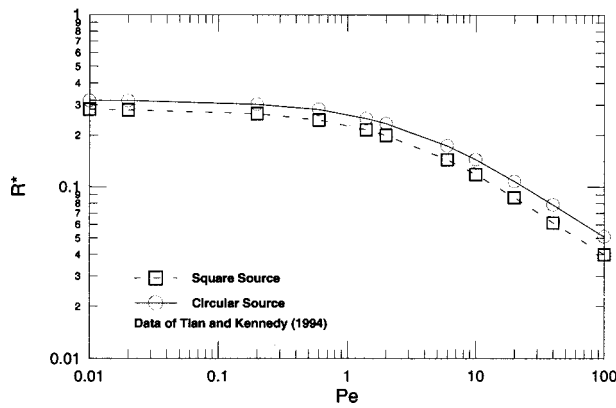


Fig. 3 \hat{R}_a^* versus Pe_a for a circular and square moving heat source

of the contact area. Comparisons of the dimensionless resistance \hat{R}^* are provided in Figs. 3 and 4 using the data for the exact analytical solutions of a isoflux heat sources from Tian and Kennedy [8]. Figure 3 shows a comparison of the results for a circular and square heat source when the characteristic length is $\mathcal{L}=a$. In Figure 4, the results for each geometry have virtually collapsed onto one another when $\mathcal{L}=\sqrt{A}$. Thus the effect of the shape of the heat source is not a significant factor, when the results are appropriately non-dimensionalized.

If the heat source is rectangular or elliptical the Peclet number must be replaced with a modified Peclet number Pe^* defined as

$$Pe_{\sqrt{A}}^* = (\epsilon_m)^{1/2} Pe_{\sqrt{A}} \quad (35)$$

The aspect ratio $\epsilon_m = b/a$ now accounts for the effect of the shape and orientation of the heat source. Since a rectangular or elliptic heat source may be oriented in the direction of motion parallel to the short or long axis of the heat source, the resistance must change based on orientation. Given the same source area and velocity, the Peclet number remains unchanged, but the resistance will decrease if the direction of motion is parallel to the short axis of the heat source. Thus, for a moving heat source, $0 < \epsilon_m < \infty$. This is quite important for the moving heat source since the resistance will increase with decreasing ϵ_m , i.e., $a > b$, and decrease with increasing ϵ_m , i.e., $b > a$. If the heat source is stationary, the orientation of the contact is not important and $0 < \epsilon_s < 1$.

Models for $0 < Pe < \infty$. In the previous sections the thermal resistances of isolated stationary and fast moving contacts were presented. These solutions represent asymptotic solutions for large

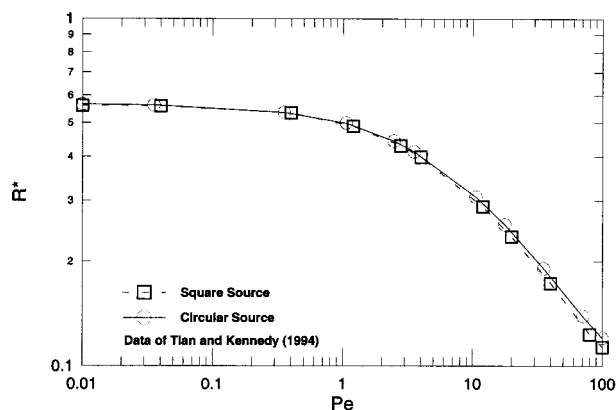


Fig. 4 $\hat{R}_{\sqrt{A}}^*$ versus $Pe_{\sqrt{A}}$ for a circular and square moving heat source

and small values of the Peclet number. If the contact is moving at moderate speeds $0.1 < Pe < 10$, a composite solution is required. Tian and Kennedy [8] combined the asymptotic results for the circular heat source using an equation which is a special case of the more general form

$$\frac{1}{R_t^n} = \frac{1}{R_s^n} + \frac{1}{R_m^n} \quad (36)$$

Equation (36) is one form of the asymptotic correlation method proposed by Churchill and Usagi [22]. This method allows the combination of asymptotic solutions, to generate a model which is valid for all values of the dependent parameter.

A single value of $n=2$ was found to give excellent agreement between the approximate model and numerical results of Tian and Kennedy [8] over the entire range of Peclet numbers for the circular heat source having a uniform or parabolic heat flux distribution and a square heat source having a uniform heat flux distribution. Thus, the parameter n does not appear to depend upon the shape of the source or the flux distribution. The models developed by Tian and Kennedy [8] are specifically for the circular heat source for uniform and parabolic flux distributions. They are not applicable to elongated contacts such as elliptic or rectangular contacts. In addition, Tian and Kennedy [8] presented their correlations in terms of contact temperatures; rather than thermal resistance. The use of thermal resistance facilitates the calculation of the partition of heat into the contacting bodies.

A general model for a moving heat source will now be obtained by combining the dimensionless resistances for a stationary and fast moving heat sources in the form of Eq. (36). As noted earlier, the definition of aspect ratio is different for the moving and stationary heat sources. The aspect ratio of the stationary heat source is now denoted by $\epsilon_s = b/a$ such that $0 < \epsilon_s < 1$, and the aspect ratio of the moving heat source is now denoted by ϵ_m such that $0 < \epsilon_m < \infty$. Also, since the effect of shape has been shown to be negligible, only the solution for the elliptic heat source will be considered in the model development.

Combining the stationary and moving heat source solutions for both the average and maximum contact surface temperatures gives

$$\bar{R}_t k \sqrt{A} = \frac{0.750}{\sqrt{(\epsilon_m)^{1/2} Pe_{\sqrt{A}} + 6.05 / (\epsilon_s \mathbf{K}^2(\epsilon_s'))}} \quad (37)$$

and

$$\hat{R}_t k \sqrt{A} = \frac{1.200}{\sqrt{(\epsilon_m)^{1/2} Pe_{\sqrt{A}} + 11.16 / (\epsilon_s \mathbf{K}^2(\epsilon_s'))}} \quad (38)$$

for the uniform flux distribution, and

$$\bar{R}_t k \sqrt{A} = \frac{0.762}{\sqrt{(\epsilon_m)^{1/2} Pe_{\sqrt{A}} + 5.77 / (\epsilon_s \mathbf{K}^2(\epsilon_s'))}} \quad (39)$$

and

$$\hat{R}_t k \sqrt{A} = \frac{1.390}{\sqrt{(\epsilon_m)^{1/2} Pe_{\sqrt{A}} + 10.79 / (\epsilon_s \mathbf{K}^2(\epsilon_s'))}} \quad (40)$$

for the parabolic flux distribution. These expressions can now be applied to arbitrarily shaped heat sources for all values of the Peclet number.

Bounds on Thermal Resistance. The expressions developed previously for the elliptic heat source assume that it is oriented with one of the axes parallel to the direction of motion, see Fig. 2. Equations (37–40) are not valid for a heat source oriented at an angle to the direction of motion. The solution for this case requires integration over the surfaces of the oblique orientation. However, Eqs. (37–40) may be used to bound the values by considering the results for the two extreme cases of ϵ_m . The limiting

cases may then be averaged in a number of ways. It is proposed that the bounding values be weighted using following expression

$$R^* = R_x^* \cos^2(\theta) + R_y^* \sin^2(\theta), \quad (41)$$

where R_x^* denotes the dimensionless resistance based upon the aspect ratio in the x -direction, and R_y^* denotes the dimensionless resistance based upon the aspect ratio in the y -direction. This formulation is proposed since it reduces to the limiting cases for $\theta = 0$ deg and $\theta = 90$ deg, and returns the arithmetic average at $\theta = 45$ deg. In the absence of an exact solution, Eq. (41) should provide good results for the average or maximum temperature prediction.

Prediction of Flash Temperatures. The concept of maximum or average flash temperature is discussed in detail in Archard [17], Blok [23], Winer and Cheng [3], and Cowan and Winer [4]. The computation of the flash temperature assumes that one of the contacting surfaces is a stationary heat source and the other a moving heat source. By accounting for the partition of heat into each of the surfaces, an estimate for the average or maximum temperature may be obtained.

In the previous section a general model for an isolated moving source for $0 < Pe < \infty$ was developed. This model may now be used to predict the average or maximum flash temperatures. The analysis begins by defining the total heat flow and the partition of each into the two contacting surfaces. The total heat generated by sliding friction is denoted $Q_g = \mu FV$, where μ is the coefficient of friction, while the heat which flows into the stationary and moving surfaces are denoted Q_s and Q_m , respectively. Through conservation of energy, the total heat flow is then

$$Q_g = Q_s + Q_m, \quad (42)$$

which may be written in terms of the temperature excess and resistance in each surface

$$\mu FV = \frac{(T_s - T_{b,s})}{R_s} + \frac{(T_m - T_{b,m})}{R_m}. \quad (43)$$

Now if perfect thermal contact is assumed at the interface, then $T_s = T_m = T_c$ at all points within the contact, and the expression given above may be solved for T_c

$$T_c = \frac{\mu FV + \frac{T_{b,s}}{R_s} + \frac{T_{b,m}}{R_m}}{\frac{1}{R_s} + \frac{1}{R_m}}. \quad (44)$$

The general expression given above may be applied to any combination of slow, moderate or fast moving sources using the expressions developed earlier. If the bulk temperatures are equal, Eq. (44) may be further simplified. In the case of a typical sliding asperity contact, the system is modelled as a stationary heat source and a moving heat source in parallel. Equation (44) may be written in terms of the dimensionless thermal resistance $R^* = Rk\sqrt{A}$ to give

$$T_c = \frac{\mu FV + \frac{T_{b,s}\sqrt{Ak_s}}{R_s^*} + \frac{T_{b,m}\sqrt{Ak_m}}{R_m^*}}{\frac{\sqrt{Ak_s}}{R_s^*} + \frac{\sqrt{Ak_m}}{R_m^*}}, \quad (45)$$

which may be further simplified to give

$$T_c = \frac{(\mu FVR_s^*R_m^*)/\sqrt{A} + T_{b,s}k_sR_m^* + T_{b,m}k_mR_s^*}{k_sR_m^* + k_mR_s^*}, \quad (46)$$

where the value for R_s^* is taken to be the appropriate value of the stationary dimensionless resistance Eqs. (29–32) and R_m^* is the appropriate expression for the dimensionless resistance of a mov-

Table 7 Comparison of average flash temperature results [12]

V m/s	Pe	Eq. (46)		[12]	
		$\bar{T}_c, ^\circ C$	$\beta = \frac{Q_m}{Q_g}$	$\bar{T}_c, ^\circ C$	$\beta = \frac{Q_m}{Q_g}$
15	16.95	1399.7	0.740	1370	0.74
10	11.30	1057.2	0.705	1040	0.70
7	7.91	816.3	0.675	810	0.67
5	5.65	632.9	0.647	630	0.64
2	2.26	299.5	0.582	300	0.58
1	1.13	161.9	0.548	160	0.54
0.7	0.79	116.5	0.536	115	0.53
0.5	0.57	84.9	0.526	85	0.52
0.2	0.23	35.0	0.517	35	0.51

ing heat source Eqs. (37–40) which were presented in the previous section. Thus, T_c may be computed for either the maximum or average value which occurs within the contact for either the isoflux or parabolic flux distribution. The validity of Eq. (46) may be questioned on the grounds that the temperature distribution of the real contact will be skewed, however, models for the stationary heat source resistance assume a symmetric temperature profile. For a slow moving contact $Pe < 0.1$ the profile is nearly symmetric and the partition of heat into each of the surfaces is equal assuming that each surface has the same thermal properties. For a fast moving heat source $Pe > 10$, the maximum temperature is located at or near the trailing edge. Most of the heat will be conducted into the moving surface since it has a lower thermal resistance. In the transition region $0.1 < Pe < 10$, the effect of temperature distribution shape should be small since the maximum temperature is located between the centroid and the trailing edge. Thus, Eq. (46) may be applied for either the average or maximum contact temperature basis. Also, due to the relatively short contact times and size of asperities, the penetration depth will be small and the assumption of a half-space is then reasonable.

Table 7 presents a comparison of results computed by Jaeger [12] for mild steel $k = 60.3$ W/mK, $\alpha = 17.7 \times 10^{-6}$ m²/s, $F = 400$ g, and $\mu = 0.23$ for a square source with half side length $a = 1 \times 10^{-5}$ m. The maximum difference between the model and the data of Jaeger [12] is 2.1 percent at $V = 15$ m/s. This error is small considering that the values presented by Jaeger [12] were based upon graphical results which are also subject to round off errors.

In the final example, the proposed model is compared with numerical results reported by Neder et al. [9]. The system examined by Neder et al. [9] consisted of a bronze substrate ($\alpha = 13.8 \times 10^{-6}$ m²/s, $k = 50$ W/mK) and a steel slider ($\alpha = 20.0 \times 10^{-6}$ m²/s, $k = 62$ W/mK). The maximum pressure considered was $P = 450$ MPa and the coefficient of friction $\mu = 0.25$. Neder et al. [9] considered sliding in directions perpendicular and parallel to the grinding direction of a real surface. Some difficulty was encountered interpreting the data reported by Neder et al. [9]. The authors reported a range for the equivalent diameter of the largest real contact spot in the direction parallel and perpendicular to the direction of sliding along with the contact width, $2a$, in the sliding direction only. The equivalent diameters which were tabulated by Neder et al. [9] have different values for each direction. It is assumed that if the same surface was considered, the equivalent diameter should be the same in both sliding directions, and that the contact spot aspect ratio may be computed assuming an elliptical contact. The area is given by $A = \pi D_e^2/4 = \pi ab$. Given D_e and $2a$, $2b$ is computed using ($8 \mu\text{m} < D_e < 10 \mu\text{m}$) and ($6 \mu\text{m} < 2a < 8 \mu\text{m}$). These dimensions were examined for both sliding directions and the maximum flash temperatures were computed

Table 8 Comparison of maximum flash temperature results [9]

V m/s	D_e μm	$2a$ μm	$2b$ μm	Eq. (46) $^{\circ}\text{C}$	\hat{T} $^{\circ}\text{C}$
1	8-10	6-8	10.7-12.5	3.83-4.81	4.33
1	8-10	10.7-12.5	6-8	3.87-4.86	5.06
10	8-10	6-8	10.7-12.5	32.01-39.17	35.4
10	8-10	10.7-12.5	6-8	34.57-41.98	40.5

using Eq. (54) along with the expressions for the dimensionless resistance based upon the maximum contact temperature. Results are summarized in Table 8. The predicted temperature range is in excellent agreement with the reported values given by Neder et al. [9]. Neder et al. [9] also reported values of $\hat{T}=32.8^{\circ}\text{C}$ and $\hat{T}=37.5^{\circ}\text{C}$ on two plots for the $V=10\text{ m/s}$ case, in the direction perpendicular and parallel to the grinding direction, respectively. These results are also within the range of temperatures computed using the proposed model.

Summary and Conclusions

A review of the important literature for stationary and moving heat sources was presented. The effects of shape and heat flux distribution for elliptic and rectangular heat sources were examined. It was shown that the dimensionless thermal resistance is a weak function of shape for stationary and moving heat sources when the results are non-dimensionalized using the square root of the heat source area. A simple model for all values of the Peclet number was developed by combining the asymptotic solutions for stationary and moving heat sources. A method was proposed for predicting the thermal resistance of an elliptic heat source oriented at any angle with respect to the direction of motion. These results were then applied to develop a general expression for determining the flash temperature for real surfaces in sliding contact. The proposed model was compared with recent numerical data for real contacts of non-circular shape. Excellent agreement between the model and data was obtained for both elliptic and square contacts.

Acknowledgments

The authors acknowledge the financial support of the Natural Sciences and Engineering Research Council of Canada under operating grant A7455. The first author would also like to thank Dr. J.B. Medley of the Department of Mechanical Engineering, University of Waterloo.

Nomenclature

- a = semi-major axis of ellipse or rectangle, radius of circle, m
- A = area, m^2
- b = semi-minor axis of ellipse or rectangle, m
- $\mathbf{E}(\cdot)$ = complete elliptic integral of the second kind
- F = applied load, N
- k = thermal conductivity, W/mK
- $\mathbf{K}(\cdot)$ = complete elliptic integral of the first kind
- \mathcal{L} = arbitrary length scale, m
- P = pressure, MPa
- $\text{Pe}_{\mathcal{L}}$ = Peclet number, $\equiv V\mathcal{L}/\alpha$
- $\text{Pe}_{\mathcal{L}}^*$ = modified Peclet number, $\equiv \sqrt{\epsilon}\text{Pe}$
- q = heat flux, W/m^2
- \bar{q} = average heat flux, $\equiv Q/A$
- Q = heat flow rate, W
- R = thermal resistance, K/W
- R^* = dimensionless thermal resistance, $\equiv Rk\mathcal{L}$
- t = time, s
- T = temperature, K

- T_b = bulk temperature, K
- T_c = contact temperature, K
- V = velocity, m/s

Greek Symbols

- α = thermal diffusivity, m^2/s
- δ = thermal penetration depth, m
- ϵ = ellipticity or aspect ratio, $\equiv b/a$
- ϵ' = complementary modulus, $\equiv \sqrt{1-\epsilon^2}$
- ϵ_m = aspect ratio, moving source, $0 < b/a < \infty$
- ϵ_s = aspect ratio, stationary source, $0 < b/a < 1$
- ϕ = angle between principal planes of contact, rad
- γ = hyperellipse parameter
- θ = temperature excess, K
- μ = coefficient of friction
- ν = Poisson's ratio
- θ = angle, rad

Superscripts

- $(\bar{\cdot})$ = based on the average temperature
- $(\hat{\cdot})$ = based on maximum temperature

Subscripts

- 1,2 = surface 1, surface 2
- \sqrt{A} = based on $\mathcal{L} = \sqrt{A}$
- b = bulk
- c = contact
- g = generated
- \mathcal{L} = arbitrary length scale \mathcal{L}
- m = moving
- s = stationary
- t = total

References

- [1] Halling, J., 1975, *Principles of Tribology*, MacMillan Education Ltd.
- [2] Williams, J. A., 1994, *Engineering Tribology*, Oxford University Press.
- [3] Winer, W. O., and Cheng, H. S., 1980, "Film Thickness, Contact Stress and Surface Temperatures," in *Wear Control Handbook*, ASME Press, New York, pp. 81-141.
- [4] Cowan, R. S., and Winer, W. O., 1992, "Frictional Heating Calculations," in *ASM Handbook, Volume 18 Friction, Lubrication, and Wear Technology*, ASM International, pp. 39-44.
- [5] Yovanovich, M. M., 1971, "Thermal Constriction Resistance Between Contacting Metallic Paraboloids: Application to Instrument Bearings," *AIAA Progress in Astronautics and Aeronautics: Heat Transfer and Spacecraft Control*, 24, J. W. Lucas, ed., MIT Press, pp. 337-358.
- [6] Yovanovich, M. M., 1978, "Simplified Explicit Elastoconstriction Resistance Expression for Ball/Race Contacts," *AIAA Paper* 78-84.
- [7] Bejan, A., 1989, "Theory of Rolling Contact Heat Transfer," *ASME J. Heat Transfer*, **111**, pp. 257-263.
- [8] Tian, X., and Kennedy, F. E., 1994, "Maximum and Average Flash Temperatures in Sliding Contacts," *ASME J. Tribol.* **116**, pp. 167-174.
- [9] Neder, Z., Varadi, K., Man, L., and Friedrich, K., 1998, "Numerical and Finite Element Contact Temperature Analysis of Steel-Bronze Real Surfaces in Dry Sliding Contact," *ASME/STLE Tribology Conference*, Toronto, Canada.
- [10] Cameron, A., Gordon, A. N., and Symm, G. T., 1968, "Contact Temperatures in Rolling/Sliding Surfaces," *Proc. R. Soc., London, Ser. A* **268**, pp. 45-61.
- [11] Carslaw, H. S., and Jaeger, J. C., 1959, *Conduction of Heat in Solids*, Oxford University Press.
- [12] Jaeger, J. C., 1942, "Moving Sources of Heat and Temperature at Sliding Contacts," *Proceedings of the Royal Society, New South Wales*, **76**, pp. 203-224.
- [13] Rosenthal, D., 1946, "The Theory of Moving Sources of Heat and Its Application to Metal Treatments," *Trans. ASME*, **68**, pp. 849-866.
- [14] Yovanovich, M. M., 1988, "Chapter 8: Theory and Applications of Constriction and Spreading Resistance Concepts for Microelectronic Thermal Management," in *Advances in Cooling Techniques for Computers*, Hemisphere Publishing.
- [15] Yovanovich, M. M., 1998, "Chapter 3: Conduction and Thermal Contact Resistance (Conductance)," in *Handbook of Heat Transfer*, W. M. Rohsenow, J. P. Hartnett, and Y. L. Cho, eds., McGraw-Hill, New York.
- [16] Yovanovich, M. M., Burde, S. S., and Thompson, J. C., 1977, "Thermal Constriction Resistance of Arbitrary Planar Contacts with Constant Heat Flux," *AIAA Progress in Astronautics and Aeronautics: Thermophysics of Spacecraft and Outer Planet Entry Probes*, **56**, A. M. Smith, ed., pp. 127-139.
- [17] Archard, J. F., 1958, "The Temperature of Rubbing Surfaces," *Wear*, **2**, pp. 438-455.

- [18] Francis, H. A., 1970, "Interfacial Temperature Distribution Within a Sliding Hertzian Contact," *ASLE Trans.*, **14**, pp. 41–54.
- [19] Holm, R., 1968, *Electric Contacts*, Springer-Verlag.
- [20] Johnson, K. L., 1985, *Contact Mechanics*, Cambridge University Press.
- [21] Yovanovich, M. M., 1986, "Recent Developments in Thermal Contact, Gap, and Joint Conductance Theories and Experiment," *Heat Transfer 1986, Proceedings of the Eighth International Heat Transfer Conference*, **1**, pp. 35–45.
- [22] Churchill, S. W., and Usgai, R., 1972, "A General Expression for the Correlation of Rates of Transfer and Other Phenomena," *American Institute of Chemical Engineers*, **18**, pp. 1121–1128.
- [23] Blok, H., 1963, "The Flash Temperature Concept," *Wear*, **6**, pp. 483–494.

The Steady Inverse Heat Conduction Problem: A Comparison of Methods With Parameter Selection

Robert Throne

Department of Electrical Engineering,
University of Nebraska,
Lincoln, NE 68588
e-mail: rthrone1@unl.edu

Lorraine Olson

Fellow ASME
Department of Mechanical Engineering and
Department of Engineering Mechanics,
University of Nebraska,
Lincoln, NE 68588

In the past we have developed the Generalized Eigensystem (GES_L) techniques for solving inverse boundary value problems in steady heat conduction, and found that these vector expansion methods often give superior results to those obtained with standard Tikhonov regularization methods. However, these earlier comparisons were based on the optimal results for each method, which required that we know the true solution to set the value of the regularization parameter (t) for Tikhonov regularization and the number of mode clusters ($N_{clusters}$) for GES_L . In this paper we introduce a sensor sensitivity method for estimating appropriate values of $N_{clusters}$ for GES_L . We compare those results with Tikhonov regularization using the Combined Residual and Smoothing Operator (CRESO) to estimate the appropriate values of t . We find that both methods are quite effective at estimating the appropriate parameters, and that GES_L often gives superior results to Tikhonov regularization even when $N_{clusters}$ is estimated from measured data. [DOI: 10.1115/1.1372193]

Keywords: Finite Element, Heat Transfer, Inverse, Numerical Methods

Introduction

Inverse problems have been studied for many years and steady inverse boundary value problems, in which we attempt to identify boundary values on a portion of the boundary, have arisen as a particular class of inverse problems. These steady inverse problems are generally associated with elliptic forward problems, and typical applications include electrostatics, magnetostatics, elasticity, flow in porous media, or steady heat transfer.

In this paper we are considering two-dimensional steady heat conduction, as shown schematically in Fig. 1. The governing equation in the domain is Laplace's equation

$$\nabla \cdot (\mathbf{k} \nabla T) = 0, \quad (1)$$

where \mathbf{k} is the conductivity which may depend on direction and position. For the forward problem, either a temperature or a heat flux must be specified at each location on all surfaces (inside and outside), and then the temperature and heat flux at all other points in the domain may be calculated. For the inverse problems under consideration in this paper, both the heat flux and the temperature are assumed known on some boundaries, and we wish to infer the temperature and heat flux on the rest of the boundaries.

For the inhomogeneous steady heat conduction equation with a known source, we would solve the inverse problem in two steps using superposition, since the equation is linear. We would first solve for the heat fluxes and temperatures due to the known source, then solve the homogeneous equation separately. However, if the source is unknown, then there are an infinite number of possible solutions and the problem can not be solved uniquely.

In a previous paper [1] we extended the Generalized Eigensystem (GES_L) methods we developed for inverse electrocardiography [2–7] to problems in steady inverse heat conduction. (A review of related work in steady inverse heat conduction is available in that paper.) We compared the GES_L techniques to truncated singular value decomposition and zero, first, and second

order Tikhonov regularization on two two-dimensional test geometries and four temperature/flux patterns. We found that GES_L generally gave more stable inverse solutions than the other techniques for all of the test cases examined. For the more complicated test patterns examined in that paper, zero order Tikhonov regularization generally outperformed higher order Tikhonov regularization. Hence, in this paper we only examine the results for zero order Tikhonov regularization.

However, Tikhonov regularization has an adjustable parameter t which must be chosen appropriately in order to obtain stable inverse solutions. GES_L also has a scalar adjustable parameter which must be chosen appropriately. All of the results in our previous work [1] used the true solution to choose the adjustable parameter; thus, these prior results were the *optimal* possible results for each case.

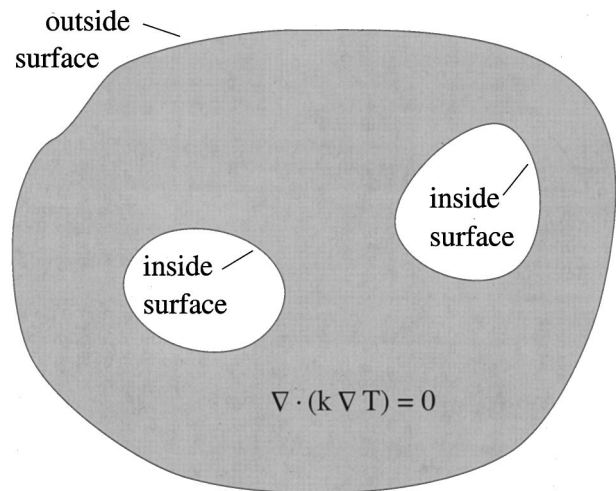


Fig. 1 Typical geometry for inverse boundary value problem in steady heat conduction

Contributed by the Heat Transfer Division for publication in the JOURNAL OF HEAT TRANSFER. Manuscript received by the Heat Transfer Division February 18, 2000; revision received February 1, 2001. Associate Editor: D. A. Kaminski.

In this paper we introduce a sensor sensitivity method for estimating appropriate values of the adjustable parameter N_{clusters} for GES_L . We compare those results with Tikhonov regularization using the Combined Residual and Smoothing Operator (CRESO) to estimate the appropriate values of t . First, we discuss the inverse algorithms and the methods for choosing the adjustable parameters. Next, we describe the test cases employed, and the results obtained with each technique. Finally, we summarize our work and give concluding remarks.

Algorithms for Steady Inverse Heat Conduction Problems

This section first discusses finite element methods for typical inverse boundary value problems in steady heat conduction. Next, we describe the inverse methods compared in this paper: Tikhonov zero-order regularization (TIK-0) and the Generalized Eigensystem method (GES_L). Both of these methods have a single scalar adjustable parameter which must be chosen based on measured data.

Numerical Discretization Using Finite Element Methods

Using standard finite element methods [8], the relationship between the temperatures and heat fluxes may be schematically represented by

$$\begin{bmatrix} \tilde{\mathbf{K}}_{oo} & \tilde{\mathbf{K}}_{or} & \tilde{\mathbf{K}}_{oi} \\ \tilde{\mathbf{K}}_{or}^T & \tilde{\mathbf{K}}_{rr} & \tilde{\mathbf{K}}_{ri} \\ \tilde{\mathbf{K}}_{oi}^T & \tilde{\mathbf{K}}_{ri}^T & \tilde{\mathbf{K}}_{ii} \end{bmatrix} \begin{bmatrix} \mathbf{T}_o \\ \mathbf{T}_r \\ \mathbf{T}_i \end{bmatrix} = \begin{bmatrix} \mathbf{M}_{oo} & \mathbf{0} & \mathbf{0} \\ \mathbf{0} & \mathbf{0} & \mathbf{0} \\ \mathbf{0} & \mathbf{0} & \mathbf{M}_{ii} \end{bmatrix} \begin{bmatrix} \mathbf{Q}_o \\ \mathbf{0} \\ \mathbf{Q}_i \end{bmatrix}, \quad (2)$$

where \mathbf{T}_o are the temperatures at nodes on the outer boundary, \mathbf{T}_i are the temperatures at nodes on the inner boundaries, and \mathbf{T}_r are the temperatures at the remaining nodes. The matrices $\tilde{\mathbf{K}}$ are the conductivity (or ‘‘stiffness’’) matrices resulting from the finite element approximation to $\nabla \cdot (\mathbf{k}\nabla T)$. \mathbf{Q}_o is the normal heat flux at the nodes on the outer boundary, with the assumption that the normal heat flux is interpolated between the nodes with the shape functions which were used to create the finite elements. (That is, if the elements are linear the normal heat flux is assumed to vary linearly between the boundary nodes, etc.) \mathbf{Q}_i is the normal heat flux at the nodes on the inner boundaries under the same interpolation assumptions. \mathbf{M}_{oo} therefore is a consistent ‘‘area’’ matrix for the outer boundary, of the form

$$\mathbf{M}_{oo} = \int \mathbf{N}^T \mathbf{N} d\Gamma_o, \quad (3)$$

where \mathbf{N} is the vector of shape functions for the outer boundary and Γ_o is the outer surface. \mathbf{M}_{ii} is a consistent ‘‘area’’ matrix for the inner boundaries. If there are n_o nodes on the outer boundary, n_i nodes on the inner boundary, and n_r nodes in the rest of the domain, then the total number of nodes is $n_{\text{tot}} = n_o + n_i + n_r$. There are then n_o entries in the vectors \mathbf{T}_o and \mathbf{Q}_o , n_r entries in \mathbf{T}_r , and n_i entries in \mathbf{T}_i and \mathbf{Q}_i . The matrices $\tilde{\mathbf{K}}$ and \mathbf{M} are square and symmetric, so that \mathbf{K}_{oo} is $n_o \times n_o$, $\tilde{\mathbf{K}}_{or}$ is $n_o \times n_r$, \mathbf{K}_{oi} is $n_o \times n_i$, etc. For any given forward problem the temperature or the heat flux must be specified on the inner and outer boundaries, so that Eq. (2) reduces to a well-posed and well-conditioned system containing n_r equations and n_r unknowns.

For computational purposes, it is useful to recognize that the boundary temperatures completely determine the remaining temperatures, so that *static condensation* [9] may be used to eliminate the volume temperatures before any inverse processing occurs. (If internal sensors are used, nodes corresponding to those locations should not be condensed out.) Solving the middle row of Eq. (2) gives

$$\mathbf{T}_r = -\tilde{\mathbf{K}}_{rr}^{-1} (\tilde{\mathbf{K}}_{ri} \mathbf{T}_i + \tilde{\mathbf{K}}_{or}^T \mathbf{T}_o). \quad (4)$$

Inserting this expression back into Eq. (2) gives

$$\begin{bmatrix} \mathbf{K}_{oo} & \mathbf{K}_{oi} \\ \mathbf{K}_{oi}^T & \mathbf{K}_{ii} \end{bmatrix} \begin{bmatrix} \mathbf{T}_o \\ \mathbf{T}_i \end{bmatrix} = \begin{bmatrix} \mathbf{M}_{oo} & \mathbf{0} \\ \mathbf{0} & \mathbf{M}_{ii} \end{bmatrix} \begin{bmatrix} \mathbf{Q}_o \\ \mathbf{Q}_i \end{bmatrix}, \quad (5)$$

where

$$\mathbf{K}_{oo} = \tilde{\mathbf{K}}_{oo} - \tilde{\mathbf{K}}_{or} \tilde{\mathbf{K}}_{rr}^{-1} \tilde{\mathbf{K}}_{or}^T \quad (6)$$

$$\mathbf{K}_{oi} = \tilde{\mathbf{K}}_{oi} - \tilde{\mathbf{K}}_{or} \tilde{\mathbf{K}}_{rr}^{-1} \tilde{\mathbf{K}}_{ri} \quad (7)$$

and

$$\mathbf{K}_{ii} = \tilde{\mathbf{K}}_{ii} - \tilde{\mathbf{K}}_{ri}^T \tilde{\mathbf{K}}_{rr}^{-1} \tilde{\mathbf{K}}_{ri}. \quad (8)$$

Naturally, the computation is performed in the computationally efficient manner indicated by Wilson [9] rather than by brute force inversion, but the concept is clearly illustrated here. In what follows therefore, we will deal primarily with the reduced equation set described by Eq. (5).

For the inverse problems under consideration in this paper, both the heat flux and the temperature are assumed known on some boundaries, and we wish to infer the temperature and heat flux on the other boundaries. The methods developed in the subsequent sections can be modified to estimate temperatures and heat fluxes from measured temperatures alone. However, using measured heat fluxes alone will not uniquely determine the temperatures since fluxes are based on gradients of temperatures.

Tikhonov Regularization. Because the structure of Eq. (5) is now identical to that which would be obtained using a boundary element method (BEM), we employ the Tikhonov regularization methods developed by Martin and Dulikravich [10–12] for steady inverse heat transfer problems derived from BEM formulations as a comparison.

Let us consider the specific case when the outer fluxes and temperatures are known and we wish to estimate the inner fluxes and temperatures. The basic forward Eq. (5) is rearranged to place the known outer fluxes and temperatures on the right-hand-side of the inverse equation, and the unknown inner fluxes and temperatures are moved to the left:

$$\begin{bmatrix} \mathbf{K}_{ii} & -\mathbf{M}_{ii} \\ \mathbf{K}_{oi} & \mathbf{0} \end{bmatrix} \begin{bmatrix} \mathbf{T}_i \\ \mathbf{Q}_i \end{bmatrix} = \begin{bmatrix} -\mathbf{K}_{oi}^T & \mathbf{0} \\ -\mathbf{K}_{oo} & \mathbf{M}_{oo} \end{bmatrix} \begin{bmatrix} \mathbf{T}_o \\ \mathbf{Q}_o \end{bmatrix}. \quad (9)$$

Since the right-hand-side is now completely known, we can write the resulting equation as

$$\mathbf{A}\mathbf{x} = \mathbf{f}, \quad (10)$$

where $\mathbf{x}^T = [\mathbf{T}_i^T \mathbf{Q}_i^T]$ is the vector of unknowns, and

$$\mathbf{A} = \begin{bmatrix} \mathbf{K}_{ii} & -\mathbf{M}_{ii} \\ \mathbf{K}_{oi} & \mathbf{0} \end{bmatrix}$$

$$\mathbf{f} = \begin{bmatrix} -\mathbf{K}_{oi}^T & \mathbf{0} \\ -\mathbf{K}_{oo} & \mathbf{M}_{oo} \end{bmatrix} \begin{bmatrix} \mathbf{T}_o \\ \mathbf{Q}_o \end{bmatrix}.$$

Notice that there may be fewer unknowns than knowns (or more, for that matter) so that \mathbf{A} is generally not square. (\mathbf{A} has $n_i + n_o$ rows and $2n_i$ columns, and \mathbf{f} is a vector with $n_i + n_o$ entries.)

Tikhonov regularization stabilizes the inverse by balancing the error in the solution to the equation with a measure of some function of the unknowns, such as the magnitude or slope. In general, we minimize Π with respect to $\hat{\mathbf{x}}$:

$$\Pi = \|\mathbf{A}\hat{\mathbf{x}} - \mathbf{f}\| + t\|\mathbf{R}\hat{\mathbf{x}}\|, \quad (11)$$

where $\hat{\mathbf{x}}$ is the estimate of the solution, \mathbf{R} is called the regularization (matrix) operator, and t is the regularization (or smoothing) parameter. In zero-order Tikhonov regularization $\mathbf{R} = \mathbf{I}$ and so we penalize the magnitude of the unknowns. In first-order regularization \mathbf{R} is chosen so that $\mathbf{R}\hat{\mathbf{x}}$ is an estimate of the gradient of the unknowns, while in second-order regularization $\mathbf{R}\hat{\mathbf{x}}$ is an estimate of the second derivative of the unknowns. First-order regularization penalizes solutions which have large slopes, while second-

order regularization penalizes solutions which have large second derivatives—i.e. solutions which are not smooth. In a previous paper [1] we investigated three choices for \mathbf{R} , but in this paper we will employ only the most common choice: zero-order regularization.

The value of $\hat{\mathbf{x}}$ which minimizes Π is given by the solution to the matrix equation

$$(\mathbf{A}^T \mathbf{A} + t \mathbf{R}^T \mathbf{R}) \hat{\mathbf{x}} = \mathbf{A}^T \mathbf{f}. \quad (12)$$

When t is zero we have a pure least-squares solution, but this is generally unstable. When t is large we have a smooth solution, but that solution may have little relationship to the original problem. By solving this equation with an appropriately chosen value of t a stable inverse solution may be obtained.

Generalized Eigensystem Methods. The Generalized Eigensystem (GES_L) methods take a different approach than Tikhonov regularization. The basic idea in GES_L is to choose basis vectors in a systematic way, yet choose vectors which will accurately represent the expected temperature and heat flux profiles with a small number of modes. This is in contrast to zero order Tikhonov regularization, where the solution is based solely on the \mathbf{A} matrix without regard to the expected nature of the temperature and heat flux profiles.

For the GES_L method, we first assume that we have a set of N_{modes} linearly independent basis vectors \mathbf{X} , which are solutions to the forward problem. (We will address the selection of these basis vectors below.) We partition the vectors as:

$$\mathbf{X} = \begin{bmatrix} \mathbf{X}_o \\ \mathbf{X}_r \\ \mathbf{X}_i \end{bmatrix}, \quad (13)$$

where \mathbf{X}_o contains the part of the basis vectors used to represent the temperature solution at the outer boundary nodes (\mathbf{X}_o is $n_o \times N_{\text{modes}}$), \mathbf{X}_i contains the part of the basis vectors used to represent the temperature solution at the inner boundary nodes (\mathbf{X}_i is $n_i \times N_{\text{modes}}$), and \mathbf{X}_r contains the basis vectors at the rest of the nodes.

Next, we calculate the normal heat fluxes on the boundaries which correspond to the temperature basis vectors. Inserting \mathbf{X}_o and \mathbf{X}_i into Eq. (5) allows us to calculate the normal boundary fluxes, \mathbf{Y}_i and \mathbf{Y}_o :

$$\begin{bmatrix} \mathbf{Y}_o \\ \mathbf{Y}_i \end{bmatrix} = \begin{bmatrix} \mathbf{M}_{oo}^{-1} & \mathbf{0} \\ \mathbf{0} & \mathbf{M}_{ii}^{-1} \end{bmatrix} \begin{bmatrix} \mathbf{K}_{oo} & \mathbf{K}_{oi} \\ \mathbf{K}_{oi}^T & \mathbf{K}_{ii} \end{bmatrix} \begin{bmatrix} \mathbf{X}_o \\ \mathbf{X}_i \end{bmatrix}. \quad (14)$$

We assume that our estimate for the temperature solution $\hat{\mathbf{T}}$ and the flux solution $\hat{\mathbf{Q}}$ can be represented as a sum of the basis vectors:

$$\hat{\mathbf{T}} = \begin{bmatrix} \hat{\mathbf{T}}_o \\ \hat{\mathbf{T}}_i \end{bmatrix} = \begin{bmatrix} \mathbf{X}_o \boldsymbol{\alpha} \\ \mathbf{X}_i \boldsymbol{\alpha} \end{bmatrix} \quad (15)$$

$$\hat{\mathbf{Q}} = \begin{bmatrix} \hat{\mathbf{Q}}_o \\ \hat{\mathbf{Q}}_i \end{bmatrix} = \begin{bmatrix} \mathbf{Y}_o \boldsymbol{\alpha} \\ \mathbf{Y}_i \boldsymbol{\alpha} \end{bmatrix}, \quad (16)$$

where $\boldsymbol{\alpha}$ is the vector of expansion coefficients (containing N_{modes} entries) for both the outer and inner temperatures and heat fluxes. If we again consider the case where the outer boundary data are measured, the GES method simply minimizes the error between the measured data on the outer boundary and the estimate evaluated at the outer boundary:

$$\Pi = \|\mathbf{T}_o - \mathbf{X}_o \boldsymbol{\alpha}\|^2 + \|\mathbf{Q}_o - \mathbf{Y}_o \boldsymbol{\alpha}\|^2. \quad (17)$$

By minimizing Π with respect to $\boldsymbol{\alpha}$ we obtain a matrix equation which allows us to solve for $\boldsymbol{\alpha}$:

$$(\mathbf{X}_o^T \mathbf{X}_o + \mathbf{Y}_o^T \mathbf{Y}_o) \boldsymbol{\alpha} = \mathbf{X}_o^T \mathbf{T}_o + \mathbf{Y}_o^T \mathbf{Q}_o. \quad (18)$$

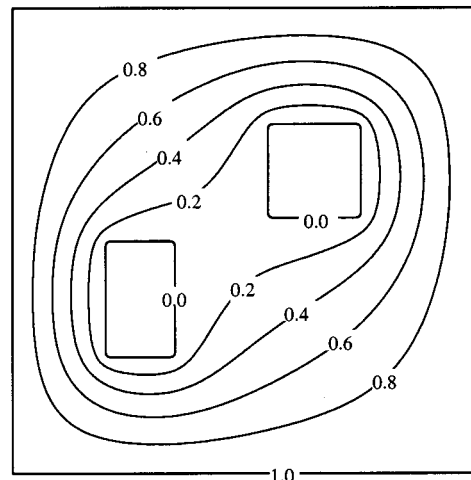
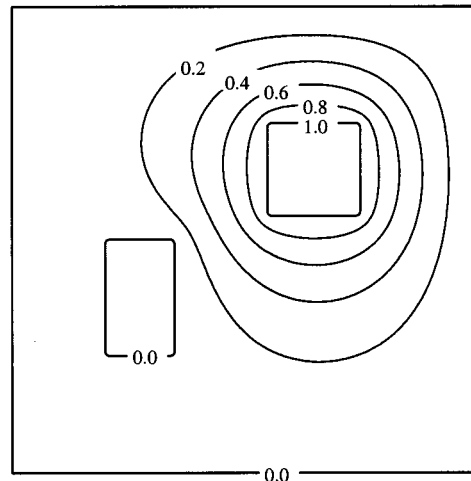
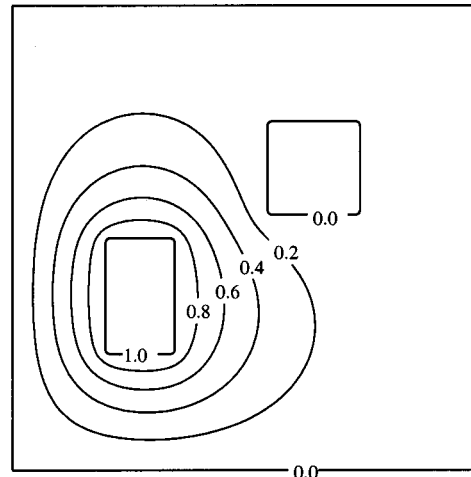


Fig. 2 First cluster for the GES_L method for the square with holes geometry

This is a system of linear algebraic equations for $\boldsymbol{\alpha}$, with N_{modes} equations in N_{modes} unknowns. Solving this equation system gives the expansion coefficients $\boldsymbol{\alpha}$. The estimate at the inner surface is then given by

$$\hat{\mathbf{T}}_i = \mathbf{X}_i \boldsymbol{\alpha} \quad (19)$$

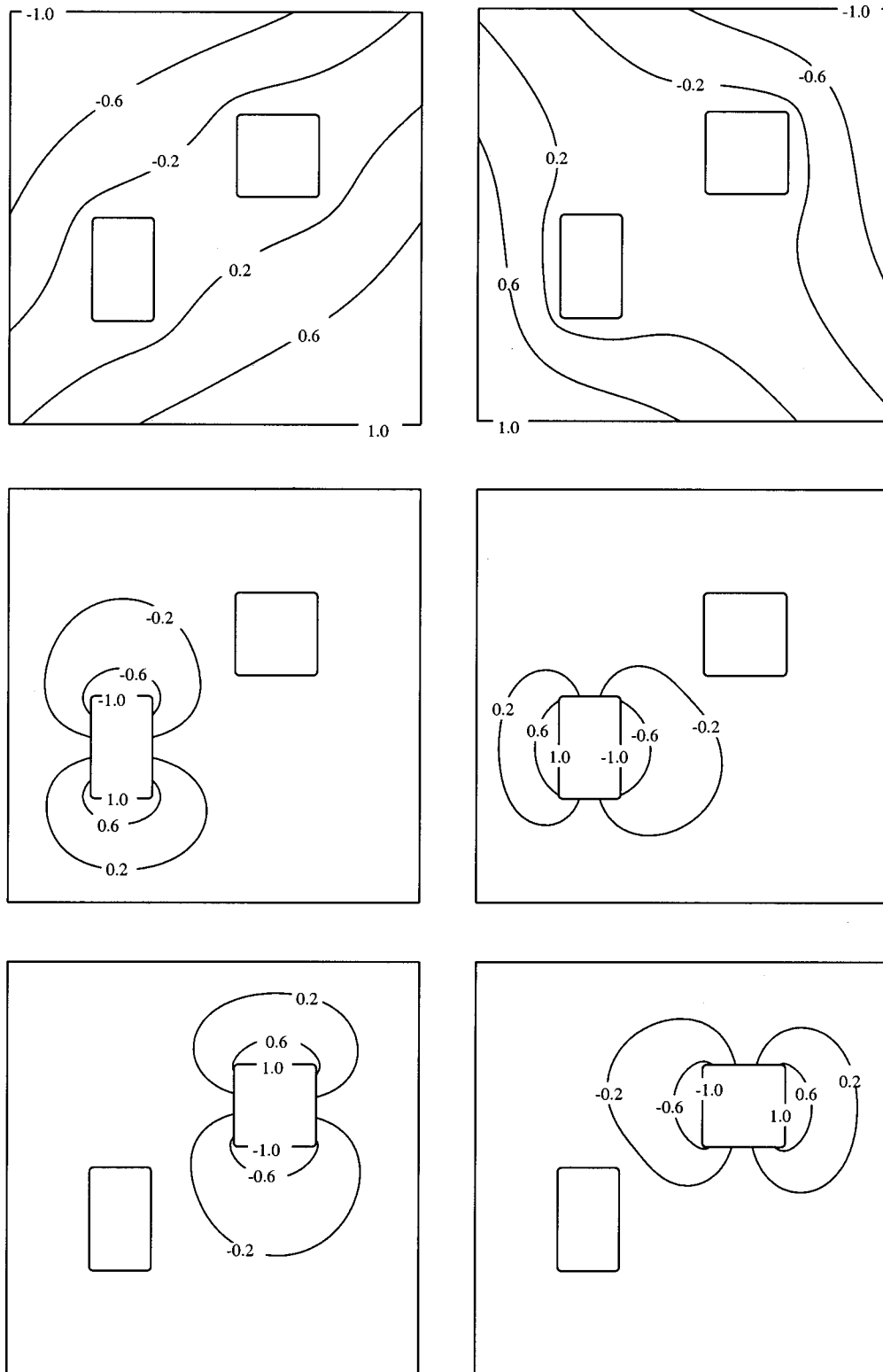


Fig. 3 Second cluster for the GES_L method for the square with holes geometry

$$\hat{Q}_i = Y_i \alpha. \quad (20)$$

Notice temperature errors and flux errors are directly summed in Eq. (17). For this to be reasonable, we should nondimensionalize the problem so that both \mathbf{T} and \mathbf{Q} are non-dimensional. In what follows we only apply the technique to dimensionless test

problems. Notice also, however, that we might have greater confidence in the temperature measurements than the heat flux measurements. Then Eq. (17) could be adjusted with confidence weighting factors.

If we use many modes in the expansion, the inverse solution will still be unstable. Again, the goal is to choose a good set of

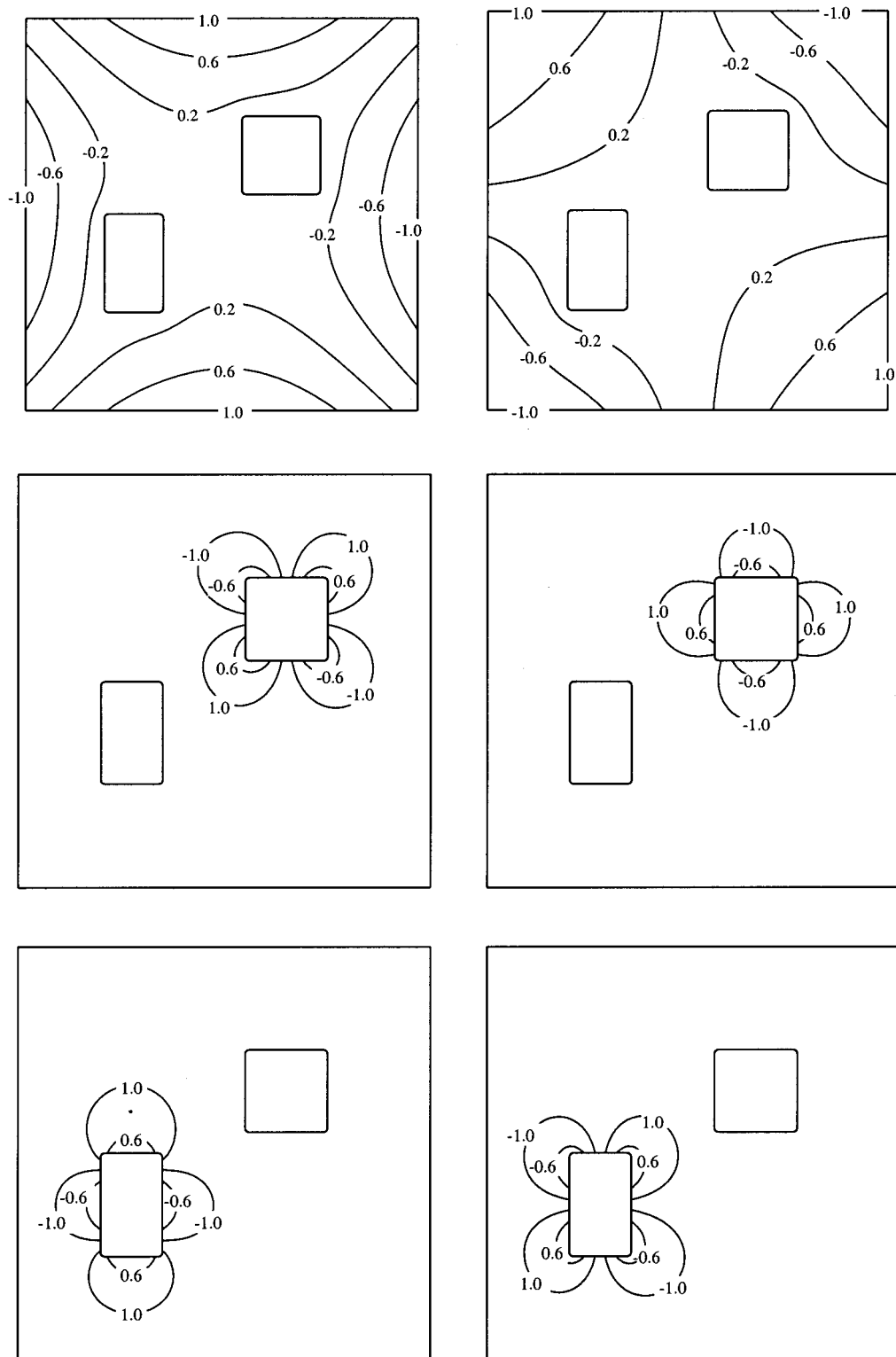


Fig. 4 Third cluster for the GES_L method for the square with holes geometry

trial forward solutions, and to order them carefully so that the truncation to N_{modes} vectors yields stable inverse solutions.

The method used in this study for selecting the vectors seeks solutions which are smooth on the boundaries, and which are ordered by the amount of oscillation in the boundary solution. We introduce a generalized eigenproblem:

$$\begin{bmatrix} \mathbf{K}_{Go} & \mathbf{0} \\ \mathbf{0} & \mathbf{K}_{Gi} \end{bmatrix} \begin{bmatrix} \mathbf{X}_o \\ \mathbf{X}_i \end{bmatrix} = \begin{bmatrix} \mathbf{M}_{oo} & \mathbf{0} \\ \mathbf{0} & \mathbf{M}_{ii} \end{bmatrix} \begin{bmatrix} \mathbf{X}_o \\ \mathbf{X}_i \end{bmatrix} \begin{bmatrix} \Lambda_{oo} & \mathbf{0} \\ \mathbf{0} & \Lambda_{ii} \end{bmatrix}. \quad (21)$$

Here \mathbf{K}_G is a surface gradient matrix [1] and \mathbf{M} is the surface area matrix. Because the eigenproblems for the boundaries are now

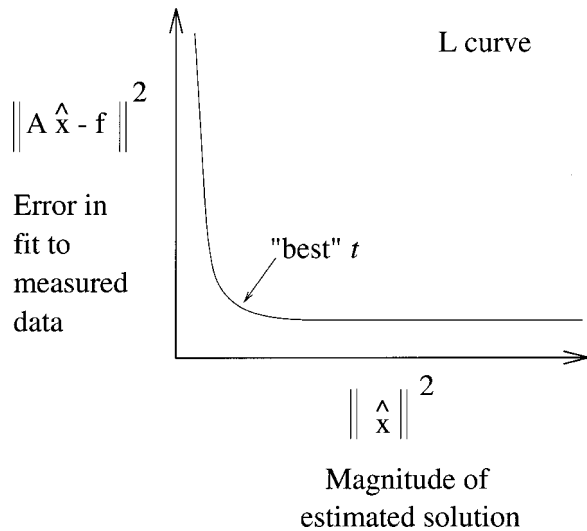


Fig. 5 L-curve used for identifying appropriate t values for zero order Tikhonov regularization

decoupled, solving Eq. (21) will find sequences of vectors which are orthogonal over each boundary and which are ordered by their smoothness on that boundary. There are as many zero eigenvalues for this problem as there are surfaces, because each surface can have one mode which has a constant temperature and hence no surface gradient.

Once the modes are identified, they are sorted into “clusters”. The first cluster includes all of the modes with a zero eigenvalue. The second cluster includes the lowest non-zero modes from each surface. The third cluster includes the second-lowest non-zero modes from each surface, and so on. Figures 2–4 show an example: the first three clusters for the square with holes test case used later in this paper. The first cluster for this geometry includes three modes with zero eigenvalues. The second cluster includes two modes (sine-like and cosine-like) for each surface, for a total of six modes. The third cluster also has 6 vectors, but now they oscillate more rapidly on the surfaces. As many clusters as desired are added to the set of vectors, and we identify the number of clusters used in the solution as N_{clusters} .

Notice that this method finds only the trial functions for the temperature. The trial functions for the heat flux are found by inserting the temperature functions into Eq. (14), and then the trial vector selection is complete. In addition, although the temperature expansion vectors we chose are uncoupled, the heat flux vectors will be coupled.

Estimation of Appropriate Adjustable Parameters. In zero-order Tikhonov regularization, the parameter t must be selected in order to adjust the balance between the magnitude of the error in solving the matrix equation and the magnitude of the estimated solution. In the GES_L method the number of clusters N_{clusters} must be chosen to balance errors in fitting the measured data against the level of oscillation in the estimated solution. Although we can find the optimal parameters t and N_{clusters} for test cases where the solution is known, in realistic problems we must estimate the parameters from known data.

In order to estimate an appropriate value of t for Tikhonov regularization, we will use the Combined Residual and Smoothing Operator (CRESO) technique developed by Colli-Franzone [13] in their studies of inverse electrocardiography, and widely used [14–16] in that field. This technique is based on L-curve concepts (see, e.g., [16–19]) Figure 5 schematically shows the L-curve, which plots the error in the fit to the measured data versus the magnitude of the estimated solution. Appropriate values of t are taken to be those at the bend, or elbow, of the curve. CRESO is a

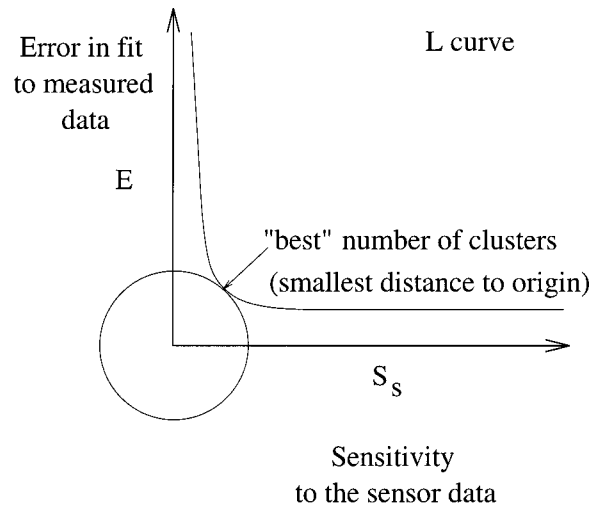


Fig. 6 L-curve used for identifying appropriate N_{clusters} values for GES_L

particular way to estimate the location of the bend: we choose t to maximize the difference between the derivative of the smoothing term $t\|\hat{\mathbf{x}}\|^2$ and the derivative of the fit to the data $\|\mathbf{A}\hat{\mathbf{x}} - \mathbf{f}\|^2$.

In order to estimate the appropriate number of clusters to use in the GES_L method, we now introduce the sensor sensitivity method, which is also based on an L-curve. Let us define E as the error in the fit to the measured data:

$$E = \|\hat{\mathbf{T}}_o - \mathbf{T}_o\|^2 + \|\hat{\mathbf{Q}}_o - \mathbf{Q}_o\|^2. \quad (22)$$

Also, define S_s as the sensitivity of the solution vector to the sensor data:

$$S_s = \sum_{j=1}^{N_s} [\|\hat{\mathbf{T}}_i - \hat{\mathbf{T}}_i^j\|^2 + \|\hat{\mathbf{Q}}_i - \hat{\mathbf{Q}}_i^j\|^2], \quad (23)$$

where N_s is the total number of sensors, $\hat{\mathbf{T}}_i$ is the estimate of the inside temperature using all of the sensors, $\hat{\mathbf{T}}_i^j$ is the estimate of the inside temperature using all sensors except sensor j , $\hat{\mathbf{Q}}_i$ is the estimate of the inside heat flux using all of the sensors, and $\hat{\mathbf{Q}}_i^j$ is the estimate of the inside heat flux using all sensors except sensor j . Figure 6 schematically shows the L-curve for this method: the error in the fit to the measured data is plotted against the sensitivity to the sensor data. Although the curve is shown as continuous for clarity, in practice it is a discrete set of points. For each possible N_{clusters} there is a value for E and a value for S_s which lies on the curve. To choose the most appropriate N_{clusters} we choose the value which falls closest to the origin. This eliminates solutions which match the measured data extremely well, and also eliminates solutions which are very sensitive to the data measurements.

This method is similar to Generalized Cross Validation (GCV) [20]. However, with GCV one attempts to minimize the overall error between predicted sensor values (estimated using all the other sensors) and the correct (measured) sensor values. Hence, GCV focuses on the predicted errors on the boundaries with known (measured) values. Our method attempts to examine the sensitivity of the estimated values on the surfaces where there are no measured values. GCV was tested as a method for choosing the number of clusters in GES_L , but performed poorly.

Test Cases

We have examined two planar test geometries: the first geometry is an annulus, and the second geometry is a square with two rounded rectangular holes. All the test cases have been nondimen-

sionalized. For the annulus geometry we considered two temperature cases, and for the square we investigated three temperature cases.

In computing the errors for the inverse solutions, we will use the percent relative error. When we are estimating the inner temperature values this is defined as

$$RE = 100 \text{ percent} \times \frac{\|\hat{\mathbf{T}}_i - \mathbf{T}_i\|}{\|\mathbf{T}_i\|} \quad (24)$$

Annulus

Figure 7 shows the geometry and finite element mesh for the annulus tests considered here, which was also studied by Maillet, Degiovanni, and Pasquetti [21], Truffart, Jarny, and Delaunay [22], Dennis and Dulikravich [23,24] and Martin and Dulikravich [10].

The geometry consists of a circle of dimensionless radius 1.0 containing a concentric circular hole with dimensionless radius 0.5. The conductivity in the region between the two circles is 1.0. The finite element mesh was generated with the I-DEAS finite element package (SDRC, Ohio) and contains 12,521 linear triangular elements and 6496 total nodes, with an element side length of approximately 0.02. There were 314 nodes on the outer circle and 157 nodes on the inner circle.

Two temperature distributions were considered for this geometry.

First Temperature Distribution. The first temperature distribution is that studied by Dennis and Dulikravich [23,24]. For the *forward* problem the temperature on the inner circle is taken to be 1.0, while the temperature on the outer circle is 0.0. For the *inverse* problem the temperatures and heat fluxes are specified on the outer boundary, and we wish to calculate the temperatures and heat fluxes on the inner boundary. The analytical solution to the forward problem is easily found to be

$$T = \frac{\ln r}{\ln 0.5}, \quad (25)$$

for the dimensionless temperature, where r is the radial coordinate, and

$$q = \frac{1}{r \ln 0.5}, \quad (26)$$

for the dimensionless heat fluxes. It should be reiterated that a proper nondimensionalization of the problem allows one to evalu-

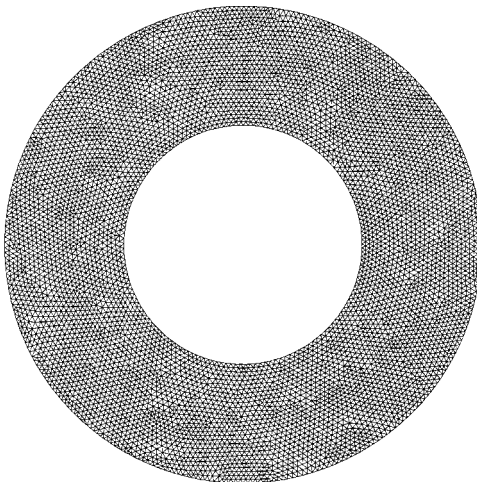


Fig. 7 Geometry and finite element mesh for annulus test case. (Inner circle has radius 0.5, outer circle has radius 1.0.)

Table 1 Inverse relative error in temperature for the first temperature distribution for the annulus test case (mean±std.)

		Noise Level					
		1	2	5	10	20	50
GES _L	Optimal	0.57±0.33	0.91±0.69	1.43±0.96	1.50±1.36	2.38±1.74	4.52±3.55
	Estimated	2.18±0.89	3.29±1.27	3.40±1.53	4.05±1.47	4.83±2.87	4.52±3.55
TIK-0	Optimal	5.48±0.76	7.26±1.50	9.77±1.67	12.15±1.83	13.92±3.20	20.74±4.25
	Estimated	7.34±1.29	8.78±1.68	13.41±2.82	14.94±3.23	17.17±3.05	20.62±5.29

ate the errors in heat flux and the errors in temperature with equal weighting, which was assumed in deriving the inverse algorithms.

For the forward problem the norm of the relative error in the computed heat flux for the mesh employed was 0.13 percent on the outer circle and 0.10 percent on the inner circle, indicating a well-converged solution.

We added white random Gaussian noise to the analytical solution on the outer boundary to examine the effects of noise on the inverse solution. For $\sigma^2 = 0.01, 0.02, 0.05, 0.10, 0.20, 0.50$ (corresponding to noise levels of 1, 2, 5, 10, 20, and 50 percent), we applied temperatures and heat flux perturbations with normal distribution and standard deviation σ . Twenty-five trials were performed for each noise level, and the relative error was computed for each inverse technique.

Tables 1 and 2 show the mean and standard deviation of the RE in temperature (Table 1) and heat flux (Table 2) on the inner boundary for each noise level and for both of the inverse algorithms under consideration. The tables indicate the *optimal* parameter and *estimated* parameter solutions for each method: the optimal solution uses the best possible choice of the free parameter for each algorithm, while the estimated uses only measured data to estimate a good value for the free parameter. GES_L performs well for this simple test case, while Tikhonov regularization is not as effective. Since the true temperature is extremely smooth on the boundaries (in fact, a constant) it is not surprising that GES_L, which orders the clusters by their smoothness, works best here. In fact, the first cluster for GES_L is all that is required to represent the exact temperature pattern completely, so that all of the boundary data can be used to estimate the amplitudes of those modes.

Second Temperature Distribution. The second temperature distribution was studied (in dimensional form) by Maillet, Degiovanni, and Pasquetti [21], and Truffart, Jarny, and Delaunay [22]. The nondimensionalized *forward* problem is to solve $\nabla^2 T = 0$ in the domain subject to the boundary conditions $T = 0$ on the inner circle ($r = 0.5$) and $\partial T / \partial r = h(T - 1)$ on the outer circle ($r = 1.0$). The heat transfer coefficient h is given on the top surface of the cylinder by

$$h = \begin{cases} 15.3846 & \text{for } \theta = 0 \text{ to } 40 \text{ deg} \\ \text{linear from } 15.3846 \text{ to } 6.1538 & \text{for } \theta = 40 \text{ to } 80 \text{ deg} \\ \text{linear from } 6.1538 \text{ to } 12.3077 & \text{for } \theta = 80 \text{ to } 180 \text{ deg} \end{cases} \quad (27)$$

and is symmetric for the bottom surface of the cylinder. (θ is measured counterclockwise from the right-hand-side of the cylinder.) No analytical solution for the forward problem is available, but Fig. 8 shows the temperature contours for the numerical forward solution.

Notice that this problem arises when *internal* measurements are used to estimate the heat transfer coefficient on the surface of a

Table 2 Inverse relative error in heat flux for the first temperature distribution for the annulus test case (mean±std.)

		Noise Level					
		1	2	5	10	20	50
GES _L	Optimal	0.36±0.20	0.42±0.34	0.89±0.60	1.29±0.89	1.25±1.04	2.51±1.67
	Estimated	2.48±1.20	3.61±2.26	2.93±2.28	2.82±1.07	2.87±1.73	2.51±1.67
TIK-0	Optimal	12.34±1.43	15.32±2.36	18.96±2.83	21.90±2.93	25.06±4.21	32.67±4.04
	Estimated	22.74±4.67	25.58±5.35	35.92±7.46	36.81±8.28	37.70±7.98	37.26±8.36

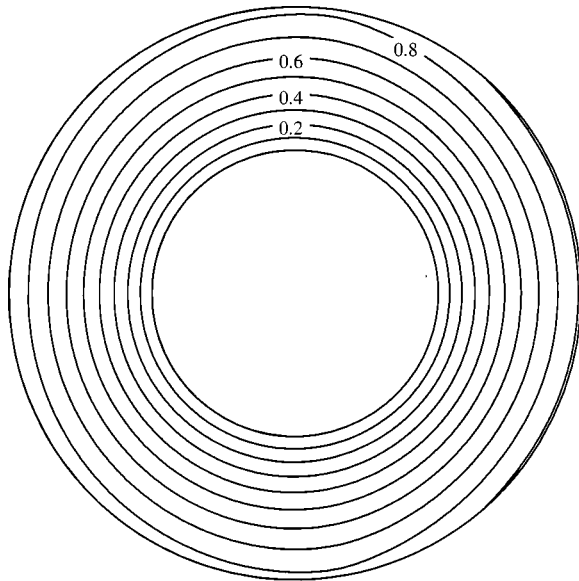


Fig. 8 Forward computed temperature contours for second annulus test case. (Temperature is zero on inner boundary; contour level intervals are 0.1.)

Table 3 Inverse relative error in temperature for the second temperature distribution for the annulus test case (mean±std.)

		Noise Level					
		1	2	5	10	20	50
GES _L	Optimal	2.92±0.47	3.45±0.48	3.76±0.75	4.22±1.18	5.15±2.15	6.55±4.03
	Estimated	3.36±0.86	4.38±1.13	6.06±2.72	7.92±5.27	9.25±3.81	3.02±5.49
TIK-0	Optimal	7.75±1.27	11.00±2.03	14.40±2.69	17.10±2.90	21.43±3.82	29.81±5.76
	Estimated	10.58±1.86	11.85±3.04	19.77±4.18	23.32±4.96	29.17±6.04	35.25±6.16

Table 4 Inverse relative error in heat flux for the second temperature distribution for the annulus test case (mean±std.)

		Noise Level					
		1	2	5	10	20	50
GES _r	Optimal	4.81±0.80	5.19±0.62	5.41±0.47	5.55±0.13	5.81±0.36	6.08±0.69
	Estimated	4.61±0.88	5.43±1.07	6.63±2.99	7.76±6.40	7.35±3.61	8.13±1.95
TIK-0	Optimal	18.49±3.03	24.65±3.20	29.13±3.99	33.86±3.72	39.73±4.36	49.71±4.93
	Estimated	32.58±6.92	31.34±8.92	49.68±10.15	53.67±11.72	65.01±15.54	57.27±8.72

cylinder, but that (following Truffart, Jarny, and Delaunay [22]) we are not attempting to estimate the coefficient but only the surface temperatures¹.

For the inverse problems with noise, we added random Gaussian noise to the forward-computed solution on the inner boundary to examine the effects of noise on the inverse solution. As before we applied temperature and heat flux perturbations, and twenty-five trials were performed for each noise level.

Tables 3 and 4 show the mean and standard deviation of the RE in temperature (Table 3) and heat flux (Table 4) on the outer boundary for each noise level and for each of the inverse algorithms under consideration. The tables indicate the optimal parameter and estimated parameter solutions for each method. For this more complicated temperature pattern both methods give less accurate inverses. The difference between the optimal and estimated parameter results is similar to the difference in the first test case.

Square with Holes. Figure 9 shows the geometry and finite element mesh for the second test geometry. This geometry is similar to that studied by Dennis and Dulikravich [23] but has been modified slightly. The original problem proposed by Dennis and Dulikravich was identical to that shown, except that the inside corners of the rectangular holes were not rounded. They chose a temperature pattern which included a constant temperature on the

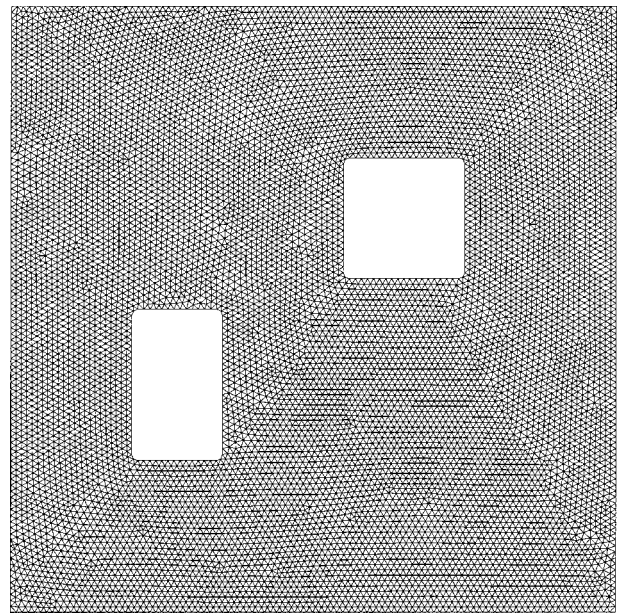


Fig. 9 Geometry and finite element mesh for square with holes. The outer square is 1.0×1.0. The first inner rectangle is centered at (0.275,0.375) and is 0.15×0.25. The second inner rectangle is centered at (0.65,0.65) and is 0.2×0.2. The radii of the corners on the inner rectangles is 0.01.

inner boundary, a constant temperature on the outer boundary, and a specified internal heat generation in the solid region. Since the internal heat generation was considered known, it can be omitted and included by superposition after the remaining fields are computed. However, the analytical solution to a constant temperature on the inner boundaries in combination with 90 deg corners on the internal edges will result in infinite heat fluxes at the corners. Hence any finite solution computed as an inverse would have an infinite error in the heat flux, which is misleading. Consequently, we have rounded the internal corners to force the heat flux at those locations to be large but finite.

The finite element mesh was generated with the I-DEAS finite element package (SDRC, Ohio) and contains 21,278 linear triangular elements and 10,638 total nodes, with an average element side length of 0.01. There were 400 nodes on the outer boundary and 80 nodes on each of the inner rectangles.

We examined three temperature distributions for this geometry.

First Temperature Distribution. In the first forward problem, the temperature on the outer boundary was nondimensionalized to 0.0 while the temperature on the inside surface of the holes was taken to be 1.0. No analytical solution for the forward problem is available, but Fig. 10 shows the temperature contours for the numerical forward solution.

We added random Gaussian noise to the forward-computed solution on the outer boundary to examine the effects of noise on the inverse solution. As before we applied temperature and heat flux perturbations, and twenty-five trials were performed for each noise level.

Tables 5 and 6 show the mean and standard deviation of the RE in temperature (Table 5) and heat flux (Table 6) on the outer boundary for each noise level and for each of the inverse algorithms under consideration, and optimal parameter and estimated parameter solutions for each method are indicated. Although this was a simple temperature pattern on the boundaries, the geometry makes the temperature and heat flux patterns within the domain more complicated. Tikhonov regularization performs poorly here, and GES_L performs ten to twenty times better. This superiority is due to the fact that the solution for the forward problem can be

¹While h can then be estimated from the surface data for temperatures and fluxes, this may not be efficient, and we will postpone that question for a subsequent study.

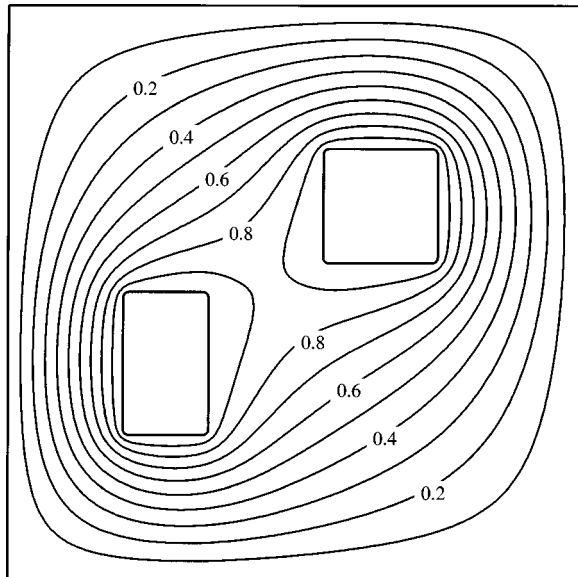
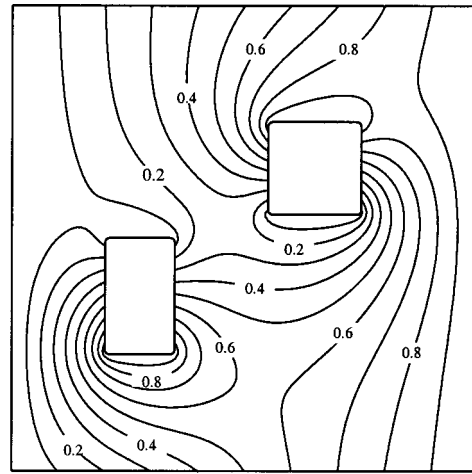


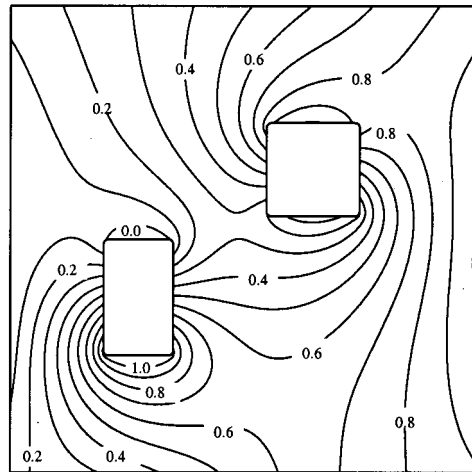
Fig. 10 Temperature contours for first square with holes test case. (Temperature is 1.0 on inner boundaries, 0.0 on outer boundary. Contours are at temperature intervals of 0.1.)

represented exactly in terms of the first GES_L cluster—those corresponding to constant temperatures on each of the surfaces. At all noise levels, the sensor sensitivity method is able to correctly identify the first cluster as the stopping point, and so the optimal and estimated results for GES_L are exactly equal. Results with Tikhonov regularization on this problem are similar to those seen with the two annulus test cases.

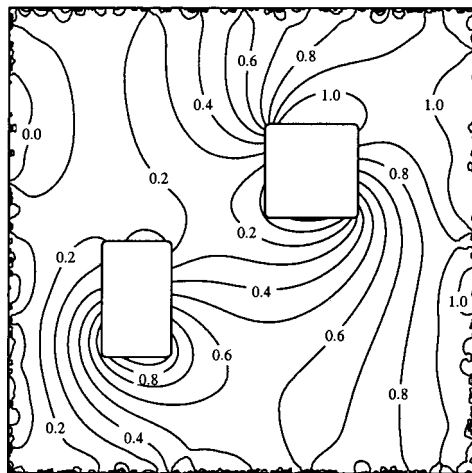
Second Temperature Distribution. The second temperature distribution tested was specifically chosen to be more difficult for the GES_L method to detect. For the forward problem, on the outer surface of the square the temperature was given by $T=1$ on the left edge, $T=0$ on the right edge, and a linear variation from 1 to 0 on the top and bottom edges. On the rectangular hole (lower left) the temperature was $T=1$ on the top edge, $T=0$ on the bottom edge, and a linear variation from 1 to 0 on the left and right edges. On the square hole (upper right) the temperature was $T=1$ on the bottom edge, $T=0$ on the top edge, and a linear variation from 0 to 1 on the left and right edges. Figure 11(a) shows temperature contours for the numerical forward (“true”) solution. This test case was treated in the same manner as the first temperature distribution for the square with holes. We added random Gaussian noise to the forward-computed solution on the outer boundary to examine the effects of noise on the inverse



(a) “TRUE”



(b) GES_L (RE=12%)



(c) TIK-0 (RE=26%)

Table 5 Inverse relative error in temperature for the first temperature distribution for the square with holes test case (mean \pm std.)

		Noise Level					
		1	2	5	10	20	50
GES_L	Optimal	0.54 \pm 0.34	0.83 \pm 0.49	1.19 \pm 0.88	1.83 \pm 0.86	2.11 \pm 1.07	3.88 \pm 2.46
	Estimated	0.54 \pm 0.34	0.83 \pm 0.49	1.19 \pm 0.88	1.86 \pm 0.86	2.11 \pm 1.07	3.88 \pm 2.46
TIK-0	Optimal	9.64 \pm 1.97	10.61 \pm 1.72	12.13 \pm 2.40	14.65 \pm 2.69	16.02 \pm 3.63	21.99 \pm 4.94
	Estimated	11.88 \pm 2.89	13.16 \pm 3.07	14.23 \pm 3.25	16.63 \pm 3.36	21.12 \pm 6.37	27.49 \pm 6.42

Table 6 Inverse relative error in heat flux for the first temperature distribution for the square with holes test case (mean \pm std.)

		Noise Level					
		1	2	5	10	20	50
GES_L	Optimal	0.34 \pm 0.19	0.57 \pm 0.35	0.69 \pm 0.38	1.33 \pm 0.81	1.94 \pm 1.11	2.46 \pm 1.27
	Estimated	0.34 \pm 0.19	0.57 \pm 0.35	0.69 \pm 0.38	1.32 \pm 0.84	1.94 \pm 1.11	2.46 \pm 1.27
TIK-0	Optimal	50.06 \pm 1.95	51.37 \pm 1.79	52.43 \pm 1.35	53.92 \pm 2.06	55.20 \pm 2.95	58.71 \pm 3.37
	Estimated	54.61 \pm 5.16	56.29 \pm 5.63	56.78 \pm 3.47	57.74 \pm 4.98	62.10 \pm 9.73	68.34 \pm 7.76

Fig. 11 Temperature contours for second square with holes test case: (a) “true” forward computed solution; (b) a GES_L inverse solution when 5 percent noise is added to the outer temperatures and fluxes; and (c) a zero-order Tikhonov inverse solution when 5 percent noise is added to the outer temperatures and fluxes. (Temperature contours at 0.0, 0.1, . . . 1.0.)

Table 7 Inverse relative error in temperature for the second temperature distribution for the square with holes test case (mean±std.)

		Noise Level					
		1	2	5	10	20	50
GES _L	Optimal	13.30±1.23	13.41±1.58	13.72±3.02	14.94±2.97	16.13±3.99	17.19±6.32
	Estimated	13.30±1.23	13.41±1.58	13.72±3.02	15.05±3.09	16.13±4.00	17.31±6.76
TIK-0	Optimal	18.87±2.40	22.65±4.62	25.00±3.46	30.26±4.16	36.95±8.97	48.23±12.51
	Estimated	20.70±4.32	22.40±3.39	28.24±7.24	30.46±4.54	69.22±3.23	71.44±3.90

Table 8 Inverse relative error in heat flux for the second temperature distribution for the square with holes test case (mean±std.)

		Noise Level					
		1	2	5	10	20	50
GES _L	Optimal	53.61±0.73	53.70±0.87	53.69±1.67	54.12±1.92	54.53±2.87	54.25±3.62
	Estimated	53.61±0.73	53.70±0.87	53.69±1.67	54.19±2.00	54.53±2.87	54.36±4.07
TIK-0	Optimal	75.58±1.34	77.28±2.45	77.65±1.99	80.07±2.42	82.08±3.84	85.53±5.64
	Estimate	77.38±3.65	77.58±2.10	80.48±5.00	81.36±4.29	98.70±0.18	98.81±0.18

solution. As before we applied temperature and heat flux perturbations, and twenty-five trials were performed for each noise level.

Tables 7 and 8 show the mean and standard deviation of the RE in temperature (Table 7) and heat flux (Table 8) on the outer boundary for each noise level and for each of the inverse algorithms under consideration, and optimal parameter and estimated parameter solutions for each method are indicated. On this problem the errors in estimated temperature with GES_L do not vary widely over all noise levels, ranging only from 13 percent at 1 percent noise to 17 percent at 50 percent noise. Although it does not always choose the optimal number of clusters, the sensor sensitivity method does an excellent job at estimating the number of clusters for this case. Tikhonov zero-order regularization does not perform particularly well here, especially at high noise levels. At modest noise levels (≤10 percent) the CRESO technique is quite good at estimating the appropriate *t* for Tikhonov regularization.

Figure 11 shows contour plots for the forward computed solution (“true”) and a typical 5 percent noise inverse solution using GES_L and zero-order Tikhonov. Notice that the GES_L inverse solution is quite reasonable, and the zero-order Tikhonov inverse solution (despite its relative error of 26 percent) gives a good qualitative representation of the true solution.

Third Temperature Distribution. In the third forward problem, we chose a source-like temperature distribution. The temperature on the boundaries of the domain was taken to be

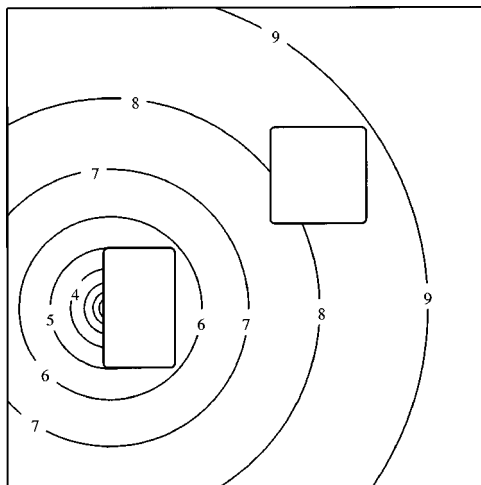


Fig. 12 Temperature contours for third square with holes test case. (Minimum temperature 0.69, maximum temperature 4.84. Contour 1:1.11 2:1.52 3:1.94 4:2.35 5:2.77 6:3.18 7:3.60 8:4.01 9:4.43).

Table 9 Inverse relative error in temperature for the third temperature distribution for the square with holes test case (mean±std.)

		Noise Level					
		1	2	5	10	20	50
GES _L	Optimal	20.23±0.19	20.21±0.24	20.34±0.41	20.36±0.45	20.57±0.66	20.78±1.14
	Estimated	20.23±0.19	20.21±0.24	20.34±0.41	20.36±0.45	20.57±0.66	20.78±1.14
TIK-0	Optimal	9.28±1.25	9.61±1.21	10.75±1.20	11.66±1.92	13.16±1.50	14.87±1.92
	Estimated	9.69±1.49	9.88±0.86	11.90±2.43	12.55±1.83	13.82±2.00	15.75±1.87

Table 10 Inverse relative error in heat flux for the third temperature distribution for the square with holes test case (mean±std.)

		Noise Level					
		1	2	5	10	20	50
GES _L	Optimal	85.50±0.07	85.55±0.11	85.58±0.19	85.58±0.27	85.74±0.41	85.94±0.88
	Estimated	85.50±0.07	85.55±0.11	85.58±0.19	85.58±0.27	85.74±0.41	85.94±0.88
TIK-0	Optimal	72.88±3.58	73.95±4.23	75.87±2.70	76.02±4.42	77.89±2.88	78.46±2.20
	Estimated	74.69±6.35	74.86±2.38	80.39±8.20	77.87±4.00	81.45±5.56	80.27±3.42

$$T = -\ln r/a, \quad (28)$$

where

$$r = \sqrt{(x-x_o)^2 + (y-y_o)^2}.$$

Here $a=2$, $x_o=0.215$, and $y_o=0.375$. This is the temperature pattern for a pure source located at x_o, y_o , and we chose the source point to lie just inside the rectangular hole. Hence, the temperature everywhere in the domain will be given by Eq. (28). The temperature on the boundaries near the source is high but not infinite, and the temperature drops off logarithmically as we move away from the source point. Figure 12 shows the temperature contours for the numerical forward solution.

We added random Gaussian noise to the forward-computed solution on the outer boundary to examine the effects of noise on the inverse solution. As before we applied temperature and heat flux perturbations, and twenty-five trials were performed for each noise level.

Tables 9 and 10 show the mean and standard deviation of the RE in temperature (Table 9) and heat flux (Table 10) on the outer boundary for each noise level and for each of the inverse algorithms under consideration, and optimal parameter and estimated parameter solutions for each method are indicated. In this case GES_L, which is seeking smooth solutions, performs poorly (although the solution is quite similar regardless of the noise level). However, the sensor sensitivity method predicts the optimal N_{clusters} perfectly at each noise level. Tikhonov zero-order regularization performs quite well on this case, and CRESO performs very well at estimating *t* for the inverse. Tikhonov zero-order regularization seeks only to limit the magnitude of the inverse, so that the steep temperature gradients present in this test case pose no problems. However, both methods produce very poor estimates of the heat flux.

Concluding Remarks

We have introduced a new method for estimating the appropriate number of clusters N_{clusters} to use with Generalized Eigensystem (GES_L) method inverses. In addition, we have compared optimal and estimated parameter results for GES_L with Tikhonov zero-order regularization. In four of the test cases, GES_L outperforms Tikhonov regularization. In the fifth test case, a square with holes and a logarithmic temperature pattern, Tikhonov zero-order regularization is substantially better than GES_L. However, in all five test cases the parameter estimation techniques worked well. The sensor sensitivity method for estimating the number of clusters N_{clusters} to be used with GES_L produced excellent results on these test cases. Also, the CRESO technique for estimating *t* for Tikhonov zero-order regularization gave good results.

However, we should note that these results were derived from simulated “data” computed by adding random zero-mean uncorrelated noise to the true solutions. Hence we have not examined

the effects of biased measurements, correlated errors, geometric errors, or other conditions which may arise in actual experiments.

It is clear from this study that vector expansion techniques such as the Generalized Eigensystem method show great promise for steady inverse heat transfer applications. In general, the effectiveness of the GES_L method is directly related to the number of expansion modes needed to accurately represent the unknown temperatures and heat fluxes. If a large number of the GES_L expansion vectors are needed relative to the number of expansion vectors required for zero order Tikhonov regularization (obtained from the singular value decomposition of the transfer matrix), then GES_L will generally not work as effectively as zero order Tikhonov regularization. Hence, for the GES_L method, it is very important to choose expansion vectors in which the expected temperature and heat flux patterns can be represented with only a few modes. In a similar manner, the GES_L method can be extended to solve coupled thermal/stress problems by choosing modes which include appropriate temperature and deformation patterns.

In this paper we have studied the effectiveness of the various techniques, with no attempt to optimize the algorithms for computational speed. Hence, we have not attempted to compare the computational efficiency of the algorithms.

In the future, we hope to further develop these methods for applications in on-line machine tool monitoring. In particular, the inverse techniques discussed in this paper could be extremely valuable in estimating tool tip/workpiece interface temperatures during turning. Here the temperature profile in the tool is quasi-steady, and the interface temperature can be treated as an unknown boundary condition on the tool. Flux and/or temperature sensors placed relatively far from the tip can then be used to estimate the interfacial temperatures, since the problem is reduced to an inverse boundary value problem in steady heat transfer.

Acknowledgment

This work was supported by the National Science Foundation Grant #0001315.

Nomenclature

- \mathbf{A} = matrix relating knowns and unknowns for Tikhonov method
- E = magnitude of the error in the fit to the measured data
- \mathbf{f} = vector of knowns for Tikhonov method
- h = convection heat transfer coefficient
- \mathbf{I} = the identity matrix
- \mathbf{k} = conductivity tensor
- \mathbf{K} = finite element conductivity matrix
- \mathbf{K}_G = finite element boundary gradient matrix
- \mathbf{K}_{Gi} = finite element boundary gradient matrix for inside boundary of domain
- \mathbf{K}_{Go} = finite element boundary gradient matrix for outside boundary of domain
- \mathbf{K}_{ii} = finite element conductivity matrix for inside boundary of domain
- \mathbf{K}_{oi} = finite element conductivity matrix coupling inside and outside boundary of domain
- \mathbf{K}_{oo} = finite element conductivity matrix for outside boundary of domain
- \mathbf{M} = finite element mass matrix
- \mathbf{M}_{ii} = finite element mass matrix for inside boundary of domain
- \mathbf{M}_{oo} = finite element mass matrix for outside boundary of domain
- n_i = number of nodes in the finite element mesh on the inside boundary of domain
- n_o = number of nodes in the finite element mesh on the outside boundary of domain

- n_r = number of nodes in the finite element mesh in the rest of the domain (not on the outside boundary and not on the inside boundary)
- n_{tot} = total number of nodes in the finite element mesh
- $N_{clusters}$ = the number of clusters used in the GES_L expansion
- N_{modes} = the number of modes used in the GES_L expansion
- N_s = the number of sensors
- \mathbf{N} = vector of finite element shape functions
- \mathbf{q} = heat flux vector
- \mathbf{Q}_i = normal nodal heat fluxes on inside boundary of domain
- \mathbf{Q}_o = normal nodal heat fluxes on outside boundary of domain
- $\hat{\mathbf{Q}}$ = inverse estimate for normal nodal heat flux solution
- $\hat{\mathbf{Q}}_i$ = inverse estimate for normal nodal heat flux solution on inside boundary of domain
- $\hat{\mathbf{Q}}_i^j$ = inverse estimate for normal nodal heat flux solution on inside boundary of domain using all sensors except sensor j
- $\hat{\mathbf{Q}}_o$ = inverse estimate for normal nodal heat flux solution on outside boundary of domain
- r = radial coordinate
- \mathbf{R} = regularization matrix
- t = penalty parameter for Tikhonov method
- T = temperature
- \mathbf{T}_i = nodal temperatures on inside boundary of domain
- \mathbf{T}_o = nodal temperatures on outside boundary of domain
- \mathbf{T}_r = nodal temperatures in the rest of the domain
- $\hat{\mathbf{T}}$ = inverse estimate for nodal temperature solution
- $\hat{\mathbf{T}}_i$ = inverse estimate for nodal temperature solution on inside boundary of domain
- $\hat{\mathbf{T}}_i^j$ = inverse estimate for nodal temperature solution on inside boundary of domain using all sensors except sensor j
- $\hat{\mathbf{T}}_o$ = inverse estimate for nodal temperature solution on outside boundary of domain
- \mathbf{x} = vector of unknowns at nodal points
- $\hat{\mathbf{x}}$ = estimate of vector of unknowns at nodal points
- \mathbf{X} = basis vectors for temperature for GES_L method
- \mathbf{X}_i = basis vectors for temperature on inside boundary for GES_L method
- \mathbf{X}_r = basis vectors for temperature for the rest of the domain for GES_L method
- \mathbf{X}_o = basis vectors for temperature on outside boundary for GES_L method
- \mathbf{Y}_i = basis vectors for normal heat flux on inside boundary for GES_L method
- \mathbf{Y}_o = basis vectors for normal heat flux on outside boundary for GES_L method
- $\boldsymbol{\alpha}$ = vector of expansion coefficients for GES_L method
- Γ_o = surface of the outer boundary
- Λ_{ii} = diagonal matrix of eigenvalues associated with inside boundary
- Λ_{oo} = diagonal matrix of eigenvalues associated with outside boundary
- θ = circumferential coordinate
- ∇ = gradient operator

References

- [1] Olson, L. G., and Throne, R. D., 2000, "A Comparison of the Generalized Eigensystem, Truncated Singular Value Decomposition, and Tikhonov Regularization for the Steady Inverse Heat Conduction Problem," *Inverse Problems in Engineering*, **8**, pp. 193–227.
- [2] Throne, R., and Olson, L., 1994, "A Generalized Eigensystem Approach to the Inverse Problem of Electrocardiography," *IEEE Trans. Biomed. Eng.*, **41**, pp. 592–600.
- [3] Throne, R. D., and Olson, L. G., 1995, "The Effects of Errors in Assumed Conductivities and Geometry on Numerical Solutions to the Inverse Problem of Electrocardiography," *IEEE Trans. Biomed. Eng.*, **42**, pp. 1192–1200.
- [4] Olson, L., and Throne, R., 1995, "Computational Issues Arising in Multidi-

- mensional Elliptic Inverse Problems: The Inverse Problem of Electrocardiography," *Eng. Comput.*, **12**, No. 4, pp. 343–356.
- [5] Throne, R. D., Olson, L. G., Hrabik, T. J., and Windle, J. R., 1997, "Generalized Eigensystem Techniques for the Inverse Problem of Electrocardiography Applied to a Realistic Heart-Torso Geometry," *IEEE Trans. Biomed. Eng.*, **44**, pp. 447–454.
- [6] Throne, R. D., Olson, L. G., and Hrabik, T. J., 1999, "A Comparison of Higher-Order Generalized Eigensystem Techniques and Tikhonov Regularization for the Inverse Problem of Electrocardiography," *Inverse Problems in Engineering*, **7**, pp. 143–193.
- [7] Throne, R. D., and Olson, L. G., 2000, "Fusion of Body Surface Potential and Body Surface Laplacian Signals for Electrocardiographic Imaging," *IEEE Trans. Biomed. Eng.*, **47**, pp. 452–462.
- [8] Bathe, K., 1982, *Finite Element Procedures in Engineering Analysis*, Prentice-Hall, Englewood Cliffs, NJ.
- [9] Wilson, E., 1974, "The Static Condensation Algorithm," *Int. J. Numer. Methods Eng.*, **8**, pp. 198–203.
- [10] Martin, T. J., and Dulikravich, G. S., 1995, "Finding Unknown Surface Temperatures and Heat Fluxes in Steady Heat Conduction," *IEEE Trans. Compon. Packag. Manuf. Technol., Part A*, **18**, pp. 540–545.
- [11] Martin, T. J., and Dulikravich, G. S., 1996, "Inverse Determination of Boundary Conditions and Sources in Steady Heat Conduction With Heat Generation," *ASME J. Heat Transfer*, **118**, pp. 546–554.
- [12] Martin, T. J., Halderman, J. D., and Dulikravich, G. S., 1995, "An Inverse Method for Finding Unknown Surface Traction and Deformations in Elastostatics," *Comput. Struct.*, **56**, pp. 825–835.
- [13] Colli-Franzone, P., Guerri, L., Taccardi, B., and Viganotti, C., 1985, "Finite Element Approximation of Regularized Solutions of the Inverse Potential Problem of Electrocardiography and Applications to Experimental Data," *Calcolo*, **22**, pp. 91–186.
- [14] Rudy, Y., and Messinger-Rapport, B. J., 1988, "The Inverse Problem in Electrocardiography: Solutions in Terms of Epicardial Potentials," *CRC Critical Reviews in Biomedical Engineering*, **16**, pp. 215–268.
- [15] Messinger-Rapport, B., and Rudy, Y., 1989, "Computational Issues of Importance to the Inverse Recovery of Epicardial Potentials in a Realistic Heart-Torso Geometry," *Math. Biosci.*, **97**, pp. 85–120.
- [16] Johnston, P. R., and Gulrajani, R., 1997, "A New Method for Regularization Parameter Determination in the Inverse Problem of Electrocardiography," *IEEE Trans. Biomed. Eng.*, **44**, pp. 19–39.
- [17] Hansen, P., 1992, "Numerical Tools for the Analysis and Solution of Fredholm Integral Equations of the First Kind," *Inverse Probl.*, **8**, pp. 849–872.
- [18] Hansen, P., 1992, "Analysis of Discrete Ill-Posed Problems by Means of the L-Curve," *SIAM Rev.*, **34**, pp. 561–518.
- [19] Hansen, P., and O'Leary, D. P., 1993, "The Use of the L-Curve in the Regularization of Discrete Ill-Posed Problems," *SIAM (Soc. Ind. Appl. Math.) J. Sci. Stat. Comput.*, **14**, pp. 1487–1503.
- [20] Trujillo, D., and Busby, D., 1997, *Practical Inverse Analysis in Engineering*, CRC Press.
- [21] Maillot, D., Degiovanni, A., and Pasquetti, R., 1991, "Inverse Heat Conduction Applied to the Measurement of Heat Transfer Coefficient on a Cylinder: Comparison Between an Analytical and a Boundary Element Technique," *ASME J. Heat Transfer*, **113**, pp. 549–557.
- [22] Truffart, B., Jarny, Y., and Delaunay, D., 1993, "A General Optimization Algorithm to Solve 2-D Boundary Inverse Heat Conduction Problems Using Finite Elements," In N. Zabarab, K. A. Woodbury, and M. Raynaud, eds., *Inverse Problems in Engineering: Theory and Practice*, Palm Coast, FL, pp. 53–60.
- [23] Dennis, B. H., and Dulikravich, G. S., 1998, "A Finite Element Formulation for the Detection of Boundary Conditions in Elasticity and Heat Transfer," in M. Tanaka and G. S. Dulikravich, eds., *Proceedings of the International Symposium on Inverse Problems in Engineering Mechanics-ISIP '98*, Nagano, Japan, pp. 61–70.
- [24] Dennis, B. H., and Dulikravich, G. S., 1999, "Simultaneous Determination of Temperatures, Heat Fluxes, Deformations, and Traction on Inaccessible Boundaries," *ASME J. Heat Transfer*, **121**, pp. 537–545.

Film Cooling of a Cylindrical Leading Edge With Injection Through Rows of Compound-Angle Holes

Y.-L. Lin

T. I.-P. Shih

Fellow ASME, Professor

Department of Mechanical Engineering,
Michigan State University,
East Lansing,
MI 48824-1226

Computations, based on the $k-\omega$ shear-stress transport (SST) turbulence model in which all conservation equations were integrated to the wall, were performed to investigate the three-dimensional flow and heat transfer about a semi-cylindrical leading edge with a flat afterbody that is cooled by film-cooling jets, injected from a plenum through three staggered rows of compound-angle holes with one row along the stagnation line and two rows along ± 25 deg. Results are presented for the surface adiabatic effectiveness, normalized temperature distribution, velocity vector field, and surface pressure. These results show the interactions between the mainstream hot gas and the cooling jets, and how those interactions affect surface adiabatic effectiveness. Results also show how "hot spots" can form about the stagnation zone because of the flow induced by the cooling jets. The computed results were compared with experimental data generated under a blind test. This comparison shows the results generated to be reasonable and physically meaningful. With the SST model, the normal spreading was under predicted from 20 to 50 percent. The lateral spreading was over predicted above the surface, but under predicted on the surface. The laterally averaged surface effectiveness was well predicted.

[DOI: 10.1115/1.1370513]

Keywords: Computational, Film Cooling, Heat Transfer, Turbines, Turbulence

Introduction

Advanced gas-turbine stages are being designed to operate at increasingly higher gas temperatures at their inlets to improve thermal efficiency. To accommodate these high temperatures, which can be higher than allowable material temperatures, film cooling in addition to internal cooling is needed to maintain acceptable temperature distributions in components such as vanes, blades, and endwalls that come in contact with the high-temperature mainstream flow. Film cooling lowers material temperature by forced convection inside film-cooling holes and by forming a protective layer of cooler air next to the vane or blade surface to insulate it from the hot gas. On film coverage, it is important to design film-cooling jets that do not lift off or move away from surfaces in need of thermal protection. Since the air used for cooling (here referred to as coolant) is extracted from the compressor, which can be harnessed for useful work, efficiency considerations demand that acceptable temperature distributions in the turbine material be achieved by using minimal amount of coolant flow while enabling a higher turbine inlet temperature.

To cool effectively with minimal cooling flow requires a good understanding of the details of the fluid mechanics and heat transfer processes involved. The importance of this problem has led many investigators to study film cooling (see review by Simoneau and Simons [1]). One region that is especially difficult to film cool efficiently is the leading edge of the first-stage stator airfoils, where there are stagnation zones and the approaching freestream temperature is the highest. Experimental studies on leading-edge film cooling have been reported by Hanus and L'Ecuyer [2], Karni and Goldstein [3], Camci and Arts [4], Mayle and Anderson [5], Ou and Han [6], Salcudean et al. [7], Cruse et al. [8], Ames [9,10], and others. Parameters investigated include mainstream

turbulence, film-cooling-hole geometry, and coolant-to-mainstream mass-flux and momentum ratios. Computational fluid dynamics (CFD) studies on leading-edge-film cooling have focused on the ability of CFD to predict adiabatic effectiveness and surface heat transfer by using mostly low-order turbulence models, such as Baldwin-Lomax, $k-\epsilon$ and $k-\omega$. Of the CFD studies, Garg and Gaugler [11] and Heidmann et al. [12] simulated realistic airfoil configurations with emphasis on film-cooling-hole exit profiles. Bohn et al. [13] also accounted for conjugate heat transfer. See Kercher [14] for a bibliography of all papers on leading-edge film cooling from 1972 to 1998.

On film cooling of leading edges, one unresolved question is why hot spots form despite seemingly more than adequate cooling flow. To address this question, Pratt and Whitney GESP organized a study involving a carefully designed and calibrated experimental study [8] and a series of CFD simulations performed by a number of invited participants (Chernobrovkin and Lakshminarayana [15], Lin, Stephens, and Shih [16], Martin and Thole [17], and Thakur, Wright, and Shyy [18]). All CFD simulations were carried out in a blind-test fashion in which experimental data are not released until the CFD simulations are completed and submitted. This paper continues the effort of Lin et al. [16] to understand the interactions between the mainstream and film-cooling jets in the thermal protection of the leading-edge region.

Problem Description

Schematic diagrams of the problem studied are given in Figs. 1 and 2. Figure 1 shows the experimental setup of Cruse et al. [8], and Fig. 2 shows the computational model of the experimental setup. The experimental setup consists of a square duct ($149 \times 149 \text{ mm}^2$) in which hot gas approaches an obstruction made up of two perpendicular plane walls connected by a quarter-cylindrical wall (radius of 50.8 mm). Within the cylindrical wall are a plenum and two rows of film-cooling holes arranged in a staggered fashion with 9 holes in each row (see Fig. 2). The di-

Contributed by the Heat Transfer Division for publication in the JOURNAL OF HEAT TRANSFER. Manuscript received by the Heat Transfer Division April 28, 1999; revision received January 9, 2001. Associate Editor: J.-C. Han.

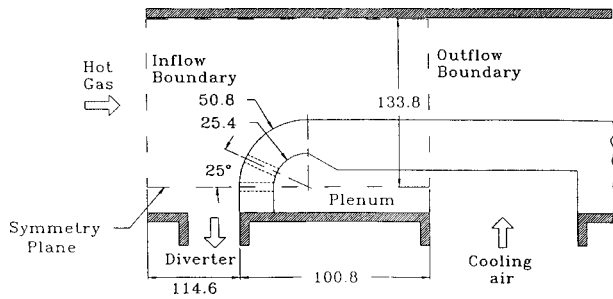


Fig. 1 Schematic of experimental setup [7]

ameter of each hole is 6.32 mm. The inclination of the holes is along the radius of the cylindrical wall and 20 deg relative to the spanwise direction. The spacing between holes in each row is 48.3 mm. The separation between the two rows of holes in the x - y plane is 25 deg. All hole edges are essentially sharp (radius less than 0.1 mm). The material of the cylindrical wall is polystyrene with a thermal conductivity of 0.025 W/m-K so that the walls are nearly adiabatic (in the measurements, a correction was made for the heat loss by conduction). Also, all surfaces are smooth (roughness is less than 100 μ m in the holes and less than 25 μ m elsewhere).

The hot gas approaching the quarter-cylindrical leading edge and the cooler gas entering through the plenum are both 50 percent dry air plus 50 percent pure N_2 with properties that are within 1.5 percent of dry air alone. At a distance of 140 mm upstream of the leading edge, the approaching flow has a nearly uniform profile with velocity (U_∞) of 10 m/s, turbulent intensity less than 0.5 percent, static pressure of 1 atm, and static temperature of 300 K. The cooling flow that enters through the plenum will produce an average coolant-to-mainstream density ratio (DR) of 1.8 and an average coolant-to-mainstream mass-flux ratio (M) of 2.0. The width of the diverter and the flow through it are adjusted to ensure that the stream surface approaching the stagnation line on the cylinder is flat and parallel to the duct axis in the absence of film cooling (measurements showed variations to be less than 1 mm). The reader is referred to Cruse et al. [8] for additional details.

For the problem just described, the computational domain is taken to be the region bounded by the dash lines shown in Fig. 1 and reproduced in Fig. 2. As can be seen, this domain assumes symmetry about the stagnation stream surface so that the leading edge is semi-cylindrical with three rows of film-cooling holes instead of quarter-cylindrical with two rows of cooling holes. This

domain also assumes periodicity in the y - z plane so that fewer holes need to be simulated. Measurements by Cruse et al. [8] show that these assumptions are reasonable.

As noted, computations were carried out in a blind-test fashion. Measurements made by Cruse et al. [8] on adiabatic effectiveness (η) and normalized temperature distributions (Θ) along selected planes for validation were provided only after submission of the computed results.

Problem Formulation

The flow and heat transfer problem about the film-cooled, semi-cylindrical leading edge is modeled by the ensemble-averaged conservation equations of mass (continuity), momentum (compressible Navier-Stokes), and total energy for a thermally and calorically perfect gas. Though the Mach number of the flow is low, the compressible form of the conservation equations was used because of the non-negligible density variations that result from temperature differences between the cooling air and the mainstream hot gas. The ensemble-averaged equations were closed by Menter's k - ω shear-stress transport (SST) turbulence model (Menter [19]), which can be applied in both the high and low Reynolds number region of the turbulent flow field. The SST model is a blend of the k - ω model of Wilcox [20] in the near-wall region and the standard k - ϵ model further away from the wall. Thus, like the k - ω model, the SST model does not require explicit damping near the wall because ω becomes extremely large as the wall is approached. The blending of the k - ϵ model is to eliminate the dependence on freestream values of ω . Also, there is a limiter, which controls the eddy viscosity so that the turbulent shear stress is bounded by a constant times the turbulent kinetic energy (a realizability constraint), which improves prediction of flows with strong adverse pressure gradients and flow separation (Kandula and Wilcox [21] and Bardina et al. [22]). The details of the ensemble-averaged equations along with the SST model used are not given here since they are well documented in the literature (see, e.g., Shih and Sultanian [23]).

The boundary conditions employed in this study for the different boundaries shown in Fig. 2 are as follows. At the inflow boundary, velocity and temperature profiles were kept uniform at 10 m/s and 300 K, respectively. Profiles of the turbulence quantities (k and ω) were also kept uniform (turbulent intensity set at 0.5 percent with effective viscosity equal to laminar viscosity). Only pressure was extrapolated. At the outflow boundary, an average back pressure of 0.999047 atm was imposed, but the pressure gradient was extrapolated. The velocity and density at that boundary were also extrapolated. At the plenum inflow, velocity and temperature (167.26 K) profiles were assumed to be uniform at

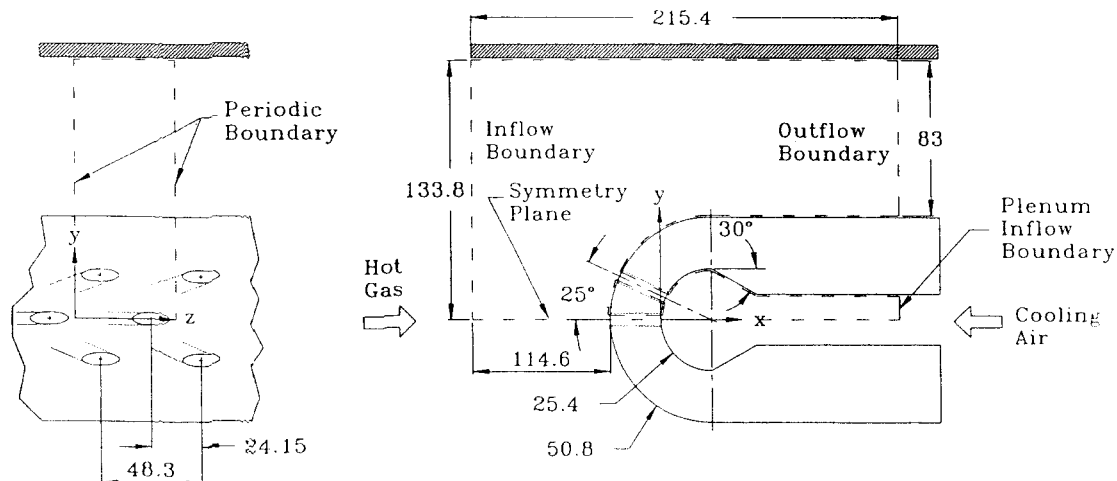


Fig. 2 Schematic of computational model

0.8591 m/s and 167.26 K, respectively. The temperature was selected to give a DR of 1.8. Since the flow rates through holes in different rows differ because of differences in pressure around the cylinder, the value of the plenum inflow velocity was iterated until an overall coolant-to-mainstream mass-flux ratio of 2.0 was obtained. The turbulence levels at the plenum inflow were taken to be negligibly small. Standard symmetry and periodic boundary conditions were imposed on the symmetry and periodic boundaries.

In this study, wall functions were not used. All equations including those for the turbulence quantities were integrated to the wall. At all walls, the no-slip and adiabatic wall conditions were imposed; the turbulent kinetic energy (k) was set to zero; and ω was set to $60\nu/(\beta Y^2)$, where ν is kinematic viscosity and Y is the normal distance from the wall.

Numerical Method of Solution

Solutions to the governing equations were obtained by using a research code called CFL3D, which is based on a cell-center finite-volume method (see Thomas et al. [24] and Rumsey and Vatsa [25]). In this study, the spatial differencing are all second-order accurate. The inviscid terms were approximated by flux-difference splitting of Roe [26,27]. All diffusion terms were approximated conservatively by differencing derivatives at cell faces. Since only steady-state solutions are sought, time derivatives were approximated by the first-order accurate Euler implicit

formula. The system of nonlinear equations that resulted from the aforementioned approximations to the space- and time-derivatives were analyzed by using a diagonalized alternating-direction implicit scheme (Pulliam and Chaussee [28]) with local time-stepping and three-level V-cycle multigrid (Ni [29], Anderson et al. [30]).

The domain of the problem (region within the dash lines in Figs. 1 and 2) was represented by a multi-block grid system with seven blocks of structured grids, some patched and some overlapped (Fig. 3). The patched/overlapped approach makes it possible to concentrate grid points where most needed and still maintain a high quality grid system in smoothness and nearly orthogonality. The seven blocks are as follows: a boundary-fitted H-H grid for the plenum, a C-H grid for the cylindrical leading edge and flat afterbody, an H-H grid for the rest of the flow domain about the leading edge, two O-H grids for the two film cooling holes, and two H-H grids to eliminate the centerline singularity associated with the two O-H grids. The O-H and H-H grids for each film-cooling hole are patched to the grid in the plenum and the grid about the leading edge. The C-H grid about the leading edge overlaps the H-H grid for the rest of the domain. The computations were carried out in one block at a time until all blocks are analyzed, and this is repeated until a converged solution is obtained. Data transfer between patched and overlapped grids is obtained by trilinear interpolation.

In this study, three different grid systems were used. For all

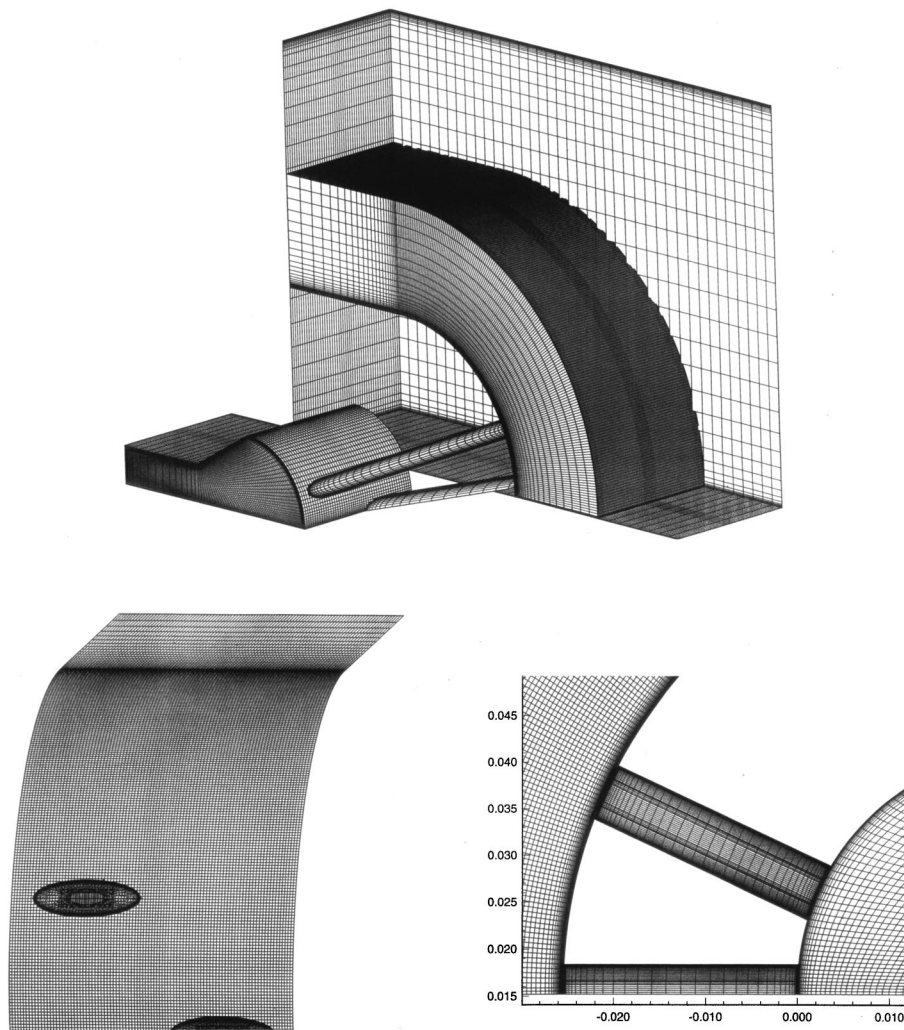


Fig. 3 Grid system used: overall grid and grid about film-cooling holes

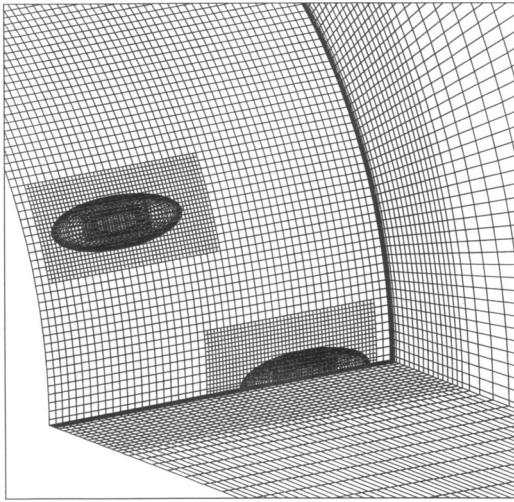


Fig. 4 Coarsest grid used for grid-independence study

three, the number of grid points and their distributions were obtained by using a very stringent set of rules established by developers of numerical methods and turbulence models to ensure accuracy. These rules include having at least five grid points within a y^+ of five and having grid spacing next to walls kept constant for at least three grid points to resolve turbulent boundary layers. Other rules include aligning grid with flow direction as much as possible and keeping grid-aspect ratio near unity in regions of recirculating flow (e.g., in mainstream-jet interaction roll-up regions). For further details on the rules, see Stephens et al. [31].

In order to satisfy the aforementioned rules, information about the solution (such as boundary-layer thickness at leading edge as well as location and size of the mainstream-jet interaction regions) is needed but unavailable for the first simulation. Thus, the first of the three grids used was generated by using estimates. The leading-edge boundary-layer thickness was estimated by using the similarity solution for stagnation flow. To estimate the mainstream-jet interaction regions, film-cooling studies on flat plates were used with a factor of safety added (i.e., used a very fine grid with grid-aspect ratio near one over a region larger than suggested by the flat plate studies). After obtaining a converged solution with the first grid, a second grid was generated that made use of the solution from the first grid. This grid system has 1.78 million grid points (Fig. 3). The converged solution obtained with the second grid is deemed excellent because all key features of the flow were well within regions where grid points were clustered and all rules were satisfied. Since the rules were quite stringent, a third grid was constructed to examine if the rules can be relaxed. The third grid system was generated by removing every other grid in the C-H grid that surrounded the leading edge and the after-body, which contained the majority of the grid points, but has a layer of fine grid embedded over each film-cooling hole to resolve the hole geometry (Fig. 4). This grid system—with 0.24 million grid points—still has 3 grid points within a y^+ of 5. The converged solution obtained with the “coarser” third grid was within 2 to 5 percent of the solution obtained by using “finer” second grid. Since this was a blind test, only the “best solution” obtained is reported, namely that generated by using the second grid.

On a Cray C-90 computer, where all computations were performed, the memory and CPU time requirements are 83.4 megawords and 33.3 hours. The CPU time given is for a converged steady-state solution, which typically involved 5000 iterations. The number of iterations needed to converge was excessively high

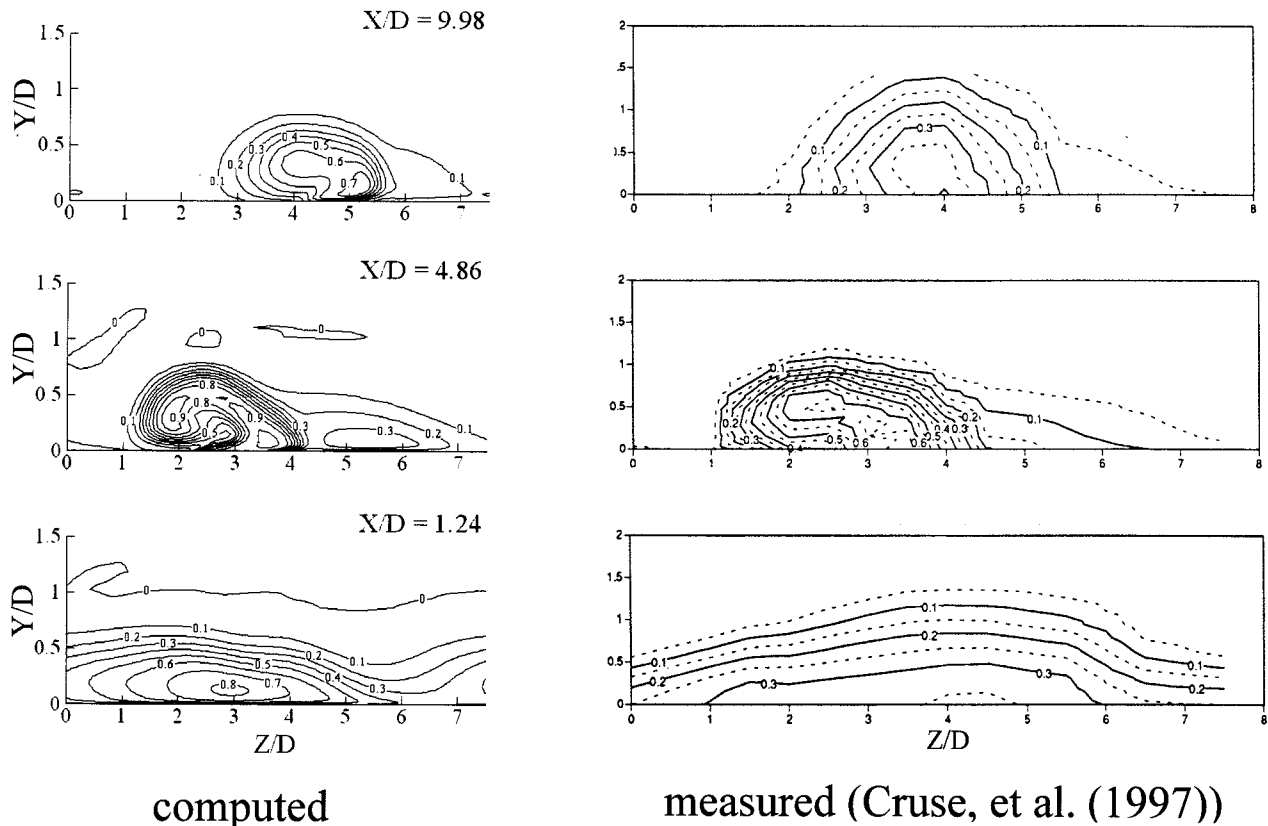


Fig. 5 Computed and measured normalized temperature Θ as a function of Z/D and Y/D at three X/D locations

because the Mach number of the flow was very low, less than 0.01. If the mainstream Mach number is 0.05 or higher, which is more typical of realistic engine conditions, then only about 1500 to 2000 iterations would be needed. Here, a solution is said to be converged when all of the following are satisfied: (1) residual drops at least three orders of magnitude; (2) the second norm of the residual is less than 10^{-13} ; and (3) normalized surface temperature Θ on the leading edge varies by less than 2 percent for over 500 iterations. At this point, it is also noted that if the "coarser" third grid is used, then only 4.5 C-90 hours would be needed to obtain a converged solution.

Results and Discussion

In this section, we first assess the capability of the CFL3D code with the SST turbulence model in predicting leading-edge film cooling in a blind test. Afterwards, we interrogate the flow field by analyzing the computed results with focus on how fluid mechanics affects adiabatic effectiveness and the formation of hot spots.

Comparison With Experiments. Figure 5 shows computed and measured normalized temperature Θ at three X/D locations.

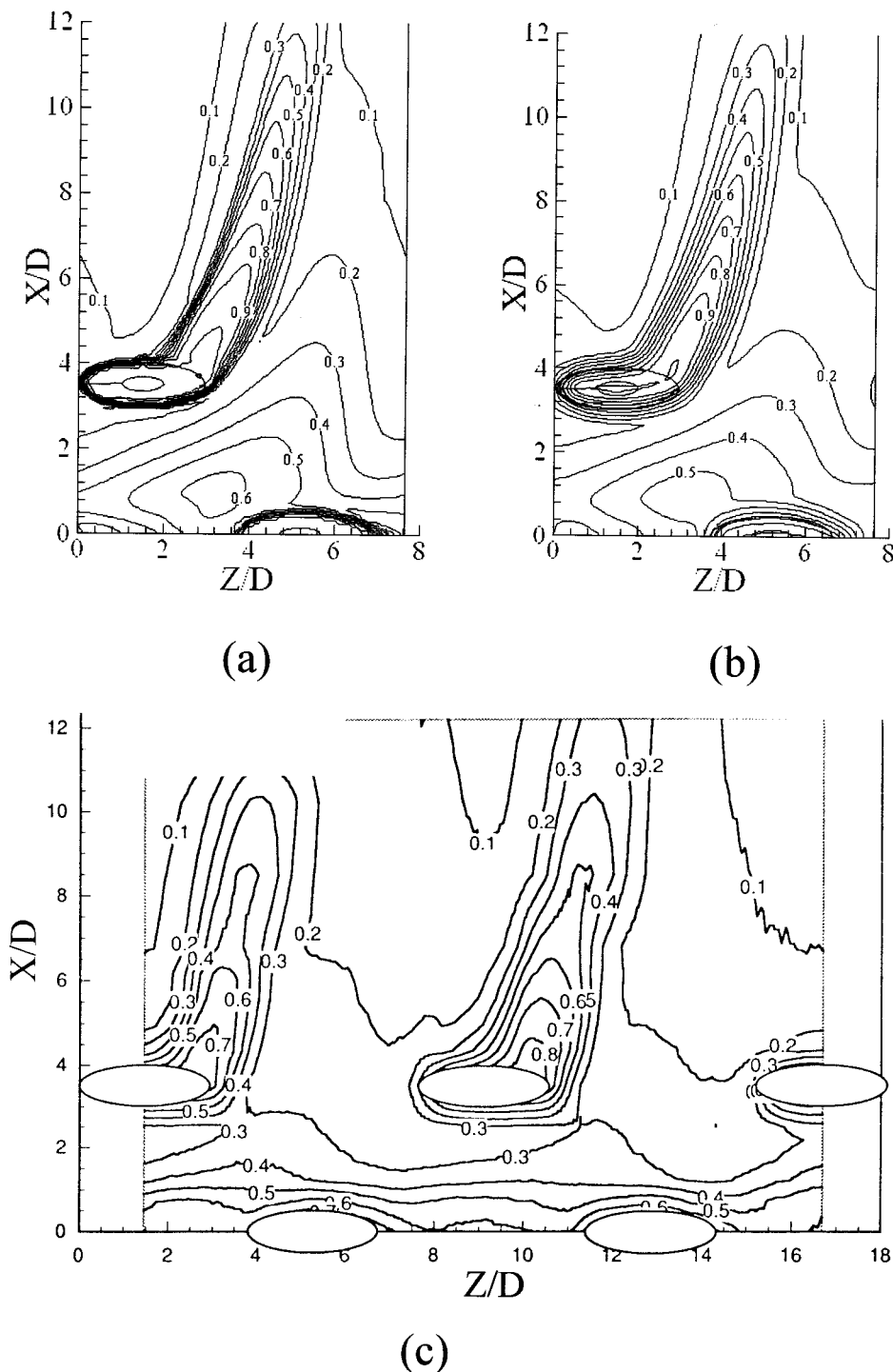


Fig. 6 Adiabatic effectiveness η : (a) computed; (b) computed, averaged over $0.43D \times 0.43D$; and (c) measured with resolution of $0.43D \times 0.43D$ [7].

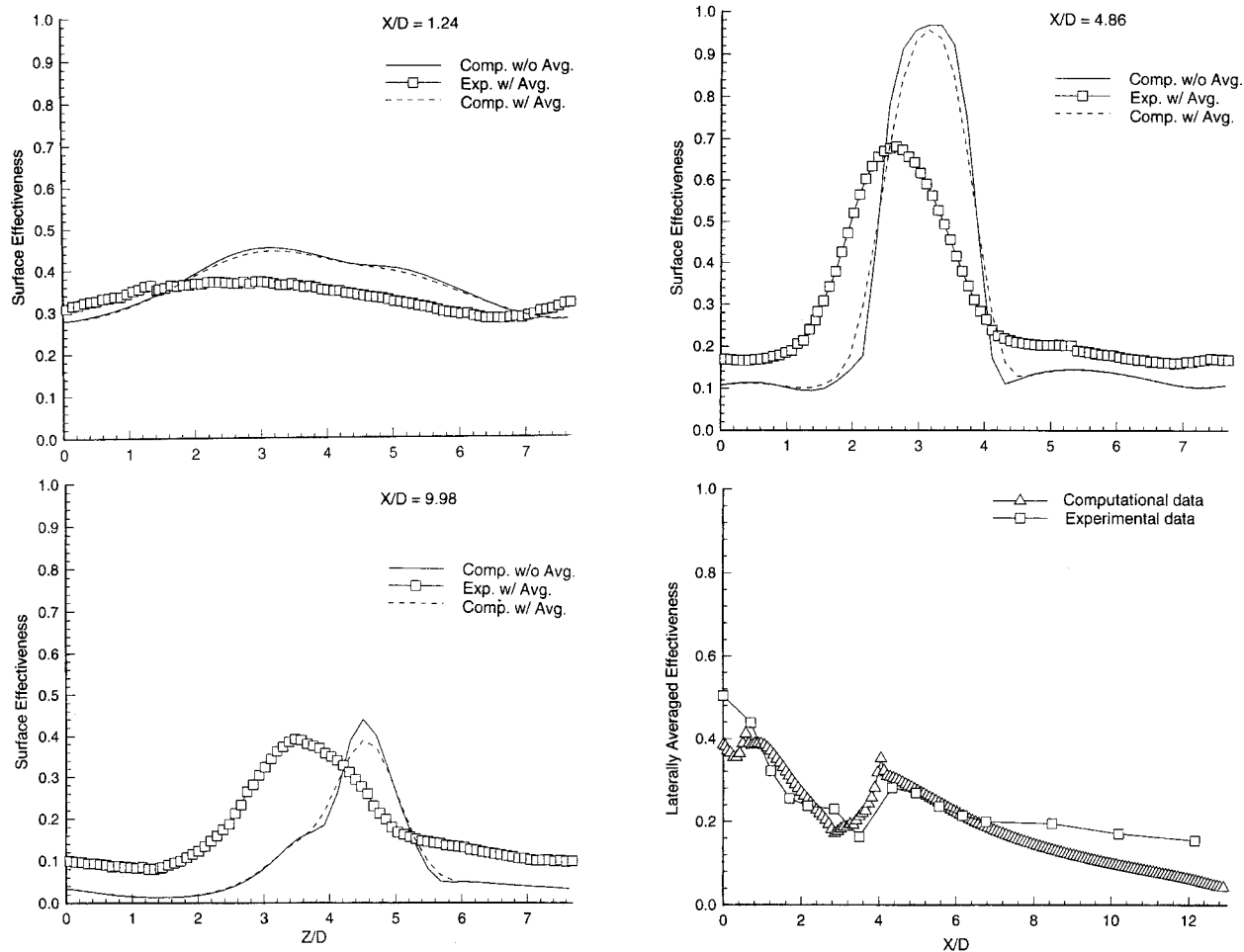


Fig. 7 Adiabatic effectiveness, local and laterally averaged

Since the temperature is a scalar transported by the cooling jet, this figure shows the spread of the cooling jets in the normal (Y) and lateral (z or Z) directions. At $X/D=1.24$, the computed and measured spreads are comparable. At $X/D=4.86$, the computations under predict the spread in the normal direction by about 20 percent. The predicted lateral spread of the coolant from the second-row holes range from about $1 < Z/D < 4.5$ above the surface to $1.5 < Z/D < 4.5$ on the surface. In the measurements, it is about $1 < Z/D < 4.5$. Note that cooler gas at Z/D greater than approximately 4.5 is due to coolant from the symmetry-plane holes. Thus, the lateral spreading is predicted more accurately above the surface than on the surface. This is because the computed results predict more entrainment of hot gas to the surface (see hot gas beneath the roll-up next to surface) than does the measurements. This error can be attributed to the turbulence model used, which cannot account for the effects of eddy flattening in the near wall region as the rolled up flow impinges on the surface. At $X/D=9.98$, the normal spread is under predicted by about 50 percent. The predicted lateral spread ranges from $2.5 < Z/D < 7$ above the surface to $3 < Z/D < 5.5$ at the surface. In the experiment, the lateral spread was $2 < Z/D < 5.5$, and was found to be largest on the surface, which was not predicted. Thus, the computations under predict the normal spreading, over predict the lateral spreading above the surface, and under predict the lateral spreading on the surface.

Figure 6 shows the computed and measured adiabatic effectiveness, which is the normalized temperature on the surface of an adiabatic wall. Note that the computed results are presented in two ways—one in which the value given at each point is the average

over an area of $0.43 D \times 0.43 D$, and another in which no averaging was used. This averaging was made because the measurement resolution on the wall is $0.43 D \times 0.43 D$. From this figure, it can be seen that the computed adiabatic effectiveness is qualitatively similar to the measured ones. Basically, the topology of the highs and the lows is in the same locations with similar shapes, and the order of magnitude of the numbers is similar. From this figure, it can be seen that the computations under predict the spread of the coolant from the symmetry-plane holes in the X/D direction. It also under predicts the spread of the coolant from the second-row holes in the Z/D direction. By comparing the $\eta=0.2$ contour line in Figs. 6(b) and 6(c) in the region on the right of the second-row holes, one can see that computations under predict the mixing of the coolant from the symmetry and the second-row holes.

A quantitative comparison of adiabatic effectiveness is shown in Fig. 7. This figure shows the adiabatic effectiveness induced by the symmetry-plane holes to be computed reasonably accurately at $X/D=1.24$. At $X/D=4.86$ and 9.98 , the adiabatic effectiveness was predicted with less accuracy. The main reason is that computations predicted more entrainment to the surface. The laterally-averaged adiabatic effectiveness, however, does agree well with measured values.

As noted, this is a blind test. The qualitative and quantitative comparisons given above show the computations to be physically reasonable.

Discussion of Computed Results. With some confidence in the computed results, this section discusses the flow field, temperature distribution, and adiabatic effectiveness associated with the leading-edge film cooling problem shown in Fig. 2.

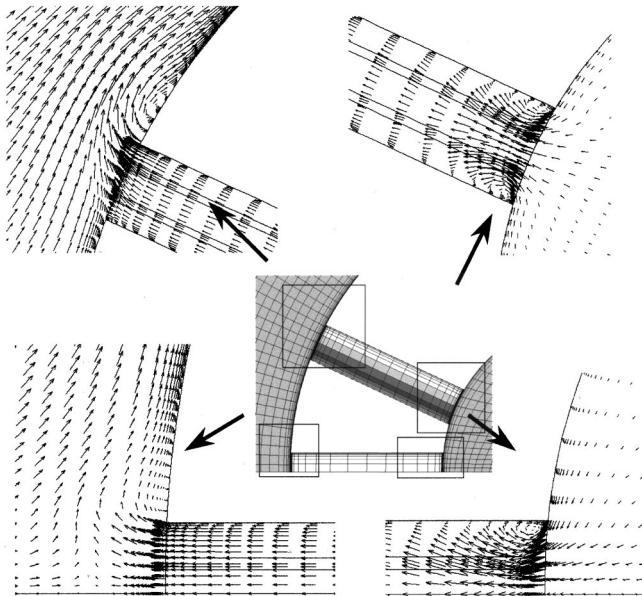


Fig. 8 Velocity-vector field about the middle of a symmetry-plane hole and the middle of a second-row hole in two x - y planes

Flow Field. The flow field can be deduced from Figs. 8–11. Figure 8 shows that there is a large separation bubble (about $D/\sin(20\text{deg})$ in length) at the inlets of the symmetry-plane and the second-row holes because of the vena contracta effect. The separation bubbles are not symmetric about the hole centerlines. They are largest in the x - y plane (shown in Fig. 8) and smallest in the y - z plane (not shown). This is because the magnitude of the

velocities is larger in the x - y plane though turning angles can be larger in the y - z plane. These asymmetric separation bubbles induce secondary flows in the cross stream. These secondary flows were also observed by Leylek and Zerkle [32]. Further downstream along the holes (about $5D$ to $6D$), the flow does become nearly axially symmetric. For this problem, the L/D ratio of the film-cooling holes is 11.75 (L is length of hole), which is much larger than 6. Thus, plenum-hole interactions are relatively unimportant here except in affecting the discharge coefficient. However, for holes with smaller L/D ratios, it can be important. For such holes, their inlets can be shaped and/or angled to create the desired symmetry or asymmetry in the flow that would bring about the best cooling jet in terms of better adiabatic effectiveness. At this point, it is noted that the mass flow rate through the symmetry-plane (1st row) holes is less than that through the second-row (2nd row) holes. This is because the pressure difference across the 1st row holes is smaller due to the stagnation zone about the symmetry plane of the leading edge. The split between the 1st and 2nd row holes is 48 to 52. Thus, the coolant-to-mainstream mass-flux ratio is less than 2.0 for the 1st row holes and greater than 2.0 for the 2nd row holes.

Once the cooling jets emerge from the 1st row holes, the following four interactions take place: jet-jet from 1st row holes, jet and mainstream, spanwise acceleration due to favorable pressure gradient induced by the curved geometry, and jets from 1st and 2nd row holes. Jet-jet interaction from 1st row holes along the z -direction causes an adverse pressure gradient region to form just upstream of each 1st row hole (Fig. 9). These adverse pressure gradients produce small separation bubbles between holes (P1 in Fig. 9). It also causes jets from 1st row holes to spread along the X -direction. The effect of the mainstream on coolant from the 1st row holes can be seen in Fig. 10 (P1, P2, and S1 to S6 for $X/D < 3$). In planes P1 and P2 of Fig. 10, the 1st row hole jets can be

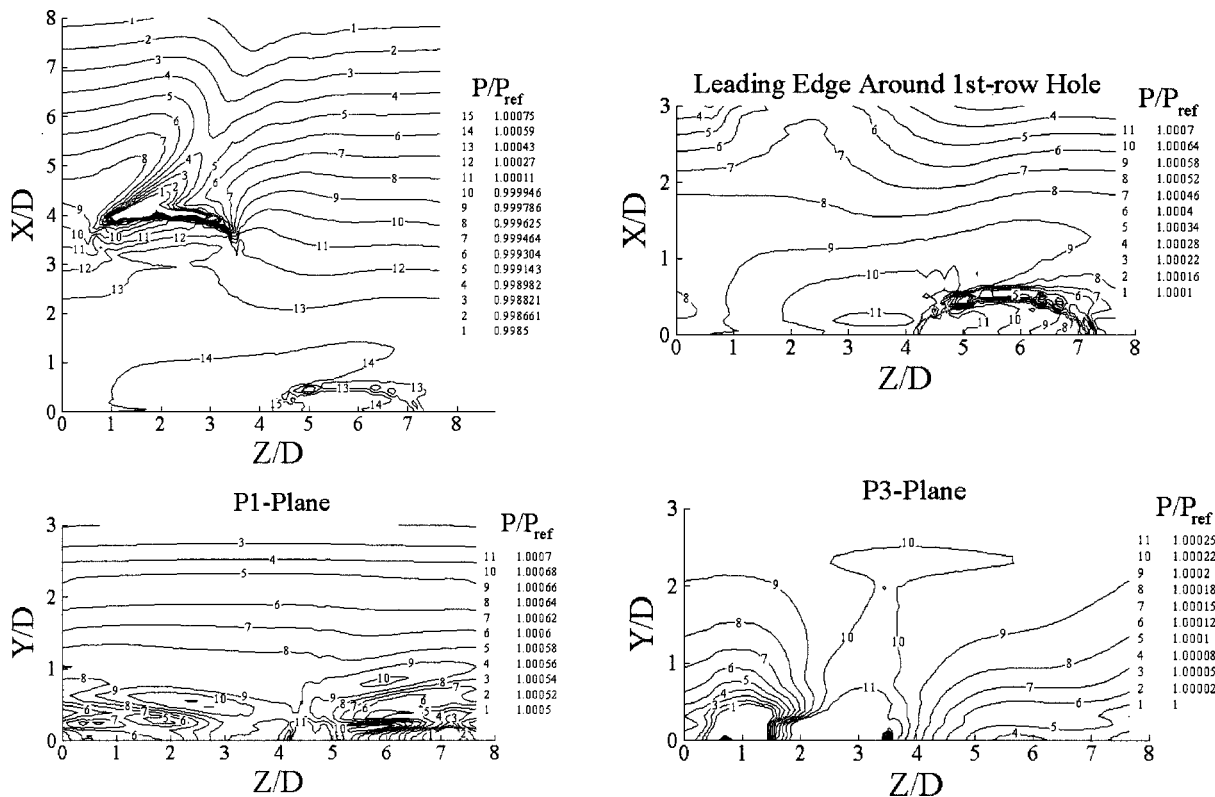


Fig. 9 Pressure contours on the cylindrical surface (X - Z plane at $Y=0$) and two Y - Z planes (P1: $X/D=0$, P3: $X/D=3.50$; see Fig. 10)

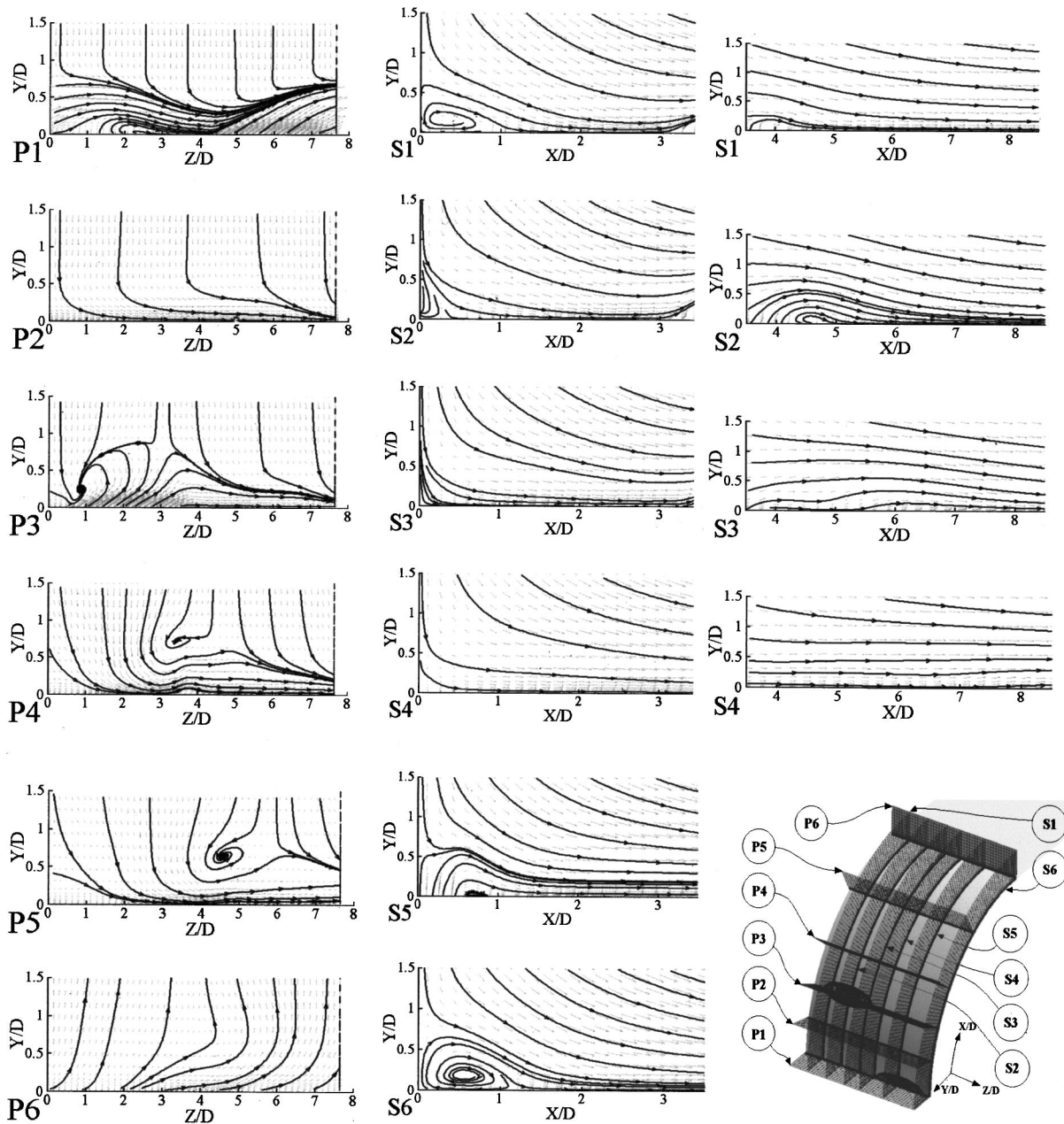


Fig. 10 Projected streamlines at selected $Y-Z$ and $X-Y$ planes. P1, . . . , P6 correspond to $X/D=0, 1.84, 3.50, 5.47, 8.47,$ and $12.72,$ respectively. S1, . . . , S6 correspond to $Z/D=1.10, 2.24, 3.37, 4.27, 5.73,$ and $7.64,$ respectively.

seen to cause the mainstream flow to acquire a velocity component in the z -direction as it approaches the leading edge because of viscous pumping. The z -component velocity acquired by the mainstream flow coupled with the outward flow of the 1st row jets against the mainstream flow caused the formation of horseshoe-like vortices that eventually get underneath the 1st row jets. This brings hot gases in the mainstream next to the vane or blade surface (Fig. 11). This indicates that coolant from 1st row holes must completely overlap each other to prevent the formation of hot spots. Figure 11 also shows the lateral spreading of the 1st row jets in the X -direction, which is affected by flow acceleration along X and coolant issuing from the 2nd row holes. In that figure, coolant from 1st row holes can be seen to flow towards the region between 2nd row holes. Some coolant from the 1st row holes can also be seen to flow over the jet issuing from the 2nd row holes (see plane B in Fig. 11).

Cooling jets from the 2nd row holes separate and lift off once

exiting the holes (see Figs. 8 and 10). This is because cooling jets from the 2nd row holes emerge with higher velocity than those from 1st row holes. Reasons for the higher velocity include higher pressure difference between the plenum and the hole exits (pressure driven) and decreased effective hole-exit area because of flow distortion. Thus, effective mass-flux ratio from the 2nd row holes is beyond the overall average of 2.0. Figure 5, planes P3, P4, P5, and S2 in Fig. 10, and plane B in Fig. 11 show the strong and asymmetric shear-layer interaction between the mainstream and the coolant issuing from the 2nd row holes. This interaction causes the mainstream hot gas to be entrained by the cooling jet and drawn to the surface, making the film-cooling jet from the second-row holes less effective.

Figure 9 shows cooling jets from both the 1st and 2nd row holes to create considerable disturbances to the aerodynamics by inducing strong pressure gradients in the streamwise and spanwise directions in the vicinity of the film-cooling holes and across the

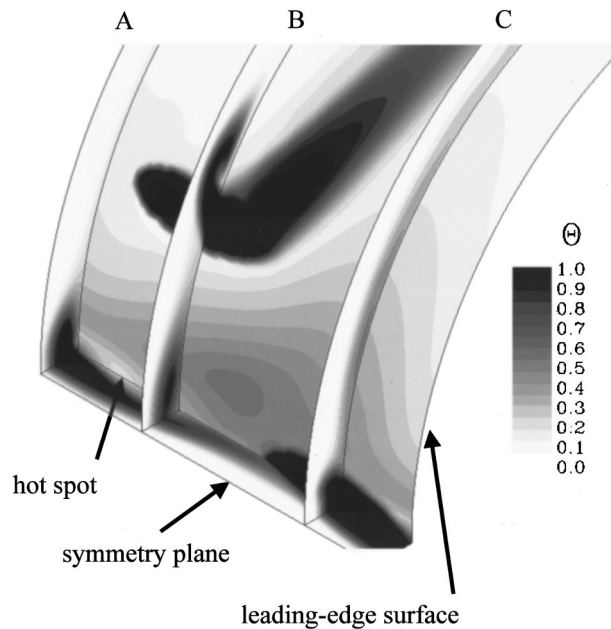


Fig. 11 Normalized temperature Θ at the symmetry plane and the leading-edge surface

wakes of cooling jets. In the symmetry plane (P1), Fig. 9 shows the coolant from the 1st row holes to affect the pressure distribution up to about $Y/D=1$ from the leading-edge stagnation zone. In the P3 plane of Fig. 9, the pressure disturbance induced by coolant jets can be seen to extend to Y/D of 2.5.

Temperature Distribution and Surface Adiabatic Effectiveness. Figures 5 and 11 show normalized temperature Θ distributions. From this figure, entrainment of hot gas into the cooling jet by mainstream-jet interaction can clearly be seen (at $X/D=4.86$ in Fig. 5 and planes B and C in Fig. 11). Basically, mainstream hot gas and coolant rolled together in layers. Cooling jets from the 2nd row holes entrain more hot gas than do cooling jets from the symmetry-plane holes. This is because the relative velocity between the mainstream flow and coolant jet issuing from 2nd row holes is higher. The entrainment of hot gas by cooling jets from the 2nd row holes is highly asymmetric. Figures 5 and 11 show the entrainment of hot gas by the vortex-like flow on the left side of the coolant jet. This was also observed by Cruse et al. [7]. The leading-edge surface becomes essentially unprotected by the cooling jets after about 50 deg measured from the symmetry plane, but there is a cool layer of gas just above it. This is because the coolant jets were lifted off by the entrained hot gas. This indicates the importance of minimizing entrainment induced by mainstream-jet interaction.

From Figs. 6 and 11, the following observations can be made about adiabatic effectiveness on the semi-cylindrical leading-edge surface. The first observation is that there is a region between the symmetry-plane holes, where adiabatic effectiveness reaches a low value. This low adiabatic effectiveness came about because horseshoe-like vortices entrained hot gases from the mainstream and got underneath the cooling jets. The second observation is that adiabatic effectiveness is low between the second-row film cooling holes. There are several reasons for this. First, cooling jets from the 1st row holes lift off when they approach the 2nd row holes due to the adverse pressure gradients induced by the cooling jets from those holes. Second, large curvature in geometry causes high flow acceleration in the streamwise direction for both the mainstream flow and the coolant jets. Thus, the coolant jets from the 2nd row holes bend rather abruptly once they emerge [3–32].

Summary

Computations were performed by using the CFL3D code with the SST turbulence model to study film cooling of a semi-cylindrical leading edge. Comparison with experimentally measured temperature distribution and adiabatic effectiveness show the computed results to be reasonable and physically meaningful. The discrepancies were in coolant jet spreading rate and the amount of hot gas entrainment. The computations under predict normal spreading, over predict lateral spreading above the surface, and under predict lateral spreading on the surface. These errors can be attributed to the isotropic turbulence model used, which cannot account for the Reynolds stress redistribution as eddies flatten as they approach the wall.

Analysis of the computed results show the following:

- Plenum-hole interactions induce separation bubbles of considerable length ($D/\sin(20\text{deg})$) in hole inlets because of the vena contracta effect. These bubbles are asymmetric from asymmetry in approach velocity and turning angles, and can produce secondary flows. These interactions are unimportant for the present problem since L/D is much larger than the separation bubble size.
- Coolant jets from the 1st row holes induce a velocity component in the spanwise direction. This component coupled with the outward flow of the cooling jets against the mainstream flow cause the formation of horseshoe-like vortices that entrain hot gases and eventually get underneath the cooling jets.
- Velocity profiles at exits of 2nd row holes are distorted significantly by the mainstream flow. The distortion further increases the local coolant-to-mainstream mass flux ratio.
- Cooling jets from the 2nd row holes interact strongly with the mainstream. These interactions entrain hot gases and cause lift off of the cooling jets.
- High acceleration induced by the curvature of the geometry causes cooling jets from 2nd row holes to bend towards the streamwise direction rather abruptly despite the 20 deg angle from which the jets emerge.

Acknowledgment

This work was supported by a grant from United Technologies Pratt and Whitney in West Palm Beach, Florida. The computer time was provided by the NAS facility. The authors are grateful for this support. The second author is also grateful for the helpful discussions with Martin Tabbita, Dean Johnson, Mark Stephens, and Fred Soechting of Pratt and Whitney and Dave Bogard of the University of Texas at Austin.

Nomenclature

D	= film-cooling hole diameter
DR	= density ratio of coolant to mainstream (ρ_c/ρ_∞)
k	= turbulent kinetic energy
L	= film-cooling hole length
M	= mass-flux ratio of coolant to mainstream ($\rho_c U_c/\rho_\infty U_\infty$)
T	= temperature
U_c	= average coolant velocity from both rows of holes
U_τ	= friction velocity
U_∞	= mainstream velocity upstream of the leading edge
x - y - z	= Cartesian coordinate system defined in Fig. 2
y^+	= normalized distance normal to surface ($\rho U_\tau Y/\mu$)
X	= streamwise coordinate tangent to leading-edge surface
Y	= coordinate normal to surface
Z	= lateral coordinate, normal to mainstream and tangent to leading-edge surface

Greek

η	= adiabatic effectiveness [$(T_{aw} - T_\infty)/(T_c - T_\infty)$]
μ	= dynamic viscosity
ρ	= density

Θ = normalized temperature $[(T - T_\infty)/(T_c - T_\infty)]$
 ω = dissipation rate per unit k

Subscripts and Superscripts

aw = adiabatic wall
c = coolant
 ∞ = mainstream

References

- [1] Simoneau, R. J., and Simon, F. F., 1993, "Progress Towards Understanding and Predicting Heat Transfer in the Turbine Gas Path," *Int. J. Heat Fluid Flow*, **14**, No. 2, pp. 106–128.
- [2] Hanus, G. J., and L'Ecuyer, M. R., 1977, "Leading Edge Injection for Film Cooling of Turbine Vanes," *J. Energy*, **1**, pp. 44–49.
- [3] Karni, J., and Goldstein, R. J., 1990, "Surface Injection Effect on Mass Transfer from a Cylinder in Cross Flow," *ASME J. Turbomach.*, **112**, pp. 477–487.
- [4] Camci, C., and Arts, T., 1991, "Effect of Incidence on Wall Heating Rates and Aerodynamics on a Film-Cooled Transonic Turbine Blade," *ASME J. Turbomach.*, **113**, pp. 493–501.
- [5] Mayle, R. E., and Anderson, A., 1991, "Velocity and Temperature Profiles for Stagnation Film Cooling," *ASME J. Turbomach.*, **113**, pp. 457–463.
- [6] Ou, S., and Han, J. C., 1992, "Influence of Mainstream Turbulence on Leading Edge Film Cooling Heat Transfer Through Two Rows of Inclined Film Slots," *ASME J. Turbomach.*, **114**, pp. 724–733.
- [7] Salcudean, M., Gartshore, I., Zhang, K., and McLean, I., 1994, "An Experimental Study of Film Cooling Effectiveness Near the Leading Edge of a Turbine Blade," *ASME J. Turbomach.*, **116**, pp. 71–79.
- [8] Cruse, M. W., Yuki, U. M., and Bogard, D. G., 1997, "Investigation of Various Parametric Influences on Leading Edge Film Cooling," *ASME Paper 97-GT-296*.
- [9] Ames, F. E., 1998, "Aspects of Vane Film Cooling with High Turbulence: Part I—Heat Transfer," *ASME J. Turbomach.*, **120**, pp. 768–776.
- [10] Ames, F. E., 1998, "Aspects of Vane Film Cooling with High Turbulence: Part II—Adiabatic Effectiveness," *ASME J. Turbomach.*, **120**, pp. 777–784.
- [11] Garg, V. K., and Gaugler, R. E., 1996, "Leading Edge Film Cooling Effects on Turbine Blade Heat Transfer," *Numer. Heat Transfer, Part A*, **30**, pp. 165–187.
- [12] Heidmann, J., Rigby, D. L., and Ameri, A. A., "A Three-Dimensional Coupled Internal/External Simulation of a Film-Cooled Turbine Vane," *ASME Paper 99-GT-186*.
- [13] Bohn, D. E., Becker, V. J., Kusterer, K. A., and Rungen, A. U., 1998, "Experimental and Numerical Conjugate Investigation of the Blowing Ratio Influence on the Showerhead Cooling Efficiency," *ASME Paper 98-GT-85*.
- [14] Kercher, D. M., 2000, "Turbine Airfoil Leading Edge Film Cooling Bibliography: 1972–1998," *Int. J. Rotating Mach.*, **6**, No. 5, pp. 313–319.
- [15] Chernobrovkin, A., and Lakshminarayana, B., 1998, "Numerical Simulation and Aerothermal Physics of Leading Edge Film Cooling," *ASME Paper 98-GT-504*.
- [16] Lin, Y.-L., Stephens, M. A., and Shih, T. I.-P., 1987, "Computations of Leading-Edge Film Cooling With Injection Through Rows of Compound Angle Holes," *ASME Paper 97-GT-298*.
- [17] Martin, C. A., and Thole, K. A., 1997, "A CFD Benchmark Study: Leading-Edge Film Cooling with Compound Angle Injection," *ASME 97-GT-297*.
- [18] Thakur, S., Wright, J., and Shyy, W., 1997, "Computation of a Leading-Edge Film Cooling Flow over an Experimental Geometry," *ASME Paper 97-GT-381*.
- [19] Menter, F. R., 1993, "Zonal Two-Equation $k-\omega$ Turbulence Models for Aerodynamic Flows," *AIAA Paper 93-2906*.
- [20] Wilcox, D. C., 1993, *Turbulence Modeling for CFD*, DCW Industries, La Canada, California.
- [21] Kandula, M., and Wilcox, D. C., 1995, "An Examination of $k-\omega$ Turbulence Model for Boundary Layers, Free Shear Layers, and Separated Flows," *AIAA Paper 95-2317*.
- [22] Bardina, J. E., Huang, P. G., and Coakley, T. J., 1997, "Turbulence Modeling Validation, Testing, and Development," *NASA TM 110446*.
- [23] Shih, T. I.-P., and Sultanian, B., 2001, "Computations of Internal and Film Cooling," *Heat Transfer in Gas Turbine Systems*, B. Suden and M. Faghri, eds., WIT Press, Ashurst, Southampton.
- [24] Thomas, J. L., Krist, S. T., and Anderson, W. K., 1990, "Navier-Stokes Computations of Vortical Flows Over Low-Aspect-Ratio Wings," *AIAA J.*, **28**, No. 2, pp. 205–212.
- [25] Rumsey, C. L., and Vatsa, V. N., 1993, "A Comparison of the Predictive Capabilities of Several Turbulence Models Using Upwind and Central-Difference Computer Codes," *AIAA Paper 93-0192*.
- [26] Roe, P. L., 1981, "Approximate Riemann Solvers, Parameter Vector and Difference Schemes," *J. Comput. Phys.*, **43**, pp. 357–372.
- [27] Roe, P. L., 1986, "Characteristic Based Schemes for the Euler Equations," *Annu. Rev. Fluid Mech.*, **18**, pp. 337–365.
- [28] Pulliam, W. R., and Chaussee, D. S., 1981, "A Diagonal Form of an Implicit Approximate Factorization Algorithm," *J. Comput. Phys.*, **39**, pp. 347–363.
- [29] Ni, R.-H., 1981, "A Multiple Grid Scheme for Solving the Euler Equations," *AIAA Paper 81-1025*.
- [30] Anderson, W. K., Thomas, J. L., and Whitfield, D. L., 1988, "Multigrid Acceleration of the Flux-Split Euler Equations," *AIAA J.*, **26**, No. 6, pp. 649–654.
- [31] Stephens, M. A., Chyu, M. K., Shih, T. I.-P., and Civinskas, K. C., 1996, "Calculations and Measurements of Heat Transfer in a Square Duct with Inclined Ribs," *AIAA Paper 96-3163*.
- [32] Leylek, J. H., and Zerkle, R. D., 1994, "Discrete-Jet Film Cooling: A Comparison of Computational Results with Experiments," *ASME J. Turbomach.*, **116**, pp. 358–368.

Time-Resolved Thermal Boundary-Layer Structure in a Pulsatile Reversing Channel Flow

Sean P. Kearney
Engineering Sciences Center, 9100,
Sandia National Laboratories,
P.O. Box 5800, MS 0834,
Albuquerque, NM 87185-0834
e-mail: spkearn@sandia.gov

Anthony M. Jacobi
Department of Mechanical
and Industrial Engineering,
University of Illinois at Urbana-Champaign,
Urbana, IL 61801

Robert P. Lucht
Department of Mechanical Engineering,
Texas A&M University,
College Station, TX 77843

In this paper, the results of an experimental study of the time-resolved structure of a thermal boundary layer in a pulsating channel flow are presented. The developing laminar regime is investigated. Two techniques were used for time-resolved temperature measurements: a nonintrusive, pure-rotational CARS method and cold-wire anemometry. Results are presented for differing degrees of flow reversal, and the data show that the primary impact of reversed flow is an increase in the instantaneous thermal boundary-layer thickness and a period of decreased instantaneous Nusselt number. For the developing laminar parameter space spanned by the experiments, time-averaged heat-transfer enhancements as high as a factor of two relative to steady flow are observed for nonreversing and partially reversed pulsating flows. It is concluded that reversal is not necessarily a requirement for enhancement. [DOI: 10.1115/1.1372317]

Keywords: Boundary Layer, Convection, Enhancement, Heat Transfer, Periodic, Pulsating

Introduction

Single-phase convective heat-transfer enhancement is important in a variety of residential and industrial end-use energy applications. Heat-transfer enhancement can be implemented using methods that are active (external energy input required) or passive (no external energy input). The introduction of high-amplitude, periodic flow pulsation shows promise as an active enhancement method. However, the literature provides conflicting reports, with some researchers reporting pulsation-induced heat-transfer enhancements (Dec et al. [1]; Niida et al. [2]; Bayley et al. [3]; Galitseyskiy et al. [4]; Fujita and Tsubouchi [5]) and others citing no impact, or even a decrease in heat transfer (Miller [6]; Feiler [7]; Jackson and Purdy [8]). The reason for these conflicting reports is that the physics of the unsteady convection process over an exceptionally broad parameter space are not fully understood. For example, a Buckingham Π analysis shows that the local time-mean Nusselt number in a low-speed, wall-bounded laminar flow may depend on as many as seven dimensionless groups:

$$\overline{Nu}_x = f(\Delta u / \bar{U}|_{\infty}, \Delta u / \omega L, a / \omega L, Wo, Re_x, Pr, Gz_T). \quad (1)$$

Additional parameters arising from flow pulsation in Eq. 1 include: (1) the Womersley number Wo , which is a ratio of the channel height to the Stokes or "acoustic" boundary-layer thickness,¹ (2) the centerline "amplitude ratio" $\Delta u / \bar{U}|_{\infty}$, which is a measure of the amplitude of the velocity waveform and is greater than unity in the case of a bulk flow reversal, (3) the parameter $a / \omega L$, which is a measure of the wavelength of the applied pressure oscillation to the relevant streamwise length scale, and (4) the grouping $\Delta u / \omega L$ which represents the relative magnitudes of the Lagrangian and convective accelerations and dictates the importance of "acoustic streaming" (as explained in Ref. [8]).

The majority of reported experiments have focused on providing empirical heat-transfer correlations for a specific geometry and flow condition and have not provided measurements of temperature and velocity profiles that are needed to fully understand

the convection process for the subset of the parameter space investigated. If the confusion that exists regarding the heat-transfer impact of pulsatile flow is to be overcome, a fundamental understanding of the unsteady convection process must be obtained. Such a detailed understanding requires knowledge of the time-resolved flow, heat-transfer and temperature behavior over a broad range of the parameter space suggested in Eq. 1.

The literature does, however, suggest a potential link between significant heat-transfer enhancement and periodic, bulk flow reversal. In an early study by Bayley et al. [3], the local, time-mean heat-transfer coefficient was measured for pulsating flow over a flat plate. The heat-transfer coefficient showed no frequency dependence, but increased with the applied pressure fluctuation amplitude if this amplitude exceeded a critical value. This critical amplitude was postulated to be associated with flow reversal, but no time-resolved velocity data were acquired to substantiate this conclusion. Hanby [9] and Keil and Baird [10] observed both nonreversing and reversing flows experimentally. In a study of a reacting, turbulent flow with 100-Hz resonant oscillations, Hanby [9] observed a decrease in the time- and space-averaged heat-transfer coefficient for nonreversing flow and heat-transfer enhancements upwards of 100 percent with flow reversal. In their study of turbulent water flow in a shell-and-tube heat exchanger with 0.4 to 1.1 Hz velocity pulsations, Keil and Baird [10] observed no heat-transfer impact for nonreversing flow and significant enhancement when the flow was reversed.

Two experimental studies (Fujita and Tsubouchi [5] and Jackson and Purdy [8]) contradict the premise that heat transfer is enhanced in reversing flows only. Fujita and Tsubouchi [5] measured local heat-transfer coefficients in a pulsed, nonreversing laminar flow over a flat plate. They observed modest heat-transfer enhancements of 10 to 20 percent for nonresonant forcing at frequencies between 2 and 23 Hz. The heat-transfer data presented by Fujita and Tsubouchi [5] also suggest that an optimal forcing frequency exists, in contrast to the earlier flat-plate measurements of Bailey and co-workers, that suggested no frequency dependence. In their study of an acoustically resonant, turbulent pipe flow, Jackson and Purdy [8] observed no overall heat transfer impact with pulsation, despite massive resonant velocity and pressure fluctuations. Jackson and Purdy did observe both enhanced and

¹The Stokes boundary layer is a measure of the penetration depth of unsteady vorticity fluctuations that are generated at the wall.

Contributed by the Heat Transfer Division for publication in the JOURNAL OF HEAT TRANSFER. Manuscript received by the Heat Transfer Division April 21, 2000; revision received February 5, 2001. Associate Editor: M. Hunt.

decreased time-mean heat-transfer coefficients at different local measurement stations that resulted in a negligible surface-averaged effect.

Three studies were found in which the time-resolved thermal boundary-layer and wall heat-flux behavior were at least partially addressed for pulsating flows with a nonzero mean mass flux. Feiler and Yeager [11] performed a qualitative flow visualization study in a highly turbulent, flat-plate boundary layer using a Schlieren method. Their results showed a dramatic thickening of the thermal boundary layer during periodic flow reversal. In their flat-plate study cited above, Fujita and Tsubouchi [5] provided the first reported time-resolved surface heat-transfer data. They found significant phase differences between the Nusselt number and the free-stream velocity oscillations. However, Fujita and Tsubouchi [5] presented time-resolved results for only a single operating condition and did not provide time-resolved boundary-layer temperature data. The study of turbulent flow and heat transfer in a pulsed combustor tailpipe by Dec and co-workers [1,12–14] is the most detailed set of time-resolved experiments to date. Dec and co-workers presented nonintrusive point measurements of boundary-layer velocity (using LDV) and temperature (using laser-induced fluorescence) as well as local wall heat flux results. Dec et al. [1] observed a distinct Nusselt-number maximum of 2.7 times the accepted value for steady, turbulent pipe flow (based on a Reynolds number evaluated with the time-mean velocity) during the positive-to-negative reversal of the free-stream flow. This heat transfer peak was followed by a period of decreasing heat flux during the negative-velocity portion of the cycle. Dec et al. [1] postulated that the enhancement mechanism during reversal was an ejection of fluid from the near-wall region. Their analysis of the time-resolved data suggested that an increased turbulence level, generated by elevated levels of shear in the Stokes boundary layer, was the dominant mechanism for time-averaged heat-transfer enhancement, with the local maxima during flow reversal accounting for only 10 to 15 percent of the total enhancement.

In this paper, new time-resolved temperature and heat flux data from a laminar, developing, pulsatile channel flow are presented. The developing channel flow is chosen because it represents a canonical problem for many heat-exchanger applications. The thermal impact of nonreversed flows and flows that are partially reversed (reversal limited to a near-wall region only) or completely reversed (reversal across the entire channel height) is investigated using a mechanical, nonresonant flow-forcing scheme. The literature cited above suggests that bulk flow reversal may lead to significant heat-transfer enhancement, but very little is understood about the interplay between the reversing flow and the time-dependent boundary-layer temperature and wall heat-flux histories. Additionally, the impact of partial flow reversal, to our knowledge, has not been previously addressed. Partial flow reversal is potentially important in heat-exchanger applications because nonresonant, mechanical forcing schemes are likely to be preferred to eliminate the high levels of noise and vibration associated with resonant, acoustic forcing. However, nonresonant forcing will provide smaller velocity oscillations than resonant forcing and may only generate partial or weak bulk flow reversals.

Pulsatile Flow Facility

A schematic of the pulsatile flow facility is provided in Fig. 1. Airflow was supplied by a blower located upstream of the settling chamber. Pulsations were imparted to the flow by four co-rotating vanes located in the settling chamber, upstream of the flow-conditioning honeycomb and screens. The vanes rotated in phase and modulated the settling chamber pressure by providing a blockage that varied the flow area between an almost fully open position and roughly 8 percent of the total settling chamber cross section. Nominal forcing frequencies of 2.5 and 5.0 Hz were used so that, $a/\omega L \gg 1$, and the wavelength of the travelling pressure wave was much longer than the length of the wind tunnel test section. Modulated blockage schemes of this type have been em-

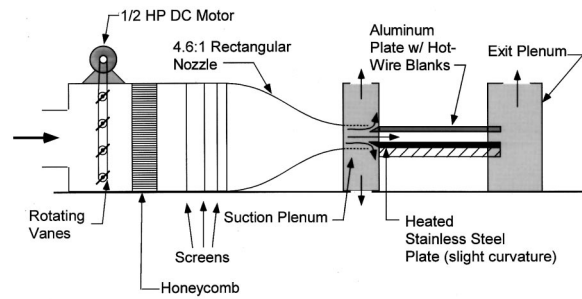


Fig. 1 Schematic of the pulsatile flow facility. The bulk flow is from left to right. Pulsations are imparted to the flow by a series of rotating vanes located upstream of the settling chamber.

ployed in previous work, [15–17] and provide sufficient velocity oscillation amplitude to reverse the flow over a limited range of forcing frequencies.

The conditioned flow was accelerated through a 4.6-to-1, two-dimensional contraction constructed using the matched-polynomial method of Morel [18]. At the exit plane of the contraction, the nozzle boundary-layer flow was removed through concentric suction slots of 10 mm minimum clearance, using an approach suggested by Swearingen and Blackwelder [19]. The suction slots were created by placing the first 25 mm of the test section inside the nozzle and enclosing the nozzle/leading edge assembly in a suction plenum where low pressures were created using a high-head blower. Removal of the nozzle boundary layer provided a well-defined origin for the thermal and momentum boundary layers, and allowed for transition between the flat nozzle walls and the large-radius curvature introduced into the floor of the test section as described below.

The test section was a rectangular channel composed of an aluminum ceiling, a stainless-steel floor, and glass side windows. To prevent leading-edge boundary-layer separation, both the ceiling and the floor of the test section were machined to sharp leading edges, and knife-edged aluminum inserts were used to form the side walls in the entrance region. The unheated ceiling of the test section was flat and constructed from an aluminum plate that was fitted with five removable blanks to allow for insertion of a hot/cold-wire probe at five streamwise locations. Uniform heat input was applied to the backside of the wind tunnel floor using Kapton resistance heaters controlled with a VARIAC. The test section floor was fabricated from stainless steel, with a small spanwise curvature machined into the floor so that the laser beams used for the nonintrusive CARS temperature measurements were not clipped as they entered the test section. The channel height was 30 mm at the spanwise centerline, where all measurements were made, and 35 mm at the side glass windows. The aspect ratio of the tunnel cross section was 5.3 when based on the centerline channel height. Potential curvature effects were minimized, as care was taken to guarantee that the local radius of curvature of the steel plate was always at least an order of magnitude greater than the half-height of the channel, which represented the maximum attainable boundary-layer thickness.

The apparatus provided a pulsatile, developing channel flow whose relative amplitude, $\Delta u/\bar{U}|_{\infty}$, could be varied to provide nonreversing, partially reversed, and completely reversed flow. Here a partially reversed flow ($\Delta u/\bar{U}|_{\infty} < 1$) is a flow where reversal is confined to some inner portion of the boundary layer, while the outer boundary-layer and the centerline or “core” flow do not reverse at any time during the cycle. A complete or “bulk” flow reversal ($\Delta u/\bar{U}|_{\infty} > 1$) is a flow that periodically reverses everywhere across the channel height. In general, lower frequencies provided higher relative amplitudes. The channel flow apparatus generated a developing laminar flow with a core velocity profile that was flat to within 3 percent, with a small (typically

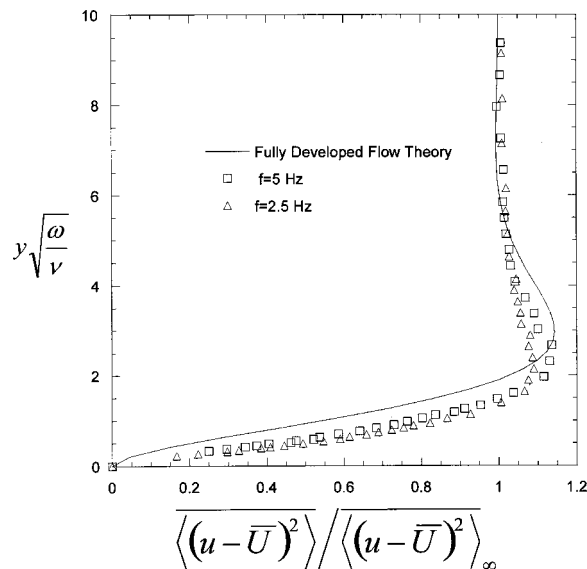


Fig. 2 A comparison of mean square velocity profiles (pulsation kinetic energy) obtained from temperature-compensated hot-wire measurements to laminar, fully developed, pulsatile flow theory from Currie [20]

less than 5 percent variation in the cycle maximum and minimum velocity amplitudes) cycle-to-cycle variation in the velocity waveform. A comparison of temperature-compensated hot-wire measurements from a nonreversing, developing channel flow in our wind tunnel with fully developed laminar pulsatile flow theory [20] is provided in Fig. 2. The flow exhibits the well-known Stokes boundary-layer behavior [21] characterized by an overshoot in the near-wall profile associated with the peak level of periodic velocity fluctuations and increased levels of mean shear within the boundary layer.

Measurement Instrumentation and Procedures

Instrumentation. Time-resolved boundary-layer temperature data were acquired using pure-rotational coherent anti-Stokes Raman scattering (CARS) and cold-wire anemometry. CARS is a nonlinear, spectroscopic technique that provides a coherent, laser-like signal whose spectral signature is similar to the rotational Raman spectrum of air, from which point measurements of temperature may be obtained. The reader is referred to Kearney et al. [22] and Kearney [23] for a detailed explanation of the nonintrusive pure-rotational CARS technique used here and an associated uncertainty analysis. The CARS probe-volume provided for a spatial resolution of $50 \mu\text{m}$ in the wall-normal and streamwise directions and for 1-mm resolution in the spanwise coordinate. The 10 ns pulse width of the Nd:YAG laser provided for an essentially infinite frequency response, but with a limited data-acquisition rate so that ten temperature profiles per forcing cycle were obtained. The uncertainty in the CARS temperature measurements was $\pm 4 \text{ K}$ (3 to 3.4 percent of the temperature difference across the boundary layer), which is primarily a random (precision) error associated with mode phase fluctuations in the broadband dye-laser output [24,25]. The uncertainty in the location of the probe volume relative to the heat-transfer surface was $\pm 50 \mu\text{m}$ (1.6 to 5 percent of the observed δ_θ), or one probe-volume diameter.

Additional time-resolved temperature measurements were performed using a constant-current anemometer (CCA) or “cold-wire” technique. The CCA supplied a 0.25 mA current through a commercially available, tungsten wire probe with copper plated ends and dimensions $d = 4.5 \mu\text{m}$, $l/d = 726$, and $l_*/d = 282$. The location of the cold-/ hot-wire probe was determined using the procedure of Quintana et al. [26], in which boundary-layer hot-

wire data from a non-reversing flow were extrapolated to a zero-velocity condition at the wall. The uncertainty in the location of the sensor relative to the wall was conservatively estimated at $\pm 200 \mu\text{m}$ (6.7 to 20 percent of the observed δ_θ) based on the results of several fits in which the number of data points was allowed to vary. The uncertainty in probe location was primarily attributed to errors associated with the number of points chosen for least-squares fitting and due to scatter in the hot-wire data. The above stated probe-location uncertainties in both the cold-wire and CARS measurements are purely bias errors, which shift the temperature profiles by the stated amounts.

The response of the CCA to temperature fluctuations in the flow was limited by the thermal inertia of the sensor. This thermal inertia effect was compensated for by using the analytically based transfer function derived by Wroblewski and Eibeck [27], which accounts for the thermal inertia of the active sensor element, plating, and support prongs:

$$H(\omega) = \frac{1}{\xi_w} \left\{ 1 + \frac{\tanh[\xi_w^{1/2} l_w]}{\xi_w^{1/2} l_w} \left[\frac{\xi_w}{\xi_c} - 1 + \frac{\xi_w}{\cosh[\xi_c^{1/2} l_c]} \right] \right\}, \quad (2)$$

where l_k and τ_k are the Bechtov cold length and the lumped-capacitance time constant of the indicated sensor elements, respectively, and $\xi_k = 1 + i\omega\tau_k$. The correction to the raw cold-wire data was made in the frequency domain by dividing the discrete Fourier transform of the “raw” time-series data by $H(\omega)$ and then inverting the corrected transform. All cold-wire time series were sampled for 100 periodic forcing cycles. The cold-wire transfer function required knowledge of the lumped-capacitance time constants, τ_w and τ_c , which depended on the local heat-transfer coefficient for the wire and support prongs. We used a time-mean heat-transfer coefficient calculated from a wire heat-transfer correlation obtained in our laboratory [23] to calculate τ_w and τ_c . This procedure neglects the cyclic variation in the wire heat-transfer coefficient, but it does allow for a tractable analysis and an approximate correction to the cold-wire data.

Local time-mean velocity data were acquired from hot-wire measurements in the pulsatile boundary layer by switching the single-wire probe to a constant-temperature bridge. Analysis of the data required an iterative procedure, as the cold-wire temperature data were also used to temperature compensate the hot-wire velocity data that were used to estimate the wire heat-transfer coefficient (see Wroblewski and Eibeck [27] or Kearney [23] for details). The process typically converged within one or two iterations. The uncertainty in the cold-wire results was largely caused by systematic errors associated with calibration, the estimated frequency compensation, and the intrusive nature of the sensor. The uncertainty relating to calibration was $\pm 2 \text{ K}$ (2 to 2.5 percent of the temperature difference across the boundary layer), while the uncertainty owed to frequency compensation and probe insertion was much more ambiguous and was difficult to quantify.

Phase-Averaging and Data Acquisition. A “triple-decomposition,” or phase-averaging, procedure was applied to all of the time-series data obtained in this study. In applying the triple-decomposition, the instantaneous value of a boundary-layer time-series quantity, in this case temperature, is written as

$$T(y, t) = \bar{T}(y) + T_{\text{osc}}(y, t) + T'(y, t), \quad (3)$$

where \bar{T} is the time-mean of the time-series data, T_{osc} is the periodic component of the signal, and T' is a random contribution resulting from small levels of turbulence and cycle-to-cycle variation in the flow. All time-series data to be presented here are in a phase-averaged form given by

$$\langle T \rangle(y, t) = \bar{T}(y) + T_{\text{osc}}(y, t). \quad (4)$$

The phase average is dependent on the cycle time, $0 \leq \omega t \leq 2\pi$, and is calculated by averaging all data within the cycle time bin, ωt to $\omega(t + \Delta t)$, where ω is the fundamental circular frequency of the applied forcing.

For the experiments reported here, the time bin for phase averaging was determined from the resolution of a shaft encoder that was fixed to the lower-most rotating vane shaft and was used to synchronize and clock all data acquisition. All results are presented in terms of a cycle time given in shaft-encoder crank-angle degrees, or CAD. Because each complete rotation of the rotating vane assembly results in two flow-forcing cycles, a single period of the forcing is 180 CAD. Use of the shaft encoder output as a time base allowed for small levels of jitter in the rotational speed and the period of the rotating-vane assembly to be taken into account.

For the CARS experiments, the encoder clock pulse provided an external time base for a series of counter/timer chips that generated triggers to properly synchronize the firing of the Nd:YAG laser and the opening of the CCD detector's mechanical shutter with the desired phase angle of the periodic flow forcing. At each vertical location within the boundary layer, 100 single-pulse CARS spectra were acquired at each of the 10 selected phase angles of 2, 30, 50, 60, 70, 80, 100, 120, 140, and 178 CAD. The single-pulse averaging time of the CARS temperature measurements was 10 ns, or the duration of the Nd:YAG laser pulse. One hundred single-pulse rotational CARS spectra were averaged in software to yield an averaged spectrum for each vertical location and phase angle. Use of 100-shot-averaged CARS spectra was required to minimize the effects of dye-laser noise. Phase-averaged temperatures were calculated from the averaged spectra using the Sandia CARSFT code [28] and the integrated-line-intensity procedure described by Kearney et al. [22]. Using this data-acquisition procedure, each CARS experimental run took about eight hours in addition to the time required for the wind tunnel floor to stabilize at temperatures between 100 to 150 K above ambient.

For the cold-wire experiments, the encoder output was used to clock the digitization of the CCA signal at a rate of one point per CAD. This increase in data-acquisition rate relative to the CARS technique provided for a more detailed picture of the unsteady thermal-boundary-layer structure at the expense of an ambiguous systematic error associated with the intrusive nature and thermal inertia of the probe. The CCA output was sampled for 100 forcing cycles, and phase-averaged temperatures were calculated after correction of the raw CCA output using Eq. 2.

Wall Heat-Flux Calculation. Nusselt-number and temperature-defect-thickness results were calculated from the boundary-layer temperature data. The temperature-defect thickness [1],

$$\langle \delta_\theta \rangle = \int_0^\infty \left(1 - \frac{\langle T \rangle(y) - T_w}{T_\infty - T_w} \right) dy, \quad (5)$$

provides a robust and unambiguous integral measure of the cyclic variation in thermal-boundary-layer thickness. The cyclically varying Nusselt number was calculated from

$$\langle Nu \rangle = \frac{\langle q'' \rangle d_h}{\kappa_\infty (T_w - \bar{T}_m)}, \quad (6)$$

where $\langle q'' \rangle$ is the wall heat flux calculated from the slope of the near-wall, phase-averaged temperature profile, and \bar{T}_m is the mixing-cup temperature obtained by integrating phase-averaged hot-wire velocity and cold-wire temperature data according to

$$\bar{T}_m(t) = \frac{1}{\dot{m}' c_p} \int_H \rho |u| c_p \langle T \rangle dy, \quad (7)$$

where H indicates a vertical integration across the channel height. In Eq. 7, the absolute value of the velocity, which the hot-wire instrument directly provides, has been used, as recommended by Zhang [29], for calculation of \bar{T}_m in reversing flows.

Calculation of the Nusselt number from a wall-gradient measurement can be advantageous because it provides for a direct measurement of the convective heat flux without any correction for radiative heat transfer. Several groups of researchers have recently used wall-gradient information to obtain heat-flux results [26,30,31] and shear-stress data [14,26]. Only the cold-wire Nusselt number results are presented here, as these data provide more points per cycle and better dynamic range.

A procedure similar to the one recently outlined by Quintana et al. [26] was used for calculation of the wall heat flux. The temperature profiles obtained displayed a characteristic linear, conduction-dominated region near the wall. A linear sublayer criterion of $y \leq 400 \mu\text{m}$ was used in selection of the points used for linear, least-squares fitting of the data. This criterion was justified based on earlier CARS temperature measurements by Kearney et al. [22] in a steady, tripped boundary layer flow conducted in the same the facility used for the present measurements. These CARS data showed that the turbulent conduction sublayer could extend as far as $y = 800 \mu\text{m}$ at Reynolds numbers similar to the time-mean values employed in the present unsteady work. A 400

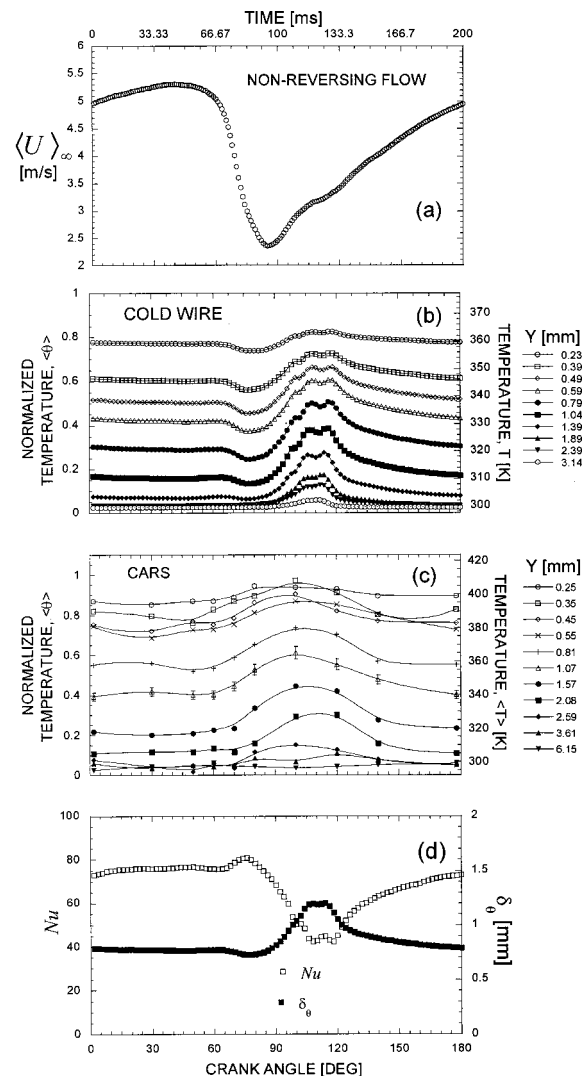


Fig. 3 Time-resolved boundary-layer temperature and heat-flux data from a nonreversing flow

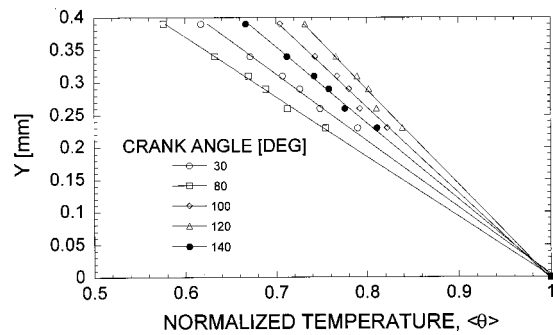


Fig. 4 Sample near-wall temperature profile obtained from the cold-wire data shown in the time series in Fig. 3(b). The plot shows that the nature of the deviation between the data and the least-squares fits is correlated for different cycle times.

μm cutoff was then justified given the $\pm 200 \mu\text{m}$ uncertainty in the location of the cold-wire probe. For the data reported in this paper, six to eight temperature points were used in the linear fits. The uncertainty in the $\langle Nu \rangle$ data obtained from the cold-wire temperature results was determined from the statistical properties of the least-squares slope estimator [23]. The absolute Nusselt-number uncertainty varied from ± 10 percent to ± 20 percent in regions of high cyclic heat flux to as high as ± 75 percent when the phase-averaged heat flux was near zero.

Surface heat-transfer and thermal boundary-layer thickness results for a nonreversing flow are shown in Fig. 3(d). The high level of negative correlation (i.e., opposing trends) between the Nusselt-number results and the robust, integral measurement of the temperature-defect thickness validates the gradient measurement of the wall heat flux. Furthermore, the scatter in the Nusselt-number data is not nearly as large as the uncertainty estimates quoted above would suggest. This is indicative of the large systematic component in the temperature-gradient error. To illustrate the systematic nature of the error, a representative set of near-wall cold-wire temperature data is shown in Fig. 4. The scatter in the temperature data about the least-squares fits is random for each individual fit, but the nature of the data scatter is correlated between the fits at different cycle times. Therefore, the scatter in the Nusselt number time-series results for a fixed number of points used in the fitting procedure is quite low. Because of the systematic nature of the temperature-gradient uncertainty, the relative error in the Nusselt number data is decreased, and trends in the cyclic heat-flux variation are readily seen.

Results and Discussion

Both CARS and cold-wire data were acquired under conditions of nonreversing, partially reversed, and fully reversing conditions, with results obtained at several streamwise measurement stations. For brevity, only a representative sample of data from the most upstream measurement location for each of the three flow regimes is presented here in time-series form. The operating conditions for the experiments are provided in Table 1. Some variation in the time-series data was observed with streamwise distance from the leading edge; however, the data were sufficiently similar to permit a discussion of the convection process using the most upstream data only. A more comprehensive presentation of the data is given by Kearney [23].

Nonreversing Flow. Phase-averaged time-series results from a nonreversing channel flow are shown in Fig. 3. A phase-averaged hot-wire trace of the centerline flow is provided in Fig. 3(a) for phase reference. Both the CARS and cold-wire results show similar temperature time histories in the nonreversing flow. However, the cold-wire results exhibit a phase lag of about 15–20 CAD relative to the CARS data, a result that is likely caused by systematic errors arising from the imperfect frequency compensa-

Table 1 Experimental parameters for representative CARS and cold-wire measurements (For all experimental runs $a/\omega L \gg 1$ so that streamwise variation in the pressure time derivative was unimportant. The parameter $\Delta u/\omega L$ was less than 1 in all experiments so that acoustic streaming effects were negligible.)

Technique	Reversal ($\Delta u/U_{\max, \text{osc}}$)	x [mm]	$\langle u \rangle_{\infty}$ [m/s]	f [Hz]	ΔT [K]	Re_x	Wo
CARS	NONE (0.47)	105	4.16	5.0	117	27,400	23.0
Cold Wire	NONE (0.55)	93	4.19	5.1	80	24,500	21.5
CARS	PARTIAL (0.75)	112	4.23	2.5	115	29,500	16.3
Cold Wire	PARTIAL (0.85)	93	4.10	2.44	81	24,000	14.9
CARS	COMPLETE (1.11)	112	1.56	2.5	133	10,900	16.3
Cold Wire	COMPLETE (1.21)	93	1.50	2.5	72	8,900	15.0

tion of the cold-wire signal and from the intrusive nature of the probe. This phase-lag is present to some extent in all of the reported data sets and is less severe for the 2.5-Hz results presented below as should be expected.

The temperature data are nearly steady during the weak acceleration at the crest of the velocity waveform and into the early stages of the fluid deceleration phase. The cold-wire results show a cycle-minimum temperature between 75 and 85 CAD during the later stages of the strong fluid deceleration phase. This temperature dip is significant because it is associated with the cycle-maximum Nusselt number. The magnitude of the temperature dip is on the order of the ± 4 K random error in the CARS measurement, which combines with the coarse time grid to mask the temperature minimum in the CARS results.

During the acceleration phase of the cycle, both the CARS and cold-wire results exhibit a temperature rise on the order of 20 percent of the wall-to-air temperature difference. This temperature peak is a result of the advection of high-enthalpy fluid associated with the increased fluid residence time and high levels of heat transfer from the wall that occur at phase angles near the cycle-minimum velocity. The boundary-layer temperature decreases during the later stages of the fluid acceleration phase as the channel is “swept clean” of high-enthalpy fluid before the beginning of the next forcing cycle. A temperature rise and decay of this nature during the fluid acceleration portion of the cycle is observed in the data for all three reversal regimes studied, and is believed to be caused by the same enthalpy-advection mechanism in all cases. From a heat-transfer enhancement standpoint, it is important that the combination of convective velocities and forcing frequencies be such that all of the high-enthalpy fluid flows through the channel before the start of the next forcing cycle.

The results from the nonreversing flow suggest that the key mechanism for the generation of periodic temperature fluctuations in this flow is the passive advection of enthalpy. Figures 3(b) and 3(c) show that the highest levels of periodic temperature fluctuation occur in the middle portion of the thermal boundary layer, where the velocity oscillations within the Stokes layer are highest, as shown in Fig. 2. The nonreversing flow data also show that the velocity oscillation and the wall heat transfer are out of phase, while the Nusselt number is in phase with the bulk temperature fluctuation. This result strongly suggests that the velocity field plays a more secondary role through the passive advection of enthalpy and invalidates the simple quasi-steady models proposed by some researchers (Hanby, [9] and Keil and Baird, [10]), where the instantaneous Nusselt number is calculated from steady-flow correlations by using the instantaneous velocity.

Partially Reversing Flow. Time-series data for a partially reversing boundary-layer flow at a forcing frequency of 2.5 Hz are shown in Fig. 5. Both near-wall and centerline hot-wire traces are

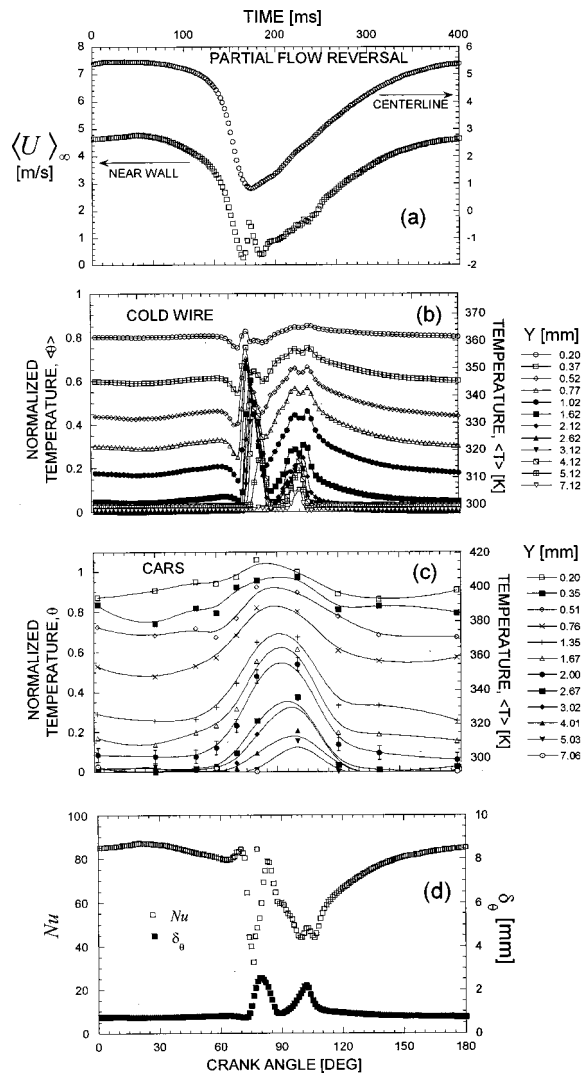


Fig. 5 Time-resolved boundary-layer temperature and heat-flux data from a partially reversed flow

shown in Fig. 5(a) for phase reference and to indicate the location of the near-wall flow reversal event. When compared to the non-reversing flow discussed above, this partially reversed flow is characterized by the same levels of convective velocity at half the forcing frequency, so that each CAD time unit is twice as large. The initiation of a local flow reversal event was determined to coincide with the rectification of the instantaneous hot-wire signal in the near-wall region. Identification of flow reversal events based upon observed hot-wire signal rectification has been employed in several previous studies of time-periodic flows including the work of Feiler [7], Despard and Miller [15], and Qiu and Simon [32]. The flow was characterized as partially reversed because hot-wire traces within the boundary layer displayed signal rectification in a limited region near the wall, but were not rectified in the outer regions of the boundary layer or in the inviscid core flow—a condition which showed that the reversal event was confined to a thin region near the wall.

Similar to the nonreversing boundary-layer flow, the boundary-layer temperature history is nearly steady during the elongated peak portion of the velocity waveform. A small temperature dip, similar to the one observed in the nonreversing flow, is observed in the cold-wire results during the steep deceleration phase of the cycle. This small temperature dip is followed by a distinct rise in temperature of up to 50 percent of the wall-to-air temperature

difference, which occurs near the time of minimum centerline velocity and the onset of flow reversal near the wall. This temperature rise is followed by an equally strong decay in the boundary-layer temperature. The rise and fall in temperature during partial flow reversal is so rapid that the coarse time grid used for the CARS measurements cannot resolve this feature. However, the nonintrusive CARS results do capture the long-time-scale features of the temperature oscillation. The cold-wire results from this 2.5 Hz data set phase-lag the CARS measurements for this case by about 10 CAD, or roughly half the observed lag for the nonreversing flow at 5 Hz presented above.

The obvious thermal impact of flow reversal, seen both in the partial reversal data and in the bulk-flow-reversal data presented below, is a significant rise in the temperature history at cycle times near flow reversal. Significant increases in $\langle \theta \rangle$ near flow reversal have been observed previously in the turbulent flow studies by Dec and Keller [1] and by Feiler and Yeager [11]. Dec and Keller [1] postulated that this rise in $\langle \theta \rangle$ is associated with an ejection of fluid from the near-wall region during a flow reversal event. The cold-wire and CARS temperature histories are also suggestive of an ejection event during flow reversal, as close examination of the data reveals that the temperature changes near the wall phase lead the changes in the outer portions of the boundary layer.

In spite of the previous observations of both Dec and Keller [1] and Feiler and Yeager [11], an explanation of this thermal boundary layer thickening has not been given. The energy equation identifies four possible sources for the generation of temperature fluctuations: (1) advection of enthalpy, (2) unsteady conduction, (3) viscous dissipation, and (4) compression heating. For the flows investigated here, dissipation and compression heating are negligible because the Eckert number is only of order 10^{-4} , and because the levels of the pressure time derivative and velocity are moderate. Conduction at times of near-stagnant fluid velocities could play a role in thickening the thermal boundary layer because of the relatively high temperature differences used and the short boundary-layer length scales involved. However, a scale analysis of the unsteady conduction equation, using length and temperature scales characteristic of our results, shows that the expected magnitude of $\partial T / \partial t$ owed to conduction is an order of magnitude less than the experimentally observed gradients.

Based on the above scaling arguments and the behavior exhibited in the data, passive advection of enthalpy must be the dominant source of temperature fluctuation in this flow. Since our experiments were conducted with constant heater input to the backside of the test plate, it is possible that the reversal-induced temperature rise is caused by streamwise advection of enthalpy from warmer downstream regions to cooler-surface-temperature, upstream locations. Analysis of the rectified portions of temperature-compensated hot-wire traces, acquired in partially reversing boundary layers at both 2.5 and 5.0 Hz forcing, showed that the maximum upstream travel of a fluid particle was only about three thermal boundary layer thicknesses. Based on this estimate of the upstream fluid particle displacement and the observed magnitude of the temperature rise, the axial (“x”) temperature gradients present in the flow would necessarily be of comparable order to the wall-normal (“y”) gradients. Such a condition is inconsistent with the concept of a thin boundary layer and with the observed wall temperature distribution. Therefore, the reversal-induced temperature rise must be caused by vertical transport of warm fluid. We believe that there are three potential mechanisms for vertical fluid transport at cycle times near flow reversal: (1) a continuity-based ejection event, (2) buoyancy induced flow, and (3) “temporary” turbulence.

An ejection event during periodic flow reversal can be explained in terms of continuity. Considering streamwise fluid motion at a fixed distance from the wall, the downstream flow will respond more quickly to temporal changes in the pressure gradient as a consequence of its lower momentum. A localized flow rever-

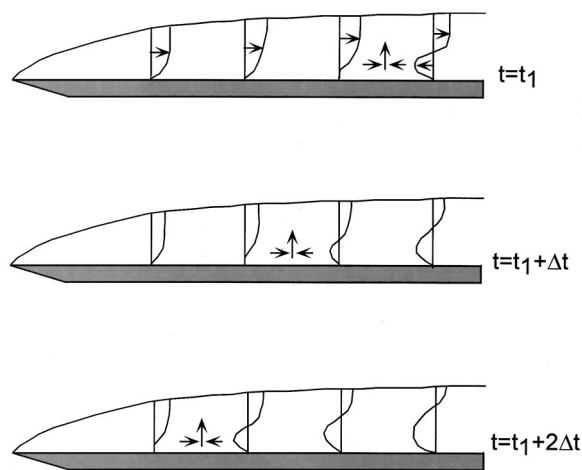


Fig. 6 Schematic of streamwise boundary-layer profiles during periodic flow reversal. The reversal initiates downstream at $t=t_1$ and rapidly propagates upstream. Continuity-based arguments show that there must be a vertical velocity event that accompanies flow reversal.

sal will then initiate near the downstream end of the channel, as shown schematically for $t=t_1$ in Fig. 6. As reversed fluid begins to move upstream, it will immediately encounter stationary or forward-moving fluid, and a secondary, transverse and/or spanwise flow must be established to preserve continuity. If we consider a two-dimensional model and neglect the changes in gas density owed to temperature (an assumption justified by similar results from low-temperature-difference cold-wire tests), then the simplified continuity relation applies

$$\frac{\partial u}{\partial x} + \frac{\partial v}{\partial y} = 0. \quad (8)$$

For a positive-to-negative, zero-velocity crossing, $\partial u/\partial x < 0$, so that $\partial v/\partial y > 0$. An ejection event must then occur almost simultaneously with a local flow reversal to satisfy both continuity and the no-slip condition. A “reversal line” then quickly moves upstream, as shown in Fig. 6, until: (1) the near-wall flow is reversed everywhere, or (2) the flow is accelerated in the positive direction again. Furthermore, any ejection must also be accompanied by a sudden inrush in order to preserve continuity, which would account for the subsequent dip in temperature following the rapid initial rise observed in the cold-wire results. This description and the necessary inflectional velocity profiles are similar in concept to steady separation, with the exception that the inviscid core flow still conforms to the shape of the wall.

Due to the high temperature differences employed in this study, buoyancy induced secondary flows in the form of thermal plumes could also be a source of vertical fluid motion at cycle times near flow reversal when the fluid velocity is nearly stagnant across the height of the channel. The impact of buoyancy was investigated experimentally by acquiring temperature time-series data in a pulsating channel flow with a cold wire. Channel floor temperatures of 4, 43, 60, 91, and 95 K above ambient were investigated. The cold-wire results, when normalized, showed that all of the temperature histories were both qualitatively and quantitatively of the same character [23]. This result is also consistent with the calculated time scale for the generation and release of a buoyant plume from a horizontal, heated wall in otherwise quiescent surroundings. Instability of the thermal boundary layer and release of a buoyant plume occurs for $Ra_\delta \sim 1000$ [33], where δ is the critical thermal-boundary-layer thickness. For the conditions of our experiments (in air with $\Delta T \sim 100$ K) this results in a length scale, δ , of about 4 to 5 mm before the thermal boundary layer becomes unstable and a plume is released. Using this length scale, the time

scale for the onset of free convection, $\tau = \delta^2/\alpha$, where α is the thermal diffusivity of air, is calculated to be of order 1 sec, which is much longer than the cycle time for which the velocities are near zero during a flow reversal event.

A third potential source of bulk fluid mixing in the vertical direction is the “temporary” turbulence that has often been reported in oscillating and pulsatile flows. It has been well documented, [34–37] that Stokes boundary layers are very receptive to transition. Transition to turbulence is often temporary but explosive, occurring during the deceleration phase of the cycle where strong adverse pressure gradients and inflectional velocity profiles destabilize the flow. This temporary turbulence is then relaminarized by the strong, favorable pressure gradient encountered during the cycle acceleration phase.

Boundary-layer hot-wire signals obtained in partially reversed flows did not display increased levels of random velocity fluctuations during the deceleration phase of the cycle where previous measurements by Hino et al. [34] suggest that transition will occur. For the case of a partial flow reversal, increased levels of random fluctuation in the hot- and cold-wire signals were observed during the initial portion of the cycle acceleration phase, from 85 to about 110 CAD, when the periodic temperature fluctuations were highest. These random fluctuations were not explosive in nature and transition to turbulence is not expected during a strong acceleration, which often has a stabilizing effect. However, the increase in random fluctuations does indicate that some level of disturbance was present in the flow during the partial flow reversal. The magnitude of this disturbance is moderate, and a good deal of the fluctuation in the anemometer output at times near flow reversal is caused by disturbed fluid that has passed over the sensor and its supports for a second and third time, and by imperfect temperature compensation of the dynamic hot-wire signal. Nevertheless, it is likely that this disturbance is due in part to some level of transition, which contributes to the rapid temperature rise associated with reversal and acts in conjunction with the bulk ejection mechanism explained above to produce a rapid increase in thermal boundary-layer thickness during a flow reversal event.

Complete Flow Reversal. Time-series data for the case of a complete flow reversal at a forcing frequency of 2.5 Hz are shown in Fig. 7. When compared to the partially reversed flow discussed above, this completely reversed flow is characterized by the same frequency and by convective velocities that are reduced by more than a factor of two. Similar to the data sets presented above, the temperature history is essentially steady during the high-velocity portion of the cycle, as high-enthalpy fluid resulting from heat transfer and vertical transport of warm fluid during the previous cycle has been advected past the measurement location before the next forcing cycle begins. Both the CARS and cold-wire results indicate a temperature rise associated with the initiation of bulk flow reversal that is similar in nature to the partially reversed flow results presented above. As in the case of a partial flow reversal, the immediate impact of a positive-to-negative zero-velocity crossing is a rapid increase in thermal boundary-layer thickness associated with a fluid ejection event and a disturbed boundary layer. This increase in thermal boundary-layer thickness is accompanied by a cyclic heat-transfer minimum followed by a short-lived thinning of the thermal boundary layer and a period of decreased heat transfer caused by the advection of high-enthalpy fluid through the measurement volume.

The duration of the period of near-cycle-minimum heat transfer is more than twice as long as observed for the case of partial flow reversal. The lower speed flow (required to generate a bulk reversal when using a mechanical forcing scheme) simply takes longer to sweep the channel clear of high-enthalpy fluid. In addition, high levels of negative velocities can couple with the downstream wall boundary conditions to further influence surface heat transfer through a streamwise advection mechanism that was unimportant for the small negative velocities observed in the partially reversed

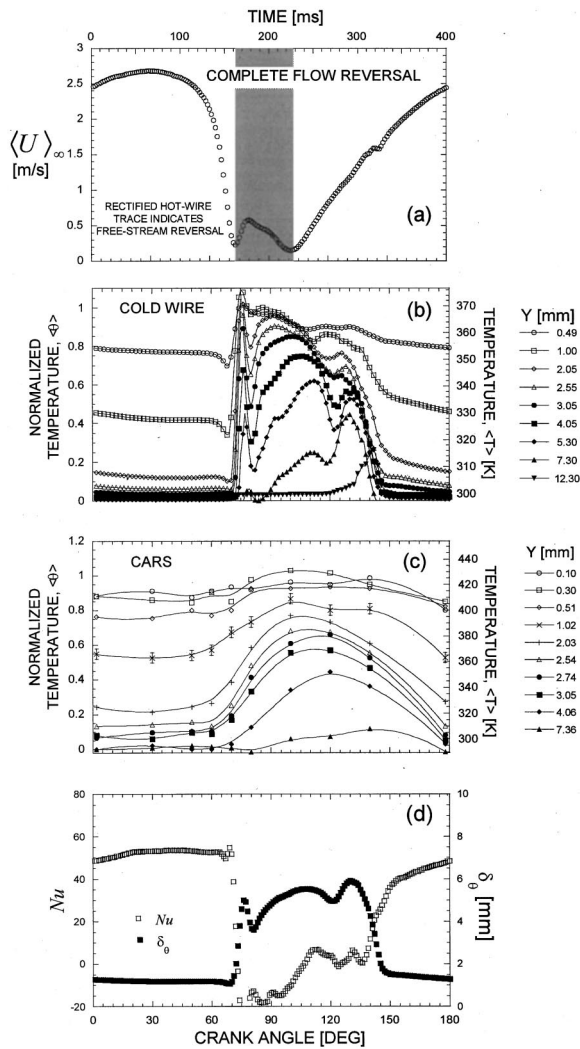


Fig. 7 Time-resolved boundary-layer temperature and heat-flux data from a fully reversing channel flow

case. Estimates obtained from rectified, temperature-compensated CTA traces acquired in the boundary layer suggest that warm fluid can travel as much as 40 percent of the channel length back toward the leading edge during a bulk flow reversal. During the strong bulk flow reversal, high-enthalpy fluid was advected upstream to “reheat” the wall and produce a reversal of the wall heat flux at this upstream measurement location for cycle times from 70 to 110 CAD. No reversal in heat flux was observed with bulk flow reversal at measurement locations further downstream. This type of conjugate effect is suggestive of an increased sensitivity of pulsatile-flow heat transfer to the surface boundary condition and is important in applications where surface temperature distributions are often not isothermal.

Time-Averaged Heat Transfer. The time-mean Nusselt number results obtained from 12 sets of cold-wire experiments are plotted against the inverse of the thermal Graetz number in Fig. 8. In construction of Fig. 8, time-mean velocities have been used to calculate the Graetz numbers for the unsteady data sets. The inverse of the Graetz number is a measure of the state of thermal boundary-layer development, and allows the effects of the thermal entry length to be accounted for in a heat-transfer comparison of the data sets.

The phase-averaged heat transfer results shown in Figs. 3, 5, and 7 indicate that the instantaneous impact of both partial and complete flow reversals is a decrease in the Nusselt number when

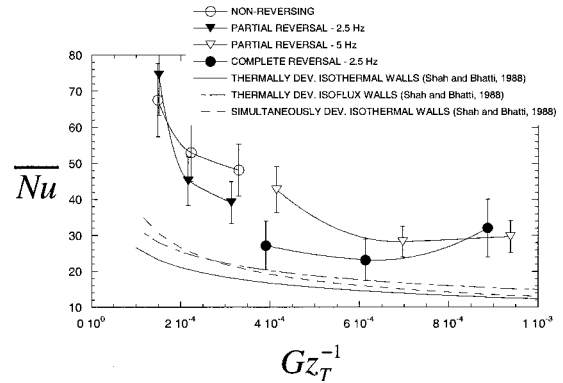


Fig. 8 Time-mean heat transfer data plotted against the inverse of the thermal Graetz number. The data are compared to accepted laminar heat transfer correlations obtained from Shah and Bhatti [38] and show a heat-transfer enhancement with flow pulsation in all cases. The error bars on the plot reflect a ± 15 percent uncertainty in time-mean Nusselt number for non-reversing and partially reversed flow and a ± 25 percent uncertainty in the Nusselt number for the case of bulk flow reversal.

compared to a nonreversing, pulsatile flow. A similar decrease in heat flux, relative to the positive-velocity cycle times, during the negative-velocity portion of the cycle was also observed in the 100 Hz, turbulent flow results of Dec and Keller [1]. Relative to the period of the applied forcing, the period of decreased heat transfer is longer if the period of reversed flow is longer, so that the lowest Nusselt numbers are obtained for a complete flow reversal.

At low Gz_T^{-1} (thin thermal boundary layers), the time-mean Nusselt-number data for the nonreversing flow at 5 Hz and the partially reversed flow at 2.5 Hz forcing differ by less than the ± 15 percent uncertainty in the measurement, but the data are still suggestive of higher heat-transfer rates for a nonreversing flow. At higher Gz_T^{-1} (thicker thermal boundary layers), the Nusselt numbers for the partial flow reversal at 5 Hz forcing are higher or equal within the measurement uncertainty to the data for bulk reversal at 2.5 Hz. Previous authors (Bayley et al. [3]; Keil and Baird [10]; Hanby [9]) have postulated that flow reversal is a requirement for heat-transfer enhancement. However, the time-mean heat transfer results presented here show that periodic flow reversal does not necessarily lead to increased heat transfer rates relative to nonreversed pulsatile flows in the developing regime. Furthermore, the heat-transfer results obtained in this study show that the time-mean Nusselt numbers are generally enhanced relative to the accepted steady flow heat-transfer correlations for laminar, two-dimensional, entry region flow provided by Shah and Bhatti [38], regardless of reversal regime. This result indicates that pulsating flows show promise as a heat-transfer enhancement technique in the developing laminar flows that are characteristic of many single-phase heat-exchanger applications.

Conclusion

The results of an experimental investigation of the time-resolved thermal boundary-layer structure and surface heat flux in a pulsatile, laminar channel flow have been reported. Two techniques, pure-rotational CARS and cold-wire anemometry, have been used to acquire phase-averaged temperature data. Pure-rotational CARS has been used for nonintrusive measurements of the long-time trends in the cyclic temperature oscillation and provides measurements with an effectively infinite frequency response. The increased data-acquisition rates offered by the invasive cold-wire technique provide a more detailed description of the temperature oscillation, at the expense of a small but finite

phase lag in the response of the probe resulting from imperfect frequency compensation and probe intrusion error.

The thermal impact of flow reversal has been systematically investigated. Time-resolved temperature data from nonreversing, partially reversed, and complete flow reversals are presented. The cycle-resolved impact of flow reversal is a dramatic thickening of the thermal boundary layer, which appears to be caused by a vertical ejection of fluid from the near-wall region and by a limited degree of turbulent transition. During the reversed-flow portion of the cycle, a cyclic heat-transfer minimum is attained. Following reversal, the wall heat transfer recovers as the accelerated boundary-layer flow sweeps the channel clear of high-enthalpy fluid.

This time-resolved description is consistent with the observed time-mean Nusselt-number results. The local time-mean Nusselt number decreases as the duration of the reversal phase, and the associated period of low heat-transfer rates, increases relative to the cycle period. For the developing, laminar regime investigated, the time-mean Nusselt number data suggest, within the bounds of the measurement uncertainty, that heat-transfer performance improves with lesser degrees of flow reversal. All of the pulsatile flows studied exhibit enhancement relative to accepted Nusselt-number data for a developing, laminar channel flow, and enhancements as high as a factor of two are observed for low values of Gz_T^{-1} . These results show that enhancement can be achieved with low-amplitude (e.g., low $\Delta u/\bar{U}_{\infty}$), mechanical forcing schemes, which will produce lower noise levels and require less energy input relative to acoustically resonant schemes that have been used previously to produce large bulk flow reversals.

Acknowledgment

The authors would like to thank the University of Illinois Air-Conditioning and Refrigeration Center (ACRC) for partial funding of this work. The ACRC is a National Science Foundation Industry/University Cooperative Research Center (IUCRC). The first author also wishes to thank the University of Illinois, Department of Mechanical and Industrial Engineering for its financial support. The constructive reviews of Steven Trujillo, Tim O'Hern, and Art Ratzel of Sandia are also gratefully acknowledged.

Nomenclature²

Roman Symbols

- a = sound speed [m/s]
 q'' = wall heat flux [W/m²]
 d = diameter [m]
 d_h = hydraulic diameter [m]
 Gz_T = Graetz number ($Gz_T = Re_x Pr / (x/d_h)$) [-]
 h = heat-transfer coefficient [W/m²-K]
 H = channel half height [m]
 L = streamwise length scale, channel length [m]
 l = Bechtov cold length, ($l = \sqrt{\tau\alpha}$), total length of cold-wire sensor [m]
 l_* = active length of cold-wire sensor [m]
 \dot{m}' = mass flux per unit depth in the spanwise direction [kg/s m]
 Nu_x = local Nusselt number ($Nu_x = q''_x d_h / \kappa_{\infty} \Delta T$) [-]
 Pr = Prandtl number ($Pr = \nu / \alpha$) [-]
 Re_x = Reynolds number ($Re_x = \bar{U} x / \nu$) [-]
 T = temperature [K]
 t = time [s]
 U, u = streamwise velocity [m/s]
 v = wall-normal velocity [m/s]
 Wo = Womersley number based on channel half height ($Wo = H\sqrt{\omega/\bar{\nu}}$) [-]

- x = streamwise coordinate [m]
 y = wall-normal coordinate [m]

Greek Symbols

- δ_{θ} = temperature defect thickness defined in Eq. 5 [m]
 κ = thermal conductivity [W/m-K]
 ν = kinematic viscosity [m²/s]
 θ = normalized temperature ($\theta = (T - T_{\infty}) / (T_w - T_{\infty})$) [-]
 τ = lumped capacitance time constant, ($\tau = \rho c_p d / 4h$) [s]
 Δu = difference between min. and max. centerline velocities [m/s]
 ω = circular frequency [s⁻¹]

Subscripts

- c = cold-wire plating property
 osc = oscillating component
 p = cold-wire prong property
 w = wall condition, cold-wire sensor property
 x = evaluated at local streamwise location
 ∞ = channel centerline condition

References

- Dec, J. E., Keller, J. O., and Arpaci, V. S., 1992, "Heat Transfer Enhancement in the Oscillating Turbulent Flow of a Pulsed Combustor Tail Pipe," *Int. J. Heat Mass Transf.*, **35**, No. 9, pp. 2311–2325.
- Niida, T., Yoshida, T., Yamashita, R., and Nakayama, S., 1974, "The Influence of Pulsation on Laminar Heat Transfer in Pipes," *Heat Transfer-Jpn. Res.*, **3**, No. 3, pp. 19–28.
- Bayley, F. J., Edwards, P. A., and Singh, P. P., 1961, "The Effect of Flow Pulsations on Heat Transfer by Forced Convection from a Flat Plate," *Proceedings of the First International Heat Transfer Conference*, Boulder, CO, pp. 499–509.
- Galitseyskiy, B. M., Danilov, Y. I., Dreyster, G. A., Kalinin, E. K., and Koshkin, V. N., 1969, "Effect of Resonant Fluctuations of Coolant Pressure on Convective Heat Transfer in Pipes," *Heat Transfer-Sov. Res.*, **1**, No. 2, pp. 177–185.
- Fujita, N., and Tsubouchi, T., 1982, "An Experimental Study of Unsteady Heat Transfer from a Flat Plate to an Oscillating Air Flow," *Heat Transfer-Jpn. Res.*, **11**, pp. 31–43.
- Miller, J. A., 1969, "Heat Transfer in the Oscillating Turbulent Boundary Layer," *J. Eng. Power*, **91**, pp. 239–244.
- Feiler, C. E., 1964, "Experimental Heat-Transfer and Boundary-Layer Behavior with 100-CPS Oscillations," NASA TN No. 2531, Washington, DC.
- Jackson, T. W., and Purdy, K. R., 1965, "Resonant Pulsating Flow and Convective Heat Transfer," *ASME J. Heat Transfer*, **87**, pp. 507–512.
- Hanby, V. I., 1969, "Convective Heat Transfer in a Gas-Fired Pulsating Combustor," *J. Eng. Power*, **91**, pp. 48–52.
- Keil, R. H., and Baird, M. H. I., 1971, "Enhancement of Heat Transfer by Flow Pulsation," *Ind. Eng. Chem. Process Des. Dev.*, **10**(4), pp. 473–478.
- Feiler, C. E., and Yeager, E. B., 1962, "Effect of Large Amplitude Oscillations on Heat Transfer," NASA TR R-142, Washington, DC.
- Dec, J. E., and Keller, J. O., 1989, "Pulse Combustor Tail Pipe Heat Transfer Dependence on Frequency, Amplitude, and Mean Flow Rate," *Combust. Flame*, **77**, pp. 359–374.
- Dec, J. E., and Keller, J. O., 1990, "Time-Resolved Gas Temperatures in the Oscillating Turbulent Flow of a Pulse Combustor Tail Pipe," *Combust. Flame*, **80**, pp. 358–370.
- Dec, J. E., Keller, J. O., and Hongo, I., 1991, "Time-Resolved Velocities and Turbulence in the Oscillating Flow of a Pulse Combustor Tail Pipe," *Combust. Flame*, **83**, pp. 271–292.
- Despard, R. A., and Miller, J. A., 1971, "Separation in Oscillating Laminar Boundary Layer Flows," *J. Fluid Mech.*, **47**, pp. 21–31.
- Charnay, G., and Mathieu, J., 1976, "Periodic Flow in a Wind Tunnel Produced by Rotating Shutters," *ASME J. Fluids Eng.*, **98**, pp. 278–283.
- Simpson, R. L., Sallas, J. J., and Nasburg, R. E., 1978, "Tailoring the Waveform of a Periodic Flow With a Programmable Damper," *ASME J. Fluids Eng.*, **100**, pp. 287–290.
- Morel, T., 1977, "Design of Two-Dimensional Wind-Tunnel Contractions," *ASME J. Fluids Eng.*, **99**, No. 2, pp. 371–378.
- Swearingen, J. D., and Blackwelder, R. F., 1987, "The Growth and Breakdown of Streamwise Vortices in the Presence of a Wall," *J. Fluid Mech.*, **182**, pp. 255–290.
- Currie, I. G., 1993, *Fundamental Mechanics of Fluids*, 2nd ed., McGraw-Hill, New York.
- Stuart, J. T., 1963, "Unsteady Boundary Layers," in *Laminar Boundary Layers*, L. Rosenhead, ed., Clarendon Press, Oxford, UK.
- Kearney, S. P., Lucht, R. P., and Jacobi, A. M., 1999, "Temperature Measurements in Convective Heat Transfer Flows Using Dual-Broadband, Pure-Rotational Coherent Anti-Stokes Raman Spectroscopy (CARS)," *Exp. Therm. Fluid Sci.*, **19**, pp. 13–26.
- Kearney, S. P., 1999, "An Experimental Investigation of Thermal Boundary

²Note: All dimensionless groups are evaluated using the properties of air evaluated at the channel centerline.

Layer Structure and Heat Transfer in Oscillating Flows Using CARS Spectroscopy and Cold-Wire Anemometry," Ph.D. dissertation, The University of Illinois, Urbana, IL.

- [24] Kröll, S., and Sandell, D., 1988, "Influence of Laser Mode Statistics on Noise in Nonlinear Optical Processes—Application to Single-Shot Broadband Coherent Anti-Stokes Raman Scattering Thermometry," *J. Opt. Soc. Am. B*, **5**, No. 9, pp. 1910–1926.
- [25] Aldén, M., Bengtsson, P. E., Edner, H., Kröll, S., and Nilsson, D., 1989, "Rotational CARS: A Comparison of Different Techniques with Emphasis on Accuracy in Temperature Determination," *Appl. Opt.*, **28**, No. 15, pp. 3206–3219.
- [26] Quintana, D. L., Amitay, M., Ortega, A., and Wagnanski, I. J., 1997, "Heat Transfer in the Forced Laminar Wall Jet," *ASME J. Heat Transfer*, **119**, pp. 451–459.
- [27] Wroblewski, D. E., and Eibeck, P. A., 1991, "A Frequency Response Compensation Technique for Cold Wires and Its Application to a Heat Flux Probe," *Exp. Therm. Fluid Sci.*, **4**, pp. 452–463.
- [28] Palmer, R. E., 1989, "The CARSFT Computer Code for Calculating Coherent Anti-Stokes Raman Spectra: User and Programmer Information," Report No. SAND89-8206, Sandia National Laboratories, Albuquerque, NM and Livermore, CA.
- [29] Zhang, L. W., 1996, "A Numerical Study of Flow and Heat Transfer in Compact Heat Exchangers," Ph.D. dissertation, The University of Illinois, Urbana, IL.
- [30] Qiu, S., Simon, T. W., and Volino, R. J., 1995, "Evaluation of Local Wall Temperature, Heat Flux, and Convective Heat Transfer Coefficient from the Near Wall Temperature Profile," *ASME-HTD*, **318**, pp. 45–52.
- [31] Volino, R. J., and Simon, T. W., 1997, "Velocity and Temperature Profiles in Turbulent Boundary Layer Flows Experiencing Streamwise Pressure Gradients," *ASME J. Heat Transfer*, **119**, No. 3, pp. 433–439.
- [32] Qiu, S., and Simon, T. W., 1994, "Measurements of Heat Transfer and Fluid Mechanics within an Oscillatory Flow in a Pipe," *ASME-HTD*, **285**, pp. 45–52.
- [33] Bejan, A., 1995, *Convection Heat Transfer*, Wiley, New York.
- [34] Hino, M., Sawamoto, M., and Takasu, S., 1976, "Experiments on Transition to Turbulence in Oscillatory Pipe Flow," *J. Fluid Mech.*, **75**, pp. 193–207.
- [35] Clamen, M., and Minton, P., 1977, "An Experimental Investigation of Flow in an Oscillating Pipe," *J. Fluid Mech.*, **81**, pp. 421–431.
- [36] Akhavan, R., Kamm, R. D., and Shapiro, A. H., 1991, "An Investigation of Transition to Turbulence in Bounded Oscillatory Stokes Flows: Part 1 Experiments," *J. Fluid Mech.*, **225**, pp. 395–422.
- [37] Verzicco, R., and Vittori, G., 1996, "Direct Simulation of Transition in Stokes Boundary Layers," *Phys. Fluids*, **8**, pp. 1341–1343.
- [38] Shah, R. K., and Bhatti, M. S., 1988, "Laminar Heat Transfer in Wall Bounded Flows," in *Handbook of Single-Phase Convective Heat Transfer*, R. K. Shah, S. Kakac, and M. Yenir, eds., McGraw-Hill, New York.

Effect of Turbulence With Different Vortical Structures on Stagnation Region Heat Transfer

Aung N. Oo

Graduate Student
Faculty of Engineering and Applied Science
Memorial University of Newfoundland
St. John's, Newfoundland, A1B 3X5, Canada
e-mail: aung@engr.mun.ca

Chan Y. Ching

Associate Professor
Dept. of Mechanical Engineering,
McMaster University,
Hamilton, Ontario, L8S 4L7, Canada
e-mail: chingcy@mcmaster.ca

The effect of freestream turbulence with different vortical structures on the stagnation region heat transfer was experimentally studied. Reynolds numbers, based on leading edge diameter of the heat transfer model with a cylindrical leading edge, ranged from 67,750 to 142,250. Turbulence generating grids of parallel rods were placed at several positions upstream of the heat transfer model in orientations where the rods were perpendicular and parallel to the stagnation line. The turbulence intensity and ratio of integral length scale to leading edge diameter were in the range 3.93 to 11.78 percent and 0.07 to 0.70, respectively. The grids with rods perpendicular to the stagnation line, where the primary vortical structures are expected to be perpendicular to the stagnation line, result in higher heat transfer than those with rods parallel to the stagnation line. The measured heat transfer data and turbulence characteristics are compared with existing correlation models. [DOI: 10.1115/1.1375165]

Keywords: Convection, Experimental, Heat Transfer, Turbulence, Vortex

Introduction

Heat transfer in the stagnation region is important in many engineering applications. A critical application would be the heat transfer from the combustion gases to the turbine blades in a gas turbine. In many instances, the temperature of combustion gases can exceed the melting point of blade materials. Accurate prediction of turbine blade heat transfer is essential to improve the design of blade cooling systems. The estimation of heat transfer to the first stage blades and vanes of a newly designed gas turbine can be in error by a factor of two or three under certain engine conditions, especially in the stagnation region [1–3].

A complete understanding of the transport mechanisms of momentum and heat in turbulent flows has not been achieved. It is, however, well established that the coherent vortical structures in a turbulent flow play an important role in momentum and heat transfer. A knowledge of the interaction of freestream vortical structures with the stagnation region boundary layer should lead to improved models of stagnation region heat transfer.

There have been several studies on the effect of freestream turbulence on stagnation region heat transfer [4–14]. Correlations between the stagnation region heat transfer and the characteristics of freestream turbulence such as turbulent intensity, integral length scale and Reynolds number have been developed. Smith and Kuethe [4] suggested a semi-empirical theory for the augmentation of heat transfer at the stagnation point of a circular cylinder. They assumed a linear relation between the stagnation point Fr ($\equiv Nu\sqrt{Re_D}$) and the freestream turbulence level for a constant Reynolds number, and their correlation was found to be valid up to a turbulence intensity of about 6 percent. Kestin and Wood [5] and Lowery and Vachon [6] used the parameter $Tu\sqrt{Re_D}$ to correlate the stagnation line heat transfer data. VanFossen et al. [12] developed a correlation model for the stagnation point heat transfer by incorporating the integral length scale in addition to Reynolds number and turbulence intensity. Yeh et al. [10] proposed a correlation model for the heat transfer at the stagnation point of a gas turbine blade based on the parameter developed by VanFossen et al. [12], but with different constants and exponents in order to best fit their experimental data. In most cases, correlations devel-

oped through specific experiments are not applicable to sets of data from other researchers. More importantly, most correlations are for nearly isotropic turbulence generated using square-mesh grids. However, turbulence in gas turbine engines is expected to be highly anisotropic [15] and well laced with coherent vortical structures [16].

Heat transfer augmentation in the stagnation region is hypothesized to be caused by vorticity amplification [17–19]. If a vortical filament, which is normal to the stagnation line and freestream flow direction, is considered, the filament is stretched and tilted as it is advected into the stagnation region due to divergence and acceleration around the bluff body (see Fig. 1). The stretching causes the vorticity to be intensified through conservation of angular momentum. The vortical filament with intensified vorticity interacts with the boundary layer and induces velocity gradients in the spanwise direction parallel to the stagnation line. The three-dimensional velocity gradients enhance the transport mechanism within the boundary layer resulting in higher heat transfer. On the other hand, a vortical filament, which is parallel to the stagnation line, is not stretched due to the lack of apparent velocity divergence in this direction as it approaches the stagnation region. VanFossen et al. [12] found that the correlation to estimate the stagnation line heat transfer from the characteristics of freestream

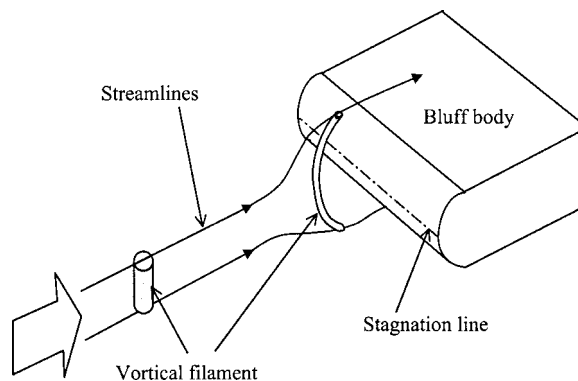


Fig. 1 Vortex stretching and vorticity intensification around the leading edge

Contributed by the Heat Transfer Division for publication in the JOURNAL OF HEAT TRANSFER. Manuscript received by the Heat Transfer Division June 30, 2000; revision received January 20, 2001. Associate Editor: M. Faghri.

turbulence generated by square mesh grids under-predicted the stagnation heat transfer rate using a grid of parallel rods. The hypothesis of vortex stretching and heat transfer enhancement can be experimentally investigated using a turbulent freestream with different coherent vortical structures. This should also provide further insight to the turbulent heat transfer mechanism in the stagnation region. This experimental study was, therefore, conducted to investigate the influence of freestream turbulence with different coherent vortical structures on the stagnation region heat transfer.

The objectives of the study are as follows:

- 1 to generate turbulence with different vortical structures (one with primary vortices susceptible to stretching and another with primary vortices not susceptible to stretching as they approach the stagnation region)
- 2 to quantify the heat transfer enhancement in the stagnation region by the two different turbulent flows in (1)
- 3 to examine the nature of heat transfer augmentation over the stagnation region by different freestream coherent vortical structures
- 4 to investigate the difference in stagnation region heat transfer due to freestream turbulence with distinct vortical structures and that due to turbulence generated using square mesh grids

Experimental Facilities and Test Procedures

The experiments were performed in an open circuit low speed wind tunnel which has a test section of $1\text{m} \times 1\text{m}$ and is over 20 m long. The wind tunnel is driven by a 19 kW centrifugal blower. The air passes through a screened diffuser and a large settling chamber with three single-piece precision screens before accelerating into the test section through a 5:1 contraction. The freestream turbulence intensity without the grids is less than 0.5 percent at all flow rates. The velocity in the test section is changed using motorized variable angle inlet vanes on the blower.

Figure 2 shows a schematic of the heat transfer model with a cylindrical leading edge to simulate the leading edge of a gas turbine vane. The leading edge is attached to a flat body 60 cm long. The after body is then streamlined with a long tapered tail in order to prevent the shift of the stagnation point due to vortex shedding at the end. The model is made of 0.635 cm thick Plexiglass. The cylindrical leading edge is 20.32 cm in diameter and 1 m in height creating a flow blockage of 20 percent.

The middle portion of the leading edge is covered with a stainless steel surface, which is to be heated for the heat transfer test. The stainless steel surface consists of nineteen strips of 0.005 cm-thick stainless steel foil, and the strips are evenly distributed over the stagnation line at the center of the cylindrical leading edge. Each strip is 15.24 cm long, located vertically in Y direction over the leading edge surface, 1.5 cm wide and separated from each other by a gap of 1 mm. The gaps between the strips are filled with super-glue and sanded until the surface is smooth and flush with the foil surface. The steel foils are connected in series,

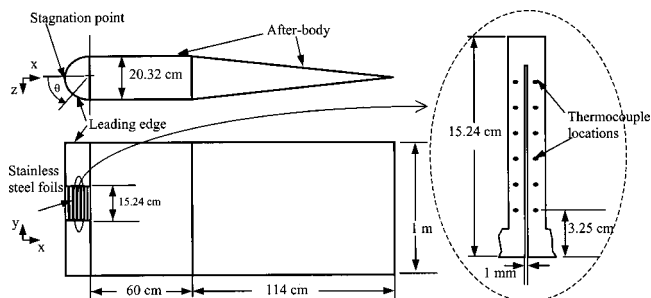


Fig. 2 Schematic diagram of heat transfer model

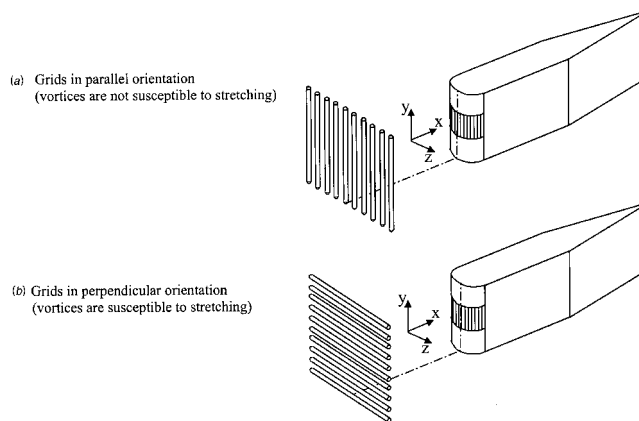


Fig. 3 Arrangements of grids

and a variable AC/DC transformer is used to supply power across the foils to obtain a constant heat flux surface at the leading edge. Six calibrated, 36-gauge T-type copper-constant thermocouples are attached to the underside of every foil strip on one half ($0 \text{ deg} \leq \theta$

$\leq 90 \text{ deg}$) of the cylindrical leading edge. The thermocouples are evenly distributed in the middle portion of the strip in such a way that the distance between the edge of the strip and the nearest thermocouple is 3.25 cm as shown in Fig. 2. One instrumented strip is also placed symmetrically opposite on the other half of the leading edge in order to check the alignment of the model with the mean flow direction. The thermocouples are threaded through small holes drilled on the leading edge. Additional thermocouples are attached on the inner wall of the leading edge to estimate the conduction heat loss through the Plexiglass.

Data from the thermocouples are acquired via two CYEXP 32 Multiplexors (Cyber Research) connected in series. Analog outputs from the Multiplexors are digitized using a DAS 1602 A/D converter (Cyber Research) and data logging is controlled by the "Labtech Buildtime" software package. Freestream velocity was measured by 8360-M-GB VelociCalc[®] Plus TSI air velocity meter, which has a resolution of 0.01 m/s. The voltage supply and current flow to the leading edge were recorded using a multimeter with a resolution of 0.01 volt and 0.01 ampere.

To generate freestream turbulence with well-defined primary vortex lines, grids of parallel rods were used. The grids were placed upstream of the model in different orientations as shown in Fig. 3. From hereafter, the grid with the rods perpendicular to the stagnation line will be called the grid in perpendicular orientation, while the grid with the rods parallel to the stagnation line will be called the grid in parallel orientation. The rods in both grid orientations are perpendicular to the streamwise direction. Three grids with rod diameters of 2.86 cm (1-1/8"), 1.59 cm (5/8") and 0.95 cm (3/8"), and 50 percent open area were used. Each grid was placed at five different positions, $25d$ to $125d$, upstream of the stagnation line of the model. The wind tunnel was operated at freestream velocities of 5, 8 and 10.5 m/s, corresponding to Re_D of 67,750, 108,350, and 142,250, for each grid position. The leading edge was heated to about 45°C for each heat transfer test. The thermocouple readings were monitored every 15 minutes until steady state conditions were reached. Three sets of temperature distributions and voltage and current flow of the DC power supply unit were recorded after steady state was attained. Each data set of temperature distributions contains 180 data points (data acquisition rate of 1.5 Hz for 2 minutes) for each thermocouple.

Single and X-wires were used to measure the freestream turbulence characteristics at several positions downstream of the rod-grids in perpendicular orientation in the absence of the heat transfer model. Two sets of X-wire data, one for the simultaneous measurement of the velocity components in X and Y directions

and another in X and Z directions (see Fig. 3), were obtained by rotating the X -wire probe 90 deg. The hot wires were operated by DANTEC 55M01 constant temperature bridges, and output voltages of the anemometers were digitized using a 16 channel 12 bit Keithley 570 System A/D converter, interfaced to a personal computer. The frequency response of the circuits was determined by standard square-wave tests, and found to be 30 kHz. The sampling frequency of the study range from 20 to 30 kHz.

Data Reduction and Experimental Uncertainties

Electrical energy supplied to the series of stainless steel foils is lost to the freestream by convection, to the surrounding by radiation, and to the leading edge of the model by conduction. The Nusselt number was estimated as follows:

$$Nu(\theta) = \frac{Q_{cov}D}{A[T_w(\theta) - T_\infty]k} \quad (1)$$

where

$$Q_{cov} = Q_{in} - Q_{rad} - Q_{cond}$$

Energy input to the leading edge, Q_{in} , is obtained from supply voltage, V_o , and current flow, I . An estimation for the radiation heat loss, Q_{rad} , was made by assuming gray body radiation to black surroundings and emissivity of 0.17 for stainless steel foil. Conduction heat losses, Q_{cond} , through the leading edge wall was computed from the measured temperature difference between the outer and inner surface of the leading edge wall. Thermal conductivity of the leading edge was 0.201 W/m-K as provided by the manufacturer. In this experiment, radiation and conduction heat losses were on the order of 2 percent and 20 percent, respectively. An uncertainty analysis was conducted using the methods of Moffat [20]. The uncertainty in Fr is 3.92 percent and 3.67 percent for the minimum and maximum freestream Reynolds number, respectively.

The average of 180 data points was obtained for each thermocouple. The spanwise temperature distribution of the stainless steel strips was found to be fairly constant and within the uncertainty of the temperature measurements. The spanwise variation of the temperatures from the six thermocouples (T1-T6) is about two percent for all heated strips (Fig. 4), where strip no. 1 is on the stagnation line. Since the thermocouples are located in the middle portion of the stainless steel foils (see Fig. 2), the end conduction heat losses from the heated strips do not significantly influence the spanwise temperature distribution at the measured locations on the strips. Therefore, an average value of the six thermocouple readings is taken as the temperature $T_w(\theta)$ of a particular strip.

A number of test runs were performed with and without the grids to estimate the conduction heat losses. During these test runs, the spanwise temperature distributions of the heated strips and the temperatures outside the strips and on the inner surfaces were recorded. A three-dimensional finite difference scheme was

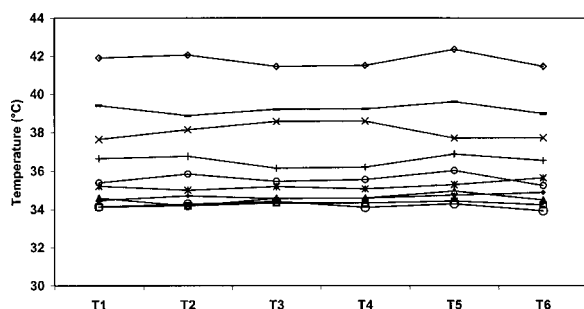


Fig. 4 Spanwise temperature distributions of heated stainless steel strips (○, strip no. 1; □, 2; △, 3; ◇, 4; *, 5; o, 6; +, 7; ×, 8; -, 9; ◇, 10)

then used to determine the total conduction heat losses taking into account the lateral end conduction heat losses. Correction factors were obtained for different freestream Reynolds numbers to estimate the conduction heat losses based on the average temperature difference between the heated outer surface and inner wall of the leading edge. Heat transfer tests were also performed without any grids to validate the heat transfer measurements. The stagnation line heat transfer Frossling numbers for the freestream with low turbulence intensity (0.5 percent for this study) ranged from 1.04 to 1.06 for the Reynolds numbers of the study, and are in good agreement with the literature [6,8].

Streamwise turbulence intensity $Tu(=u/U)$ and integral length scale (λ_x) were calculated from the single hot wire data. The method proposed by VanFossen et al. [12] was used to estimate λ_x by fitting the auto-correlation data with an exponential function. The rms fluctuating velocity components in spanwise directions (v and w) were calculated from the X -wire data. Experimental uncertainties in the v and w components and λ_x , based on the uncertainty analysis of hot wire data by Yavuzkurt [21], were estimated to be 3.09 percent and 10.95 percent, respectively. The turbulence characteristics were found to be uniform in the spanwise direction at all streamwise downstream locations, i.e., x/d of 25 to 125. This is consistent with the results of Roach [22], where the turbulence was found to be homogeneous beyond ten mesh lengths, i.e., $x/d=20$ for this study.

Results and Discussion

The streamwise turbulence intensity downstream of the three rod-grids are almost independent of Reynolds number (Fig. 5), and well represented with the power law of Roach [22].

$$Tu = C_1 \left(\frac{x}{d} \right)^{-\frac{5}{7}} \quad (2)$$

The values of C_1 are 1.12, 1.24, and 1.20 for the rod-grids of 2.86 cm, 1.59 cm, and 0.95 cm, respectively. The turbulence intensity decreases approximately from 12 percent to 4 percent as the grid-to-model distance increases from $25d$ to $125d$. The streamwise distributions of the ratio of integral length scale to the diameter of the grid-rods (λ_x/d) for the sample $Re_D = 108,350$ are given in Fig. 6. Unlike the turbulence intensity, λ_x/d is dependent on Reynolds number, and the best-fit lines with the power law are also presented in Fig. 6. The form of the power law used has the same growth rate of λ_x proposed by Roach [22].

$$\lambda_x = C_2 \left(\frac{x}{d} \right)^{\frac{1}{2}} \quad (3)$$

The values of C_2 for the different rod-grids and Reynolds numbers are presented in Table 1. The λ_x/d increases by about 45 percent as x/d increases from 25 to 125, and is in reasonable agreement with the results of Roach [22]. It should be noted that

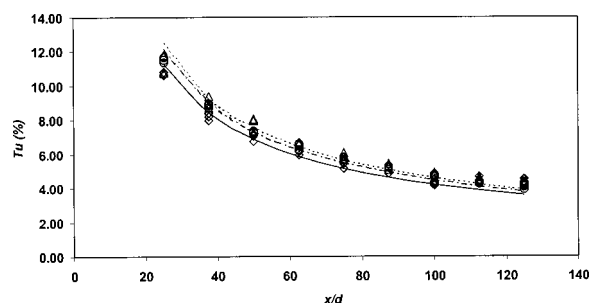


Fig. 5 Streamwise turbulence intensity downstream of the grids (◇, —, 2.86 cm rod-grid; △, ---, 1.59 cm rod-grid; ○, - · -, 0.95 cm rod-grid)

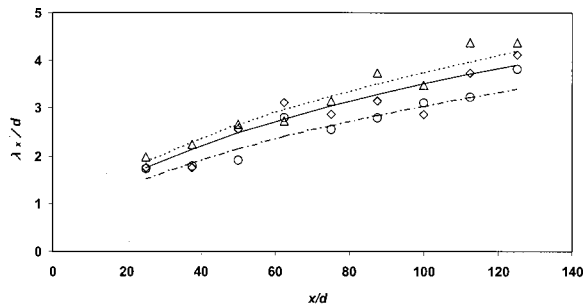


Fig. 6 Streamwise integral length scale downstream of the grids for $Re_D=108,350$ (\diamond , —, 2.86 cm rod-grid; Δ , ---, 1.59 cm rod-grid; \circ , - - -, 0.95 cm rod-grid)

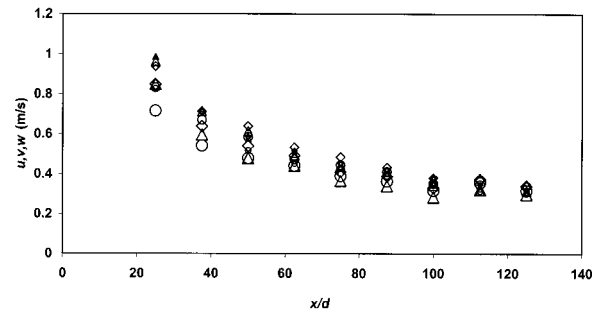


Fig. 7 RMS fluctuating velocity components of grids in perpendicular orientation for $Re_D=108,350$ (2.86 cm rod-grid: \diamond , u ; Δ , v ; \circ , w ; 1.59 cm rod-grid: \diamond , u ; Δ , v ; \circ , w ; 0.95 cm rod-grid: \diamond , u ; Δ , v ; \circ , w)

both rod-grids in perpendicular and parallel orientations give the same Tu and λ_x/d since they are calculated based on the streamwise velocity fluctuations.

The rms of fluctuating velocity components, u , v , and w , downstream of the rod-grids in perpendicular orientation for $Re_D = 108,350$ are presented in Fig. 7. At locations close to the grid, v and u are approximately equal ($v/u \approx 1$), and higher than the w component (w/u is in the range 0.85 to 0.91). This is due to the fact that most turbulence eddies are aligned with the turbulence generating rods and velocity fluctuation in the direction parallel to the rods are not as intense as in other directions. As x/d increases, the difference between the three components decreases. At $x/d = 125$, v/u , and w/u range from 0.99 to 0.9 and from 0.88 to 0.99, respectively. A plausible conclusion from Fig. 7 is that the distinct structures of turbulence due to the parallel array of rods become more homogeneous with distance from the grid.

Heat transfer curves for the three grids of 2.86 cm, 1.59 cm, and 0.95 cm rods, where R and L denote rods in perpendicular and parallel orientations, are presented in Fig. 8. The results for five grid locations for the sample $Re_D (=108,350)$ are shown in the figures. The semi-theoretical solution of Frossling [23] for a uniform freestream is also provided for reference. Heat transfer in the stagnation region decreases with increasing grid-to-model distance for a given Reynolds number. This is expected since the turbulence intensity of the freestream decreases with downstream distance from the grid. Heat transfer augmentation at the stagnation line over the uniform freestream ranges from 37 percent to 75 percent for a grid-to-model distance (x/d) of 25. The augmentation is reduced to the range 15 percent to 34 percent as x/d increases to 125. For a given x/d , the lowest heat transfer augmentation is obtained with the 2.86 cm rod-grid in parallel orientation while the highest is obtained with the 0.95 rod-grid in perpendicular orientation. Heat transfer increases with increasing Reynolds number for a given rod-grid and grid-to-model distance. For example, the Frossling number at the stagnation line increases by about 10 percent at $x/d=125$ as Re_D increases from 67,750 to 142,250. At $x/d=25$, the increase in Frossling number is about 15 percent for the same increase in Re_D . For the same x/d and Re_D , a smaller rod-grid gives higher heat transfer. For example, at the stagnation line, Frossling number with the 0.95 cm rod-grid is about 5 percent higher than that with the 2.86 cm rod-grid.

Table 1 The constant C_2 of Eq. (3)

	$Re = 67,750$	$Re = 108,350$	$Re = 142,250$
2.86-cm rod	0.3235	0.3500	0.3873
1.59-cm rod	0.3299	0.3751	0.3984
0.95-cm rod	0.2767	0.3046	0.3105

Heat transfer at the stagnation line ($\theta=0$) with the rod-grids in perpendicular and parallel orientation are compared to investigate the effect of different freestream vortical structures (Fig. 9, 10, and 11). The best-fit lines to the data are also presented in the figures to highlight the trends. The detailed quantitative data of these figures are given in Table 2. In all cases, heat transfer enhancement by the grids in perpendicular orientation is larger than that by the grids in parallel orientation. It can be speculated that the larger heat transfer with the rod-grids in perpendicular orientation is due to the greater vortex stretching of the primary vortices, which are parallel and align with the grid-rods. The increase in heat transfer augmentation with the grids in perpendicular orientation over grids in parallel orientation decreases with the rod size. At $x/d=25$, the average increase in Frossling number from the perpendicular orientation over the parallel orientation is about 7.39 percent, 4.63 percent, and 2.46 percent for the 2.86 cm, 1.59 cm, and 0.95 cm grid-rods, respectively. As evident in Fig. 9, 10, and 11, the difference between the two heat transfer curves for the two different grid orientations decreases with increasing grid-to-model distance, and this is more pronounced for the bigger grid-rod. As x/d increases from 25 to 125, the average difference in Frossling number between the perpendicular and parallel orientations decreases from 7.39 percent to 1.06 percent for 2.86 cm rods, 4.63 percent to 0.81 percent for 1.59 cm rods and 2.46 percent to 0.89 percent for 0.95 cm rods.

Since the literature on vortical structures behind grids of parallel rods is very limited, the vortex dynamics of wakes behind circular cylinders can be used to speculate on the freestream turbulent structure downstream of the grids used in this study. The Reynolds number based on the rod size, Re_d , in this study ranges from 3175 to 20,000. Hence, the wake is in the flow regime of shear layer transition [24]. Besides the primary vortices, which are parallel and aligned with the circular cylinder, intense shedding of near wake ($x/d < 1$) streamwise vortices are present in this regime. Furthermore, three-dimensional vortical structures with sizes ranging from the shear layer thickness to the Karman vortices are expected to develop in this flow regime [25,26]. The streamwise vortices, which evolve from the primary vortices in the near wake region, deform into three-dimensional structures as they travel further downstream. The primary vortices become dislocated and cannot be precisely traced beyond $x/d > 50$ in this flow regime [24]. It is plausible to assume a similar vortex structure downstream of the grids in this study. At downstream distances close to the grid ($x/d \leq 75$), the two grid orientations generate freestream turbulence with primary vortices apparently in different spanwise planes. The primary vortices from the perpendicular grid orientation are primarily aligned normal to the stagnation line, and are more susceptible to stretching as they approach the stagnation region. This would explain the higher heat transfer with the grids in perpendicular orientation. As the distance from the grids increases, the three-dimensionality of the

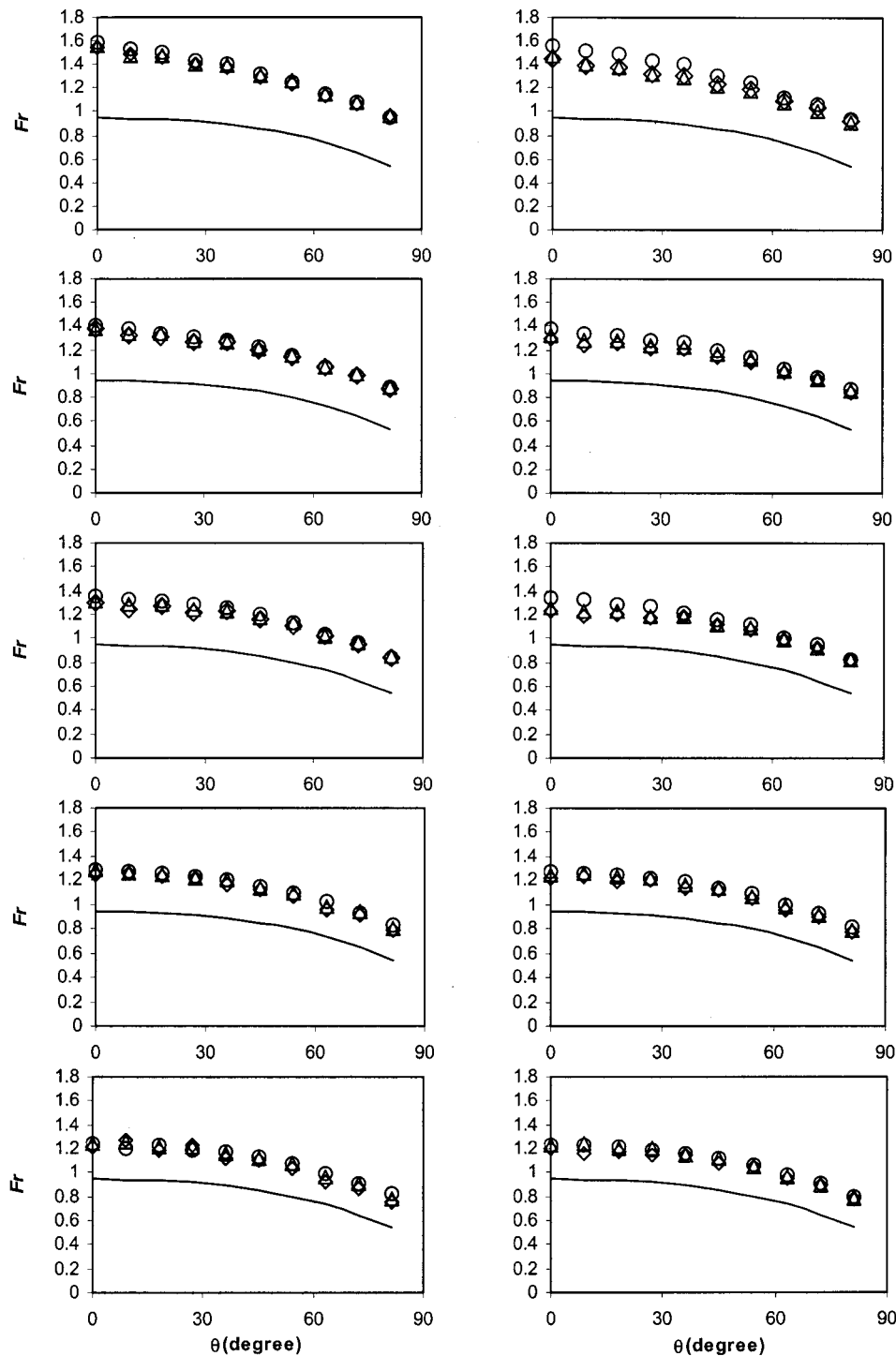


Fig. 8 Distribution of Frossling number in the stagnation region for $Re_D=108,350$ grids (\diamond , 2.86 cm rod-grid; \triangle , 1.59 cm rod-grid; \circ , 0.95 cm rod-grid; — Frossling solution)

vortices increases, resulting in a smaller difference in heat transfer with the perpendicular and parallel grid orientations.

While the size of the primary vortices depends on the size of the turbulence generating rod, the size of streamwise vortices are more dependent on the flow regime rather than the size of primary vortices [26]. Within a flow regime, there are relatively small changes in the character of vortex shedding over a large range of Re_d [26]. For the Re_d range of the present study, it seems likely that the size and strength of streamwise vortices, which promote the three-dimensionality of the vortical structure downstream of the grids, are somewhat comparable for all rod-grids. However,

the sizes of primary vortices are relatively different for the three different rod-grids. It can be speculated that the greater difference in heat transfer rates between perpendicular and parallel orientations for the grid with larger rods is due to the more apparent distinction between primary and secondary vortices with the larger rods.

The difference in heat transfer augmentation with the two different grid orientations over the entire stagnation region ($0 \text{ deg} < \theta < 90 \text{ deg}$) are presented in Fig. 12 for all rod-grids at $Re_D = 108,350$. For the 2.86 cm rod-grid, the difference in heat transfer augmentation between the two grid-orientations is highest at

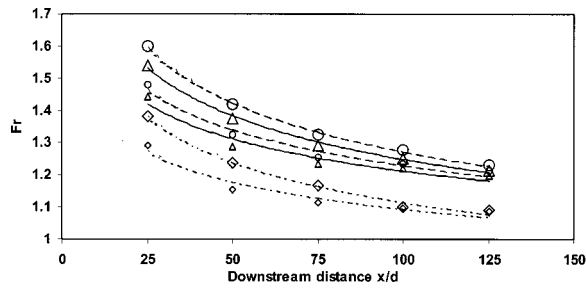


Fig. 9 Stagnation line Frossling number for 2.86 cm rod-grid (\diamond , $Re_D=67,750$ (R); \diamond , $67,750$ (L); \triangle , $108,350$ (R); \triangle , $108,350$ (L); \circ , $142,250$ (R); \circ , $142,250$ (L))

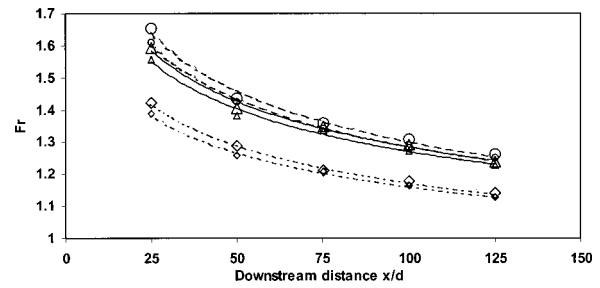


Fig. 11 Stagnation line Frossling number for 0.95 cm rod-grid (\diamond , $Re_D=67,750$ (R); \diamond , $67,750$ (L); \triangle , $108,350$ (R); \triangle , $108,350$ (L); \circ , $142,250$ (R); \circ , $142,250$ (L))

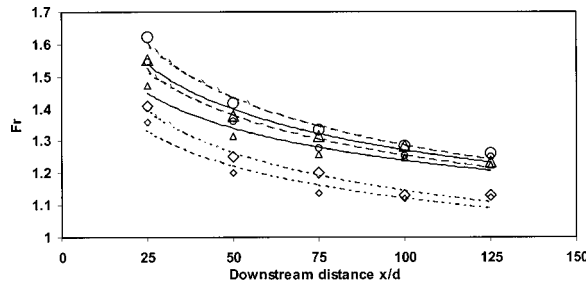


Fig. 10 Stagnation line Frossling number for 1.59 cm rod-grid (\diamond , $Re_D=67,750$ (R); \diamond , $67,750$ (L); \triangle , $108,350$ (R); \triangle , $108,350$ (L); \circ , $142,250$ (R); \circ , $142,250$ (L))

the stagnation line ($\theta=0$ deg), and decreases with streamwise distance from the stagnation line. The percentage difference in heat transfer decreases by about three as θ increases from 0 deg to 80 deg for grid-to-model distances of $25d$, $50d$, $75d$, and $100d$. The heat transfer characteristics at grid-to-model distance of $125d$ are anomalous, where the heat transfer with the parallel orientation is higher than with the perpendicular orientation in the off-

stagnation region. This distinct phenomena could be related to the large scale secondary vortical structures, called double rollers in the literature [24,27], found in the far wake ($x/d > 100$) of a circular cylinder; however, a detailed explanation for this cannot be offered at this point. For the 1.59 cm and 0.95 cm rod-grids, the difference in heat transfer for the two grid orientations remains relatively constant over the whole stagnation region for all grid-to-model distances and Re_D . The observed characteristics of the off-stagnation region heat transfer indicate that the nature of heat transfer enhancement in the stagnation region by different vortical structures are dependent on the size of primary vortices, since the grid size is a determining factor of the size of primary vortices.

The data from the three grids are compared with the correlation of VanFossen et al. [12] for freestream turbulence from square bar mesh grids in Fig. 13.

$$Fr = 0.008 \sqrt{Tu Re_D^{0.8} \left(\frac{\lambda_x}{D}\right)^{-0.574}} + 0.939 \quad (4)$$

The discrepancy between the present experimental data and Eq. (4) is significant for the 2.86 cm rod-grid, but the agreement improves with decreasing size of rod. For the 0.95 cm rod-grid, 87

Table 2 Stagnation line Frossling numbers

	2.86 cm rods			1.59 cm rods			0.95 cm rods		
	R	L	% Inc.	R	L	% Inc.	R	L	% Inc.
I. 25d upstream of the model									
U_1	1.3827	1.2915	7.06	1.4079	1.3593	3.58	1.4218	1.3873	2.49
U_2	1.5406	1.4407	6.93	1.5524	1.471	5.53	1.5916	1.5572	2.21
U_3	1.601	1.4801	8.17	1.6213	1.5473	4.78	1.6526	1.6094	2.68
II. 50d upstream of the model									
U_1	1.2368	1.1555	7.04	1.2518	1.2004	4.28	1.2892	1.2571	2.55
U_2	1.3755	1.2872	6.86	1.3783	1.3154	4.78	1.4051	1.3828	1.61
U_3	1.4175	1.3244	7.03	1.4175	1.3604	4.20	1.4366	1.4243	0.86
III. 75d upstream of the model									
U_1	1.1678	1.1131	4.91	1.1997	1.1374	5.48	1.2094	1.206	0.28
U_2	1.2913	1.2344	4.61	1.3137	1.2576	4.46	1.3494	1.3355	1.04
U_3	1.326	1.2561	5.56	1.3358	1.2777	4.55	1.3585	1.3417	1.25
IV. 100d upstream of the model									
U_1	1.1018	1.0956	0.57	1.1312	1.1196	1.04	1.1774	1.1642	1.13
U_2	1.252	1.2197	2.65	1.2846	1.2471	3.01	1.2918	1.2705	1.68
U_3	1.2791	1.2336	3.69	1.2863	1.2544	2.54	1.3066	1.2825	1.88
V. 125d upstream of the model									
U_1	1.0901	1.0887	0.13	1.1292	1.1228	0.57	1.14	1.1275	1.11
U_2	1.2157	1.1975	1.52	1.2361	1.2259	0.83	1.2382	1.2293	0.72
U_3	1.2321	1.2136	1.52	1.2624	1.2497	1.02	1.2626	1.2519	0.85

- R and L represent the grids in perpendicular and parallel orientations, respectively.
- U_1 , U_2 and U_3 are the mean freestream velocity of 5 m/s, 8 m/s and 10.5 m/s, respectively.

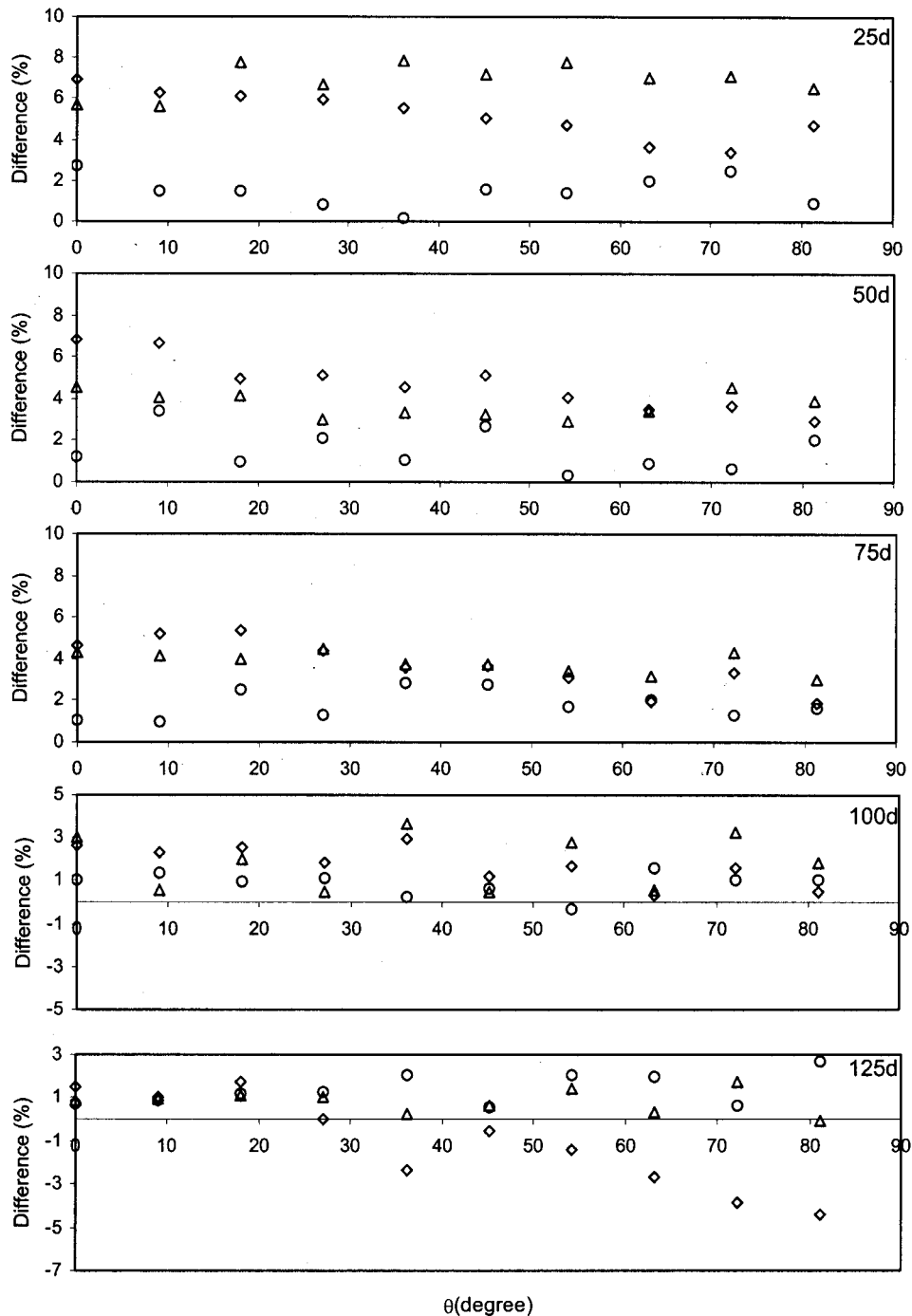


Fig. 12 Difference in heat transfer with grid in perpendicular over parallel orientation for $Re_D=108,350$ (\diamond , 2.86 cm rod-grid; \triangle , 1.59 cm rod-grid, \circ , 0.95 cm rod-grid)

percent of data falls within ± 4 percent of Eq. (4). It is clear from Fig. 13 that the correlations developed for isotropic turbulence generated by square mesh grids should be corrected to predict the heat transfer due to the turbulence with distinct coherent vortical structures. The errors are more serious for turbulence with higher integral length scales. Therefore, care should be taken in estimating heat transfer to gas turbine blades where the wake turbulence from the preceding blades could have integral length scales comparable to the leading edge diameter of the blades.

An attempt was made to highlight the distinct nature of stagnation region heat transfer by freestream turbulence with different vortical structures by developing a correlation using a functional

form similar to that of VanFossen et al. [12]. The best fit obtained by the regression analysis for all data sets, i.e., for both orientations of rod-grids, is plotted in Fig. 14. The data fall within ± 6 percent of the correlation given in Eq. (5).

$$Fr = 0.0018 \sqrt{Tu^{1.3463} Re_D^{1.2053} \left(\frac{\lambda_x}{D}\right)^{-0.2463}} + 0.939 \quad (5)$$

Since the rod-grids in perpendicular orientation give higher heat transfer in the stagnation region than those in parallel orientation, correlations for each grid orientation were also developed (Fig. 15

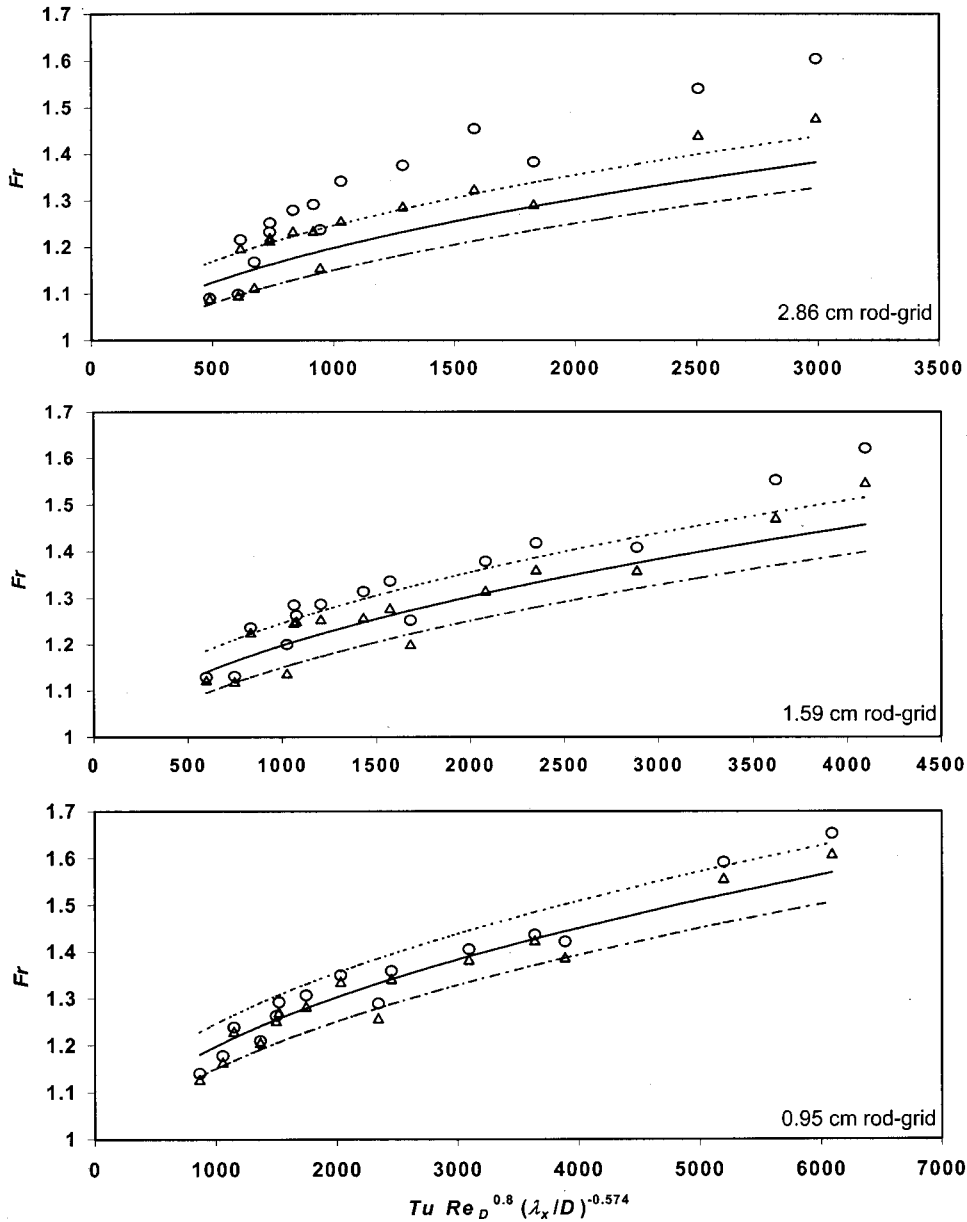


Fig. 13 Stagnation line Fr versus correlation parameter proposed by VanFossen et al. [12] (Orientation of rod-grids: \circ , perpendicular; \triangle , parallel, Correlation lines: —, van Fossen et al.; ---, +4%; - - -; -4%)

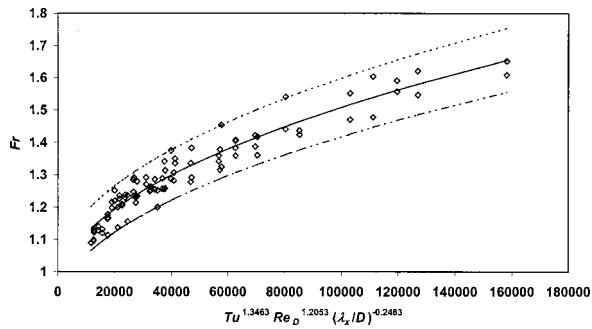


Fig. 14 Stagnation line Fr versus correlation parameter for both grid orientations (\diamond , Data, Correlation lines: —, Eq. (5); ---, +6%; - - -; -6%)

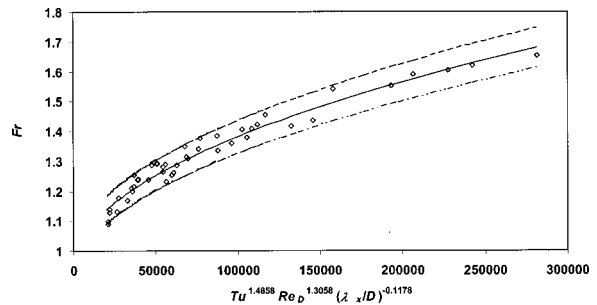


Fig. 15 Stagnation line Fr versus correlation parameter for rod-grids in perpendicular orientation (\diamond , Data, Correlation lines: —, Eq. (6); ---, +4%; - - -; -4%)

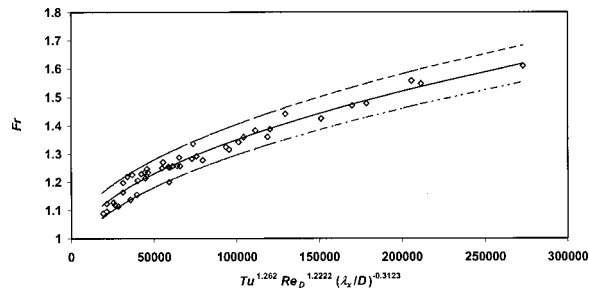


Fig. 16 Stagnation line Fr versus correlation parameter for rod-grids in parallel orientation (◇, Data, Correlation lines: —, Eq. (7); ---, +4%; - - -, -4%)

and 16). The best-fit equations using the regression analysis are given in Eq. (6) for the rod-grids in perpendicular orientation and in Eq. (7) for those in parallel orientation.

$$Fr = 0.0014 \sqrt{Tu^{1.4858} Re_D^{1.3058} \left(\frac{\lambda_x}{D}\right)^{-0.1178}} + 0.939 \quad (6)$$

$$Fr = 0.0013 \sqrt{Tu^{1.2620} Re_D^{1.2222} \left(\frac{\lambda_x}{D}\right)^{-0.3123}} + 0.939 \quad (7)$$

The data for each grid orientation are within ± 4 percent of the correlation line. The different correlations that can be obtained to best fit a given data set highlights the difficulty of obtaining a correlation for gas turbine blade heat transfer. It is clear that freestream turbulence with different orientations of coherent vortical structures have different influences over the heat transfer in the stagnation region.

Conclusions

An experimental study has been performed to investigate the effect of freestream turbulence with different vortical structures on stagnation region heat transfer. Freestream turbulence with different orientations of primary vortices were generated using grids of 2.86 cm, 1.59 cm, and 0.95 cm diameter parallel rods in perpendicular and parallel orientations. Heat transfer measurements were made in the stagnation region using a heat transfer model with the grids $25d$ to $125d$ upstream of the model at three different Re_D of 67,750, 108,350, and 142,250. The main conclusions can be summarized as:

- 1 Heat transfer in the stagnation region decreases with increasing grid-to-model distance for a given Reynolds number. The increase in the Frossling number at the stagnation line over a uniform freestream ranges from 37 percent to 75 percent at $x/d=25$, and 15 percent to 34 percent at $x/d=125$ for the three different grids.
- 2 Heat transfer increases with increasing Re_D for a given rod-grid and grid-to-model distance. The stagnation line Frossling number increases by 10 percent and 15 percent at x/d of 125 and 25 as Re_D increases from 67,750 to 142,250.
- 3 For a given grid-to-model distance, x/d , and Re_D , the grid with smaller diameter rods gives higher heat transfer. At the stagnation line, the Frossling number with the 0.95 cm rod-grid is about 5 percent higher than that with the 2.86 cm rod-grid. This can be attributed to the smaller length scales associated with the smaller rod-grid.
- 4 The heat transfer enhancement by the grids in perpendicular orientation is larger than that by the grids in parallel orientation. This can be speculated to be caused by greater vortex stretching, since the primary vortices generated by the perpendicular orientation are primarily aligned normal to the stagnation line, and more susceptible to stretching as they approach the stagnation region.

- 5 The difference in heat transfer augmentation by grids in perpendicular and parallel orientations decreases with the size of grid-rods. This could be due to a more apparent distinction between primary and secondary vortices with the bigger rods. At a grid-to-model distance of $25d$, the average difference in the Frossling number is 7.39 percent, 4.63 percent, and 2.46 percent for the 2.86 cm, 1.59 cm, and 0.95 cm rods, respectively.
- 6 The difference in heat transfer augmentation with grids in perpendicular and parallel orientations decrease with increasing grid-to-model distance. This is likely due to the greater three-dimensionality of the freestream vortical structures as the distance from the grid increases.
- 7 For the 2.86 cm rod-grid, the difference in heat transfer between perpendicular and parallel grid-orientations is highest at the stagnation line, and decreases with streamwise distance. However, this difference remains fairly constant over the whole stagnation region for the 1.59 cm and 0.95 cm rod-grids. This indicates that the heat transfer enhancement by different vortical structures are dependent on the size of primary vortices.
- 8 The nature of heat transfer enhancement in the stagnation region by freestream turbulence with distinct coherent vortical structures is quite distinct from that by turbulence generated using square-mesh grids. The heat transfer data of this study are poorly predicted using existing correlation models for turbulence generated from square-mesh grids. The discrepancies increase for the larger grid-rods. Any correlation model should take into account the distinct nature of the coherent vortical structures of the turbulence to improve its predictive capability.

Acknowledgments

The support of the Natural Sciences and Engineering Research Council (NSERC) of Canada is gratefully acknowledged.

Nomenclature

- A = area of the heated portion of the leading edge (m^2)
- d = diameter of a grid-rod (m)
- D = diameter of cylindrical leading edge (m)
- Fr = Frossling number ($Nu/\sqrt{Re_D}$)
- I = current (ampere)
- k = thermal conductivity (W/m-K)
- Nu = Nusselt number
- Q_{cond} = conduction heat loss (W)
- Q_{cov} = convection heat transfer (W)
- Q_{in} = heat input (W)
- Q_{rad} = radiation heat loss (W)
- Re_d = Reynolds number based on d
- Re_D = Reynolds number based on D
- Tu = streamwise turbulence intensity
- $T_w(\theta)$ = temperature of the leading edge at angle θ (K)
- T_∞ = temperature of freestream (K)
- u = rms of fluctuating velocity component in streamwise direction (m/s)
- U = mean freestream velocity (m/s)
- v = rms of fluctuating velocity component in spanwise Y direction (m/s)
- V_0 = voltage (V)
- w = rms of fluctuating velocity component in spanwise Z direction (m/s)
- x = distance downstream of the grid (m)
- θ = angle measured from the stagnation point (degree)
- ν = kinematic viscosity of freestream (m^2/s)
- λ_x = streamwise integral length scale of turbulence (m)

Appendix

Analysis of Experimental Uncertainties. Following the uncertainty analysis methods of Moffat [20] the uncertainty in Fr can be expressed as:

$$(Un_{Fr})^2 = (Un_{Nu})^2 + 0.25(Un_{ReD})^2$$

where Un_{Fr} = Uncertainty in Fr (%)

Un_{Nu} = Uncertainty in Nu (%)

Un_{ReD} = Uncertainty in Re_D (%)

The uncertainty in Fr and the influencing variables with 95 percent confidence levels are given in Table 3 for both maximum and minimum freestream velocities. Uncertainties in temperature were considered in estimating conduction heat loss, radiation heat losses and convection heat transfer. Uncertainties associated with leading edge diameter (D), thermal conductivity (k) and area (A) are assumed to be negligible since these values are based on the data specified by manufacturers.

The techniques proposed by Yavuzkurt [21] were used to estimate the uncertainties in Tu and λ_x . The uncertainties are given in Table 4.

Table 3 Experimental uncertainty in Fr (%)

Variable	Bias Error		Precision Error	
	Experimental Reynolds Number Range			
	Maximum	Minimum	Maximum	Minimum
Current I	0.18	0.26	0.53	0.51
Voltage V_D	0.06	0.08	0.20	0.21
Temperature difference ΔT	3.20	3.20	0.53	0.53
Conduction heat Q_{cond}	4.60	4.60	0.75	0.75
Radiation heat Q_{rad}	12.80	12.80	2.12	2.12
Convection heat Q_{cov}	1.61	2.10	0.55	0.60
Reynolds number Re_D	0.05	0.10	0.32	0.37
Frossling number Fr	3.58	3.83	0.79	0.82

Table 4 Experimental uncertainty in Tu and λ_x (%)

	Experimental Reynolds Number Range	
	Maximum	Minimum
Velocity Calibration (Tu , λ_x)	0.07	0.14
Velocity Curve Fitting (Tu , λ_x)	2.18	2.18
Autocorrelation Curve Fitting (λ_x)	10.50	10.50
Turbulence Intensity Tu	3.09	3.09
Integral Length Scale λ_x	10.95	10.95

References

- [1] Maciejewski, P. K., and Moffat, R. J., 1992, "Heat Transfer with Very High Freestream Turbulence: Part I — Experimental Data; Part II — Analysis of Results," ASME J. Heat Transfer **114**, pp. 827–839.
- [2] Larsson, J., 1997, "Turbine Blade Heat Transfer Calculations Using Two-equation Turbulence Models," Proc. Instn. Mech. Engrs. **221**, Part A, pp. 253–262.
- [3] Guo, S. M., Jones, T. V., Lock, G. M., and Dancer, S. N., 1998, "Computational Prediction of Heat Transfer to Gas Turbine Nozzle Guide Vanes with Roughened Surfaces," ASME J. Turbomach. **120**, pp. 343–350.
- [4] Smith, M. C., and Kuethe, A. M., 1966, "Effects of Turbulence on Laminar Skin Friction and Heat Transfer," Phys. Fluids **9**, No. 12, pp. 2337–2344.
- [5] Kestin, J., and Wood, R. T., 1971, "The Influence of Turbulence on Mass Transfer from Cylinders," ASME J. Heat Transfer **93C**, pp. 321–327.
- [6] Lowery, G. W., and Vacon, R. L., 1975, "Effect of Turbulence on Heat Transfer from Heated Cylinders," Int. J. Heat Mass Transf. **18**, No. 11, pp. 1229–1242.
- [7] O'Brien, J. E., and VanFossen, G. J., 1985, "The Influence of Jet-Grid Turbulence on Heat Transfer from the Stagnation Region of a Cylinder in Cross-flow," ASME Paper 85-HT-58.
- [8] Mehendale, A. B., Han, J. C., and Ou, S., 1991, "Influence of High Mainstream Turbulence on Leading Edge Heat Transfer," ASME J. Heat Transfer **113**, pp. 843–850.
- [9] Han, J. C., Zhang, L., and Ou, S., 1993, "Influence of Unsteady Wake on Heat Transfer Coefficients from a Gas Turbine Blade," ASME J. Heat Transfer **115**, pp. 904–911.
- [10] Yeh, F. C., Hippensteele, S. A., VanFossen, G. J., Poinatte, P. E., and Ameri, A., 1993, "High Reynolds Number and Turbulence Effects on Aerodynamics and Heat Transfer in a Turbine Cascade," AIAA-93-2252.
- [11] Zhang, L., and Han, J. C., 1994, "Influence of Mainstream Turbulence on Heat Transfer Coefficients from a Gas Turbine Blade," ASME J. Heat Transfer **116**, pp. 896–903.
- [12] VanFossen, G. J., Simoneau, R. J., and Ching, C. Y., 1995, "Influence of Turbulence Parameters, Reynolds Number and Body Shape on Stagnation Region Heat Transfer," ASME J. Heat Transfer **117**, pp. 597–603.
- [13] Ahmaed, G. R., and Yovanovich, M. M., 1997, "Experimental Study of Forced Convection from Isothermal Circular and Square Cylinders and Toroids," ASME J. Heat Transfer **119**, pp. 70–79.
- [14] Du, H., Ekkad, S., and Han, J. C., 1997, "Effect of Unsteady Wake with Trailing Edge Coolant Ejection on Detailed Heat Transfer Coefficient Distributions for a Gas Turbine Blade," ASME J. Heat Transfer **119**, 242–248.
- [15] Johnston, J. P., 1974, "The Effects of Rotation on Boundary Layers in Turbomachine Rotors," NASA SP 304.
- [16] Lakshminarayana B., 1996, *Fluid Dynamics and Heat Transfer of Turbomachinery*, John Wiley & Sons, Inc., New York.
- [17] Suter, S. P., Maeder, P. F., and Kestin, J., 1963, "On the Sensitivity of Heat Transfer in the Stagnation-point Boundary Layer to Free-stream Vorticity," J. Fluid Mech. **16**, part 3, pp. 497–520.
- [18] Suter, S. P., 1965, "Vorticity Amplification in Stagnation-point Flow and its Effect on Heat Transfer," J. Fluid Mech. **21**, part 3, pp. 513–534.
- [19] Morkovin, M. V., 1979 "On the Question of Instabilities Upstream of Cylindrical Bodies," MASA CR-3231.
- [20] Moffat, R. J., 1988, "Describing the Uncertainties in Experimental Results," Exp. Therm. Fluid Sci. **1**, pp. 3–17.
- [21] Yavuzkurt, S., 1984, "A Guide to Uncertainty Analysis of Hot-Wire Data," ASME J. Fluids Eng. **106**, pp. 181–186.
- [22] Roach, P. E., 1987, "The generation of Nearly Isotropic Turbulence by Means of Grids," Heat and Fluid Flow, **8**, No. 2, pp. 82–92.
- [23] Frossling, N., 1958, "Evaporating Heat Transfer and Velocity Distribution in Two-Dimensional and Rotationally Symmetric Laminar Boundary Layer Flow," NACA TM-1432.
- [24] Zdravkovich, M. M., 1997, *Flow Around Circular Cylinders, Vol 1: Fundamentals*, Oxford Science Publications, Oxford University Press; Oxford, United Kingdom.
- [25] Wei, T., and Smith, C. R., 1986, "Secondary Vortices in the Wake of Circular Cylinders," J. Fluid Mech. **169**, pp. 513.
- [26] Williamson, C. H. K., 1996, "Vortex Dynamics in the Cylinder Wake," Annu. Rev. Fluid Mech. **28**, pp. 477–539.
- [27] Corke, T., Krull, J. D., and Ghassemi, M., 1992, "Three-dimensional Mode Resonance in Far Wake," J. Fluid Mech. **239**, pp. 99–132.

Effects of Rib Arrangements on Heat Transfer and Flow Behavior in a Rectangular Rib-Roughened Passage: Application to Cooling of Gas Turbine Blade Trailing Edge

Robert Kiml

Assistant Professor

E-mail: robert@mmlab.mech.tuat.ac.jp

Sadanari Mochizuki

Professor, Mem. ASME

Akira Murata

Professor

Tokyo University of Agriculture and Technology,
Department of Mechanical Systems Engineering,
Nakacho 2-24-16, Koganei-shi, Tokyo
184-8588, Japan

Experimentation was conducted to examine the heat transfer and pressure drop characteristics in a rib-roughened rectangular passage with aspect ratio 2:1 for four rib configurations: 90 deg, 75 deg, 60 deg and 45 deg oblique ribs. The ribs were attached to two opposing long side walls instead of short side walls. In this study the oblique ribs were intended to function as secondary flow inducers as well as turbulators to improve the heat transfer of the bottom wall (one of the short side walls). The results revealed that, in order to enhance the heat transfer of the bottom wall, the oblique ribs should be arranged so that the secondary flow along the ribs hits the top wall instead of the bottom wall. Flow visualization test was performed to understand the heat transfer mechanisms. It was confirmed that the heat transfer enhancement at the bottom wall was attributed to the rib-induced secondary flow where the flow along the ribs hit the top wall, turned back and carried cold air from the passage core region towards the bottom wall. The highest average heat transfer was achieved for the 60 deg rib pattern due to the strong rotational momentum of the secondary flow and higher heat transfer enhancement on the rib-roughened walls in comparison to the other three rib patterns.

[DOI: 10.1115/1.1378019]

Keywords: Cooling, Flow, Heat Transfer, Thermocouples, Visualization

Introduction

With an increase in demands for the higher thermal efficiency, components of a modern gas turbine engine, especially the first moving stage blades, are exposed to the higher and higher turbine inlet gas temperature. Cooling techniques such as forced convection cooling, impingement cooling, film cooling and their combinations have been employed in order to maintain acceptable air-foil temperature and secure blade life.

Internal forced convection cooling of a gas turbine rotor blade has been studied by many scientists. Johnson et al., [1], Taslim [2], Rau et al. [3], Mochizuki et al. [4], Han [5], Kiml [6], and Wagner [7] studied the heat transfer and friction characteristics in rib-roughened passages with different rib arrangements. They focused on the effects of the Reynolds number and rib geometry on the heat transfer and pressure drop in the fully developed region of a uniformly heated square and rectangular channels. All these studies showed that angled ribs provide better heat transfer enhancement than transverse ribs. Further studies Dutta et al. [8], Dutta et al. [9], Dutta and Han [10], El-Husayni and Han [11], and Mochizuki et al. [12] examined the effects of Coriolis forces, centrifugal force and buoyancy force on the heat transfer characteristics with different rib configurations. Studies by Taslim and Kercher [13], Hu and Shen [14], Han et al. [15,16], Ekkad and Han [17], and Johnson et al. [18] presented the heat transfer results for the parallel, broken and V-shaped ribs mounted on two opposite walls. The effects of the 180 deg or 90 deg sharp turn on

the flow and heat transfer in a serpentine passage have been reported by Cheng et al. [19], Cheng and Shi [20], Metzger et al. [21], and Kiml et al. [22].

However, with the advancement of gas turbine technology, it became necessary to focus the attention on the regions exposed to the most severe thermal conditions, leading and trailing edges, as shown in Fig. 1. In particular, the trailing edge, due to its significant shortage of cooling space for internal cooling, is becoming one of the most important problems to realize more effective gas turbine engines. In order to cool the trailing edge of a blade, cooling-air ejection has been commonly used. However, ejection of air degrades both the aerodynamic performance of the blade and thermal efficiency of the engine. Therefore, for future advanced engines, especially for the power plant use, cooling air should be recovered from the blade after it passed through the internal cooling passages. To accomplish this, installation of oblique ribs in the internal passage near the trailing edge as secondary-flow inducers as well as turbulators can be one solution. Recently, study by Dutta et al. [19], Zhang et al. [23], Kiml et al. [24,25] and Hirota et al. [26] showed the heat transfer data for the smooth and ribbed rectangular channels. However, the authors investigated channels with different geometrical properties or they did not focus on the examination of the secondary flow induced by the oblique rib patterns.

The present study focuses on the detailed examination of the flow behavior and its effects on the local heat transfer distribution in a rectangular passage with aspect ratio 2:1 where the ribs are attached on the two opposing long side walls. The emphasis is placed on the investigation of rib-induced secondary flow and its effects on the heat transfer and pressure drop characteristics pro-

Contributed by the Heat Transfer Division for publication in the JOURNAL OF HEAT TRANSFER. Manuscript received by the Heat Transfer Division August 27, 1999; revision received January 8, 2001. Associate Editor: J.-C. Han.

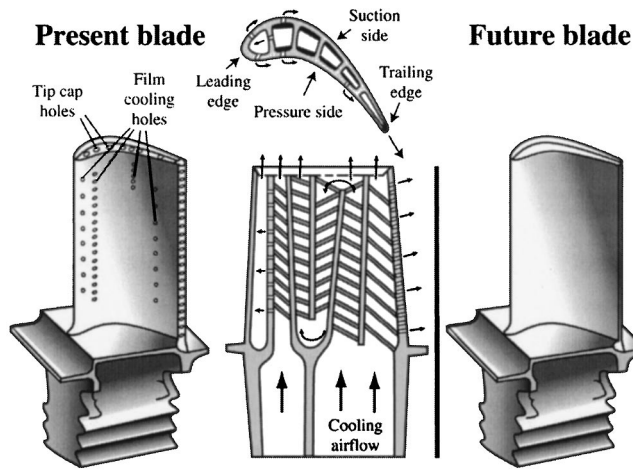


Fig. 1 Schematic of internal and external cooling structures of a gas turbine rotor blade

duced by 4 different rib patterns: 45 deg, 60 deg, 75 deg, and 90 deg ribs. The heat transfer and flow visualization experiments were performed only under stationary conditions.

Experimental Apparatus and Procedure

Heat Transfer Experiment. The heat transfer experiment was performed in a rib-roughened passage with the aspect ratio 2:1 ($15 \times 30 \text{ mm}^2$, equivalent diameter $d_e = 20 \text{ mm}$) with the ribs attached on the two opposing long-side walls. From this point on, the walls of the cooling channel will be called the “top,” “bottom,” “left” and “right” walls, as presented in Fig. 2. The heat transfer test section was constructed from 5 mm thick Bakelite plates. This material was chosen for its low thermal conductivity, high mechanical strength and easy machining. The inside surfaces of the test section were covered with thin electric conductive plastic films, consisting of 180 μm thick polyethylene terephthalate (PET) layer and a 20 μm thick conductive layer (see Fig. 2). Uniform wall heat flux conditions were achieved by passing an electric current through the conductive layer of the film. Its specific characteristics of highly uniform electric resistance fulfill the requirement for uniform heat generation. The test section and

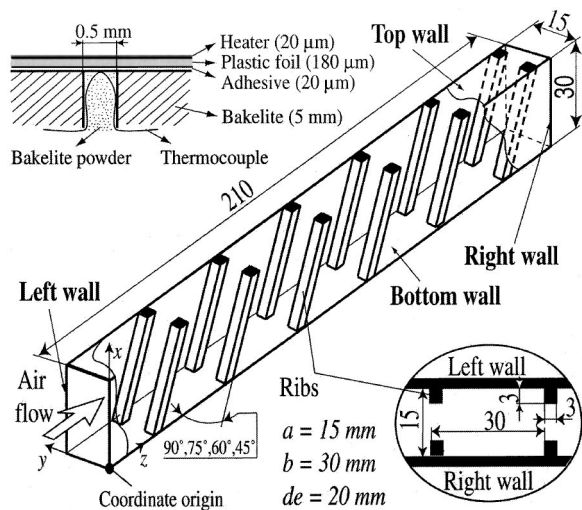


Fig. 2 Schematic of rib-roughened passage in which heat transfer experiment was performed

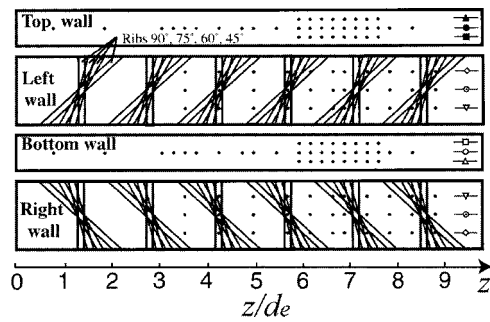


Fig. 3 Thermocouple layout and rib patterns tested in present study

mixing device were insulated by an insulation material (SAN PERKA) with a heat conductivity of 0.0417 W/(mK). The insulation thickness was 20 mm.

Air from the turbo blower flows into the test section after passing through a straight entrance region, with length of 660 mm, which has a rectangular flow cross section identical to the flow passage inside the test section. Air temperature at the inlet to the test section was measured by means of two K-type thermocouples (0.3 mm in diameter). The outlet bulk mean temperature was calculated from temperature obtained from 12 thermocouples (50 μm in diameter) behind a flow mixing device which was installed at the exit of the test section.

The wall surface temperature was measured by means of 152 K-type thermocouples (50 μm in diameter) mounted on back side of the conductive plastic heater, as can be also observed in Fig. 2. The thermocouples on all walls were located in three lines, as shown in Fig. 3. The ribs with a square cross section (rib height $e = 3 \text{ mm}$), machined from the bakelite, were attached to two opposing long side walls (right and left walls) instead of short side walls (top and bottom walls). This material was chosen for its low weight and high mechanical strength, which enables to perform the heat transfer experiments under rotating conditions. Experiments were performed for 45 deg, 60 deg, 75 deg, and 90 deg rib patterns which were intended to function as secondary flow inducers to improve the heat transfer of the bottom wall (one of the short side walls). The Reynolds number was set to $\text{Re} = 15,000$.

Flow Visualization Experiment. The flow visualization using fine particles as tracers was carried out in a 6 m long water channel with a test section located 5 m downstream of the settling

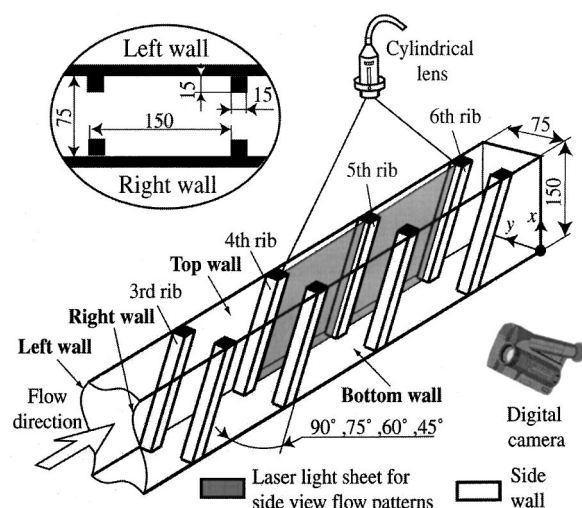


Fig. 4 Schematic of flow visualization test section

chamber. The test section, made of transparent Plexiglas plates, had a rectangular cross section ($150 \times 75 \text{ mm}^2$). Water was mixed with the chemical compound NaSO_4 , with increased the specific weight of the water so that the particles (about $70 \mu\text{m}$ in diameter) had the same specific weight with that of the water. These particles were illuminated between the fifth and sixth ribs by an argon laser light-sheet (3 mm thick) and photographed by a still digital camera and video camera, as shown in Fig. 4. The camera exposure time was set to 0.5 second to allow the particles to create path lines. Top view patterns were photographed at 5 locations $x = 0.66e$ (near-bottom wall region), $2.66e$, $5e$ (center), $7.33e$ and $9.33e$ (near-top wall region) from the bottom wall surface. Side view patterns were obtained at $y = 0.33e$ (near right wall region); $0.66e$, $1e$, $1.66e$, and $2.5e$ (central vertical plane) from the right wall surface. The ribs, made of transparent Plexiglas with a square cross section ($15 \times 15 \text{ mm}^2$), were mounted on the left and right walls of the channel. Geometric proportions of the water channel, ribs, rib angle and rib pitch correspond to those used in heat transfer experiments. The Reynolds number was varied from $Re = 10,000$ to $20,000$.

Data Reduction

The Reynolds number, wall heat flux, local heat transfer coefficient, friction coefficient and Nusselt numbers are calculated, respectively, as follows:

$$Re = u_m d_e / \nu \quad (1)$$

$$\dot{q}_w = \dot{m} c_p (T_{out} - T_{in}) / A_h \quad (2)$$

$$\alpha = \dot{q}_w / (T_w - T_b) \quad (3)$$

$$Nu = \alpha d_e / k \quad (4)$$

$$Nu_\infty = 0.022 Re^{0.8} Pr^{0.5} \quad (5)$$

$$C_f = \Delta p d_e / (2L \rho u_m^2) \quad (6)$$

$$Nu_m = \frac{\sum_{i=1}^n (Nu_i A_i)}{\sum_{i=1}^n A_i} \quad (7)$$

An uncertainty analysis using the ASME Performance Test Codes (ANSI/ASME PTC 19.1-1985), was carried out for the heat transfer experiment and it was estimated that the maximum uncertainties of the Nusselt number were estimated to be less than 9 percent.

Experimental Results and Discussion

Figure 5 shows the effects of rib configurations on the ratio of the wall mean Nusselt number and Nusselt number for a fully developed flow in a smooth passage, Nu_m / Nu_∞ , on the top, bottom, right and left walls. It can be clearly observed from this figure that the Nu_m for 90 deg (\blacklozenge) rib pattern achieves its maximum value on the rib-roughened walls (left and right walls) and

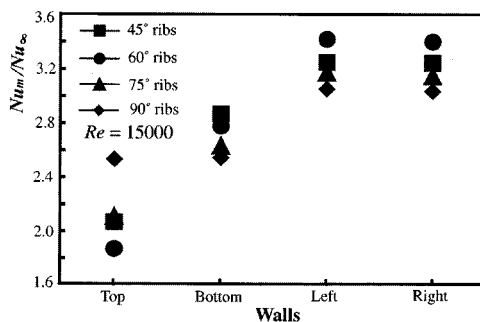


Fig. 5 Effect of rib configuration on average Nusselt number on all four walls

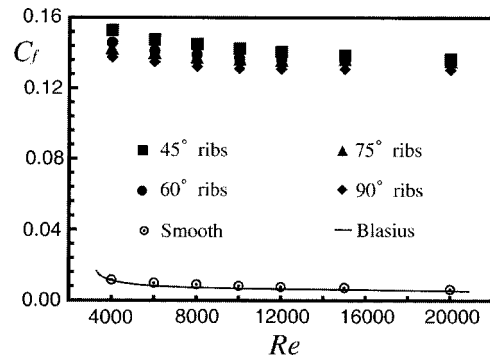


Fig. 6 Effects of rib configuration on friction coefficient, C_f : (a) flow pattern at $x = 0.66e$ (near the bottom wall); (b) flow pattern at $x = 5e$ (channel center); (c) flow pattern at $x = 9.33e$ (near the top wall); (d) flow pattern at $y = 0.33e$ (close to the right wall); and (e) flow pattern at $y = 2.5e$ from right wall (channel central vertical plane).

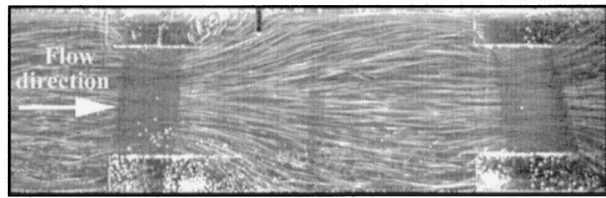
considerably lower value on the top and bottom walls. In comparison to the 90 deg rib patterns, the oblique [60 deg (\bullet), 75 deg (\blacklozenge) and 45 (\blacksquare)] rib patterns show a considerably lower wall Nu_m on the top wall and higher on the bottom, right and left walls. Particularly, the 30 percent higher Nu_m on the bottom wall in contrast to that on the top wall, where one might have expected opposite situation due to the ribs' inclination (confirm in Fig. 2), may attract ones attention. It can be also seen from this figure that the Nu_m on the rib-roughened walls (right and left walls) is the highest for 60 deg (\bullet) rib pattern, but on the bottom wall it is the highest for the 45 deg (\blacksquare) rib pattern. The Nu_m enhancement caused by the use of ribs as secondary flow inducers is paid by a considerably larger pressure drop increase as shown in Fig. 6.

The effects of all rib patterns on the passage mean Nu_{mp} and the friction coefficient in comparison to a Smooth passage (\circ) are summarized in Table 1. The passage mean Nu_{mp} in comparison to the wall mean Nu_m is evaluated from the Nu distribution on the left, right and bottom walls. The top wall is excluded because it is not as important in this case due to the near location another cooling passage, as is shown in the blade internal structure in Fig. 1.

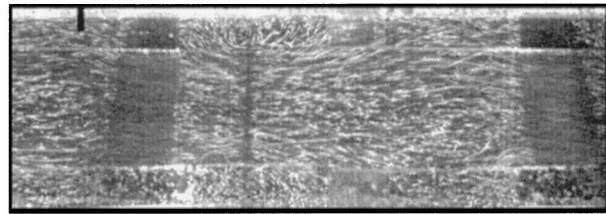
It can be seen from this table that every Nu_{mp} enhancement causes a large increase of C_f . As mentioned above, the 90 deg rib pattern achieves the lowest Nu_{mp} and C_f of all rib patterns. The most efficient rib patterns in terms of heat transfer are 60 deg and 45 deg parallel rib patterns. Unfortunately, while the heat transfer is only 2.67 or 2.60 times higher in comparison with the case of the Smooth passage, the pressure drop is 16.24 or 16.72 times

Table 1 Passage mean Nusselt number and friction coefficient of four rib patterns compared to the smooth (\circ) surfaces

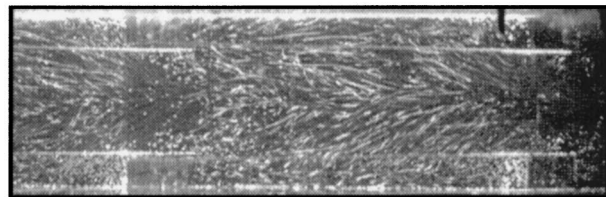
Rib pattern	Nu_{mp}/Nu_{mp0}	C_f/C_{f0}
Smooth	1.00	1.00
90°	2.34	15.45
75°	2.49	15.97
60°	2.67	16.24
45°	2.60	16.72



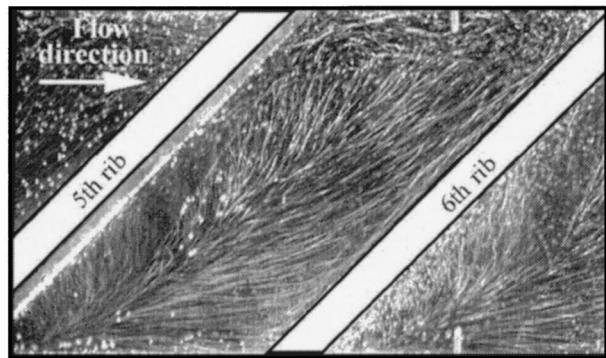
(a)



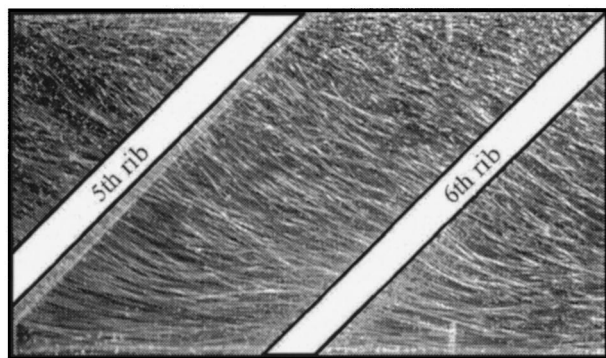
(b)



(c)



(d)



(e)

Fig. 7 Flow visualization results for 45 deg ribs, $Re = 20,000$

higher. It may be also noted that 60 deg pattern shows very similar heat transfer with the case of the 45 deg rib patterns, but a slightly lower pressure drop.

To explain these heat transfer and pressure drop characteristics,

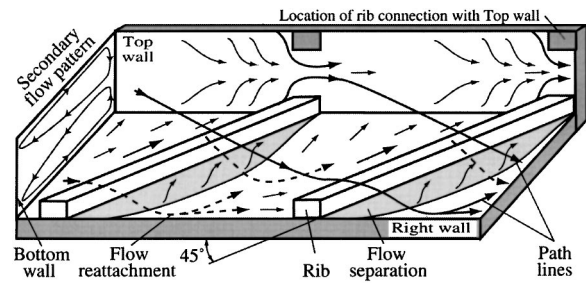


Fig. 8 Schematic of secondary flow induced by 45 deg ribs

as presented in Figs. 5, 6, and Table 1, one has to focus on the detailed Nu distribution and flow visualization results.

Flow Visualization. Figure 7 represents the flow visualization results between the fifth and sixth ribs for the case of 60 deg parallel ribs. The top view flow pattern, taken near the bottom wall (see Fig. 7(a)), shows the creation of a separation bubble behind the fifth rib and a flow reattachment between those two ribs. From the flow reattachment the flow proceeds in the main flow direction and due to the rib's inclination is forced to move along the rib towards the top wall (see Fig. 7(d)). Here, due to its encounter with the top wall and a similar flow stream induced by the ribs mounted on the opposite rib-roughened wall, the flow sharply turns 180 deg and flows back towards the bottom wall, as can be confirmed by Figs. 7(c) and 7(e). This flow behavior causes a development of the secondary flow in form of two vortices, which carry cold fluid from the central core region towards the bottom wall, as schematically illustrated in Fig. 8. From the Figs. 7(e) and 8 it can be also noted that the flow near the center of the bottom wall creates a boundary layer with the flow proceeding in the main flow direction, so that the secondary flow does not impinge the bottom wall directly at this location, but in the near rib-roughened wall regions.

Local Heat Transfer. The flow visualization results confirmed that the heat transfer enhancement at the bottom wall is attributed to the rib-induced secondary flow where the flow is forced to proceed along the ribs, hit the top wall, turn back and carry cold and large momentum air from the passage core region towards the bottom wall, as was schematically illustrated in Fig. 8 and as was shown in Figs. 7. This introduction of fresh cold air on the bottom wall enhances the heat transfer appreciably. The big difference between the Nu distributions on the top and bottom walls for the 45 deg rib pattern is presented in detail in Figs. 9 and 10, where the Nu on the bottom wall [(○), (△), (□) in Fig. 10] is significantly higher than on the top wall [(●), (◆), (■) in Fig. 9]. It may be noted from these figures that the Nu appreciably en-

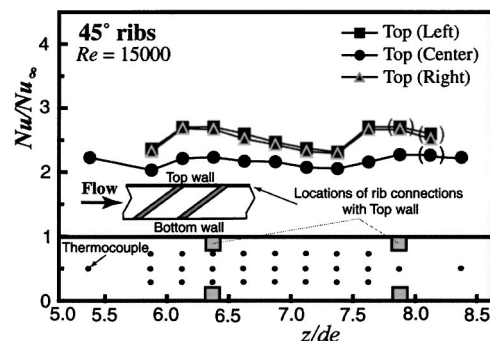


Fig. 9 Local Nu distribution on top wall for 45 deg ribs

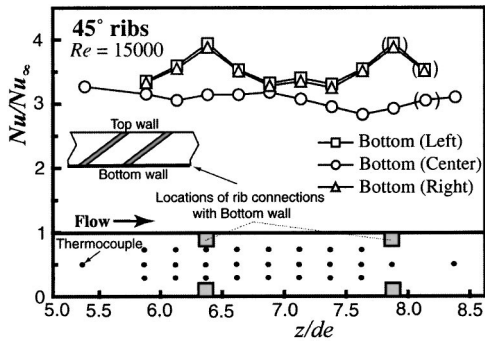


Fig. 10 Local Nu distribution on bottom wall for 45 deg ribs

hances in the regions closer to the rib-roughened walls [(\diamond) , (\blacksquare) , and (\triangle) , (\square)] in contrast to the central regions [Top Center (\circ) and Bottom Center (\bullet)].

(For better understanding of this complicated Nu distribution and due to the different location of thermocouples between the ribs Nu value plotted in brackets, “(,)” substituted with the Nu value obtained by thermocouples located upstream or downstream of the previous rib.)

In the case of the top wall, the Nu enhancement in the near rib-roughened walls regions takes place especially downstream and between the ribs’ connections with the top wall (confirm in Fig. 9). It is caused by (1) the impingement of the local flow streams proceeding along the oblique ribs and impinging the top wall in this area (see in Figs. 7(d) and (8) and (2) the high flow velocity caused by the space contraction between the ribs. From this local maximum, the Nu gradually deteriorates due to the boundary layer growth.

In contrast to the Nu distribution on the top wall, the Nu enhancement in the near rib-roughened wall regions on the bottom wall, [Right (\triangle) , Left (\square)], is more peaked and can be clearly observed only in the regions near the ribs (see Fig. 10) due to the space contraction between the ribs which increases the flow velocity appreciably. As the flow velocity quickly deteriorates from its peak within the space contraction, the Nu distribution decreases likewise until it is very similar to the Nu in the central region [Bottom Center (\circ)].

The detailed Nu distribution on the left wall (rib-roughened wall) for 45 deg rib pattern between the fourth and fifth and fifth and sixth ribs is presented in Fig. 11. The Nu in the area just behind the fourth or fifth ribs is relatively low. This is because the area is covered by the separation bubble. In the area farther from the rib, the Nu strongly enhances, particularly along the Left Bottom (\triangle) and Left Center (\circ) lines of measurement points due to the existence of the flow reattachment. This Nu enhancement rap-

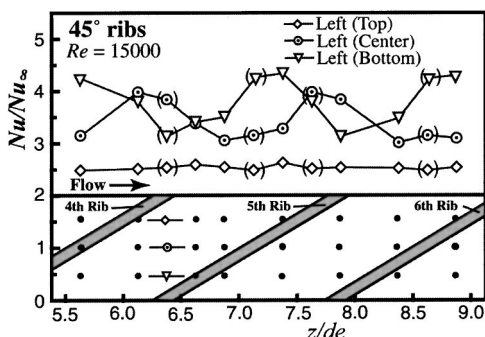


Fig. 11 Local Nu distribution on left wall for 45 deg ribs

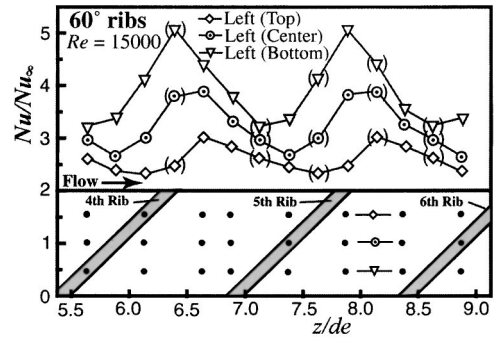


Fig. 12 Local Nu distribution on left wall for 60 deg ribs

idly deteriorates with the distance from the reattachment region due to the boundary layer growth and the flow separation in front of the fifth or sixth ribs.

Comparison between 45 Deg and 60 Deg Rib Patterns. As was noticed above, the wall mean Nu_m on the bottom wall was the highest for the 45 deg rib pattern and on the rib-roughened walls it was the highest for the 60 deg rib pattern. It was also shown in Table 1 that while the Nu_m was very similar for both rib patterns, the pressure drop was slightly higher for the 45 deg rib pattern.

The higher Nu_m for the 60 deg rib pattern on the rib-roughened walls in comparison to that of the 45 deg rib pattern is caused by the strong Nu enhancement between the adjacent ribs, as can be seen in Fig. 12. The Nu deterioration in the spanwise direction for the 60 deg rib pattern is much smaller than in the case of the 45 deg rib pattern due to (1) the smaller boundary layer growth between the 60 deg ribs and (2) the higher Nu enhancements, especially in the near top wall regions [Left Top (\diamond)] compare Figs. 12 and 11.

The slightly higher mean Nu_m on the bottom wall and higher pressure drop for the 45 deg rib pattern in contrast to that of the 60 deg rib pattern is considered to be caused by a stronger rotational momentum of the secondary flow which impinges the bottom wall under greater angle and enhances the Nu appreciably, as can be confirmed by comparing Figs. 13 and 7.

Comparison With the Other Researcher’s Results. Recently Hirota et al. [26] examined the flow velocities and turbulent stresses in 90 deg rib-roughened passage with the aspect ratio 2:1 where the channel width-to-height ratio was $w/e = 50$. The authors showed secondary flow distribution near the rib-roughened walls, however due to the different geometrical size (channel width-to-height ratio used in this study $w/e = 5$) and only 90 deg rib arrangement, the effects of the secondary flow induced by the rib inclination could not be compared.

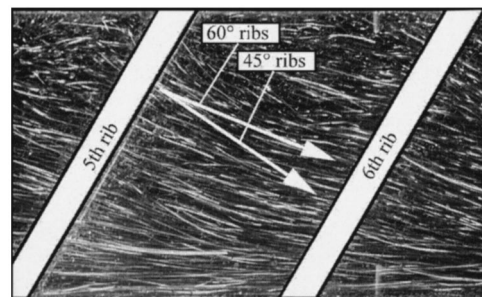


Fig. 13 Flow pattern taken for 60 deg ribs at $y=2.5e$ (central vertical plane). Comparison of secondary flow angle between 45 deg and 60 deg ribs.

Zhang et al. [23] examined the effects of compound turbulators on friction factors and heat transfer coefficients inside a high aspect ratio rectangular channel (aspect ratio 10:1) with two opposite ribbed-grooved walls. However, as in the previous study the authors investigated only 90 ribbed-grooved channel, where they could not observe the flow behavior presented in this study.

To the authors knowledge there are no references describing a flow behavior and heat transfer distribution inside a similar rectangular passage with the aspect ratio 2:1, width-to-height ratio $w/e=5$ and similar rib configurations, except Kiml et al. [24,25] (study for the channel with the aspect ratio 5:1).

Conclusion

The heat transfer experiments and flow visualization were performed in a rectangular rib-roughened channel with aspect ratio 2:1. Ribs were attached to two opposing long side walls. Four rib patterns were tested: 90 deg, 75 deg, 60 deg, and 45 deg ribs. The following conclusions were drawn:

1 The flow visualization and heat transfer results revealed that the heat transfer enhancement at the bottom wall is attributed to the rib-induced secondary flow which conveys the cold air from the passage core region towards the bottom wall. This introduction of fresh cold air on the surface of the bottom wall enhances the heat transfer appreciably.

2 The highest mean Nu_m on the bottom wall and the highest friction coefficient were achieved for the 45 deg parallel rib pattern due to the stronger rotational momentum of the secondary flow which impinges the bottom wall under larger angle than in the other cases.

3 The highest mean Nu_m on the rib-roughened walls was achieved for the 60 deg rib pattern. It was considered to be caused by (a) the stronger Nu enhancement between the adjacent ribs than for the other rib patterns and (b) the smaller Nu deterioration in the spanwise direction.

Acknowledgments

The authors would like to express their gratitude to Mr. M. Yagi and Mr. T. Yokoyama who were very helpful in carrying out the experiments.

Nomenclature

a = passage width [m]
 A_i = cross sectional area of channel [m^2]
 A_h = heat transfer surface area [m^2]
 b = passage side length [m]
 c_p = specific heat of air [J/kgK]
 C_f = friction coefficient ($f/4$)
 d_e = equivalent diameter ($4ab/[2(a+b)]$)
 e = rib height [m]
 k = air thermal conductivity [W/mK]
 L = passage length [m]
 \dot{m} = air mass flow rate [kg/s]
 Nu = Nusselt number, Eq. (4)
 Nu_{∞} = Nusselt number for fully developed flow in smooth passage, Eq. (5)
 Nu_m = wall mean Nusselt number, Eq. (7)
 Nu_{mp} = passage mean Nusselt number
 Nu_{m0} = mean Nusselt number for the smooth passage
 \dot{q}_w = wall heat flux [W/m^2], Eq. (2)
 Δp = pressure loss [Pa]
 Pr = Prandtl number of air
 Re = Reynolds number, Eq. (1)
 T_b = local bulk temperature [K], ($T_{in} + (z/L)(T_{out} - T_{in})$)
 T_{in} = inlet bulk temperatures [K]
 T_{out} = outlet bulk temperatures [K]
 T_w = wall temperature [K]
 u_m = air or water mean velocity [m/s]

\dot{V} = volumetric flow rate of air or water [m^3/s]
 w = channel width
 z = passage length [m]
 α = local heat transfer coefficient [$W/m^2 K$], Eq. (3)
 ρ = air density [kg/m^3]
 ν = air or water kinematic viscosity [m^2/s]

References

- [1] Johnson, B. V., Wagner, J. H., Steuber, G. D., and Yeh, F. C., 1993, "Heat Transfer in Rotating Serpentine Passages With Selected Model Orientations for Smooth or Skewed Trip Walls," ASME Paper 93-GT-305.
- [2] Taslim, M. E., 1991, "An Experimental Investigation of Heat Transfer Coefficients in a Spanwise Rotating Channel With Two Opposite Rib-Roughened Walls," ASME J. Turbomach., **113**, pp. 75–82.
- [3] Rau, G., Cakan, M., Moeller, D., and Arts, T., 1996, "The Effect of Periodic Ribs on the Local Aerodynamic and Heat Transfer Performance of a Straight Cooling Passage," *Proceedings, International Gas Turbine and Aeroengine Congress and Exhibition*, Birmingham, UK, June 10–13, 1996.
- [4] Mochizuki, S., Murata, A., and Fukunaga, M., 1997, "Effects of Rib Arrangement on Pressure Drop and Heat Transfer in a Rib-roughened Channel with a Sharp 180° Turn," ASME J. Turbomach., **119**, pp. 610–616.
- [5] Han, J. C., 1985, "Heat Transfer Enhancement in Channels With Turbulence Promoters," ASME J. Eng. Gas Turbines Power, **106**, pp. 774–781.
- [6] Kiml, R., 2000, "Internal Cooling of Gas Turbine Blades," Doctoral thesis, Tokyo University of Agriculture and Technology, pp. 1–190.
- [7] Wagner, J. H., 1992, "Heat Transfer in Rotating Serpentine Passages With Trips Normal to the Flow," ASME J. Turbomach., **114**, pp. 847–857.
- [8] Dutta, S., Han, J.-C., and Zhang, Y.-M., 1995, "Influence of Rotation on Heat Transfer from a Two-Pass Channel with Periodically Placed Turbulence and Secondary Flow Promoters," *Int. J. Rotating Mach.*, **1**, pp. 129–144.
- [9] Dutta, S., Andrews, J. M., and Han, J.-C., 1996, "Prediction of Turbulent Flow and Heat Transfer in Rotating Square and Rectangular Smooth Channels," ASME Paper 96-GT-234.
- [10] Dutta, S., and Han, J.-C., 1996, "Local Heat Transfer in Rotating Smooth and Ribbed Two-Pass Square Channels with Three Channel Orientations," ASME J. Turbomach., **118**, pp. 587–584.
- [11] El-Husayni, H. A., Taslim, M. E., and Kercher, D. M., 1994, "Experimental Heat Transfer Investigation of Stationary and Orthogonally Rotating Asymmetric and Symmetric Heated Smooth and Turbulated Channels," ASME J. Turbomach., **116**, pp. 124–132.
- [12] Mochizuki, S., Beier, M., and Murata, A., 1996, "Detailed Measurement of Convective Heat Trans. In Rotating Two-Pass Rib-Roughened Coolant Channels," ASME Paper 96-TA-6.
- [13] Taslim, M. E., Li, T., and Kercher, D. M., 1994, "Experimental Heat Transfer and Friction in Channels Roughened with Angled V shaped and Discrete Ribs on Two Opposite Walls," Paper 94-GT-163.
- [14] Hu, Z., and Shen, J., 1996, "Secondary Flow and Its Contribution to Heat Transfer Enhancement in a Blade Cooling Passage with Discrete Ribs," *Proceedings, International Gas Turbine and Aeroengine Congress & Exhibition Birmingham*, UK, June 10–13, 1996.
- [15] Han, J. C., and Zhang, Y. M., 1992, "High Performance Heat Transfer Ducts with Parallel, Broken, and V-shaped ribs," *Int. J. Heat Mass Transf.*, **35**, pp. 513–523.
- [16] Han, J. C., Zhang, Y. M., and Lee, C. P., 1991, "Augmented Heat Transfer in Square Channels With Parallel, Crossed, and V-Shaped Angled Ribs," ASME J. Heat Transfer, **113**, pp. 590–596.
- [17] Ekkad, S. V., and Han, J.-C., 1997, "Detailed Heat Transfer Distribution in Two-Pass Square Channels with Rib Turbulators," *Int. J. Heat Mass Transf.*, **40**, No. 11, pp. 2525–2537.
- [18] Johnson, B. V., Wagner, J. H., Steuber, G. D., and Yeh, F. C., 1994, "Heat Transfer in Rotating Serpentine Passages With Trips Skewed to the Flow," ASME J. Turbomach., **116**, pp. 113–123.
- [19] Cheng, K. C., Shi, L., and Kurokawa, M., 1992, "Visualization of Flow Patterns in a 180-Degree Sharp Turn of a Square Duct," *Proceedings, 4th International Symposium on Transport Phenomena and Dynamics of Rotating Machinery*, USA, Hawaii, A, pp. 124–132.
- [20] Cheng, K. C., and Shi, L., 1996, "Visualization of Flow Patterns in a 90-Degree Sharp Turn of a Square Duct," *Proceedings, 6th International Symposium on Transport Phenomena and Dynamics of Rotating Machinery*, USA, Hawaii, 2, pp. 651–660.
- [21] Metzger, D. E., Plevich, C. W., and Fan, C. S., 1984, "Pressure Loss Through Sharp 180 Degree Turn in Smooth Rectangular Channels," *Trans. ASME J. Eng. Gas Turbines Power*, **106**, pp. 677–681.
- [22] Kiml, R., Mochizuki, S., and Murata, A., 1998, "Influence of 180 Degree Sharp Turn on the Heat Transfer and Flow Behavior in a Smooth Square Cross Sectional Serpentine Channel," *8th International Symposium on Flow Visualization*, CD Rom Proc. of 8th International Symposium on Flow Visualization, Sorrento, Italy (Paper No. 067), pp. 1–8.

- [23] Zhang, Y. M., Gu, W. Z., and Han, J. C., 1994, "Heat Transfer and Friction in Rectangular Channels Ribbed and Ribbed-Grooved Walls," *ASME J. Heat Transf.*, **116**, pp. 58–65.
- [24] Kiml, R., Mochizuki, S., and Murata, A., 2000, "Influence of the Gap Size between Side Walls and Ribs on the Heat Transfer in a Stationary and Rotating Straight Rib-Roughened Duct," *Int. J. Rotating Mach.* **6**, No. 4, pp. 253–263.
- [25] Kiml, R., Mochizuki, S., and Murata, A., 2000, "Function of Ribs as Turbulators and Secondary Flow Inducers," *9th International Symposium on Flow Visualization*, CD Rom Proc. of 9th International Symposium on Flow Visualization, Edinburgh, United Kingdom (Paper File No. 164), pp. 1–10.
- [26] Hirota, M., Fujita, H., Yokosawa, H., and Tanaka, Y., 1996, "Characteristics of Turbulent Flow in a Rectangular Duct With Rib-Roughened Long-Side Walls," *Proc. of the 9th International Symposium on Transport Phenomena in Thermal-Fluids Engineering*, Singapore, June 25–28, 1996.

Energy Separation and Acoustic Interaction in Flow Across a Circular Cylinder

R. J. Goldstein

University of Minnesota,
Department of Mechanical Engineering,
111 Church Street, S.E.,
Minneapolis, MN 55455

Boyong He

510 Maloney Road,
Poughkeepsie, NY 12603

Energy separation in a flow around an adiabatic circular cylinder is investigated using a surface-mounted thermocouple. Energy separation mechanisms in different regions around the cylinder are discussed. Velocity measurements near the rear stagnation point and acoustic measurements indicate that shedding vortices and the wind tunnel intrinsic resonant acoustics can strengthen each other when their frequencies match producing strong energy separation. [DOI: 10.1115/1.1378020]

Keywords: Heat Transfer, Measurement Techniques, Vortex, Wakes

Introduction

Fluid in motion without any heat sources or heat sinks can separate spontaneously into high energy (total temperature or enthalpy) regions and neighboring low energy regions. This phenomena is called energy separation. Energy separation occurs in various flow situations, including laminar and turbulent boundary layers, and vortex flows. The intensity of energy separation can be quantitatively measured with the energy separation factor. Energy separation associated with vortex flows is a much stronger process compared with that associated with boundary layer flows. The mechanisms of energy separation have been a topic of discussion for many years and continue to be in dispute.

Steady Boundary Layer Flow. The unsteady energy equation assuming constant specific heat and no body force can be written from Eckert and Drake [1] as

$$\rho C_p \frac{DT_t}{Dt} = \frac{\Omega P}{\partial t} + \frac{\partial}{\partial x_i} \left(k \frac{\partial T_s}{\partial x_i} \right) + \frac{\partial}{\partial x_j} (u_j \tau_{ij}), \quad (1)$$

where

$$\frac{D}{Dt} = \frac{\partial}{\partial t} + u_i \frac{\partial}{\partial x_i} \quad (2)$$

and for Newtonian fluid,

$$\tau_{ij} = \mu \left(\frac{\partial u_i}{\partial x_j} + \frac{\partial u_j}{\partial x_i} \right) + \delta_{ij} \mu' \frac{\partial u_k}{\partial x_k}. \quad (3)$$

For steady state two-dimensional boundary layer flow,

$$\frac{\partial}{\partial y} \gg \frac{\partial}{\partial x}, \frac{\partial}{\partial z} \quad (4)$$

and Eq. (1) reduces to

$$\rho C_p \left(u \frac{\partial T_t}{\partial x} + v \frac{\partial T_t}{\partial y} \right) = \frac{\partial}{\partial y} \left(k \frac{\partial T_s}{\partial y} \right) + \frac{\partial}{\partial y} \left(u \mu \frac{\partial u}{\partial y} \right), \quad (5)$$

where x is the streamwise direction, y in the direction normal to the wall, and z is the direction orthogonal to x and z .

The total energy (temperature) can vary due to the imbalance between the energy transferred by conduction and shear stress. Within a boundary layer, energy separation is a relatively weak process dependent on the Prandtl number. For a flow over a flat plate laminar boundary layer has a recovery factor,

$$r = \sqrt{\text{Pr}} \quad (6)$$

or

$$S_l = \sqrt{\text{Pr}} - 1,$$

while for a turbulent boundary layer,

$$r \cong \sqrt[3]{\text{Pr}} \quad (7)$$

or

$$S_l \cong \sqrt[3]{\text{Pr}} - 1.$$

Here r is the recovery factor and S_l is the energy separation factor based on the free stream velocity immediately outside the boundary layer.

Unsteady Flow Without Friction and Conduction. For unsteady flow without friction and conduction, Eq. (1) reduces to

$$\rho C_p \frac{DT_t}{Dt} = \frac{\partial p}{\partial t}. \quad (8)$$

Equation (8) indicates that the total energy of a fluid particle will change along path-line due to the pressure fluctuations at a fixed location in the low field. Strong pressure fluctuations, for example in vortex type flows, can cause a large energy separation.

Energy separation due to pressure fluctuations caused by vortices has been studied for flow in vortex tubes (Ranque [2], Hilsch [3], Hartnett and Eckert [4], Marshall [5], and Kurosaka [6]), in resonant tubes (Sprenger [7]), in a free shear layer (O'Callaghan and Kurosaka [8]), and in jet flows (Goldstein et al. [9], Goldstein et al. [10], Fox et al. [11] and Seol [12]).

Eckert and Weise [13] observed energy separation in the flow around a circular cylinder; and an energy separation factor of -1.1 was reached at the rear stagnation line. This means that the cylinder surface recovery temperature at the rear stagnation line is even lower than the static temperature of the upstream fluid. Ryan [14] and Thomann [15] confirmed Eckert's experimental results. Eckert [16] presented a model to analyze cross energy transport through a pathline in a single vortex which can also be used in the analysis of the energy separation in a vortex street. He assumed the vortex has a viscous core and inviscid outer layer, and the maximum and minimum total temperature T_t are located at a place close to the border between the viscous and inviscid part of the vortex. Energy separation starts as the vortex is generated and decreases as the strength of the vortex decreases. Kurosaka and Gertz [17] also investigated energy separation phenomena around a circular cylinder in the Mach number range of $0.2 \leq Ma \leq 0.5$. They found that the pressure fluctuations due to the convective vortex separate the flow field instantaneously into hot spots and

Contributed by the Heat Transfer Division for publication in the JOURNAL OF HEAT TRANSFER. Manuscript received by the Heat Transfer Division April 18, 2000; revision received February 12, 2001. Associate Editor: B. Chung.

cold spots and resonance has very strong effects on the energy separation. Ng et al. [18] used an aspirating probe to measure the transient total pressure and total temperature simultaneously in the wake of a circular cylinder at free stream Mach number of 0.4 and Reynolds number of 2.3×10^5 . From the frequency domain of the measured transient total temperature and total pressure signals, it was confirmed that both signals have a dominant frequency which is the same as the vortex shedding frequency.

It can be seen from the above discussion that energy separation across a circular cylinder and its relation with the shedding vortex and the acoustic sound has been studied since 1940 and it is generally agreed that the pressure fluctuation caused by the shedding vortex will intensify the energy separation around the cylinder rear stagnation point and acoustic resonance will have strong effect on the energy separation. It is paper's intention to answer if the acoustic sound will intensify the vortex shedding thus the energy separation through temperature, flow and acoustic measurement.

Experimental Apparatus

The Wind Tunnel. The suction-type subsonic tunnel used has an entrance section with a bell-mount inlet, a flow straightener and filter, three turbulence reducing screens and two stages of area contraction to the test section. The total area contraction ratio is 15:1. The test section constructed of 19 mm thick Plexiglas has a 120 mm (width) \times 103 mm (height) cross section and 1345 mm overall length. With this design, the velocity in the wind tunnel test section without a cylinder inside can reach 120 m/s. Measured by a TSI 1218-T1.5 hot wire, the velocity across the wind tunnel test section with no cylinder present is uniform and the turbulence intensity is 0.3 percent.

The Test Cylinder and Its Stepper Motor Control. The test cylinder, made of phenolic and shown in Fig. 1 has an OD of 19.05 mm and an ID of 10.16 mm. Phenolic has a thermal conductivity of 0.3344 W/m·K and a thermal diffusivity of 1.6×10^{-7} m²/s. The hot-wire probe leads and a thermocouple leads come out of the hollow cylinder center. The test cylinder, by connection through a 6.4 mm diameter circular extension shaft, can be rotated by a Superior Electric M063-LS09 model stepper motor with a resolution of 400 steps per revolution (0.9 deg per step). The stepper motor is controlled by a Unislide NF-90-3 Pro-

grammable Stepper Motor Controller (Velmex Inc.) connected to a computer through an IO Tech Serial-to-IEEE 488 Converter and an IEEE 488 cable.

The Splitter Plates. A splitter plate installed immediately behind the cylinder can eliminate the shedding vortex in the cylinder wake. Two different splitter plates with thicknesses of 3.0 mm and 9.4 mm are used. The splitter plates have a contoured face toward the cylinder with curvature equal to that of the cylinder and 1.0 mm away from it.

Surface Hot Wire and Thermocouple Mounting. A TSI T1.0 tungsten wire with a 2.54 μ m diameter is soldered on the cylinder surface as shown in Fig. 1. The wire is approximate 120 μ m above the cylinder surface and can be used as both hot wire and cold wire. When used as a hot wire, it is calibrated against the potential flow and used to measure the fluid velocity immediately outside the boundary layer, $U(\theta)$. The velocity in the potential flow region (outside the cylinder boundary layer) before the separation can be expressed as follows:

$$U(\theta) = 2U_\infty \sin(\theta). \quad (9)$$

Calculating the boundary layer thickness from the similarity solution of Wang [19], the hot wire is outside the boundary layer for the potential flow at least to $\theta=30$ deg. This provides a velocity reference for an approximate calibration of the surface mounted hot wire against the potential flow velocity (Eq. 9), while the incoming fluid velocity, U_∞ , is measured with a pitot tube.

A calibrated T-type 30 gauge thermocouple, flush mounted on the cylinder surface with an insulator as shown in Fig. 1, measures the cylinder surface recovery temperature T_r . Before mounting the surface thermocouple, a groove in the cylinder's longitude direction and an angled hole were cut as shown in Fig. 1. Then the thermocouple was laid down on the groove and both thermocouple wires can be pulled out of the hollowed cylinder center from the angled hole. The thermocouple insulation cement was then used to glue thermocouple wire and the thermocouple junction in position. During this process, one took care that the thermocouple junction is just slightly above the cylinder surface. The cylinder was put back to the original shape by machining away the extra insulation cement. A sand paper with very fine grain size was then used to carefully sand the cylinder and the thermocouple junction so that the cylinder surface is smooth and the thermocouple junction is flush with the cylinder surface. Four T-type 30 gauge thermocouples mounted on the entrance section of the wind tunnel monitor the room temperature, which closely approximates the total temperature of the incoming fluid, T_∞ .

Microphone Acoustic Measurement. One objective of this test is to investigate acoustic effects. A Radio Shack 270-092B microphone mounted on the top wall of the test section three diameters (D) downstream of the cylinder monitors the dominant acoustic frequency. A hole in the top wall enables flush mounting of the microphone to the inside of the wind tunnel.

Flow Visualization. In order to investigate the relationship between the moving vortices and energy separation around a circular cylinder, the flow pattern around the cylinder was studied. The near surface flow was visualized using a mixture of oil and black powder painted on the cylinder.

Uncertainty Analysis. The uncertainty in energy separation factor S_∞ depends on the uncertainties in incoming fluid total temperature $T_{t,\infty}$, recovery temperature T_r and dynamic temperature T_d , according to the definition of S_∞ . From the uncertainty analysis method (Coleman and Steele [20]), it is estimated that the uncertainty in energy separation factor S_∞ is 5.23 percent at the cylinder rear stagnation point with $U_\infty=84.25$ m/s (He [21]).

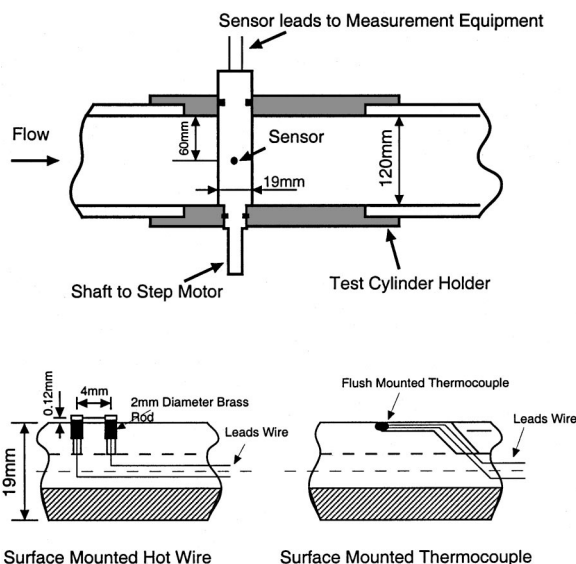


Fig. 1 Schematic drawing of cylinder and surface mounted hot wire

Results and Discussion

Energy Separation Without a Splitter Plate. Figure 2 shows the variation of energy separation with θ along with flow visualization when $U_\infty \approx 84$ m/s. The energy separation factor, S_∞ , decreases continuously from a value of zero at the front stagnation point (recovery factor $r=1.0$) to a value of -1.2 at the rear stagnation point (recovery factor $r=-0.2$). The negative recovery factor at the rear stagnation point indicates that the recovery temperature is even lower than the incoming fluid static temperature. For $U_\infty \approx 84$ m/s case, the energy separation is surprisingly strong. During the recovery temperature measurements at this free stream velocity, an extremely strong resonant acoustic sound was heard and it was suspected that the surprisingly strong energy separation phenomena (low recovery temperature) in the region near the rear stagnation point is related to the resonant acoustic sound.

The distribution of S_∞ , local velocity $U(\theta)$ and turbulence intensity T_u around the cylinder can be separated into five regions (Fig. 3) which correspond to the five regions from the flow visualization shown in Fig. 2.

1 Region 1 extends from the front stagnation point ($\theta=0$ deg) to about 72 deg. In this region, S_∞ continuously decreases from zero to -0.4 at a moderate slope. Both the $U(\theta)$ distribution and the flow visualization indicate a laminar boundary layer flow in this region and separation point at 72 deg, somewhat lower than often observed. In region 1, the energy separation is dominated by laminar boundary layer flow and is relatively weak.

2 Region 2 extends from about 72 deg to about 90 deg. In this region, the energy separation factor changes very little. It is suspected from the flow visualization that this region has a near stagnant flow—a very weak flow exists so that the energy separation

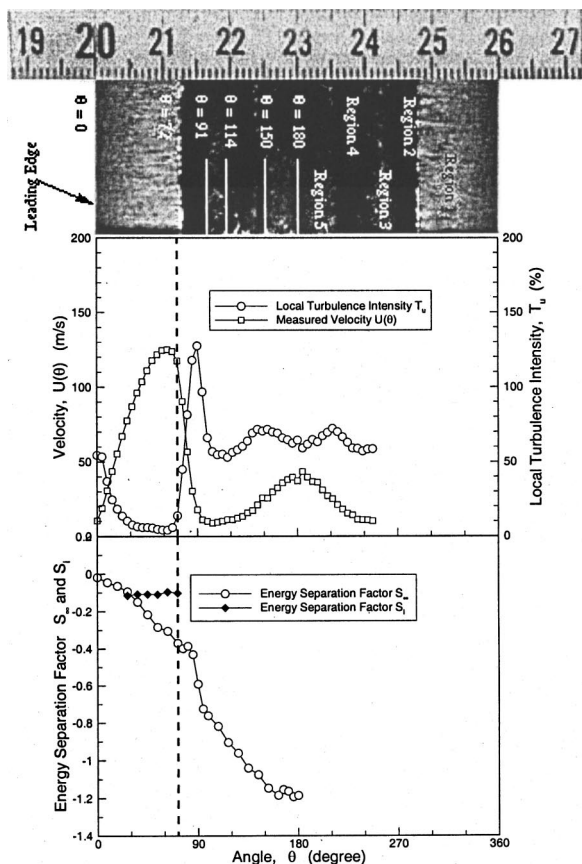


Fig. 2 Comparison of energy separation factor, S_∞ , and flow visualization around the cylinder for $U_\infty \approx 84$ m/s

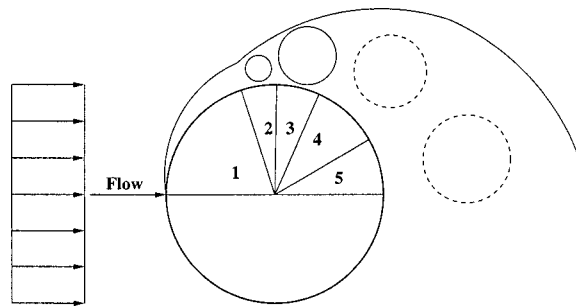


Fig. 3 Proposed traveling vortex pattern around a circular cylinder

factor S_∞ does not change significantly. It also can be seen from the $U(\theta)$ distribution that the velocity decreases dramatically in this region.

3 Region 3 extends from about 90 deg to about 110 deg. S_∞ decreases dramatically from -0.4 to -0.75 . It is expected from the flow visualization picture that the negative pressure gradient in θ direction due to the laminar separation creates a clockwise vortex in this region as shown in Fig. 3. As this clockwise vortex moves away from the cylinder surface in region 3, main stream fluid is drawn close to the cylinder surface and the cylinder surface recovery temperature drops dramatically.

4 Region 4 extends from about 110 deg to 150 deg. S_∞ decreases from -0.75 to -1.2 at a moderate rate but still greater slope than that in region 1. The moving clockwise vortex creates a strong pressure fluctuation which dominates the energy separation in this region, but the cylinder surface recovery temperature does not drop as sharply as that in region 3.

5 Region 5 extends from 150 deg to 180 deg. In this region, the clockwise vortices from the upper part of the cylinder and the counter-clockwise vortex from the bottom part of the cylinder alternatively affect the flow near the cylinder surface. Pressure fluctuations due to the alternately shedding vortex produce the lowest S_∞ in this region.

The energy separation factor distribution around the cylinder for five different velocities are shown in Fig. 4. S_∞ distributions for all velocity cases generally follow the five regions discussed above. At $U_\infty = 84$ m/s case, the acoustic sound is the strongest; the sound levels for $U_\infty = 72$ m/s, 93 m/s, and 100 m/s cases are weaker than that when $U_\infty = 84.25$ m/s. No acoustic sound is heard when $U_\infty = 43$ m/s. Up to the laminar separation points, the S_∞ distributions for all velocity cases are virtually the same and match Eckert and Weise [13] very well. The resonant acoustics have no effects on the energy separation inside the laminar bound-

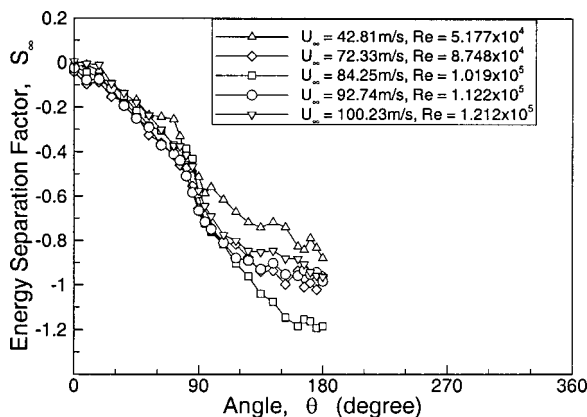


Fig. 4 Energy separation factor, S_∞

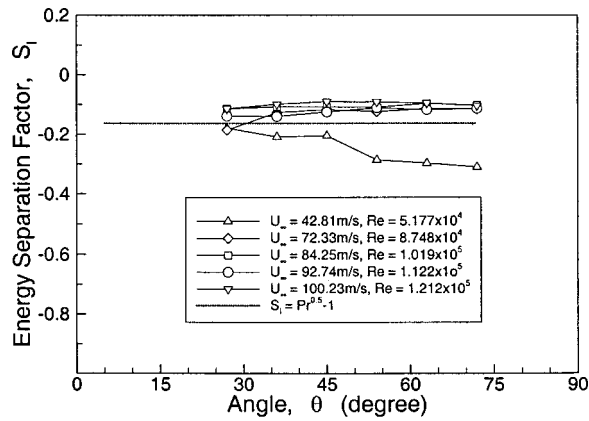


Fig. 5 Energy separation factor, S_l , distributions for 5 different velocities

ary layer and this is also demonstrated in Fig. 5 which shows that the S_l distributions for all five cases inside the laminar boundary layer before the separation point are virtually the same. Both Fig. 2 and Fig. 5 indicate that before flow separation, S_l which is based on the local velocity, closely matches the recovery factor (\sqrt{Pr}) for a laminar boundary layer. But it is very evident in Fig. 4 that S_∞ at a free stream velocity of $U_\infty = 84$ m/s decreases from 90 deg to 180 deg at larger slope than at other free stream velocities.

It is interesting to compare the S_∞ distributions in region 4 and 5 for different free stream velocities. S_∞ has lowest value in region 4 and 5 when $U_\infty = 84$ m/s. The greater the difference in U_∞ from $U_\infty = 84$ m/s, the larger S_∞ is. If there is a resonance in the wind tunnel used at $U_\infty = 84$ m/s, then the energy separation effect in the area after the laminar separation point will be weaker if the incoming fluid velocity is further away from this resonant velocity ($U_\infty = 84$ m/s).

Acoustic Effects on Energy Separation. It has been found by Ryan [14] and confirmed by Kurosaka and Gertz [17] that acoustic sound has strong effect on energy separation around a circular cylinder. By using a surface mounted hot wire an flush mounted microphone, the effect of acoustic on the flow, vortex shedding can be related to energy separation.

Figure 6 indicates that there is no dominant frequency inside the acoustic signal when $U_\infty \approx 84$ m/s without a cylinder present. But once a circular cylinder is present, certain dominant frequencies appear in the acoustic signal. The first dominant frequency is $f_{a1} = 810$ Hz, the n^{th} dominant frequency is $f_{an} = n \times f_{a1}$, but the amplitude of the first dominant frequency is much higher than the others. The hot wire signal measured at the cylinder rear stagna-

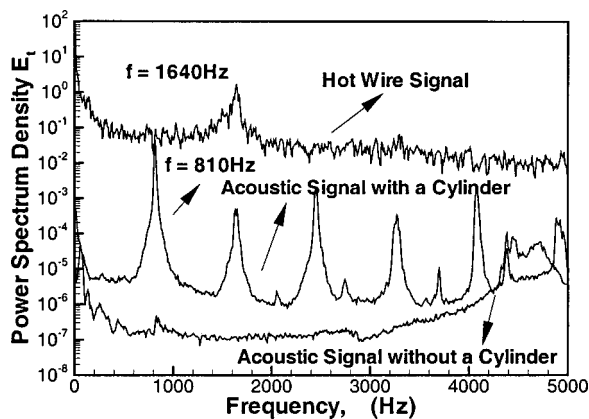


Fig. 6 Acoustic measurement for $U_\infty = 84$ m/s

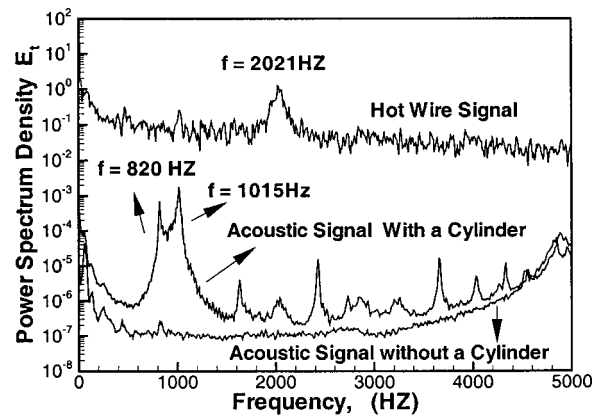


Fig. 7 Acoustic measurement for $U_\infty = 100$ m/s

tion point has a dominant frequency of 1640 Hz, so the single vortex shedding frequency is 820 Hz, which is virtually the same as the first dominant acoustic frequency. The calculated Strouhal number, S_l , from the 820 Hz single shedding vortex frequency is 0.186 which closely matches the value found by Ericsson and Reding [22]. This suggests that there is an intrinsic resonant acoustic frequency around 810 Hz. Taking the intrinsic acoustic wavelength, λ , to be 2 times the wind tunnel height (203 mm) and the sound speed ($c = \sqrt{\gamma RT} = 344.8$ m/s), then the frequency for a standing wave in the wind tunnel can be calculated as $f = c/\lambda = 850$ Hz. This frequency is very close to the measured first dominant acoustic frequency and the shedding vortex frequency when $U_\infty \approx 84$ m/s.

When there is a shedding vortex at the same frequency as the wind tunnel intrinsic resonant acoustic frequency, the resonant acoustic will be excited to a stronger level, but at the same time, this strong acoustic sound also strengthens the shedding vortex after the separation point around the cylinder. This is why S_∞ decreases with a large slope after separation and has the low value of -1.2 at the rear stagnation point for the case of $U_\infty = 84$ m/s.

With no cylinder present there is also no dominant frequency inside the acoustic signal for $U_\infty = 100$ m/s (c.f. Fig. 7), but with a cylinder present, there are two dominant frequencies whose amplitudes are substantially higher than the others. The first one is $f_{a1} = 820$ Hz, which is related to the wind tunnel intrinsic resonant frequency. The second one is $f_{a2} = 1015$ Hz ($S_l = 0.193$) which is essentially the shedding vortex frequency for this velocity. But the acoustic signal level at both frequencies is substantially lower than the acoustic signal level at 810 Hz for $U_\infty = 84$ m/s case. The hot wire signal amplitude at the dominant shedding vortex frequency is also lower than at $U_\infty = 84$ m/s. As the shedding vortex frequency gets close to the wind tunnel intrinsic resonant frequency, both the shedding vortex strength and the resonant acoustic get quite strong and the energy separation gets larger in the region after the laminar separation point where the energy separation is dominated by the shedding vortex, as occurs at $U_\infty = 84$ m/s. When the shedding vortex frequency is away (but not too far away) from the wind tunnel intrinsic resonant frequency (cases for $U_\infty = 100$ m/s, 93 m/s, and 72 m/s), both the resonant acoustic at the wind tunnel intrinsic resonant frequency (810 Hz) and the acoustic at the shedding vortex frequency will be excited by the shedding vortex, but at a weaker level than when $U_\infty = 84$ m/s as there is a weaker interaction between the resonant acoustic and the shedding vortex. The weaker shedding vortex results in smaller energy separation in the region after the laminar separation point. When $U_\infty = 43$ m/s case, there is very little interaction between the shedding vortex and the resonant acoustic since the shedding vortex frequency is away from the wind tunnel intrinsic resonant frequency, resulting in a relatively weak energy separation in the rear of the cylinder (Fig. 4).

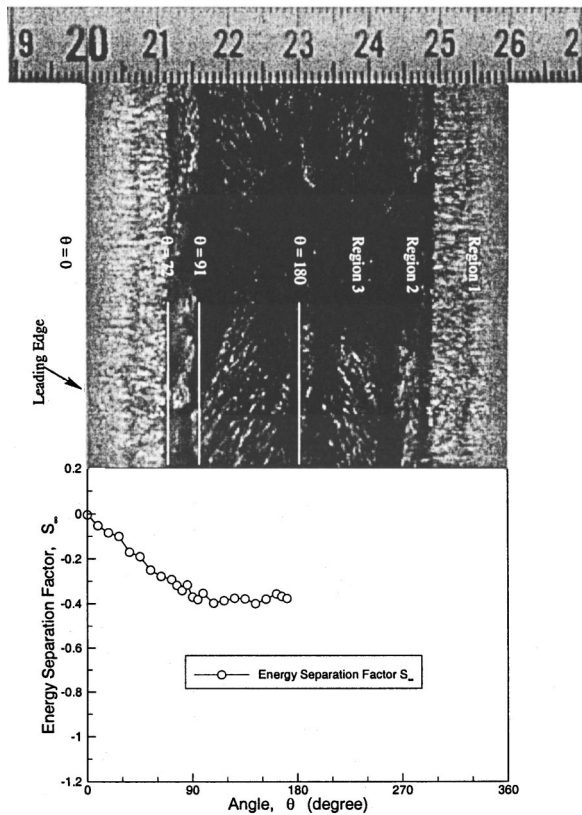


Fig. 8 Comparison between energy separation factor, S_z , distributions and flow visualization around the cylinder for $U_\infty = 84$ m/s with 3.0 mm splitter plate

Energy Separation With a Splitter Plate. It was found (see previous section) that the wind tunnel's intrinsic acoustic and-shedding vortex will have strong interaction only when the shedding vortex frequency matches to wind tunnel's intrinsic acoustic frequency. In this case, the energy separation around the cylinder's rear stagnation point is greatly intensified. Thus, it is expected the energy separation around the rear stagnation point of the cylinder will be much weaker if a splitter plate is placed at the rear stagnation point to eliminate the shedding vortex.

Figure 9 shows energy separation distributions around the cylinder with 3.0 mm and 9.4 mm splitter plates and without a splitter plate at $U_\infty \approx 84$ m/s. Up to 72 deg, the S_z distributions are

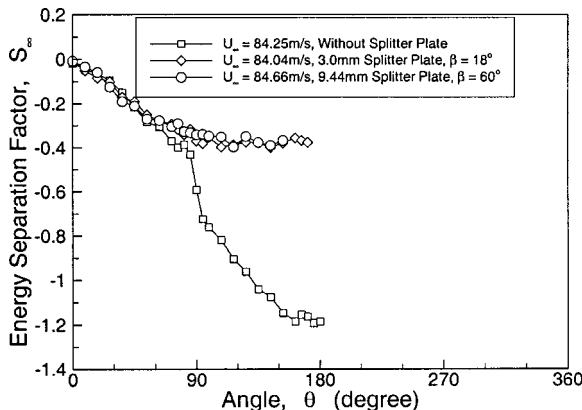


Fig. 9 Energy separation factor, S_z , comparison among cases with 3.0 mm, 9.4 mm and without splitter plate for $U_\infty \approx 84$ m/s

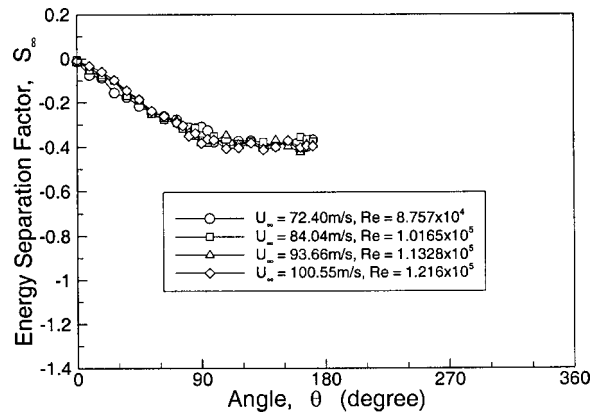


Fig. 10 Energy separation factor, S_z , comparison among cases with 3.0 mm splitter plate for $U_\infty = 72$ m/s, 84 m/s, 94 m/s, 100 m/s

virtually the same for all three cases, but there is a profound difference after 90 deg. S_z remains constant at -0.4 with either splitter plate. The energy separation is much weaker with a splitter plate. During the recovery temperature measurements with splitter plates, no acoustic sound is heard. A comparison between the energy separation factor, distributions and the flow visualization around the cylinder with a 3.0 mm splitter plate in Fig. 8 shows that the flow still separates at $\theta \approx 72$ deg even with a splitter plate present and laminar boundary layer flow still dominates the region from 0 deg to 72 deg. This is why the S_z distributions for all three cases in Fig. 9 are the same up to the laminar separation point. After the separation, flow visualization in Fig. 8 shows that the flow reattaches at $\theta \approx 91$ deg and a separation bubble is present in the region between $\theta \approx 72$ deg and $\theta \approx 91$ deg. So with a splitter plate, there is no moving convective vortex after the separation; the flow in the cylinder wake region after the separation is not dominated by vortex type flow, but rather by reattached boundary layer type flow. That is why the energy separation is so weak with a splitter plate present. The flow pattern differences in the region after the laminar separation point with and without a splitter plate causes profound differences in energy separation in this region.

Figure 10 shows S_z distributions with a 3.0 mm splitter plate present for four velocities. Unlike the distribution without a splitter plate, the S_z distributions in Fig. 10 are similar for all four velocities all around the cylinder even in the region after the laminar separation point at $\theta \approx 72$ deg. The S_z distributions with a 9.4 mm splitter plate present at same velocities as 3.0 mm splitter plate are exactly the same as that in Fig. 10. The presence of a splitter plate has eliminated the shedding vortex after the separation and energy separation is totally independent of splitter plate and Reynolds number in the region studied.

Conclusions

In this paper, the energy separation effect around a circular cylinder is measured using a surface mounted thermocouple. To reveal the direct relationship between the acoustic and energy separation, a surface mounted hot wire is used to measure the shedding vortex frequency and a flush mounted microphone was used to measure the acoustic signal inside the wind tunnel. Thus, the relationship between the strength of shedding vortex and the acoustic sound can be found. Then from the energy separation measurement around the cylinder at the same flow conditions, a relationship between the energy separation and the acoustic is obtained.

Around a cylinder in cross flow, the flow in the region from $\theta = 0$ deg to $\theta = 72$ deg is laminar; the energy separation is due to the imbalance between conduction heat transfer and shear stress work and is relatively weak. After flow separation, the flow

around the cylinder is dominated by shedding vortices and the energy separation in this region is due to the strong pressure fluctuations due to the shedding vortices.

Shedding vortices can interact with the wind tunnel intrinsic acoustics. If the shedding vortex frequency is close to the tunnel intrinsic resonant acoustic frequency, both the shedding vortex and the resonant acoustic will be strengthened by each other and the energy separation in the rear of the cylinder is strong due to the strong shedding vortex. The energy separation gets weaker because of a weaker interaction between the shedding vortex and the intrinsic resonant acoustic as the shedding vortex frequency shifts further from the wind tunnel intrinsic resonant acoustic frequency. Interaction between the shedding vortices and the resonant acoustic has little effects on energy separation in the region before flow separates.

With a splitter plate present, the shedding vortices are not present. The flow still separates at $\theta \approx 72$ deg, but reattaches at $\theta \approx 90$ deg. Energy separation in this case is dominated by boundary layer type flow. The incoming flow velocity and the splitter plate thickness have little effect on energy separation.

Acknowledgment

This work was supported by the Engineering Research Program of the Office of Basic Energy Sciences at the Department of Energy. We also wish to thank Dr. Bumsoo Han for his helpful suggestions.

Nomenclature

c	= speed of sound
c_p	= specific heat at constant pressure
D	= cylinder diameter
f	= frequency
f_{a1}	= first dominant frequency inside acoustic signal
f_{an}	= n^{th} dominant signal inside acoustic signal
f_s	= vortex shedding frequency
k	= fluid thermal conductivity
P	= pressure
Pr	= prandtl number
r	= recovery factor, $r = 1 + S_\infty$
R	= universal gas constant
Re	= Reynolds number, $Re = \rho U_\infty D / \mu$
S_∞	= energy separation factor based on incoming fluid velocity, $S_\infty = T_r - T_{t,\infty} / T_d$
S_l	= energy separation factor based on local fluid velocity immediately outside the boundary layer, $S_l = T_r - T_{t,\infty} / 0.5 U(\theta)^2 / C_p$
St	= Strouhal number, $St = f_s D / U_\infty$
t	= time
$T_{t,\infty}$	= incoming fluid total temperature
$T_{s,\infty}$	= incoming fluid static temperature
T_r	= recovery temperature
T_d	= dynamic temperature, $T_d = T_{t,\infty} - T_{s,\infty} = U_\infty^2 / 2 C_p$
u	= fluid velocity in flow direction inside a flat plate boundary layer
U_∞	= incoming fluid velocity
$U(\theta)$	= potential flow velocity around circular cylinder at angle θ
u_i	= velocity component in Cartesian coordinate system

x_i	= coordiante in Cartesian coordinate system
x	= coordiante along flow direction
y	= coordiante perpendicular to flow direction
z	= coordiante orthogonal to x and y
δ_{ij}	= Kronecker delta
θ	= angle around cylinder measured from forward stagnation point
λ	= acoustic wavelength
μ	= fluid kinetic viscosity
μ'	= viscosity
ν	= specific heat ratio
ρ	= fluid density
τ_{ij}	= shear stress tensor

References

- [1] Eckert, E. R. G., and Drake, R. M. J., 1972, *Analysis of Heat and Mass Transfer*, McGraw-Hill, New York, pp. 265–270.
- [2] Ranque, G., 1933, "Expériences sur la Détente Giratoire avec Productions Simultanées d'un échappement d'air chaud et d'un échappement d'air Froid," *J. Phys. Radium*, **4**, pp. 112–114.
- [3] Hilsch, R., 1947, "The Use of Expansion of Gases in a Centrifugal Field as a Cooling Process," *Rev. Sci. Instrum.*, **18**, pp. 108–113.
- [4] Hartnett, J. P., and Eckert, E. R. G., 1957, "Experimental Study of the Velocity and Temperature Distribution in a High-Velocity Vortex-Type Flow," *Trans. ASME*, **79**, pp. 751–758.
- [5] Marshall, J., 1977, "Effect of Operating Conditions, Physical Size and Fluid Characteristics on the Gas Separation Performance on the Linderstrom-Lang Vortex Tube," *Int. J. Heat Mass Transf.*, **20**, pp. 227–231.
- [6] Kurosaka, M., 1982, "Acoustic Streaming in Swirling Flow and the Ranque-Hilsch (Vortex Tube) Effect," *J. Fluid Mech.*, **124**, pp. 139–172.
- [7] Sprenger, H., 1954, "Über Thermische Effekte in Resonanzrohren," *Mitteilungen aus dem Institut für Aerodynamik, Eidgen. Tech. Hochschule Zürich*, **21**, pp. 18.
- [8] O'Callaghan, J. J., and Kurosaka, M., 1993, "Vortex-Induced Energy Separation in Shear Flow," *AIAA J.*, **13**, pp. 1157–1159.
- [9] Goldstein, R. J., Behbahani, A. I., and Heppelmann, K. K., 1986, "Streamwise Distribution of the Recovery Factor and the Local Heat Transfer Coefficient in an Impinging Air Jet," *Int. J. Heat Mass Transf.*, **29**, pp. 1227–1235.
- [10] Goldstein, R. J., Sobolik, K. A., and Seol, W., 1990, "Effect of Entrainment on the Heat Transfer to a Heated Circular Air Jet Impinging on a Flat Surface," *J. Fluid Mech.*, **112**, pp. 608–611.
- [11] Fox, M., Kurosaka, M., and Hirano, K., 1990, "Total Temperature Separation in Jets," *AIAA Paper 90-1621*.
- [12] Seol, W., 1993, "Energy Separation in a Jet Flow," Ph.D. thesis, Department of Mechanical Engineering, University of Minnesota, Minneapolis, MN.
- [13] Eckert, E. R. G., and Weise, W., 1940, "Messung der Temperaturverteilung auf der Oberfläche Schnell Angeströmter umbeheizter Körper," *Jahrbuch 1940 der Deutschen Luftfahrtforschung*, **2**, pp. 25–31.
- [14] Ryan, L. F., 1951, "Experiments on Aerodynamic Cooling," Ph.D. thesis, Eidgen. Tech. Hochschule, Zürich.
- [15] Thomann, H., 1959, "FFA Report 84," Stockholm, Sweden.
- [16] Eckert, E. R. G., 1987, "Cross Transport of Energy in Fluid Stream," *Wärme und Stoffübertragung*, **21**, pp. 73–81.
- [17] Kurosaka, M., and Gertz, J. B., 1987, "Energy Separation in a Vortex Street," *J. Fluid Mech.*, **178**, pp. 1–29.
- [18] Ng, W. F., Chakroun, M., and Kurosaka, M., 1990, "Time-Resolved Measurement of Total Temperature and Pressure in the Vortex Stress Behind a Cylinder," *Phys. Fluids A*, **12**, pp. 971–978.
- [19] Wang, H. P., 1997, "Local Mass Transfer from a Turbine Blade: Influence of High Turbulence with Large Length Scale on Heat/Mass Transfer," Ph.D. thesis, Department of Mechanical Engineering, University of Minnesota, Minneapolis, MN.
- [20] Coleman, H. W., and Steele, W. G. S. J., 1989, *Experimentation and Uncertainty Analysis for Engineers*, Wiley, New York, pp. 75–116.
- [21] He, B., 1997, "Energy Separation for High Speed Flow Across a Circular Cylinder," Master's thesis, Department of Mechanical Engineering, University of Minnesota, Minneapolis, MN.
- [22] Ericsson, L. E., and Reding, J. P., 1979, "Criterion for Vortex Periodicity in Cylinder Wakes," *AIAA J.*, **17**, pp. 1013.

Experimental and Numerical Study of Conjugate Heat Transfer in a Horizontal Channel Heated From Below

Wilson K. S. Chiu

Cristy J. Richards

Yogesh Jaluria

Fellow ASME

Department of Mechanical
and Aerospace Engineering,
Rutgers, The State University of New Jersey,
New Brunswick, NJ 08903

Conjugate heat transfer has significant relevance to a number of thermal systems and techniques which demand stringent temperature control, such as electronic cooling and chemical vapor deposition. A detailed experimental and numerical study is carried out to investigate conjugate heat transfer in a common configuration consisting of a horizontal channel with a heated section. Experimental data obtained from this study provides physical insight into conjugate heat transfer effects and facilitates validation of numerical conjugate heat transfer models. The basic characteristics of the flow and the associated thermal transport are studied. The numerical model is used to carry out a parametric study of operating conditions and design variables, thus allowing for the characterization of the conjugate heat transfer effects. It is found that the numerically predicted flow field and heat transfer results validate well to experimental observations. Conjugate heat transfer is shown to significantly affect the temperature level and uniformity at the heated section's surface, channel walls and the gas phase, thus impacting the rate of heat transfer. This study provides guidelines and fundamental insight into temperature control during the combined modes of heat transfer, with implications to various thermal manufacturing methods. [DOI: 10.1115/1.1372316]

Keywords: Conjugate, Experimental, Heat Transfer, Manufacturing, Mixed Convection

Introduction

Many investigators have demonstrated the importance of conjugate heat transfer in a number of important technological areas, where the coupling of conduction, convection and/or radiation heat transfer significantly affects the temperature distribution and rate of heat transfer. Examples where conjugate heat transfer analysis has important and significant impact include electronic cooling [1–3], solar collectors [4], chemical vapor deposition (CVD) [5,6], and extrusion of materials [7]. Conjugate heat transfer analysis is critical in predicting the system's temperature distribution and heat transfer rate. However, there is a need to further understand how the different modes of heat transfer affect the thermal characteristics of the system (i.e., temperature distribution, heat transfer rate), and provide experimental data for conjugate model validation.

A limited amount of work on mixed-mode heat transfer studies exist in the literature. In CVD, for example, Chinoy et al. [8] numerically modeled thermal radiation exchange using a uniform temperature heated region coupled with conservation equations. The study demonstrated that a two-band model is able to satisfactorily predict GaAs growth rates in a horizontal CVD reactor. Durst et al. [9] and Fotiadis et al. [10] investigated radiation heat transfer coupled with heat conduction through quartz walls and ambient convection heat loss. Durst et al. [9] examined conjugate effects using an electrically heated region in a channel reactor, while Fotiadis et al. [10] considered a vertical channel with induction heating and radiation heating by heat lamps. Both investigators stressed the importance of wall conduction, and found significant differences in heated surface temperatures when conjugate

effects are considered. Fotiadis et al. [10] further showed that different wall materials in a vertical channel altered the isotherms, but did not significantly affect the flow field.

The preceding literature review indicates the importance of conjugate heat transfer effects. Several researchers have numerically investigated conjugate transport, but a need exists for experimental data, satisfactory model validation, and characterizing of the conjugate effects for a wide range of operational parameters. This paper presents an experimental and numerical study of conjugate heat transfer of air flow in a horizontal channel with conducting walls, as motivated by CVD systems. Conjugate heat transfer effects are considered for different wall materials and wall thicknesses. The flow field is visualized using a light sheet with smoke injection at the inlet, while wall and gas phase temperature distributions are measured using thermocouple probes. Experimental results obtained at different flow rates, heating rates and heated region materials are compared to numerical predictions. Good agreement between the two is observed.

Experimental Apparatus

The experimental system shown in Fig. 1 consists of a plexiglass channel, flow regulation system with a smoke generator, DC power supply, light source, and temperature measurement probes connected to a data acquisition system. The 91.4 cm long plexiglass channel measures 5.08 cm high by 25.4 cm wide from the inside. The channel is insulated on all sides with 5.08 cm thick fiberglass insulation to minimize heat loss.

Air is pressure-regulated and introduced into the channel using a variable area float-type flowmeter. A $1.89 \times 10^{-2} \text{ m}^3$ stagnation chamber is used to provide a flow at constant temperature and to dampen pressure fluctuations associated with compressed air supplied by the house line. The stagnation chamber is also used to premix smoke for flow visualization. Smoke is generated using a commercial smoke generating device (ROSCO Laboratories 1600) which vaporizes heated aqueous glycol solution, producing

Contributed by the Heat Transfer Division for publication in the JOURNAL OF HEAT TRANSFER. Manuscript received by the Heat Transfer Division August 16, 1999; revision received February 1, 2001. Associate Editor: D. A. Kaminski.

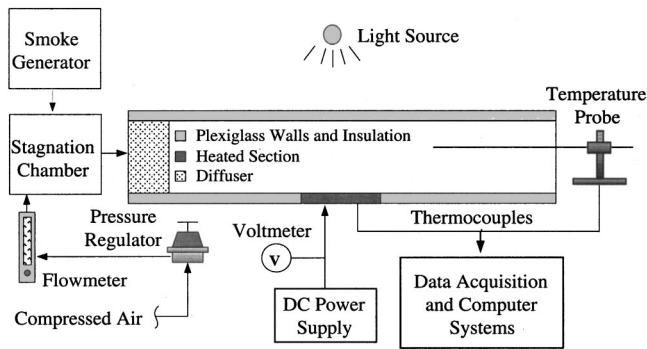


Fig. 1 Diagram of the experimental system

glycol particles in suspension. The gas mixture is injected into the channel, where 10.16 cm of high porosity polyurethane is used as a diffuser and flow straightener to give rise to a uniform laminar entrance flow.

The heated section consists of a 16.51 cm long by 21.22 cm wide by 6.35 mm thick heated region plate (susceptor) mounted in a G-10 Garolite fiberglass tub, as shown in Fig. 2. G-10 Garolite is chosen because of its high thermal resistance and excellent machinability. The plate is mounted flush to the top surface using ceramic spacers. Heating pads are constructed of 0.13 mm thick by 2.03 mm wide inconel wire sandwiched between two 0.06 mm thick kapton sheets (Technical Heaters, CA). The heating pads are secured to the back of the heated region plate using a high temperature acrylic adhesive to ensure good thermal contact. Heating power is supplied by a DC power supply. Power input is calculated by measuring the heater resistance and the amount of voltage supplied to the heaters. Heater resistance deviates less than 0.5 percent under the temperature range considered.

Heated section temperature measurements are obtained by embedding 0.25 mm diameter Type K thermocouples using OME-GABOND high thermal conductivity cement. A total of five thermocouples are centered in the plate, placed 3.31 cm apart along the longitudinal centerline and at half the plate thickness. Two more thermocouples are centered along the plate's transverse centerline, spaced 5.08 cm apart, to measure transverse temperature distributions within the plate. Since the embedded thermocouples are placed at half the plate thickness, a one-dimensional conduction calculation is performed to obtain the surface temperature. Two upstream and three downstream thermocouples are mounted on the bottom plexiglass wall with similar uniform spacing. A thermocouple probe consisting of eight thermocouples mounted on a rack is used to measure gas phase temperatures. On the rack, the bottom four thermocouples are spaced 3.2 mm apart with the bottom thermocouple 6.4 mm from the bottom wall. The next three thermocouples are spaced 6.4 mm apart, and the top thermocouple is 6.4 mm from the top wall.

A vertical light sheet is passed through the top of the channel for flow visualization. A side view is obtained by centering the sheet along the longitudinal direction, giving a two-dimensional view of flow traveling down the channel. The image is captured using a CCD camera, and video editing software (ADOBE Pho-

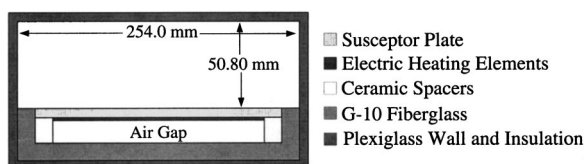


Fig. 2 Cross sectional view of the heated region (susceptor) assembly

toshop and Premiere) is used for image post-processing. A data acquisition system (National Instruments SCXI and LabView) is used to record outputs from the thermocouples. Graphical presentation of the results are carried out on workstations connected to the data acquisition system.

Convective Heat Flux Calculation. Since the bottom wall is not perfectly insulated, heat loss from the bottom of the experimental arrangement is accounted for by using the following expression:

$$q_{\text{ref}} = q_{\Omega} - q_k \quad (1)$$

where the amount of thermal energy input to the heated region (q_{ref}) is the difference between the heat flux due to resistance heating (q_{Ω}) and heat flux due to conduction loss through the bottom. Since temperature measurements show small temperature differences between the heated bottom surface and the bottom wall, radiative heat loss through the bottom is neglected in Eq. (1). Assuming uniform heat flux q_{Ω} and q_k through the bottom wall, q_k is calculated using a one-dimensional conduction model with a 12.7 mm thick air gap, 6.4 mm thick G-10 Garolite and 50.8 mm thick fiberglass insulation. This correction is incorporated in all cases presented in this study. Heat flux into the heated surface (q_{ref}) is used to calculate numerical parameters for the model. There is a minimal feedback effect from numerically corrected q_{ref} used for validation studies since q_{ref} is determined using a separate one-dimensional conduction model, and contribution from the conduction component is small, where $q_k/q_{\Omega} \leq 5$ percent.

In calculating the total convective heat flux (q) at the heated region, one must determine the amount of conduction and radiation contribution to the overall heat flux. The heat flux across the heated region q is written as the uniform heat input q_{ref} less conduction loss q'_k to the walls and radiation loss q_r in the channel:

$$q = q_{\text{ref}} - q'_k - q_r \quad (2)$$

Conduction losses are calculated using the current conjugate heat transfer model. Radiative heat flux is calculated using a net radiative enclosure model [11]. Calculations show that radiative effects contribute between 2.5 percent to 7.5 percent of q_{ref} , with the largest q_r contribution occurring at the highest heated section temperature. Furthermore, q_r remains fairly constant (<5 percent deviation) over the range of temperatures considered, and can be easily factored out as a constant in the results. Since these results show that convective and conductive heat transfer components dominate heat transfer, radiative effects are not included in this study.

Uncertainty Analysis. Many experiments were repeated to ensure that the results and imposed conditions were accurate and repeatable. An uncertainty in repeatability of less than 10 percent was found for the results presented here. The uncertainty in the data is also estimated to be of this order based on the inaccuracies in the measuring instrumentation.

Other uncertainties arising in the experimental study include the measurement of dimensional values (H, L, X_{sep}), heat fluxes, flow rates and temperature values. Embedded thermocouples fluctuate less than $\pm 0.1^\circ\text{C}$, while gas phase temperature readings are within $\pm 0.25^\circ\text{C}$. All thermocouples are calibrated to within $\pm 0.1^\circ\text{C}$ using a constant water bath at temperatures bounding the range encountered in this study (300 K–400 K). Thermocouples mounted in the spanwise direction recorded less than $\pm 0.1^\circ\text{C}$ from the centerline temperature, revealing negligible heat loss in the spanwise direction. Spanwise flow visualization revealed negligible flow variation across the heated plate when measurements are taken at least one channel height away from the sidewalls. It is estimated that temperature and other measurements account for less than 10 percent uncertainty in experimental measurements. The majority of uncertainty arises from material property evaluation, where uncertainties up to 15 percent have been observed for

some materials used in this study. These uncertainties will have a significant impact on experimental parameter calculations (Re, Gr, Pr, K) and on consequent comparisons with numerical predictions.

Numerical Model

The full elliptic governing equations for a two-dimensional steady-state laminar flow in a horizontal channel with constant properties are considered. The two-dimensional assumption is valid if the channel aspect ratio is large and buoyancy effects do not dominate (Gr/Re^2 small), as verified by observing the corresponding two-dimensional flow in the experimental study. In the present study, buoyancy effects are considered using the Boussinesq approximations [12]. The dimensionless governing equations for continuity, momentum, and energy are

$$\frac{\partial u}{\partial x} + \frac{\partial v}{\partial y} = 0 \quad (3)$$

$$\frac{\partial(u\phi)}{\partial x} + \frac{\partial(v\phi)}{\partial y} = \frac{1}{\Gamma} \left[\frac{\partial^2 \phi}{\partial x^2} + \frac{\partial^2 \phi}{\partial y^2} \right] + S(x, y), \quad (4)$$

where the general dependent variable ϕ , the effective diffusion coefficient $1/\Gamma$, and the source term $S(x, y)$ for momentum and energy conservation are defined as

$$\phi = \begin{bmatrix} u \\ v \\ \theta \end{bmatrix}, \quad \Gamma = \begin{bmatrix} Re \\ Re \\ RePr \end{bmatrix}, \quad S(x, y) = \begin{bmatrix} -\frac{\partial P}{\partial x} \\ -\frac{\partial P}{\partial y} + \frac{Gr}{Re^2} \theta \\ 0 \end{bmatrix}. \quad (5)$$

Nondimensional variables are scaled using the channel height H , free stream velocity U_∞ , reference heat flux q_{ref} , and properties evaluated at the reference temperature T_{ref} . Thermal buoyancy effects are represented by the mixed convection parameter, Gr/Re^2 , appearing in the source term of the second momentum equation, Eq. (5). In the energy conservation equation, an order of magnitude analysis [12] shows that viscous dissipation and pressure work are negligible, and are, therefore, not included in this study.

Conjugate Modeling. Conjugate heat transfer couples heat transfer in the solid and fluid regions. The present problem considers heat transfer through the gas and bottom wall of thickness H_s . Conjugate effects due to fiberglass insulation and plexiglass walls are accounted for using convective boundary conditions with total heat transfer coefficients. Energy transfer in the fluid is governed by Eq. (4). The dimensionless energy equation for the solid region is given as

$$\frac{K}{RePr} \left[\frac{\partial^2 \theta}{\partial x^2} + \frac{\partial^2 \theta}{\partial y^2} \right] = 0. \quad (6)$$

Interface conditions are derived by performing an energy balance across the solid-fluid interface. Using these equations, energy transport in the entire region, including solid and gas regions, is solved simultaneously.

In the non-conjugate model, only the fluid region is considered (i.e., $H_s = 0$). Conjugate boundary conditions (Eqs. 7 to 9) are still used, but surface heating input goes directly into convectively heating the gas flow, as achieved by specifying $K_{sus} = K_{insul} = 1$.

Boundary Conditions. The velocity of the flow entering the channel is prescribed as the analytically obtained parabolic profile $u = 6(y - y^2)$ [13]. The flow enters at the ambient temperature T_∞ ($\theta = 0$). The inlet flow conditions are experimentally verified by velocity and temperature measurements at the inlet. The upper boundary is a no-slip, impermeable wall consisting of a plexiglass

wall covered with fiberglass insulation and convective losses from the insulation surface to the ambient (Fig. 3(b)), resulting in a convective boundary condition of the form

$$\text{Top Wall: } \frac{\partial \theta}{\partial y} \Big|_{\text{top}} = -Bi_{\text{top}} \theta_{\text{top}}. \quad (7)$$

The value of Bi_{top} is calculated by considering the total thermal resistance arising from a 9.5 mm thick plexiglass wall ($k = 0.25$ W/mK), 50.8 mm thick fiberglass insulation ($k = 0.04$ W/mK), and natural convection heat transfer from the insulation surface into the environment approximated by $h = 5.0$ W/m²K [14]. The resulting total heat transfer coefficient at the top boundary is calculated as $h_{\text{top}} = 0.66$ W/m²K, corresponding to $Bi_{\text{top}} = 1.27$.

The lower boundary is a no-slip, impermeable solid material of finite thickness (H_s). It is composed of three sections as shown in Fig. 3(a). To replicate experimental conditions, thermal contact resistance between each section is prescribed a 1 mm air gap ($K = 1.0$). The heated region's (susceptor) surface is electrically heated from the bottom by resistance heaters, and approximated by a constant source of uniform heat flux (q_{ref}) as shown in Fig. 3(c). The insulation sections to the left and right of the heated region are solved using the conjugate model, while heat loss through the remaining insulation material at $y < 0$, composing of plexiglass and fiberglass (Fig. 3(d)), is approximated using a total heat transfer coefficient. At the $y = 0$ boundary, convective heat loss into the ambient occurs through a 28.6 mm thick plexiglass wall ($k = 0.25$ W/mK), 50.8 mm thick fiberglass insulation ($k = 0.04$ W/mK), and convectively from the outer insulation surface, as approximated by $h = 5.0$ W/m²K representing natural convection to the ambient [14]. The total heat transfer coefficient at the bottom boundary is calculated as $h_{\text{insul}} = 0.63$ W/m²K, corresponding to $Bi_{\text{insul}} = 1.22$. In summary, the thermal boundary conditions for the bottom wall are

$$\text{Heated Region: } \frac{\partial \theta}{\partial y} \Big|_{\text{sus}} = -1/K_{\text{sus}} \quad (8)$$

$$\text{Insulation: } \frac{\partial \theta}{\partial y} \Big|_{\text{insul}} = \frac{Bi_{\text{insul}}}{K_{\text{insul}}} \theta_{\text{bottom}}, \quad (9)$$

where $Bi_{\text{insul}} = h_{\text{insul}} H / k_{\text{insul}}$, and θ_{bottom} is the temperature at the bottom wall ($y = 0$). The ends of the insulation section are exposed to the ambient, hence are assumed to be at the ambient temperature ($\theta = 0$).

The flow exiting the channel is quite complex due to flow recirculation and entrainment of ambient gas from the exit. In such cases, gas exiting the channel is assumed to be dominated by convection heat transfer, hence the fully developed thermal and velocity boundary condition is prescribed. If gas is entrained into the channel at the exit ($u \leq 0$), it enters at the ambient temperature under fully developed flow conditions [15]. In summary, the exit boundary conditions are

$$\frac{\partial u}{\partial x} = v = 0$$

$$\theta = 0 \quad \text{if } u \leq 0 \quad (\text{inflow}) \quad (10)$$

$$\frac{\partial \theta}{\partial x} = 0 \quad \text{if } u > 0 \quad (\text{outflow}).$$

The inflow temperature was experimentally measured as the ambient temperature. This technique is verified to ensure overall mass conservation in the computational domain. Pressure boundary conditions are not needed since the SIMPLER algorithm [16] calculates pressure values directly from the velocity field. Since pressure differences are calculated in this study, the ambient pressure is specified at one point at the inlet to eliminate drifting of the absolute pressure.

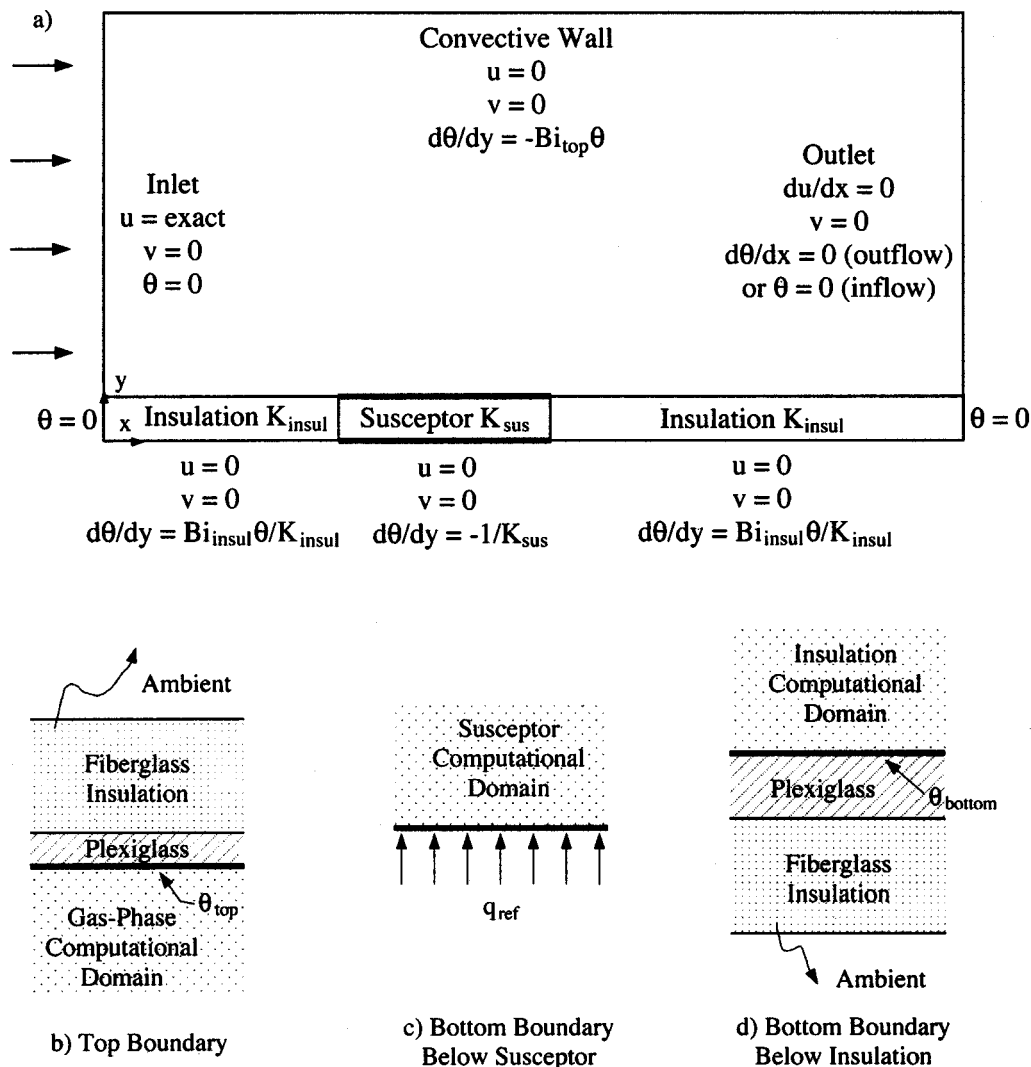


Fig. 3 Boundary conditions and parameters used in the numerical model. The heated region is labeled as the susceptor.

Numerical Method. The numerical model solves the coupled non-linear partial differential equations governing continuity, momentum, and energy conservation. A finite volume technique is used with a uniform staggered grid arrangement, while different grid sizing of uniform spacing is used in the fluid and solid regions. The algorithm solves for primitive variables in velocity (u, v), pressure (p), and temperature (θ). Since momentum and heat transfer are strongly coupled, the continuity (pressure), momentum, and energy conservation equations are solved simultaneously. This coupling arises through buoyancy effects and conjugate boundary conditions. The resulting non-linearly coupled system is solved using Successive Over Relaxation (SOR) for the pressure equation and the Tridiagonal Matrix Algorithm (TDMA) for the remaining equations. Under-relaxation values of 0.1–0.4 are used during iteration of the linearized equations [17].

Typical cases use a grid size of 280×40 in the fluid region and 10 grid points per $H_s = 0.10$ thickness in the solid region. The grid size is chosen based on solution accuracy and computational effort. Grid density is increased until the converged solution differs by less than 1 percent between sizes. This procedure ensures the independence of results on grid size. Iterative convergence is achieved when two consecutive comparisons of the calculated values do not indicate significant differences ($< 10^{-6}$). Convergence is ensured by comparing intermediate flow and thermal fields and

by verifying mass and energy conservation to less than 1 percent discrepancy. The independence of other user prescribed variables, such as initial guess, relaxation factors, outflow boundary conditions, and channel length are varied for all cases to ensure that the results are independent of values chosen.

Results and Discussion

Experimental and numerical results are presented for a horizontal channel heated from below. The channel is 5.08 cm high by 28 cm long with a 12 cm long entrance length defined as insulation in Fig. 3. Consider a system where air enters the chamber at a freestream velocity of $U_\infty = 1.24$ cm/s. The bottom wall is 3.18 mm thick, while the heat region material is ceramic ($k = 1.26$ W/mK) and the insulation material is composed of plexiglass ($k = 0.25$ W/mK). The heated region is heated uniformly at $q_{ref} = 12.7$ W/m², yielding $T_{ref} = 25.3$ K. Transport properties are evaluated at 300 K as $\nu_{ref} = 15.89 \times 10^{-6}$ m²/s, $k_{ref} = 26.3 \times 10^{-3}$ W/mK, and $\alpha_{ref} = 22.5 \times 10^{-6}$ m²/s. Using these values, nondimensional parameters for the reference case are calculated as $Re = 39.8$, $Pr = 0.7$, $Gr = 4.3 \times 10^5$, $K_{sus} = 47.9$, $K_{insul} = 9.5$, and $H_s = 0.125$.

The flow field is studied by comparing the experimentally observed flow field to numerical predictions. The study then pro-

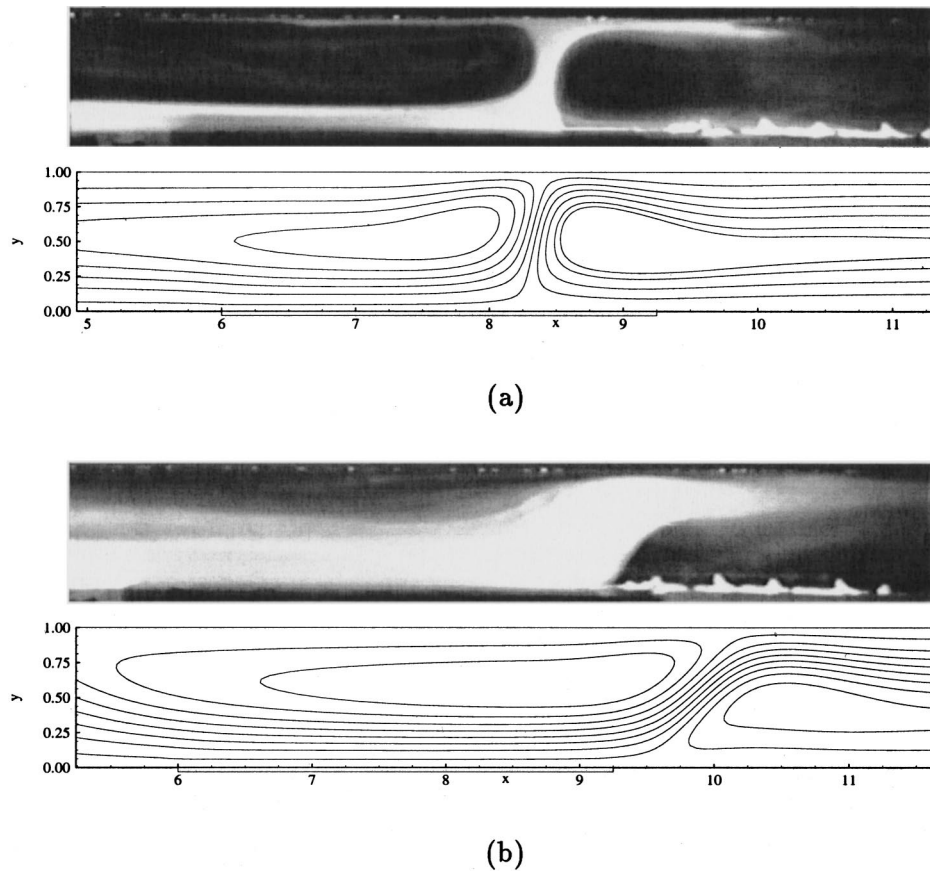


Fig. 4 Comparison between experimental observations and numerical predictions of streamlines for a ceramic heated region at (a) $Re=9.48$ and (b) $Re=29.7$

ceeds to compare numerically calculated and experimentally measured temperature distributions in the channel for different heat region materials and flow rates. A parametric study of several conjugate heat transfer parameters, namely K_{sus} , K_{insul} , and H_s , are performed to quantify their impact on temperature uniformity and heat transfer at the heated region's surface, yielding better physical insight and provide quantitative information for the thermal design of thermal manufacturing systems.

Flow Field. Predicted streamlines are compared to experimental observations for flow of air over a region heated by a uniform heat flux source. The comparison is presented for the reference case with two flow rates given by $Re=9.48$ and 29.7 , as shown in Fig. 4. As the gas travels over the heated region ($6.0 \leq x \leq 9.25$), gas heating causes buoyancy effects to arise. In the case of low Re ($Re=9.48$), a plume develops above the heated region. This flow pattern generates two transverse rolls, with their axis of rotation perpendicular to the flow direction. The upstream roll produces a recirculation region, while the downstream roll entrains flow from outside. These rolls can have significant alterations to the surface temperature and heat transfer rates. In chemical vapor deposition (CVD), for example, deposition rate and film uniformity can be affected by the convective displacement of reactants. As Re is increased (Fig. 4(b)), the plume shifts downstream due to bulk gas flow. Consequently, the two transverse rolls become smaller and flow entrainment from the outside is reduced. The appearances of oscillatory flow, turbulent flow, transverse and longitudinal rolls are observed to be dependent on the channel cross-sectional aspect ratio, flow rate and heating rate. These findings are reported in Chiu et al. [18].

The plume location is measured by calculating the distance from the heated region's leading edge to the plume's center (point

of flow separation), as given by X_{sep} . Figure 5 shows predicted X_{sep} compared to experimentally measured values for a range of mixed-convection parameter $2.71 \times 10^2 \leq Gr/Re^2 \leq 6.79 \times 10^4$. With the exception of the numerical data point at $Gr/Re^2 = 2.71 \times 10^2$, there is good agreement between numerical and experimental results. Discrepancy between numerical and experimental X_{sep} at $Gr/Re^2 = 2.71 \times 10^2$ is due to inherent difficulty in matching exit boundary conditions to experimental conditions. When the plume observed in Fig. 4 reaches near the exit, flow across the outlet deviates from the fully developed conditions given by Eq. (10). Other numerical outflow boundary conditions, such as zero-diffusion and different channel lengths, have been investigated. The zero-diffusion outflow boundary condition is a less stringent form of Eq. (10), where a zero second gradient is defined for u , v , and θ . This choice of boundary condition assumes negligible diffusion across the boundary, but does not demand fully developed flow at the exit. Both methods have been investigated without success. Since it was experimentally observed that the plume intensifies across the channel exit under these conditions, a possible solution is to extend to numerical domain to include flow into the environment. This option was not pursued in this study due to computational limitations.

Parameters in the conjugate model characterizing heat transfer in the solid material, namely K_{sus} , K_{insul} , and H_s , are systematically varied in order to investigate the generation of transverse rolls. For each case, the separation distance relative to the non-conjugate model $X_{sep}/X_{sep,nc}$ is numerically calculated and plotted in Fig. 6. Reference conditions are prescribed to the remaining operating parameters. Results show that a variation in the heated region's thermal conductivity (K_{sus}) does not significantly alter X_{sep} . This is expected since a thin solid material yields low ther-

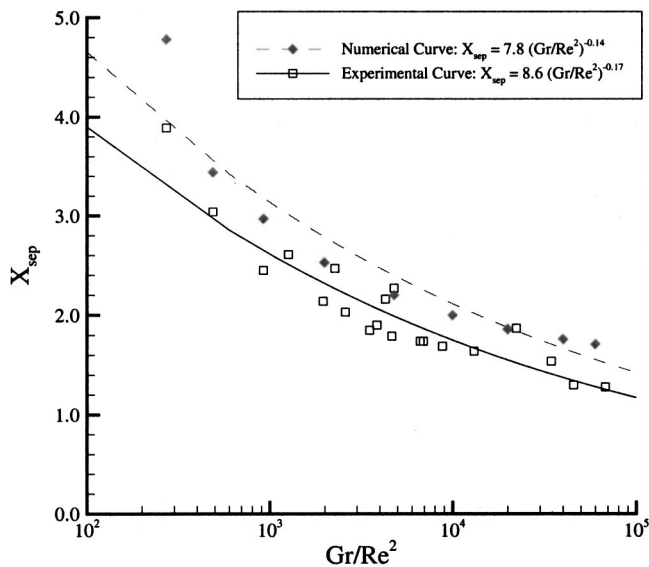


Fig. 5 Thermal plume generation as characterized by flow separation at various Gr/Re^2

mal resistance, thereby allowing convection to be the dominant mode of heat transfer. As the insulation thermal conductivity is increased, the energy is redirected into the surrounding insulation. Small X_{sep} deviations occur at $K_{insul} < 2.5$ because gas heating primarily occurs when the fluid flows over the heated region. At $K_{insul} > 2.5$, significant heat loss to the insulation results in reduced thermal buoyancy, hence increasing the separation distance. At very large K_{insul} , heat transfer is limited to the heated region's conduction toward the insulation, resulting in a leveling of the curve. For small solid material thickness ($H_s \rightarrow 0$), the conjugate model approaches the non-conjugate case, as expected. When the solid material thickness is increased, enhanced heat transfer through the insulation reduces heat transfer into the gas flow, thereby reducing buoyancy effects and delaying plume separation, as indicated by an increase in X_{sep} .

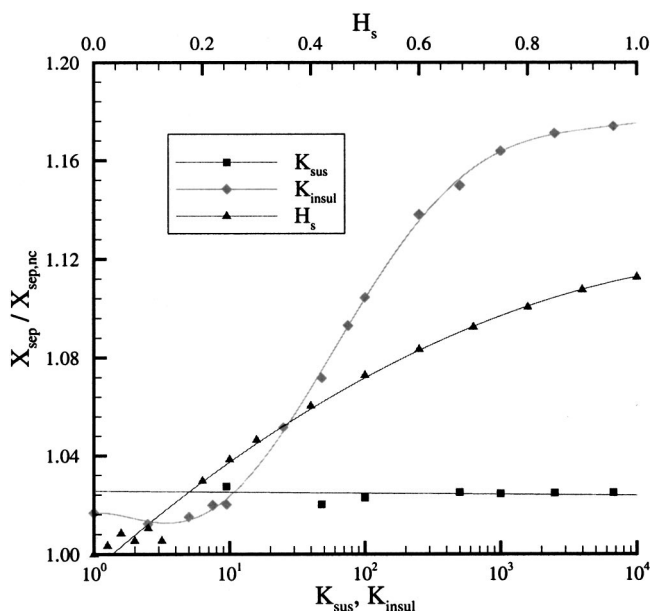


Fig. 6 Flow separation dependence on conjugate parameters. Flow separation predicted by the non-conjugate model is $X_{sep,nc} = 4.67$.

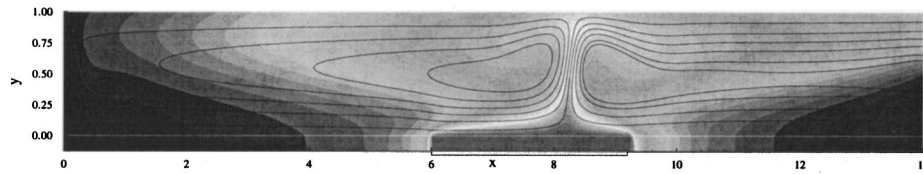
Temperature Field. Numerically predicted temperature fields shown in Fig. 7 are compared to experimental measurements. Figure 7(a) shows streamlines overlaying isotherms for the reference case with $Re = 9.48$ and an aluminum heated region ($K_{sus} = 6730$). It demonstrates the coupling of strong mixed convection effects with conjugate heat transfer modeling to predict a highly isothermal aluminum heated region in the wall and flow field comparable to experimental observations. Further information may be obtained by examining horizontal temperature profiles in the channel.

Corresponding temperature distributions at various y locations are obtained and plotted with experimental data in Fig. 7(b). At temperature distributions above the surface ($y > 0.0$) in Fig. 7(b), the thermal plume produces a peak in the temperature profile near $x \approx 8.25$. This trend is also observed in the experimental data, reinforcing the validity of numerical model in gas phase temperature predictions. Horizontal asymmetry in temperature profiles is caused by bulk gas flow through the channel. The temperature field shows that the heated region remains at high temperature relative to the insulation material, resulting in the generation of a thermal plume above the heated region surface. Due to aluminum's high thermal conductivity, the heated region surface temperature ($6.0 \leq x \leq 9.25$) is highly uniform, as indicated by the last temperature distribution ($y = 0.0$) in Fig. 7(b). Comparison of experimental measurements and numerical predictions show good agreement on the wall and gas phase temperature measurements, with less than 5 percent deviation at the heated region's surface.

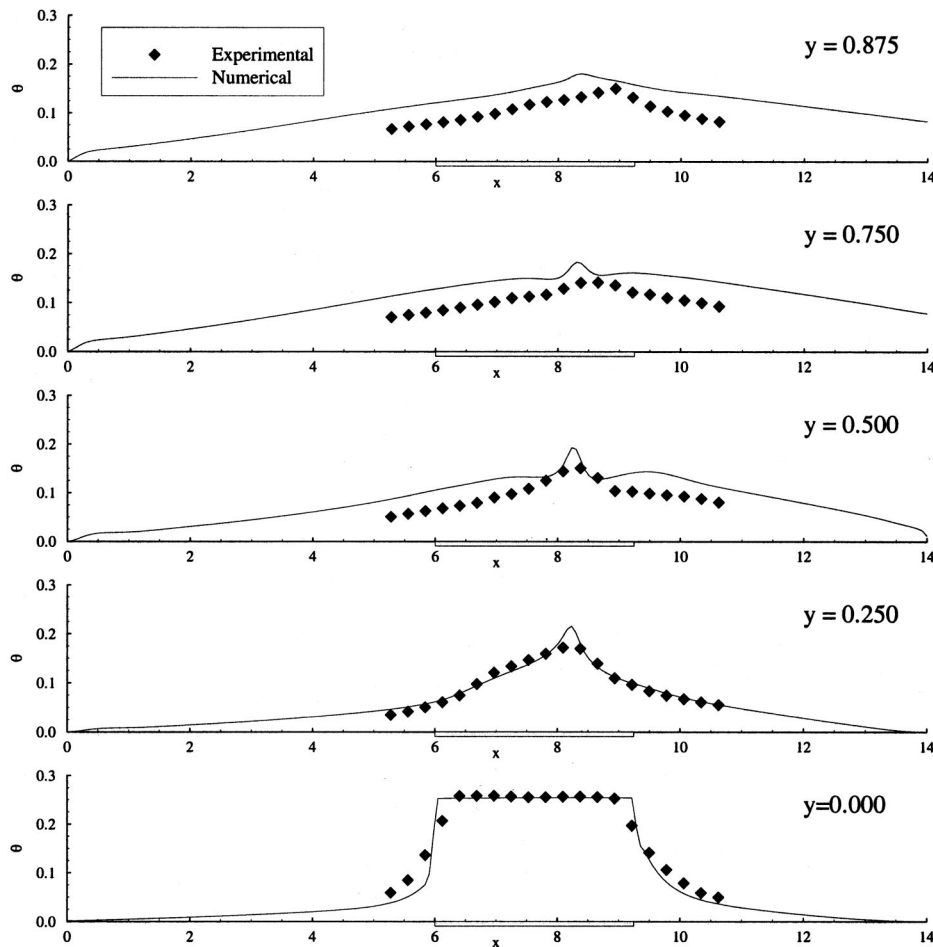
When low thermal conductivity materials such as ceramics are used for the heated region, the temperature characteristics differ significantly from the aluminum case, as shown in Fig. 8. In this comparison, the surface temperature distribution ($y = 0.0$) for a ceramic heated region ($K_{sus} = 47.9$) at two different flow rates ($Re = 9.48$ and 39.8) is shown, with less than 12 percent deviation between numerical and experimental values. A low thermal conductivity heated region material reduces the surface temperature uniformity. This is due to a number of factors, such as increased heat transfer to the insulation and poor thermal diffusivity characteristics of low K_{sus} materials. Discussion and explanation of this phenomenon will be presented later. At increased flow rates, the flow field (Fig. 4) shows a gradual transition where the two transverse rolls created by the plume decrease in size as the plume shifts downstream. In consequence, enhanced cooling will decrease the heated region's temperature, as shown in Fig. 8. Discrepancies at $x > 9.25$ are again due to difficulties in matching the exit boundary conditions to experimental conditions, as discussed earlier. The numerical and experimental cases compare well at other flow rates as well.

Parametric Study. Operational parameters describing the heated region and surrounding materials, namely K_{sus} , K_{insul} and H_s have a direct impact on conjugate heat transfer. This section presents a systematic numerical investigation of these three parameters in detail. The parameters are varied in the range $1.0 \leq K_{sus}$, $K_{insul} \leq 6730$, and $0.0 \leq H_s \leq 1.0$, where $H_s = 0.0$ represents the nonconjugate case. The effect of each parameter on the heated region's surface temperature and uniformity is characterized by the average heated region surface temperature θ_{avg} and heated region surface temperature deviation of the mean θ_{σ} , respectively. Besides K_{sus} , K_{insul} , and H_s , other operational parameters are kept at the reference values.

The significance and importance of conjugate heat transfer modeling is demonstrated in Fig. 9, where the wall surface temperature predicted using a non-conjugate model is compared to temperature predictions using conjugate heat transfer modeling under similar conditions. The conjugate parameters used in this comparison are $H_s = 0.125$, $K_{insul} = 9.5$ (plexiglass) and various heated region thermal conductivities. Heated region conductivities of $K_{sus} = 9.5, 47.9, 100, 500,$ and 6730 are typical values for plexiglass, ceramics, stainless steel and aluminum, respectively. When heated by a uniform heat flux source, which is typical with radia-



(a)



(b)

Fig. 7 (a) Streamline and temperature contours and (b) experimental temperature data comparison (symbols) with numerically predicted results for an aluminum heated region

tion or electrical heating, the non-conjugate model predicts a highly nonuniform wall temperature profile. The temperature immediately upstream of the heated region section is heated above the ambient temperature ($\theta > 0$) due to axial diffusion of thermal energy. A slight dip in the wall temperature at $x \approx 11.0$ is due to the presence of a plume, as discussed previously. When conjugate effects are considered, thermal energy transport besides convection heat transfer into the flowing gas becomes increasingly important. As the heated region conductivity (K_{sus}) is increased, not only does thermal energy redistribute itself within the heated region to produce a highly uniform temperature distribution, thermal energy loss to the insulation also increase. In consequence, paths of thermal energy transfer are manifold compared to the non-conjugate model. Under uniform heating of the heated re-

gion's bottom, the non-conjugate model directs all available thermal energy into the gas phase. Conjugate modeling demonstrates that thermal energy also travels through the solid material, eventually being lost to the ambient or reintroduced into the channel at locations other than the heated region's surface. Since these processes are highly temperature sensitive, these issues must be resolved in order to improve temperature and heat transfer rate predictions. In CVD processing, these quantities are strongly related to film quality, uniformity and productivity.

In order to evaluate the importance of heated region surface temperature predictions using conjugate heat transfer modeling, the average heated region temperature θ_{avg} predicted at various K_{sus} , K_{insul} , and H_s are compared to the non-conjugate prediction ($\theta_{\text{avg,nc}}$) by using the ratio $\theta_{\text{avg}}/\theta_{\text{avg,nc}}$. Using this ratio, the effect

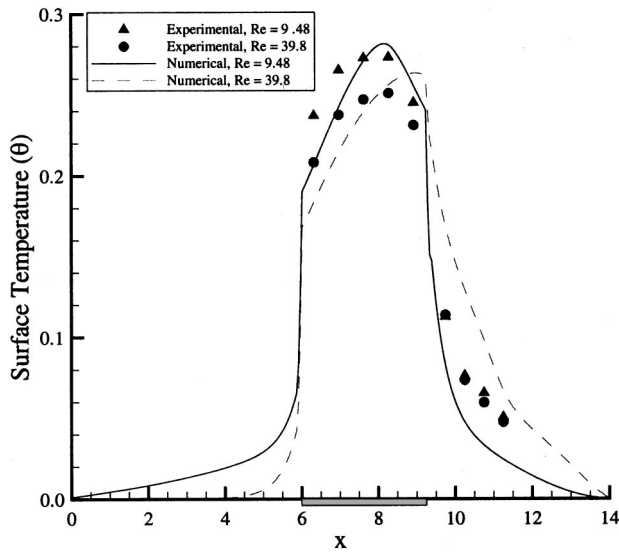


Fig. 8 Surface temperature comparisons for a ceramic heated region

of increasing K_{sus} is shown in Fig. 10. The figure shows a resultant increase in the average temperature due to enhanced heat transfer of the heated region material coupled with limited convective heat transfer to the gas flow. Furthermore, Fig. 11 shows a dramatic drop in temperature deviation θ_σ across the heated region's surface when K_{sus} is increased. A decrease in θ_σ is indicative of a high thermal conductivity material's ability to redistribute thermal energy, thus producing a nearly isothermal surface. Low K_{sus} materials exhibit highly non-isothermal behavior, resulting in large temperature deviations across the heated region's surface.

An increase in insulation thermal conductivity (K_{insul}) allows for thermal energy loss to the insulation, resulting in the reduction of θ_{avg} (Fig. 10) and increased θ_σ (Fig. 11). In consequence, a temperature drop occurs at locations where the heated region is in contact with the insulation; a phenomena known as an "edge effect." This phenomenon, although important particularly near the heated region's edges, is fairly insensitive to variations in K_{insul} , as indicated by small variations in θ_σ in Fig. 11. When the

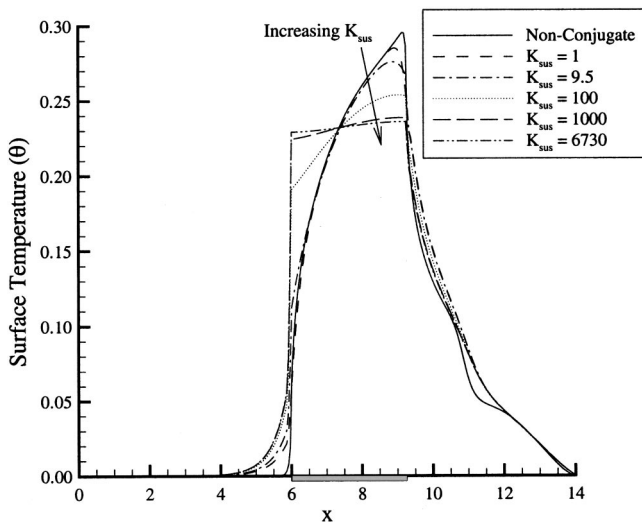


Fig. 9 Effect of heated region (susceptor) material on surface temperature distribution

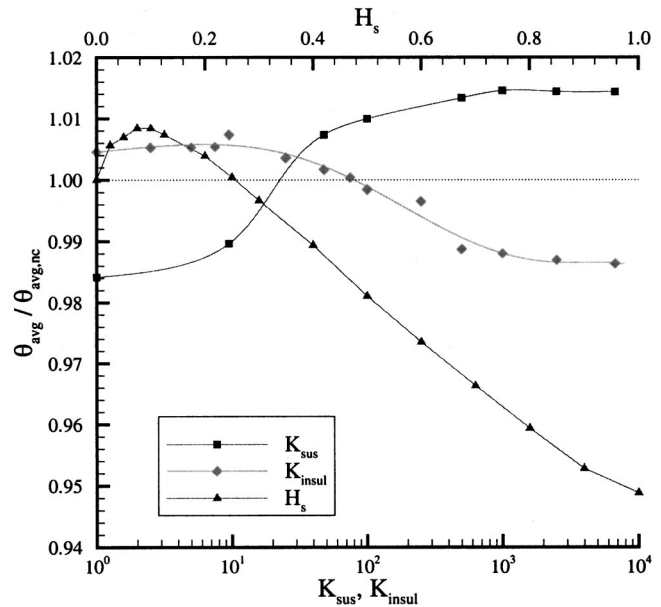


Fig. 10 Deviation of average heated region temperature from the non-conjugate case ($\theta_{avg,nc}=0.229$)

solid material thickness is increased incrementally from $H_s=0.0$ (non-conjugate) to a thickness of one channel height ($H_s=1.0$), heat loss through the insulation is the major contributor to a large drop in θ_{avg} and decreasing heated region temperature deviation (θ_σ), as indicated in Figs. 10 and 11. These aspects are very important when a process is temperature sensitive, and when predictable and controllable temperatures are desirable.

A further understanding of conjugate effects is achieved by quantifying the amount of energy transfer into the gas phase under conjugate conditions for a variety of parameters K_{sus} , K_{insul} , and H_s . Figure 12 compares total convective heat transfer across the heated region surface predicted using conjugate modeling and non-conjugate modeling. Comparison to non-conjugate predictions is achieved by scaling the total convective heat transfer to

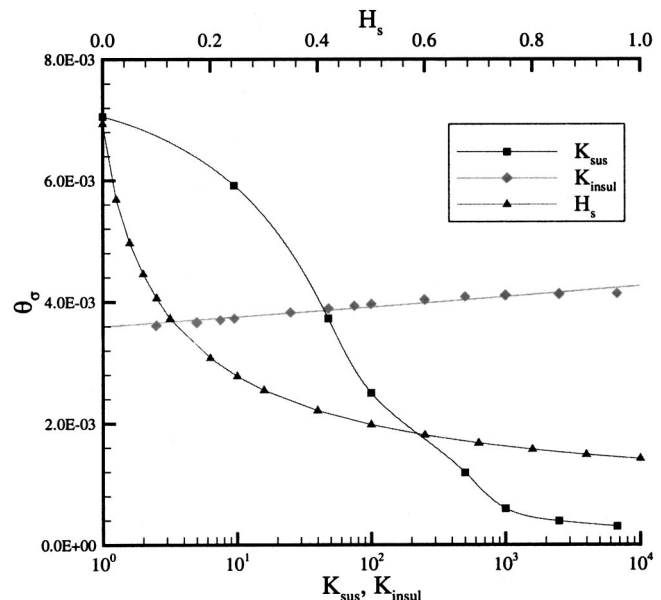


Fig. 11 Heated region temperature uniformity dependence on solid material thickness (H_s), heated region thermal conductivity (K_{sus}) and insulation thermal conductivity (K_{insul})

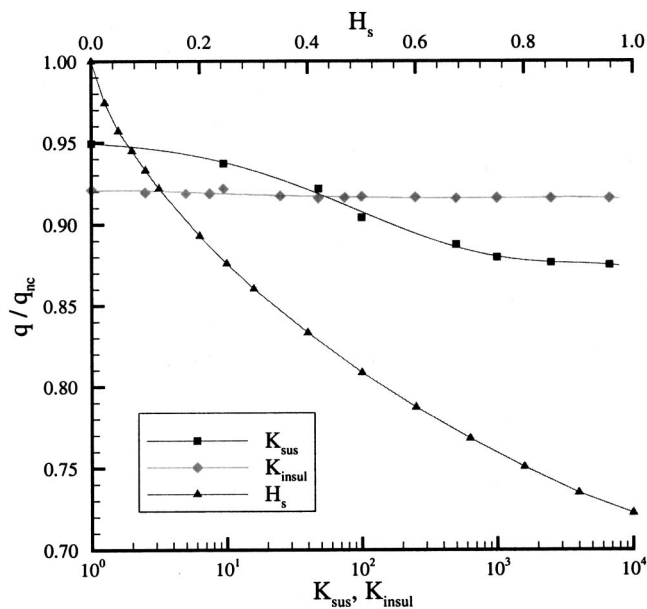


Fig. 12 Fraction of thermal energy across the heated region surface as compared to non-conjugate modeling

the non-conjugate value q/q_{nc} . For example, since the non-conjugate model has a zero-thickness wall, heat input goes directly into the gas flow, i.e., $q/q_{nc} = 1.0$. When conjugate effects are considered, alternate routes of thermal energy transfer become significant, and q/q_{nc} becomes less than unity. Increasing K_{sus} or K_{insul} reduces convection heat transfer across the heated region's surface, and thermal energy reroutes into the insulation. In the range of K_{sus} considered, convective heat transfer into the channel (q/q_{nc}) drops as much as 12 percent with highest thermal losses occurring when an aluminum heated region ($K_{sus} = 6730$) produces a hot (high θ_{avg}) isothermal heated region. Heat losses of 8 percent occurred at $K_{insul} = 1$, and has slightly increased at $K_{insul} = 6730$, indicating that K_{insul} has a fairly weak effect on heat loss through the insulation. However, the inclusion of insulation conjugate heat transfer is necessary to account for a significant amount of thermal energy loss (up to 9 percent) in the solid material and resultant edge effects on the heated region. When the solid material thickness is increased up to $H_s = 1.0$, thermal energy loss through the insulation becomes very significant, with as much as 28 percent of the thermal energy being lost to the insulation at $H_s = 1.0$.

These observations indicate that the inclusion of conjugate heat transfer effects is necessary, as evident from a significant (up to 12 percent) drop in convective heat transfer due to material property variations in the heated region and the insulation (K_{sus}, K_{insul}), and as much as 28 percent of the thermal energy input is lost through the insulation due to H_s variations. Numerical models incorporating conjugate heat transfer are needed to capture these effects. For certain cases, especially where the walls are very thin, and low K_{insul} material is used to contain thermal energy in the heated region, conjugate modeling may not be critical. In such instances, a high K_{sus} material may be approximated as an isothermal surface, while low K_{sus} material may be modeled using a prescribed heat flux condition. Care must be taken in choosing the appropriate model, and a detailed investigation incorporating conjugate heat transfer modeling may be necessary in order to identify the appropriate design variables.

Conclusions

A detailed experimental and numerical study is carried out to investigate conjugate heat transfer in horizontal channels with a heated section, and its impact on thermal processing techniques.

In the experimental study, the gas flow field, temperature distribution and paths of heat transfer are examined for different conditions. The ranges of operational parameters are further extended to numerically examine conjugate effects by considering a variety of materials and wall thicknesses and studying their effects on temperature uniformity and heat transfer.

Experimental data obtained in this study provides valuable insight into the physical phenomenon which governs conjugate heat transfer. The flow and temperature field in a heated horizontal channel with thermally conducting walls of different materials can be quite complicated. This is demonstrated experimentally by the appearance of a two-dimensional thermal plume and transverse roll structures, and by large deviations in experimentally measured temperature distributions for different heated region materials. The aluminum heated region exhibited nearly isothermal conditions, while a ceramic plate yielded highly non-uniform temperature along its surface, illustrating the importance of conjugate effects in system material selection. Comparisons of experimental results with numerical predictions show good agreement.

A parametric study of operational parameters related to the conjugate heat transfer (K_{sus} , K_{insul} , and H_s) revealed that the addition of conjugate heat transfer significantly affects the temperature and heat transfer rates at the heated region's surface. In consequence, channel wall design and modeling of thermal processes with high temperature sensitivity require proper treatment of conjugate heat transfer effects. Situations where non-conjugate modeling is satisfactory are also discussed in detail.

Acknowledgments

Computational resources are provided by the National Partnership for Advanced Computational Infrastructure (NPACI) under Grant No. RUT206 and the High Performance Computing Project (HPCP) of the Information Sciences Strategic Planning Committee at Rutgers University. The authors thank Professor N. G. Glumac for many helpful discussions. The authors also wish to acknowledge partial support provided by the Center for Computational Design (CCD) at Rutgers University. The help provided by Troy Kim in some of the experiments is also acknowledged.

Nomenclature

- Bi = Biot number ($= hH/k$)
- Gr = Grashof number ($= g\beta T_{ref}H^3/v_f^2$)
- Gr/Re² = mixed convection parameter ($= g\beta T_{ref}H/(U_\infty)^2$)
- H = channel height
- h = heat transfer coefficient
- K = thermal conductivity ratio ($= k/k_f$)
- k = thermal conductivity
- L = channel length
- P = local pressure in the fluid
- Pr = Prandtl number ($= v_f/\alpha_f$)
- q = heat flux
- Re = Reynolds number ($= U_\infty H/v_f$)
- T = temperature
- T_{ref} = reference temperature difference ($= q_{ref}H/k_{ref}$)
- U_∞ = free stream velocity
- u, v = velocity components along the x and y axes, respectively
- X_{sep} = flow separation distance from the heated region's leading edge
- x, y = dimensionless coordinates (scaled by H)

Greek Letters

- α = thermal diffusivity ($= k/\rho c_p$)
- β = coefficient of thermal expansion ($= -1/\rho \partial \rho / \partial T|_p$)
- Γ = effective diffusion coefficient
- ν = kinematic viscosity

θ = dimensionless temperature ($= (T - T_{\infty}) / T_{\text{ref}}$)
 ϕ = generalized dependent variable

Subscripts

∞ = ambient or free stream
avg = arithmetic mean
insul = insulation
nc = obtained from non-conjugate model
ref = reference value
s = solid
sus = susceptor (heated region)
top = top wall

References

- [1] Fedorov, A. G., and Viskanta, R., 2000, "Three-Dimensional Conjugate Heat Transfer in the Microchannel Heat Sink for Electronic Packaging," *Int. J. Heat Mass Transf.*, **43**, pp. 399–415.
- [2] Heindel, T. J., Ramadhyani, S., and Incropera, F. P., 1995, "Conjugate Natural Convection from an Array of Discrete Heat Sources: I. Two- and Three-Dimensional Model Validation," *Int. J. Heat Mass Transf.*, **16**, pp. 501–510.
- [3] Sugavanam, R. A., Ortega, A., and Choi, C. Y., 1995, "A Numerical Investigation of Conjugate Heat Transfer from a Flush Heat-Source on a Conductive Board in Laminar Channel Flow," *Int. J. Heat Mass Transf.*, **38**, pp. 2969–2984.
- [4] Aronov, B., and Zvirin, Y., 1999, "A Novel Algorithm to Investigate Conjugate Heat Transfer in Transparent Insulation: Application to Solar Collectors," *Numer. Heat Transfer, Part A*, **35**, pp. 757–777.
- [5] Chiu, W. K. S., Glumac, N. G., and Jaluria, Y., 2000, "Numerical Simulation of Chemical Vapor Deposition Processes Under Variable and Constant Property Approximations," *Numer. Heat Transfer, Part A*, **37**, pp. 113–132.
- [6] Mahajan, R. L., 1996, "Transport Phenomena in Chemical Vapor-Deposition Systems," *Adv. Heat Transfer*, **28**, pp. 339–425.
- [7] Lin, P., and Jaluria, Y., 1998, "Conjugate Thermal Transport in the Channel of an Extruder for Non-Newtonian Fluids," *Int. J. Heat Mass Transf.*, **41**, pp. 3239–3253.
- [8] Chinoy, P. B., Kaminski, D. A., and Ghandhi, S. K., 1991, "Effects of Thermal Radiation on Momentum, Heat, and Mass Transfer in a Horizontal Chemical Vapor Deposition Reactor," *Numer. Heat Transfer, Part A*, **19**, pp. 85–100.
- [9] Durst, F., Kadinski, L., and Schäfer, M., 1995, "A Multigrid Solver for Fluid Flow and Mass Transfer Coupled with Grey-Body Surface Radiation for the Numerical Simulation of Chemical Vapor Deposition Processes," *J. Cryst. Growth*, **146**, pp. 202–208.
- [10] Fotiadis, D. I., Kieda, S., and Jensen, K. F., 1990, "Transport Phenomena in Vertical Reactors for Metalorganic Vapor Phase Epitaxy," *J. Cryst. Growth*, **102**, pp. 441–470.
- [11] Siegel, R., and Howell, J. R., 1992, *Thermal Radiation Heat Transfer*, Taylor & Francis, Philadelphia, PA.
- [12] Gebhart, B., Jaluria, Y., Mahajan, R. L., and Sammakia, B., 1988, *Buoyancy-Induced Flows and Transport*, Taylor & Francis, Philadelphia, PA.
- [13] Panton, R. L., 1984, *Incompressible Flow*, John Wiley & Sons, Inc., NY.
- [14] Incropera, F. P., and DeWitt, D. P., 1990, *Fundamentals of Heat and Mass Transfer*, John Wiley & Sons, Inc., NY.
- [15] Ku, A. C., Doria, M. L., and Lloyd, J. R., 1976, "Numerical Modeling of Buoyant Flows Generated by Fire in a Corridor," *Proc. 16th Symp. (Int.) on Combustion*, Combustion Institute, pp. 1372–1384.
- [16] Patankar, S. V., 1980, *Numerical Heat Transfer and Fluid Flow*, Taylor & Francis, Philadelphia, PA.
- [17] Jaluria, Y. and Torrance, K. E., 1986, *Computational Heat Transfer*, Hemisphere Publishing Corporation, USA.
- [18] Chiu, W. K. S., Richards, C. J., and Jaluria, Y., 2000, "Flow Structure and Heat Transfer in a Horizontal Converging Channel Heated from Below," *Phys. Fluids*, **37**, pp. 2128–2136.

Conjugate Mixed Convection With Surface Radiation From a Vertical Plate With a Discrete Heat Source

C. Gururaja Rao

Research Scholar and Lecturer
Department of Mechanical Engineering,
Regional Engineering College,
Warangal—506 004 (AP), India

C. Balaji

Assistant Professor

S. P. Venkateshan

Professor
e-mail: spv46@usa.net

Heat Transfer and Thermal Power Laboratory,
Department of Mechanical Engineering,
Indian Institute of Technology Madras,
Chennai-600 036, India

The results of a numerical study of the problem of two-dimensional, steady, incompressible, conjugate, laminar, mixed convection with surface radiation from a vertical plate with a flush-mounted discrete heat source are reported. The governing equations, written in vorticity-stream function form, are solved using a finite-volume based finite difference method. A hybrid grid system has been employed for discretization of the computational domain. The effects of (i) the magnitude and location of the heat source, (ii) the material and surface properties of the plate, and (iii) the free-stream velocity on both heat transfer and fluid flow have been studied. Based on a large set of (more than 550) numerical data, correlations have been developed for maximum and average non-dimensional plate temperatures and mean friction coefficient. A method for evaluating the forced convection mean friction coefficient component, which may be used in estimating the power input required for maintaining the flow, has been proposed. [DOI: 10.1115/1.1373654]

Keywords: Conjugate, Finite Difference, Heat Transfer, Mixed Convection, Radiation

Introduction

Interaction of different modes of heat transfer continues to be a topic of interest because of its application in several areas, like the cooling of electronic equipment. Vertical board mounted electronic components are cooled by the removal of the heat generated in the components, with air as one of the promising cooling media. Zinnes [1] presented both numerical and experimental results of the problem of interaction of conduction with natural convection from a vertical plate with arbitrary surface heating, and showed that the degree of coupling between plate conduction and natural convection in the fluid is influenced by the plate-fluid thermal conductivity ratio. Gorski and Plumb [2] numerically investigated the problem of conjugate heat transfer from a single discrete heat source, flush-mounted in a flat plate. Here, the problem was solved using the well-known Blasius velocity profile for laminar forced convection as the input, and a correlation relating the average Nusselt number to Peclet number, the heat source size and the length ratio was developed. Hossain and Takhar [3] numerically investigated the effect of radiation on mixed convection from a heated vertical plate with uniform free-stream and surface temperatures. Cole [4] addressed, numerically, the problem of electronic cooling, from the perspective of scaling, applied to a steady viscous flow over a heated strip on a plate. However, the results for the problem of conjugate laminar mixed convection with surface radiation from a vertical plate with a flush-mounted discrete heat source are not available in the literature. Hence, a detailed numerical analysis of this problem is reported here.

Mathematical Formulation

The governing equations for two-dimensional, steady, incompressible, laminar, mixed convection from a vertical plate are available in a number of references, e.g., Bejan [5]. The schematic of the problem geometry, consisting of a vertical plate with a flush-mounted discrete heat source, is shown in Fig. 1. The left, top and bottom faces of the plate are insulated, while heat transfer occurs from the right face, by convection (free and forced) and surface radiation. The governing equations are first converted into

vorticity-stream function (ω - ψ) form and are then normalized. As the present problem involves “conjugate” heat transfer, an “obvious” reference temperature difference does not exist. Hence, a “modified” reference temperature difference is introduced as $\Delta T_{\text{ref}} = (q_v L_h t / k_s)$. The normalized governing equations are

$$U \frac{d\omega}{dX} + V \frac{\partial \omega}{\partial Y} = -\text{Ri}_L^* \frac{\partial \theta}{\partial Y} + \frac{1}{\text{Re}_L} \left[\frac{\partial^2 \omega}{\partial X^2} + \frac{\partial^2 \omega}{\partial Y^2} \right] \quad (1)$$

$$\frac{\partial^2 \psi}{\partial X^2} + \frac{\partial^2 \psi}{\partial Y^2} = -\omega \quad (2)$$

$$U \frac{\partial \theta}{\partial X} + V \frac{\partial \theta}{\partial Y} = \frac{1}{\text{Pe}_L} \left[\frac{\partial^2 \theta}{\partial X^2} + \frac{\partial^2 \theta}{\partial Y^2} \right] \quad (3)$$

Computational Domain

Based on an earlier work of the present authors, Gururaja Rao et al. [6], the computational domain in this case is extended beyond the trailing edge of the plate by a length equal to that of the plate (L), while the width (W) of the domain is taken equal to the plate length.

Boundary Conditions

At the bottom, as the fluid enters with a uniform velocity, u_∞ , and temperature, T_∞ , $(\partial \psi / \partial Y) = 1$, $\omega = 0$ and $\theta = 0$. Along the plate, $\psi = 0$ and $\omega = -\partial^2 \psi / \partial Y^2$. Energy balance on the plate element, which is shown, enlarged, in the inset to Fig. 1, yields the following equation for the plate temperature distribution, in the non-dimensional form:

$$\frac{\partial^2 \theta}{\partial X^2} + \gamma \left(\frac{\partial \theta}{\partial Y} \right)_{Y=0} + A_{r_1} A_{r_2} - \varepsilon \gamma \text{N}_{RF} \left[\left(\frac{T}{T_\infty} \right)^4 - 1 \right] = 0 \quad (4)$$

Equation (4) is valid in the region that contains the heat source. In the region outside the heat source, the term $A_{r_1} A_{r_2} = 0$. Energy balance on the bottom and top insulated ends will give the appropriate equations, depending on whether or not these two ends are part of the heat source. With regard to the extended length of the left boundary, because of symmetry, $V = 0$, which means that $(\partial \psi / \partial X) = 0$, implying that ψ is a constant. Since $\psi = 0$ has been taken along the plate, the same is used along the extended length

Contributed by the Heat Transfer Division for publication in the JOURNAL OF HEAT TRANSFER. Manuscript received by the Heat Transfer Division May 30, 2000; revision received November 25, 2000. Associate Editor: R. Skocypec.

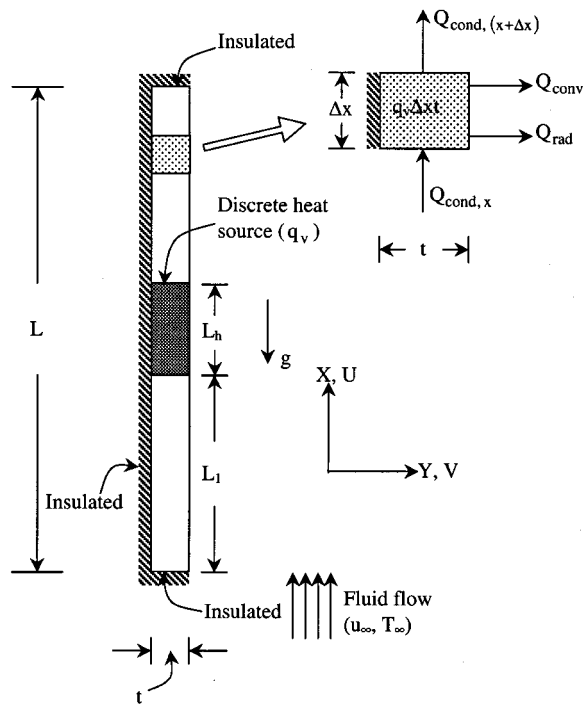


Fig. 1 Schematic of the problem geometry (inset showing an enlarged plate element)

of the left boundary also. The vorticity, $\omega=0$ here. Because there is no heat transfer across the extended length, $(\partial\theta/\partial Y)=0$. On the top, the fully developed condition, $(\partial\psi/\partial X)=0$, has been used for ψ . Since the domain is extended, $\omega=0$. When U is positive, the fully developed condition $(\partial\theta/\partial X)=0$ is used for θ , and when U is negative, $\theta=0$. On the right, a mixed condition, $(\partial^2\psi/\partial X\partial Y)=0$, is imposed on ψ , while ω and θ are each taken to be zero.

Method of Solution

The governing Eq. (1)–(3) are transformed into finite difference equations using a finite-volume based finite difference method of Gosman et al. [7] and are then solved using the Gauss-Seidel iterative procedure. The details of the solution procedure are available in Gururaja Rao et al. [6]. A hybrid grid system is used for discretizing the computational domain, keeping in mind the fact that the temperature distribution along the plate depends on the height and the position of the heat source. Based on a grid sensitivity test to be discussed in the ensuing section a grid size of 111×111 is chosen. The grid pattern used for a typical case is shown in Fig. 2, which also shows all the boundary conditions. All the calculations are done for air ($Pr=0.71$) and the range of parameters used in the present work is listed in Table 1.

Results and Discussion

Grid Sensitivity Analysis. To study the effect of grid size ($M \times N$) on the solution, a case with $q_v=5 \times 10^5 \text{ W/m}^3$, $A_1=0.4375$, $k_s=0.25 \text{ W/m K}$, $\varepsilon=0.45$, $Re_L=1275$, and $Ri_L^*=2$ is considered, and the results are shown in Table 2. The analysis is made in two stages—first with M fixed and then with N fixed. The results of the former show that the difference in θ_{\max} between grid sizes 111×111 and 111×131 is 0.06 percent, while the difference in \bar{C}_f between the same grid sizes is 0.62 percent. The results of the grid sensitivity with N fixed show that the differences in θ_{\max} and \bar{C}_f between grid sizes 111×111 and 131×111 are 0.07 percent and 0.54 percent, respectively. In view of the above, M and N have both been fixed as 111. The nodal number 111 is considered as the basis after some initial studies with various other numbers.

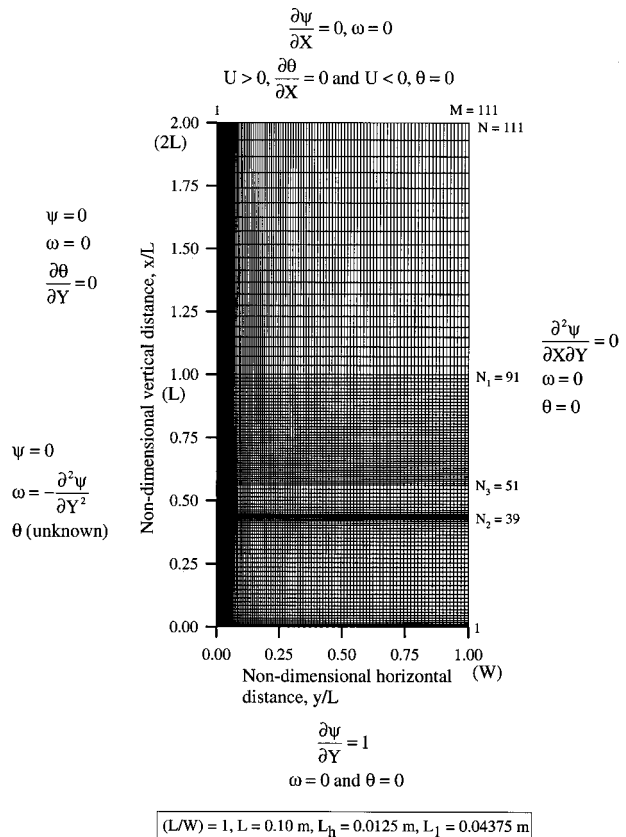


Fig. 2 Grid pattern used for a typical case along with boundary conditions

Validation

The fundamental difference between the boundary conditions for laminar mixed convection from an isothermal vertical plate, e.g., Gururaja Rao et al. [6] and those used in the present work is the temperature variation along the plate. In the former, the temperature was considered uniform along the plate, while here, the temperature varies along the plate, provided with a heat source, due to multi-mode heat transfer. Thus, the validation of results for the entire mixed convection regime, provided in Gururaja Rao et al. [6] with reference to both numerical and experimental results available in the literature, will ensure the accuracy of the present results.

Table 1 Range of parameters [$L=0.10 \text{ m}$, $t=0.0015 \text{ m}$, $L_h=0.0125 \text{ m}$, $L_1=0.04375 \text{ m}$]

Parameter	Unit
$10^5 \leq q_v \leq 10^6$	W/m^3
$0 \leq A_1 < 1$	-
$0.25 \leq k_s \leq 1$	W/m K
$0 < \gamma \leq 10$	-
$0 < N_{RF} \leq 1000$	-
$0.05 \leq \varepsilon \leq 0.85$	-
$80 \leq Re_L \leq 8000$	-
$0.1 \leq Ri_L^* \leq 25$	-

Table 2 Grid sensitivity analysis [$L=0.10$ m, $L_h=0.0125$ m, $t=0.0015$ m, $L_f=0.04375$ m, $q_v=5 \times 10^5$ W/m³, $k_s=0.25$ W/m K, $\varepsilon=0.45$, $k_f=0.0291$ W/m K, $Re_L=1275$ and $Ri_L^*=2$]

Stage	Grid size (M×N)	θ_{max}	Percentage change (abs.)	\bar{C}_f (total)	Percentage change (abs.)
(1) M = 111, N varied	111×91	1.0429	-	0.0642	-
	111×111	1.0348	0.78	0.0648	0.86
	111×131	1.0355	0.06	0.0644	0.62
(2) N = 111, M varied	91×111	1.0357	-	0.0652	-
	111×111	1.0348	0.09	0.0648	0.57
	131×111	1.0341	0.07	0.0644	0.54

The results of the present problem are also tested for mass and energy balance. For this, a typical case with $q_v=10^6$ W/m³, $k_s=0.25$ W/m K, $\varepsilon=0.85$, $Re_L=2500$, and $Ri_L^*=1$ is taken up. As many as 13 different positions for the discrete heat source ($0 \leq A_1 \leq 0.875$) are considered. The mass and the energy balance are found satisfactory within ± 0.007 percent and ± 4.02 percent, respectively.

Variation of Maximum Plate Temperature (θ_{max}) With Other Parameters

Figure 3 shows the variation of θ_{max} with non-dimensional heat source position (A_1), for two values of u_∞ ($Ri_L^*=25$ and 0.1) and two values of surface emissivity ($\varepsilon=0.05$ and 0.85), for the case with $q_v=10^6$ W/m³ and $k_s=0.25$ W/m K. It is clear that there is a sharp increase in θ_{max} from $A_1=0$ to $A_1=0.125$ and again from $A_1=0.825$ to $A_1=0.875$, with a considerably slower increase for $A_1=0.125$ to 0.825. As Ri_L^* decreases from 25 to 0.1, the amount by which θ_{max} increases between the positions $A_1=0.125$ and $A_1=0.825$ also increases. In the case considered here, the increase in θ_{max} , between $A_1=0.125$ and $A_1=0.825$, for $Ri_L^*=25$ and $\varepsilon=0.85$, is only 2.8 percent, while that for $Ri_L^*=0.1$ is 14.4 percent. The θ_{max} decreases with increasing Re_L (or decreasing Ri_L^*), for a given A_1 . The figure shows that the best position for the heat source is $A_1=0$ (leading edge of the plate), while the least advisable position is $A_1=0.875$ (heat source ending on the trailing edge) for all values of Ri_L^* and ε . For example, for $Ri_L^*=0.1$ and

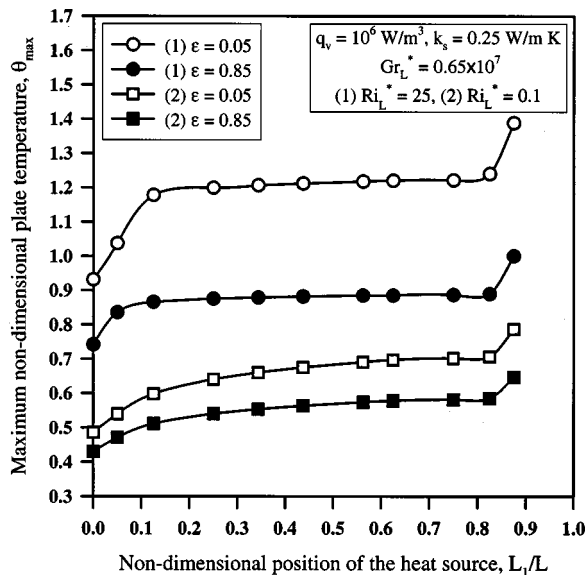


Fig. 3 Maximum non-dimensional plate temperature with modified Richardson number and surface emissivity for various positions of the discrete heat source

$\varepsilon=0.85$, θ_{max} increases by as much as 51 percent as the heat source shifts from $A_1=0$ to $A_1=0.875$. Further, θ_{max} decreases with increasing ε for a given Ri_L^* . The effect of ε on θ_{max} is more pronounced in the free convection dominant regime than in the forced convection dominant regime, which is consistent with the findings of earlier studies on natural convection-surface radiation interaction in enclosures, e.g., Dehghan and Behnia [8].

Heat Transfer Characteristics

Figure 4 shows the contributions of convection and radiation, plotted against A_1 , for two values of Ri_L^* (25 and 0.1) and two values of ε (0.05 and 0.85), for the case with $q_v=10^6$ W/m³, $k_s=0.25$ W/m K. A notable feature is the behavior of the two curves drawn for $Ri_L^*=25$ and $\varepsilon=0.85$. It is seen that the contribution of convection decreases from 45 percent for $A_1=0$ to about 41.5 percent for $A_1=0.05$, but from then increases monotonically to a maximum of 65 percent for $A_1=0.875$. An exact "mirror image" variation is noticed for radiation. The two curves cross each other for $A_1=0.625$, implying equal contributions from the two modes. The contribution from radiation decreases continuously from the free convection limit ($Ri_L^*=25$) to the forced convection limit ($Ri_L^*=0.1$), for a given ε . For $Ri_L^*=25$ and $\varepsilon=0.85$, radiation is significant with maximum and minimum contributions of 58.5 percent and 36 percent, respectively, depending on the position of the heat source. Even for $Ri_L^*=0.1$ (and the same $\varepsilon=0.85$), radiation plays a key role with maximum and minimum contributions of 30.5 percent and 18.3 percent, respectively. Convection is the dominant mode of heat transfer for a good reflecting surface ($\varepsilon=0.05$). For the case of the heat source located at the center of the plate, for $Ri_L^*=0.1$ and $\varepsilon=0.05$, convection takes away as much as 97.6 percent of the heat, while the radiation contribution is only 2.4 percent. The contribution from radiation increases with ε , with a proportionate decrease in convection. For $Ri_L^*=25$ and $A_1=0$, radiation contributes about 6.1 percent for $\varepsilon=0.05$, while, for $\varepsilon=0.85$, there is more than nine fold increase to 55.1 percent.

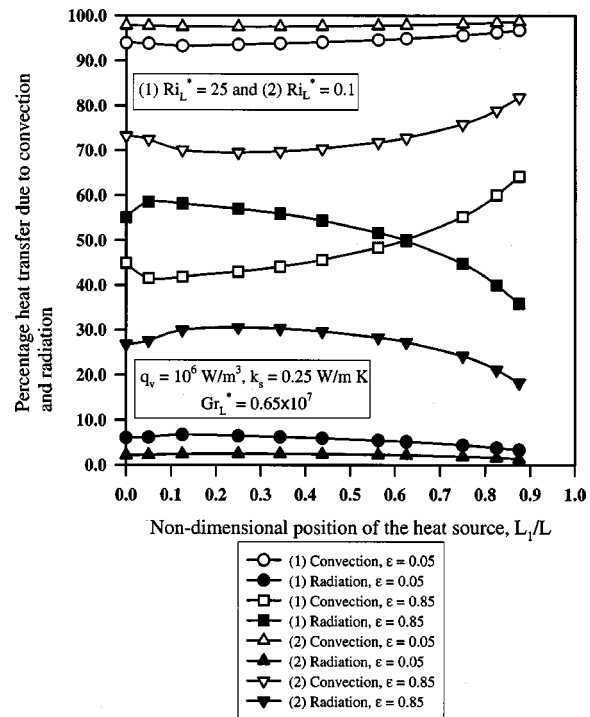


Fig. 4 Percentage heat transfer due to convection and radiation with modified Richardson number and surface emissivity for various positions of the discrete heat source

Effect of Thermal Conductivity of the Plate

The thermal conductivity of the plate (k_s) is present in ΔT_{ref} , which, in turn, is present in Gr_L^* , Ri_L^* , and N_{RF} . Thus, k_s alone cannot be varied by setting all the three dimensionless variables, Gr_L^* , Ri_L^* , and N_{RF} , for a given q_v . However, keeping all the primary variables fixed and letting k_s alone vary (0.25, 0.5, and 1 W/m K), the dimensional maximum plate temperature (T_{max}) is calculated for a representative case with $q_v = 10^6$ W/m³, $u_\infty = 0.25$ m/s, $T_\infty = 25^\circ\text{C}$ (298 K), $\varepsilon = 0.45$, and $A_1 = 0.4375$. It has been noticed that T_{max} decreases by 18.9 percent as k_s increases from 0.25 to 1 W/m K, in this particular case. This demonstrates the importance of k_s in the present problem.

Correlations

A correlation, having a correlation coefficient of 0.99 and an error band of ± 5.8 percent, is evolved for θ_{max} , based on a large set of 514 data, as

$$\theta_{max} = 51.5181(1 - A_1)^{-0.14} \gamma^{-0.69} \left(\frac{N_{RF}}{1 + N_{RF}} \right)^{0.07} (1 + \varepsilon)^{-0.51} \times (1 + Ri_L^*)^{-0.139} Re_L^{-0.323}. \quad (5)$$

A correlation, having a correlation coefficient of 0.986 and an error band of ± 6.1 percent, is developed for θ_{av} as

$$\theta_{av} = 54.4132(1 - A_1)^{0.25} \gamma^{-0.89} \left(\frac{N_{RF}}{1 + N_{RF}} \right)^{-1.91} (1 + \varepsilon)^{-0.78} \times (1 + Ri_L^*)^{-0.179} Re_L^{-0.415}. \quad (6)$$

Two separate correlations are generated for \bar{C}_f for two different ranges of Ri_L^* , viz., $0.1 \leq Ri_L^* \leq 1$ and $1 < Ri_L^* \leq 25$. The \bar{C}_f for ‘‘low’’ modified Richardson number range ($0.1 \leq Ri_L^* \leq 1$), based on 245 data, having a correlation coefficient of 0.992 and an error band of ± 4.6 percent, correlated as

$$\bar{C}_f = 6.8719(1 - A_1)^{0.03} \gamma^{-0.08} \left(\frac{N_{RF}}{1 + N_{RF}} \right)^{-0.8} (1 + \varepsilon)^{-0.05} \times (1 + Ri_L^*)^{0.239} Re_L^{-0.672}. \quad (7)$$

The correlation for \bar{C}_f for ‘‘high’’ modified Richardson number range ($1 < Ri_L^* \leq 25$), based on 196 data, having a correlation coefficient of 0.99 and an error band of ± 5.4 percent, came out as

$$\bar{C}_f = 38.155(1 - A_1)^{0.39} \gamma^{-0.47} \left(\frac{N_{RF}}{1 + N_{RF}} \right)^{-0.25} (1 + \varepsilon)^{-0.54} \times (1 + Ri_L^*)^{0.493} Re_L^{-0.792}. \quad (8)$$

Calculation of Forced Convection Friction Coefficient Component

Equations (7) and (8) give the sum of the free and forced convection components of the mean friction coefficient. Of these, only the forced convection component requires the power input (pumping power), through a fan or blower, for maintaining the flow. The free convection related flow, results from buoyancy, and hence does not need any power input. Now, the point of interest is to obtain \bar{C}_f (forced) from the correlations for the total \bar{C}_f evolved above. For this, the present problem is solved for two typical cases, for as many as eight values of Ri_L^* covering the entire range $0.1 \leq Ri_L^* \leq 25$ in each case. The problem is solved first as such and later with $\beta = 0$ (no free convection), which, respectively, gave the values of \bar{C}_f (total) and \bar{C}_f (forced). From these, the values of \bar{C}_f (free) are obtained. The percentages of the two components are plotted against Ri_L^* , for both the cases, as shown in Fig. 5, which reveals that $Ri_L^* = 0.1$ and 25 could be taken as the forced and free convection limits, respectively, with pure mixed

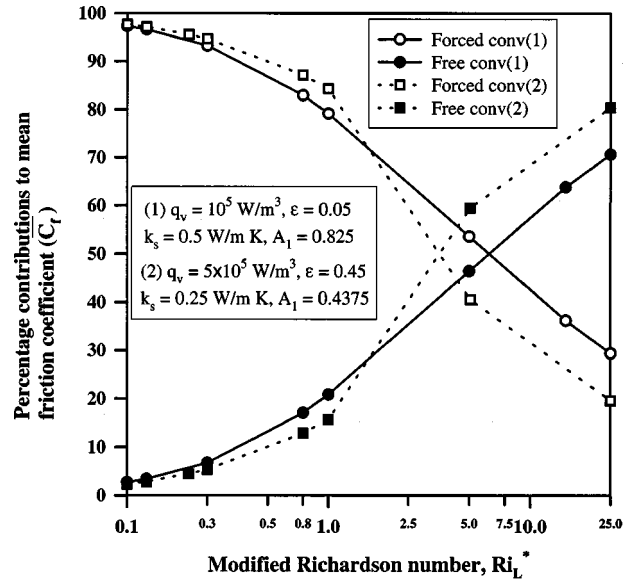


Fig. 5 Percentage contributions to mean friction coefficient from forced and free convection components

convection falling in the range $1 \leq Ri_L^* \leq 10$. In view of this, it has been decided to check whether $0.1 \leq Ri_L^* \leq 1$ would serve as the forced convection asymptote. To do this, 26 randomly chosen data, covering the entire range ($0.1 \leq Ri_L^* \leq 25$), are generated with $\beta = 0$ (no free convection). The values of \bar{C}_f (forced), thus obtained, are compared with the values of \bar{C}_f obtained by letting $Ri_L^* = 0$ in Eq. (7), and a very good agreement, with an error band of ± 6.3 percent, is noticed. Therefore, \bar{C}_f (forced) for the whole range of Ri_L^* ($0.1 \leq Ri_L^* \leq 25$) may be obtained from Eq. (7), by simply setting $Ri_L^* = 0$, as

$$\bar{C}_f(\text{forced}) = 6.8719(1 - A_1)^{0.03} \gamma^{-0.08} \left(\frac{N_{RF}}{1 + N_{RF}} \right)^{-0.8} \times (1 + \varepsilon)^{-0.05} Re_L^{-0.672}. \quad (9)$$

From the \bar{C}_f (forced), the wall shear, the drag force and thus the fan power input may be calculated.

Conclusions

The best position for the heat source is the leading edge of the plate and the least preferable position is the trailing edge, as the latter position increases θ_{max} by 35–50 percent for the entire range of Ri_L^* . The θ_{max} , for the given values of q_v and k_s , decreases with ε for any given Re_L or Ri_L^* . However, the degree of decrease of θ_{max} with ε decreases, as one moves from the free convection limit ($Ri_L^* = 25$) to the forced convection limit ($Ri_L^* = 0.1$). Radiation is found to play a significant role in the present problem. For example, for $\varepsilon = 0.85$, for $Ri_L^* = 25$, radiation is found to contribute 35–60 percent of heat transfer, depending on the position of the heat source. While, for the same $\varepsilon = 0.85$, for $Ri_L^* = 1$ and 0.1, the radiation contributions have been found to be 28–45 percent and 18–30 percent, respectively. For a given Ri_L^* (say for $Ri_L^* \sim 1$), convection is dominant, taking away as much as 90–95 percent of the heat generated, in the case of a good reflecting surface ($\varepsilon = 0.05$), with radiation being insignificant. However, the radiation contribution increases with ε for the same Ri_L^* and it may be as high as 45–50 percent, in the case of a good emitting surface ($\varepsilon = 0.85$). Correlations are developed for θ_{max} and θ_{av} along with two separate correlations for \bar{C}_f for two different

ranges of Ri_L^* . A method for evaluating the forced convection friction coefficient component is provided, which helps in the estimation of the fan or blower power input required for maintaining the flow.

Nomenclature

A_1 = non-dimensional position of the heat source, (L_1/L)
 A_{r_1}, A_{r_2} = aspect ratios pertaining to problem geometry, (L/t) , (L/L_h) , respectively
 \bar{C}_f = mean friction coefficient, $(2/Re_L) \int_0^1 (\partial U / \partial Y)_{Y=0} dX$
 Gr_L^* = modified Grashof number based on L , $g\beta\Delta T_{ref} L^3 / \nu^2$
 g = acceleration due to gravity, 9.81 m/s^2
 H, W = height and width of the computational domain, respectively, m
 k = thermal conductivity, W/m K
 L, t = length and thickness of the vertical plate, respectively, m
 L_h, L_1 = height and starting length of the discrete heat source, respectively, m
 M, N = number of grid points in horizontal and vertical directions, respectively
 N_{RF} = radiation-flow interaction parameter, $\sigma T_\infty^4 \Delta T_{ref} / (k_f / L)$
 P = pressure at any location, Pa
 Pe_L = Peclet number based on L , $u_\infty L / \alpha$
 q_v = volumetric heat generation rate in the discrete heat source, W/m^3
 Q = heat transfer rate, W
 Re_L = Reynolds number based on L , $u_\infty L / \nu$
 Ri_L^* = modified Richardson number based on L , (Gr_L^* / Re_L^2) or $g\beta\Delta T_{ref} L / u_\infty^2$
 T = temperature at any location, K
 u_∞ = free-stream velocity of the fluid, m/s
 u = vertical velocity, m/s
 U = non-dimensional vertical velocity, u/u_∞ or $\partial\psi/\partial Y$
 v = horizontal velocity, m/s
 V = non-dimensional horizontal velocity, v/u_∞ or $-\partial\psi/\partial X$
 x, y = vertical and horizontal distances, respectively, m
 X, Y = non-dimensional vertical and horizontal distances, $x/L, y/L$, respectively
 α = thermal diffusivity of the fluid, m^2/s
 β = isobaric cubic expansivity of the fluid, $-(1/\rho) \times (\partial\rho/\partial T)_P, K^{-1}$

ΔT_{ref} = modified reference temperature difference, $q_v L_h t / k_s, K$
 Δx = height of the plate element, m
 ΔX = non-dimensional height of the plate element, $\Delta x/L$
 ε = emissivity of the plate surface
 δ = convergence criterion in percentage form, $|(\zeta_{new} - \zeta_{old}) / \zeta_{new}| \times 100$ percent
 γ = non-dimensional thermal conductivity parameter, $k_f L / k_s t$
 ν = kinematic viscosity of the fluid, m^2/s
 ω' = vorticity, s^{-1}
 ω = non-dimensional vorticity, $\omega' L / u_\infty$
 ρ = density of the fluid, kg/m^3
 σ = Stefan-Boltzmann constant, $5.6697 \times 10^{-8} \text{ W/m}^2 \text{ K}^4$
 ψ' = stream function, m^2/s
 ψ = non-dimensional stream function, $\psi' / u_\infty L$
 θ = non-dimensional temperature, $(T - T_\infty) / \Delta T_{ref}$
 ζ = dependent variable (ψ, ω , or θ) over which convergence test is applied

Subscripts

av, max, p = average, maximum and local values of the plate temperature, respectively
 f, s = fluid and plate material, respectively
 new, old = values of the dependent variable from present and previous iterations, respectively

References

- [1] Zinnes, A. E., 1970, "The Coupling of Conduction with Laminar Natural Convection From a Vertical Flat Plate With Arbitrary Surface Heating," ASME Journal of Heat Transfer, **92**, pp. 528–534.
- [2] Gorski, M. A., and Plumb, O. A., 1992, "Conjugate Heat Transfer from an Isolated Heat Source in a Plane Wall," Proc. Winter Annual Meeting of The American Society of Mechanical Engineers, ASME HTD-210, pp. 99–105.
- [3] Hossain, M. A., and Takhar, H. S., 1996, "Radiation Effect on Mixed Convection Along a Vertical Plate with Uniform Surface Temperature," Heat and Mass Transfer/Warme-und Stoffubertragung, **31**, pp. 243–248.
- [4] Cole, K. D., 1997, "Conjugate Heat Transfer from a Small Heated Strip," Int. J. Heat Mass Transf., **40**, pp. 2709–2719.
- [5] Bejan, A., 1984, *Convection Heat Transfer*, Wiley, New York, pp. 112–114.
- [6] Gururaja Rao, C., Balaji, C., and Venkateshan, S. P., 2000, "Numerical Study of Laminar Mixed Convection from a Vertical Plate," I. J. Trans. Phenomena, **2**, pp. 143–157.
- [7] Gosman, A. D., Pun, W. M., Runchal, A. K., Spalding, D. B., and Wolfshtein, M., 1969, *Heat and Mass Transfer in Recirculating Flows*, Academic Press, London, pp. 89–137.
- [8] Dehghan, A. A., and Behnia, M., 1996, "Combined Natural Convection—Conduction and Radiation Heat Transfer in a Discretely Heated Open Cavity," ASME Journal of Heat Transfer, **118**, pp. 56–64.

Minoru Takahashi

e-mail: mtakahas@nr.titech.ac.jp
Research Laboratory for Nuclear Reactors,
Tokyo Institute of Technology,
2-12-1 O-okayama, Meguro-ku,
Tokyo 152-8550, Japan

Arun Kumar Nayak

e-mail: redths@apsara.barc.ernet.in
Reactor Engineering Division,
Bhabha Atomic Research Centre,
Trombay, Mumbai 400085, India

Shin-ichi Kitagawa

Hiroyuki Murakoso

Department of Nuclear Engineering,
Tokyo Institute of Technology,
2-12-1 O-okayama, Meguro-ku,
Tokyo 152-8550, Japan

Heat Transfer in Direct Contact Condensation of Steam to Subcooled Water Spray

The condensation heat transfer of saturated steam to a hollow-cone spray of subcooled water was investigated experimentally and analytically. The spray water temperature rose more steeply in flow direction than those in the previous studies, because of the use of smaller thermocouple which was capable of measuring the temperature in a thin water sheet and water droplets more accurately. The result of the condensation heat transfer coefficient suggested the breakup of the water sheet into droplets. A pure conduction model underpredicted the heat transfer in the sheet region significantly, which was better predicted by considering turbulence in the sheet. The heat transfer in the droplet region was well estimated by considering internal circulation and mixing inside the droplets. [DOI: 10.1115/1.1370510]

Keywords: Condensation, Cooling, Droplet, Heat Transfer, Sprays

1 Introduction

The study of direct contact condensation of steam on spray of water has been of great interest to researchers because of its numerous applications in nuclear industries, e.g., the pressure control in the pressurizers of the Pressurized Water Reactors (PWR), the emergency core cooling in the Boiling Water Reactors (BWR), the containment cooling during the loss of coolant accident (LOCA) of the Light Water Reactors (LWR), and the bleed condensers of the Indian Pressurized Heavy Water Reactors (PHWR). The other applications include direct contact condensers used in chemical industries, geothermal power plants, etc.

Figure 1 depicts the structure of a spray flow issuing from a pressure-swirl hollow-cone nozzle. The liquid moves through spiral like channels inside the nozzle, which discharges it tangentially into a vortex or swirl chamber. The liquid thus emerging from the nozzle forms a conical sheet at the nozzle outlet due to its tangential, radial and axial momentum forces. After some distance, the sheet breaks into ligaments and finally into droplets due to the destabilizing forces. Therefore, the spray flow can be broadly classified into two distinct regions, viz., a continuous liquid sheet region followed by a droplet region.

Many experimental and analytical studies have been carried out in the past to investigate the hydrodynamics and the heat transfer mechanism in the above two regions. Studies on vapor condensing on single moving drops have been carried out by Brown [1], Letic and Ford [2], Sundararayan and Ayyaswamy [3,4], Chung and Chang [5] and Celata et al. [6] and on liquid sheet formed out of a spray by Lee and Tankin [7]. Hasson et al. [8] studied the heat transfer behavior during direct contact condensation of steam on a water sheet analytically. Weinberg [9] studied experimentally and analytically the heat transfer behavior considering both sheet and droplet regions. Mayinger and Chavez [10] carried out experiments to reveal the heat transfer behavior in the sheet and droplet regions by using pulsed laser holography.

In spite of all these works, there is a greater need for further research in this area in order to generate more reliable experimental data which are scanty and to understand the heat transfer be-

havior at the interface of steam and spray. That is because it has been technically difficult to measure the temperature profile across the sheet whose thickness may vary from few hundred micrometer to few micrometer depending on the structure of spray cone. The previous researchers have not mentioned about the sizes of thermocouples used for measuring the spray water temperature. If they have employed relatively large thermocouples to measure the temperature of the sheet, their measurements may provide much different spray temperatures from each other. For example, they are a spatially averaged temperature in a certain volume having the water sheet and a steam flow, and not the average temperature across the sheet which has higher temperature in thermal boundary layers adjacent to the sheet surfaces but a local low bulk temperature at one point inside the sheet. The measurement of

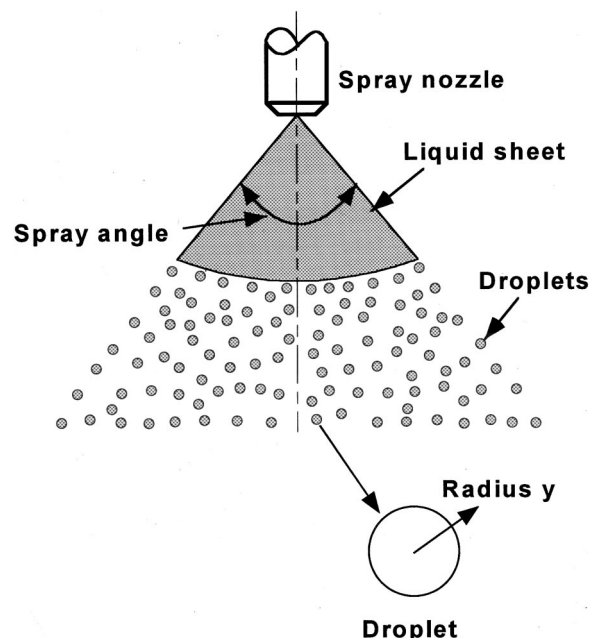


Fig. 1 Hollow-cone spray

Contributed by the Heat Transfer Division for publication in the JOURNAL OF HEAT TRANSFER. Manuscript received by the Heat Transfer Division July 10, 2000; revision received January 30, 2001. Associate Editor: H. H. Bau.

temperature profiles across the sheet thickness require the use of thermocouples which are smaller than the sheet thickness and have short response time, and a fast data acquisition system. The temperature profile across the sheet thickness can be measured by traversing the thermocouples normal to the spray flow path, which can be averaged to obtain the local average temperature.

Further, there are many analytical models for the heat transfer behavior in the sheet and droplet regions with different assumptions in literature. However, the models have not been adequately tested especially for steam condensing on a hollow-cone spray of water. In order to clarify the heat transfer mechanism in the sheet and droplet regions, it is required to predict the heat transfer behavior using these analytical models and compare the result with the experimental data.

For this purpose, experiments were carried out to study the heat transfer behavior of steam condensing on a hollow-cone spray. The temperature profiles across the sheet and droplet regions were measured using very small thermocouples and a fast data acquisition system. The effect of thermocouple response time on the spray temperature was studied by varying the size of thermocouples in the experiment. The temperature rise in the flow direction in the sheet and droplet regions were predicted using analytical models. The heat transfer mechanism in the sheet and droplet regions are discussed from the comparison of the test data with the predictions.

2 Experiment

2.1 Experimental Apparatus and Procedure. Figure 2 shows a schematic diagram of the experimental apparatus which consists of a water circulation loop and a steam supply system. Water was circulated by the pump from the tank below the test vessel through the subcooler, the orifice, the flow control valve to the test vessel. Saturated steam was generated in the boiler and supplied into the test vessel maintained at near atmospheric pressure. In order to keep the water level in the test vessel and boilers constant, the amount of the water accumulated in the vessel due to condensation was returned to the boiler continuously using a pump, and thermally steady condition was maintained throughout the operation. The inlet temperatures of steam and subcooled wa-

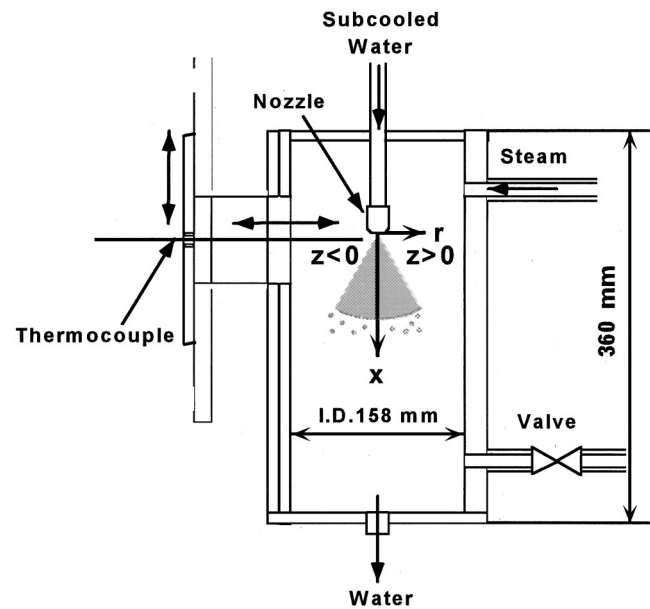


Fig. 3 Test section

ter to the test vessel, and the temperature in the test vessel were measured with sheathed thermocouples 1 mm in diameter. The vessel pressure was measured with a semi-conductor type pressure transducer. In order to prevent the steam from condensing inside the transducer, a tube introduced into the transducer was filled with silicon oil and electrically heated to the saturation temperature of steam, while the tube near the transducer was water-cooled to keep the sensor at the room temperature. During the measurement, the outlet valve was closed, and the pressure in the test vessel was controlled to be the one corresponding to the saturation temperature in the boiler.

A spray condensation was realized in a cylindrical test vessel made of stainless steel shown in Fig. 3. The hollow-cone spray

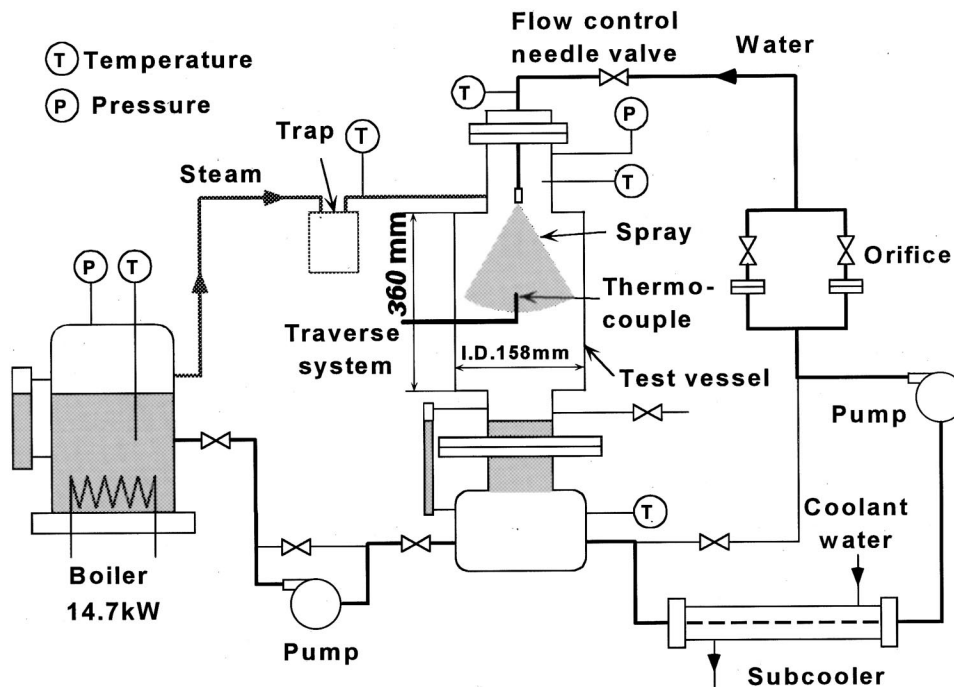


Fig. 2 Experimental apparatus

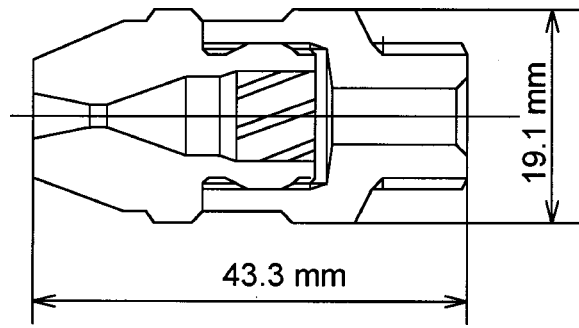


Fig. 4 Hollow-cone spray nozzle (B1/4GG-SS3030HC of Spraying Systems Japan Co.)

nozzle: Spraying Systems Japan Co., B1/4GG-SS3030HC, was inserted from the top into the vessel, and a subcooled water was discharged from the nozzle into the vessel, which resulted into a hollow-cone spray. The inside diameter of the nozzle is 3.6 mm. The configuration of the nozzle is shown in Fig. 4, and the dependences of the flow rate and the spray angle on the pressure drop are shown in Fig. 5. It is found that the spray angle is nearly constant with the flow rate except for the conditions of low flow rate. Thus, the present experiment was not performed with the parameter of the spray angle.

The outside of the entrance pipe from the top of the vessel to the nozzle was thermally insulated with a silicon rubber sheet 3 mm in thickness. The temperature rises from the measuring position of the inlet water temperatures to the nozzle outlet were estimated to be $0.3^{\circ}\text{C} - 0.5^{\circ}\text{C}$, which was 1.3 percent of $T_{\text{sat}} - T_i$ and negligibly small compared with the temperature rise in the spray. Thus, it is valid to consider the measured inlet temperature as the nozzle outlet temperature.

Non-condensable gas was removed from the vessel by blowing the steam through the steam outlet valve for about 30 minutes before each operation and also for about 15 minutes before every measurement. The experimental conditions are listed in Table 1, where the superficial nozzle outlet velocity indicates the cross-sectional average velocity estimated from the cross-sectional area of the nozzle and the volumetric flow rate without considering an air core that exists inside the present centrifugal nozzle.

To measure the temperature of the spray with the steam condensation, two types of thermocouples (K-type) with bead diameters of 0.025 mm and 0.05 mm shown in Fig. 6 were used in order to investigate the influence of the thermocouple size on the spray temperature measurement. Chromel and alumel wires with the diameters of 0.025 mm and 0.05 mm were spot-welded to make the hot junctions. From the microscope observation, it was

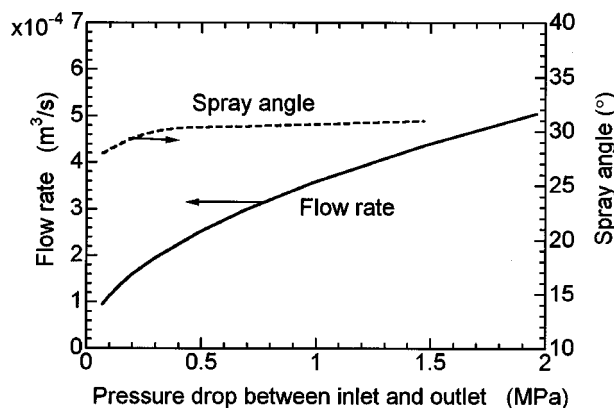


Fig. 5 Performance of hollow-cone spray nozzle (B1/4GG-SS3030HC of Spraying Systems Japan Co.)

Table 1 Experimental conditions

Nozzle inside diameter	3.6 mm
Water mass flow rate	0.057 – 0.081 kg/s
Superficial nozzle outlet velocity	5.7 – 8.2 m/s
Nozzle outlet temperature	65.0 – 76.5 °C
Steam temperature	100.0 – 103.5 °C
Steam pressure	0.10 – 0.12 MPa

confirmed that the sizes of the beads were nearly the same of the wire diameters. The hot junction was directed toward the upstream of the spray in order not to disturb the water sheet. The thin thermocouple wires were connected to the thick wires with a lead-tin alloy solder. The surface of the wires except for the hot junction were covered with the silicon glue for electrical insulation and also to support the thin thermocouple wires. In order to avoid splashing of the water at the surface of the thermocouple assembly, which may affect the measured temperature signal, the glue cover was made as small as possible. The thermocouple was inserted through the side wall, and traversed both radially and axially to measure the temperature distributions in the region of the spray sheet and droplets.

The response time of the 0.025 mm thermocouple was estimated to be approximately 0.03 ms if the unsteady heat conduction is considered in a cylindrical thermocouple wire. This was estimated from the convective heat transfer coefficient of steam and water on the surface of the thermocouple wire and found to be about 0.05–0.15 ms for water flowing with velocity of 1–14 m/s, respectively, and about 9–28 ms for steam flowing with velocity of 1–14 m/s, respectively. The data of the fluctuating temperature in the saturated steam and subcooled water sheet or droplets were stored using a fast data acquisition system with the data sampling frequency of 50 kHz which was high enough compared with the temperature fluctuation frequency less than 1 kHz which could be estimated from the characteristic period of the data shown in Fig. 7.

As shown in Fig. 7, the fluctuating temperature in the saturated steam and subcooled water sheet or droplets was successfully detected with fast response. It is found that the practical response time is much shorter than that estimated from the heat transfer in a steam flow. If it is assumed that the axial velocity is equal to the superficial velocity listed in Table 1 and does not change in the flow direction, the sheet thickness is estimated to be 108 μm –540 μm depending on the radius of the spray sheet r at the water mass flow rate of 0.081 kg/s as shown in Table 2. Practically these estimated values of the thickness may be valid in the order of the magnitude. Inside the sheet with the thickness, there are two thin thermal boundary layers adjacent to the both sheet surfaces in which temperature is higher than in the bulk of the sheet. It may

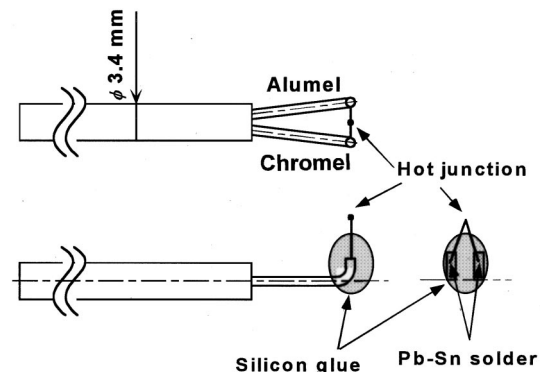


Fig. 6 Thermocouple used for spray temperature measurement

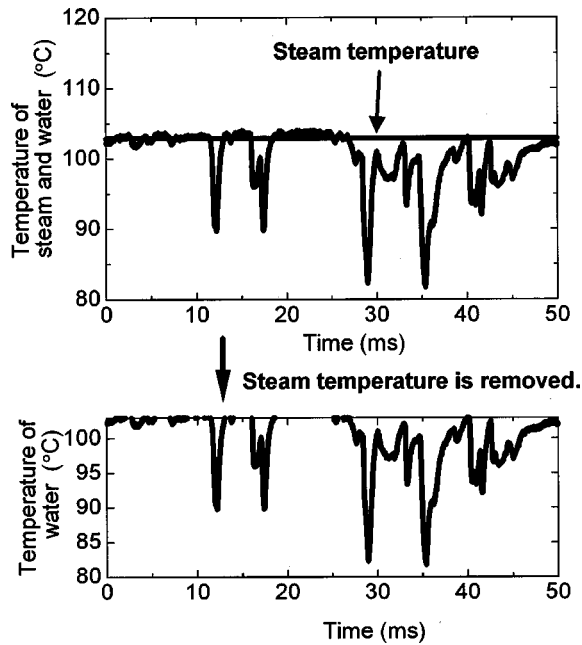


Fig. 7 Temperature fluctuation

Table 2 Estimated sheet thickness at the water mass flow rate of 0.081 kg/s

r (mm)	3	5	10	15
Sheet thickness (μm)	540	324	162	108

be difficult to detect the higher temperature in the thin thermal boundary layers using thermocouples larger than the thickness of the sheet. Since the mixing of the hot and cold water inside the sheet cannot be expected when the sheet contacts the thermocouples, only the lower temperature inside the bulk of the sheet may be detected with the large thermocouple. With the small thermocouple with short response time the size of which is comparable with the thickness of the thermal boundary layers, the higher temperature in the boundary layers can be detected.

At the interface of steam and sheet of the spray, the thermocouple output signal sometimes contain the steam temperature due to the instability of the sheet and hence the thermocouple touches the steam. Similarly in the droplet region, since the droplet flow is discontinuous and dispersed at any axial and radial location, the thermocouple output contains the mixture of steam and droplet temperature at any position. Hence, to estimate the spray temperature at any position, the steam temperature signal is removed from the thermocouple output signal so that the measured temperature is only the spray temperature as shown in Fig. 7. Then, the water temperature was time-averaged to obtain mean local water temperature in the sheet and droplets of the spray.

The errors of the measured radial distance was within ± 0.05 mm when the thermocouple was traversed horizontally. The measured temperature signal had some electrical noise, but it was reduced to be less than 1 K in the noise peak-to-peak values. Thus, the error of the measured temperature was within ± 0.5 K. The error of the measured T_i was also within ± 0.5 K.

2.2 Experimental Results and Discussion. The temperature profiles in the spray sheet and droplets for different spray inlet temperatures are shown in Fig. 8, where r and x are the radial and axial coordinates respectively. It is found that the temperature profiles are steep near the nozzle outlet. However, in the downstream region, the temperature profiles are broader and higher.

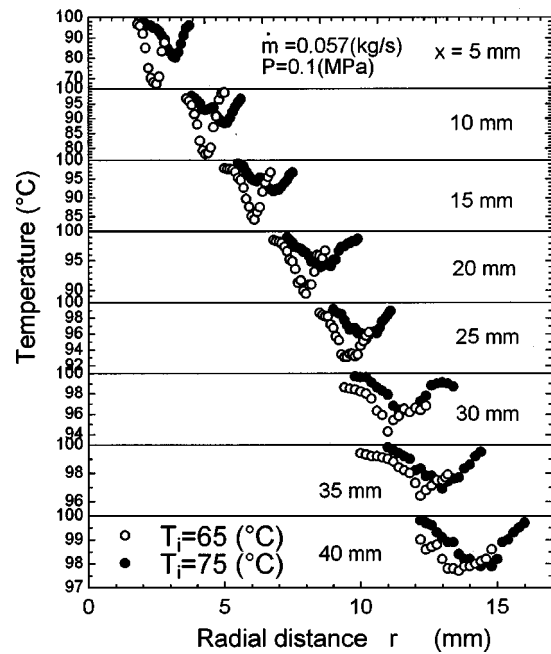


Fig. 8 Radial temperature profiles at various axial distance from the nozzle outlet

This is because, the sheet is very stable near the nozzle outlet. However, as the spray moves downstream, it becomes unstable due to the dynamic shear between the water sheet and the ambient steam and the sheet vibrates at any position. After some distance from the nozzle outlet, the sheet breaks into ligaments and finally drops. In the sheet region, even though the thickness of sheet reduces with distance from nozzle, the sheet vibrates away from nozzle outlet due to instability which makes as if a thicker sheet. The phenomena is a thinner sheet having a wider radial movement away from the nozzle. So the thermocouple measures a wider temperature profile at any downstream position. In the droplet region, various sizes of droplets are formed from the breakup of sheet. All the drops do not move in the same direction. In fact the smaller droplets move towards the center of spray as they move downstream. So at any axial position, the thermocouple finds the droplets over a wider region.

It is also found that the temperature profiles for $T_i = 65^\circ\text{C}$ are slightly narrower than that of $T_i = 75^\circ\text{C}$ at any vertical positions, that is, the sheet is thinner and droplet region is narrower for higher nozzle outlet water subcooling. This may be possibly because the higher subcooling increases the heat flux, and then the steam inflows to the sheet and droplets from both sides, and as a result reduces the radial expanding motions or instability of the sheet and droplets flow. Furthermore, the spray angle is smaller for the higher subcooling condition. This is possibly because of the lower pressure inside the hollow cone due to the higher vapor condensation rate at the higher subcooling condition.

The average water temperature \bar{T} at each elevation was calculated by integrating the radial temperature profile as

$$\bar{T} = \int_{r_1}^{r_2} 2T(r) r dr / (r_2^2 - r_1^2). \quad (1)$$

The local average heat transfer coefficient was estimated from the local average heat flux between two measuring positions and the temperature rise across them. The local average heat flux \bar{q} between two positions was calculated from the axial enthalpy rise as

$$\bar{q} = \dot{m} C_p \frac{1}{4\pi r} \frac{\Delta T}{\Delta x / \cos \phi}, \quad (2)$$

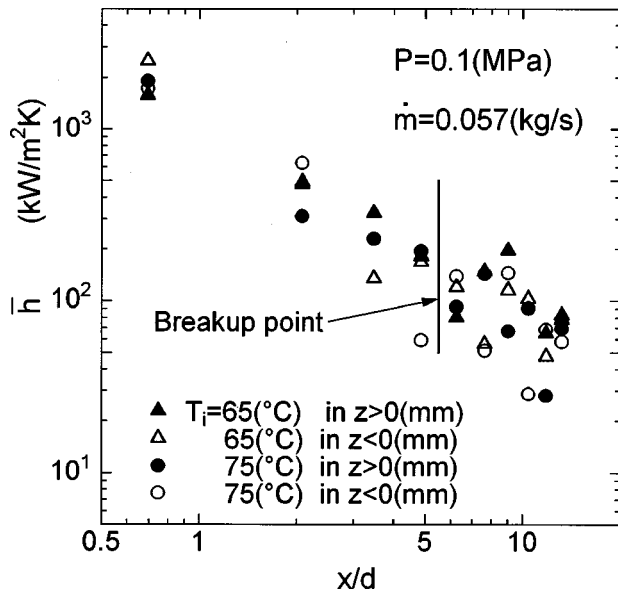


Fig. 9 Variation of heat transfer coefficient in the flow direction

where \dot{m} is the spray mass flow rate, ΔT is the spray temperature rise between two positions for which the vertical distance is Δx , ϕ is the spray angle and \bar{r} is the spray radius, and the over-bar means the arithmetical average of variables at two positions. The local average heat transfer coefficient \bar{h} is given by

$$\bar{q} = \bar{h}(T_{\text{sat}} - \bar{T}). \quad (3)$$

The magnitude of the error in the estimate of \bar{h} is smaller as the axial temperature rise ΔT is larger and the average spray temperature \bar{T} is lower because of the smaller errors in the estimate of ΔT and the heat flux \bar{q} in Eq. (2) and the smaller error in the estimate of the heat transfer coefficient \bar{h} in Eq. (3). The errors of \bar{h} are estimated to be ± 8 percent at $x/d=0.69$, ± 23 percent at $x/d=2.08$, ± 32 percent at $x/d=3.47$, ± 48 percent at $x/d=4.86$, ± 70 percent at $x/d=6.25$, and ± 105 percent at $x/d=7.64-10.4$.

The experimental results for the local average heat transfer coefficient \bar{h} is shown in Fig. 9. There appears two sheets and droplets regions in the temperature measurement plane, that is, the region of $z < 0$ and that of $z > 0$ as shown in Fig. 3. The heat transfer coefficients obtained in the regions of $z < 0$ and $z > 0$ are separately shown in Fig. 9, although appreciable differences are not observed between these results. It is found that the heat transfer coefficient is high near the nozzle outlet, and it decreases in the x -direction. The breakup point indicated in Fig. 9 is determined from the temperature fluctuation data, assuming that when measured temperature reaches the saturation temperature periodically, the sheet has broken up into droplets. It is assumed that if the thermocouple measures continuously temperature less than the steam temperature as it penetrates radially at any axial position along the spray, it is the sheet region of spray. On the other hand, if it measures sometimes low temperature and sometimes saturation temperature as it penetrates along the spray at any axial position, it measures the droplet temperature. This is because of the discontinuity of the flow of droplets at any axial and radial position unlike that of a liquid sheet which is continuous along its thickness. The breakup point obtained from the temperature profile measurement occurs at $5.5x/d$ which is almost the same as that predicted from the empirical correlation of Lee and Tankin [7].

It is obvious that the heat transfer coefficient in the sheet region is comparatively higher than that in the droplet region, as a result

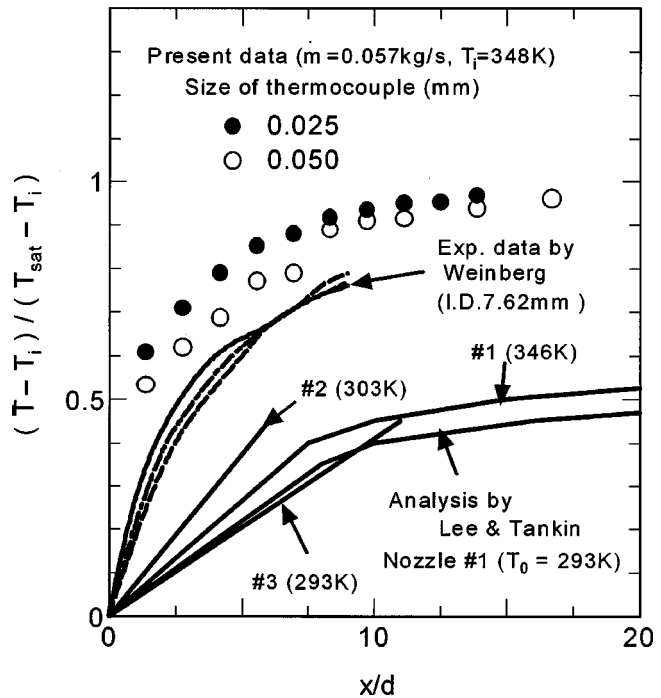


Fig. 10 Variation of condensation efficiency in the flow direction

significant heat transfer takes place in the sheet region as compared to that in the droplet region, even though the length of the sheet region is very small.

The axial rise in the water average temperature, or the condensation efficiency is shown in Fig. 10, where $T - T_i$ is the water temperature rise from the nozzle outlet to the measuring position, and $T_{\text{sat}} - T_i$ is the difference between the saturation temperature and the water temperature at the nozzle outlet. The axial distance from the nozzle x is normalized by the nozzle diameter, d . The error in the estimate of the condensation efficiency is within ± 0.04 due to the errors of \bar{T} and T_i mentioned above. The temperature measured with the thermocouple having the diameter of 0.05 mm is somewhat lower than that measured with the thermocouple having the diameter of 0.025 mm in the region where $x/d < 10$. This is because it is difficult to detect the higher temperature in the thin thermal boundary layers using thermocouples larger than the thickness of the sheet. While only the lower temperature inside the bulk of the sheet may be detected with the large thermocouple, the higher temperature in the thermal boundary layers can be detected using the small thermocouple with short response time the size of which is comparable with the thickness of the thermal boundary layers, and as a result the average temperature appears to be higher with the small thermocouples having shorter response time as shown from the comparison of the results with the thermocouples with the sizes of 0.025 mm and 0.05 mm in Fig. 10.

In addition, the present data are found to be higher than the data obtained by Weinberg [9] for a nozzle with the inner diameter of 7.62 mm. It means that with smaller thermocouples the response time is short enough compared with the time scale of temperature fluctuation. Hence, such small thermocouples are required to measure reliable spray water temperatures. However, the analytical results by Lee and Tankin [7], who assumed a laminar flow in the smooth spray sheet, are much lower than the present experimental result and Weinberg's data. This suggests that the condensation heat transfer may be influenced greatly by disturbed interfaces, a turbulent flow inside the water sheet and recirculating flows in droplets.

3 Analysis

3.1 Analytical Model

3.1.1 Summary. As mentioned before, the structure of the spray can be characterized by two distinct regions, viz., (a) continuous liquid sheet region and (b) droplet region. There are many analytical models in the literature for the heat transfer behavior in these regions. Depending on the assumptions made in these models, the heat transfer mechanism in the sheet and droplet regions can be broadly classified into two modes, i.e., (i) heat transfer taking place by purely conduction with negligible resistance of condensate film, and (ii) consideration of a turbulent thermal conductivity in the sheet region or internal circulation and mixing in the droplet region. The models considered in the present analysis are discussed below.

3.1.2 Modeling of Heat Transfer in the Sheet Region. If conduction is assumed to be the only mode of heat transfer from the surface of the sheet to the center without considering the growth of condensate film on the surface, the model due to Hasson et al. [8] developed for a fan spray sheet can be directly applied. A numerical solution similar to that carried out by Lee and Tankin [7] for the sheet region is possible, but the Hasson et al. model [8] is easier to apply provided the sheet thickness is known at any axial distance from the nozzle. The present analysis considers this model and the sheet thickness is estimated from the equation of continuity

$$s = \frac{m}{2\pi r \rho V}, \quad (4)$$

where V is the velocity in the flow direction, m is the mass flow rate of spray, and r is the radius of spray cone at a distance x from the nozzle outlet.

The mean temperature rise in the sheet can be expressed as

$$\bar{\theta} = \frac{8}{\pi^2} \exp(-4\pi^2/3Gz), \quad (5)$$

for small Graetz numbers Gz ; and

$$\bar{\theta} = 1 - \frac{8}{\sqrt{3\pi Gz}}, \quad (6)$$

for large Graetz numbers.

However, the spray discharged from the nozzle possesses certain amount of turbulence which damps along the flow path of the spray. To the authors' knowledge, no theoretical model has ever considered this phenomenon in the sheet region of the spray. One complex problem with spray condensation phenomena is modeling the turbulence generated inside the swirl chamber of the nozzle, and how it propagates with the spray after it issues from the nozzle while condensation occurring on it. However, some analytical studies have considered this behavior for circular jets (Kutateladze [11]; Celata et al. [12]; Celata et al. [13]) issuing from nozzles. Hence, an attempt has been made here to consider the turbulent thermal conductivity model of Celata et al. [13] on the heat transfer behavior in the sheet region. This model is given by

$$K_{\text{tot}} = K(1 + A(B + C)) \quad (7)$$

where

$$A = (H/d)(\text{Pe})^{(d/H)^{0.12}}, \quad (8)$$

$$C = 3.6 \times 10^{-4} (T_{\text{sat}} - T) / (T_{\text{sat}} - T_i), \quad (9)$$

$$B = 1.36 \times 10^{-3} (L_{tb}/x)^{1.8} (\alpha_L/d) \exp[-(L_{tb}/x)(H/d)^{0.3}], \quad (10)$$

$$\alpha_L = \sqrt{\gamma/g\Delta\rho} \quad (11)$$

$$L_{tb} = 1.875 \times 10^{-4} V d^2 / \nu + 0.11, \quad (12)$$

which takes into account (i) the effect of radial velocity profile development along the jet axis; (ii) the decrease of the turbulence caused by the lack of solid walls; (iii) the edge effects at the nozzle exit due to the surface tension and the viscosity; (iv) the effect of surface instability; (v) the thermal effect due to the settling of the radial temperature profile; (vi) the effect of the interface shear stress between the condensate and the liquid jet. The K_{tot} obtained by the model is substituted into Eqs. (5) or (6) to calculate $\bar{\theta}$. An empirical K_{tot} similar to the above cannot be easily found out in the spray condensation case. That is because the propagation of turbulence generated inside the swirl chamber of a hollow-cone nozzle is quite different from that of a jet issuing from a pipe. Besides, the sheet thickness and the turbulence intensity reduce with distance from the nozzle outlet, which is a completely different phenomena unlike that observed from the cylindrical jets. Further, the sheet is never stable and the droplet flow is highly dispersed. So it is impossible to estimate accurately the heat flux from the measured temperature in the surface of the sheet which is unstable and the highly dispersed flow of droplets. The present temperature measurements are only good enough for the average temperature of the sheet or the droplet region at any axial position.

3.1.3 Modeling of Heat Transfer in the Droplet Region. The heat transfer in the droplet regions depends on the size of the droplets. Since droplets of different sizes are formed due to the breakup of the liquid sheet, many analytical models consider a droplet size distribution parameter. However, it is required to determine the maximum droplet diameter and other distribution parameters from experiments. In the absence of that, it is possible to evaluate the heat transfer behavior by considering a mean diameter of the droplets. Weinberg [9] carried out experiments using various types of spray nozzles with water as fluid. The size of nozzle varied from a minimum of 0.07 in (1.78 mm) to a maximum of 3.75 in (95.25 mm) which covered the present nozzle size of 3.6 mm. Weinberg developed the correlation which is applicable for flow parameter F up to 500 and pressure up to 20 psi and given by

$$D = 0.0047 \times 10^{-6} (F^3/\Delta p)^{1/7}, \quad (13)$$

where $F = Q/\sqrt{\Delta p}$, Q is the flow rate in gph and Δp is the pressure drop across the nozzle in psi. Since in the present case, the maximum value of F was 33, and the pressure was atmospheric, which was in the range of the Weinberg's ones, Eq. (13) was used for the prediction of the droplet diameter.

If we assume the droplet to be a sphere and the mode of heat transfer is by conduction from the surface to the center, the applicable differential equation is (Ford and Lekic [14])

$$\frac{\partial \theta}{\partial t} = \alpha \left(\frac{\partial^2 \theta}{\partial y^2} + \frac{2}{y} \frac{\partial \theta}{\partial y} \right) \quad (14)$$

where $\theta = (T - T_i)/(T_{\text{sat}} - T_i)$ with the following boundary conditions: (i) droplet initially at a uniform temperature: $\theta(y,0) = 0$; (ii) droplet surface immediately reaches saturation temperature: $\theta(R,t) = 1$; (iii) symmetry: $(\partial \theta / \partial y)_{y=0} = 0$; and (iv) heat balance at the interface: $K(T_{\text{sat}} - T_i)(\partial \theta / \partial y)_{y=R} = \lambda \rho dR/dt$. The temperature distribution, considering (as an approximation necessary for the solution) that the heat flux at $y = R$ is the same for a sphere with constant radius, is given by

$$\theta(y,t) = 1 - \frac{2R}{\pi y} \sum_{n=1}^{\infty} \frac{(-1)^n}{n} \sin\left(n\pi \frac{y}{R}\right) \exp\left(-\alpha \frac{\pi^2 n^2 t}{R^2}\right). \quad (15)$$

The rate of droplet growth due to condensation can be expressed as

$$\frac{D}{D_i} = 1 + \varphi \left[1 - \exp\left(-\frac{4\pi^2\alpha t}{D_i^2}\right) \right]^{1/2};$$

$$\varphi = \left[1 + \frac{C_p(T_{\text{sat}} - T_i)}{\lambda} \right]^{1/3} - 1. \quad (16)$$

The motion of the droplet in the vapor environment can be expressed as (Weinberg [9])

$$\frac{\pi}{6} D^3 \rho \frac{dV}{dt} = \frac{\pi}{6} D^3 (\rho - \rho_g) g - \frac{1}{8} C_D \rho_g \pi D^2 V^2, \quad (17)$$

or

$$\frac{dV}{dt} = g \left(1 - \frac{\rho_g}{\rho} \right) - \frac{3}{4} C_D \frac{\rho_g}{\rho} \frac{V^2}{D}. \quad (18)$$

The diameter and velocity of the droplet at any time can be estimated from Eqs. (16) and (18). The average non-dimensional temperature of the droplet at any time can be written as

$$\theta_m = 1 - \frac{6}{\pi^2} \sum_{n=1}^{\infty} \frac{1}{n^2} \exp\left(-n^2 \frac{4\pi^2\alpha t}{D_i^2}\right). \quad (19)$$

Many researchers have considered the effects of both internal circulation and mixing inside the droplet (Ohba et al. [15]; Rose and Kinter [16]; Skelland and Wellek [17]). Adding both internal circulation and mixing inside the droplet to the pure conduction hypothesis, the mean temperature the mean temperature of the droplet can be expressed as (Celata [18])

$$\theta_m = 1 - \frac{6}{\pi^2} \sum_{n=1}^{\infty} \frac{1}{n^2} \exp\left(-n^2 C \frac{4\pi^2\alpha t}{D_i^2}\right), \quad (20)$$

where C is a factor which takes into account the effects of turbulence inside the droplets.

3.2 Analytical Results and Discussion. Figure 11 shows a comparison of the predictions with the experimental data for spray velocity of 0.057 kg/s with its inlet temperature at 75°C. The region I and region II shown in the figure are the estimated sheet region and droplet regions respectively. The breakup length was estimated using the empirical correlation of Lee and Tankin [7] which was obtained from the photographs of a spray, since the present breakup length which agreed well with the predicted from the above correlation was only demarcated from the measured temperature profile of the spray with just an approximate method.

The diameter of the droplet is estimated to be about 0.295 mm for the condition by using Eq. (13). The droplet Reynolds number $Re \equiv VD/v$ is estimated to be 107 if the velocity of the droplet V is approximately equal to the maximum superficial nozzle velocity of 8.2 m/s, and the steam kinematic viscosity ν is 2.26×10^{-7} m²/s. This value is much lower than the oscillation criteria of 200. Thus, the effect of the oscillations of the droplets on heat transfer has been neglected.

It can be observed that when pure conduction is assumed in both the sheet and droplet regions, the mean temperature of the spray is very much under-predicted. However, if the turbulence is considered, the heat transfer increases significantly especially in the sheet region. Even though, the predictions are lower than the experimental data, still it clarifies the mechanism of heat transfer in the sheet region which has never been considered before. The previous analytical studies (Lee and Tankin [7]; Hasson et al. [8]) have considered only heat conduction in the sheet, but the present results show that this assumption is not true. In fact, the turbulence generated inside the swirl chamber of a hollow-cone nozzle greatly augments the heat transfer in the sheet region even though the sheet is laminar (nearly 90 percent of thermal efficiency is achieved in this region).

In addition, it is also found from the experimental results that even at a distance of 5 mm from the nozzle outlet, the temperature

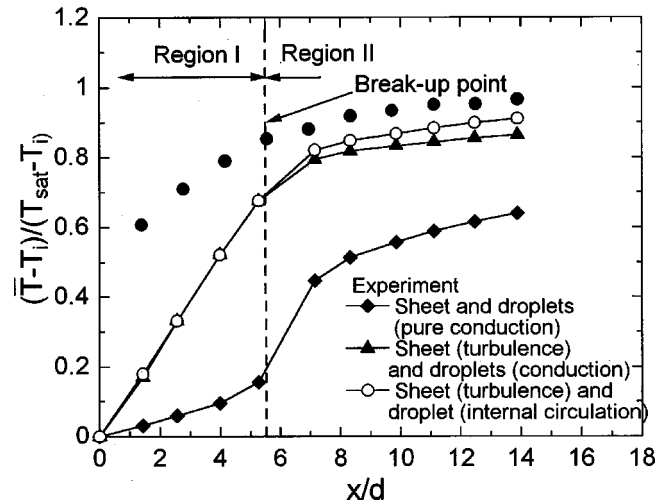


Fig. 11 Variation of condensation efficiency in the flow direction (comparison of experiment and analysis)

rise is more than 60 percent of the total ΔT . This may be due to the fact that the turbulence intensity is the largest at the nozzle outlet and decreases in the flow direction. Previous experimental studies of Weinberg [9] and Mayinger and Chavez [10] have shown similar behavior very close to the nozzle outlet. Lee and Tankin [7] have attributed the high heat transfer in the experimental data of Weinberg [9] to the inaccuracy of temperature measurement. Whereas, it is due to the turbulence generated inside the swirl chamber that enhances the heat transfer in the sheet region, which needs to be considered in the analytical model. Further, the present calculations show that the turbulent thermal conductivity model due to Celata et al. [13] is not adequate to reveal the heat transfer in the sheet region.

If we consider the internal circulation inside the droplet, there is an increase in the heat transfer over that of a simple conduction model which is very close to the experimental data in the region II.

4 Conclusions

The spray condensation heat transfer were investigated experimentally and analytically. The following conclusions are obtained from the above study:

1 Reliable temperature in the spray can be obtained for both sheet and droplet regions by using smaller size thermocouples with fast response.

2 The experimental results indicate that the spray water temperature rises more steeply in flow direction than those obtained by previous investigators. Further, maximum heat transfer is achieved in the sheet region as compared to that in the droplet region.

3 The measured temperature rise in water spray is much higher than those predicted by the pure heat conduction models both in spray sheet and droplets. The temperature prediction is much improved by considering turbulence in a spray sheet and internal circulation and mixing inside droplets, which clarifies the heat transfer mechanism during direct contact condensation of steam on subcooled water spray.

Nomenclature

- C = constant, $C = a(Pe')^b$ where $a = 0.153$ and $b = 0.454$ [6]
- C_D = drag coefficient
- C_p = specific heat (J/kg-K)
- D = droplet diameter (m)

d = nozzle diameter (m)
 g = acceleration due to gravity (m/s^2)
 Gz = Graetz number ($Gz=4s^2V/\alpha$)
 H = length of nozzle (m)
 h = heat transfer coefficient ($\text{W/m}^2\text{K}$)
 \bar{h} = local average heat transfer coefficient ($\text{W/m}^2\text{K}$)
 K = thermal conductivity (W/mK)
 L = axial distance (m)
 \dot{m} = mass flow rate (kg/s)
 Δp = pressure drop in nozzle (psi)
 Pe = Peclet number (dV/α)
 Pe' = modified Peclet number
 $(Pe' = (dV/\alpha)(\mu_g/(\mu_g + \mu)))$
 q = heat flux (W/m^2)
 \bar{q} = axially average heat flux (W/m^2)
 Q = flow rate (gph)
 r = radius (m)
 \bar{r} = spray radius (m)
 R = radius of droplet (m)
 s = sheet thickness (m)
 t = time (s)
 T = temperature (K)
 \bar{T} = integral average temperature across sheet and droplet region (K)
 V = velocity in flow direction (m/s)
 x = vertical downward distance from nozzle outlet (m)
 y = local radius of droplet (m)
 z = horizontal coordinate with $z=0$ on the center axis in the temperature measurement plane (m)

Greek Symbols

α = Thermal diffusivity (m^2/s)
 ϕ = Spray angle (rad)
 λ = latent heat of vaporization (J/kg)
 μ = dynamic viscosity (N-s/m^2)
 ν = kinematic viscosity (m^2/s)
 θ = non-dimensional local temperature inside droplet, $\theta = (T - T_i)/(T_{\text{sat}} - T_i)$
 $\bar{\theta}$ = non-dimensional mean temperature, $\bar{\theta} = (T_{\text{sat}} - \bar{T})/(T_{\text{sat}} - T_i)$
 θ_m = condensation efficiency in Eq. (19), $\theta_m = (\bar{T} - T_i)/(T_{\text{sat}} - T_i)$
 ρ = density (kg/m^3)
 σ = surface tension (N/m)

Subscripts

d = droplet
 g = Vapor
 i = initial or nozzle outlet

m = mean
 sat = saturation

Superscripts

$-$ = average

References

- [1] Brown, G., 1951, "Heat Transmission by Condensation of Steam on a Spray of Water Drops," *Proc. of General Discussion on Heat Transfer*, Institution of Mechanical Engineers.
- [2] Lekic, A., and Ford, J. D., 1980, "Direct Contact Condensation on a Spray of Subcooled Liquid Droplets," *Int. J. Heat Mass Transf.*, **23**, pp. 1531–1537.
- [3] Sundararayan, T., and Ayyaswamy, P. S., 1984, "Heat and Mass Transfer Associated with Condensation of a Moving Drop: Solutions for Intermediate Reynolds Numbers by a Boundary Layer Formulation," *ASME J. Heat Transfer*, **107**, pp. 409–415.
- [4] Sundararayan, T., and Ayyaswamy, P. S., 1985, "Hydrodynamics and Heat Transfer Associated with Condensation on a Moving Drop: Solution for Intermediate Reynolds Numbers," *J. Fluid Mech.*, **149**, pp. 33–58.
- [5] Chung, J. N., and Chang, T. H., 1984, "A Mathematical Model of Condensation Heat and Mass Transfer to a Moving Droplet in its Own Vapor," *J. Heat Mass Transf.*, **106**, pp. 417–424.
- [6] Celata, G. P., Cumo, M., D'Annibale, F., and Farello, G. E., 1991, "Direct Contact Condensation of Steam on Droplets," *Int. J. Multiphase Flow*, **17**, pp. 191–211.
- [7] Lee, S. Y., and Tankin, R. S., 1984, "Study of Liquid Spray (Water) in a Condensable Environment (Steam)," *Int. J. Heat Mass Transf.*, **27**, pp. 363–374.
- [8] Hasson, D., Luss, D., and Peck, R., 1964, "Theoretical Analyses of Vapor Condensation on Laminar Liquid Jets," *Int. J. Heat Mass Transf.*, **7**, pp. 969–981.
- [9] Weinberg, S., 1952, "Heat Transfer to Low Pressure Sprays of Water in a Steam Atmosphere," *Proc. Inst. Mech. Engrs, London*, Vol. **1B**, No. 6, p. 240–252.
- [10] Mayinger, F., and Chavez, A., 1992, "Measurement of Direct Contact Condensation of Pure Saturated Vapor on an Injection Spray by Applying Pulsed Laser Holography," *Int. J. Heat Mass Transf.*, **35**, pp. 691–702.
- [11] Kutateladze, S. S., 1952, "Heat Transfer in Condensation and Boiling," 2nd ed. Chpt. 7, Moscow-Leningrad, English translation by U.S. Atomic Energy Commission, AEC-tr-3770.
- [12] Celata, G. P., Cumo, M., Farello, G. E., and Focardi, G., 1986, "Direct Contact Condensation of Steam on Slowly Moving Water," *Nucl. Eng. Des.*, **96**, pp. 21–31.
- [13] Celata, G. P., Cumo, M., Farello, G. E., and Focardi, G., 1989, "A Comprehensive Analysis of Direct Contact Condensation of Saturated Steam on Subcooled Liquid Jets," *Int. J. Heat Mass Transf.*, **32**, pp. 639–654.
- [14] Ford, J. D., and Lekic, A., 1973, "Rate of Growth of Drops During Condensation," *Int. J. Heat Mass Transf.*, **16**, pp. 61–64.
- [15] Ohba, K., Kitada, H., and Nishiguchi, A., 1982, "Direct Contact Condensation on a High Spray Jet of Subcooled Water," *Heat Transfer in Nuclear Reactor Safety*, S. G. Bankoff and N. H. Afgan, eds., Hemisphere Publishing Corporation.
- [16] Rose, P. M., and Kintner, R. C., 1966, "Mass Transfer from Large Oscillating Drops," *AIChE J.*, **12**, pp. 530–534.
- [17] Skelland, A. H. P., and Wellek, R. M., 1964, "Resistance to Mass Transfer Inside Droplets," *AIChE J.*, **10**, pp. 491–496.
- [18] Celata, G. P., 1991, "Direct Contact Condensation of Steam on Subcooled Water," *Invited Lecture in Phase-Interface Phenomena in Multiphase Flow*, G. F. Hewitt, F. Mayinger, and J. R. Riznic, eds., pp. 345–371.

Experimental and Theoretical Study of Heating/Drying of Moist Paper Sheet With a Gas-Fired Infrared Emitter

J. Seyed-Yagoobi

A. N. Husain¹

Drying Research Center,
Department of Mechanical Engineering,
Texas A&M University,
College Station, TX 77843-3123

Infrared (IR) radiation is used for heating/drying of moist paper in the paper making process owing to its penetration characteristic inside porous media and a high absorptivity of water in the IR wavelength range. However, there is a lack of fundamental understanding of the transport phenomena occurring within moist paper during IR heating/drying. A series of experiments has been conducted along with the development of a theoretical model to fundamentally understand IR heating/drying of moist paper. The experimental results confirm the IR radiation energy penetration into the paper sheet and the theoretical analysis indicates that the penetration depth decreases with increasing sheet moisture content. [DOI: 10.1115/1.1372324]

Keywords: Drying, Emitting, Heat Transfer, Moisture, Porous Media, Radiation

Introduction

Heating of media and surfaces is achieved using various modes of heat transfer namely conduction, convection, and radiation. Paper manufacturing is an energy intensive process that involves drying of paper primarily with steam-heated cylinders. A method that has been used to increase drying efficiency is infrared (IR) radiation heating/drying. Though IR energy use in the US paper industry accounted for less than 3 percent in 1980 [1], the usage has increased significantly in the past decade, and a survey conducted in 1996 for US and Canadian paper industries indicated that 27 percent of the paper machines were using IR energy for drying purposes [2].

The wide application of IR radiation for paper drying purposes is because of the fact that IR radiation is not solely a surface-heating source, rather the energy penetrates inside the medium, imparting volumetric heating. IR heating also offers the priceless benefit of heating/drying of media in a non-contact mode that makes its application very attractive for the drying of coated paper. Two conventional types of IR heaters are being commercially used namely electric heaters and gas-fired heaters. Electric IR heaters emit radiation by passing an electric current through a resistance, which raises its temperature. These are operated up to a temperature of 2200°C, and emit near IR radiation (0.7 to 1.4 μm) which does not correspond to a high absorptivity in moist paper, and a portion of the energy is either transmitted through the paper thickness or reflected [3]. In many applications, the transmitted energy is redirected by placing back reflectors on the opposite side of the web thus increasing the efficiency of the electric IR heaters. Gas-fired IR heaters produce combustion on the burner surface by ignition of a premixed air and fuel stream. The combustion raises the surface temperature to ranges of 800–1100°C. The heater surface, which can be a ceramic plate with many holes, a matrix from metallic or ceramic fibers, or porous ceramic foam, incandesces at high temperatures to emit radiation. The radiation emitted at these temperatures is mainly in the medium wavelength range (1.6 to 10 μm) of the spectrum, which is absorbed well by moist paper due to presence of water in the web (see Fig. 1).

Though it has been used for a long time, insufficient fundamental information is available on paper drying with IR heaters. Riikonen et al. [4] developed a computer simulation, which combined IR and convective drying of pulp by adding the radiation contribution to a previously developed model for convective and conductive heat transfer. The IR energy was considered to be absorbed into the top-most layer of the pulp sheet. It was found that the observed experimental drying rates were smaller compared to the model predictions.

Kuang et al. [5] developed a numerical model to study the drying of paper using a gas-fired IR dryer, taking into account the three modes of heat transfer. The model took into account the radiation heating as a volumetric absorption that attenuated progressively in paper thickness direction. The absorption coefficient was calculated by the volumetric weighted average of the absorption coefficients of water and solid fiber. Local scattering and emission within the medium were neglected. The model developed demonstrated a high sensitivity to water and paper absorption coefficients. The simulated moisture content profiles were in agreement with the experimental results. However, no data were available for temperature profiles within the paper thickness direction for comparison with the simulation results.

Ojala and Lampinen [6] studied the efficiency of gas and electric IR emitters using radiation exchange calculations. Various dryer configurations were studied. Optical properties of paper were evaluated over discrete wavelength intervals (0.4 to 20 μm) and used in the radiation exchange calculations. A comparison of the model with a pilot unit was made but it was vague owing to the differences in operating conditions and geometry of the pilot unit and those used in the theoretical model. The optical properties determined for paper (with varying moisture content) by Ojala and Lampinen have been used extensively for modeling the IR radiation absorption in the paper thickness direction.

Fernandez and Howell [7] developed a one-dimensional model that took into account the three modes of heat transfer with mass transfer. The radiation was assumed to be a volumetric phenomenon, with the material internally absorbing, scattering, and emitting energy. The absorption and scattering coefficients were spectrally dependent. Water was assumed to exist in three phases; bound liquid, free liquid, and vapor. The model accounted for spectral dependence of radiative properties, and the radiation heat flux was calculated for two different spectral bands. Model simu-

¹Current Address: Carrier Corporation, Carrier Parkway, Syracuse, NY 13221

Contributed by the Heat Transfer Division for publication in the JOURNAL OF HEAT TRANSFER. Manuscript received by the Heat Transfer Division July 24, 2000; revision received January 22, 2001. Associate Editor: F. B. Cheung.

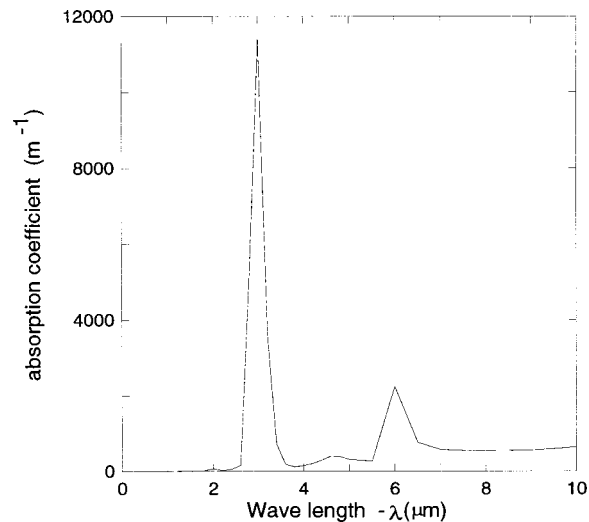


Fig. 1 Spectral absorption coefficient of water [16]

lations were not compared with any experimental data to validate the model and the values used for the optical properties.

Pettersson and Stenstrom [8] proposed a model based on multi-layered idealization of a paper sheet as proposed earlier by Scallan and Borch [9]. Their argument, based on microscopic analysis of paper structure, was that a beam of radiation had to pass a number of parallel layers within the paper depth to propagate through the medium. The reflectivity and the transmissivity of a single layer were fitted to the experimental literature data for the reflectivity and transmissivity of paper at different wavelengths. The model developed predicts the IR energy penetration inside the paper thickness without accounting for other transport mechanisms that are present during heating/drying of moist paper. It is therefore not possible to compare the model with any drying data.

As presented above, limited work has been carried out in the past to analyze the drying process of moist paper with IR radiation energy. Specifically, there is a lack of fundamental understanding of the transport phenomena occurring within the moist sheet during IR heating/drying. The intent of this paper is to provide such information through experimental study and theoretical analysis.

Experimental Set-Up

Details regarding the experimental facility can be found in Wirtz [10] and Husain [11]. The facility, shown in Fig. 2, consists of a single gas-fired IR surface burner in a look down configuration, suspended in the middle of an aluminum enclosure (214 cm high, 154 cm wide, and 123 cm deep). The purpose of the enclosure is to minimize the effect of outside air entrainment. The burner consists of a porous ceramic matrix, which is 60 cm wide and 40 cm deep. Combustion air and natural gas are fed into a mixing tube located upstream of the IR emitter. The premixed stream passes through the ceramic matrix and ignites at the surface of the porous structure. The ignition produces a very uniform flame at the exit face of the ceramic that protrudes about 1 mm from the surface. The combustion heat is partially transferred to the ceramic surface, which incandesces to produce the desired IR radiation. Aluminum cooling air shroud is provided around the IR emitter with a 2 mm gap between the edges of the ceramic face and the cooling shroud. Cooling air is introduced through four independent ports and passes out through the gap between the shroud and the ceramic face.

On the floor of the rig, parallel to the firing face, is a large water-cooled heat exchanger, for absorbing incident IR radiation energy. The top surface of the heat exchanger, facing the IR emitter, is painted black to increase its absorptivity. Located in the center of the water-cooled heat exchanger on the floor of the test

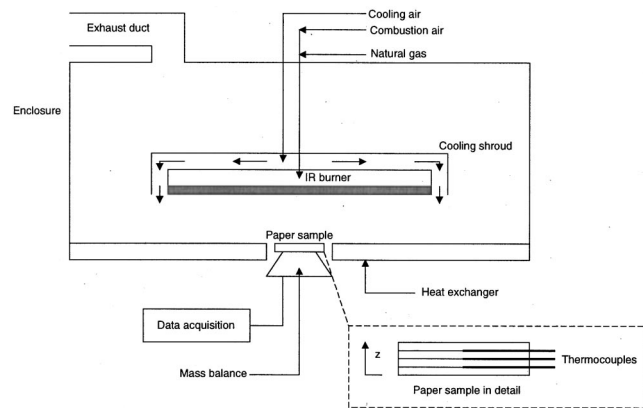


Fig. 2 Schematic of experimental set-up

chamber, is a 16.50 cm circular sample port provided for positioning the test samples parallel to the IR emitter. The sample port is flush with the upper plate of the heat exchanger, which forms the floor of the enclosure. The paper samples are placed on a mesh stand (0.0083 m² open area versus a total area of 0.0188 m²) which in turn is placed on a digital weighing balance. The digital balance has a resolution of one milligram and a signal output frequency of 2.5 Hz. The balance is calibrated to account for the mass reading indicated due to air flow over the sample. The data acquisition system used for collecting the sample transient temperature and the heat flux data has a data output frequency of 5 Hz.

The sample port is covered with a radiation insulating shield prior to the drying experiment. A 0.127 mm diameter T type (copper-constantan junction) thermocouple is mounted on the outer periphery of the sample for signaling the starting time in heating/drying process when the sample port is exposed to the IR radiation. For surface heat flux measurements, a circular foil heat-flux gage (Vatell Corporation, model number 1000-1) with a surface total hemispherical emissivity of 0.94 is used. The IR emitter surface temperature measurements are made with an IR camera (Mikron, model 6T62). These measurements are based on the IR emitter surface emissivity of 0.99 determined with the IR camera.

Paper Samples Construction

The paper samples were made in accordance with the Technical Association of Pulp and Paper Industries (TAPPI) standard 205. The paper samples were all fabricated from linerboard fibers. The experimental program consisted of two different sets of samples. In the first set, the initial dry basis moisture content (DBMC) of the samples was kept constant at 1.5. Fibers with 605 Canadian Standard Freeness (CSF) were used in preparation of samples. CSF is a measure of drainability of free water from the stock. The basis weights (BW) of the samples were selected to be 100, 200, and 300 g/m². In the second set, fibers with 680 CSF were used and the basis weight of all the samples was 200 g/m² with initial DBMC of 1.5, 1.0, and 0.5.

Single and multi layer samples were tested for both of the studies. Multi layer samples were used to obtain temperature profiles within the thickness direction. The multi layer samples consisted of four layers of equal weight with the total weight equal to the required basis weight of the sample. Three T type micro thermocouples of 0.08 mm diameter were inserted in between the adjacent layers prior to adhering them together with a press roll according to TAPPI-205 procedure. Table 1 provides the information on the location of the thermocouples inserted within the samples prior to heating/drying process. For each sample, the initial thickness was measured at four locations (25 mm in from the edge on 90 degree intervals). These measurements were performed with a dual-plate dial micrometer. Using the assumption

Table 1 Initial sample thickness and thermocouple locations measured from sample surface exposed to IR emitter; initial DBMC~1.5; Samples: linerboard with 605 CSF.

Basis Weight (g/m ²)	Total Thickness (mm)	Top Thermocouple (mm)	Middle Thermocouple (mm)	Bottom Thermocouple (mm)
100	0.510	0.127	0.255	0.382
200	0.890	0.220	0.441	0.667
300	1.600	0.401	0.803	1.200

that each target sample was uniform, the depth of the thermocouples from the sample top surface was determined. The maximum standard deviation for the data given in Table 1 was 0.020 mm.

Error Analysis

For each individual measurement, the propagation of uncertainty was calculated using the method proposed by Kline and McClintock [12]. The uncertainty associated with each measurement term was comprised of error induced due to uncertainty associated with the measurement device itself and the error induced due to the variance within the experimental data (the t-value corresponding to the confidence level of 90 percent was used). The uncertainty values for the calculated DBMC of 100 g/m² samples were less than 20 percent while for 200 and 300 g/m² samples they were below 15 percent. The high uncertainty values corresponded to the low moisture contents. For temperature measurements, the uncertainty values with initial DBMC of 1.5 were below 15 percent for the top, middle, and bottom thermocouples. The total uncertainty associated with the heat flux measurement on the target surface was 6.7 percent. As described above, this uncertainty was comprised of uncertainty due to the sensitivity of the heat flux meter (± 6 kW/m²) and the uncertainty in the measured data. Further details in the error analyses are given in Husain [11].

Theoretical Analysis

The theoretical model predicts the temperature and moisture distributions inside paper with IR as a heat source and is based on transport equations developed by Asensio and Seyed-Yagoobi [13] for simulation of conventional steam heated cylinder drying of paper. A volumetric heat source term to account for radiation penetration is added to this basic model. Boundary conditions are also modified to represent the experimental conditions of this study. Note that the sheet shrinkage and porosity variation that occur due to moisture and temperature changes are also accounted for in the original model by Asensio and Seyed-Yagoobi. The following provides a brief description of the theoretical model.

The local moisture content and temperature of the sheet are assumed to be function of z (see Fig. 2) and IR exposure time. The conservation of mass for water is given by

$$\frac{\partial M}{\partial t} = -\frac{\partial J_w}{\partial z} - \frac{\partial J_v}{\partial z} \quad (1)$$

The actual mass of vapor and air within the paper, especially in the early stages of drying (this is the case here), will be much smaller than the liquid mass. Thus, under the assumption of no vapor or air accumulation, only a single continuity equation needs to be written.

The conservation of energy is as follows:

$$\begin{aligned} [c_w \rho_w S \varepsilon + c_f \rho_f (1 - \varepsilon)] \frac{\partial T_{sh}}{\partial t} = & -\frac{\partial q''}{\partial z} - \frac{\partial (H_w J_w + H_v J_v)}{\partial z} \\ & + \frac{\partial q''_r|_z}{\partial z}, \end{aligned} \quad (2)$$

where the effect of water vapor and air components on the average specific heat of the sheet has been considered negligible. The conduction heat flux is given by the Fourier's law

$$q'' = -k_{\text{eff}} \frac{\partial T_{sh}}{\partial z} \quad (3)$$

and water flux is given by the Darcy's law

$$J_w = -\left(\frac{K}{v_w}\right) \cdot \frac{\partial P_{ca}}{\partial z} \quad (4)$$

The vapor flux is given by Fick's law

$$J_v = -\left[\frac{D_{ap} \cdot MW_v}{(1 - y_v)}\right] \frac{\partial C_v}{\partial z} \quad (5)$$

Details for determining parameters such as P_{ca} , D_{ap} , K , C_v , and ε are given in Asensio and Seyed-Yagoobi [13]. Similar to the average specific heat of the sheet (see Eq. (2)), the effective thermal conductivity of the sheet is also calculated assuming a parallel heat flow model where fluid and solid phases are parallel, cross-sectional areas are proportional to void and solid fractions, and phase lengths are equal to the sheet thickness

$$k_{\text{eff}} = (1 - \varepsilon)k_f + S\varepsilon k_w + (1 - S)\varepsilon k_a, \quad (6)$$

where the effect of water vapor on the effective thermal conductivity has been considered negligible.

The two relevant boundary conditions for the present case are for the paper bottom surface in contact with the unheated mesh on which the samples are placed, and for the paper top surface exposed to the IR radiation heat flux. The surface nodes are modeled as half thickness control volumes in the energy and mass balance equations. For the bottom control volume, the mass balance equation is given as

$$\frac{\partial M}{\partial t} = \frac{1}{\Delta z} (-J_w - J_v + J_{v,o}) \quad (7)$$

and the energy conservation equation is

$$\begin{aligned} [c_w \rho_w \varepsilon S + c_f \rho_f (1 - \varepsilon)] \frac{\partial T_{sh}}{\partial t} \\ = \frac{1}{\Delta z} \left(k_{\text{eff}} \frac{\partial T_{sh}}{\partial z} - J_w H_w - J_v H_v + J_{v,o} H_v \right. \\ \left. + h_{\text{bottom}} (T_{\text{amb}} - T_{sh}) + q''_r|_{z=\Delta z} - q''_r|_{z=0} \right). \end{aligned} \quad (8)$$

For the top control volume exposed to IR radiation, the mass balance equation is given as

$$\frac{\partial M}{\partial t} = \frac{1}{\Delta z} (+J_w + J_{v,i} - J_{v,o}), \quad (9)$$

and the energy conservation equation includes the radiation and convection (promoted mainly by the IR emitter) heat flux terms

$$\begin{aligned} [c_w \rho_w \varepsilon S + c_f \rho_f (1 - \varepsilon)] \frac{\partial T_{sh}}{\partial t} \\ = \frac{1}{\Delta z} \left(-k_{\text{eff}} \frac{\partial T_{sh}}{\partial z} + J_w H_w + J_{v,i} H_v - J_{v,o} H_v \right) \\ + q''_{\text{conv}} + q''_r|_{z=Z} - q''_r|_{z=Z-\Delta z} \end{aligned} \quad (10)$$

q''_{conv} represents the convective contribution of heating on the top surface of the sample. This value is determined by deducting the calculated incident radiative heat flux from the measured total heat flux. This is discussed at length in Husain [11]. For the

evaporation at the paper-air interface, $J_{v,o}$, the mass transfer coefficient is determined from the Chilton-Colburn form of the Reynolds analogy as described in Asensio [14].

The radiation heat flux term in Eqs. (2), (8), and (10) represents the amount of energy that penetrates into the paper in the thickness direction and is given by Bouguer's law

$$q_r''|_z = q_r''|_Z \exp\left(-\int_Z^z a \cdot dz\right), \quad (11)$$

where $q_r''|_Z$ represents the radiation heat flux incident on the surface of paper exposed to the IR emitter. Note that the z -direction is defined from the paper sample bottom surface toward the top (IR exposed) surface (see Fig. 2). The amount of energy that penetrates up to a certain thickness decays exponentially as a function of the penetration thickness and absorption coefficient "a." The radiation penetration given by Eq. (11) does not take the scattering of radiation within the paper into account. Thus, this analysis is not precise, however, it allows for significant simplification of the problem especially that insufficient data are available in the literature for optical properties of the paper fibers.

To determine the net radiation heat flux incident at the top surface of paper (i.e., $q_r''|_Z$), a classical radiation exchange calculation was performed among the IR emitter surface, paper sample top surface, heat exchanger top surface, and the surroundings [11]. The gas within the enclosure was assumed to be nonparticipating. The magnitude of $q_r''|_Z$ was mainly a function of the IR emitter surface temperature and the distance between the emitter and the paper sample.

The absorption coefficient in Eq. (11) has been determined by taking a weighted average of absorption coefficient for dry fiber and water

$$a = a_f(1 - \varepsilon) + \varepsilon S a_w. \quad (12)$$

The above equation for calculating the absorption coefficient is an approximation. The porosity and saturation in Eq. (12) at various moisture content levels are determined from the paper structure model given by Asensio [14]. The absorption coefficient for paper fiber is determined from the following equation based on Bouguer's law, in terms of the total hemispherical absorptivity and reflectivity of fiber.

$$a_f = \frac{1}{L} \ln\left(1 - \frac{\alpha_f}{(1 - R_f)}\right). \quad (13)$$

The total hemispherical absorptivity of fiber, α_f , was obtained on the basis of spectral absorptivity from 0.4 to 20.0 μm for a 41 g/m^2 basis weight paper with a moisture content of 6 percent, measured by Ojala and Lampinen [6]. Potential differences in the fiber types used in this paper and the ones studied by Ojala and Lampinen contribute towards errors in the theoretical predictions. However, there is very limited information available in the literature about optical properties of paper. The value for the total hemispherical reflectivity of fiber, R_f , was obtained from Kuang [15]. The value for absorption coefficient of water, a_w , has been taken from Kuang et al. [5] for a temperature that corresponded to the operating temperature of the IR heater in the current experiments. Table 2 gives the values of these properties along with the other parameters utilized in this study.

The theoretical model presented above was solved numerically using finite difference techniques. A marching technique (fully explicit) in the time direction was employed. The paper thickness was divided into twelve equally spaced nodal points. The step size in the time direction was 1×10^{-4} s. There was no observable difference in the moisture or temperature values when more nodal points in the z -direction or smaller steps in time direction were used. Numerical convergence with respect to the temperature and moisture content (weight of water divided by weight of dry fiber) in the z -direction corresponded to 10^{-3} K and 10^{-3} , respectively. More details on the numerical solutions are given in [11] and [14].

Table 2 Parameters used for theoretical analysis

$q_r'' _{z=Z}$ (kW/m^2)	66.0
q_{conv}'' (kW/m^2)	2.4
h_{bottom} ($\text{W/m}^2\text{K}$)	20
IR T_{surface} ($^{\circ}\text{C}$)	934
c_w (kJ/kgK)	4.17
a_f ($1/\text{m}$)	57000
R_f	0.27
ε	0.73
c_f (kJ/kgK)	1.34
a_w ($1/\text{m}$)	44000
α_f	0.73
ρ_f (kg/m^3)	1500
k_f (W/mK)	0.12
ε_e	0.99

Experimental Results

The experimental results discussed in this section are provided in terms of the average moisture content and temperature distribution of the sample sets specified earlier. All the experiments presented here are carried out at an emitter fuel consumption rate corresponding to 50.1 kW (209 kW/m^2 , based on emitter surface area) and an emitter to paper sample surface spacing of 11.5 cm. At this operating condition, the ceramic surface temperature of the IR emitter is measured (with an IR camera) to be 934°C (flame temperature of 1500°C) resulting in 66.0 kW/m^2 (determined from classical radiation calculations) of incident radiation heat flux on the paper sample surface. Note that this incident radiation heat flux is much lower than the heat flux generated at the emitter surface (based on the fuel heating value) since only a portion of the heat generated at the emitter results in radiation emission from the IR ceramic surface. More details and additional experimental data for different operating conditions can be found in Husain [11].

Figure 3 shows the effect of varying sample basis weight on IR drying. Higher basis weight samples take a longer duration to achieve a certain DBMC due to large amount of water present in the sample. A brief period of approximately one second of constant DBMC (no moisture loss) is visible for the 300 g/m^2 basis weight samples which represents the initial sensible heating. The lower basis weights of 100 g/m^2 and 200 g/m^2 do not indicate a constant DBMC period, rather, rapid moisture reduction is evident in both cases. This is primarily due to the fact that the thermal mass (water and fiber) associated with lower basis weight samples at identical initial DBMC of 1.5 is small resulting in a very short sensible heating period under similar IR radiation energy level. Note that all the samples at initial DBMC of 1.5 are saturated with water. This shorter duration of sensible heating for lower basis weight samples has not been captured in Fig. 3 owing to relatively low frequency of data acquisition system for the weight measurement.

Figure 4 illustrates the effect of initial DBMC on IR drying for 200 g/m^2 basis weight samples (680 CSF). The drying time is shorter for lower initial DBMC samples due to smaller amount of

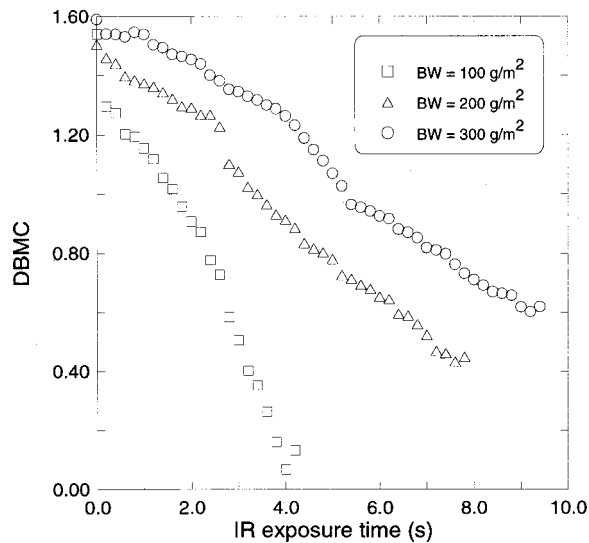


Fig. 3 Effect of basis weight on IR drying; initial DBMC~1.5; samples: linerboard with 605 CSF.

water content within the sample. A sensible heating period of approximately 1.0 s and 0.7 s is visible for samples with initial DBMC of 0.5 and 1.0, respectively. The sensible heating period was not captured for samples with initial DBMC of 1.5. The longer duration of sensible heating for samples with initial DBMC of 0.5 can be related primarily to the unavailability of water on the sample surface. For samples with the initial DBMC of 1.5, the surface is saturated with water and with the interception of the IR energy, the water rapidly evaporates.

The discussion on the temperature distribution in the paper thickness direction is based on the temperature data obtained from the thermocouples embedded within the layers of paper, as mentioned earlier. The initial calculations indicated no need for the radiative corrections on the thermocouple outputs. The top, middle, and bottom layers represent the temperature measured by the thermocouples between the first and second, second and third, and third and fourth layers, respectively. See Table 1 for the initial location of the embedded thermocouples. Note that the location of the thermocouples changes due to the shrinkage of samples with

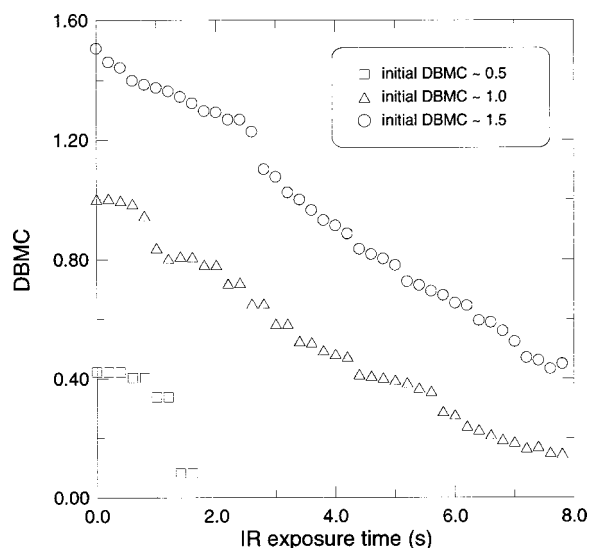


Fig. 4 Effect of initial DBMC on IR drying; basis weight = 200 g/m²; samples: linerboard with 680 CSF.

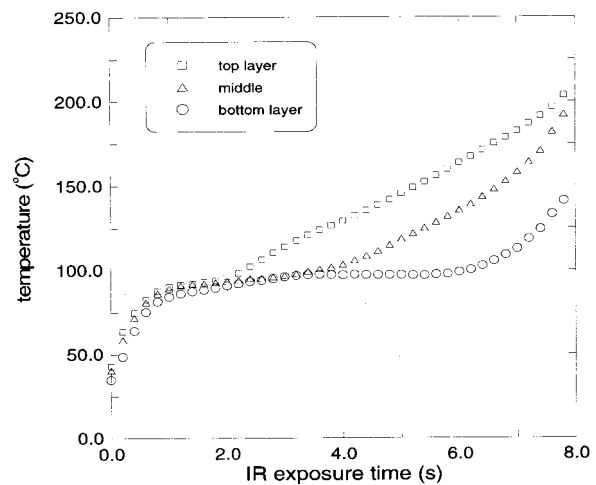


Fig. 5 Temperature profile for 100 g/m² basis weight sample; initial DBMC~1.5; samples: linerboard with 605 CSF.

drying. However, initially the sheet thickness, thus, the location of the thermocouples remain unchanged due to the lack of significant moisture loss in the early stage of the sample exposure to the IR energy.

Figure 5 illustrates the temperature profile of 100 g/m² (605 CSF) basis weight samples with an initial DBMC of 1.5. The temperature response for all the layers in Fig. 5 can be divided into three distinct regimes. The process starts with sensible heating indicated by an increase in temperature. The initial sensible heating is followed by evaporation at constant temperature, towards the end of which, the process of moisture removal is essentially completed. At the completion of constant temperature evaporation, a second sensible heating follows. From Fig. 5, a sharp temperature rise is evident for all the three layers. However, the top layer demonstrates the most rapid temperature rise, owing to its closer location to the surface exposed to IR emitter. The energy that reaches the top, middle, and bottom layers can be due to IR radiation penetrating to this depth, as well as the energy that propagates by conduction and convection through the thickness. The response of the middle and bottom layers demonstrates that the magnitude of initial temperature rise decreases with increasing distance from the surface exposed to the IR emitter.

As shown in Fig. 5, the duration of constant temperature evaporation stage for the top layer is shorter compared to the middle and bottom layers. This is representative of moisture transport mechanism within paper during drying process. Transport of water vapor from the top layer occurs in either direction with evaporation occurring from the surface exposed to the IR heating as well as vapor transfer to the lower layers. The water vapor reaching the lower layers condenses back to liquid phase first followed by evaporation period. This was observed experimentally by Wirtz [10] through weight measurement of the individual layers at different times. In addition to the above, the evaporation time is longer for lower layers because the amount of energy reaching the lower layers decreases with distance. In Fig. 5, the evaporation temperature is below 100°C corresponding to partial saturation pressure of the water vapor. As shown in Fig. 5, the middle layer temperature approaches the top layer temperature following 7 s of IR exposure time because the top layer starts to discolor, crack, and eventually ignite.

Effect of an increased basis weight on the temperature profile is illustrated in Fig. 6, which shows the temperature response of 300 g/m² samples (605 CSF). Distinct regimes of sensible heating, evaporation, and final sensible heating are visible. A delay in response time, especially of the bottom layer temperature, in contrast to the top layer immediate response, is indicative of the fact that the IR energy initially does not penetrate this far (1.600 mm

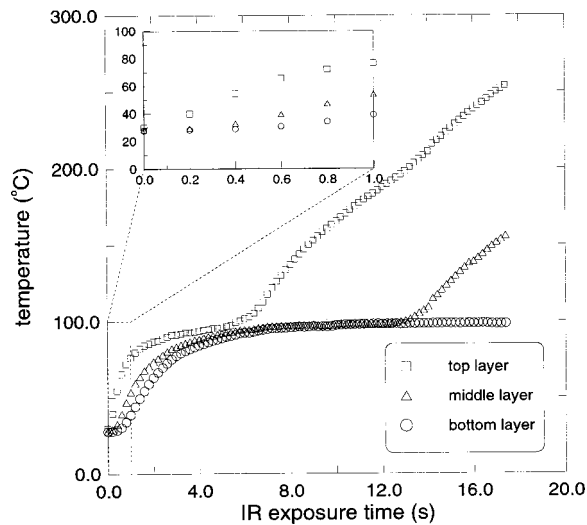


Fig. 6 Temperature profile for 300 g/m² basis weight sample; initial DBMC~1.5; samples: linerboard with 605 CSF.

and beyond from Table 1). The depth of penetration of the IR energy into the sheet is dependent on various parameters including IR emitter operating conditions and paper sheet moisture level.

To estimate the initial penetration depth of the IR energy under the operating conditions corresponding to Fig. 6, a classical conduction heat transfer analysis was carried out to determine the temperature rise in the locations of the first, second, and third thermocouples that would have resulted if the incident radiation heat flux on the sample upper surface was only a surface phenomenon. Since the sample at DBMC of 1.5 is completely saturated, the heat transfer due to mass transport within the sheet is initially absent. Assuming that the IR energy incident on the sample surface does not penetrate into the sheet, the only mode of transfer of heat into the sample will be by conduction. A heat conduction analysis for a semi-infinite body under a constant surface heat flux (sum of the radiation and convection heat fluxes) was performed and the results are summarized in Table 3. In the conduction analysis, it was assumed that the saturated sheet had properties of water, thus exaggerating the calculated temperature values. Also included in this table are the corresponding measured temperatures. The micro thermocouples used in this study have a response time of approximately 0.05 s. According to Table 3, the contribution of the pure conduction heat transfer to temperature rise is negligible during the first 0.2 s of exposure to IR energy. On the other hand, the measured temperature rise is significant even at 0.1 s of exposure to IR energy at 0.401 mm from the surface. For 0.803 mm from the surface, there is a small 0.3°C temperature rise at 0.1 s indicating a negligible portion of the IR radiation energy penetrating this far into the sample. It must be mentioned that with the IR energy penetrating into the sheet, the conduction heat transfer (in the early stage of exposure to IR energy) from the IR penetrated region to the region unaffected by the IR energy is promoted due to the increase in the temperature of the IR affected region. A similar analysis was carried out for a 100 g/m² sample based on the data given in Fig. 5, and it was concluded that the IR energy did penetrate to the third thermocouple location (i.e. 0.382 mm, see Table 1). In the case of 200 g/m² samples, the experimental data (not given in this paper, see Husain [11]) revealed that the IR energy reached the middle thermocouple location (0.441 mm) but barely penetrated up to the third thermocouple location (0.667 mm). From the above discussion, one can assume that under the corresponding operating conditions, the IR radiation energy penetrated into the saturated sheet up to approximately 0.667 mm from the surface. As previously mentioned, the exact

Table 3 Calculated initial temperature rise (based on pure conduction heat transfer analysis) versus measured initial temperature rise (from Fig. 6); basis weight=300 g/m², initial DBMC~1.5; samples: linerboard with 605 CSF

IR exposure time (s)	Location* (mm)	Calculated temperature rise (°C)	Measured temperature rise (°C)
0.1	0.401	0.0	≈4.7 [†]
0.2	0.401	0.8	9.7
0.1	0.803	0.0	≈0.3 [†]
0.2	0.803	0.1	1.0
0.1	1.200	0.0	≈0.0 [†]
0.2	1.200	0.0	0.2

*interpolated from 0 to 0.2 s temperature readings

[†]measured from sample surface exposed to IR emitter

magnitude of the depth of penetration is dependent on the operating conditions. The data presented here, however, prove the fact that the IR radiation energy should be treated as a volumetric phenomenon rather than a surface phenomenon with respect to a porous paper sheet.

Comparison of Numerical and Experimental Results

The numerical solutions presented here are based on the theoretical model presented earlier. Transient moisture content and local temperature profiles in the paper sheet are simulated and compared with the experimental data. The values used for the parameters in the theoretical model are given in Table 2. Parameters, such as water properties, not listed in this table are readily available in the literature. As shown in the theoretical model, the properties are saturation dependent and their values do change during the drying process. The net IR energy incident on paper sheet surface, $q''_r|_{z=Z}$, is a calculated value as described earlier in the paper. The convection heat flux on the top surface of the paper sample, q''_{conv} , is determined by subtracting $q''_r|_{z=Z}$ from the total measured heat flux using the heat flux sensor.

Figure 7 compares the theoretical and experimental DBMC as a function of IR exposure time for 100, 200, and 300 g/m² samples. Results are provided up to an IR exposure time of 3.0 s to avoid

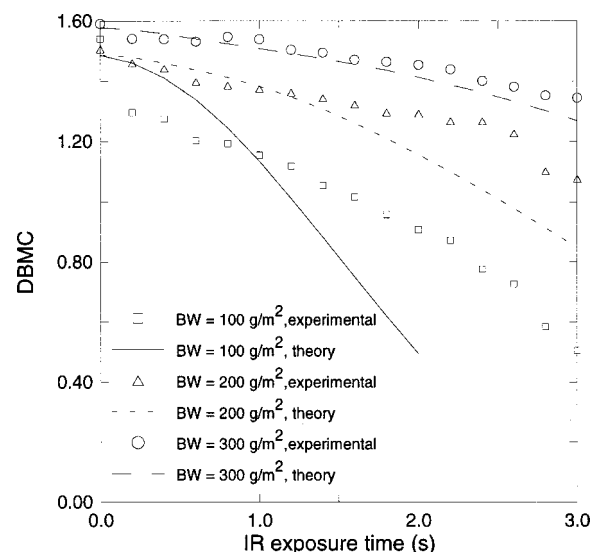


Fig. 7 Comparison of theoretical predictions with experimental data; DBMC versus IR exposure time for three different basis weights; samples: linerboard with 605 CSF.

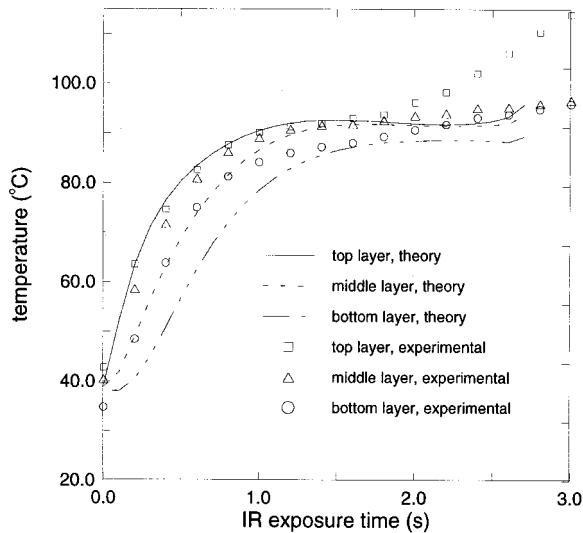


Fig. 8 Comparison of theoretical predictions with experimental data; temperature versus IR exposure time for BW = 100 g/m², initial DBMC ~ 1.5; samples: linerboard with 605 CSF.

theoretical predictions in the hygroscopic region. This is because the theoretical model does not take into account the effect of bound water transport that becomes pronounced at low moisture content levels. According to Fig. 7, the theory demonstrates a trend that is similar to the experimental data. For basis weight of 300 g/m², the agreement between the theory and the experimental data is very good, however, the agreement becomes worse at lower basis weights where the samples dry quickly. This is primarily due to (1) limitation of the theoretical model, especially at low moisture content levels (e.g., exclusion of bound water effects), (2) limitation of the IR energy penetration model due to neglecting internal scattering within the paper, and (3) lack of data for optical properties of paper fibers. The optical properties of paper fibers significantly affect the IR radiation energy penetration into the sheet. Their effect on drying of a thin paper (low BW) becomes more pronounced since the depth of IR energy penetration becomes comparable to the sheet thickness. As presented later in this section, the depth of IR energy penetration increases with a decrease in the moisture content indicating the importance of the values of the optical properties of paper fibers especially at the later stage of drying.

Figure 8 compares the predicted temperature profiles with the experimental data for a basis weight of 100 g/m² and initial DBMC of 1.5. The trend demonstrated by the simulation is very similar to the experimental data. Sensible heating is predicted for all the three layers with the most rapid temperature rise demonstrated for the top layer followed by the middle and bottom layers. Quantitatively, the theoretical predictions compare well with the experimental data for the top layer, but the deviation becomes larger with the progressive layers. The deviation becomes worse for the 300 g/m² sample, which shows a qualitative, rather than a quantitative agreement with the experimental data. The theoretical predictions also deviate from the experimental data for the top layer once this layer reaches the second sensible heating region. The shrinkage and degradation of the top layer, because of the over exposure to the IR emitter, contribute to this deviation.

In the early stage of the sample exposure to the IR emitter, due to the lack of significant moisture loss, the contribution of the convective liquid phase and vapor phase energy transfer (the second term on the right hand side of Eq. (2)) to the total energy balance within the moist sheet is negligible. Furthermore, as discussed earlier in this paper, the conduction term (the first term on the right hand side of Eq. (2)), especially during the early stage of

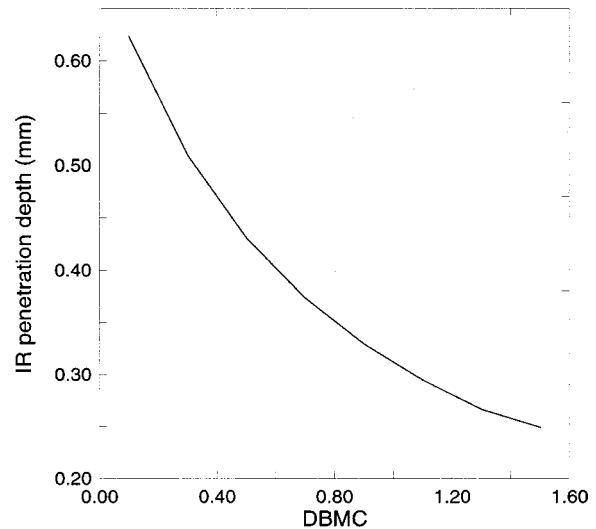


Fig. 9 Theoretical penetration depth for 1 percent of incident radiation energy versus DBMC (distributed uniformly); samples: linerboard with 605 CSF.

the exposure to the IR energy, is very small compared to the radiative heat source term (the last term on the right hand side of Eq. (2)). Therefore, one can conclude that in the beginning (e.g., within the IR exposure time of less than 1.0 s), the dominant terms in the energy balance (i.e. Eq. (2)) are the transient and radiative heat source terms, indicating that the IR energy initially raises the sheet temperature over time as illustrated in Figs. 7 and 8. Following the initial stage of the exposure to IR energy, all the terms given in Eq. (2), contribute to the local energy balance within the sheet. Further details on the transport mechanisms taking place within a moist sheet during the drying process in the absence of exposure to the IR energy are given in [13].

Using Eqs. (11), (12), and (13), the initial depth of IR energy penetration (defined based on 1 percent of the radiation energy incident at the surface) is presented as a function of initial moisture content in Fig. 9. The radiation penetration depth decreases with increasing moisture content. This is because of high absorptivity of water versus fiber within the corresponding wavelength range of the IR radiation energy. According to Fig. 9, the depth of penetration at DBMC of 1.5 is approximately 0.24 mm. This is much lower than the experimentally predicted value. However, it must be realized that the experimentally determined depth of penetration was determined primarily based on the temperature values corresponding to 0.1 s of IR exposed time. As shown in Fig. 3, the DBMC of the sample, especially with BW of 100 g/m², decreases within this time period. This drop in the moisture content is solely from the top layer giving a lower DBMC for this layer, which should result in a slightly higher theoretical depth of penetration than 0.24 mm. Nevertheless, the theoretically predicted value is much smaller than the experimentally determined value. The discrepancy between the theoretical and experimental results is primarily attributed to the errors associated with the values assumed for the optical properties. The depth of penetration is strongly dependent on the absorption coefficient (see Eq. (11)). Other factors discussed earlier in this section also contribute to this discrepancy.

Conclusion

Experimental and theoretical results of drying of paper using IR radiation energy as a heating source have been presented. The measurement of temperature distribution inside the paper thickness and transient DBMC provide a good basis for understanding of the IR paper drying process. The theoretical model gives qualitatively comparable trends to experimental data. The experimental

data indicate a higher IR energy depth of penetration into the paper sample than the numerical prediction. Absorption coefficient theoretically determines the level of IR penetration within a medium and it is therefore a critical parameter in the theoretical model. Thus, there is a great need for accurate measurement of optical properties of various types of paper fibers.

Acknowledgment

This work was partially supported by the Drying Research Center at Texas A&M University. The gas-fired IR burner was provided by Measurix-Devron.

Nomenclature

A = area of the sample (m^2)
 a = absorption coefficient (1/m)
 BW = basis weight; (weight of air dry sheet/sheet area), (g/m^2)
 C = molar concentration ($kmol/m^3$)
 c = specific heat ($J/kg\ K$)
 CSF = Canadian Standard Freeness
 D = diffusivity (m^2/s)
 $DBMC$ = dry basis moisture content, $DBMC = W_{ins} - W_{bd} / W_{bd}$
 h_{bottom} = heat transfer coefficient for bottom paper surface exposed to ambient conditions (W/m^2K)
 H = enthalpy (J/kg)
 J = mass flux ($kg/m^2\ s$)
 K = permeability (m^2)
 k = thermal conductivity ($W/m\ K$)
 k_m = mass transfer coefficient ($kg/m^2\ s$)
 L = thickness of bone dry sheet with 41 g/m^2 basis weight
 M = mass of water in sheet (kg/m^3)
 MW = molecular weight ($kg/kmol$)
 P = pressure (Pa)
 q = heat transfer (W)
 q'' = heat flux (W/m^2)
 R = total hemispherical reflectivity
 S = saturation; volume of liquid/volume of voids
 t = instantaneous drying time (s)
 T = temperature (K)
 W = weight of sample (kg)
 y = mole fraction
 z = paper thickness direction (m)
 Z = paper sample thickness (m)

Greek Symbols

α = total hemispherical absorptivity
 Δz = step size in z direction (m)
 ϵ = emissivity
 ϵ = porosity; volume of voids/total volume
 λ = wavelength (μm)
 ν = kinematic viscosity (m^2/s)
 ρ = density (kg/m^3)

Subscripts

a = air
 amb = ambient
 ap = apparent
 bd = bone dry
 ca = capillary
 $conv$ = convection
 e = emitter
 eff = effective
 f = fiber
 ins = instantaneous
 r = radiation
 sh = paper sheet
 v = vapor
 v,i = vapor from interior
 v,o = vapor to exterior
 w = water

References

- [1] McConell, R. R., 1980, "A Literature Review of Drying Research in the Pulp and Paper Industry," *Drying*, Hemisphere Publishing Corp., Washington, D.C., **2**, p. 330.
- [2] Bean, C. E., and Cocagne, J. M., 1996, "Assessment of Gas-fired Infrared Heaters in the Paper Industry," Topical Report, GRI-96/0087, Gas Research Institute, Chicago, IL, p. 3.
- [3] Pettersson, M., and Strenstrom, S., 1998, "Evaluation of Gas-fired and Electrically Heated Industrial Infrared Paper Dryers," *Proceedings of International Gas Research Conference*, San Diego, CA, p. 213.
- [4] Riikonen, J., Jarkonen, E., and Palosaari, S., 1987, "Modeling of Infrared Drying of Pulp," *Drying '87*, Hemisphere Publishing Corp., New York, NY, pp. 18–23.
- [5] Kuang, H., Thibault, J., Grandjean, B., and Chen, R., 1994, "Study of Heat and Mass Transfer during Drying of Paper," *Drying Technol.*, **3**, pp. 545–575.
- [6] Ojala, K. T., and Lampinen, M. J., 1995, "Modeling, Measurements, and Efficiencies of Infrared Dryers for Paper Drying," *Handbook of Industrial Drying*, 2, A. S. Mujumdar, ed., ISBN no. 0-8247-9644-6, pp. 931–976.
- [7] Fernandez, M. L., and Howell, J. R., 1997, "Radiative Drying Model of Porous Materials," *Drying Technol.*, **15**, No. 10, pp. 2377–2339.
- [8] Pettersson, M., and Strenstrom, S., 1998, "Absorption of Infrared Radiation and Radiation Transfer Mechanism in Paper," *J. Pulp Pap. Sci.*, **24**, No. 11, pp. 349–355.
- [9] Scallan, A. M., and Borch, J., 1972, "An Interpretation of Paper Reflectance Based upon Morphology: I. Initial Considerations," *Tappi J.*, **55**, No. 7, pp. 583–588.
- [10] Wirtz, J. W., 1999, "An Experimental Study of Gas-Fired Infrared Drying of Paper," M.S. thesis, Texas A&M University, College Station, TX.
- [11] Husain, A. N., 2000, "Measurement and Analysis of Heating of Paper with Gas-Fired Infrared Burner," M.S. thesis, Texas A&M University, College Station, TX.
- [12] Kline, S., and McClintock, F., 1953, "Describing Uncertainties in Single Sample Experiments," *Mech. Eng. (Am. Soc. Mech. Eng.)*, **75**, pp. 3–8.
- [13] Asensio, M. C., and Seyed-Yagoobi, J., 1993, "Simulation of Paper-Drying Systems With Incorporation of an Experimental Drum/Paper Thermal Contact Conductance Relationship," *ASME J. Energy Resour. Technol.*, **115**, No. 4, pp. 291–300.
- [14] Asensio, M. C., 1992, "Simulation of Paper Drying with Incorporation of an Experimental Drum/Paper Thermal Contact Conductance Relationship," M.S. thesis, Texas A&M University, College Station, TX.
- [15] Kuang, H., 1994, "Le Sechage du Papier Par Infrarouge," Ph.D. dissertation, Universite Laval, Quebec, Canada.
- [16] Siegel, R., and Howell, J. R., 1992, "Thermal Radiation Heat Transfer," Third Edition, Hemisphere Publishing Corp., Washington, D.C., pp. 175–176.

The Effect of Dissolving Gases or Solids in Water Droplets Boiling on a Hot Surface

Qiang Cui

Sanjeev Chandra

Mem. ASME
e-mail: chandra@mie.utoronto.ca

Susan McCahan

Department of Mechanical and
Industrial Engineering,
University of Toronto,
Toronto, Ontario M5S 3G8, Canada

We conducted experiments on the effect of dissolving either a gas (carbon dioxide) or a solid salt (sodium carbonate or sodium bicarbonate) in water droplets boiling on a hot stainless steel surface. Substrate temperatures were varied from 100°C to 300°C. We recorded the boiling of droplets with a video system, and photographed droplet impact using short-duration flash photography. At surface temperatures that were too low to initiate nucleate boiling, dissolved salts were found to reduce the evaporation rate since they lower the vapor pressure of water. Dissolved gas had the opposite effect: it came out of solution and formed bubbles in the liquid, enhancing evaporation. In the nucleate boiling regime dissolved carbon dioxide enhanced heat transfer by a small amount. However, sodium carbonate prevented coalescence of vapor bubbles and produced foaming in the droplet, greatly enhancing heat transfer and reducing the droplet lifetime to approximately half that of a pure water drop. Sodium bicarbonate, which decomposes to give carbon dioxide and sodium carbonate when heated, produced an even larger enhancement of heat transfer. When the surface temperature was raised above the Leidenfrost temperature of water, droplets went into film boiling and bounced off the surface following impact. Dissolved carbon dioxide was found to suppress heterogeneous bubble formation in the droplet during impact. However, dissolved salts promoted bubble formation and led to droplet break-up during impact. [DOI: 10.1115/1.1376394]

Keywords: Additives, Boiling, Droplet, Enhancement, Heat Transfer, Sprays

Introduction

Spray cooling is frequently used in industrial processes to dissipate extremely high heat fluxes. A solid surface loses heat much more rapidly to small droplets of liquid impinging on it than it does to the same liquid flowing continuously over it. High heat transfer rates are beneficial because they allow the size, cost, and complexity of heat exchange equipment to be reduced. Practical applications of water sprays include quenching of metals in foundries, fire fighting, and emergency core cooling in nuclear plants.

To design spray cooling equipment we need to know how the heat transfer rate from the surface varies with the size, velocity and physical properties of impacting spray droplets. To provide such information many experimental studies have examined water droplets evaporating on a hot surface (e.g., [1–3]). The water used in all these experiments was carefully degassed and purified to eliminate any impurities that could influence boiling. However, water sprays used in industrial applications typically contain significant amounts of dissolved salts and gases. We need to understand the effect of these contaminants on boiling heat transfer to accurately predict cooling rates. Even more usefully, if some impurities are found to significantly enhance heat transfer, we can deliberately add controlled amounts of them to the water to increase cooling efficiencies. For example, Qiao and Chandra [4,5] have demonstrated that adding traces of a surfactant to droplets or sprays impinging on a heated surface can increase nucleate boiling heat transfer by up to 300 percent.

The use of additives to enhance spray cooling has taken on added importance in the light of efforts to find replacements for Halon 1301, which is a very effective fire suppression agent, but whose manufacture has been banned because it depletes atmospheric ozone. Environmental considerations make water the most

attractive fire extinguishing agent available; unfortunately it is not efficient enough to use on board aircraft and vehicles, where the weight of liquid that can be carried is severely restricted. Much recent research has been directed at finding additives that can enhance the fire suppression capabilities of water. Finnerty [6] dissolved an assortment of inorganic and organic salts in water sprays used to extinguish a liquid pool fire of standard size. A pure water spray took 31.9 s to extinguish the fire. Sprays in which a salt was dissolved took from 3.2 s to 42.7 s depending on the additive used. The reason for this large variation was not clear. King et al. [7] studied the effect of some of the salts that Finnerty

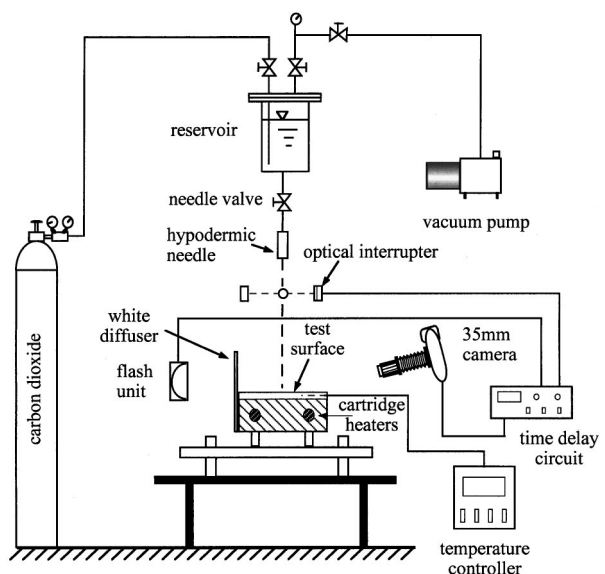


Fig. 1 Schematic diagram of the experimental apparatus

Contributed by the Heat Transfer Division for publication in the JOURNAL OF HEAT TRANSFER. Manuscript received by the Heat Transfer Division July 31, 2000; revision received January 11, 2001. Associate Editor: F. B. Cheung.

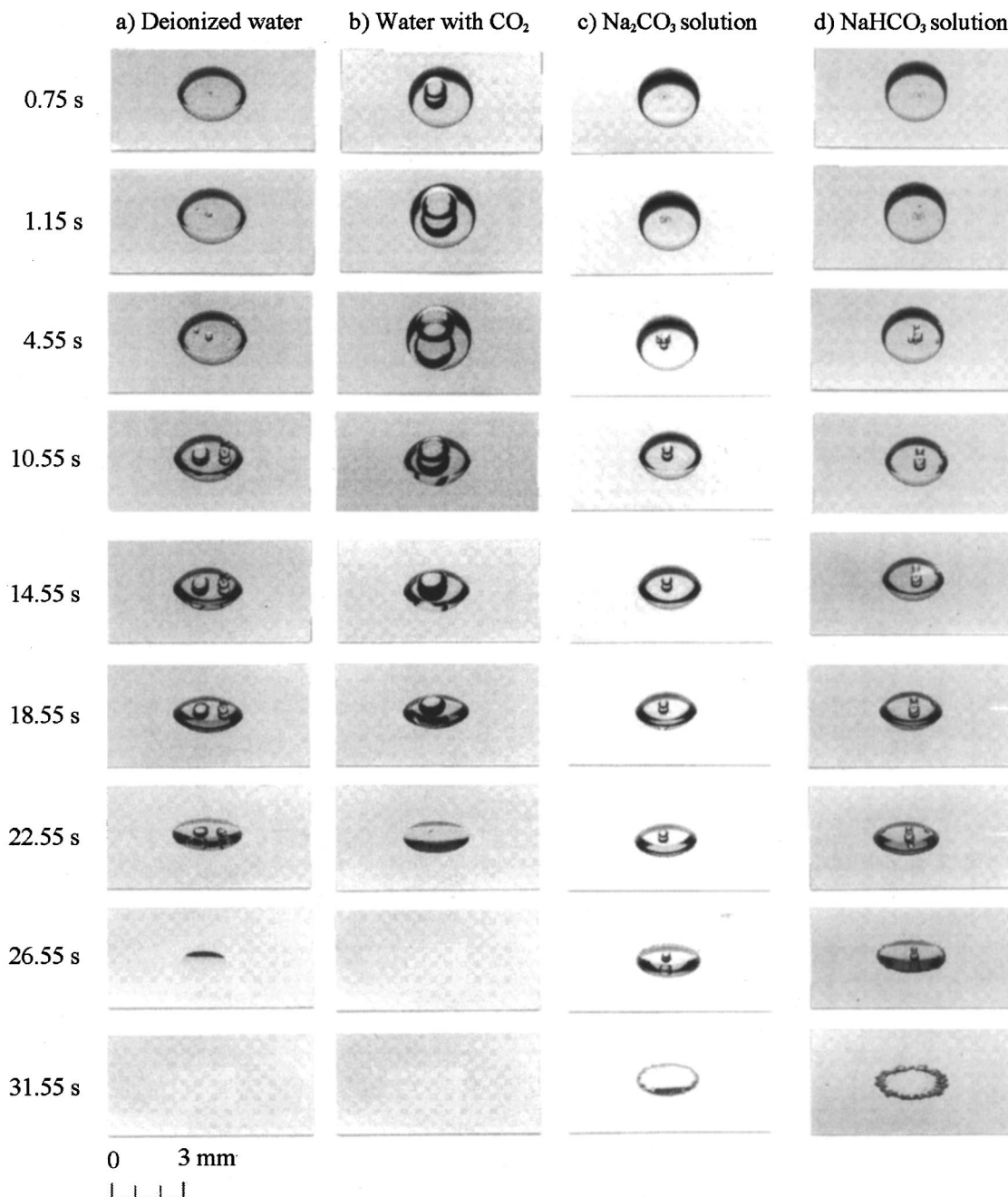


Fig. 2 Evaporation of droplets on a hot surface at 100°C: (a) pure water; (b) water containing dissolved CO₂; (c) 1 percent by weight solution of Na₂CO₃; (d) 1 percent by weight solution of NaHCO₃

[6] had found to have a large effect, by placing droplets of salt solution on a hot surface (at temperatures below the boiling point of water) and photographing their evaporation. They found that dissolved salts decreased droplet evaporation rates.

In the absence of any information on the effect of solid or gaseous impurities in droplets boiling on a hot surface, the most relevant information is available from pool boiling experiments. Jamialahmadi and Müller-Steinhagen [8] and Najibi et al. [9] investigated the effect of dissolved salts on pool boiling of water. They found that, in general, dissolved salts reduce heat transfer. This effect was most pronounced for salts with low solubility that precipitated on to the heater surface and formed a thermal barrier.

Dissolved gases also affect pool boiling heat transfer. Muller-Steinhagen et al. [10] studied sub-cooled boiling of heptane and water and established that dissolved gases always increased heat

transfer coefficients. The magnitude of heat transfer enhancement increased with gas solubility. Torikai et al. [11] observed that the wall superheat necessary to initiate pool boiling of water decreased with increasing air content. You et al. [12] did an extensive experimental investigation on the enhancement of pool boiling heat transfer using highly wetting dielectric fluids (FC series). Dissolved gases were found to influence boiling initiation only when gas content was high. Jeschar et al. [13] measured the cooling rate of a hot sphere dropped into a water bath in which carbon dioxide and various salts were dissolved. They reported that high concentration of dissolved gas yielded a more stable vapor film on the heater surface and reduced the temperature at which film boiling was initiated.

Studies on the effect of dissolving gases and salts in boiling water have not considered the case of droplets placed on a hot

surface. Boiling of droplets is distinct from pool boiling in that heat transfer is to a thin liquid film, so that vapor bubbles produced at the hot surface cannot rise away but tend to coalesce. This large vapor mass distorts the droplet shape and alters the liquid-solid contact area. Therefore, additives that can influence bubble nucleation and coalescence are of interest in the study of droplet boiling.

We deposited water droplets, in which either a solid salt or gas was dissolved, on a heated stainless steel surface and photographed them as they boiled. Based on information found in the pool boiling literature and some preliminary experiments, we expected sodium carbonate (Na_2CO_3) to have significant influence on droplet boiling and selected it as the first salt to study. The gas used was carbon dioxide (CO_2), because it is highly soluble in water. Finally we experimented with dissolving sodium bicarbonate (NaHCO_3), which decomposes when heated to yield Na_2CO_3 and CO_2 , thus combining their individual effects. Substrate temperature was varied in our experiments from 100°C to 300°C , encompassing the entire range of heat transfer regimes from nucleate to film boiling.

Experimental Method

The water used in our experiments was successively distilled, deionized and degassed. Distilled water was deionized in a NANOpure Bioresearch Deionization System (Model #D4754, Barnstead Thermolyne Corporation) to an electrical resistivity of $18.3 \text{ M}\Omega\text{-cm}$. A stainless steel chamber (88.9 mm diameter and 152.4 mm height) was filled with deionized, distilled water and placed in a Dewar flask filled with dry ice. Once the water froze the space above it was evacuated for over an hour. The water was then allowed to melt, after which the freezing and evacuation process was repeated two more times.

Salt solutions were prepared by dissolving 1 percent by weight of powdered Na_2CO_3 or NaHCO_3 (99.7 percent pure, ACP Chemical Inc.) in purified water at room temperature, and then allowing the solution to stand for about 12 hours to ensure complete mixing. The salt concentrations were well below their solubility limits in water, which are 18 percent by weight for Na_2CO_3 and 9 percent by weight for NaHCO_3 at room temperature [14].

Carbon dioxide was dissolved directly in water contained in the stainless steel vessel used for degassing water by pressurizing it with gas at 1 bar from a CO_2 tank for two days. The container was shaken occasionally to speed up the diffusion rate of carbon dioxide into the water. A Natelson microgasometer (Model #650, Scientific Industries Inc.) that adapts the classical Van Slyke [15] manometric method, was used to determine the gas content. The carbon dioxide content of water measured in the tests was typically $0.74 \text{ mm}^3/\text{mm}^3$ at STP, which was close to the saturated value ($0.75 \text{ mm}^3/\text{mm}^3$ at STP) reported in the literature [16].

The apparatus shown in Fig. 1 was used to record the impact and boiling of a single droplet on a hot surface. It consisted of a droplet generation and delivery system, a heated test surface on which droplets were placed, and a camera. The test surface, 50.8 mm square and 6.35 mm thick, was made of stainless steel and finished with 600 grit emery cloth and metal polish. During experiments it was cleaned with a cotton swab soaked in distilled water each time a droplet was deposited on it. The test plate was bolted to a copper block in which two cartridges heaters were embedded. Chromel-Alumel thermocouples were used to measure surface temperature, which was held constant within $\pm 0.5^\circ\text{C}$ by a temperature controller before depositing a droplet on it.

Droplets were formed by allowing water to flow from the reservoir through a needle valve and detach under its own weight from the tip of a 33-gauge stainless steel needle held 50 mm above the test surface. Droplet diameter was measured from photographs of spherical droplets falling after detachment and found to be $2.0 \pm 0.02 \text{ mm}$ in all our experiments. There was no measurable difference between the diameter of droplets in which any of the three additives was dissolved, from which we concluded that

they did not significantly change surface tension. Previous measurements of the effects of these additives on the surface tension of water [17,18] confirm that they have little influence at low concentrations.

Evaporation of droplets deposited on the hot surface was recorded using a video camera, and evaporation time for each droplet measured using a video timer. The resolution of our measurements was 33 ms, corresponding to the 30 frames per second recording rate of the video camera. Droplet diameter and liquid-solid contact angle during evaporation was measured by importing video images into a computer-based image analysis package. The resolution of our measurement was restricted to the size of a single pixel of the video image, which, at the magnification used in our experiments, was $\pm 0.02 \text{ mm}$. Impacting droplets were photographed by using either a 35 mm camera or a digital still camera to take a single flash photograph of an impacting droplet. By varying the time between the droplet landing on the surface and triggering the flash, different stages of droplet impact could be recorded. The impact process was repeatable enough that we

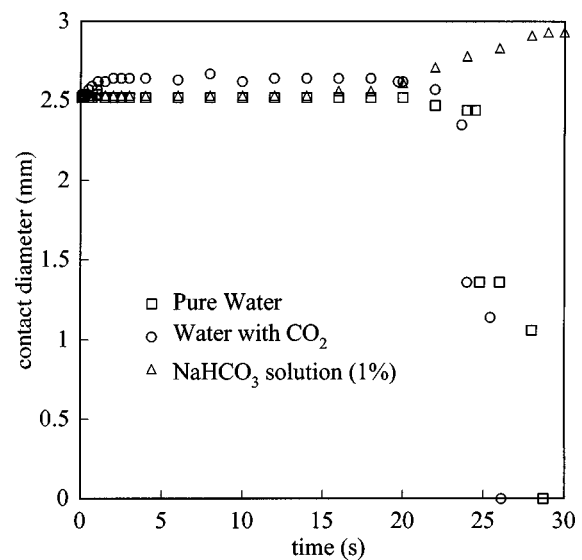


Fig. 3 Variation of liquid-solid contact diameter with time during evaporation of droplets on a stainless steel surface at 100°C

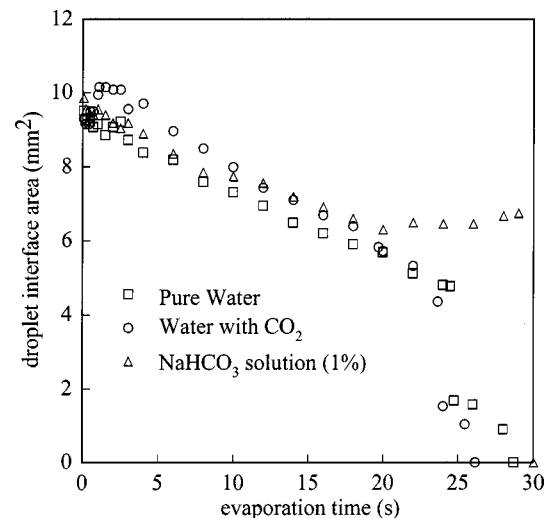


Fig. 4 Variation of droplet-air interface area during evaporation of droplets on a stainless steel surface at 100°C

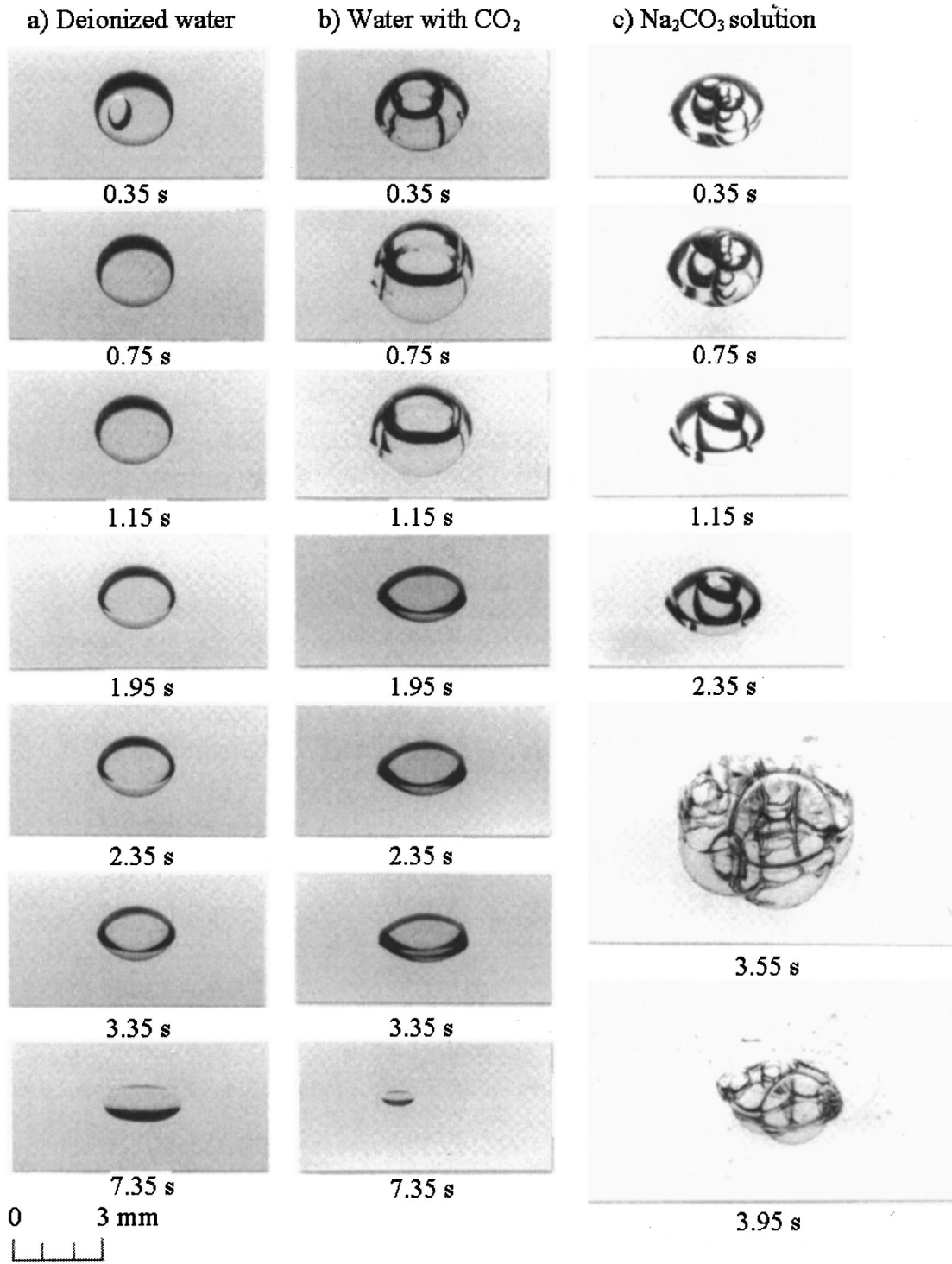


Fig. 5 Boiling of droplets on a hot surface at 130°C: (a) pure water; (b) water containing dissolved CO₂; (c) 1 percent by weight solution of Na₂CO₃

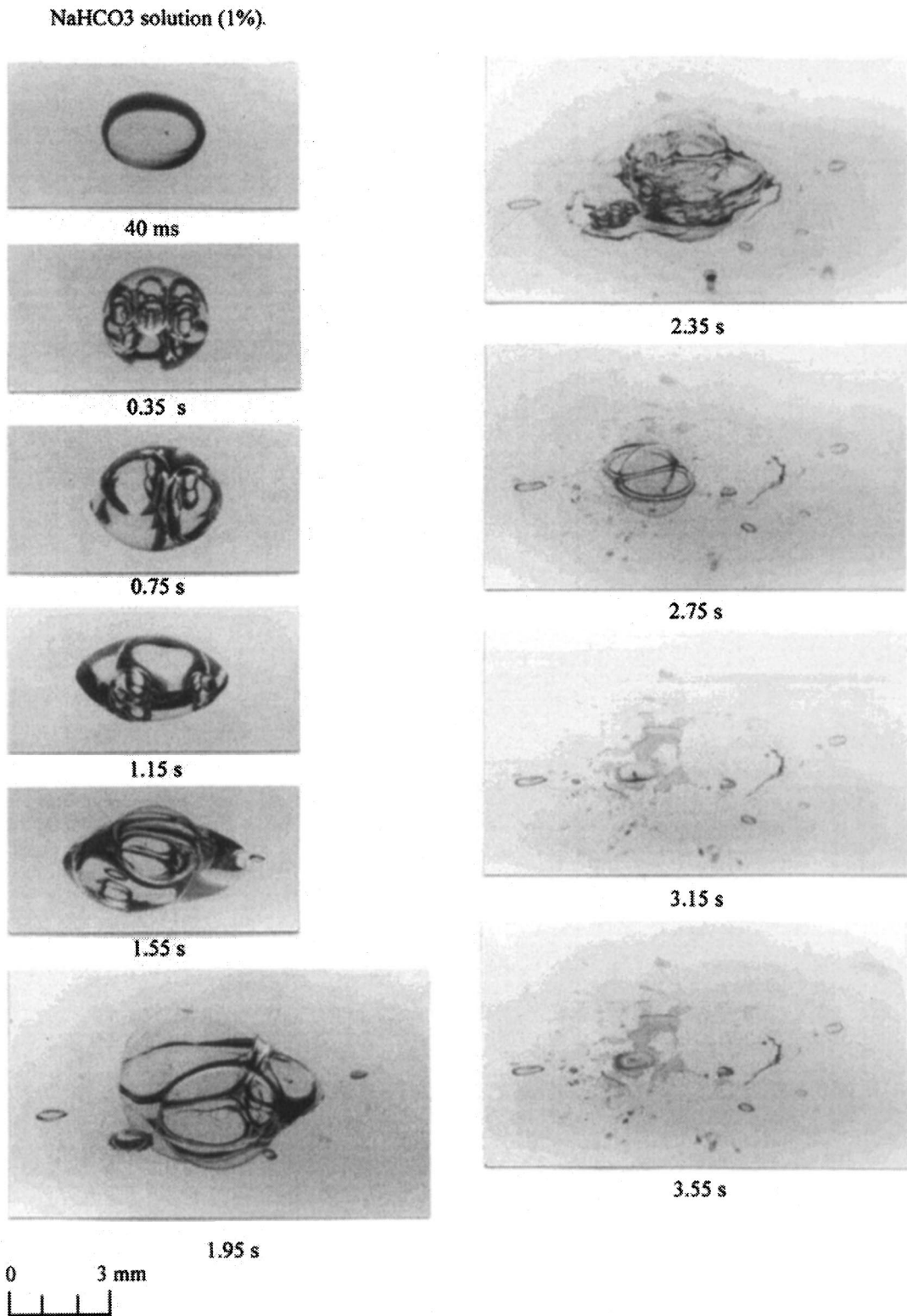


Fig. 6 Boiling of 1 percent by weight solution of NaHCO₃ droplets on a hot surface at 130°C

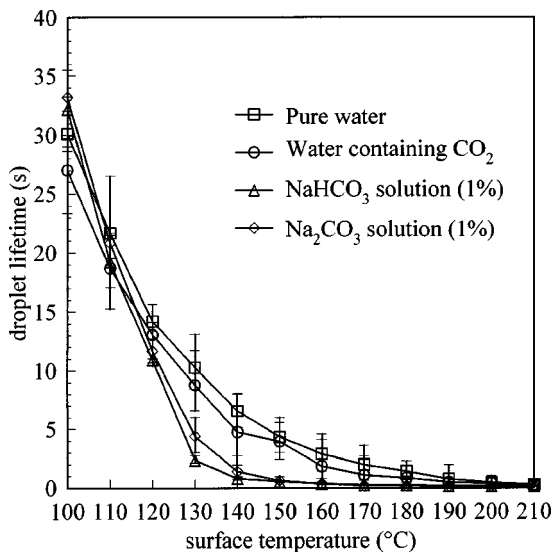


Fig. 7 Variation of droplet lifetime for droplets deposited on a stainless steel surface at temperatures ranging from 100°C to 210°C

could reconstruct droplet impact dynamics from a sequence of such photographs. Qiao and Chandra [3,4] have described the method in greater detail.

Results and Discussion

When water droplets were deposited on a stainless steel plate at a temperature below 120°C, the surface temperature was not high enough to trigger bubble nucleation and droplets evaporated without initiating nucleate boiling. Figure 2 shows photographs of water droplets, and those containing the three different additives used in our experiments, evaporating on a surface at 100°C. Each column in Fig. 2 shows successive stages during the droplet lifetime. Each row of photographs shows droplets photographed at the same time (t), measured from the instant of droplet impact on the surface. The time t in s is indicated to the left of each row.

A small air bubble was trapped at the center of a water droplet when it landed on the surface (see Fig. 2(a), $t=0.75$ s). The bubble grew larger as the droplet evaporated. Measurements from photographs showed that as the volume of liquid diminished, the liquid-solid contact angle decreased while the contact area between the droplet and substrate remained constant. Eventually, when the contact angle reached a lower limit, equal to the receding contact angle (measured by Qiao and Chandra [4] to be approximately 10 deg), the contact diameter began to decrease rapidly until the droplet disappeared. We measured the evolution of contact diameter during droplet evaporation with the results shown in Fig. 3. The contact diameter of pure water droplets was constant for $t < 20$ s, after which it decreased rapidly. We also calculated the surface area of the droplet exposed to air (from which liquid evaporated) by measuring the droplet height and diameter and assuming it to be a segment of a sphere. The variation of droplet surface area is shown in Fig. 4, and a steady decrease in area is evident as the droplet evaporates. The rate at which the surface area diminished increased towards the end of the droplet lifetime ($t > 20$ s) when the contact diameter began to shrink.

Dissolving CO₂ in a water droplet placed on a surface at 100°C slightly reduced its evaporation time (see Fig. 2(b)). Inspection of videotapes of evaporating droplets showed that several vapor bubbles nucleated within the drop immediately after it was deposited on the surface. These rapidly merged with each other, so that by $t=0.75$ s (the first frame in Fig. 2) there remained a single large bubble. The solubility of CO₂ decreases with rising temperature and gas escaping from solution made the bubble much larger

than that in a drop of pure water. The bubble produced little change in the contact diameter (Fig. 3), though it did increase the droplet surface area exposed to air (see Fig. 4, $0 < t < 5$ s). The increased area for evaporation produced a small decrease in droplet lifetime. The effect is not very significant because, as shown by computer simulations [1,2], most heat transfer to an evaporating droplet occurs around its edge where the substrate is hottest and the liquid film is thinnest. Therefore the length of its periphery, rather than surface area, principally determines droplet evaporation time.

Addition of Na₂CO₃ or NaHCO₃ to water droplets placed on a surface at 100°C led to an increase in their lifetime (Fig. 2(c) and (d)), in agreement with the findings of King et al. [7]. Dissolving a salt in water is known to reduce its vapor pressure. The magnitude of this effect can be calculated using the method described by Cisternas et al. [19]. We estimated that the reduction of vapor pressure is small for dilute solutions: dissolving 1 percent by weight of NaHCO₃ reduces the vapor pressure to 100 kPa at 100°C, only slightly lower than that of pure water (101 kPa). However, as the droplet evaporated and its salt concentration increased, the lowering in vapor pressure would become more pronounced. The decrease of vapor pressure would diminish the rate of mass transfer from the droplet surface and increase droplet evaporation time.

As the droplets of salt solution became smaller salt crystals precipitated along their edges, where the evaporation rate was highest (see Fig. 2(c) and (d) at $t=31.55$ s). The ring of salt prevented inward movement of liquid at the edges of the droplets (see Fig. 2(c) and (d), $t=31.55$ s). In fact droplets spread out slightly towards the end of their life, as is evident in both photographs (see Fig. 2(c) and (d) at $t=26.55$ s) and our measurements of droplet diameter. Figure 3 shows that droplet contact diameter remained constant for droplets that had NaHCO₃ dissolved in them, whereas droplets of pure water and those containing CO₂ shrank rapidly towards the end of their lifetime ($t > 20$ s). The salt stain left after all the water had evaporated was in the form of a circle along which there were regularly spaced fingers, perhaps created by a surface tension driven instability [20].

Increasing the surface temperature to 130°C led to the formation of vapor bubbles in droplets deposited on the surface and the onset of nucleate boiling. Figure 5 shows photographs of pure water droplets (Fig. 5(a)) and droplets containing dissolved CO₂ droplets (Fig. 5(b)) and Na₂CO₃ droplets (Fig. 5(c)) on a surface at 130°C. By examining the video record of droplet evaporation it was evident that a number of small bubbles nucleated inside the droplets immediately after impact, formed in cavities on the heater surface. However, for both pure water droplets and those with dissolved CO₂ these bubbles rapidly coalesced, so that by $t=0.35$ s (the first frame in Fig. 5) only one large bubble was evident. This bubble grew larger as the droplet evaporated, until it finally broke through the droplet surface. No more bubbles were produced in the droplet; heat loss to the liquid cooled the stainless steel substrate too much to support further nucleation. Dissolving CO₂ in the droplet increased the number of bubbles nucleated immediately after impact, and they coalesced to produce a large bubble. The bubble grew as CO₂ came out of solution and increased the droplet diameter. Droplet lifetime was therefore slightly reduced.

Dissolved Na₂CO₃ had two significant effects on nucleate boiling of a water droplet (Figure 5(c)). First, the bubbles that formed immediately after the droplet was deposited did not coalesce (see Figure 5(c), $t=0.35$ s). Second, at approximately $t=3$ s, a large number of new vapor bubbles nucleated. These also did not combine, but grew larger, greatly expanding the droplet diameter. The bubbles burst, reducing the droplet lifetime by almost half compared to that for pure water.

The ability of dissolved salts to prevent coalescence of vapor bubbles has been well documented (e.g., [21–24]). The merging of two bubbles is inhibited if the liquid film between them is

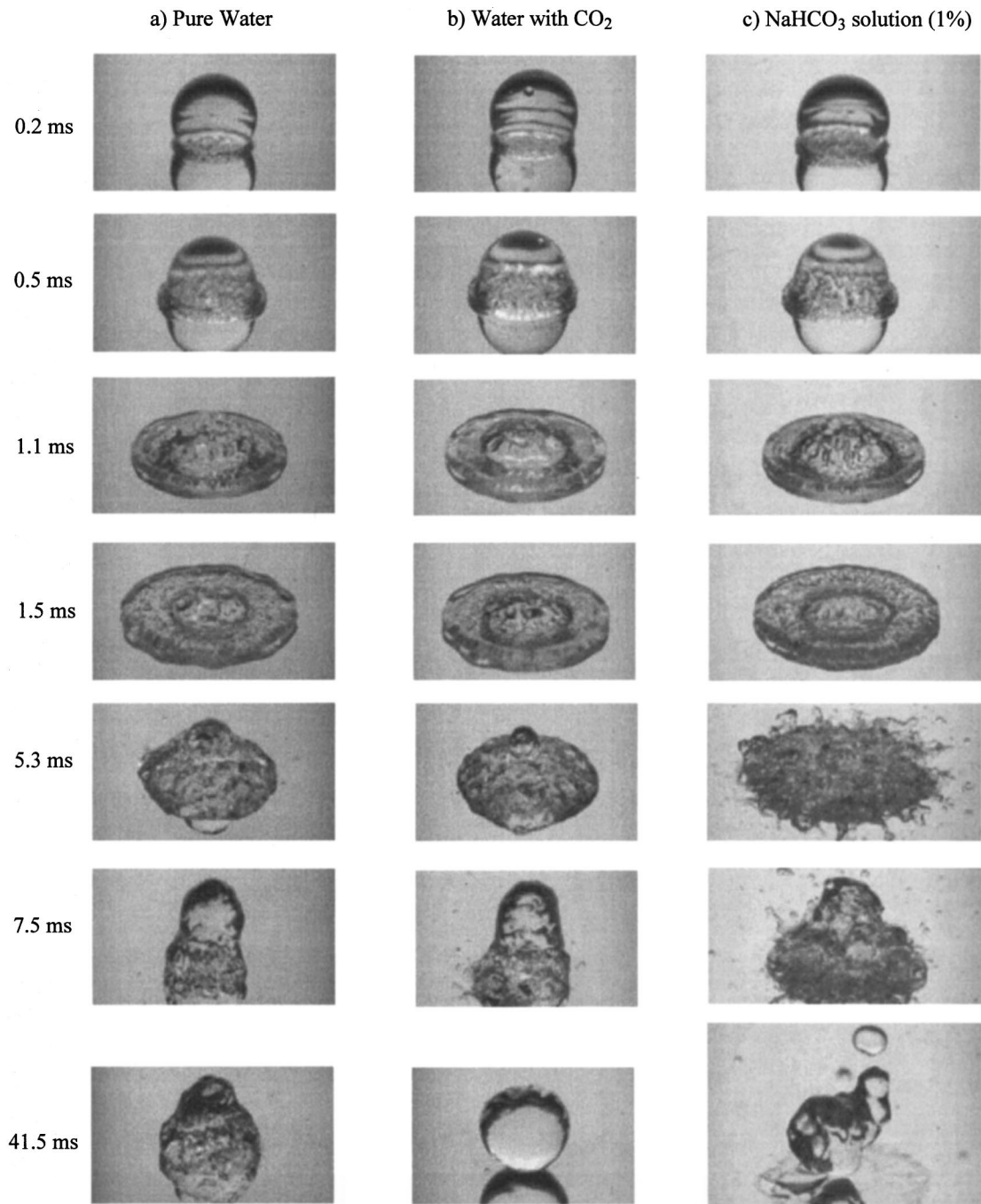


Fig. 8 Impact of droplets on a surface at 220°C: (a) pure water; (b) water containing dissolved CO₂; and (c) 1 percent by weight solution of NaHCO₃

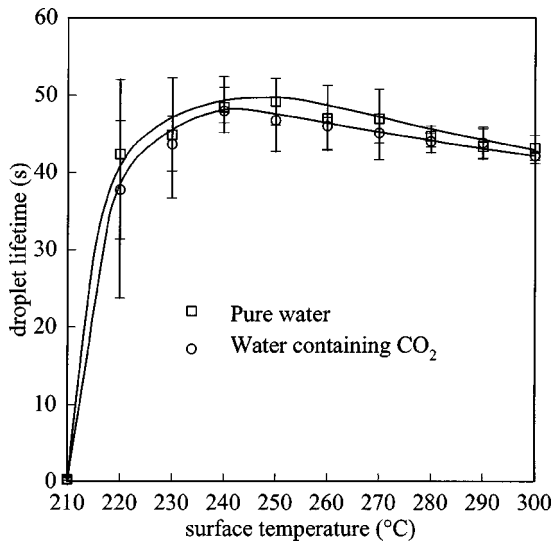


Fig. 9 Variation of droplet lifetime for droplets deposited on a stainless steel surface at temperatures ranging from 210°C to 300°C

stabilized. Surfactants achieve this by altering the surface tension of the liquid. Qiao and Chandra [4] demonstrated that adding a surfactant to water droplets boiling on a hot surface prevents bubble coalescence, making the liquid foam and greatly reducing droplet lifetime. It is unlikely that inorganic salts change surface tension enough to produce foaming [21]. Using published data for the surface tension and viscosity of Na_2CO_3 and NaHCO_3 solutions we concluded that adding 1 percent by weight of solute would produce a negligible change in both surface tension and viscosity. The ability of salts to prevent coalescence is linked to their ionic strength: electric charge accumulated on the surfaces of bubbles produces a repulsive force, preventing them from approaching each other [24]. There is also a more complex effect, in which dissolved electrolytes strengthen the electrostatic bonds between water molecules and make the liquid film separating bubbles stronger [23].

The sudden nucleation of bubbles in the droplets of Na_2CO_3 solution fragmented them and produced a large decrease in droplet lifetime (see Fig. 5(c) at $t=3.55$ s). We believe that this was caused by salt particles precipitating from the evaporating droplet, which serve as nuclei to trigger bubble formation. The particles were too small to observe directly, but to test our hypothesis, we sprinkled a few salt particles on the hot surface before a droplet was deposited on it. These produced instantaneous nucleation of bubbles in water droplets dropped on them.

The boiling rate of water droplets in nucleate boiling was increased by a small amount by dissolving CO_2 in them, and by a much larger amount by dissolving Na_2CO_3 . Though dissolved CO_2 increased the number of vapor bubbles nucleated, they quickly merged. Dissolved Na_2CO_3 , which prevented bubble coalescence, had a much larger effect on droplet lifetime. We therefore expected that a combination of the two additives, in which CO_2 enhanced bubble production and Na_2CO_3 prevented their merger, would reduce droplet lifetimes even further. To achieve this combined effect we selected sodium bicarbonate (NaHCO_3) as an additive, because it decomposes into Na_2CO_3 and CO_2 at high temperatures: $2\text{NaHCO}_3 \rightarrow \text{Na}_2\text{CO}_3 + \text{H}_2\text{O} + \text{CO}_2$. We estimated the decomposition rate of NaHCO_3 using kinetic data from the literature [25], and calculated that approximately 10 percent of the NaHCO_3 in a 1 percent by weight aqueous solution decomposes during the droplet lifetime. This would produce about 10 percent of the mass of CO_2 that was dissolved in pure water during our previous tests, i.e., 0.07 mm^3 of CO_2/mm^3 water at STP.

The boiling of a droplet of 1 percent by weight solution of NaHCO_3 is shown in Fig. 6. A larger number of bubbles were visible in the droplet soon after impact (Fig. 6, $t=0.35$ s), probably because of CO_2 released by decomposition of NaHCO_3 . These did not coalesce, but grew larger. The abrupt nucleation of more bubbles was again observed at approximately $t=1.2$ s, much earlier than for droplets in which Na_2CO_3 was dissolved. The bubbles disrupted the droplet so that it evaporated in approximately 3 s. As expected, NaHCO_3 reduced the droplet lifetime more than either CO_2 or Na_2CO_3 alone.

Our measurements of droplet lifetime on surfaces at temperatures (T_w) ranging from 100°C to 210°C are shown in Fig. 7. Each data point represents the average of five measured values with error bars marking the highest and lowest measured values. To summarize our findings, at a low surface temperature ($T_w=100^\circ\text{C}$), CO_2 reduced the droplet lifetime slightly, while the two salts increased it. At higher temperatures ($T_w>120^\circ\text{C}$) both salts produced a large reduction in droplet lifetime, NaHCO_3 having a larger effect than Na_2CO_3 .

Droplets dropped on a surface at a temperature higher than 210°C went into a state of transition boiling. Water droplets evaporated so rapidly that the pressure of vapor generated at the liquid-solid interface was sufficient to lift them off the surface. Figure 8 shows three sequences of photographs of the impact and recoil of droplets of water (Fig. 8(a)), water with dissolved CO_2 (Fig. 8(b)), and NaHCO_3 solution (Fig. 8(c)), on a surface at 220°C. Since Na_2CO_3 had an effect similar to that of NaHCO_3 , a separate set of photographs for Na_2CO_3 solution droplets is not shown. Dissolved CO_2 had no significant effect on droplet behavior. However NaHCO_3 solution droplets had a visibly larger number of bubbles in them (see Fig. 8, $t=1.1$ ms) whose coalescence was inhibited by the salt. Bubbles bursting out of the liquid made the droplet disintegrate ($t=5.3$ ms).

To record the evaporation time of droplets on surfaces with $T_w>210^\circ\text{C}$, they were dropped on a stainless steel plate machined to make the upper surface slightly concave, which prevented droplets from rolling off. Measured droplet lifetimes for $210^\circ\text{C} \leq T_w \leq 300^\circ\text{C}$ are shown in Fig. 9. Data for the two salt solutions is not shown, since the droplets shattered during impact, and it was not possible to define a meaningful droplet lifetime. There was little difference in measurement for pure water droplets and those with dissolved CO_2 . Droplet lifetimes increased with substrate temperature for $210^\circ\text{C} \leq T_w \leq 240^\circ\text{C}$. The surface temperature corresponding to the maximum droplet lifetime is known as the ‘Leidenfrost temperature’ [3,4]. Above this droplets are fully levitated on a thin film of their own vapor, and are in a state of stable film boiling. Droplet lifetimes then decrease with further increases of temperature.

Figure 10 shows photographs of droplets landing on a surface at 300°C. Droplets containing CO_2 had far fewer bubbles than those of pure water (see Fig. 10, $t=1.5$ ms). Vapor bubbles are formed by heterogeneous nucleation when liquid touches the solid surface. When a droplet approached the heated plate, dissolved CO_2 quickly escapes from the bulk liquid since the solubility of CO_2 decreases sharply with increasing water temperature. Gas emerging from under the droplet would form a film that prevents liquid from contacting the hot substrate, suppressing nucleation. Jeschar et al. [13] have also noted that dissolved gas makes the vapor film formed around a heated sphere immersed in water more stable. On the other hand NaHCO_3 promoted bubble nucleation, which was vigorous enough to fragment the droplet (Fig. 10(c), $t=7.5$ ms).

Conclusions

We observed the effects of dissolving either a gas (CO_2) or a salt (Na_2CO_3 or NaHCO_3), in water droplets impinging on a heated surface. At surface temperatures too low to initiate nucleate boiling it was found that droplet lifetime was determined by heat and mass transfer around the periphery of the droplet. Dissolved NaHCO_3 and Na_2CO_3 both reduced droplet evaporation

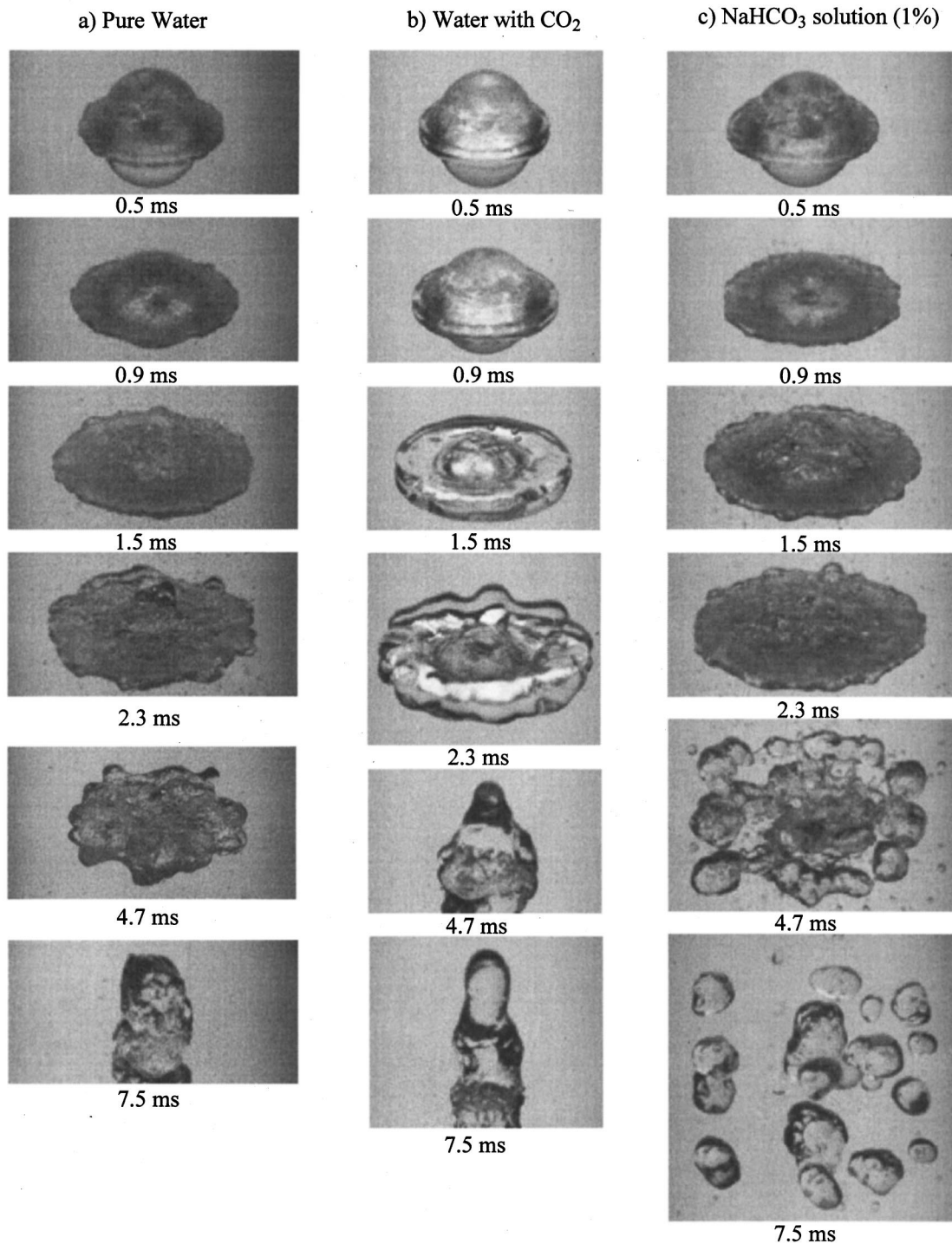


Fig. 10 Impact of droplets on a surface at 300°C: (a) pure water; (b) water containing dissolved CO₂; and (c) 1 percent by weight solution of NaHCO₃

rates since they lower the vapor pressure of water. Dissolved CO₂ enhanced the evaporation rate slightly, because the gas bubble trapped in the droplet made it swell and increased its circumference. In the nucleate boiling regime, Na₂CO₃ prevented coalescence of bubbles in the liquid and promoted foaming, reducing droplet lifetimes. Salt particles precipitated from the solution during evaporation also triggered vapor nucleation. Dissolved NaHCO₃ reduced droplet lifetimes even more than Na₂CO₃, because it decomposed when heated to produce CO₂, further augmenting bubble formation. When a droplet was deposited on a surface above the Leidenfrost temperature, dissolved CO₂ escaped

from below the drop and prevented it touching the substrate, suppressing heterogeneous nucleation. Conversely, both salts promoted bubble nucleation and foaming so vigorously that droplets disintegrated upon impact.

References

- [1] di Marzo, M., Evans, D. D., 1989, "Evaporation of Water Droplet Deposited on a Hot High Thermal Conductivity Solid Surface," *ASME J. Heat Transfer*, **111**, pp. 210–213.
- [2] Chandra, S., di Marzo, M., Qiao, Y. M., and Tartarini, P., 1996, "Effect of

- Liquid-Solid Contact Angle on Droplet Evaporation," *Fire Saf. J.*, **27**, pp. 141–158.
- [3] Qiao, Y. M., and Chandra, S., 1996, "Boiling of Droplets on a Hot Surface in Low Gravity," *Int. J. Heat Mass Transf.*, **39**, No. 7, pp. 1379–1393.
- [4] Qiao, Y. M., and Chandra, S., 1997, "Experiments on Adding a Surfactant to Water Drops Boiling on a Hot Surface," *Proc. Phys. Soc., London, Sect. A*, **453**, pp. 673–689.
- [5] Qiao, Y. M., and Chandra, S., 1998, "Spray Cooling Enhancement by Addition of a Surfactant," *ASME J. Heat Transfer*, **120**, pp. 92–98.
- [6] Finnerty, A. E., 1995, "Water-Based Fire-Extinguishing Agents," *Proceedings of Halon Options Technical Working Conference*, pp. 461–471.
- [7] King, M. D., Yang, J. C., Chien, W. S., and Grosshandler, W. L., 1997, "Evaporation of a Small Water Droplet Containing an Additive," *Proceedings of the 22nd National Heat Transfer Conference*, **4**, Baltimore, MD, pp. 45–57.
- [8] Jamialahmadi, M., and Muller-Steinhagen, H., 1990, "Pool Boiling Heat Transfer to Electrolyte Solutions," *Chem. Eng. Process.*, **28**, pp. 79–88.
- [9] Najibi, S. H., Muller-Steinhagen, H., and Jamialahmadi, M., 1996, "Boiling and Non-Boiling Heat Transfer to Electrolyte Solutions," *Heat Transfer Eng.*, **17**, No. 40, pp. 46–63.
- [10] Muller-Steinhagen, H., Epstein, N., and Watkinson, A. P., 1987, "Subcooled Boiling of Heptane and of Water with Various Dissolved Gases," *Proceedings of 1987 ASME-JSME Thermal Engineering Joint Conference*, pp. 125–131.
- [11] Torikai, K., Shimamune, H., and Fujishiro, T., 1970, "The Effects of Dissolved Gas Content Upon Incipient Boiling Superheats," *Proceedings of 4th International Heat Transfer Conference*, **V**, pp. B2.11.
- [12] You, S. M., Simon, T. W., Bar-Cohen, A., and Hong, Y. S., 1995, "Effects of Dissolved Gas Content on Pool Boiling of a Highly Wetting Fluid," *ASME J. Heat Transfer*, **117**, pp. 687–692.
- [13] Jeschar, R., Kraushaar, H., and Griebel, H., 1996, "Influence of Gases Dissolved in Cooling Water on Heat Transfer During Stable Film Boiling," *Steel Res.*, **67**, No. 6, pp. 227–234.
- [14] Stephen, H., and Stephen, T., 1963, "Solubilities of Inorganic and Organic Compounds," *Binary Systems*, Part 1, **1** Pergamon Press, New York, pp. 115–116.
- [15] Van Slyke, D. D., and Neill, J. M., 1924, "The Determination of Gases in Blood and Other Solutions by Vacuum Extraction and Manometric Measurement-I," *J. Biol. Chem.*, **61**, pp. 523–573.
- [16] Fogg, P. G. T., and Gerrard, W., 1991, "Solubility of Gases in Liquids: A Critical Evaluation of Gas/Liquid Systems in Theory and Practice," Chichester, Wiley, New York.
- [17] Jho, C., Nealon, D., Shogbola, S., and King, Jr., A. D., 1977, "Effect of Pressure on the Surface Tension and Water: Adsorption of Hydrocarbon Gases and Carbon Dioxide on Water at Temperatures Between 0 and 50°C," *J. Colloid Interface Sci.*, **65**, No. 1, pp. 141–154.
- [18] *International Critical Table*, 1933, Vol. II and V, McGraw-Hill, New York.
- [19] Cisternas, L. A., and Lam, E. J., 1991, "An Analytic Correlation for the Vapor Pressure of Aqueous and Non-Aqueous Solutions of Single and Mixed Electrolytes, Part II. Application and Extension Fluid Phase Equilibria," **62**, pp. 11–27.
- [20] Zhang, N., Wang, B. X., and Xu, Y., 1987, "Thermal Instability of Evaporating Droplets on a Flat Plate and Its Effects on Evaporation Rate," *Int. J. Heat Mass Transf.*, **30**, No. 3, pp. 469–478.
- [21] Marrucci, G., and Nicodemo, L., 1967, "Coalescence of Gas Bubbles in Aqueous Solution of Inorganic Electrolytes," *Chem. Eng. Sci.*, **22**, pp. 1257–1265.
- [22] Lessard, R. R., and Zieminski, S. A., 1971, "Bubble Coalescence and Gas Transfer in Aqueous Electrolytic Solutions," *Ind. Eng. Chem. Fundam.*, **10**, No. 2, pp. 260–269.
- [23] Zieminski, S. A., and Whittemore, R. C., 1971, "Behavior of Gas Bubbles in Aqueous Electrolyte Solutions," *Chem. Eng. Sci.*, **26**, pp. 509–520.
- [24] Keitel, G., and Onken, U., 1982, "Inhibition of Bubble Coalescence by Solutes in Air/Water Dispersions," *Chem. Eng. Sci.*, **17**, pp. 1635–1638.
- [25] Hu, W., Smith, J. M., Dogu, T., Dogu, G., 1986, "Kinetics of Sodium Bicarbonate Decomposition," *AIChE J.*, **32**, No. 9, pp. 1483–1490.

Interface Shape and Thermally-Driven Convection in Vertical Bridgman Growth of Gallium Selenide: A Semiconductor With Anisotropic Solid-Phase Thermal Conductivity

Hanjie Lee

Postdoctoral Research Associate
e-mail: hanjie@ajphp1.me.uiuc.edu

Arne J. Pearlstein

Professor of Mechanical Engineering
e-mail: ajp@uiuc.edu
Mem. ASME

Department of Mechanical and Industrial
Engineering,
University of Illinois at Urbana-Champaign,
1206 West Green Street,
Urbana, IL 61801

For vertical Bridgman growth of thermally anisotropic semiconductors, we present a detailed model accounting for heat transfer, flow driven by thermal buoyancy and solidification shrinkage, and interface deformation. The model allows for anisotropic solid-phase thermal conductivity, characteristic of nonlinear optical materials, as well as conduction in the ampoule wall, and conduction and convection in the liquid. The interface shape is determined as part of the solution of a moving boundary problem. For the nonlinear optical material gallium selenide and a range of growth conditions of practical interest, we present steady axisymmetric computations of the isotherms, flow, and interface shape. For ampoule-wall temperature profiles typical of three-zone Bridgman furnaces, the strength of the flow and deflection of the interface increase considerably with increasing growth rate, while the temperature distribution is relatively insensitive, except near the interface. Interface deflection decreases as the maximum ampoule-wall temperature gradient increases. The flow depends significantly on whether the melting temperature is “centered” between the high and low temperatures. The 23°C uncertainty in the melting temperature of GaSe is shown to have little effect on the flow and interface shape over the entire range of growth conditions. We show that properly accounting for thermal anisotropy is critical to predicting the flow and interface shape, both of which are relatively insensitive to the temperature dependence of the viscosity and thermal conductivities. We also show that localized heating along the ampoule wall can both reverse the direction of flow along the interface, which is expected to significantly influence distribution of dopants or impurities in the solid phase, as well as reduce interfacial curvature. When GaSe is grown under zero gravity conditions, the only flow is due to solidification shrinkage, and is essentially normal to the interface, whose shape is similar to those computed at normal gravity. Comparison of results for GaSe to previous work for benzene, a surrogate for organic nonlinear optical materials, shows that the qualitatively different results are associated with differences in the anisotropy of the thermal conductivity. [DOI: 10.1115/1.1372194]

Keywords: Crystal Growth, Microgravity, Solidification

1 Introduction

Crystals of nonlinear optical materials have anisotropic optical and electro-optical properties. In many cases, the solid-phase thermal conductivity and thermal expansivity are also anisotropic, and can have important effects on crystal growth. First, anisotropy of the solid-phase conductivity can significantly affect heat transfer from the liquid to solid, as well as removal of latent heat liberated at the liquid/solid interface, thereby affecting interface shape and liquid flow. Second, anisotropic thermal expansion (or contraction [1]) can lead to development of either cracks that degrade crystal quality [1–3], or gaps between the growing boule and the ampoule wall into which impurity- or dopant-enriched liquid can infiltrate and solidify [4].

The importance of vertical Bridgman growth of anisotropic op-

tical, magnetic, and other materials has been discussed elsewhere [5]. Reference [5] also reviews previous work on directional solidification in which thermal anisotropy has been considered, including experiments by Gau and Viskanta [6] in horizontal plane layers of apparently quiescent fluid heated from below, and computations by Weaver and Viskanta [7] in which heat transfer occurs only by conduction. (Conduction calculations by Huang, Elwell, and Feigelson [8] for CdGeAs₂, a nonlinear optical material whose solid-phase thermal conductivity is thought to be anisotropic on the basis of its crystal structure, do not account for flow, latent heat, or crystal growth.)

We have recently reported [5,9] the first numerical simulations of vertical Bridgman growth of benzene, a thermally anisotropic material, with thermophysical properties similar to those of most organic nonlinear optical materials for which property data is available. The results of those calculations are consistent with the work of Huang et al. [8] in that they show that solid-phase conductivity anisotropy plays an important role in determining inter-

Contributed by the Heat Transfer Division for publication in the JOURNAL OF HEAT TRANSFER. Manuscript received by the Heat Transfer Division August 29, 2000; revision received February 2, 2001. Associate Editor: C. Beckermann.

Table 1 Dimensionless property value ratios

Material	$k_{zz,s}/k_{rr,s}$ ^a	$k_{zz,s}/k_l^a$	$Pr = \nu/k_l$	$\rho_s/\rho_l - 1$ ^b	Source
GaSe	0.123 ^b	0.484 ^b	2.8 ^b	0.024	present work
benzene	2.2	4.8	8.5 ^b	0.132	5
CdGeAs ₂	0.1-3 ^c	0.1-3 ^c	no flow	not applicable	8
Ge	1	0.436	0.007	0	19
Hg _{0.8} Cd _{0.2} Te	1	0.148	0.11	0.01	21
CdTe	1	0.836	0.406	0	23

^a values of $k_{zz,s}$ and $k_{rr,s}$ are those adopted in the axial and radial directions in this and previous simulations. For GaSe with the c axis aligned with the ampoule axis, $k_{zz,s} = k_c$ and $k_{rr,s} = k_l$.

^b evaluated at the melting temperature (937 °C for GaSe)

^c liquid conductivity and conductivity tensor for solid unknown; ranges provided in [8]

face shape. Depending on growth conditions, qualitatively different interface shapes are found, including shapes for which neither the liquid nor solid region is convex¹.

Gallium monoselenide (GaSe) is a nonlinear optical material whose large nonlinear susceptibility and birefringence, transparency over the wavelength range 0.65–18 μm , and relatively high thermal conductivity perpendicular to the preferred optical axis make it attractive in a number of frequency conversion applications [11–12]. Reviews of the properties, growth, and characterization of GaSe are available [13–16]. Vertical Bridgman growth is the dominant [14] approach used to produce single crystals of GaSe.

Gallium selenide differs significantly in several key respects from benzene [5], and from semiconductors [17–27] for which Bridgman growth has previously been simulated.

First, all known GaSe polytopes consist of hexagonally symmetric layers, leading to isotropy about the c axis [28–29]. Thus, there are exactly two distinct thermal conductivities, both of which have been measured (see §2). For benzene, the crystal structure is orthorhombic bipyramidal [30], and one might expect the thermal conductivity to assume three different values along the principal axes, even though only two have been measured [5]. In all previous simulations of Bridgman solidification of semiconductors, the material has been (or has been taken to be) isotropic. Table 1 shows that the solid-phase thermal conductivity of GaSe is highly anisotropic, with the conductivity along the c axis (parallel to the sixfold symmetry axis) being about one-eighth the conductivity along the orthogonal a and b axes [16,31]. In our work for benzene [5], the ratio of the axial conductivity to the lateral conductivity in the solid was 2.2, whereas for the c axis of GaSe aligned with the growth direction, the corresponding ratio is about 0.12. Thus, we see that radial conduction in the solid will be a much more efficient means to remove heat from the interface (relative to axial conduction) in GaSe than in benzene. Anisotropy and liquid/solid conductivity ratios are expected to strongly influence interface shape (cf. [8]), which in turn is known to affect twinning and other determinants of crystal quality in Bridgman-grown materials [32–33].

Second, beyond its anisotropic solid-phase thermal conductivity, GaSe has liquid- and solid-phase thermophysical properties quite different from those of other semiconductors and benzene, as shown in dimensionless terms in Table 1. The Prandtl number for GaSe (~2.8 at the melting temperature) is smaller than that for benzene by a factor of three, but is more than two orders of magnitude higher than for Ge.

¹In what follows, we use “convex-solid” and “concave-solid” as adjectives to unambiguously describe interfaces bounding convex and concave solid regions, respectively. Use of “convex” and “concave” to modify regions rather than interfaces is consistent with standard topological nomenclature [10], is shorter than “convex to the solid,” etc., and avoids confusion.

Finally, the larger kinematic viscosity of GaSe relative to other molten semiconductors gives rise to a much larger Schmidt number, $Sc = \nu/D$, and considerably thinner concentration boundary layers, critical to distribution of dopants or impurities in the liquid. Thus, accurate computation of the flow and the temperature distribution that drives it will be important in predicting distributions of dopants (e.g., [11,34–39]) and impurities [40–42] in Bridgman-grown GaSe, as well as in doped crystals of other III–VI semiconductors, including InSe [43].

To date, the only computational work on melt growth of GaSe is that described in papers by Singh and co-workers [39,40]. The first [39] presented axial temperature distributions “near the center” of the ampoule at five instants based on a “pure conduction” model apparently accounting for conduction in the GaSe, ampoule, and boron oxide encapsulant, but not for convection in the liquid. It is unclear whether the growth rate was nonzero, since no mention was made of it or the interfacial position or shape. Exclusion of convection was justified by the statement that “the Prandtl number of GaSe is very low,” although no Prandtl number was cited. (As shown in Table 1, the Prandtl number for GaSe at 1000°C is about 2.8, compared to 0.01 for Ge [18] and 0.11 for Hg_{0.8}Cd_{0.2}Te [22].) The second paper [40] presented the “pure conduction” axial temperature profile at one additional time, and for two times showed an apparently axisymmetric interface, whose shape cannot be discerned. The partial differential equations shown included a momentum equation with thermal and solutal Rayleigh numbers in the buoyancy terms, which terms did not depend on temperature or composition. No physical property values were given in either paper.

Here, we focus on temperature distributions, interface shapes, and flow in vertical Bridgman growth of GaSe in quartz ampoules of circular cross-section, used in almost all previous experimental work. The temperature distribution is critical to predicting stress distributions and dislocation formation (cf. [33,44]). The interface shape is shown to be important in understanding and avoiding secondary nucleation and growth in GaSe [14] and other crystals [45], while the flow is important in dopant transport [9,18,19]

2 Model and Numerical Approach

We consider vertical Bridgman growth in a quartz [11,31,38,46–51] ampoule of inner radius r_i , moving downward at velocity $-U\mathbf{e}_z$ on a vertical axis past a fixed temperature distribution $T_b(z)$, which we take to obtain on the outer wall of the ampoule, as shown in Fig. 1. Except in §3.4, we consider the hyperbolic tangent profile

$$T_b(z) = \frac{1}{2} [T_c + T_h + (T_h - T_c) \tanh \lambda z], \quad (1)$$

where the temperatures in the liquid and solid far from the interface, T_h and T_c , respectively, bracket the melting temperature T_M . The ampoule-wall temperature profile (1) is an excellent approximation to those in Bridgman growth experiments (cf. references cited in [5,9] as well as in other experimental and computational [52,53] work), in which an “adiabatic zone” lies between hot and cold constant-temperature zones. Here, $\lambda = 2(dT_b(0)/dz)/(T_h - T_c)$, where $dT_b(0)/dz$ is the maximum axial derivative of the ampoule-wall temperature profile (1). As in previous simulations of Bridgman growth of electronic materials (cf. [23,27,54]), we neglect radiative transfer within the liquid and solid. Assessment of the effect of this approximation on growth of GaSe, which is essentially transparent over most of the infrared, is beyond the scope of the present work.

We consider GaSe growing as a single crystal, with its c axis parallel to the ampoule axis, as in a number of experimental investigations [11,39–41,46]. (Crystals of GaSe can also be grown perpendicular to the c axis [41,46,55].) In that case, the conductivity can be written as $\mathbf{k}_s = k_l \mathbf{e}_r \mathbf{e}_r + k_t \mathbf{e}_\phi \mathbf{e}_\phi + k_c \mathbf{e}_z \mathbf{e}_z$, where k_c and k_t are the conductivities parallel and transverse to the c axis, respectively. We consider the situation in which the temperature

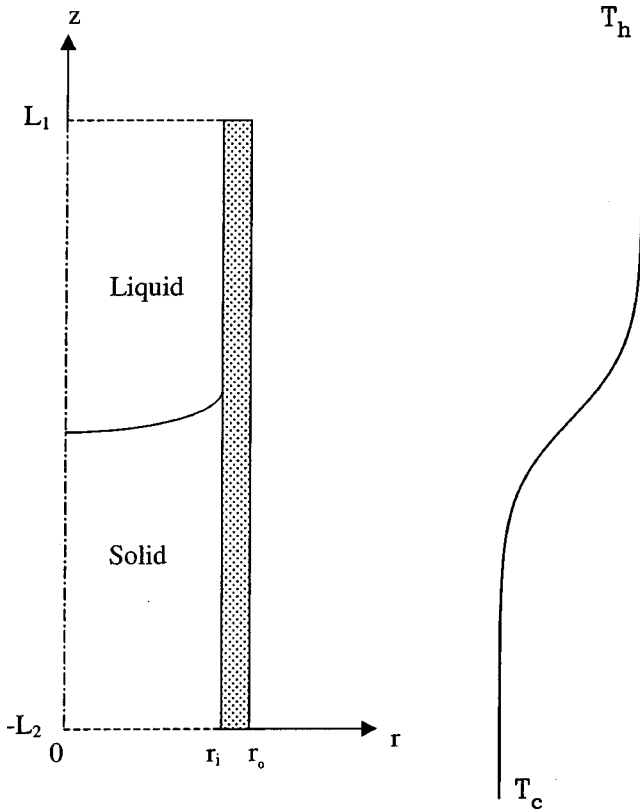


Fig. 1 Schematic of vertical Bridgman growth with imposed ampoule-wall temperature distribution $T_b(z)$

distribution, interface shape, and flow are axisymmetric [27,54], and steady in an interface-fixed reference frame in which the solid and ampoule translate downward at $-U\mathbf{e}_z$. The ampoule is taken to be unbounded in the vertical direction, corresponding to a long boulev grown under steady conditions. The relevance of this growth regime to the production of axially uniform boules has been discussed elsewhere [9,52].

With these assumptions, the dimensionless governing equations for conservation of energy, mass, and momentum are

$$-Pe_{IM} \frac{\kappa_{IM}}{\kappa_a} \frac{\partial \theta_s}{\partial \eta} = \nabla \cdot (\mathbf{b}_s \nabla \theta_s), \quad (2a)$$

$$Pr_M \mathbf{u} \cdot \nabla \theta_l = \nabla \cdot [f_{k,l}(\theta_l) \nabla \theta_l], \quad (2b)$$

$$-Pe_{IM} \frac{\kappa_{IM}}{\kappa_a} \frac{\partial \theta_a}{\partial \eta} = \nabla^2 \theta_a, \quad (2c)$$

$$\nabla \cdot \mathbf{u} = 0, \quad (3)$$

$$\mathbf{u} \cdot \nabla \mathbf{u} = -\nabla \Pi + \nabla \cdot \{f_v(\theta_l) [\nabla \mathbf{u} + (\nabla \mathbf{u})^T]\} + Gr \mathbf{e}_\eta, \quad (4)$$

where the temperature (θ_l , θ_s , and θ_a , in the liquid, solid, and ampoule wall, respectively), relative velocity \mathbf{u} , and cylindrical coordinates (axial η and radial ξ) have been scaled with $\Delta T = T_h - T_c$, ν_M/r_i , and r_i , respectively [5]. We take the specific heats ($c_{p,l}$, $c_{p,s}$, and $c_{p,a}$), ampoule conductivity (k_a), and densities of the solid (ρ_s) and ampoule (ρ_a) to be constant. The liquid density is to be taken to be constant in the inertial term and continuity equation, and to vary linearly with temperature (as amply justified by the data for GaSe [56]) in the body force. The functions $f_v = \nu(T)/\nu_M$ and $f_{k,l} = k_l(T)/k_{IM}$ account for the temperature dependence of the kinematic viscosity and liquid-phase thermal conductivity, respectively, while $\mathbf{b}_s \equiv \mathbf{k}_s/k_{IM}$ is a dimensionless ten-

sor accounting for the temperature dependence of the solid-phase thermal conductivity. The subscript M denotes a property evaluated at the melting temperature.

As in Ref. [5], the temperature dependence of the viscosity is accounted for using an Arrhenius fit to the data. Results presented in §3.3 show that these variable-property effects are small. Aside from the viscosity, liquid- and solid-phase conductivities, and liquid density (*vide supra*), all other thermophysical properties are taken as constant. We account for shrinkage flow due to the difference between the liquid and solid densities. The heat flux singularity associated with the discontinuous thermal conductivity across the liquid/solid interface, and the moving contact singularity associated with shrinkage, both at the liquid/solid/ampoule wall three-phase junction, are discussed in [9].

The Grashof number and liquid-phase Péclet numbers are defined by $Gr = \alpha g r_i^3 \Delta T / \nu_M^2$ and $Pe_{IM} = U r_i / \kappa_{IM}$, respectively. Here, α , g , and U are the thermal expansivity of the liquid, magnitude of the gravitational acceleration, and growth rate, respectively, while $\kappa_{IM} = k_{IM} / (\rho_{IM} c_{p,l})$, $\kappa_{IM} = k_{IM} / (\rho_s c_{p,s})$, and $\kappa_a = k_a / (\rho_a c_{p,a})$ are the thermal diffusivities in the liquid, solid (transverse to the c axis), and ampoule wall.

We assume that on the liquid/solid interface, the deflection $\eta_l(\xi)$ is a single-valued function of the radial coordinate, and that the dimensionless interfacial boundary conditions are

$$\theta_l(\xi, \eta_l(\xi)) = \theta_s(\xi, \eta_l(\xi)) = \theta_M \quad (5a)$$

$$\frac{k_{cM}}{k_{IM}} \frac{\partial \theta_s(\xi, \eta_l(\xi))}{\partial \eta} - \eta'_l(\xi) \frac{\partial \theta_s(\xi, \eta_l(\xi))}{\partial \xi} - \frac{k_{IM}}{k_{IM}} \left[\frac{\partial \theta_l(\xi, \eta_l(\xi))}{\partial \eta} - \eta'_l(\xi) \frac{\partial \theta_l(\xi, \eta_l(\xi))}{\partial \xi} \right] = \frac{\kappa_{IM}}{\kappa_{IM}} Pe_{IM} St \quad (5b)$$

$$\mathbf{e}_n \cdot \mathbf{u}(\xi, \eta_l(\xi)) = -\frac{Pe_{IM}}{Pr} \frac{1}{\sqrt{1 + \eta'_l(\xi)^2}} \frac{\rho_s}{\rho_{IM}}, \quad (5c)$$

$$\mathbf{e}_s \cdot \mathbf{u}(\xi, \eta_l(\xi)) = -\frac{Pe_{IM}}{Pr} \frac{\eta'_l(\xi)}{\sqrt{1 + \eta'_l(\xi)^2}}, \quad (5d)$$

corresponding to an isothermal interface at T_M , conservation of energy, conservation of mass, and no-slip, respectively. Here, \mathbf{e}_n and \mathbf{e}_s are unit vectors normal and tangential to the interface, respectively, $St = \Delta H_f / (c_{p,s} \Delta T)$ is the Stefan number, and ΔH_f is the heat of fusion.

On the inner wall of the ampoule, we have

$$\theta_l(1, \eta) = \theta_a(1, \eta) \quad (6a)$$

$$\frac{\partial \theta_l(1, \eta)}{\partial \xi} = \frac{k_a}{k_{IM}} \frac{\partial \theta_a(1, \eta)}{\partial \xi} \quad (6b)$$

$$\mathbf{u} = -(Pe_{IM}/Pr_M) \mathbf{e}_\eta \quad (6c)$$

above the liquid/solid/ampoule junction ($\eta > \eta_l(1)$), and

$$\theta_s(1, \eta) = \theta_a(1, \eta) \quad (6d)$$

$$\frac{\partial \theta_s(1, \eta)}{\partial \xi} = \frac{k_a}{k_{IM}} \frac{\partial \theta_a(1, \eta)}{\partial \xi} \quad (6e)$$

below that junction ($\eta < \eta_l(1)$).

On the axis, symmetry and boundedness of the velocity and temperature require

$$\mathbf{e}_\xi \cdot \mathbf{u} = 0 \quad (7a)$$

$$\mathbf{e}_\eta \cdot \mathbf{u} \text{ finite} \quad (7b)$$

$$\frac{\partial \theta_l(0, \eta)}{\partial \xi} = 0 \quad (7c)$$

Table 2 Parameters in terms of which results are presented

$dT_b(0)/dz$	maximum axial temperature gradient in ampoule wall
T_c	cold-end temperature
T_h	hot-end temperature
U	growth velocity
T_M	melting temperature of GaSe
$2r_i$	inner diameter of ampoule
L_1	dimensionless location of far-field liquid boundary, scaled with r_i
L_2	dimensionless location of far-field solid boundary, scaled with r_i

$$\frac{\partial \theta_s(0, \eta)}{\partial \xi} = 0. \quad (7d)$$

In the liquid, solid, and ampoule, the velocity and temperature should approach finite limits far from the interface. These values can be obtained by seeking η -independent solutions of the governing equations (2)–(4) subject to the radial boundary conditions (6), (7)

$$\lim_{\eta \rightarrow \infty} \mathbf{u} = -(Pe_{lM}/Pr_M)[1 + 2(\rho_s/\rho_{lM} - 1)(1 - \xi^2)]\mathbf{e}_\eta \quad (8a)$$

$$\lim_{\eta \rightarrow \infty} \theta_l = 1 \quad (8b)$$

$$\lim_{\eta \rightarrow -\infty} \theta_s = 0 \quad (8c)$$

$$\lim_{\eta \rightarrow \infty} \theta_a = 1 \quad (8d)$$

$$\lim_{\eta \rightarrow -\infty} \theta_a = 0. \quad (8e)$$

For $\rho_s \neq \rho_{lM}$, the far-field flow (8a) corresponds to superposition of the growth velocity and a Poiseuille flow driven by solidification shrinkage.

The model determines the interface shape as part of the solution [9,54], and accounts for latent heat release at the interface, convection in the liquid, conduction in the liquid, solid, and ampoule wall, and anisotropy of the solid-phase thermal conductivity, a ubiquitous property of nonlinear optical materials [5,9].

The computational approach, involving domain decomposition, Chebyshev collocation, and iterative solution of a nonlinear algebraic equation system, is as described for benzene [5], with the exception that a longer computational domain is required, as described below. Compared to benzene, the relatively more vigorous flows in GaSe growth give rise to primary toroidal vortex cells that penetrate considerably farther upward into the liquid, as discussed in §§3 and 4. This requires that the far-field computational boundary for the liquid (L_1 in dimensionless terms [5]) be farther from the interface. This question, and the effects of domain size on convergence, are discussed in §3.

For $r-z$ coordinates, two distinct streamfunction definitions satisfy the continuity equation. We use here the one for which the standard two-dimensional interpretation of “no flow across a streamline” pertains. As in our earlier work for benzene [5,9], all streamlines shown are referred to a frame translating with the ampoule and solid.

For ease of reference, we define in Table 2 the parameters in terms of which results are presented. These quantities and the symbols denoting them are identical to those used for benzene [5]. The property values used are listed in Table 3, along with the sources of data (Refs. [14,31,56–67]).

3 Results

We have computed temperature distributions, interface shapes, and the corresponding thermally-driven flows for several sets of growth conditions.

In most previous simulations of vertical Bridgman growth (cf. [5,18,19]), the high and low temperatures were chosen so that T_M lies midway between. Except where otherwise stated (in §3.2), we also choose the temperatures of the hot and cold zones to “center” T_M . We use $\Delta T = T_h - T_c = 150^\circ\text{C}$, corresponding to the difference between hot- and cold-zone temperatures reported by Singh and co-workers for vertical Bridgman growth of GaSe [39,40]. For this ΔT , temperatures that “center” $T_M = 937^\circ\text{C}$ are $T_h = 1012^\circ\text{C}$, and $T_c = 862^\circ\text{C}$. We refer to these temperatures and a maximum ampoule-wall temperature gradient of $dT_b(0)/dz = 30^\circ\text{C cm}^{-1}$ [39,40,69,70] as the “standard” thermal conditions.

The fused quartz ampoule was taken to have an inner diameter $2r_i = 1$ cm [11,36,41,48,55,70–75] and outer wall thickness of 1 mm.

Resolution convergence was established by increasing the number of radial and axial expansion functions. For $L_1 = 30$ and $L_2 = 15$ (where L_1 and $-L_2$ are the locations of the upper and lower computational boundaries, respectively [5,9]), Table 4 shows that for the “standard case” and $U = 1.0 \mu\text{m sec}^{-1}$, the streamfunction and temperature $\theta_l = [T_l - T_c]/\Delta T$ at six points (axial positions in the primary and secondary vortices; radial positions near the centerline and ampoule wall, and midway between), and the overall interface deflection $\Delta z = [z(r_i) - z(0)]/r_i$, are well converged for $M = 20$ radial and $N = 60$ axial expansion functions.

For $M = 20$ and $N = 60$, we assess domain convergence using domains of varying dimensionless axial extent. We consider the

Table 3 Thermophysical properties of GaSe

Property	Symbol	Value or functional form	Source
melting temperature	T_M	937°C	14,57-60
enthalpy of fusion	ΔH_f	376.65 J g^{-1}	58
thermal expansivity	α_T	$1.287 \times 10^{-4} \text{ }^\circ\text{C}^{-1}$	56 ^a
liquid thermal conductivity	k_l	$(3.168 \times 10^{-3} + 3.243 \times 10^{-5} T/\text{K}) \text{ W cm}^{-1}\text{K}^{-1}$	61 ^a
kinematic viscosity	ν	$4.0237 \times 10^{-4} \exp(3588.64 \text{ K}/T)$	62 ^a
liquid specific heat	$c_{p,l}$	$0.56 \text{ J K}^{-1}\text{g}^{-1}$	63-65 ^b
conductivity along c axis	k_c	$6.09(T/\text{K})^{-1.045} \text{ W cm}^{-1}\text{K}^{-1}$	31 ^a
conductivity \perp to c axis	k_t	$55.58(T/\text{K})^{-1.063} \text{ W cm}^{-1}\text{K}^{-1}$	31 ^a
solid specific heat	$c_{p,s}$	$0.34 \text{ J K}^{-1}\text{g}^{-1}$	66 ^c
ampoule-wall density	ρ_a	2.2 g cm^{-3}	67
ampoule-wall specific heat	$c_{p,a}$	$1.25 \text{ J K}^{-1}\text{g}^{-1}$	67
ampoule-wall conductivity	k_a	$0.026 \text{ W cm}^{-1}\text{K}^{-1}$	67
solid density	ρ_s	4.93 g cm^{-3}	56
liquid density at T_M	ρ_{lM}	4.814 g cm^{-3}	56

^a cited data used to perform least-squares fit

^b computed from specific heats of GaTe, InSe, and InTe using Kopp's law ([68], p. 58)

^c Dulong Petit high-temperature approximation ([68], pp. 53-54), in excellent agreement with high-temperature asymptote [66]

Table 4 Resolution convergence for $dT_b(0)/dz = 30^\circ\text{C cm}^{-1}$, $U = 1.0 \mu\text{m sec}^{-1}$, $L_1 = 30$, $L_2 = 15$

	$M = 20$	$N = 60$	$M = 30$	$N = 60$	$M = 20$	$N = 80$
$\psi(0,1,0.5)$	8.535×10^{-3}		8.535×10^{-3}		8.537×10^{-3}	
$\psi(0,5,0.5)$	4.233×10^{-2}		4.233×10^{-2}		4.232×10^{-2}	
$\psi(0,9,0.5)$	1.273×10^{-2}		1.273×10^{-2}		1.265×10^{-2}	
$\psi(0,1,3,0)$	3.675×10^{-3}		3.674×10^{-3}		3.658×10^{-3}	
$\psi(0,5,3,0)$	2.010×10^{-2}		2.010×10^{-2}		1.999×10^{-2}	
$\psi(0,9,3,0)$	1.004×10^{-2}		1.004×10^{-2}		9.938×10^{-3}	
$\theta_l(0,1,0,5)$	0.5519		0.5519		0.5519	
$\theta_l(0,5,0,5)$	0.5522		0.5522		0.5522	
$\theta_l(0,9,0,5)$	0.5517		0.5517		0.5517	
$\theta_l(0,1,3,0)$	0.7671		0.7671		0.7671	
$\theta_l(0,5,3,0)$	0.7671		0.7671		0.7671	
$\theta_l(0,9,3,0)$	0.7674		0.7674		0.7674	
$\Delta z/r_i$	0.2149		0.2127		0.2159	

Table 5 Domain convergence for $dT_b(0)/dz=30^\circ\text{C cm}^{-1}$, $U=1.0 \mu\text{m sec}^{-1}$, $M=20$, $N=60$, $L_2=L_1/2$

	$L_1=3$	$L_1=7.5$	$L_1=15$	$L_1=30$
$\psi(0.1,0.5)$	8.545×10^{-3}	8.519×10^{-3}	8.536×10^{-3}	8.535×10^{-3}
$\psi(0.5,0.5)$	4.237×10^{-2}	4.224×10^{-2}	4.227×10^{-2}	4.232×10^{-2}
$\psi(0.9,0.5)$	1.250×10^{-2}	1.247×10^{-2}	1.258×10^{-2}	1.273×10^{-2}
$\psi(0.1,3.0)$	0.336×10^{-3}	3.639×10^{-3}	3.667×10^{-3}	3.675×10^{-3}
$\psi(0.5,3.0)$	1.668×10^{-3}	1.984×10^{-2}	2.010×10^{-2}	2.010×10^{-2}
$\psi(0.9,3.0)$	2.964×10^{-3}	9.766×10^{-3}	9.852×10^{-3}	1.004×10^{-2}
$\theta_i(0.1,0.5)$	0.5519	0.5519	0.5518	0.5519
$\theta_i(0.5,0.5)$	0.5522	0.5522	0.5522	0.5522
$\theta_i(0.9,0.5)$	0.5517	0.5517	0.5517	0.5517
$\theta_i(0.1,3.0)$	0.7685	0.7671	0.7671	0.7671
$\theta_i(0.5,3.0)$	0.7685	0.7671	0.7671	0.7671
$\theta_i(0.9,3.0)$	0.7685	0.7674	0.7674	0.7674
$\Delta z/r_i$	0.2156	0.2156	0.2154	0.2149

standard case with $U=1.0 \mu\text{m sec}^{-1}$ and $L_2=L_1/2$ for $3 \leq L_1 \leq 30$ (corresponding to $4.5 \leq L_1+L_2 \leq 45$). This range contrasts to $L_1+L_2=4$ [18] and $L_1 \approx 6$ [19] used for Ge, and $L_1+L_2 \geq 8$ [5] used for benzene. For these growth conditions, Table 5 shows that the interface deflection and liquid temperature are all well converged even for the smallest computational domain. Not surprisingly, convergence of the streamfunction values at $z/r_i=3$ re-

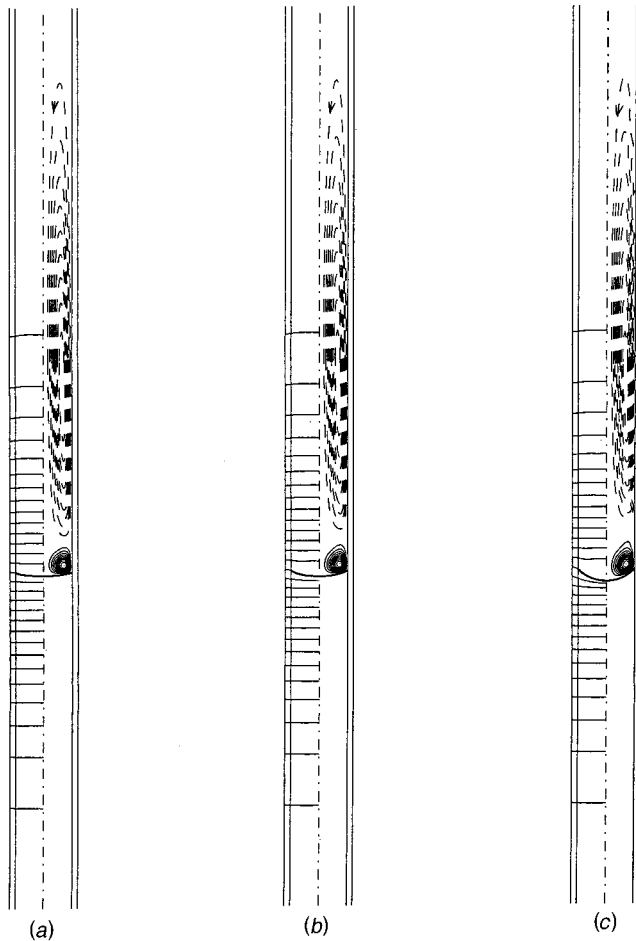


Fig. 2 Isotherms and streamlines for $dT_b(0)/dz=30^\circ\text{C cm}^{-1}$. (a) $U=0.25 \mu\text{m sec}^{-1}$: $\psi_{\min}=-0.0261$, $\psi_{\max}=0.0432$; (b) $U=1.0 \mu\text{m sec}^{-1}$: $\psi_{\min}=-0.0253$, $\psi_{\max}=0.0708$; and (c) $U=3.0 \mu\text{m sec}^{-1}$: $\psi_{\min}=-0.0233$, $\psi_{\max}=0.116$.

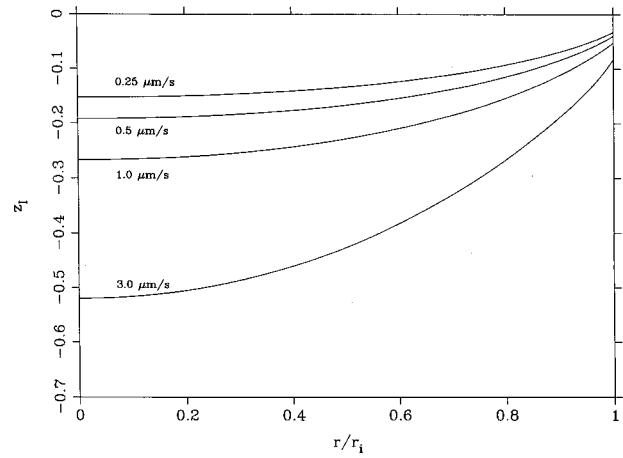


Fig. 3 Interface shapes for $dT_b(0)/dz=30^\circ\text{C cm}^{-1}$. $U=0.25 \mu\text{m sec}^{-1}$, $\Delta z/r_i=0.120$; $U=0.50 \mu\text{m sec}^{-1}$, $\Delta z/r_i=0.152$; $U=1.0 \mu\text{m sec}^{-1}$, $\Delta z/r_i=0.215$; $U=3.0 \mu\text{m sec}^{-1}$, $\Delta z/r_i=0.437$.

quires a larger domain than for $z/r_i=0.5$. At both axial locations, however, the streamfunction is well converged for the two largest domains ($L_i=15$ and 30).

Together, these results demonstrate convergence of the computed solutions.

3.1 Effect of Growth Rate and Maximum Temperature Gradient.

Vertical Bridgman growth of GaSe has been reported at rates between 0.1 and 12 mm hr^{-1} ($0.028 \mu\text{m sec}^{-1} \leq U \leq 3.33 \mu\text{m sec}^{-1}$), for $10^\circ\text{C cm}^{-1} \leq dT_b(0)/dz \leq 80^\circ\text{C cm}^{-1}$ [37–39,41,46–49,55,69,70,72–74,76,77]. After first considering growth rates covering most of the U range for the standard case, we then consider additional values of $dT_b(0)/dz$ covering most of the range studied in previous experiments.

Figures 2(a–c) show isotherms and streamlines for $U=0.25$, 1.0 , and $3.0 \mu\text{m sec}^{-1}$. For these growth rates and $U=0.5 \mu\text{m sec}^{-1}$, Fig. 3 shows the corresponding interface shapes. Figure 2(a) shows that at the lowest U , the thermally-driven buoyant flow consists of two counter-rotating toroidal cells. The upper “primary” vortex extends many diameters into the liquid, while the smaller “secondary” vortex is confined to a region adjacent to the interface. (This nomenclature was adopted in our work on benzene [5], in which sometimes only a single large vortex extending far into the liquid was found.) The thermal Péclet number in the liquid $Pe_{IM} = Ur_i \rho_{IM} c_{p,i} / k_{IM}$ is so small (4.5×10^{-3} , based on the growth rate $U=0.25 \mu\text{m sec}^{-1}$) that the liquid-phase isotherms (Fig. 2(a)) are almost horizontal except near the interface and wall. (In this and all other contour plots, the dashed and solid streamlines shown are at equal increments between ψ_{\min} and 0 , and between 0 and ψ_{\max} , respectively. The isotherms shown are at increments of $\Delta T/30$.) Slight isotherm curvature near the wall reflects thermal boundary layers associated with locally upward and downward flows of the primary and secondary vortices, respectively. The primary vortex (dashed streamlines, corresponding to negative streamfunction values) transports hot fluid down toward the interface along the centerline, while heat released at the interface is conducted down into the solid. Isotherms in the solid are essentially horizontal, i.e., perpendicular to the growth direction. The aspect ratio (L_1+L_2) of the domain required to adequately capture the flow is larger than in our benzene computations, since $[dT_b(0)/dz]/[(T_h-T_c)/r_i]$ is relatively smaller (0.1 for $dT_b(0)/dz=30^\circ\text{C cm}^{-1}$, $\Delta T=150^\circ\text{C}$, and $2r_i=1 \text{ cm}$, with a range of 0.05 – 0.4 for the GaSe cases considered, compared to a range of 0.375 – 3 for benzene [5]). As a consequence, the primary vortex extends much farther up into the liquid. Figure 3 shows that at $U=0.25 \mu\text{m sec}^{-1}$, the interface shape is concave-solid, with maximum deflection $\Delta z/r_i=0.120$ on the centerline.

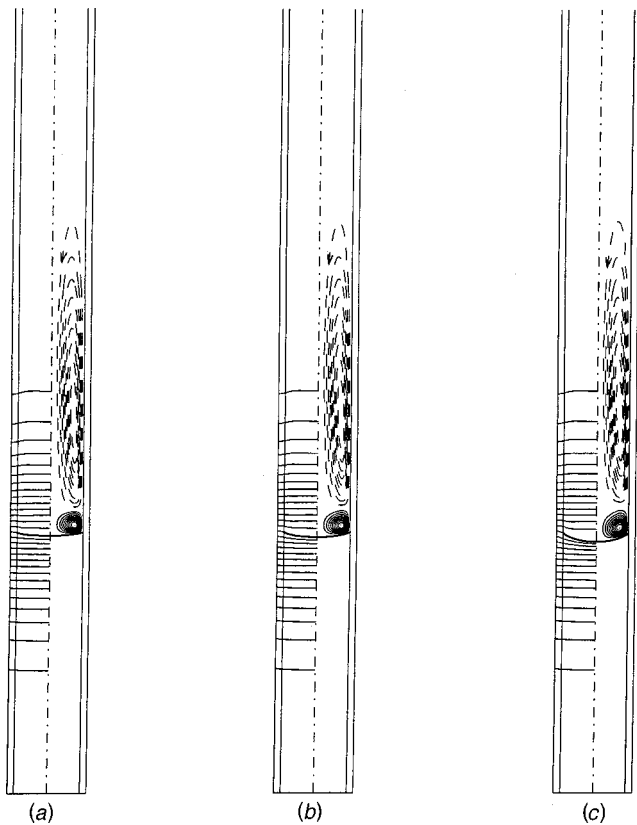


Fig. 4 Isotherms and streamlines for $dT_b(0)/dz=60^\circ\text{C cm}^{-1}$, with $L_1=30$ and $L_2=8$. (a) $U=0.25\ \mu\text{m sec}^{-1}$: $\psi_{\min}=-0.0608$, $\psi_{\max}=0.0490$; (b) $U=1.0\ \mu\text{m sec}^{-1}$: $\psi_{\min}=-0.0598$, $\psi_{\max}=0.0704$; and (c) $U=3.0\ \mu\text{m sec}^{-1}$: $\psi_{\min}=-0.0572$, $\psi_{\max}=0.117$.

For $U=0.5\ \mu\text{m sec}^{-1}$, the thermal Péclet number based on U is still so small (9×10^{-3}) that the temperature distribution is dominated by conduction. Except near the interface, the isotherms (not shown) are indistinguishable from those for $U=0.25\ \mu\text{m sec}^{-1}$ (Fig. 2(a)). Hence, the thermally-driven primary vortex is nearly identical to that computed for $0.25\ \mu\text{m sec}^{-1}$. On the other hand, the secondary vortex is driven by the temperature variation near the interface, which depends on interface curvature. Figure 3 shows that the interface is somewhat more deformed than for $0.25\ \mu\text{m sec}^{-1}$, but maintains its concave-solid shape; the maximum deflection is $\Delta z/r_i=0.152$. For $U=1.0\ \mu\text{m sec}^{-1}$, Fig. 2(b) shows that the maximum streamfunction value, which occurs in the secondary vortex, is significantly higher than for $0.25\ \mu\text{m sec}^{-1}$. (The maximum ψ values in the primary vortex are nearly unchanged between $U=0.25$ and $1.0\ \mu\text{m sec}^{-1}$.) Figure 3 shows that the interface deflection continues to increase, reaching $\Delta z/r_i=0.215$. For $U=3.0\ \mu\text{m sec}^{-1}$, Fig. 2(c) shows that the flow in the secondary vortex has intensified still more. Figure 3 shows that the interface deflection is significantly higher, with $\Delta z/r_i=0.437$. The volume of the nearly isothermal region immediately above the interface is considerably larger than at lower growth rates.

When the maximum ampoule-wall temperature gradient is doubled to 60°C cm^{-1} , thermal variation in the liquid and solid is considerably more localized. Figures 4(a–c) shows that the secondary vortex is confined to a volume near the interface somewhat smaller than for 30°C cm^{-1} . This diminution is accompanied by an increase in the maximum magnitude of the streamfunction in the secondary vortex, which more than doubles (compared to the

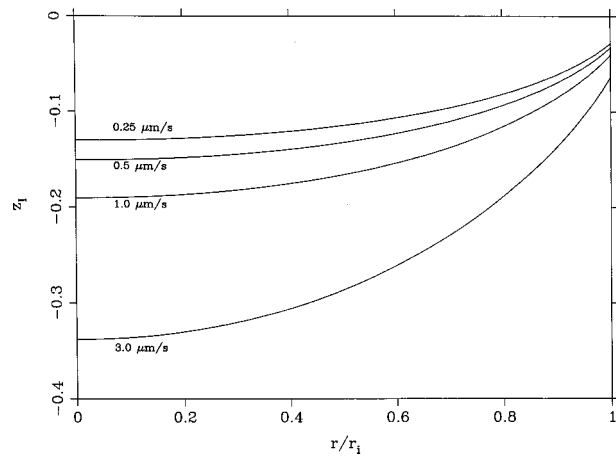


Fig. 5 Interface shapes for $dT_b(0)/dz=60^\circ\text{C cm}^{-1}$. $U=0.25\ \mu\text{m sec}^{-1}$, $\Delta z/r_i=0.102$; $U=0.50\ \mu\text{m sec}^{-1}$, $\Delta z/r_i=0.117$; $U=1.0\ \mu\text{m sec}^{-1}$, $\Delta z/r_i=0.150$; $U=3.0\ \mu\text{m sec}^{-1}$, $\Delta z/r_i=0.275$.

30°C cm^{-1} case), while there is little change in the corresponding value for the primary vortex. However, the primary vortex is significantly shortened.

For $dT_b(0)/dz=60^\circ\text{C cm}^{-1}$, Fig. 5 shows that the interfacial curvature increases significantly with growth rate, as for 30°C cm^{-1} , but with considerably smaller deflections at 60°C cm^{-1} . The ratio of the interfacial deflection at 60°C cm^{-1} to that at 30°C cm^{-1} decreases from $0.111/0.120=0.92$ at $0.25\ \mu\text{m sec}^{-1}$ to $0.275/0.437=0.63$ at $3.0\ \mu\text{m sec}^{-1}$.

For $dT_b(0)/dz=15^\circ\text{C cm}^{-1}$ [14], results (not shown) demonstrate that the strengths of the flow in the primary vortex and especially the secondary vortex are reduced, while the vertical extent of the former and the deflection of the concave-solid interface are both considerably greater than for the standard 30°C cm^{-1} case.

3.2 Effect of Hot- and Cold-Zone Temperatures and Melting Temperature Uncertainty. As stated above, most previous simulations of vertical Bridgman growth have considered the case where T_M lies midway between T_h and T_c . There is, however, evidence suggesting that “off-centered” temperature distributions can give rise to interface shapes with more favorable curvature [2,78]. Moreover, for GaSe the melting temperature is uncertain by about 23°C (cf. [79–84] and compare references cited in Table 3). Thus, the dependence of the solidification process on whether the melting temperature lies midway between T_h and T_c is of interest.

We first consider hot- and cold-zone temperatures of 1050 and 900°C , respectively, as used by Singh et al. [39,40], with the same overall temperature difference as for the standard case, to which we compare the results. We again take $T_M=937^\circ\text{C}$.

Figure 6 shows that, at $U=0.25\ \mu\text{m sec}^{-1}$, the secondary vortex adjacent to the interface is highly distended, compared to the standard (“centered”) case. This is due to the fact that the maximum ampoule-wall temperature gradient lies more than two radii above the interface, rather than near the interface (as in the standard case). As a consequence, the primary vortex is shifted upward (with little change in form), and the secondary vortex driven by it is free to occupy a larger volume. The separation streamline (shown as a dotted curve) between the primary and secondary vortices now lies about 1.5 diameters above the interface, compared to about 0.6 diameters in the centered case. The distended secondary vortex persists to $U=3.0\ \mu\text{m sec}^{-1}$. As in the centered case, the temperature distribution and the form of the flow it drives (although not the strength) are essentially independent of U

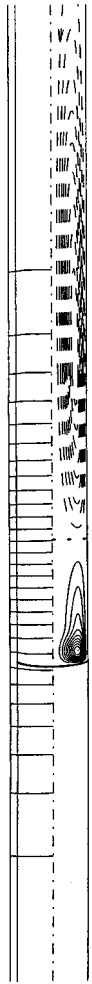


Fig. 6 Isotherms and streamlines for $dT_b(0)/dz=30^\circ\text{C cm}^{-1}$, $U=0.25 \mu\text{m sec}^{-1}$, with $T_c=900^\circ\text{C}$, $T_h=1050^\circ\text{C}$, and $T_M=937^\circ\text{C}$: $\psi_{\min}=-0.0292$, $\psi_{\max}=0.0538$.

over $0.25\text{--}3.0 \mu\text{m sec}^{-1}$. Figure 7 shows that at each growth rate, the interface deflection is 20–30 percent higher than for the standard case.

On the other hand, when we use the “alternate” melting temperature of 960°C [79–84] with the standard T_h and T_c , the flow and interface shape (not shown) are quite similar to the corresponding “standard-case” results at $U=0.25, 0.5, 1.0$, and $3.0 \mu\text{m sec}^{-1}$. Although this “alternate- T_M ” case is also not centered, it differs from the previous uncentered case in that the maximum vertical temperature gradient occurs more than one diameter *below* the interface (i.e., in the solid), as opposed to in the liquid. Consequently, the primary vortex is somewhat closer to the interface than in the standard case, rather than farther away as in the other uncentered computations. The result is a slight axial compression of the secondary vortex. At each growth rate, the interface deflection differs by only a few percent from the corresponding value computed for $T_M=937^\circ\text{C}$.

3.3 Effect of Neglecting Anisotropy or Temperature-Dependence of Properties. The importance of solid-phase thermal conductivity anisotropy can be clearly identified by considering the fictitious case in which the conductivity is taken to be isotropic. We take the conductivity to be one-third of the trace of the conductivity tensor ($k_{\text{iso}}=(2k_t+k_c)/3$), an approximation in excellent agreement with experiment and computations for many microscopically anisotropic polycrystalline materials [85].

The streamlines and isotherms shown in Figs. 8(a–c) and inter-

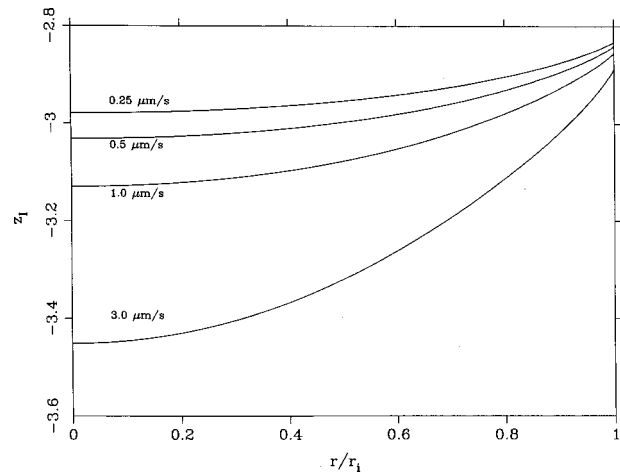


Fig. 7 Interface shapes for $dT_b(0)/dz=30^\circ\text{C cm}^{-1}$, with $T_c=900^\circ\text{C}$, $T_h=1050^\circ\text{C}$, and $T_M=937^\circ\text{C}$. $U=0.25 \mu\text{m sec}^{-1}$, $\Delta z/r_i=0.146$; $U=0.50 \mu\text{m sec}^{-1}$, $\Delta z/r_i=0.190$; $U=1.0 \mu\text{m sec}^{-1}$, $\Delta z/r_i=0.274$; $U=3.0 \mu\text{m sec}^{-1}$, $\Delta z/r_i=0.563$.

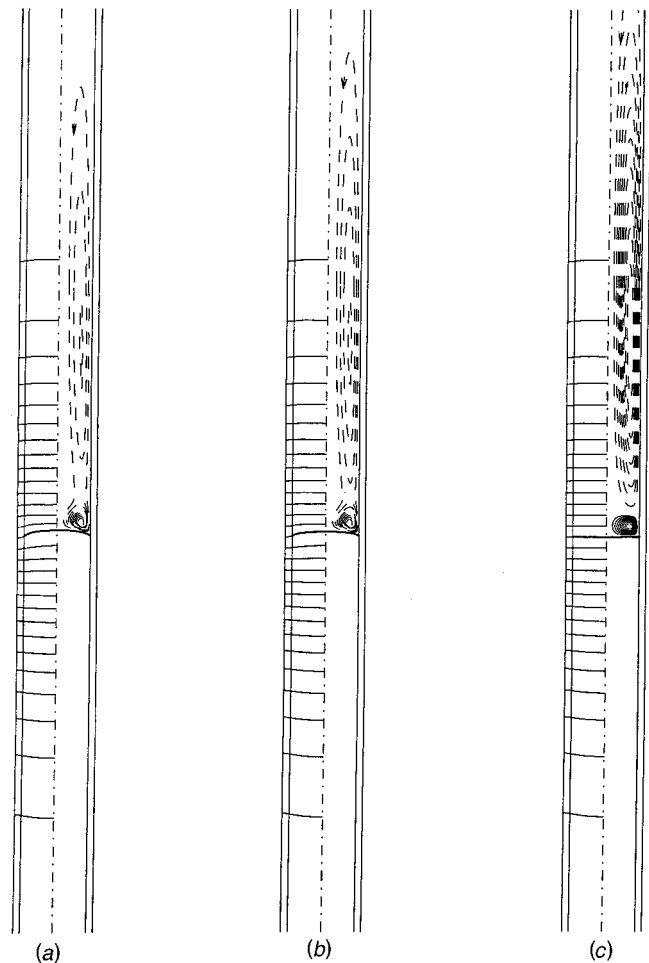


Fig. 8 Isotherms and streamlines for a fictitious material with isotropic solid-phase conductivity $k_{\text{iso}}=tr(k_s)/3$ and $dT_b(0)/dz=30^\circ\text{C cm}^{-1}$. (a) $U=0.25 \mu\text{m sec}^{-1}$: $\psi_{\min}=-0.0712$, $\psi_{\max}=0.893 \times 10^{-4}$; (b) $U=1.0 \mu\text{m sec}^{-1}$: $\psi_{\min}=-0.0507$, $\psi_{\max}=0.0$; and (c) $U=3.0 \mu\text{m sec}^{-1}$: $\psi_{\min}=-0.0572$, $\psi_{\max}=0.117$.

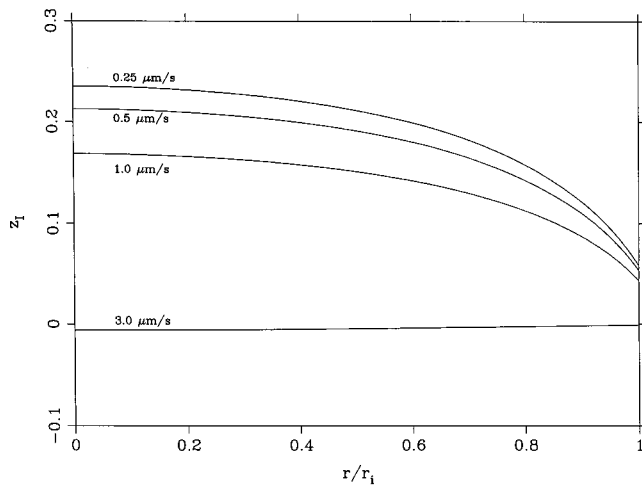


Fig. 9 Interface shapes for $dT_b(0)/dz=30^\circ\text{C cm}^{-1}$ for a fictitious material with isotropic solid-phase thermal conductivity $k_{iso}=tr(k_s)/3$ and $dT_w(0)/dz=30^\circ\text{C cm}^{-1}$. $U=0.25 \mu\text{m sec}^{-1}$, $\Delta z/r_i=-0.177$; $U=0.50 \mu\text{m sec}^{-1}$, $\Delta z/r_i=-0.159$; $U=1.0 \mu\text{m sec}^{-1}$, $\Delta z/r_i=-0.125$; $U=3.0 \mu\text{m sec}^{-1}$, $\Delta z/r_i=4.9\times 10^{-3}$.

face shapes shown in Fig. 9 reveal several key differences compared to the anisotropic case (Figs. 2(a-c) and 3). First, for $U=0.25$ and $1.0 \mu\text{m sec}^{-1}$, the interface is now decidedly convex-solid, rather than concave-solid as for the real material. For $3.0 \mu\text{m sec}^{-1}$, the interface is nearly horizontal, but slightly concave-solid, with $\Delta z/r_i=4.91\times 10^{-3}$ (about 4 percent of the deflection for the real material). Second, for $U=0.25$ and $1.0 \mu\text{m sec}^{-1}$, the vortical flow has not split into counter-rotating vortices. Rather, the flow in the small cell near the interface and the much larger co-rotating cell above are divided by a separatrix, rather than by a separation streamline, as is the case for the anisotropic material. Third, at all growth rates considered, the isotherms in the solid display noticeable curvature well below the interface. Away from the immediate vicinity of the interface, the isotherms are essentially independent of growth rate, as was the case for the real material (Fig. 2). This, and the thin thermal boundary layers in the liquid adjacent to the wall, again indicate that heat transfer in this system is conduction-dominated, and is unaffected by either flow or ampoule translation.

These profound differences are due to the differences in $k_{z,z,s}/k_{r,r,s}$ (unity for the isotropic case, as opposed to 0.12 for the real material), and of $k_{z,z,s}/k_l$ (2.83 for the isotropic case, compared to 0.48 for the real material). The higher ratio of vertical to radial conductivity in the solid allows for much more efficient conduction down into the "isotropic" solid than in the anisotropic case, and reduces the outward radial flux. As discussed by Feigelson and Route [2], this is largely responsible for the qualitative differences in interface shape. Specifically, in the isotropic case, axial conduction through the solid is more efficient than in the anisotropic case, so that liquid penetrates less deeply on the centerline. As U increases, however, latent heat must be removed more rapidly, and the depth of liquid penetration increases until by $3.0 \mu\text{m sec}^{-1}$, the interface is slightly concave-solid.

The lower radial conductivity in the isotropic case (two-thirds of the radial value in the anisotropic case) allows for development of somewhat larger radial temperature gradients in the solid, giving rise to greater isotherm curvature away from the interface.

The nature of the vortical flow near the interface is directly related to the interface shape. At small growth rates, when the interface shape is convex-solid in the isotropic case, hot fluid from the upper part of the melt cools as it falls, and continues "downhill" along the interface as it moves radially outward to the wall. As this downgoing fluid approaches the wall, on which the tem-

perature exceeds T_M above the liquid/solid/ampoule junction, it warms and rises. For the real material (and for the isotropic case at $3.0 \mu\text{m sec}^{-1}$) the interface curvature is opposite, and so is the flow on the interface. One consequence of this flow reversal is that dopants or impurities rejected at the interface (i.e., with segregation coefficients less than unity) will be transported radially outward along the interface, and will tend to accumulate near the ampoule wall, as for pyridine-doped benzene [9] under growth conditions that gave a convex-solid interface. (Conversely, for solutes with segregation coefficients greater than unity, which are preferentially incorporated into the solid, the solid-phase mass fraction will be higher near the centerline.)

It is also useful to understand how the results depend on whether one accounts for the temperature dependence of the viscosity and liquid and solid-phase thermal conductivities, since for many materials, detailed data on the temperature dependence of these properties is not readily available. To make such an assessment, we take all of the properties to be independent of T , except the liquid density, which we allow to depend linearly on temperature, as before. The computed flows and interface shapes (not shown) are essentially unchanged, with the centerline interface deflections at each growth rate differing from the corresponding standard (variable-property) case by less than 1 percent.

3.4 Effect of Localized Ampoule-Wall Heating.

Here, we explore the possibility of using the ampoule-wall temperature profile to manipulate the flow and interface shape. The results of §3.1 show that increasing the maximum gradient in the hyperbolic tangent ampoule-wall temperature profile (1) can significantly reduce interface curvature, especially at higher growth rates.

Specifically, we consider ampoule-wall temperature gradients of the form

$$T_b(z) = \frac{1}{2}[T_c + T_h + (T_h - T_c)\tanh \lambda z](1 + \chi e^{-\sigma(z-z_0)^2/r_i^2}), \quad (9)$$

corresponding to localized heating near $z=z_0$. The quantities χ , z_0/r_i , and σ measure the amplitude, location, and degree of localization of the additional heating. The distribution (9) corresponds to a "multiplicative" Gaussian "bump" superimposed on the underlying hyperbolic tangent temperature profile. It should be possible to obtain distributions qualitatively similar to (9) using a ring heater centered about an axial position z_0 in the "adiabatic" zone of a three-zone Bridgman furnace.

For $\chi=0.1$, $z_0/r_i=-0.05$, and $\sigma=2$, Figs. 10(a-c) show how the flow depends on growth rate. At $U=0.25 \mu\text{m sec}^{-1}$, the flow differs from the standard case (Fig. 2(a)) in that a third toroidal vortex has formed between the interface and secondary vortex. (Note that the senses of rotation of the primary and secondary vortices are unaffected by the local heating.) The effect of the third vortex, whose sense of rotation is opposite to that of the secondary vortex normally adjacent to the interface, will be to reverse the direction of flow along the interface. This is expected to alter dopant transport in the liquid, and consequently segregation in the solid. As U increases to $0.50 \mu\text{m sec}^{-1}$ and subsequently to $1.0 \mu\text{m sec}^{-1}$, a fourth vortex appears between the third one and the interface. Its sense of rotation is the same as that of the secondary vortex, but with a much lower strength. Its appearance leads to reversion to radially inward interfacial flow.

For $U=0.25, 0.5$, and $1.0 \mu\text{m sec}^{-1}$, Fig. 11 shows that localized heating significantly reduces the curvature of concave-solid interfaces, especially at high growth rates. We have not yet, however, found conditions for which a convex-solid interface shape is achieved.

3.5 Zero-Gravity Simulations.

Simulations absent gravity are of interest for two reasons. First, initial experiments on microgravity Bridgman growth of an anisotropic semiconductor have recently been reported [86]. The material studied, tellurium, has

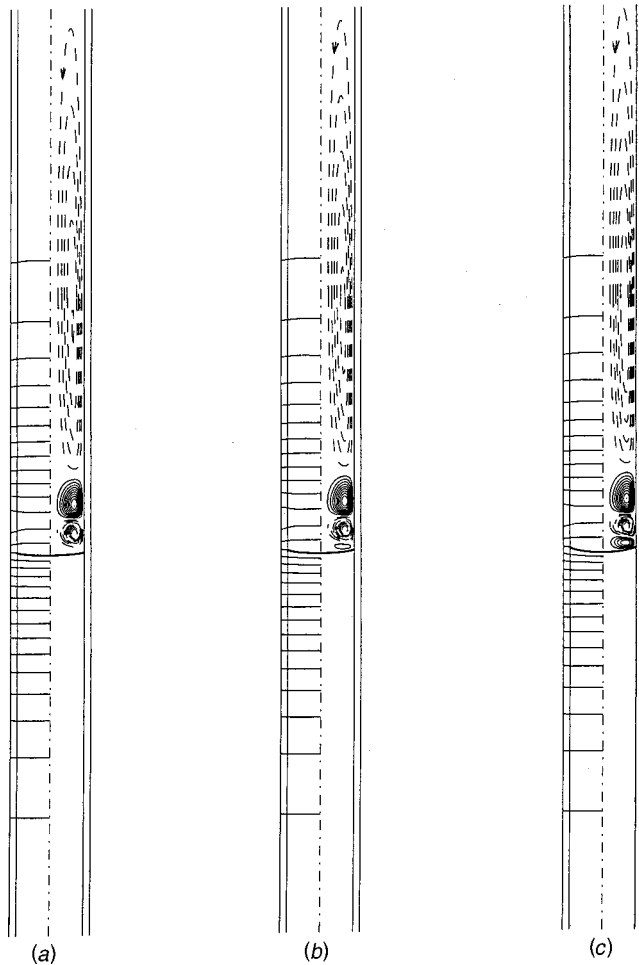


Fig. 10 Isotherms and streamlines for localized ampoule-wall heating with $\chi = -0.1$, $z_0/r_i = -0.05$, $\sigma = 2$, and $\lambda = 0.4 \text{ cm}^{-1}$, corresponding to $dT_b(0)/dz = 30^\circ\text{C cm}^{-1}$ when $\chi = 0$. (a) $U = 0.25 \mu\text{m sec}^{-1}$: $\psi_{\min} = -0.0515$, $\psi_{\max} = 0.0387$; (b) $U = 0.5 \mu\text{m sec}^{-1}$: $\psi_{\min} = -0.0481$, $\psi_{\max} = 0.0389$; and (c) $U = 1.0 \mu\text{m sec}^{-1}$: $\psi_{\min} = -0.0425$, $\psi_{\max} = 0.0402$.

hexagonal symmetry, like GaSe, so that its thermal conductivity is isotropic about the c axis. Second, elimination of gravity in our computations lays bare its role in determining the shape of the interface and structure of the flow.

As indicated in §2, the difference between the liquid and solid densities gives rise to solidification-shrinkage driven flow even absent gravity. For $U = 1.0 \mu\text{m sec}^{-1}$, Fig. 12 shows that the shrinkage-driven flow is normal to the interface, with no recirculation. (As indicated in §2, the streamlines shown are for a frame moving with the ampoule; streamlines for a frame moving with the interface would be exactly normal to the interface.) Results for $U = 0.25 \mu\text{m sec}^{-1}$ (not shown) are similar, with less interface deflection, and maximum and minimum streamfunction values approximately one-fourth those shown for $1.0 \mu\text{m sec}^{-1}$. The weakness of the flow, as indicated by the small magnitudes of the maximum and minimum values of the streamfunction, strongly suggests that dopant transport will be largely by diffusion, as for zero- g growth of pyridine-doped benzene [9]. We can use the maximum magnitude of the streamfunction to compute a mass transfer Péclet number based on the velocity \mathbf{u} and a diffusion coefficient of $2 \times 10^{-5} \text{ cm}^2 \text{ sec}^{-1}$. For $U = 1.0 \mu\text{m sec}^{-1}$, this gives $Pe_{D,\mathbf{u}} = (v_M/r_i)|\mathbf{u}|r_i/D = 390 \max|\psi| = 0.03$, compared to $Pe_{D,\mathbf{u}} = 27$ at the same growth rate for normal gravity. We thus see that mass transfer will be dominated by diffusion at zero g .

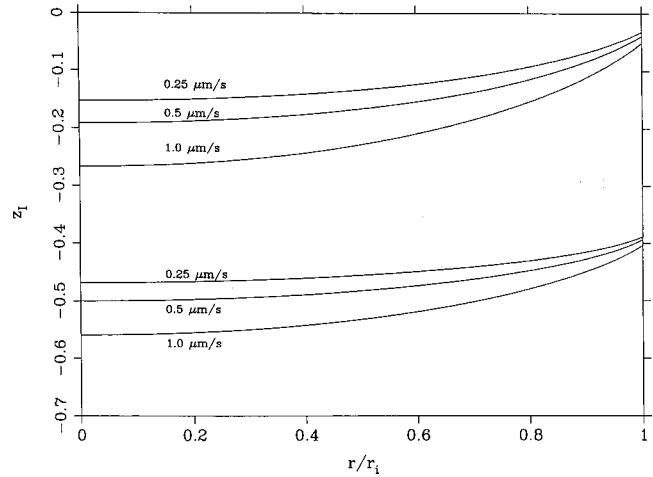


Fig. 11 Interface shapes (below) for localized ampoule-wall heating with $\chi = 0.1$, $\sigma = 2$, $z_0/r_i = -0.05$, and $\lambda = 0.4 \text{ cm}^{-1}$ (corresponding to $dT_b(0)/dz = 30^\circ\text{C cm}^{-1}$ when $\chi = 0$). $U = 0.25 \mu\text{m sec}^{-1}$, $\Delta z/r_i = 0.080$; $U = 0.50 \mu\text{m sec}^{-1}$, $\Delta z/r_i = 0.106$; $U = 1.0 \mu\text{m sec}^{-1}$, $\Delta z/r_i = 0.156$. Upper curves are for $\chi = 0$: $U = 0.25 \mu\text{m sec}^{-1}$, $\Delta z/r_i = 0.120$; $U = 0.50 \mu\text{m sec}^{-1}$, $\Delta z/r_i = 0.152$; $U = 1.0 \mu\text{m sec}^{-1}$, $\Delta z/r_i = 0.215$.

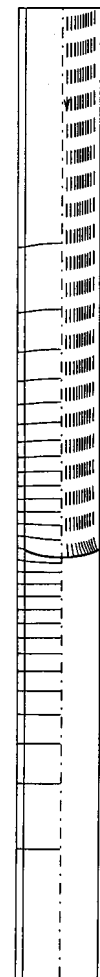


Fig. 12 Isotherms and streamlines for zero g at $dT_b(0)/dz = 30^\circ\text{C cm}^{-1}$, $U = 1.0 \mu\text{m sec}^{-1}$: $\psi_{\min} = -7.79 \times 10^{-5}$, $\psi_{\max} = -5.09 \times 10^{-8}$.

The liquid-phase temperature distributions differ from their normal-gravity counterparts in several respects. First, the zero-gravity isotherms in the primary vortex exhibit more curvature near the centerline than in the normal-gravity case, due to less radial mixing associated with “countercurrent” normal-gravity flow (see Fig. 2). Second, the zero-gravity isotherms show more curvature along the centerline in the secondary vortex. The lower curvature in the normal-gravity case is due to significant upward flow along the centerline, which reduces isotherm curvature associated with the curved interface immediately below.

The interface shapes (not shown) are very similar to those computed for normal gravity at the same growth rates, differing by less than 7 percent at the four growth rates considered. It is clear that while thermally-driven buoyant convection will play a dominant role in determining solute distributions, it has little effect on the interface shape and solid-phase temperature distribution.

4 Discussion

The present results are qualitatively different from those for benzene [5], the only other material with anisotropic solid-phase thermal conductivity for which simulations of vertical Bridgman growth have been performed. Computations (§3.3) for a fictitious material with all properties the same as those of GaSe, except for an isotropic thermal conductivity, show that the interface shape is strongly influenced by anisotropy. Computations for benzene [5] also revealed that thermal anisotropy played an important role in determining interface shape. One fundamental difference between benzene and GaSe is that for benzene the ratio of the conductivity parallel to the growth direction to the conductivity perpendicular to the growth direction was 2.2, while for GaSe it is about 0.12. An important consequence is that, unlike the benzene case, we have found no monotonic ampoule-wall temperature profile that gives a convex-solid interface shape. As for the case of benzene, the isotherms are insensitive to the growth rate, except near the interface.

Our far-field computational boundary in the liquid is placed far enough from the interface that the vertical extent of the primary vortex is determined by the thermophysical properties and growth conditions (including thermal boundary conditions on the ampoule wall). As a consequence, the computed flow should faithfully model flows in long ampoules used to grow boules with low degrees of axial segregation [9].

The computed interface shapes are qualitatively similar to those earlier calculated for vertical Bridgman growth of Ge [19], with the deflection at the centerline increasing monotonically with growth rate. At the higher growth rates considered, our computed dimensionless interface deflections are in excess of twice the largest values computed earlier for Ge.

The qualitatively different (convex-solid, and at $3.0 \mu\text{m sec}^{-1}$, nearly planar) interface shapes obtained using an isotropic thermal conductivity in the solid emphasize the importance of properly accounting for anisotropy in simulations of vertical Bridgman growth of materials with significant thermal anisotropy. The reversal of flow will have the effect of changing the predicted location of maximum solute enrichment from the centerline to the ampoule wall for dopants rejected at the interface, and from the wall to the centerline for dopants preferentially incorporated into the solid.

The fact that the flow and interface shape do not significantly depend on whether account is taken of the temperature dependence of the viscosity and conductivities bodes well for prediction of vertical Bridgman growth for materials for which less extensive thermophysical property data is available than for GaSe.

Unlike the benzene case [5], zero-gravity simulations show that elimination of buoyancy-driven convection does not lead to a convex-solid interface shape. This is again a consequence of the high lateral conductivity compared to the conductivity in the growth direction. Also, unlike the benzene case (see Figs. 4 and 8 of Ref. [5]), the isotherms are affected very little by the buoyancy-

driven flow. This is a consequence of the smaller Péclet number for GaSe (4.5×10^{-3} – 5.4×10^{-2} , depending on growth rate), compared to 0.11–0.33 for growth of benzene.

The ability to use localized heating to control interface shape and the direction and strength of the flow adjacent to the interface provides a means to influence dopant distributions and reduce twinning and other crystal defects over a range of growth rates. This approach points the way to tailoring the ampoule-wall temperature profile so as to achieve not only desirable interface shapes [53,87], but also buoyancy-driven flows conducive to favorable solid-phase dopant distributions.

Finally, the availability of a complete set of measured values of the thermal expansion coefficients and elastic coefficients [16] for GaSe provides the basis for calculating the stress distribution in Bridgman-grown boules of this anisotropic material.

5 Conclusions

This first analysis and computation of flow, heat transfer, and interface shape in vertical Bridgman growth of an anisotropic semiconductor shows that when the c axis of GaSe is aligned with the growth direction, anisotropy can have important consequences. Interface shapes computed using experimental anisotropic thermal conductivity data are decidedly concave-solid, as opposed to the convex-solid shapes predicted using an isotropic conductivity appropriate to a polycrystalline or amorphous material at low growth rates, and slightly concave-solid shapes predicted for isotropic conductivity at higher growth rates. For concave-solid interfaces corresponding to the anisotropy of the real material, the flow on the interface is radially inward toward the centerline, while for the convex-solid interface shapes, the flow is outward to the ampoule wall. The different flows and interface shapes will lead to profoundly different solid-phase dopant or impurity distributions, which we are currently investigating.

The results also show that the interface shape is not convex-solid for any of the growth conditions investigated. However, by use of a ring heater in the “adiabatic” zone between the hot and cold zones, one or two additional vortices (beyond the two that exist absent the additional heating) can be introduced in the region overlying the interface. Depending on growth rate and other conditions, the flow direction on the interface can be reversed compared to the case without additional heating, leading to a change in the location of solute accumulation. Such local heating can also reduce interfacial curvature.

Acknowledgments

The authors gratefully acknowledge the comments, suggestions, and information provided by Drs. Nils C. Fernelius, Valeriy G. Voevodin, and two anonymous reviewers. We also very much appreciate the efforts of several people, including Donna Swischer, Irina Bereznyaya, Barbara Loomis, Tina Chrzastowski, and Joseph Bentsman to obtain a copy of Reference [62], without which this work would not have been possible. The authors gratefully acknowledge support of the Microgravity Science and Applications Division of the National Aeronautics and Space Administration through Grant NAG3-1121 during the early stages of the development of the code used herein. The computations were performed using the facilities of the National Center for Supercomputing Applications.

References

- [1] Feigelson, R. S., and Route, R. K., 1990, “Improved Yield of Bridgman Grown AgGaSe₂ Crystals using Shaped Crucibles,” *J. Cryst. Growth*, **104**, pp. 789–792.
- [2] Feigelson, R. S., and Route, R. K., 1980, “Vertical Bridgman Growth of CdGeAs₂ with Control of Interface Shape and Orientation,” *J. Cryst. Growth*, **49**, pp. 261–273.
- [3] Prazak, M., and Holecek, S., 1995, “Directional Solidification of AlZn Eutectic in Microgravity Conditions,” *Cryst. Res. Technol.*, **30**, pp. 927–932.
- [4] McGhie, A. R., and Sloan, G. J., 1976, “Impurity Distribution in Organic

- Crystals I. The System Naphthalene/2-Chloronaphthalene," *J. Cryst. Growth*, **32**, pp. 60–67.
- [5] Lee, H., and Pearlstein, A. J., 2000, "Simulation of Vertical Bridgman Growth of Benzene, a Material with Anisotropic Solid-Phase Thermal Conductivity," *J. Cryst. Growth*, **209**, pp. 934–952.
- [6] Gau, C., and Viskanta, R., 1985, "Effect of Crystal Anisotropy on Heat Transfer During Melting and Solidification of a Metal," *ASME J. Heat Transfer*, **107**, pp. 706–708.
- [7] Weaver, J. A., and Viskanta, R., 1989, "Effects of Anisotropic Heat Conduction on Solidification," *Numer. Heat Transfer*, **15A**, pp. 181–195.
- [8] Huang, C. E., Ewell, D., and Feigelson, R. S., 1983, "Influence of Thermal Conductivity on Interface Shape During Bridgman Growth," *J. Cryst. Growth*, **64**, pp. 441–447.
- [9] Lee, H., and Pearlstein, A. J., 2000, "Simulation of Radial Dopant Segregation in Vertical Bridgman Growth of Pyridine-Doped Benzene, a Surrogate for Binary Organic Nonlinear Optical Materials," *J. Cryst. Growth*, **218**, 354–352.
- [10] Kasriel, R. H., 1971, *Undergraduate Topology*, W. B. Saunders, Philadelphia, PA, p. 116.
- [11] Fernelius, N. C., Singh, N. B., Suhre, D. R., and Balakrishna, V., 1999, "Modified Gallium Selenide Crystals for High Power Nonlinear Optical Applications," U.S. Patent 5,980,789, issued Nov. 9, 1999.
- [12] Fernelius, N. C., Hopkins, F. K., and Ohmer, M. C. 1999, "Nonlinear Optical Crystal Development for Laser Wavelength Shifting at AFRL Materials Directorate," in *Operational Characteristics and Crystal Growth of Nonlinear Optical Materials*, Proc. SPIE, **3793**, SPIE, Bellingham, Wash. pp. 2–8.
- [13] Lieth, R. M. A., 1977, "III-VI Compounds," in *Preparation and Crystal Growth of Materials with Layered Structures*, R. M. A. Lieth, ed., Reidel, Dordrecht, pp. 225–254.
- [14] Gousskov, A., Camassel, J., and Gousskov, L., 1982, "Growth and Characterization of III-VI Layered Crystals like GaSe, GaTe, InSe, GaSe_{1-x}Te_x and Ga_xIn_{1-x}Se," *Prog. Cryst. Growth Charact.*, **5**, pp. 323–413.
- [15] Maschke, K., and Lévy, F., 1983, "III-VI Compounds," in *Numerical Data and Functional Relationships in Science and Technology*, Landolt-Börnstein, New Series, Group III, **17f**, O. Madelung, ed., Springer-Verlag, Berlin, pp. 9–102.
- [16] Fernelius, N. C., 1994, "Properties of Gallium Selenide Single Crystal," *Prog. Cryst. Growth Charact. Mater.*, **28**, pp. 275–353.
- [17] Holmes, D. E., and Gatos, H. C., 1981, "Convective Interference and 'Effective' Diffusion-Controlled Segregation during Directional Solidification under Stabilizing Vertical Temperature Gradients; Ge," *J. Electrochem. Soc.*, **128**, pp. 429–437.
- [18] Chang, C. J., and Brown, R. A., 1983, "Radial Segregation Induced by Natural Convection and Melt/Solid Interface Shape in Vertical Bridgman Growth," *J. Cryst. Growth*, **63**, pp. 343–364.
- [19] Adomato, P. M., and Brown, R. A., 1987, "Convection and Segregation in Directional Solidification of Dilute and Non-dilute Binary Alloys: Effects of Ampoule and Furnace Design," *J. Cryst. Growth*, **80**, pp. 155–190.
- [20] Adomato, P. M., and Brown, R. A., 1987, "Petrov-Galerkin Methods for Natural Convection in Directional Solidification of Binary Alloys," *Int. J. Numer. Methods Fluids*, **7**, pp. 761–791.
- [21] Kim, D. H., and Brown, R. A., 1989, "Models for Convection and Segregation in the Growth of HgCdTe by the Vertical Bridgman Method," *J. Cryst. Growth*, **96**, pp. 609–627.
- [22] Kim, D. H., and Brown, R. A., 1991, "Modelling of the Dynamics of HgCdTe Growth by the Vertical Bridgman Method," *J. Cryst. Growth*, **114**, pp. 411–434.
- [23] Kuppuraio, S., Brandon, S., and Derby, J. J., 1995, "Modeling the Vertical Bridgman Growth of Cadmium Zinc Telluride: I. Quasi-Steady Analysis of Heat Transfer and Convection," *J. Cryst. Growth*, **155**, pp. 93–102.
- [24] Liang, M. C., and Lan, C., 1996, "Three-Dimensional Convection and Solute Segregation in Vertical Bridgman Crystal Growth," *J. Cryst. Growth*, **167**, pp. 320–332.
- [25] Lan, C. W., and Chen, F. C., 1996, "A Finite Volume Method for Solute Segregation in Directional Solidification and Comparison with a Finite Element Method," *Comput. Methods Appl. Mech. Eng.*, **131**, pp. 191–207.
- [26] Lan, C. W., 1999, "Effects of Ampoule Rotation on Flows and Dopant Segregation in Vertical Bridgman Growth," *J. Cryst. Growth*, **197**, pp. 983–991.
- [27] Ma, N., and Walker, J. S., 2000, "A Model of Dopant Transport During Bridgman Crystal Growth with Magnetically Damped Buoyant Convection," *ASME J. Heat Transfer*, **122**, pp. 159–164.
- [28] Jandl, S., Brebner, J. L., and Powell, B. M., 1976, "Lattice Dynamics of GaSe," *Phys. Rev. B*, **13**, pp. 686–693.
- [29] Bastow, T. J., Campbell, I. D., and Whitfield, H. J., 1981, "A ⁶⁹Ga, ¹¹⁵In NQR Study of Polytypes of GaS, GaSe and InGe," *Solid State Commun.*, **39**, pp. 307–311.
- [30] Cox, E. G., Cruickshank, D. W. J., and Smith, J. A. S., 1958, "The Crystal Structure of Benzene at -3°C," *Proc. R. Soc. London, Ser. A*, **247**, pp. 1–21.
- [31] Guseinov, G. D., Abdullayeva, S. G., Ramazanade, A. M., Ismailov, M. Z., Viscakas, J. K., Vaitkus, J. J., and Baltramiejūnas, R. A., 1975, "Anisotropy of Lattice Heat Conductivity of Complex Chalcogenides," *Phys. Lett.*, **54A**, pp. 378–380.
- [32] Tiller, W. A., 1963, "Principles of Solidification," *The Art and Science of Growing Crystals*, J. J. Gilman, ed., Wiley, New York, pp. 276–342.
- [33] Huang, C. E., Elwell, D., and Feigelson, R. S., 1984, "Computation of Stress in Bridgman Crystals," *J. Cryst. Growth*, **69**, pp. 275–280.
- [34] Abdullaev, G. B., Abasova, A. Z., Zaitov, F. A., Lepnev, L. S., Stafeyev, V. I., and Chkuna, V. N., 1982, "Influence of Gamma and Neutron Irradiation on the Photoluminescence Spectra of p-type GaSe Single Crystals," *Sov. Phys. Semicond.*, **16**, pp. 729.
- [35] Shigetomi, S., Ikari, T., and Nakashima, H., 1993, "Optical and Electrical Properties of Layer Semiconductor p-GaSe Doped with Zn," *J. Appl. Phys.*, **74**, pp. 4125–4129.
- [36] Lee, W.-S., Kim, N.-O., and Kim, B.-I., 1996, "Optical Properties of GaSe:Er³⁺ Single Crystals," *J. Mater. Sci. Lett.*, **15**, pp. 1644–1645.
- [37] Singh, N. B., Suhre, D. R., Rosch, W., Meyer, R., Marable, M., Fernelius, N. C., Hopkins, F. K., Zelmon, D. E., and Narayanan, R., 1999, "Modified GaSe Crystals for Mid-IR Applications," *J. Cryst. Growth*, **198/199**, pp. 588–592.
- [38] Micocci, G., Serra, A., and Tepore, A., 1997, "Electrical Properties of n-GaSe Single Crystals Doped with Chlorine," *J. Appl. Phys.*, **82**, pp. 2365–2369.
- [39] Singh, N. B., Narayanan, R., Zhao, A. X., Balakrishna, V., Hopkins, R. H., Suhre, D. R., Fernelius, N. C., Hopkins, F. K., and Zelmon, D. E., 1997, "Bridgman Growth of GaSe Crystals for Nonlinear Optical Applications," *Mater. Sci. Eng., B*, **49**, pp. 243–246.
- [40] Singh, N. B., Suhre, D. R., Balakrishna, V., Marable, M., Meyer, R., Fernelius, N., Hopkins, F. K., and Zelmon, D., 1998, "Far-Infrared Conversion Materials: Gallium Selenide for Far-Infrared Conversion Applications," *Prog. Cryst. Growth Charact. Mater.*, **37**, pp. 47–102.
- [41] Anis, M. K., 1981, "The Growth of Single Crystals of GaSe," *J. Cryst. Growth*, **55**, pp. 465–469.
- [42] Anis, M. K., 1988, "Thermopower Measurements in p-GaSe Single Crystals Parallel and Perpendicular to the c-Axis," *Int. J. Electron.*, **65**, pp. 215–221.
- [43] Segura, A., Guesdon, J. P., Besson, J. M., and Chevy, A., 1979, "Photovoltaic Effect in InSe. Application to Solar Energy Conversion," *Rev. Phys. Appl.*, **14**, pp. 253–257.
- [44] Parfeniuk, C., Weinberg, F., Samarasekera, I. V., Schvezov, C., and Li, L., 1992, "Measured Critical Resolved Shear Stress and Calculated Temperature and Stress Fields during Growth of CdZnTe," *J. Cryst. Growth*, **119**, pp. 261–270.
- [45] Brice, J. C., 1973, *The Growth of Crystals from Liquids*, North-Holland, Amsterdam, p. 209.
- [46] Cardetta, V. L., Mancini, A. M., and Rizzo, A., 1972, "Melt Growth of Single Crystal Ingots of GaSe by Bridgman-Stockbarger's Method," *J. Cryst. Growth*, **16**, pp. 183–185.
- [47] Sampaio, H., Gousskov, A., and Arguello, Z. P., 1977, "Orientations of the Basal Plane of Single Crystals of GaSe Grown by Vertical Bridgman Technique," *J. Cryst. Growth*, **41**, pp. 275–277.
- [48] Shtanov, V. I., Komov, A. A., Tamm, M. E., Atrashenko, D. V., and Zlomanov, V. P., 1998, "Phase Diagram of the Gallium-Selenium System and Photoluminescence Spectra of GaSe Crystals," *Dokl. Chem.*, **361**, pp. 140–143.
- [49] Gousskov, L., Gousskov, A., Lemos, V., May, W., and Sampaio, H., 1977, "Electrical Properties of GaTe_xSe_{1-x} Crystals," *Phys. Status Solidi A*, **39**, pp. 65–71.
- [50] Sulewski, P. E., Bucher, E., Stücheli, N., Oglesby, C. S., Friemelt, K., Vögt, M., Baumann, J. R., and Kloc, C., 1992, "Search for Giant Franz-Keldysh-Like Effects in GaSe and Other Layered Semiconductors," *Appl. Phys. A*, **54**, pp. 79–83.
- [51] Sakai, E., Nakatani, H., Tatsuyama, C., and Takeda, F., 1998, "Average Energy Needed to Produce an Electron-Hole Pair in GaSe Nuclear Particle Detectors," *IEEE Trans. Nucl. Sci.*, **35**, pp. 85–88.
- [52] Pfeiffer, M., and Mülhberg, M., 1992, "Interface Shape Observation and Calculation in Crystal Growth of CdTe by the Vertical Bridgman Method," *J. Cryst. Growth*, **118**, pp. 269–276.
- [53] Lan, C. W., and Ting, C. C., 1996, "A Study of the Interface Control of Vertical Bridgman Crystal Growth using a Transparent Multizone Furnace," *Chem. Eng. Commun.*, **145**, pp. 131–143.
- [54] Zhang, H., Zheng, L. L., Prasad, V., and Larson, D. J., 1998, "Local and Global Simulations of Bridgman and Liquid-Encapsulated Czochralski Crystal Growth," *ASME J. Heat Transfer*, **120**, pp. 85–873.
- [55] Anis, M. K., and Piercy, A. R., 1977, "Growth of Single Crystals of GaSe with Natural Facets at Large Angles to the Layers," *Phys. Status Solidi A*, **44**, pp. K5–K6.
- [56] Glazov, V. M., Makhmudov, S., and Mavlonov, S., 1972, "Thermal Expansion and Volume Changes During the Melting of Gallium and Indium Selenides" (translated), *Izv. Akad. Nauk Tadzh. SSR, Otd. Fiz.-Mat. Geol.-Khim. Nauk*, No. 1, pp. 20–24.
- [57] Suzuki, H., and Mori, R., 1974, "Phase Study on Binary System Ga-Se," *Jpn. J. Appl. Phys.*, **13**, pp. 417–423.
- [58] Dieleman, J., Sanders, F. H. M., and van Dommelen, J. H. J., 1982, "The Phase Diagram of the Ga-Se System," *Philips J. Res.*, **37**, pp. 204–229.
- [59] Dieleman, J., and Engelfriet, R. G., 1971, "The Phase Diagram of the System Ga_{1-x}Se_x for 0.5 ≤ x ≤ 0.6 and 300 K ≤ T ≤ 1500 K," *J. Less-Common Met.*, **25**, pp. 231–233.
- [60] Zavrzhnov, A. Y., Turchen, D. N., Goncharov, E. G., and Prigorodova, T. A., 1999, "Scanning of T-X Projections of Phase Microdiagrams based on Data on Gas Solubility in Melts. Homogeneity Area of GaSe at Premelting Temperatures," *Russ. J. Gen. Chem.*, **69**, pp. 1692–1697.
- [61] Fedorov, V. I., and Machuev, V. I., 1972, "Thermal Conductivity of Selenium and of Indium and Gallium Selenides in the Liquid and Solid States," *Sov. Phys. Semicond.*, **6**, pp. 142–144.
- [62] Glazov, V. M., Makhmudov, S., and Mavlonov, S., 1978, "Temperature Dependence of the Viscosity of Gallium and Indium Selenides" (translated), *Elektricheskie Svoistva Slozhnykh Poluprovodnikov i Kristallov*, S. M. Mav-

- Ionov and R. A. Karieva, eds., Donish, Dushanbe, pp. 28–41.
- [63] Takeda, S., Okazaki, H., and Tamaki, S., 1982, "Specific Heat of Liquid In-Te Alloys," *J. Phys. C*, **15**, pp. 5203–5210.
- [64] Takeda, S., Tamaki, S., Takano, A., and Okazaki, H., 1983, "Specific Heat of Liquid Ga-Te Alloys," *J. Phys. C*, **16**, pp. 467–471.
- [65] Mills, K. C., 1976, "Molar Heat Capacities and Enthalpies of Transition for InSe(c), InSe_{1.2} and In₂Se₃," *High Temp.-High Press.*, **8**, pp. 225–230.
- [66] Mamedov, K. K., Kerimov, I. G., Kostyukov, V. N., and Mekhtiev, M. I., 1967, "Specific Heat of Gallium Selenide and Thallium Selenide," *Sov. Phys. Semicond.*, **1**, pp. 363–364.
- [67] Goldsmith, A., Waterman, T. E., and Hirschhorn, H. J., 1961, *Handbook of Thermophysical Properties of Solid Materials*, Vol. III, Ceramics, Macmillan, New York, pp. 891–896.
- [68] Lewis, G. N., and Randall, M., 1961, *Thermodynamics*, 2nd ed., revised by K. S. Pitzer and L. Brewer, McGraw-Hill, New York.
- [69] Singh, N. B., Henningsen, T., Balakrishna, V., Suhre, D. R., Femelius, N., Hopkins, F. K., and Zelmon, D. E., 1996, "Growth and Characterization of Gallium Selenide Crystals for Far-Infrared Conversion Applications," *J. Cryst. Growth*, **163**, pp. 398–402.
- [70] Manfredotti, C., Murri, R., Rizzo, A., Galassini, S., and Ruggiero, L., 1974, "Deep Hole Traps in *p*-type GaSe Single Crystals," *Phys. Rev. B*, **10**, pp. 3387–3393.
- [71] Nakatani, H., Sakai, E., Tatsuyama, C., and Takeda, F., 1989, "GaSe Nuclear Particle Detectors," *Nucl. Instrum. Methods Phys. Res. A*, **283**, pp. 303–309.
- [72] Rizzo, A., DeBlasi, C., Catalano, M., and Cavaliere, P., 1988, "Dislocations in A^{III}B^{VI} Single Crystals," *Phys. Status Solidi A*, **105**, pp. 101–112.
- [73] De Blasi, C., Manno, D., and Rizzo, A., 1989, "Convergent-Beam Electron Diffraction Study of Melt- and Vapour-Grown Single Crystals of Gallium Chalcogenides," *Il Nuovo Cimento*, **11D**, pp. 1145–1163.
- [74] Manfredotti, C., Mancini, A. M., Murri, R., Rizzo, A., and Vasanelli, L., 1977, "Electrical Properties of *p*-Type GaSe," *Il Nuovo Cimento*, **39B**, pp. 257–268.
- [75] Lendvay, E., Kuhn, A., Chevy, A., and Ceva, T., 1971, "Dislocation Etching of GaSe Single Crystals," *J. Mater. Sci.*, **6**, pp. 305–308.
- [76] Rustamov, P. G., Melikova, Z. D., Nasirov, Y. N., and Alidzhanov, M. A., 1969, "Preparation of Single Crystals of Solid Solutions of Alloys of the System GaS-GaSe and Study of Their Physical Properties," *Inorg. Mater.*, **5**, pp. 750–752.
- [77] Guseinov, G. D., and Rasulov, A. I., 1966, "Heat Conductivity Study of GaSe Monocrystals," *Phys. Status Solidi*, **18**, pp. 911–922.
- [78] Brandon S., and Derby, J. J., 1992, "Heat Transfer in Vertical Bridgman Growth of Oxides: Effects of Conduction, Convection, and Internal Radiation," *J. Cryst. Growth*, **121**, pp. 473–494.
- [79] Rustamov, P. G., Il'yasov, T. M., Safarov, M. G., and Sadykhova, S. A., 1979, "Projection of the Liquidus of the As, Ga|Se, Te System," *Russ. J. Inorg. Chem.*, **24**, pp. 263–266.
- [80] Il'yasov, T. M., and Rustamov, P. G., 1982, "Chemical Interaction and Glass Formation in Chalcogenide Systems of the As₂X₃-GaX Type," *Russ. J. Inorg. Chem.*, **27**, pp. 1500–1503.
- [81] Rustamov, P. G., Melikova, Z. D., Safarov, M. G., and Alidzhanov, M. A., 1965, "Solid Solutions in the System GaS-GaSe," *Inorg. Mater.*, **1**, pp. 387–389.
- [82] Rustamov, P. G., Babaeva, B. K., and Luzhnaya, N. P., 1965, "The Interaction of Gallium with Selenium," *Inorg. Mater.*, **1**, pp. 775–776.
- [83] Muschinsky, W. P., and Pawelenko, N. M., 1969, "Untersuchung des Systems GaSe-InSe," *Krist. Tech.*, **4**, No. 2, pp. K5–K7.
- [84] Palatnik, L. S., and Belova, E. K., 1996, "Investigation of the Ga-Se Phase Diagram," *Inorg. Mater.*, **2**, pp. 657–659.
- [85] Kumar, S., and Singh, R. N., 1995, "Thermal Conductivity of Polycrystalline Materials," *J. Am. Ceram. Soc.*, **78**, pp. 728–736.
- [86] Parfeniev, R. V., Farbshtein, I. I., Shulpina, I. L., Yakimov, S. V., Shalimov, V. P., Turchaninov, A. M., Ivanov, A. I., and Savin, S. F., 2000, "Solidification of Anisotropic Semiconducting Material—Tellurium under Microgravity Conditions," *Mater. Sci. Forum*, **329/330**, pp. 297–304.
- [87] Batur, C., Srinivasan, A., Duval, W. M. B., and Singh, N. B., 1995, "Control of Crystal Growth in Bridgman Furnace," *Prog. Cryst. Growth Charact. Mater.*, **30**, pp. 217–236.

Molecular Dynamics Simulation of Nanodroplet Evaporation

J. H. Walther

Postdoctoral Fellow
e-mail: walther@inf.ethz.ch

P. Koumoutsakos¹

Professor
e-mail: petros@inf.ethz.ch

Institute of Computational Sciences,
ETH Zentrum,
Weinbergstrasse 43,
CH-8092 Zürich, Switzerland

Molecular dynamics simulations are used to study the sub-critical evaporation of a nanometer-size droplet at 300 K and 3 MPa. Classical molecular dynamics techniques are combined with an adaptive tree data structure for the construction of the neighbor lists, allowing efficient simulations using hundreds of thousands of molecules. We present a systematic convergence study of the method demonstrating its convergence for heat conduction problems in submicron scales. These high resolution simulations compute values of the evaporation coefficient that are in excellent agreement with theoretical predictions. [DOI: 10.1115/1.1370517]

Keywords: Nanofluidics, Nanodroplet, Molecular Dynamics Simulation

1 Introduction

Phenomena associated with droplet dynamics are of fundamental importance to non-premixed combustion studies. Such phenomena include the formation of sprays and droplets, droplet coalescence and breakup, and droplet evaporation and combustion [1–4]. At subcritical conditions the droplet evaporation is well described by the classical D^2 evaporation law [5]

$$\frac{dD^2}{dt} = -\beta_v, \quad (1)$$

where β_v is the evaporation coefficient, and D is the droplet diameter. At supercritical conditions the continuum analysis of the problem is faced with suitable modeling of transport and thermodynamic properties, equations of state, and proper specification of the interface [6,7]. Using molecular dynamics simulations the modeling issues reduce to the specification of proper interatomic potentials.

Molecular dynamics simulations of nanometer-size droplets in equilibrium with a vapor have been applied for the study of the droplet pressure and density profile, and to the calculation of the surface tension as function of vapor temperature and droplet size [8–11]. Studies of non-equilibrium systems have included condensation and evaporation of argon slabs [12–14], evaporation of argon clusters [15], and evaporation of argon droplets [16,17], which recently have been extended to studies of supercritical evaporation of liquid oxygen [18]. Related molecular dynamics simulations also include studies of droplet collision cf. Svanberg et al. [19], Sikdar and Chung [20] and Murad and Law [21] and the cluster formation of a Lennard-Jones fluid during anisotropic expansion Ashurst and Holian [22].

The molecular dynamics simulations by Long, Micci, and Wong [16] involved sub-critical evaporation of an argon droplet in an argon vapor at high Knudsen numbers. At a droplet size of 5 nm (droplet consisting of 1000 atoms), they found good agreement with the theoretical correlation by assuming an evaporation coefficient of 0.3.

Little [17] simulated the sub and super-critical evaporation of nanometer-size droplets using parameters similar to the present study. For droplet sizes of 8 nm (using 5587 atoms), the evaporation coefficient was found within 20 percent of the D^2 evaporation law.

In this paper we consider the possibility of studying non-premixed combustion from the molecular level, by applying large

number of molecules to approach the macro-scale physics. To validate this approach the present study involves subcritical evaporation of a droplet in a quiescent vapor allowing direct comparison with the D^2 evaporation law.

We conduct a series of high resolution simulations using several tens of thousands of computational molecules by efficiently employing tree data structures. We present a systematic convergence study to examine the influence of the different parameters imposed by the numerical method, including the size of the computational domain, cutoff radius, droplet diameter, heating frequency and size of heating region, initialization period, and time step size. It is shown that molecular dynamics simulations converge to the D^2 evaporation law to desired accuracy by using large number of computational molecules. The paper is organized as follows: Section 2 outlines the numerical method including a description of the applied tree data structure and of the heating algorithm. Section 3 presents the convergence study and the predicted evaporation rates.

2 Molecular Dynamics

The evaporation of an argon droplet in its own vapor is studied using molecular dynamics simulations. The atoms are assumed to interact via the 12–6 Lennard-Jones pair potential

$$V(r) = 4\epsilon \left[\left(\frac{\sigma}{r} \right)^{12} - \left(\frac{\sigma}{r} \right)^6 \right], \quad (2)$$

where r is the distance between the atoms. For argon, the zero energy distance σ is 3.4 Å, and the depth of the potential ϵ is $120k_B$, where k_B is Boltzmann's constant. The N atoms move according to Newton's law

$$m \frac{d^2 r_p}{dt^2} = -\nabla V(r_p), \quad p = 1, \dots, N \quad (3)$$

and

$$\nabla V(r_p) = \sum_{q=1}^N \nabla V(|r_p - r_q|), \quad p = 1, \dots, N, \quad (4)$$

where m is the mass of the atom. Numerical integration of Eq. (3) nominally requires $\mathcal{O}(N^2)$ operations, where N is the number of atoms, but is rendered an $\mathcal{O}(N)$ algorithm by the short range nature of the potential. The computational problem is reduced then to efficiently identifying the neighboring particles at each computational element. In the present work the neighbors are considered for cutoff radii of $r_c/\sigma = 2.5, 5$, and 10.

¹Also at CTR, NASA Ames 202A-A-1, Moffett Field, CA-94035, USA.

Contributed by the Heat Transfer Division for publication in the JOURNAL OF HEAT TRANSFER. Manuscript received by the Heat Transfer Division September 10, 1999; revision received November 20, 2000. Associate Editor: T. Avedisian.

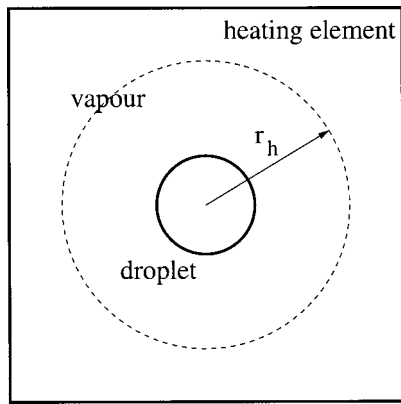


Fig. 1 Sketch of computational domain and heating element

The system of equations is integrated in time using the leap-frog scheme and a constant number of atoms and in a constant volume. Periodic boundary conditions are imposed in all spatial directions.

For a single droplet evaporating into a vapor, the far-field temperature (\tilde{T}_v^*) boundary condition is

$$T_v^*(r) \rightarrow \tilde{T}_v^* \text{ as } r \rightarrow \infty, \quad (5)$$

which is enforced by a momentum scaling of the atoms located sufficiently far away from the droplet [16,23,24]. The velocity is scaled according to

$$v_i^{\text{new}} = v_i^{\text{old}} \sqrt{\frac{3T_v k_B N_h}{2E_{\text{kin}}}}, \quad (6)$$

where E_{kin} is the total kinetic energy of the N_h atoms found in the heating region ($r_i > r_h$), and r_i is the radial co-ordinate of the atom measured from the center of the computational box cf. Fig. 1. The size (r_h) of the heating element and the heating frequency are adjusted to minimize thermal noise and to obtain a good approximation of Eq. (5).

Non-dimensional quantities are marked with an asterisk and are based on σ , ϵ , k_B , and m . Specifically, time is non-dimensionalised by $\tau^* = \tau \sqrt{\epsilon / (m \sigma^2)}$. A non-dimensional time step of $\delta \tau^* = 0.005$ (≈ 10 fs) is used unless otherwise specified.

2.1 Tree Algorithm. Traditionally, molecular dynamics simulations use the Verlet neighbor list in combination with a linked list [25–27] to reduce the $\mathcal{O}(N^2)$ operations required by the direct implementation of the force evaluation cf. Eq. (4). However, for systems involving large density variations (as in the present case), the regular mesh imposed by these methods often results in inefficient load balancing on parallel computers [17,28]. The present code adopts a different strategy, by using an adaptive tree data structure to sort the atoms and to build the neighbor list. The tree is constructed at every time step by recursively dividing the computational box in eight equal sized boxes. The division of the boxes is terminated if the size of the box is less than $2r_c$, or if the number of atoms in the box is less than some prescribed value. The latter criterion allows for efficient computations of problems with large density variations. A threshold value of 40 atoms per box was used in this work. Figure 2 shows an example of a two-dimensional (quad) tree created for 16 atoms (shown as circles) using a threshold value of one atom per box. The resulting tree has four levels.

The list of neighboring boxes is constructed for each box that has no further subdivisions (childless boxes). Two boxes are said to be neighbors if they share at least one corner. The neighbor list is constructed in two steps. First, neighboring boxes at the same level in the tree (colleagues), are found for each box in the tree (a box has a maximum of 26 colleagues). The list of colleagues is

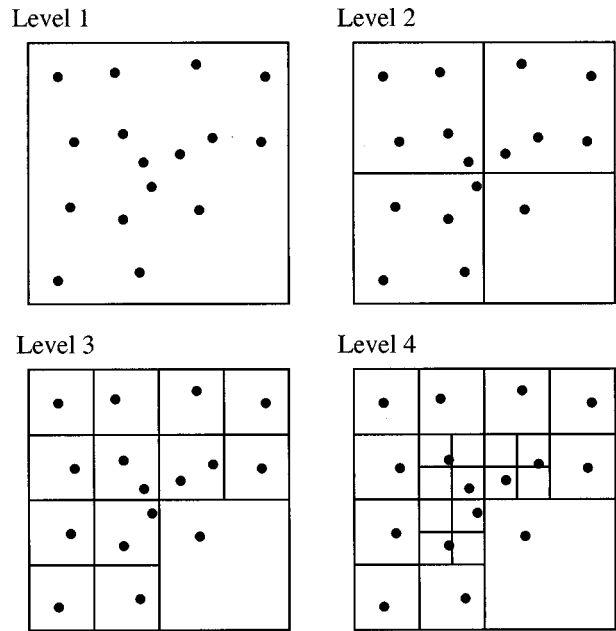


Fig. 2 Example of a two-dimensional tree created for 16 atoms and allowing one particle per box

built by traversing the tree bottom-up, starting at the next coarsest level where all (at most 8) boxes are colleagues. At higher levels of the tree the colleagues of a box are searched from the children of colleagues of the box's parent. This effectively limits the search to 6^3 boxes for each box. The colleagues (marked with an \times) of the shaded boxes are shown in Fig. 3. The neighbor list for the childless boxes is finally constructed by considering the colleagues and their descendents of the childless box cf. Fig. 4. The construction of the tree and the neighbor list takes less than 15 percent of the total CPU time.

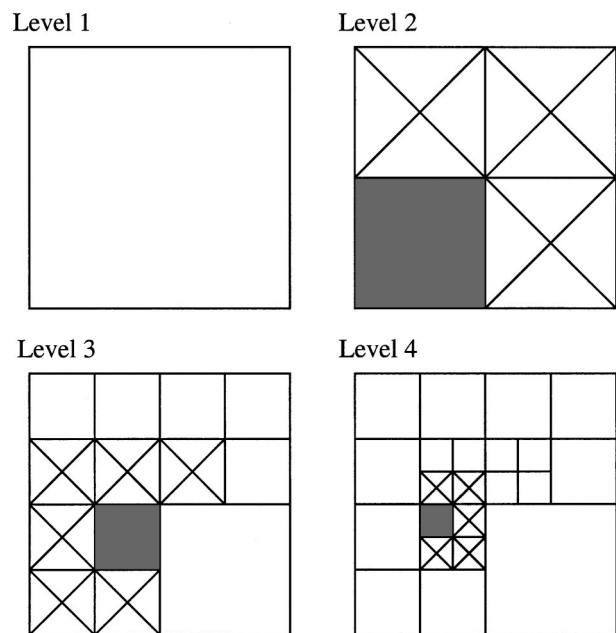


Fig. 3 Example of colleagues of boxes in the two-dimensional tree created for the 16 atoms shown in Fig. 2. The colleagues of the filled boxes are marked with an \times .

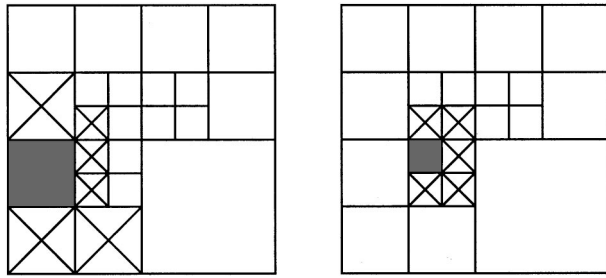


Fig. 4 Example of neighbors of boxes in the two-dimensional tree created for the 16 atoms shown in Fig. 2. The neighbors of the filled boxes are marked with an X. The interactions of the particles in the two (filled) neighboring boxes are computed at the level of the larger box (left) utilizing the symmetry of Eq. (4).

To allow efficient computations, the atoms are mapped onto the boxes using the so called Morton ordering [29,30], in which atoms in neighboring boxes are stored in consecutive memory locations (cf. Fig. 5). This ordering can furthermore be utilized in a parallel domain decomposition of the atoms onto the processors cf. e.g. [31]. Another technique currently being investigated uses the lower levels of the tree to obtain information of the spatial distribution of the atoms and thus guiding the decomposition. After the decomposition the remaining levels of the tree can be constructed independently.

Periodic boundary conditions are handled by explicitly copying the particles in the outer regions to a ‘ghost layer’ outside the computational box before the construction of the tree.

2.2 Initialization. The atoms corresponding to the liquid and vapor phases are initially placed on a face-centered-cubic (f.c.c.) lattice with a liquid and vapor density of $\rho_l^* = 0.715$ and $\rho_v^* = 0.0292$, respectively, corresponding to a non-dimensional saturation temperature of $T_{sat}^* = 0.83$ cf. [32]. The droplet is ‘cut’ from the cubic f.c.c. lattice into a spherical shape to reduce the required relaxation period.

The atoms are assigned a Maxwellian velocity distributed with the desired initial temperature ($T_l^* = T_v^* = T_{sat}^*$) corresponding to a saturation pressure of $p^* = 0.0076$ and well below the critical pressure for argon of $p_{crit}^* = 0.1154$ cf. [33]. At these conditions the droplet will be in equilibrium with the surrounding vapor. The initial mean drift velocity is computed and subtracted accordingly.

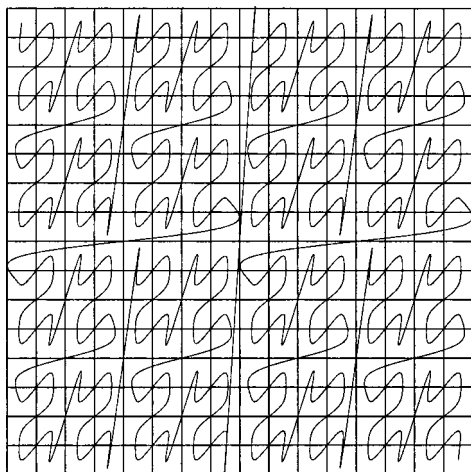


Fig. 5 Atoms in neighboring boxes are stored in consecutive memory locations to allow efficient computations using Morton ordering

Table 1 List of spatial systems investigated. $D^* = D/\sigma$ is the initial droplet diameter, $L^* = L/\sigma$ is size of the computational domain, N_{drop} and N_{vapour} are the initial number of atoms in the droplet and vapor phases respectively. $\alpha = L/D$ is the relative size of the computational domain, and $r_h^* = r_h/\sigma$ the position of the heating element.

System	D^*	L^*	N_{drop}	N_{vapour}	α	r_h^*
I	22	77	5768	13260	6	25
II	22	87	5768	19316	7	25
III	22	103	5768	31664	8	25
IV	38	113	22360	41432	6	30
V	51	155	51105	105480	6	40

The system is subsequently relaxed for 25 or 50 non-dimensional time units by heating the complete system to a temperature of 0.83 at every $\tau_h/\delta\tau$ time step, where $1/\tau_h$ is the heating frequency. During this initial heating the change in droplet diameter is less than 2 percent confirming that the droplet is in equilibrium with the surrounding vapor. After the relaxation, the temperature of the ‘far-field’ vapor atoms is increased to the desired value of $T_v^* = 2.5$.

The size of the computational box ($L \times L \times L$) is chosen sufficiently large to avoid large density and pressure increases during the evaporation, and to accommodate the temperature far-field boundary condition. Using a non-dimensional box size of ($\alpha \equiv L/D$) 6 to 8, where D is the droplet diameter results in pressure rises of 0.012 to 0.0285 (15–40 percent pressure increase), which are both well below p_c^* .

Five spatial systems are investigated including three different droplet diameters ($D = 8, 13, \text{ and } 17 \text{ nm}$) and three different sizes of the computational domain cf. Table 1. The number of atoms range from 5769 and 13260 to 51105 and 105480 for the liquid and vapor phases, respectively. In all the cases, the heating was performed on atoms located well beyond the region of the droplet ($r_h/\sigma > 25, 30, \text{ and } 40$).

2.3 Diagnostics. The density and temperature profiles presented in the following are instantaneous profiles obtained by sampling the enumeration of atoms and the associated kinetic energy in concentric shells of constant radial spacing around the system’s center of mass. A total of fifty shells were found to give a good resolution of the extracted fields.

The size of the droplet is given by the number of atoms found in the liquid phase as [17]

$$D^2 \approx \left(6 \frac{N_{drop} m}{\pi \rho_l} \right)^{2/3}, \quad (7)$$

where a spherical shape has been assumed. Using a simple Cartesian binning of the atoms, and assigning atoms in bins with a sufficiently high density to the liquid phase was found to give insufficient resolution. Instead, the local density is computed at the position of each atom using a spherical binning. A radius of interrogation of $1.5r_c$ provides sufficient statistics while at the same time retaining the spatial resolution. Atoms with a local density exceeding a threshold density (ρ_c^*) are assigned to the liquid phase. The threshold value was found to determine the size of the drop to within a constant and hence not to influence the predicted evaporation rate. Thus, using a fixed value of ρ_c^*

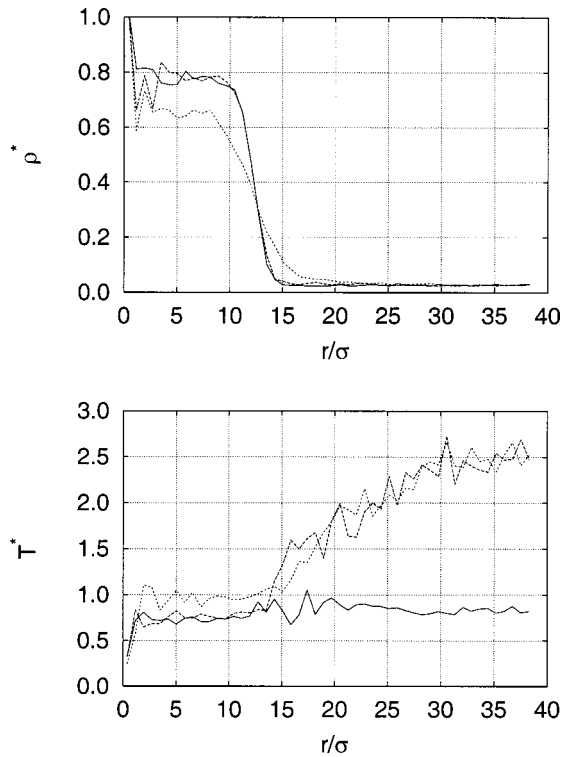


Fig. 6 Droplet density and temperature profiles during accommodation and evaporation of the 5768 atom droplet (Case E01). (—: $\tau^*=25$; ---: $\tau^*=30$; ···: $\tau^*=100$)

=0.298, and applying this procedure to the initial f.c.c. lattice resulted in deviations in number of liquid atoms of less than 3 percent.

2.4 Evaporation. After the initial relaxation, the reduced temperature of the vapor is raised to 2.5 corresponding to a pressure of 0.071. The droplet is heated by the vapor until the saturation temperature is reached at $T^*=1.156$, when the droplet starts to evaporate. The radial density and temperature profiles during heating and evaporation at $\tau^*=25, 30$, and 100 are shown in Fig. 6 for Case I. At $t^*=30$ the center of the droplet is seen to be slightly sub-cooled at a temperature of 0.83.

At these subcritical conditions the droplet is expected to evaporate according to the D^2 evaporation law (1)

$$\frac{d(D^2)}{dt} = -\beta_v,$$

where the evaporation coefficient β_v is given by [5]

$$\beta_v = \left(\frac{8\rho_s \mathcal{D}_s}{\rho_l} \right) \ln(1+B), \quad (8)$$

where ρ_s and \mathcal{D}_s are the density and self-diffusion at the surface of the droplet. The transfer number B is

$$B = \frac{c_p(T_v - T_s)}{h_{fg}}, \quad (9)$$

where c_p and h_{fg} are the specific heat and heat of vaporization, and T_v and T_s are the temperature of the vapor and the droplet surface temperature, respectively. The coefficient of self-diffusion is found from [34]

$$D = 2.6280 \times 10^{-22} \frac{\sqrt{T_v^3/M}}{p_v \sigma^2 \Omega^{(1,1)*}(T_v^*)}, \quad (10)$$

where p_v is the vapor pressure, M the molar mass, and $\Omega^{(1,1)*}$ the collision integral.

Since (ρD) varies slowly with temperature, $(\rho_v \mathcal{D}_v)$ can replace $(\rho_s \mathcal{D}_s)$, and \mathcal{D}_v is the self-diffusion of the vapor. Using the parameters for argon ($c_p = 548$ J/kg K, and $h_{fg} = 88$ kJ/kg) [32], and ($\Omega^{(1,1)*} = 0.996$) [34] the transfer number is close to unity and the diffusion coefficient is 623×10^{-9} m²/s.

The self-diffusion coefficient of the bulk vapor has also been computed in separate equilibrium molecular dynamics simulations for system sizes of 1372 and 2916 atoms, respectively. The self-diffusion is computed from the Green-Kubo relation [26]

$$D = \frac{1}{3N} \int_0^\infty \sum_j^N \mathbf{v}_j(t) \cdot \mathbf{v}_j(0) dt, \quad (11)$$

where $\mathbf{v}_j(t)$ is the velocity of the j th atom at time t . The predicted values are 592×10^{-9} m²/s and 639×10^{-9} m²/s for the two system sizes and within 5 percent of the theoretical value given by Eq. (10).

3 Results

A range of simulations were conducted to study the consistency and convergence of the MD approach and to determine the influence of the cutoff radius, the temporal and spatial resolution, and the heating frequency. The list of simulations is shown in Table 2, and the computational cost for each case is listed in Table 2. The present tree code was compared with a traditional cell index code for System I and V using cutoff values of 2.5 and 5.0, respectively. The cell index was found to be 20–30 percent faster for the smaller cutoff value and for the smaller system (System I), whereas the tree code is approximately 40 percent faster for the larger system (System V) using a cut-off value of 5.0. The comparison was performed on a SGI (Octane R10k) workstation. During the simulations the droplet remained close to the geometrical center of the computational box, and hence no drift adjustment was required.

3.1 Convergence Study. The sensitivity of the different numerical parameters is studied for the radial density and temperature profiles during the evaporation of the 5766 atom droplet.

3.1.1 Spatial Convergence. Simulations are conducted to study the influence of the cutoff radius using $r_c/\sigma = 2.5, 5.0$, and 10.0, respectively. The influence on the non-dimensional radial density and temperature profiles at a non-dimensional time of 200 is shown in Fig. 7. The simulation using the smaller cutoff radius ($r_c/\sigma = 2.5$) clearly exhibits increased evaporation and lower droplet density due to the discontinuous cutoff of the potential and the reduced surface tension [35]. The mean difference between the simulation using a cutoff radius of 2.5 and the simulations using higher cutoff value is 12 percent, whereas the difference between the simulations of 5.0 and 10.0 is less than 1.0 percent. Similar but less severe trends can be observed in the temperature profile (Fig. 7) exhibiting difference less than 1.0 percent between the simulations.

Three different sizes of the computational box, $\alpha = 6, 7$, and 8 are tested, and differences of 2.9 percent and 5.3 percent are observed in the temperature profiles for a non-dimensional time of 100 and 200, respectively (not shown). The corresponding deviations in the density profiles are less than 0.5 percent, consistent with a prediction of the evaporation rate that is insensitive to α .

3.1.2 Temporal Convergence. The temporal convergence is studied using different non-dimensional time step sizes of 0.005 (Case E01) and 0.010 (Case E08), respectively. The differences in both the density and temperature profiles are less than 1.7 percent (not shown). Similar deviations are observed for the length of the initialization period (Cases E01 and E09 using 25 and 50 non-dimensional time units, respectively). The effect of doubling the

Table 2 List of simulation cases. The “system” refers to the spatial systems listed in Table 1, r_c/σ is the cutoff radius, $\alpha=L/D$ the size of the computational box, $\delta\tau^*$ the non-dimensional time step, $\tau_h/\delta\tau$ the heating frequency, $\tau_i/\delta\tau$ the initialization period, CPU time per time step (in seconds on a Sun Ultra 2 workstation), and β_v is the predicted evaporation rate. The theoretical evaporation rate is $1.7 \times 10^{-7} \text{ m}^2/\text{s}$.

Case	System	r_c/σ	α	$\delta\tau^*$	$\tau_h/\delta\tau$	$\tau_i/\delta\tau$	CPU time	β_v
E01	I	2.5	6	0.0050	100	5000	1.0	1.43×10^{-7}
E02	I	5	6	0.0050	100	5000	1.2	1.13×10^{-7}
E03	I	10	6	0.0050	100	5000	3.8	1.13×10^{-7}
E04	II	2.5	7	0.0050	100	5000	-	1.43×10^{-7}
E05	III	2.5	8	0.0050	100	5000	-	1.43×10^{-7}
E06	IV	2.5	6	0.0050	100	5000	-	1.76×10^{-7}
E07	V	2.5	6	0.0050	100	5000	-	1.78×10^{-7}
E08	I	2.5	6	0.0100	50	2500	-	-
E09	I	2.5	6	0.0050	100	10000	-	-
E10	I	2.5	6	0.0050	500	5000	-	-
E11	I	2.5	6	0.0050	1000	5000	-	-

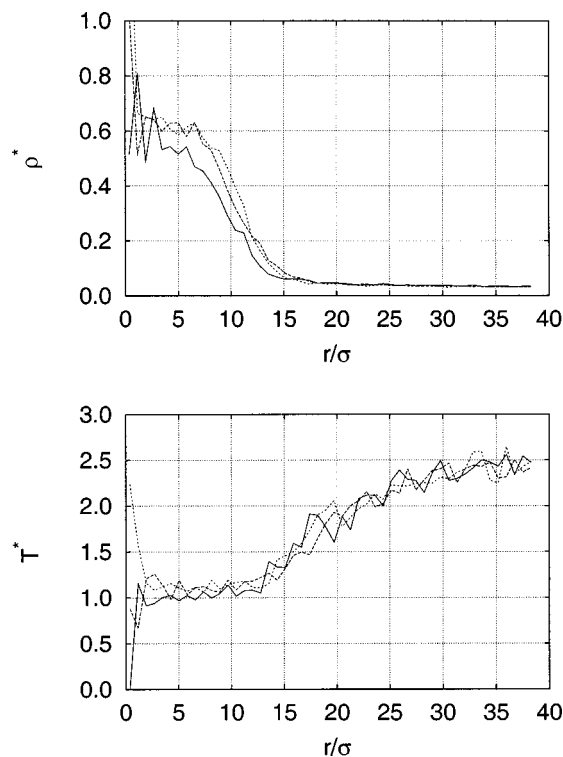


Fig. 7 Convergence of the density and temperature profiles as function of the cutoff radius for the 5768 droplet at $\tau^*=200$. —: $r_c/\sigma=2.5$ (Case E01); ----: $r_c/\sigma=5.0$ (Case E02); - - -: $r_c/\sigma=10.0$ (Case E03)

initialization period results in a difference in the profiles of less than 1.7 percent (not shown). Thus, an initialization period of 25 is used throughout.

3.1.3 Heating Frequency. The effect of the heating frequency ($1/\tau_h$) is studied using three different heating rates: $\tau_h/\delta\tau=100, 500, 1000$ (Cases: E01, E10, and E11), and the difference in the density and temperature profiles are found to be less than 0.5 percent and 1.3 percent, respectively. One simulation was conducted to study the initial heat contents of the system. In this

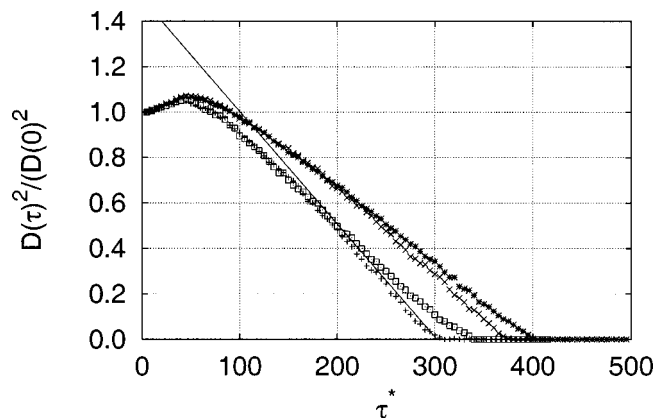


Fig. 8 Evaporation curve for the 5768 droplet. +: E01 ($r_c/\sigma=2.5$); ×: E02 ($r_c/\sigma=5.0$); *: E03 ($r_c/\sigma=10.0$); □: E05 ($r_c/\sigma=2.5$); —: Theory.

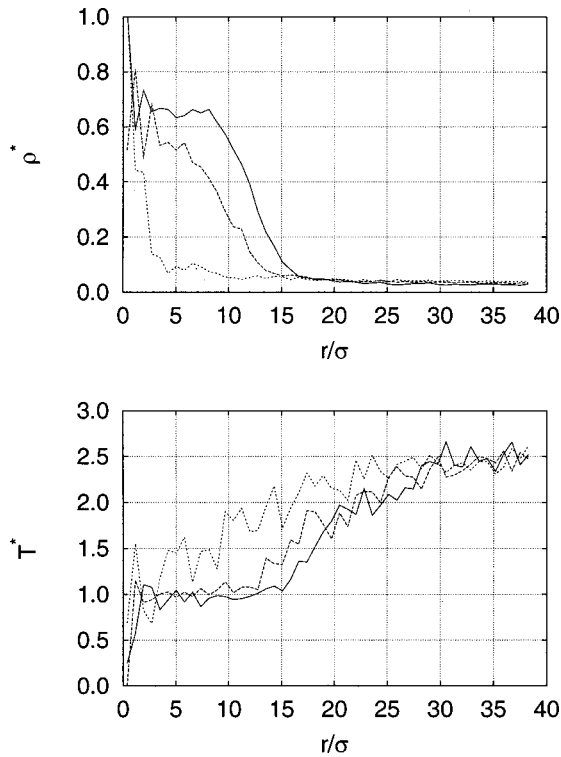


Fig. 9 Density and temperature profiles during evaporation for the 5867 atom droplet (Case E02). —: $\tau^*=100$; ----: $\tau^*=200$; - - -: $\tau^*=300$.

case the heating was stopped after the initialization and the droplet reached an equilibrium with a radius close to the initial.

3.2 Evaporation Coefficient. The non-dimensional evaporation rate (D^2/D_0^2) for the 5867 atom droplet simulation is shown in Fig. 8 for the different cutoff values. D_0 is the initial droplet diameter. The initial relaxation during the first 25 non-dimensional time units, and the subsequent heating of the droplet including condensation of vapor on the droplet [36], is clearly visible until $\tau^* \approx 100$. As the droplet reaches saturation, the evaporation follows the D^2 evaporation law.

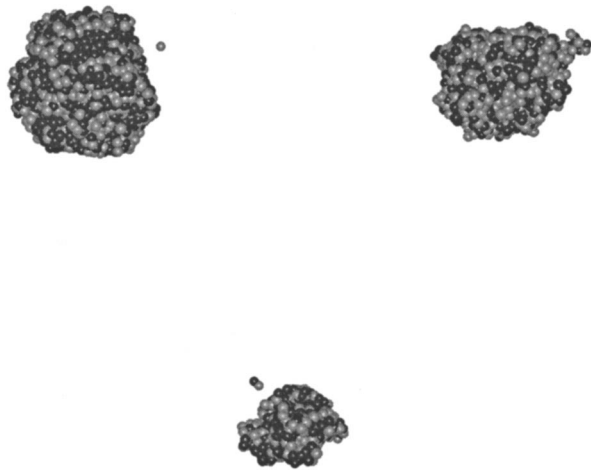


Fig. 10 Time history of the 5867 atom droplet during evaporation (Case E02) (vapor not shown). From left to right: $\tau^* = 100, 200, \text{ and } 300$.

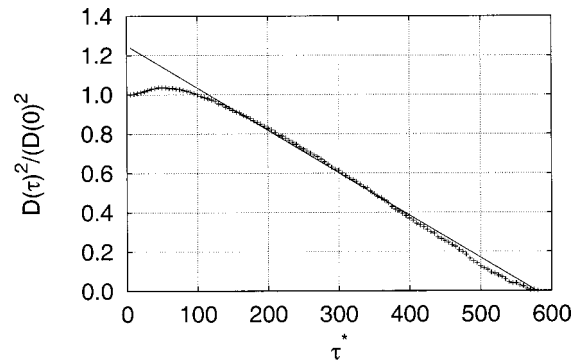


Fig. 11 Evaporation curve for the 22360 atom droplet. +: E06; —: Theory.

The “numerical” heating and evaporation caused by the discontinuous cutoff of the potential is seen for the simulations E01 and E05 as compared to the E02 and E03 cases.

Using Eq. (8) and a mean liquid density of 0.6, see e.g., Fig. 7 gives a theoretical evaporation coefficient of $1.7 \times 10^{-7} \text{ m}^2/\text{s}$. The simulated values extracted from Fig. 8 are $1.43 \times 10^{-7} \text{ m}^2/\text{s}$ and $1.13 \times 10^{-7} \text{ m}^2/\text{s}$ for the small and large cutoff simulation (cf. Table 2). Hence, the predicted evaporation coefficients are within

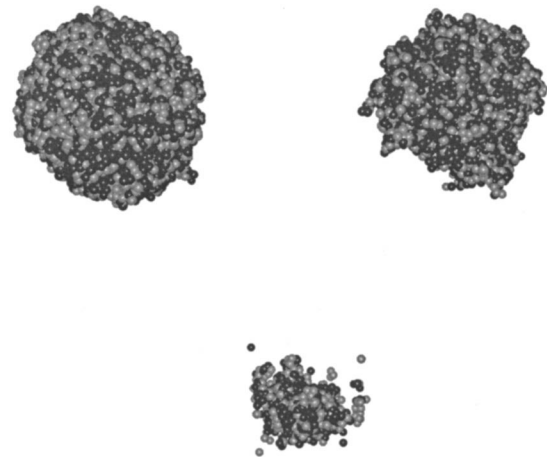


Fig. 12 Time history of the 22360 atom droplet during evaporation (vapor not shown). From left to right: $\tau^* = 100, 300, \text{ and } 500$.

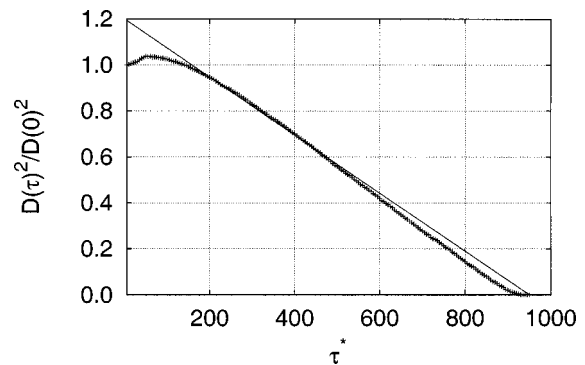


Fig. 13 Evaporation curve for the 51104 atom droplet. +: E07; —: Theory.

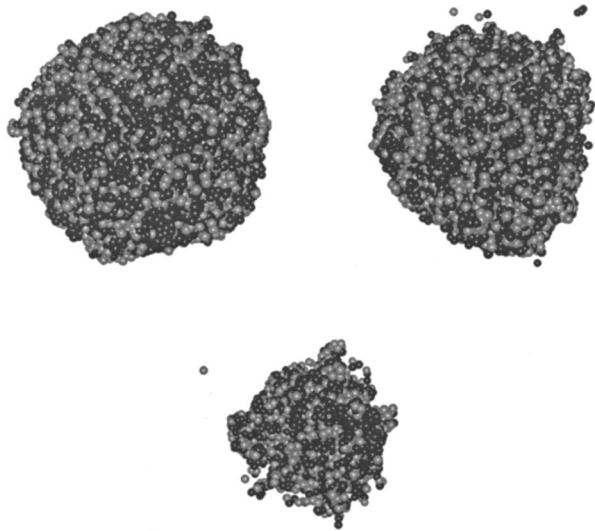


Fig. 14 Time history of the 51104 droplet during evaporation. From left to right: $\tau^* = 100, 400, \text{ and } 700$.

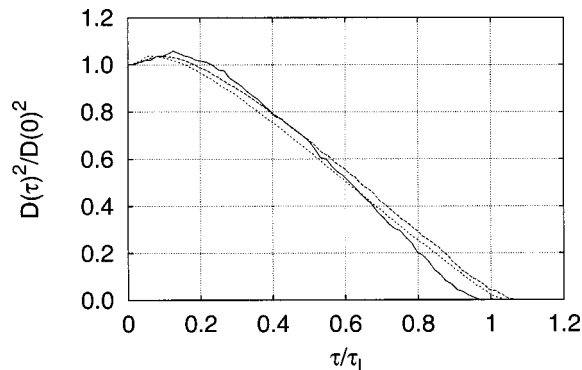


Fig. 15 Evaporation rate. —: 5678 atom droplet; ----: 22310 atom droplet; - · - ·: 51104 atom droplet.

16 percent to 34 percent of the theoretical value. Deviations of the same magnitude were also found by Little [17], using similar number of atoms.

The corresponding radial density and temperature profiles are shown in Fig. 9. The instantaneous position of the liquid atoms during evaporation (Case E02) as determined from the local density method is shown in Fig. 10. Atoms originally in the vapor or liquid phases are coloured light gray and black, respectively. The atoms are plotted in scale as spheres with a radius of σ .

Higher resolution simulations were run in order to establish the convergence of the method with respect to theoretically predicted values. The evaporation curve, density and temperature profiles, and snapshots for the 22360 and 51104 atom droplets are shown in Figs. 11–12 and 13–14, respectively. The simulated evaporation coefficients are $1.76 \times 10^{-7} \text{ m}^2/\text{s}$ and $1.78 \times 10^{-7} \text{ m}^2/\text{s}$ cf. Table 2, both in excellent agreement with the theoretical value. Thus, the simulations converge to the theoretical values as the number of droplet atoms is increased beyond 10^4 .

To combine the evaporation curves for the different droplet sizes, time is non-dimensionalized using the macro-scale droplet life time,

$$\tau_l = \frac{\beta_v}{D_0^2} \quad (12)$$

where D_0 is the initial droplet diameter extrapolated from Figs. 8, 11, and 13. The evaporation rate consequently collapses as shown in Fig. 15.

4 Conclusion

The sub-critical evaporation of a nanometer-size droplet has been simulated using the method of molecular dynamics. The far-field boundary condition for the temperature is implemented by a regional heating technique, allowing correct prescription of far-field conditions.

An adaptive tree data structure is employed to sort the particles and to build the neighbor lists in order to reduce the computational cost. The efficiency is further enhanced by mapping the particles consecutively in memory using Morton ordering.

Convergence of the method has been demonstrated by varying the numerical parameters such as droplet size, domain size, cutoff range, time step size, initialisation length, and heating frequency.

Three argon droplets with diameters of approximately 8, 13, and 17 nm corresponding to 5768, 22360, and 51105 liquid atoms, respectively, were evaporated into an argon vapor at a non-dimensional temperature of 2.5 and a pressure of 0.071. For the 8 nm droplet, the evaporation rate was found within 35 percent of the theoretical predictions, whereas the evaporation rate of the two larger droplets deviated less than 5 percent.

In the investigated parameter range, the largest differences were observed for the simulations using different cutoff values resulting in increasing the evaporation rate for the smaller cutoff values.

The results of the simulations demonstrate that molecular dynamics simulations can be a consistent numerical method for the simulation of thermodynamics of nano-scale phenomena. New computational techniques and algorithms allow us to conduct routine calculations using tens of thousands and hundred of thousands of atoms, thus reaching more realistic behavior of the system being simulated.

Nomenclature

Greek

- α = non-dimensional box size
- β_v = evaporation coefficient
- $\delta\tau$ = non-dimensional time step
- ϵ = energy scale of Lennard-Jones potential
- ρ = density
- σ = zero energy distance of Lennard-Jones potential
- τ = time
- τ_l = droplet life time
- τ_h = heating time interval
- $\Omega^{(1,1)}$ = collision integral

Roman

- B = transfer number
- \mathcal{D} = self-diffusion coefficient
- \mathcal{D}_s = self-diffusion coefficient at the surface of the droplet
- \mathcal{D}_v = self-diffusion coefficient of the vapor
- D = droplet diameter
- E_{kin} = kinetic energy
- L = size of computational box
- N = total number of atoms
- N_h = number of atoms in heating region
- N_{drop} = number of atoms in the droplet
- T = temperature
- V = potential
- c_p = specific heat
- h_{fg} = heat of vaporisation
- k_B = Boltzmann's constant
- m = atomic mass
- r = distance
- r_c = cutoff radius
- r_h = distance from center of box to heating region

r_i = distance from center of box to i -th atom
 p = pressure
 v = velocity
 T = temperature
 T_{sat} = saturation temperature
 t = time

Superscripts

* = non-dimensional quantity

Subscripts

0 = initial value
 crit = critical
 v = vapor
 l = liquid
 c = cutoff
 h = belonging to heating region
 i = initialisation
 sat = saturation

References

- [1] Glassman, I., 1994, "A Look Forward: The Next 25 Years," *Combust. Sci. Technol.*, **98**, pp. 217–222.
- [2] Brezinsky, K., 1994, "The Next Twenty Five Years of Combustion Research: One Researcher's Perspective," *Combust. Sci. Technol.*, **98**, pp. 237–243.
- [3] Sirignano, W. A., 1993, "Fluid Dynamics of Sprays—1992 Freeman Scholar Lecture," *J. Fluids Eng.*, **115**, pp. 345–378.
- [4] Aggarwal, S. K., and Peng, F., 1995, "A Review of Droplet Dynamics and Vaporization Modeling for Engineering Calculations," *ASME J. Eng. Gas Turbines Power*, **117**, pp. 453–461.
- [5] Kuo, K. K.-Y., 1986, *Principles of Combustion*, John Wiley & Sons, New York.
- [6] Shuen, J. S., Yang, V., and Hsiao, C. C., 1992, "Combustion of Liquid-Fuel Droplets in Supercritical Conditions," *Combust. Flame*, **89**, pp. 299–319.
- [7] Yang, V., Lin, N. N., and Shuen, J.-S., 1994, "Vaporization of Liquid Oxygen (LOX) Droplets in Supercritical Hydrogen Environments," *Combust. Sci. Technol.*, **97**, pp. 247–270.
- [8] Protzenko, S. P., and Skripov, V. P., 1977, "Molecular-Dynamics Calculation of Thermodynamic Properties and Structure System of Liquid Argon Nuclei," *Sov. J. Low Temp. Phys.*, **3**, No. 1, pp. 1–4.
- [9] Rusanov, A. I., and Brodskaya, E. N., 1977, "The Molecular Dynamics Simulation of a Small Drop," *J. Colloid Interface Sci.*, **62**, No. 3, pp. 542–555.
- [10] Powles, J. G., Fowler, R. F., and Evans, W. A. B., 1983, "A New Method for Computing Surface Tension Using a Drop of Liquid," *Chem. Phys. Lett.*, **96**, No. 3, pp. 289–292.
- [11] Thompson, S. M., Gubbins, K. E., Walton, J. P. R. B., Chantry, R. A. R., and Rowlinson, J. S., 1984, "A Molecular Dynamics Study of Liquid Drops," *J. Chem. Phys.*, **81**, No. 1, pp. 530–542.
- [12] Yasuoka, K., Matsumoto, M., and Kataoka, Y., 1994, "Evaporation and Condensation at a Liquid Surface of Argon," *J. Chem. Phys.*, **101**, No. 9, pp. 7904–7911.
- [13] Matsumoto, M., 1996, "Molecular Dynamics of Liquid Surfaces," *Mol. Simul.*, **16**, pp. 209–217.
- [14] Zhakhovskii, V. V., and Anisimov, S. I., 1997, "Molecular-Dynamics Simulation of Evaporation of a Liquid," *JETP*, **84**, No. 4, pp. 734–745.
- [15] Rytönen, A., Valkealahti, S., and Manninen, M., 1997, "Melting and Evaporation of Argon Clusters," *J. Chem. Phys.*, **106**, No. 5, pp. 1888–1892.
- [16] Long, L. N., Micci, M. M., and Wong, B. C., 1996, "Molecular Dynamics Simulations of Droplet Evaporation," *Comput. Phys. Commun.*, **96**, pp. 167–172.
- [17] Little, J. K., 1996, "Simulation of Droplet Evaporation in Supercritical Environments Using Parallel Molecular Dynamics," Ph.d. thesis, The Pennsylvania State University.
- [18] Kaltz, T. L., Long, L. N., Micci, M. M., and Little, J. K., 1998, "Supercritical Vaporization of Liquid Oxygen Droplets Using Molecular Dynamics," *Combust. Sci. Technol.*, **136**, pp. 279–301.
- [19] Svanberg, M., Marković, N., and Petterson, J. B. C., 1998, "Collision Dynamics of Large Water Clusters," *J. Chem. Phys.*, **108**, No. 14, pp. 5888–5897.
- [20] Sikdar, S., and Chung, J. N., 1997, "A Quasimolecular Approach for Discrete Study of Droplet Collision," *Int. J. Comput. Fluid Dyn.*, **8**, pp. 189–200.
- [21] Murad, S., and Law, C. K., 1999, "Molecular Simulation of Droplet Collision in the Presence of Ambient Gas," *Mol. Phys.*, **96**, No. 1, pp. 81–85.
- [22] Ashurst, W. T., and Holian, B. L., 1999, "Droplet Size Dependence Upon Volume Expansion Rate," *J. Chem. Phys.*, **111**, No. 6, pp. 2842–2843. (Letters to the Editor).
- [23] Grönbeck, H., Tománek, D., Kim, S. G., and Rosén, A., 1997, "Does Hydrogen Pre-Melt Palladium Clusters?," *Chem. Phys. Lett.*, **264**, pp. 39–43.
- [24] Westergren, J., Grönbeck, H., Kim, S.-G., and Tománek, D., 1997, "Noble Gas Temperature Control of Metal Clusters: A Molecular Dynamics Study," *J. Chem. Phys.*, **107**, No. 8, pp. 3071–3079.
- [25] Verlet, L., 1967, "Computer Experiments on Classical Fluids," *Phys. Rev.*, **159**, pp. 98–103.
- [26] Allen, M. P., and Tildesley, D. J., 1987, *Computer Simulation of Liquids*, Clarendon Press, Oxford.
- [27] Grest, G. S., and Dünweg, B., 1989, "Vectorized Link Cell FORTRAN Code for Molecular Dynamics Simulations for a Large Number of Particles," *Comput. Phys. Commun.*, **55**, pp. 269–285.
- [28] Plimpton, S., 1995, "Fast Parallel Algorithms for Short-Range Molecular Dynamics," *J. Comput. Phys.*, **117**, pp. 1–19.
- [29] Samet, H., 1989, *The Design and Analysis of Spatial Data Structures*, Addison-Wesley Publishing Company.
- [30] Cottet, G.-H., and Koumoutsakos, P., 2000, *Vortex Methods: Theory and Practice*, Cambridge University Press, New York.
- [31] Salmon, J. K., and Warren, M. S., 1993, "Skeletons From the Treecode Closet," *J. Chem. Phys.*, **111**, pp. 136–155.
- [32] Rabinovich, V. A., Vasserma, A. A., Nedostup, V. I., and Veksler, L. S., 1988, *Thermophysical Properties of Neon, Argon, Krypton, and Xenon*, Hemisphere.
- [33] Reynolds, W. C., 1979, *Thermodynamic Properties in SI*, Stanford University.
- [34] Hirschfelder, J. O., Curtiss, C. F., and Bird, R. B., 1967, *Molecular Theory of Gases and Liquids*, 4th ed., John Wiley & Sons, New York.
- [35] Mecke, M., Winkelmann, J., and Fischer, J., 1997, "Molecular Dynamics Simulation of the Liquid-Vapor Interface: The Lennard-Jones Fluid," *J. Chem. Phys.*, **107**, No. 21, pp. 9264–9270.
- [36] Margerit, J., and Sero-Guillaume, O., 1996, "Study of the Evaporation of a Droplet in Its Stagnant Vapor by Asymptotic Matching," *Int. J. Heat Mass Transf.*, **39**, No. 18, pp. 3887–3898.

Monte Carlo Study of Phonon Transport in Solid Thin Films Including Dispersion and Polarization

Sandip Mazumder

e-mail: sm@cfdr.com

Assoc. Mem. ASME

CFD Research Corporation,

215 Wynn Drive,

Huntsville, AL 35805

Arunava Majumdar

6185 Etcheverry Hall,

Department of Mechanical Engineering,

University of California,

Berkeley, CA 94720-1740

e-mail: majumdar@me.berkeley.edu

The Boltzmann Transport Equation (BTE) for phonons best describes the heat flow in solid nonmetallic thin films. The BTE, in its most general form, however, is difficult to solve analytically or even numerically using deterministic approaches. Past research has enabled its solution by neglecting important effects such as dispersion and interactions between the longitudinal and transverse polarizations of phonon propagation. In this article, a comprehensive Monte Carlo solution technique of the BTE is presented. The method accounts for dual polarizations of phonon propagation, and non-linear dispersion relationships. Scattering by various mechanisms is treated individually. Transition between the two polarization branches, and creation and destruction of phonons due to scattering is taken into account. The code has been verified and evaluated by close examination of its ability or failure to capture various regimes of phonon transport ranging from diffusive to the ballistic limit. Validation results show close agreement with experimental data for silicon thin films with and without doping. Simulation results show that above 100 K, transverse acoustic phonons are the primary carriers of energy in silicon. [DOI: 10.1115/1.1377018]

Keywords: Conduction, Heat Transfer, Microscale, Monte Carlo, Non-Equilibrium, Thin Films

1 Introduction

During the past decade, aggressive scale-down in the feature sizes of electronic devices has renewed interest in the physics of energy carriers in solid crystalline materials. The central focus of the device physics community, however, has been on electron transport, which is primarily responsible for the electronic performance of a material. The miniaturization of electronic devices, coupled with faster processing speeds, results in a very large quantity of heat being generated per unit volume in these devices. The efficient removal of heat from such devices is a daunting task, and overheating is one of the most common causes of device failure. Recent trends show that thermal issues are rapidly becoming the central focus. In order to address this problem, it is first necessary to understand the fundamental physics of heat conduction in microscale solid thin films.

Heat conduction in crystalline materials occurs by lattice vibrations, which produce quanta of energy called phonons. A detailed discussion on the wave versus particle nature of energy transport in solids may be obtained from classical texts by Ziman [1], Kittel [2], or from more recent ones by Tien et al. [3]. The phonons travel through space and engage in anharmonic interactions with one another (phonon-phonon scattering), and with electrons, impurities, and geometric boundaries. The average distance a phonon travels before it interacts with another phonon is its mean free path. The drift (or ballistic movement) of phonons result in deviation from thermodynamic equilibrium. Phonon-phonon scattering helps restore thermodynamic equilibrium. Other forms of scattering do not necessarily restore thermodynamic equilibrium. If the characteristic size of a solid material is much larger than the mean free path of the resident phonons, the number of scattering events is large, and local thermodynamic equilibrium is restored. Under

these conditions, a temperature gradient is established within the medium, and the overall transport process is diffusion-like. This regime (diffusion limit) can be described accurately using the Fourier Law of heat conduction. If the characteristic dimension of the medium is significantly smaller than the mean free path of the phonons (ballistic limit), scattering events are rare, and thermodynamic equilibrium may not exist in the material. Here, the Fourier Law of heat conduction is invalid. The effective mean free path of phonons in undoped silicon is approximately 300 nm [4]. This is already much larger than the characteristic dimension of some of the devices used today. This implies that the transport phenomena in such devices cannot be described using diffusion approximations.

The Boltzmann Transport Equation (BTE) is the most suitable candidate for describing phonon transport in crystalline solids. This is attributed to its ability to correctly describe both equilibrium and non-equilibrium phenomena. In the 1950s and 1960s, when computers were in their infancy, solid state physicists attempted to obtain closed-form analytical solutions of the BTE for phonon transport [5–11]. This, however, is possible only after a number of simplifying assumptions, some of which are not justifiable from a physical standpoint, and therefore, result in significant discrepancies with experimentally observed behavior. For example, Ju and Goodson [4] pointed out that if phonon dispersion in silicon is neglected, the average mean free path of phonons is only about 43 nm, as opposed to 300 nm when dispersion is accounted for. With the advent of modern high-speed computers, it is now possible to remove these assumptions, and solve the BTE in its most general form. Over the last decade or so, there has been tremendous advancement in the development of solution techniques for the BTE for charge carriers [12–16]. However, limited progress has been made in the area of solution of the BTE for phonon transport. Recent works by Majumdar et al. [17], Chen and Tien [18], Goodson [19], and Chen [20] have presented solution strategies for both the diffusion and the ballistic limit. However, in such calculations dispersion was neglected, and the dual

Contributed by the Heat Transfer Division for publication in the JOURNAL OF HEAT TRANSFER. Manuscript received by the Heat Transfer Division April 24, 2000; revision received January 20, 2001. Associate Editor: D. Poulikakos.

polarizations of phonon propagation were replaced by a single “average” (or “effective”) polarization branch. Furthermore, such calculation strategies can only be adopted for considerably simplified geometry. If all these assumptions are removed, it is extremely difficult to solve the BTE for phonons by a deterministic approach in an arbitrary geometry, simply because the number of independent variables is too large, and would render any kind of discretization scheme too complex to be practical. Furthermore, the nonlinear scattering events are difficult to incorporate without an overall relaxation time approximation [3], in which case, individual scattering events cannot be treated in isolation. The alternative is to solve the BTE using stochastic or Monte Carlo techniques. Monte Carlo techniques have been used with success for electron transport simulations, and they have also been used for phonon transport by Klistner [21] and by Peterson [22]. Peterson’s work assumes the linear Debye theory and may be considered useful as a starting point. Some of the ideas in this article are borrowed from Peterson’s work [22]. However, Peterson’s work is far from complete, and makes the same simplifying assumptions, discussed earlier. Klistner’s work focuses on the ballistic limit only. It is now necessary to develop comprehensive solution strategies for the BTE phonon transport to study thermal behavior of solid state devices, and to bring phonon transport computations at par with its electronic counterpart. This is the first attempt at a comprehensive Monte Carlo solution technique for the solution of the BTE for phonons. The objective is to present a solution technique and algorithm, which removes most assumptions that have been made in the past, and is sufficiently general to be adopted for future modeling work in this area. It is demonstrated here that modeling of this nature can help extract critical information pertaining to the physics of phonon transport.

2 Theory

Although, the following material may be found in any fundamental text on solid state physics, it is necessary to briefly discuss the underlying theory of phonons and the BTE of phonons, prior to discussion of numerical techniques pertaining to the solution of the BTE for phonons.

2.1 Lattice Vibrations and Phonons. A crystal lattice can be visualized as a complex three-dimensional array of masses (representing individual atoms) and springs (representing atomic bonds). The deviation from the equilibrium position of an individual atom within the lattice result in vibrational waves, which propagate through the crystal and carry energy. The vibrational energy of the atoms is quantized, and each quantum is called a phonon. A phonon is an ensemble of travelling waves having a certain frequency, ν , a certain group velocity, \mathbf{V}_g , and carrying with it energy equal to $h\nu$, where h is the Planck constant.

Under thermodynamic equilibrium, the temperature of a medium is well defined. At a temperature, T , the equilibrium phonon occupation number, $\langle n \rangle$, is given by the Bose-Einstein distribution [2]

$$\langle n \rangle = \frac{1}{\exp\left[\frac{\hbar\omega}{k_B T}\right] - 1}, \quad (1)$$

where ω is the angular frequency (radians/s) of the phonon ($=2\pi\nu$), $\hbar = h/2\pi$, and k_B is the Boltzmann constant. The total vibrational energy in a material of volume $V=L^3$ is written as [2]

$$E \cdot V = \sum_p \sum_{\mathbf{K}} \left(\langle n \rangle + \frac{1}{2} \right) \hbar \omega, \quad (2)$$

where E is the energy per unit volume of the material. The summations in Eq. (2) have been performed over all polarizations of the various modes of phonon propagation (longitudinal optical, transverse optical, longitudinal acoustic and transverse acoustic), p , and wave-vector, \mathbf{K} . The wave-vector space over which the

summation in Eq. (2) is performed, is the first Brillouin zone. Optical phonons do not contribute significantly to thermal transport [2,5]. They are eliminated from the summation over the various modes for our current needs. For a large crystal, the wave vector space is very dense, and can be assumed to be continuous. This enables replacement of the summation in Eq. (2) by an integral, yielding

$$E \cdot V = \sum_p \int_{\mathbf{K}} \left(\langle n \rangle + \frac{1}{2} \right) \hbar \omega \frac{d\mathbf{K}}{(2\pi/L)^3}. \quad (3)$$

The integration over wave-vector space can be transformed to an integration over frequency space by invoking the dispersion relation, $\mathbf{K}=\mathbf{K}(\omega, p)$, and assuming that the Brillouin zone is isotropic, yielding

$$E = \sum_p \int_{\omega} \left(\langle n \rangle + \frac{1}{2} \right) \hbar \omega D(\omega) d\omega, \quad (4)$$

where $D(\omega)$ is the density of state, and is expressed as [2]

$$D(\omega) = \frac{K^2}{2\pi^2} \frac{dK}{d\omega}. \quad (5)$$

The quantity $D(\omega)d\omega$ represents the number of vibrational states between ω and $\omega + d\omega$. The second term within parenthesis in Eq. (4) is independent of temperature, and can be summed up to yield the so-called zero-point energy. Finally, the group velocity of phonons is defined as [2]:

$$\mathbf{V}_g = \nabla_{\mathbf{K}} \omega. \quad (6)$$

The above six equations completely describe the state of a phonon, and are sufficient for the realization of the numerical scheme to be discussed in Section 3.

2.2 BTE for Phonons. The Boltzmann Transport Equation is a transport equation describing the transport of an ensemble of particles (or stochastic samples). In the case of phonons, it assumes the following form [3]:

$$\frac{\partial f}{\partial t} + \mathbf{V}_g \cdot \nabla f = \left[\frac{\partial f}{\partial t} \right]_{\text{scat}} = \sum_{\mathbf{K}'} [\Phi(\mathbf{K}, \mathbf{K}') f(\mathbf{K}') - \Phi(\mathbf{K}', \mathbf{K}) f(\mathbf{K})], \quad (7)$$

where $f(t, \mathbf{r}, \mathbf{K})$ is the distribution function of an ensemble of phonons, and \mathbf{r} is the position vector describing the position of an individual stochastic particle. The left-hand side of Eq. (7) represents drift, and causes departure from equilibrium, while the scattering term on the right-hand side of Eq. (7) restores equilibrium. The distribution function is, in general, a function of seven independent variables, namely, time, three space variables, and three wave-vector variables. $\Phi(\mathbf{K}, \mathbf{K}')$ is the scattering rate from state \mathbf{K}' to \mathbf{K} , and is usually a nonlinear function of \mathbf{K} . These complexities render the solution of the BTE extremely difficult by deterministic means.

3 Monte Carlo Solution Technique

In a Monte Carlo solution technique, samples are drawn from the six individual stochastic spaces. These include the three wave-vector components and the three position vector components. The samples (phonons, in this case) are then allowed to drift (or unrestrained motion) and scatter in time, and their statistics is collected at various points in time and space, and processed to extract the necessary information.

3.1 Initial Conditions.

Number of Phonons. The first step is to initialize the states of the ensemble of phonons that are to be used for the Monte Carlo simulation. Prior to initialization, it is first necessary to determine how many phonons need to be initialized within each control volume. The number of phonons per unit volume, and polarization p , excluding the zero-point number, is given by [from Eq. (4)]

$$N(p) = \sum_{i=1}^{N_b} \langle n(\omega_{0,i}, p) \rangle D(\omega_{0,i}, p) \Delta \omega_i, \quad (8)$$

where the integral over frequency space has been replaced by a discrete summation. N_b is the number of spectral intervals or bands into which the frequency space is broken into, and $\Delta \omega$ is the spectral band width. The central frequency of the i th spectral band is $\omega_{0,i}$. The number of phonons, resulting from Eq. (8), is usually an extremely large number (for example, at 80 K, silicon has approximately 4.5×10^{22} phonons/m³). In practice, it is not feasible to simulate that many phonons, and therefore, a scaling factor is required. First a decision is made as to how many phonons will be traced (an input to the code). Let this number be $N_{\text{prescribed}}$. The code then calculates a scaling factor from the expression

$$W = \frac{N_{\text{actual}}}{N_{\text{prescribed}}}, \quad (9)$$

where N_{actual} is computed using Eq. (8) after summing over all polarizations. This scaling factor, W , is then stored permanently, and used for the remainder of the computational process. Each stochastic sample used during the simulation actually represents an ensemble of W phonons. During the simulation, of course, the total number of samples within the computational domain may change depending on the boundary conditions.

Position. The numerical scheme to initialize the position of a phonon depends on the type of control volume cells used for spatial sampling of the phonons. For example, if all control volumes are rectangular orthogonal hexahedra, the initialization consists of drawing three random numbers to assign a random set of coordinates (x, y, z) within the hexahedron. This may well be sufficient for the simulation of simple geometries. However, since our goal is to develop a solution technique, which is to be used eventually for the thermal analysis of entire semiconductor devices, it is necessary to adopt a more general strategy. In general, a spatial bin (or cell) may be an arbitrary polyhedron in three-dimensional and arbitrary polygon in two-dimensional. It is always possible to dissect this cell into its smallest element, which is a tetrahedron in three-dimensional and triangle in two-dimensional. Details of such procedure are beyond the scope of this article, and may be obtained from references on unstructured grid generation [23]. The position vector, \mathbf{r}_P , of any point P , within a triangle (in two-dimensional) or tetrahedron (in 3D) is expressed as

$$\mathbf{r}_P = \begin{cases} \mathbf{r}_A + R_1 \mathbf{a} + R_2 \mathbf{b} & \mathbf{2D} \\ \mathbf{r}_A + R_1 \mathbf{a} + R_2 \mathbf{b} + R_3 \mathbf{c} & \mathbf{3D} \end{cases} \quad (10)$$

where R_1 , R_2 , and R_3 are random numbers between zero and unity, and \mathbf{r}_A is the position vector of point A . In addition, R_1 and R_2 must obey the inequality: $R_1 + R_2 < 1$. The vectors \mathbf{a} , \mathbf{b} , and \mathbf{c} are illustrated in Fig. 1.

Frequency. As a first step, the dispersion relationship of the material is provided to the code in the form of a table. From this data, the maximum cut-off frequencies of the longitudinal acoustic (LA) and transverse acoustic (TA) branches are determined. They are denoted by $\omega_{\text{max,LA}}$ and $\omega_{\text{max,TA}}$, respectively. The frequency space between zero and $\omega_{\text{max,LA}}$ is then discretized into spectral intervals, $\Delta \omega_i = \omega_{\text{max,LA}} / N_b$, where N_b is the number of spectral intervals. It was determined by trial-and-error studies, that for most cases, 1000 equal-sized spectral intervals serves the pur-

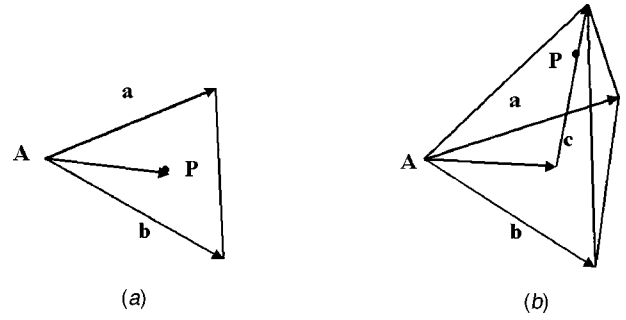


Fig. 1 Pictorial representation of phonon initial position, P , in (a) two-dimensional triangular element, and (b) three-dimensional tetrahedral element

pose. At low temperatures, where the frequency distribution is highly nonlinear, it may be worthwhile to have more than 1000 spectral intervals. However, this will increase computational cost, and will result in poor statistical sampling within some spectral intervals. Furthermore, as our computations will show, 1000 intervals, even at low temperatures, result in less than 2 percent errors in solutions.

The number of phonons per unit volume in the i th spectral interval is given by

$$N_i = \langle n(\omega_{0,i}, LA) \rangle D(\omega_{0,i}, LA) \Delta \omega_i + 2 \langle n(\omega_{0,i}, TA) \rangle D(\omega_{0,i}, TA) \Delta \omega_i, \quad (11)$$

where the equilibrium distribution is now evaluated at the central frequency of the spectral interval in question. In order to determine the frequency of a phonon, the normalized cumulative number density function is first constructed

$$F_i = \frac{\sum_{k=1}^i N_k}{\sum_{k=1}^{N_b} N_k}. \quad (12)$$

A random number, R , is then drawn. If $F_{i-1} < R < F_i$, then the phonon belongs to the i th spectral interval. A blind search to locate i would be far too expensive. In the current scheme, the search is conducted using a bisection algorithm, which requires the execution of at most 11 such checks. Having determined the spectral interval, the actual phonon frequency is then given by

$$\omega = \omega_{0,i} + (2R - 1) \frac{\Delta \omega_i}{2}, \quad (13)$$

where R is the same random number used to select the spectral interval from Eq. (12). A random number relation has been employed to distribute the frequencies linearly between $\omega_{0,i} - \Delta \omega/2$ and $\omega_{0,i} + \Delta \omega/2$. The assumption here is that the phonon frequency distribution is linear between $\omega_{0,i} - \Delta \omega/2$ and $\omega_{0,i} + \Delta \omega/2$. The advantage of this approach is that instead of having discrete frequencies of $\omega_{0,i}$, we now have an almost continuous frequency space.

Polarization. Any phonon, initialized within the computational domain has to be assigned to either a LA branch or a TA branch. To determine which branch the phonon will belong to, first, the Bose-Einstein distribution is utilized to calculate the probability of LA to TA phonons at the i th spectral interval (or frequency)

$$P_i(LA/TA) = \frac{N_i(LA)}{N_i(TA) + N_i(LA)} = \frac{\langle n(\omega_{0,i}, LA) \rangle D(\omega_{0,i}, LA)}{2 \langle n(\omega_{0,i}, TA) \rangle D(\omega_{0,i}, TA) + \langle n(\omega_{0,i}, LA) \rangle D(\omega_{0,i}, LA)}, \quad (14)$$

where the equilibrium number of phonons is computed using the thermodynamic temperature of the cell (or spatial bin) in which the phonon is to be initialized, and i is the spectral interval to which the phonon belongs (determined by the procedure outlined in the previous sub-section). Next, a random number between zero and unity is drawn. If the random number is less than $P_i(LA/TA)$, then the phonon belongs to the LA branch. Otherwise, it belongs to a TA branch.

Wave Vector. Once the phonon frequency has been sampled, the wave-vector can be determined directly using the dispersion relationship. In general, given a frequency, ω , an interpolation can be performed within the three-dimensional dispersion table to find K_x , K_y , and K_z . In most cases, however, dispersion relationships are available only in the (100) and (111) directions, and it is, perhaps, best to assume isotropy, as a first step. If we assume isotropy, then K_x is first determined (and this is equal to K_y and K_z). It then follows that the magnitude of the wave-vector $|\mathbf{K}| = \sqrt{3}K_x$ in three-dimensional, and $|\mathbf{K}| = \sqrt{2}K_x$ in two-dimensional cases. The direction of the wave-vector is expressed as

$$\hat{\mathbf{s}} = \begin{pmatrix} \sin \theta \cdot \cos \psi \\ \sin \theta \cdot \sin \psi \\ \cos \theta \end{pmatrix}, \quad (15)$$

where $\psi = 2\pi R_2$, $\cos \theta = 2R_1 - 1$, and $\mathbf{K} = |\mathbf{K}|\hat{\mathbf{s}}$, R_1 and R_2 being random numbers between zero and unity. θ and ψ are polar and azimuthal angles, respectively, and are shown in Fig. 2. In two-dimensional cases, only one random number is necessary, and the direction vector is given by

$$\hat{\mathbf{s}} = \begin{pmatrix} \cos \psi \\ \sin \psi \end{pmatrix}. \quad (16)$$

Once the initialization is complete, the next task is to provide boundary conditions for the simulation scheme.

3.2 Boundary Conditions. Since the primary focus of this article is heat transport, various kinds of thermal boundary conditions will be discussed in this section. The two most common types are isothermal and prescribed heat flux boundary conditions, of which a prescribed heat flux of zero results in a special kind of boundary, namely an adiabatic boundary. In this article, only the treatment of isothermal and adiabatic boundaries is discussed. The treatment of conjugate walls (material interfaces) is required for the study of superlattices, and may be found elsewhere [20,24,25].

An isothermal wall is analogous to a black wall for photon radiation. All phonons that strike it are thermalized (analogous to absorption by a blackbody). Depending on its temperature, the boundary also emits phonons into the computational domain, the

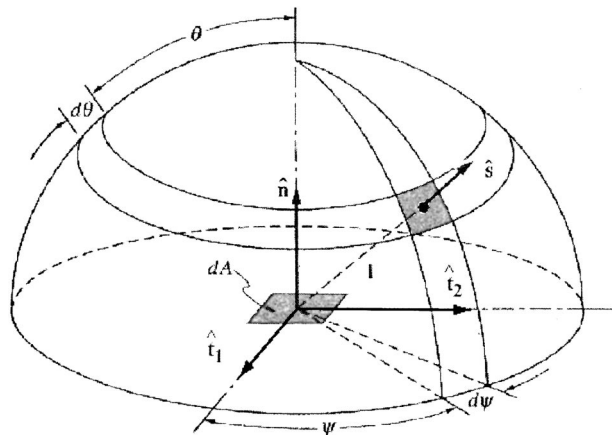


Fig. 2 Coordinate system showing the direction of phonon emission and the associated angles

frequency distribution being governed by Bose-Einstein statistics. The state of emitted phonons is completely independent of the state of incident phonons. In the numerical scheme, any phonon incident on an isothermal wall is tallied, and then deleted from the simulation. This provides the net incident energy during a time interval Δt . The number of phonons emitted from a boundary face of area, A , and temperature, T , is given by

$$N_{\text{face}} = A \cdot \Delta t \cdot \left(\sum_p \sum_{i=1}^{N_b} \langle n(\omega_{0,i}, p) \rangle \langle \mathbf{V}_g(\omega_{0,i}) \cdot \hat{\mathbf{n}} \rangle \times D(\omega_{0,i}, p) \Delta \omega_i \right), \quad (17)$$

where $\mathbf{V}_g(\omega_{0,i}) \cdot \hat{\mathbf{n}}$ represents the phonon velocity normal to the face (Fig. 2). In general, phonons will be emitted from a face in all directions (over a solid angle 2π). The quantity $\mathbf{V}_g(\omega_{0,i}) \cdot \hat{\mathbf{n}}$, therefore, has to be directionally averaged (as indicated by the angled brackets in Eq. (17)) in order to obtain the average normal velocity to the boundary face. In two-dimensional, for example, Eq. (17), after appropriate directional averaging, reduces to

$$N_{\text{face}} = \frac{A}{\pi} \cdot \Delta t \cdot \left(\sum_p \sum_{i=1}^{N_b} \langle n(\omega_{0,i}, p) \rangle \mathbf{V}_g(\omega_{0,i}) D(\omega_{0,i}, p) \Delta \omega_i \right), \quad (18)$$

where N_{face} is the actual number of phonons that should be emitted into the computational domain from the boundary face. The representative number emitted in the simulation would be N_{face}/W .

The emission location of a phonon is determined by drawing random numbers, and distributing the phonons uniformly over the entire face. In three-dimensional, a basic surface element is a triangle, and the procedure described earlier for volumetric two-dimensional elements can be used for three-dimensional surface elements. The frequency of the emitted phonon, the magnitude of the wave-vector, and the polarization of the phonon can be determined by following a procedure similar to the one discussed in Section 3.1. The difference is that the volumetric number density has to be replaced everywhere by face number flux. The direction of the wave-vector depends on the surface normal of the surface in question, and is expressed as follows:

$$\hat{\mathbf{s}} = \sin \theta \cos \psi \hat{\mathbf{t}}_1 + \sin \theta \sin \psi \hat{\mathbf{t}}_2 + \cos \theta \hat{\mathbf{n}}, \quad (19)$$

where $\hat{\mathbf{n}}$ is the unit surface normal, and $\hat{\mathbf{t}}_1$ and $\hat{\mathbf{t}}_2$ are unit surface tangents (Fig. 2), which must be perpendicular to each other. The two surface tangents and the surface normal must follow the right-handed system. First, the surface normal is computed using Gauss-divergence theorem. Next, one of the surface tangents is computed using the coordinates of the vertices of the triangular face in question. The second tangent is computed from the relationship: $\hat{\mathbf{t}}_1 \times \hat{\mathbf{t}}_2 = \hat{\mathbf{n}}$. This ensures that both the above criteria are satisfied.

An adiabatic wall acts as a perfect reflector for the phonons. Most surfaces, irrespective of their polish, act as partially specular reflectors. An excellent discussion on surface reflection characteristics and their impact on boundary scattering of phonons may be found in Klistner [21]. In the current numerical scheme, the degree of specularity, d , can be prescribed. The value of d may vary between zero (completely diffuse reflection) and unity (completely specular). The former scenario results in intense boundary scattering, while the latter poses no resistance to the flow of phonons. The preceding discussion clarifies the point that in the current numerical procedure, boundary scattering is not treated indirectly using so-called geometric factors [5,7,8] and boundary scattering time-scales, but rather, by actual interaction of a traversing phonon with the true geometric boundary. When a phonon

strikes an adiabatic boundary, a random number is first drawn. If this random number is less than the prescribed value of d , the phonon is specularly reflected using the relation

$$\hat{\mathbf{s}}_r = \hat{\mathbf{s}}_i + 2|\hat{\mathbf{s}}_i \cdot \hat{\mathbf{n}}|\hat{\mathbf{n}}, \quad (20)$$

where $\hat{\mathbf{s}}_i$ and $\hat{\mathbf{s}}_r$ are the direction vectors of the incident and reflected phonon, respectively. If this number is larger than d , the phonon is reflected diffusely at the surface using Eq. (19).

3.3 Scattering. Phonons move inside a crystalline material with velocity \mathbf{V}_g and engage in scattering as they move. Scattering is caused by lattice boundaries (intrinsic scattering), defects or dislocations, charge carriers such as electrons, and by external boundaries or material interfaces. Electron-phonon scattering may alter the thermal conductivity of a material under certain situations, but this effect is not well understood. For the current study, such electron-phonon or phonon-free-carrier scattering is neglected. All other types of scattering can potentially affect the thermal conductivity, and, therefore, heat transport in a crystalline material. In the current numerical scheme, the events occurring within a time-step Δt is split into two distinct sequential phases, namely drift¹ and scattering. During the drift phase, phonons move linearly from one location to another. Their positions are tracked using an explicit first-order time integration

$$\mathbf{r}(t + \Delta t) = \mathbf{r}(t) + \mathbf{V}_g \cdot \Delta t. \quad (21)$$

Following the drift phase, phonons are tallied within each spatial bin, and the energy of each spatial bin is computed and stored. This will, henceforth, be referred to as the target energy of the cell, and will be denoted by E_T . At this juncture, the pseudo-temperature, \tilde{T} , of each spatial bin is computed by numerical inversion of Eq. (4):

$$\frac{E_T W}{V} = \sum_p \sum_{i=1}^{N_b} \frac{\hbar \omega_{0,i} D(\omega_{0,i}, p) \Delta \omega_i}{\exp[\hbar \omega_{0,i} / k_B \tilde{T}] - 1}. \quad (22)$$

The pseudo-temperature is an artificial temperature that may be computed for every spatial bin assuming that thermodynamic equilibrium exists in that bin. It is necessary to compute the probability of LA to TA phonons within each spectral bin. For this, Eq. (14) is used, in which the thermodynamic temperature is replaced by the pseudo-temperature. Although it is not clear at this point why these quantities should be computed, it will become clear once the scattering algorithm is discussed. During the second phase of the scheme, phonons within a spatial bin are allowed to engage in three-phonon scattering processes, and are also scattered by impurities when they are present.

Three-Phonon Scattering (Normal and Umklapp Processes). Phonons engage in three-phonon elastic interactions [2] of two types: Normal scattering and Umklapp scattering. The latter directly poses resistance to energy transport, while the former indirectly affects the transport process by altering the frequency distribution of the resident phonons. An immense volume of literature is available, which studies the details of three-phonon interactions of all types in a variety of different materials. At the heart of three-phonon interactions lie the conservation laws of energy and momentum:

$$\omega_1 + \omega_2 \leftrightarrow \omega_3 \quad (\text{Energy Conservation; All})$$

$$\mathbf{K}_1 + \mathbf{K}_2 \leftrightarrow \mathbf{K}_3 \quad (\text{Momentum Conservation; Normal}) \quad (23)$$

$$\mathbf{K}_1 + \mathbf{K}_2 \leftrightarrow \mathbf{K}_3 + \mathbf{G}$$

$$(\text{Momentum Conservation; Umklapp}),$$

¹“Drift”, as described here, is not to be confused with motion under the influence of an external force, such as an electric field. Here, “drift” implies unrestrained ballistic motion from point A to point B.

where \mathbf{G} is the reciprocal lattice vector. During any three-phonon process, energy and momentum must both be satisfied simultaneously. This disallows certain types of transitions between the two polarization branches. It can be shown mathematically [5,7] that the only allowable ones are $LA \leftrightarrow LA + TA$ and $LA \leftrightarrow TA + TA$. In principle, it is possible to incorporate three-phonon scattering by treating each phonon as a potential candidate for scattering and allowing it to interact with every other phonon in its vicinity. The frequency and wave-vector combinations of the interacting phonons would then automatically decide, subject to satisfaction of Eq. (23), if an interaction between them is at all possible. This is the most fundamental approach to computing a phonon’s lifetime. However, in a Monte Carlo scheme, since only limited number of samples are traced, the ω and \mathbf{K} spaces are generally far from being continuous to the degree that all possible triadic interactions can be accounted for. Secondly, such computations would be immensely expensive, and not acceptable for practical problems. The problem is circumvented using perturbation analysis. The equilibrium distribution is first perturbed linearly, and all triadic interactions are considered at a given temperature, allowing the system to come back to equilibrium. By this way, phonon lifetimes can be computed. Discussion on such techniques may be obtained from early work by Klemens [5]. Subsequent analyses, including polarization and normal scattering effects, were performed by Holland [7,8] for a variety of important semiconductor materials. The final outcome of such analysis is expressions for phonon lifetimes, for the two polarization branches, as a function of frequency and temperature.

Once the scattering time-scales for the two polarization branches are known as a function of frequency and temperature, the three-phonon scattering processes can be implemented in the following manner. First, based on the time-scale of scattering and the time-step used, a probability of scattering is computed: $P_{NU} = 1 - \exp(-\Delta t / \tau_{NU})$ [22]. The time-scale, τ_{NU} , is an effective time-scale which accounts for both normal and Umklapp processes, i.e., $\tau_{NU}^{-1} = \tau_U^{-1} + \tau_N^{-1}$, where τ_U and τ_N are time-scales for Umklapp and normal processes, respectively. Next, a random number is drawn and compared with P_{NU} . If the random number is less than P_{NU} , the phonon is scattered. Scattering is implemented by resetting the phonon frequency, wave-vector, and polarization. The frequency is sampled from the equilibrium distribution computed at \tilde{T} . Once the frequency is known, the wave-vector can be determined using the procedure outlined in Section 3.1. The polarization is determined using the LA/TA probability based on \tilde{T} , which was computed and stored after the drift phase. Resetting the state of the phonon essentially thermalizes the phonon and helps restore equilibrium, which is the sole function of three-phonon scattering processes. When the frequency of a certain phonon is changed, energy conservation is violated. After all scattering processes have been completed, the actual energy of each spatial bin is again tallied. This actual energy, E_A , is likely to be different from the cell’s target energy E_T , due to violation of energy conservation. A creation/destruction scheme is next implemented. In this scheme, phonons are continuously added and/or deleted from a cell until the actual energy of the cell matches the target energy of the cell within a certain tolerance. Investigations revealed that a tolerance level equal to $\hbar \omega_{\max,TA}$ is adequate. The added or deleted phonons are drawn from the equilibrium distribution, so that the overall effect of the phonon creation/destruction process is also to restore thermodynamic equilibrium. Depending on the phonon lifetimes, during a given time period, all phonons within the computational domain may not scatter. At low temperature, for example, very few of them will scatter. Thus, although the scattering algorithm may restore local thermodynamic equilibrium, this may only be attained partially, thereby retaining the non-equilibrium nature of transport. This scattering scheme captures all of the essential physics of three-phonon scattering processes. It allows transition between polarization branches, conserves energy, and helps restore ther-

modynamic equilibrium. Momentum conservation is violated, as would be by Umklapp scattering. The shortcoming of the scheme lies in that it cannot treat normal and Umklapp scattering in isolation. The authors are currently in the process of investigating procedures where this may be possible.

Scattering by Impurities. Scattering by impurities, defects and dislocations are treated in the Monte Carlo scheme in isolation from normal and Umklapp scattering. This is difficult in deterministic approaches. The time-scale for scattering due to impurities, τ_i , is used to compute a probability of scattering, and a selection based on a new random number is performed, as discussed earlier. In this case, however, the frequency of the scattered phonon is left unaltered (implying that the magnitude of the wave-vector is also left unaltered). The direction of the wave-vector is changed, the new direction vector being described by Eq. (15) or (16). The time-scale for scattering by impurities is expressed using a simple model proposed by Vincenti and Kruger [26]

$$\tau_i^{-1} = \alpha \sigma \rho |\mathbf{V}_g|, \quad (24)$$

where α is a constant of the order of unity, ρ is the defect density per unit volume, and σ is the scattering cross-section expressed as [17]

$$\sigma = \pi r^2 \left(\frac{\chi^4}{\chi^4 + 1} \right), \quad (25)$$

where r is the atomic radius of the impurity, and $\chi = r|\mathbf{K}|$. In the current study, it is assumed that the main effect of an impurity atom is point scattering. Impurities may alter hole concentrations in the material, resulting in additional scattering, but such effects are neglected, primarily due to the lack of understanding of the physics underlying such scattering.

The scattering procedure, outlined above, employs a relaxation time approximation for the various scattering events. Although this is not as accurate as using the selection rules directly to compute the nonlinear scattering rates, the Monte Carlo procedure does allow treatment of each scattering event in isolation, and this is very important when accounting for the various regimes of transport. The physics of various types of scattering are quite different. For example, intrinsic scattering results in frequency and polarization change, while defect scattering changes the direction of the propagating phonon only. Therefore, it would be grossly incorrect to treat all scattering processes in a similar manner by employing an overall relaxation time, computed using the Matthiessen rule. This is a clear advantage of using the Monte Carlo approach over deterministic approaches used in almost all past studies.

This completes the description of the models and the numerical scheme underlying solution of the BTE for phonons. The commercial engineering analysis software, CFD-ACE+, provided the framework on which the numerical scheme was developed. In choosing a time-step for simulation of phonon transport, it must be ascertained that the chosen time-step is smaller than the smallest scattering time-scale. Furthermore, the time-step should be small enough so that the fastest traveling phonon does not travel a distance, which exceeds the characteristic spatial bin size.

4 Results and Discussion

The code was first tested to ensure that it reproduces the correct limiting behavior and trends. Following such verification, it was used to compute the thermal conductivity of pure and doped silicon films between the temperature of 10–300 K.

4.1 Verification of Numerical Scheme. As discussed earlier, there exist two well-defined limiting scenarios: (1) $l \gg L$ (ballistic limit); and (2) $l \ll L$ (diffusion limit), where l is the average mean free path of the phonons, and L is the characteristic film thickness. The first case results in ballistic transfer of phonons between the boundaries of the film, and the resulting temperature

profile is one that may be obtained in the case of radiative equilibrium [17]. The second case would result in a linear temperature profile, as would be predicted by the Fourier law of heat conduction [3].

Simulations were performed in a simple one-dimensional gallium arsenide film of thickness $L = 400$ nm. The left end of the film was maintained at $T_L = 20$ K, while the right end was maintained at $T_R = 10$ K, and symmetry boundary conditions at the top and bottom surfaces. The Debye temperature of GaAs is approximately 345 K [8]. It is well known, that at temperatures well below the Debye temperature, the heat conduction is governed by the Stefan-Boltzmann law [3]. Under this condition, the temperature of the entire film would assume a constant value of $[(T_L^4 + T_R^4)/2]^{1/4}$ [17], with discontinuities at the two boundaries. A comparison of the numerical results against analytical results is shown in Fig. 3. The maximum error between the two solutions is approximately 2 percent. At low temperature, the equilibrium distribution of phonons (Eq. (1)) is strongly nonlinear [2]. The small error in solution is actually caused by the fact that in the numerical scheme, this non-linear distribution is approximated by a piecewise linear function of $N_b = 1000$ segments. The accuracy of temperature profile in the ballistic limit proves that the numerical treatment of isothermal boundaries, described earlier, is accurate.

Verification of the code in the diffusion limit was performed both for one-dimensional and two-dimensional films, since analytical solutions are obtainable in both cases. For the one-dimensional case, a simulation was performed in a gallium arsenide film with $T_R = 300$ K and $T_L = 500$ K. At these temperatures, intrinsic scattering is very strong, and transport is in the diffusion limit. It was estimated that the average mean free path of the resident phonons is approximately $0.05L$. The dispersion relationship for GaAs was used from Waugh and Dolling [27]. The scattering time-scale expressions were adopted from Bhandari and Verma [9]. Impurity and boundary scattering effects were neglected. The simulation was performed with just 20,000 samples. The steady-state temperature profiles are depicted in Fig. 4, which exhibits a good match. The noisy nature of the numerical profile is due to statistical errors, to be discussed in detail in later sections. The two-dimensional simulations were performed in a $400\text{nm} \times 400\text{nm}$ square geometry with four different temperatures on the four different walls. The material was GaAs, and 100,000 samples were used for initialization, and 100 spatial bin were used. The results are illustrated in Figs. 5(a)–(c), where the quantity, “Error_T”, in 5(c) is the difference in temperature between analytical

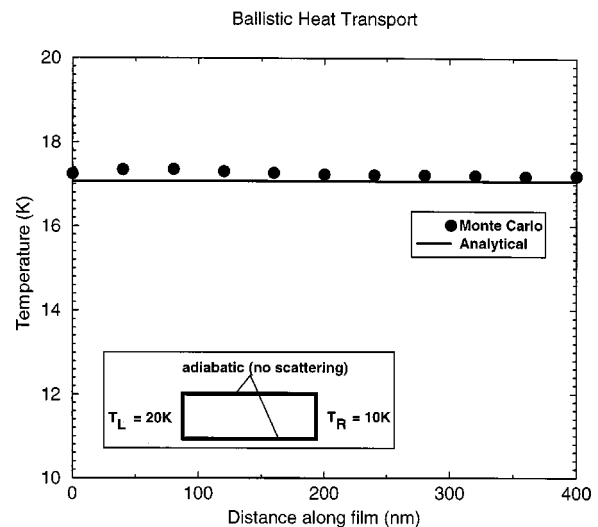


Fig. 3 Comparison of temperature profile obtained by Monte Carlo solution of the BTE for phonons with analytical results in the ballistic limit

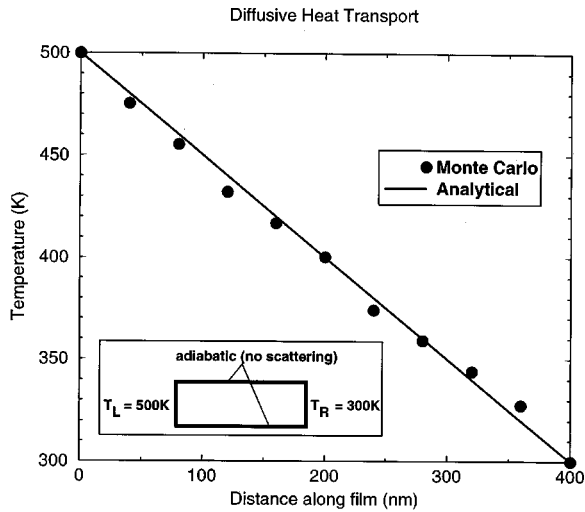


Fig. 4 Comparison of temperature profile obtained by Monte Carlo solution of the BTE for phonons with analytical results in the diffusion limit

and Monte Carlo solutions. It is seen that the maximum error is about 20 K, which corresponds to about 6.7 percent. The maximum error regions, as expected, are clustered around the junction of the 600 K and 300 K walls, where the thermal gradients are largest. These results lend validity to the numerical implementation of intrinsic scattering, described in Section 3.3.

Following the verification of the two limits, the boundary and impurity scattering mechanisms were tested individually to ascertain that they reproduce correct behavior, at least qualitatively. First, simulations were performed in GaAs films with cross-plane (left to right) thickness of 1 μm and in-plane (bottom to top) thickness of 100 nm. The left boundary was set to 20 K and the right boundary was set to 10 K. The top and bottom boundaries represent adiabatic scattering walls. The degree of specularity of these surfaces was varied from zero to unity. Simulation results are shown in Fig. 6. All other forms of scattering were deactivated. As the degree of specularity is decreased, boundary scattering becomes increasingly strong, and a temperature gradient is established across the film. In the absence of intrinsic scattering, these temperature profiles are not likely to be linear [21], as seen in Fig. 6.

Another set of simulations was performed for the same film, where all other forms of scattering, other than scattering by im-

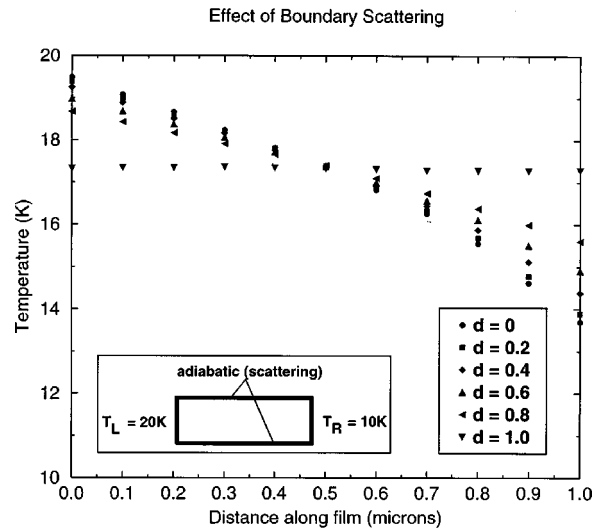


Fig. 6 Temperature profiles in a one-dimensional GaAs film for various degrees of specularity (d) of the film boundaries

purities were deactivated. The degree of specularity at the top and bottom boundaries was set to unity, so that the boundaries do not pose any resistance to the phonons. The results are shown in Fig. 7. It is seen that as the defect density is increased, the temperature drop across the film increases, as would be expected.

The above exercises lend credibility and help gain confidence in the various models and their numerical implementation. Following these exercises, the code was used to perform thermal conductivity studies in silicon thin films.

4.2 Validation Study for Silicon Thin Films. Silicon is probably the most important electronic material to date. Several researchers have performed studies on silicon in the past, and as a result its dispersion characteristics are well known. Furthermore, Holland [7] has provided comprehensive guidelines pertaining to phonon lifetimes in silicon. Although, a large number of thermal conductivity measurements of silicon has been made in the past, most of these data are for thick samples, where transport is in the diffusion limit, and important effects such as the effect of temperature and boundary scattering become mute. For study of such important effects, it is important to use thin-film data. The data used here for validation was collected recently by Asheghi [28],

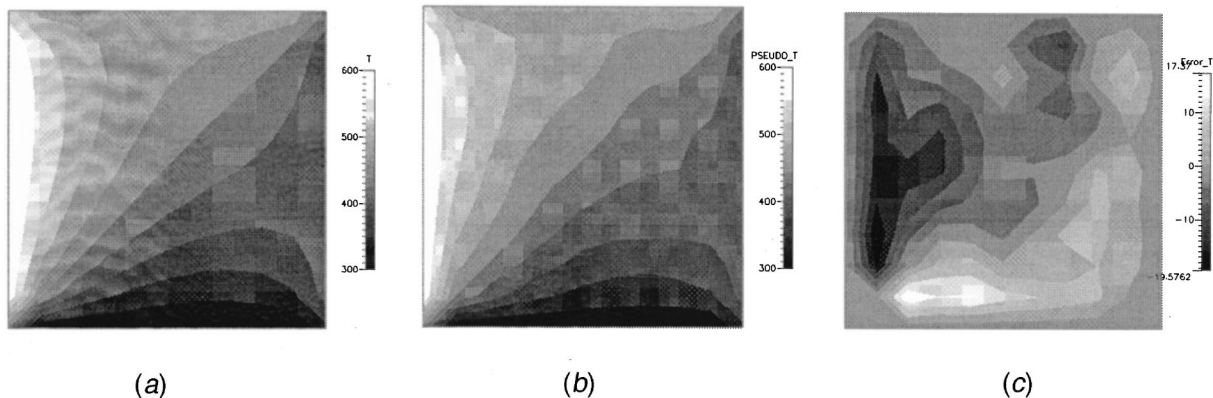


Fig. 5 Comparison of temperature profile obtained by Monte Carlo solution of the BTE for phonons with analytical results in the diffusion limit for a two-dimensional geometry: (a) analytical solution, (b) Monte Carlo solution of BTE, and (c) difference in (a) and (b). The left wall was set to 600 K, the top wall to 500 K, the right wall to 400 K, and the bottom wall to 300 K.

Effect of Impurities/Defects on Heat Conduction

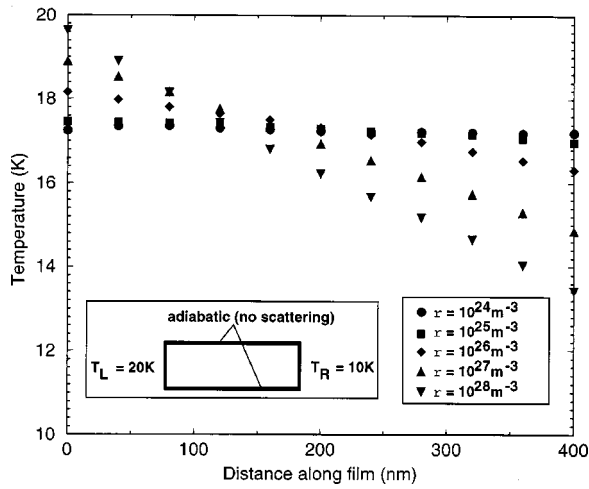


Fig. 7 Temperature profiles in a GaAs film for various levels of impurity (r)

and to our knowledge, is the most comprehensive and reliable data available. The dispersion relationship for silicon in the (001) direction is available from early studies by Brockhouse [29], and the acoustic branches have been reproduced and shown in Fig. 8, for the sake of completeness.

The relaxation times for the various three-phonon scattering processes were adopted from Holland [7]

$$\begin{aligned} \tau_{NU}^{-1} &= B_L \omega^2 T^3 \quad (LA, \text{Normal} + \text{Umklapp}) \\ \tau_N^{-1} &= B_{TN} \omega T^4 \quad (TA, \text{Normal}) \\ \tau_U^{-1} &= \begin{cases} 0 & (TA, \text{Umklapp for } \omega < \omega_{1/2}) \\ B_{TU} \omega^2 / \sinh\left(\frac{\hbar \omega}{k_B T}\right) & (TA, \text{Umklapp for } \omega > \omega_{1/2}) \end{cases} \end{aligned} \quad (26)$$

where $\omega_{1/2}$ is the frequency corresponding to $K/K_{\max} = 0.5$. For silicon, $\omega_{1/2} = 2.417 \times 10^{13}$ radians/s (Fig. 8). The constants B_L , B_{TN} , and B_{TU} can be obtained directly from Holland [7]. A series of simulations were performed for a 3 μm thick silicon film at different temperatures all the way from 10 K to 300 K. The difference in temperature between the two boundaries of the film was always maintained at 20 K and it is assumed that the computed thermal conductivity from the simulation is the representative thermal conductivity at the average temperature of the film. For

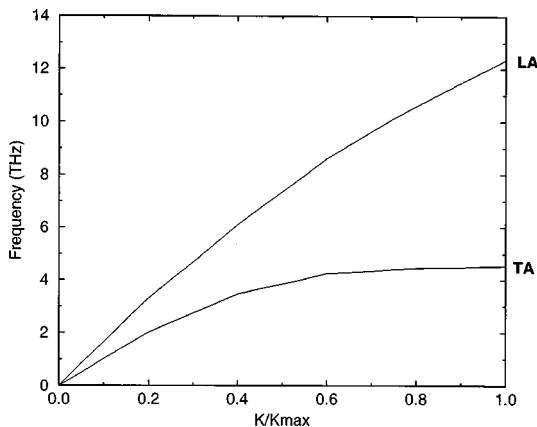


Fig. 8 Dispersion relation (only acoustic branches shown) of silicon in the (001) direction (adopted from Brockhouse [29])

Thermal Conductivity of Pure Silicon

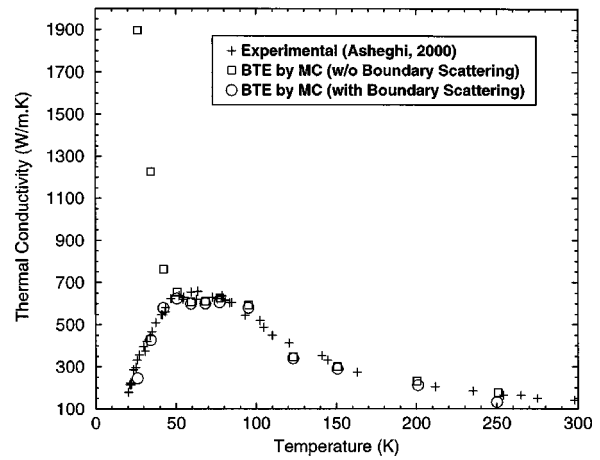


Fig. 9 Thermal conductivity across a 3 μm pure silicon film: numerical predictions with and without boundary scattering compared to experimental data [28]

example, if a simulation is performed between 10 K and 30 K, the average film temperature is about 25.4 K,² and consequently, it is assumed that the thermal conductivity computed by this simulation is the thermal conductivity at 25.4 K. The simulations were allowed to proceed until steady state; following this, a time averaging over 10 time-steps was performed to extract the final results of the computation. Soon after the dispersion relationship of the material is read, the code computes the highest and lowest velocity that any resident phonon may have. Theoretically, the lowest velocity is zero (at the edge of the Brillouin zone). However, due to discretization of the \mathbf{K} -space, the lowest velocity is non-zero in the numerical treatment. From this lowest velocity, and the characteristic film dimension, the time required to reach steady state can be estimated. For the current study, all simulations were performed up to twice this estimated steady-state time to ensure that the solutions are indeed steady state solutions. Another indication of steady state is that the total number of phonons (i.e., the total energy) in the computational domain becomes constant, barring statistical fluctuations.

Figure 9 shows the results of the simulations. At low temperatures, the mean free path of the phonons due to intrinsic lattice scattering is much larger than the film dimension, and the transport is ballistic. The thermal conductivity, in such cases, is arbitrarily large. Heat conduction, in the low temperature regime, is purely dominated by boundary scattering. The phonons impinge on the film boundaries directly and scatter. When boundary scattering was introduced, it was found the thermal conductivity drops drastically. Of course, the magnitude is determined by the combined effect of the degree of specularly of the scattering surfaces and the distance by which they are apart. For the current study, neither the distance between the scattering planes, nor the degree of specularly of the scattering planes, was known. First, the distance between the planes was fixed at 10 μm . Next, the degree of specularly was calibrated to match the experimental thermal conductivity value at 25 K. The calibrated value for d was found to be 0.6. This value was finally used for the remaining simulations at all other temperatures. At higher temperatures, Umklapp scattering is dominant, and the effect of boundary scattering is negligible. It is clear from Fig. 9 that the match between experimental and numerical result is excellent. It must be emphasized that the results have been plotted on a linear scale (as opposed to all previous research, where differences between model predictions and

²At this temperature, transport is still in the ballistic limit, and the temperature of the medium is the average of the fourth power of the boundary temperatures.

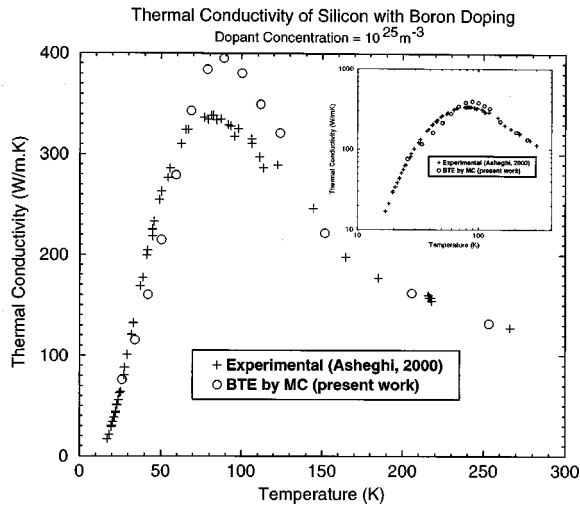


Fig. 10 Thermal conductivity across a 3 μm boron-doped (10^{25} atoms/ m^3) silicon film: numerical predictions compared to experimental data [28]. The same plot is plotted on a logarithmic scale and shown in the inset.

experimental data are hardly noticeable because they are always plotted on a logarithmic scale) to highlight the fact that the match is indeed excellent.

The task of predicting thermal conductivity of doped silicon films was undertaken next. Asheghi [28] has measured thermal conductivity of boron-doped silicon films at three different doping levels of 10^{23} , 10^{24} , and 10^{25} atoms/ m^3 . The constant, α , in Eq. (24) was first calibrated using the data for 10^{24} atoms/ m^3 . The calibration was done by performing a least square fit of the data at all temperatures, and yielded a value of $\alpha=7.7$. This value was then used to compute the thermal conductivity for a doping level of 10^{25} atoms/ m^3 . The results are shown in Fig. 10. Some discrepancy is observed between predicted results and experimental data. This may be attributed to the simplistic model used for the relaxation time for impurity scattering.

One critical issue, which has remained unresolved over the past several decades, is the relative role of *LA* and *TA* phonons in energy transport at various temperatures. Past studies [9,30] have tried to isolate the role of the two branches, but no firm conclusion has been reached. Part of the reason is that these analytical studies have neglected transition between the two branches, and according to Klemens [30], this could result in misleading deductions, especially for materials in which dispersion is strong. In the

Table 1 Role of *LA* phonons in Silicon at various temperatures

T (K)	$\frac{E_{LA}}{E_{total}}$ (%)	
	Left (Hot) boundary	Right (cold) boundary
26.1	15.1	14.9
50.5	26.2	24.5
68.7	43.7	29.0
78.6	55.4	30.0
88.9	72.4	19.1
100.0	100.0	4.8

Table 2 Statistical errors associated with thermal conductivity calculations

T (K)	# phonons	\bar{k} (W/mK)	σ_k (W/mK)	σ_k/\bar{k} (%)
26.1	126,000	76.46	1.6	2.1
50.5	123,000	213.68	3.5	1.64
78.6	112,000	384.84	23.2	6.02
123.9	119,000	321.07	24.2	7.53
151.8	101,000	221.87	27.6	12.43
205.6	102,000	162.03	31.2	19.25
253.1	107,000	131.89	29.8	22.59

framework of a Monte Carlo simulation, the role of the *LA* and *TA* phonons can be easily isolated by sampling their contributions to the overall heat flux at each boundary, separately. The results are shown in Table 1, for the same silicon film described earlier. From Table 1, it is clear that at low temperature, almost all of the *LA* phonons that are emitted from the hot boundary of the film reach the cold boundary. As the temperature of the film is increased, although the number of *LA* phonons increase, their lifetimes are much shorter, and a large fraction of them transition to *TA* phonons, indicating that $LA \Rightarrow TA + TA$ is probably the most dominant three-phonon process. Above 100 K, the *TA* phonons are the primary energy carriers. The results shown here corroborate remarks by Bhandari and Verma [9] who claimed that at high temperature transport in GaAs is dominated by *TA* phonons.

4.3 Numerical Error Estimates. The results, presented in the preceding sections, have statistical errors associated with them. The errors depend primarily on the number of stochastic samples used in the simulation (i.e., $N_{\text{prescribed}}$), and the number of scattering events that occur. To estimate the magnitude of the statistical errors, simulations were performed at each temperature with ten different random number seeds. Computations were performed only at seven selected temperatures to keep the total computational time within reasonable limits. Depending on the number of scattering events, each simulation takes between two to three hours on a DEC Alpha 500 MHz workstation. Following simulations at each temperature, the raw data was analyzed to compute the mean thermal conductivity and its standard deviation. The results are shown in Table 2. In order to compare the errors at different temperatures, it is necessary to run the simulations at all temperatures with the same number of samples at steady state. This, however, is difficult to control because the number of samples changes due to scattering. For the current study, an effort was made to attain a steady state count of 100,000 for each simulation. This was done by trial-and-error adjustment of $N_{\text{prescribed}}$. However, as evident in Table 2, this goal was only achieved partially. With an increase in temperature, the statistical errors increase. This is because the number of scattering events increases with temperature, and larger number of samples is necessary to account for all possible interactions accurately. Beyond about 100 K, the number of scattering events are so large that further change in that number does not affect the statistical accuracy significantly.

5 Summary and Conclusions

The BTE for phonons best describe the non-equilibrium transfer of heat in thin films, where the mean free path of the energy-carrying phonons may be larger than the film thickness. In this article, a detailed solution technique for the BTE was presented. A novel three-phonon scattering algorithm has been presented, which accounts for transition of phonons between the polarization

branches, and frequency dependent phonon lifetimes. The model was used to compute the thermal conductivity of silicon thin films between 10–300 K. Numerical predictions exhibit very close match with experimental data for pure silicon. For doped silicon films, it was found that a model, which accounts for the mass difference between the base and the dopant atoms, is necessary to produce a better match. It was also found that TA phonons play a dominant role in heat transport in silicon above 100 K. Future research will focus on enhancing the scattering model to allow treatment of normal and Umklapp scattering as isolated events, and the implementation of truly anisotropic Brillouin zones. It is our hope that this preliminary effort will provide a sound platform for future research pertaining to numerical solution of the BTE for phonons.

Acknowledgments

This work was funded by the National Science Foundation through a SBIR Phase I award (Award #9960172; Program Officer: Dr. Cynthia Ekstein). The authors gratefully acknowledge this support. The authors would also like to thank Drs. Mehdi Asheghi and Kenneth Goodson of the Department of Mechanical Engineering, Stanford University for providing the original files containing the experimental data.

Nomenclature

A	= area of boundary face [m ²]
B_L, B_{TN}, B_{TU}	= constant in relaxation time expression
d	= degree of specularly
$D(\omega)$	= density of state [m ⁻³ ·s]
E	= energy per unit volume [J/m ³]
f	= distribution function
F	= cumulative number density function
\mathbf{G}	= reciprocal lattice vector [m ⁻¹]
h	= Planck constant (= 6.6262 × 10 ⁻³⁴ J·s)
\hbar	= $h/2\pi$ (= 1.05459 × 10 ⁻³⁴ Js)
k_B	= Boltzmann constant (= 1.38062 × 10 ⁻²³ J/K)
\bar{k}	= ensemble averaged thermal conductivity [W/m·K]
K	= component of wave vector [m ⁻¹]
\mathbf{K}	= wave vector [m ⁻¹]
L	= characteristic length [m]
N	= number density (number/volume) [m ⁻³]
$\langle n \rangle$	= phonon occupation number
$\hat{\mathbf{n}}$	= unit surface normal
N_b	= number of spectral bands
N_{face}	= number of phonons emitted from a face
p	= polarization
P_{NU}	= probability of intrinsic scattering
$P(LA/TA)$	= probability of LA versus TA
\mathbf{r}	= position vector
R, R_1, R_2, R_3	= random numbers between 0 and 1
$\hat{\mathbf{s}}$	= direction of wave-vector
t	= time [s]
Δt	= time-step size [s]
T	= thermodynamic temperature [K]
\tilde{T}	= pseudo temperature [K]
$\hat{\mathbf{t}}_1, \hat{\mathbf{t}}_2$	= unit surface tangents
V	= volume [m ³]
\mathbf{V}_g	= group velocity of phonon [m/s]
\tilde{W}	= scaling factor

Greek

α	= calibrated constant [Eq. 24]
ν	= frequency [Hz]
Φ	= scattering rate [s ⁻¹]
θ	= polar angle
ρ	= defect density [atoms/m ³]

σ	= scattering cross section [m ²]
σ_k	= standard deviation in thermal conductivity calculations [W/m·K]
τ_{NU}	= combined relaxation time for intrinsic scattering [s]
τ_i	= relaxation time for impurity scattering [s]
τ_N	= relaxation time for normal scattering [s]
τ_U	= relaxation time for Umklapp scattering [s]
ω	= angular frequency [radians/s]
$\omega_{\text{max},LA}$	= maximum cut-off frequency for LA branch [radians/s]
$\omega_{\text{max},TA}$	= maximum cut-off frequency for TA branch [radians/s]
$\omega_{0,i}$	= central frequency of i -th band [radians/s]
$\Delta\omega$	= band width [radians/s]
ψ	= azimuthal angle

References

- [1] Ziman, J. M., 1960, *Electrons and Phonons*, Oxford University Press, London.
- [2] Kittel, C., 1986, *Introduction to Solid State Physics*, John Wiley & Sons Inc., Sixth Edition.
- [3] Tien, C. L., Majumdar, A., and Gerner, F. M., eds., 1998, *Microscale Energy Transport*, Taylor and Francis.
- [4] Ju, Y. S., and Goodson, K. E., 1999, "Phonon Scattering in Silicon Films with Thickness of Order 100 nm," *Appl. Phys. Lett.*, **74**, No. 20, pp. 3005–3007.
- [5] Klemens, P. G., 1958, "Thermal Conductivity and Lattice Vibrational Modes," in *Solid State Physics*, 7, F. Seitz and D. Turnbull, eds., Academic Press, NY.
- [6] Callaway, J., 1959, "Model for Lattice Thermal Conductivity at Low Temperatures," *Phys. Rev.*, **113**, No. 4, pp. 1046–1051.
- [7] Holland, M. G., 1963, "Analysis of Lattice Thermal Conductivity," *Phys. Rev.*, **132**, No. 6, pp. 2461–2471.
- [8] Holland, M. G., 1964, "Phonon Scattering in Semiconductors from Thermal Conductivity Studies," *Phys. Rev.*, **134**, No. 2A, pp. A471–A480.
- [9] Bhandari, C. M., and Verma, G. S., 1965, "Role of Longitudinal and Transverse Phonons in Lattice Thermal Conductivity of GaAs and InSb," *Phys. Rev.*, **140**, No. 6A, pp. A210–A214.
- [10] Guyer, R. A., and Krumhansl, J. A., 1966, "Solution of the Linearized Phonon Boltzmann Equation," *Phys. Rev.*, **148**, No. 2, pp. 766–778.
- [11] Hardy, R. J., 1970, "Phonon Boltzmann Equation and Second Sound in Solids," *Phys. Rev. B*, **2**, No. 4, pp. 1193–1206.
- [12] Mogilestue, C., 1982, "Monte Carlo Particle Modeling of Small Semiconductor Devices," *Comput. Methods Appl. Mech. Eng.*, **30**, pp. 173–208.
- [13] Jacoboni, C., and Reggiani, L., 1983, "The Monte Carlo Method for the Solution of Charge Transport in Semiconductors with Applications to Covalent Materials," *Rev. Mod. Phys.*, **55**, No. 3, pp. 642–705.
- [14] Lugli, P., Bordone, P., Reggiani, L., Reiger, M., Kocovar, P., and Goodnick, S. M., 1989, "Monte Carlo Studies of Nonequilibrium Phonon Effects in Polar Semiconductors and Quantum Wells. I. Laser Photoexcitation," *Phys. Rev. B*, **39**, No. 11, pp. 7852–7865.
- [15] Fischetti, M. V., and Laux, S. E., 1988, "Monte Carlo Analysis of Electron Transport in Small Semiconductor Devices Including Band-Structure and Space-Charge Effects," *Phys. Rev. B*, **38**, No. 14, pp. 9721–9745.
- [16] Fischetti, M. V., and Laux, S. E., 1993, "Monte Carlo Study of Electron Transport in Silicon Inversion Layers," *Phys. Rev. B*, **48**, No. 4, pp. 2244–2274.
- [17] Majumdar, A., 1993, "Microscale Heat Conduction in Dielectric Thin Films," *ASME J. Heat Transfer*, **115**, No. 7, pp. 7–16.
- [18] Chen, G., and Tien, C. L., 1993, "Thermal Conductivities of Quantum Well Structures," *J. Thermophys. Heat Transfer*, **7**, No. 2, pp. 311–318.
- [19] Goodson, K. E., 1996, "Thermal Conduction in Nonhomogeneous CVD Diamond Layers in Electronic Microstructures," *ASME J. Heat Transfer*, **118**, pp. 279–286.
- [20] Chen, G., 1998, "Thermal Conductivity and Ballistic Phonon Transport in the Cross-Plane Direction of Superlattices," *Phys. Rev. B*, **57**, No. 23, pp. 14958–14973.
- [21] Klistner, T., VanCleve, J. E., Henry, E. F., and Pohl, R. O., 1988, "Phonon Radiative Heat Transfer and Surface Scattering," *Phys. Rev. B*, **38**, No. 11, pp. 7576–7594.
- [22] Peterson, R. B., 1994, "Direct Simulation of Phonon-Mediated Heat Transfer in a Debye Crystal," *ASME J. Heat Transfer*, **116**, pp. 815–822.
- [23] Mavriplis, D. J., 1995, "Unstructured Mesh Generation and Adaptivity," *Institute for Computer Applications in Science and Engineering*, Technical Report #TR-95-26.
- [24] Cahill, D. G., 1997, "Heat Transport in Dielectric Thin Films and at Solid-Solid Interfaces," *Microscale Thermophys. Eng.*, **1**, pp. 85–109.

- [25] Sverdrup, P. G., Ju, Y. S., and Goodson, K. E., 1999, "Sub-Continuum Simulations of Heat Conduction in Silicon-on-Insulator Transistors," *IMECE 1999, Nashville, TN*, HTD **363-3**.
- [26] Vincenti, W. G., and Kruger, C. H., 1977, *Introduction to Physical Gas Dynamics*, Robert Kreiger Publ., New York, NY.
- [27] Waugh, J. L., and Dolling, G., 1963, "Crystal Dynamics of Gallium Arsenide," *Phys. Rev.*, **132**, pp. 2410-2412.
- [28] Asheghi, M., 2000, "Thermal Transport Properties of Silicon Films," *Thesis in Mechanical Engineering*, Stanford University.
- [29] Brockhouse, B. N., 1959, "Lattice Vibrations in Silicon and Germanium," *Phys. Rev. Lett.*, **2**, pp. 256.
- [30] Klemens, P. G., 1981, "Theory of Lattice Thermal Conductivity: Role of Low-Frequency Phonons," *Int. J. Thermophys.*, **2**, No. 1, pp. 55-62.

Integrative Thermodynamic Optimization of the Crossflow Heat Exchanger for an Aircraft Environmental Control System

Jose V. C. Vargas

Adrian Bejan

Department of Mechanical Engineering
and Materials Science,
Duke University, Box 90300,
Durham, NC 27708-0300

David L. Siems

The Boeing Company,
MC S106-7075, PO Box 516,
Saint Louis, MO 63166-0519

This paper documents the process of determining the internal geometric configuration of a component by optimizing the global performance of the installation that uses the component. The example chosen is the crossflow heat exchanger used in the environmental control system of a modern aircraft. The optimization of global performance is achieved by minimizing the total entropy generation rate of the installation. There are three degrees of freedom in the heat exchanger configuration (the length-to-width and height-to-width aspect ratios, and the separator plate spacing ratio), which is subjected to two global constraints: total component volume, and total wall material volume (or weight/density) of wall material. Numerical results show how the optimal configuration responds to changes in specified external parameters such as volume, weight, Mach number, diffuser inlet cross-sectional area, and the pressure at which the cabin air is initially bled from the engine compressor. It is shown that the optimal configuration is robust and that major features such as the ratios of channel spacings and flow lengths are relatively insensitive to changes in some of the external parameters. It is also shown that the optimal heat exchanger geometry is insensitive to the thermodynamic irreversibility caused by discharging the used ram air into the ambient. [DOI: 10.1115/1.1375811]

Keywords: Geometry, Heat Exchangers, Optimization, Second Law, Thermodynamics

1 Introduction

The thermodynamic optimization of heat exchangers has attracted considerable attention during the past two decades, and is now an established subfield in heat transfer and engineering thermodynamics. It is now recognized as the mechanism for the generation of architecture in flow systems everywhere, in engineering and nature [1]. Thermodynamic imperfection is due to currents (fluid, heat) that must overcome resistances. Better performance at the global level is achieved when the resistances are minimized together, i.e., when the imperfection is distributed in space optimally [1]. Optimal distribution of imperfection represents flow architecture, or constructal design.

Heat exchangers have often been subjected to thermodynamic optimization (or entropy generation minimization) in isolation, i.e., removed from the larger installation that uses them. Examples are the counterflow, crossflow, parallel flow and phase-change heat exchanger optimizations documented in [2–13].

The existing work is based on the important assumption that the component (heat exchanger) can be optimized in isolation. The successful execution of this step is known as the principle of thermodynamic isolation, and depends on a careful understanding of how the component interacts with the rest of the installation. Paradoxical conclusions result when this principle is not respected (for an illustration, see [14], pp. 606–609).

The much surer alternative is to pursue the thermodynamic optimization of the heat exchanger as a component installed in the larger system. This consists of optimizing the larger system by varying the geometric features of the component. This is the integrative approach used in this paper. The result is that the entire

architecture of the component emerges as a consequence of the global optimization of the entire system, subject to the constraints faced by the entire system.

Objectives other than thermodynamic optimization can be pursued as an integrative design, for example, minimum total cost, or minimum total weight. The integrative design methodology can be summarized as follows: an entire system can be conceived from the beginning as a system designed to achieve certain global objectives optimally, not as an ensemble of already existing parts [15].

When should the global optimization of the system be based on entropy generation minimization? In brief, the methods of exergy analysis (EA), entropy generation minimization (EGM) and thermoeconomics (TE) are the most established changes that have taken place in modern engineering thermodynamics during the past three decades [16–25]. The emphasis is now on identifying the mechanisms and system components that are responsible for thermodynamic losses (EA), the sizes of these losses (EA), minimizing the losses subject to the global constraints of the system (EGM), and minimizing the total costs associated with building and operating the energy system (TE). Thermodynamic optimization (EGM) may be used by itself (without cost minimization) in the preliminary stages of design [26], in order to identify trends and the existence of optimization opportunities. The optima and structural characteristics identified based on thermodynamic optimization can be made more realistic through subsequent refinements based on global cost minimization.

Thermodynamic optimization can be useful by itself in cases where the total cost of the installation is dominated by the cost due to thermodynamic irreversibility. The classical example of this kind is cryogenics, or refrigeration at very low temperatures, where the power requirement is substantial and proportional to the entropy generated in the cold space [16,27]. Another example is the subject of this paper: environmental control systems for aircraft.

To see why aircraft energy systems can be conceptualized on

Contributed by the Heat Transfer Division for publication in the JOURNAL OF HEAT TRANSFER. Manuscript received by the Heat Transfer Division June 9, 2000; revision received January 20, 2001. Associate Editor: D. Poulikakos.

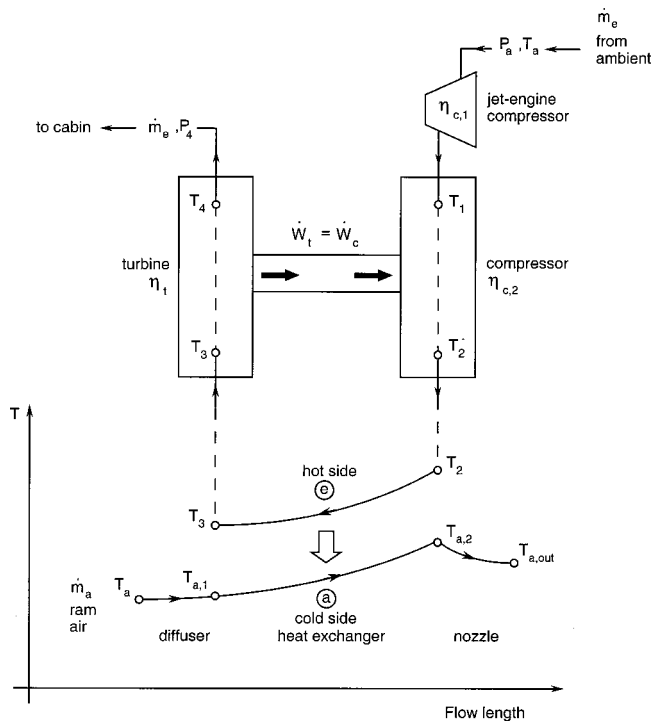


Fig. 1 Environmental control system with compression and expansion on the engine-air side (\dot{m}_e), and heat exchanger for cooling with ram air (\dot{m}_a)

the basis of thermodynamic optimization, consider their objectives and physical constraints. Power and refrigeration systems are assemblies of streams and hardware (components). The size of the hardware is always constrained (e.g., weight, volume). Each stream carries exergy (useful work content), which is the life blood of the power system, i.e., another form of the fuel brought on board and burned in order to drive the system. Exergy is destroyed (or entropy is generated) whenever streams interact with each other and with components. The design objectives are: (i) to optimize streams and components so that they destroy the least exergy subject to constraints, and (ii) to make sure that the optimized entities “match,” or can be “fitted” together (wrapped around each other) into a new integrative design of the larger system. What emerges is a design, i.e., the visible structure that reflects the optimization principle and the various constraints.

The new feature of the optimization approach presented herein is that it determines the entire geometry of the subject component (in this case, a heat exchanger). The optimal geometry is *deduced* from the minimization of the thermodynamic imperfection of the installation in which the component is used. This is in contrast to the optimization methodology that is currently used in the aircraft industry (i.e., the trade study), which attempts to select analytically the optimal geometry from some arbitrarily defined and limited field of candidates.

2 Model

Consider the model with two streams shown in Fig. 1. The upper stream \dot{m}_e is originally drawn from the ambient (P_a, T_a), and is compressed to the state (P_1, T_1) in the low-pressure stages of the jet engine. This “engine” air stream (\dot{m}_e) is a fraction of the air flow rate processed by the jet-engine compressor. The stream \dot{m}_e is compressed further in a separate compressor, which raises its pressure and temperature (P_2, T_2). Next, the stream temperature is lowered to T_3 in a crossflow heat exchanger, and then the stream is expanded through a turbine. The shaft power produced by the turbine is used to drive the separate compressor,

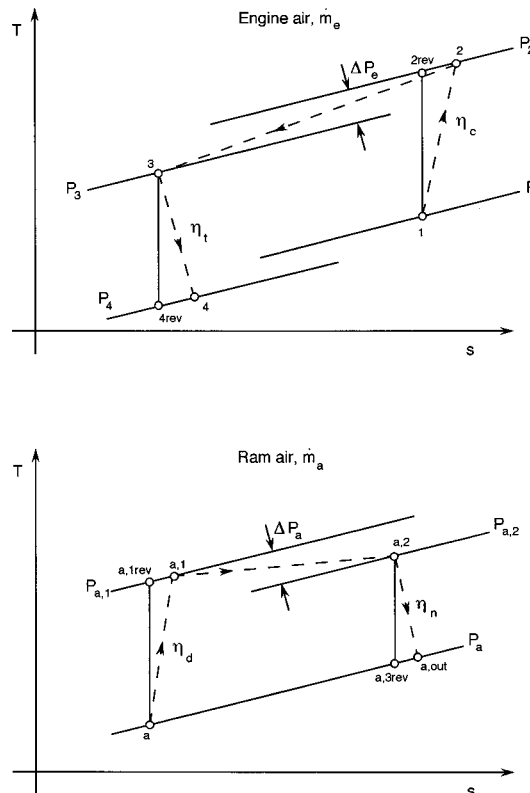


Fig. 2 The T - s diagrams of the processes undergone by the engine-air and ram-air streams

$\dot{W}_t = \dot{W}_c$. The purpose of the expansion through the turbine is to decrease the pressure and temperature to the specified cabin conditions (P_4, T_4). The air flow rate \dot{m}_e is also specified by the environmental design of the cabin.

The lower stream \dot{m}_a shown in Fig. 1 is the ram air used on the cold side of the crossflow heat exchanger. The ram air enters the system at ambient conditions (P_a, T_a), and initially it has the same speed as the aircraft (V_a). It is decelerated to the state ($P_{a,1}, T_{a,1}, V_{a,1}$) in a diffuser, and continues through the heat exchanger, where it is heated to the state ($P_{a,2}, T_{a,2}, V_{a,2}$). Before being discharged into the ambient, the \dot{m}_a stream is accelerated to the state ($P_{a,out}, T_{a,out}, V_{a,out}$). The ram air mass flow rate \dot{m}_a is not specified.

The processes undergone by the engine-air and ram-air streams are shown on their respective T - s diagrams in Fig. 2. Each process is irreversible. The upper diagram shows that the compression process (1)–(2) is not isentropic: the isentropic efficiency is $\eta_{c,2} < 1$. Similarly, the expansion (3)–(4) is characterized by the turbine isentropic efficiency $\eta_t < 1$. The flow (2)–(3) on the hot side of the heat exchanger is accompanied by the frictional pressure drop ΔP_e . The preliminary compression (a)–(1) executed in the jet-engine compressor is not shown; its isentropic efficiency is $\eta_{c,1} < 1$.

The lower diagram of Fig. 2 shows the deceleration process (a)–($a,1$) through the diffuser, where the isentropic efficiency is η_d . The pressure drop experienced by the ram air while flowing on the cold side of the heat-exchanger surface is ΔP_a . The isentropic efficiency of the nozzle acceleration process ($a,2$)–(a,out) is η_n .

To be true to the integrative design philosophy, the model should have included “everything” that is affected by, or is coupled to the environmental control system. One step toward more realism and greater complexity would have been to include the jet-engine compressor (Fig. 1) in the greater system that is subjected to entropy generation analysis and minimization. We

stopped short of doing this, because of time and computational cost limitations. We felt that the environmental control system of Fig. 1 is large enough (certainly larger than the heat exchanger) to illustrate the integrative approach, i.e., why this approach differs from optimizing the heat exchanger alone.

3 Entropy Generation Analysis

The objective is to select and arrange the geometric features of the system so that its penalty (entropy generation, exergy destruction) to the aircraft power output is minimized. The analysis developed in this section establishes the relation between the entropy generation rate and the physical features of the system. To start with, the entropy generation rate due to the complete system defined in Fig. 1 is

$$\begin{aligned} \dot{S}_{gen,1} = \dot{m}_e & \left[\left(c_p \ln \frac{T_1}{T_a} - R \ln \frac{P_1}{P_a} \right) + \left(c_p \ln \frac{T_2}{T_1} - R \ln \frac{P_2}{P_1} \right) \right. \\ & + \left(c_p \ln \frac{T_3}{T_2} - R \ln \frac{P_3}{P_2} \right) + \left. \left(c_p \ln \frac{T_4}{T_3} - R \ln \frac{P_4}{P_3} \right) \right]_e \\ & + \dot{m}_a \left(c_p \ln \frac{T_{out}}{T_{in}} - R \ln \frac{P_{out}}{P_{in}} \right)_a. \end{aligned} \quad (1)$$

The terms collected in this expression correspond to the sequence of components recognized in Figs. 1 and 2. The two fluids are modeled as ideal gases with constant specific heat, $(R, c_p)_e$ and $(R, c_p)_a$. It is convenient to introduce the nondimensional variables

$$\tilde{P} = \frac{P}{P_4} \quad \tau = \frac{T}{T_4} \quad (2)$$

$$N_S = \frac{\dot{S}_{gen}}{\dot{m}_e c_{pe}} \quad \mu = \frac{\dot{m}_a c_{pa}}{\dot{m}_e c_{pe}}, \quad (3)$$

where (P_4, T_4, \dot{m}_e) are the fixed cabin conditions, N_S is the entropy generation number, and μ is the ratio of the two capacity rates. Equation (1) becomes

$$\begin{aligned} N_{S1} = & \left(\ln \frac{\tau_1}{\tau_a} - b \ln \frac{\tilde{P}_1}{\tilde{P}_a} \right) + \left(\ln \frac{\tau_2}{\tau_1} - b \ln \frac{\tilde{P}_2}{\tilde{P}_1} \right) + \left(\ln \frac{\tau_3}{\tau_2} - b \ln \frac{\tilde{P}_3}{\tilde{P}_2} \right) \\ & + \left(\ln \frac{1}{\tau_3} - b \ln \frac{1}{\tilde{P}_3} \right) + \mu \ln \frac{\tau_{a,out}}{\tau_a}, \end{aligned} \quad (4)$$

where $b = R/c_p$. It is assumed that the two streams have the same b value, namely $b = 0.286$, which corresponds to $\gamma = c_p/c_v = 1.4$.

An alternative to Eq. (4) is to include in the entropy generation rate calculation the contribution made by the discharging of the spent stream $(T_{a,out})$ into the ambient (T_a) . Equation (1) is replaced by

$$\begin{aligned} \dot{S}_{gen,2} = \dot{m}_e & \left[\left(c_p \ln \frac{T_1}{T_a} - R \ln \frac{P_1}{P_a} \right) + \left(c_p \ln \frac{T_2}{T_1} - R \ln \frac{P_2}{P_1} \right) \right. \\ & + \left(c_p \ln \frac{T_3}{T_2} - R \ln \frac{P_3}{P_2} \right) + \left. \left(c_p \ln \frac{T_4}{T_3} - R \ln \frac{P_4}{P_3} \right) \right]_e \\ & + \dot{m}_a \left(c_p \ln \frac{T_{out}}{T_{in}} - R \ln \frac{P_{out}}{P_{in}} \right)_a + \dot{m}_a c_p \ln \frac{T_a}{T_{a,out}} + \frac{\dot{Q}_e}{T_a}, \end{aligned} \quad (5)$$

where the cooling experienced by the discharged air is

$$\dot{Q}_e = \dot{m}_a c_p (T_{a,out} - T_a). \quad (6)$$

Using the dimensionless variables defined in Eqs. (2, 3), we rewrite Eq. (5) as a second entropy generation number

$$\begin{aligned} N_{S2} = & \left(\ln \frac{\tau_1}{\tau_a} - b \ln \frac{\tilde{P}_1}{\tilde{P}_a} \right) + \left(\ln \frac{\tau_2}{\tau_1} - b \ln \frac{\tilde{P}_2}{\tilde{P}_1} \right) + \left(\ln \frac{\tau_3}{\tau_2} - b \ln \frac{\tilde{P}_3}{\tilde{P}_2} \right) \\ & + \left(\ln \frac{1}{\tau_3} - b \ln \frac{1}{\tilde{P}_3} \right) + \mu \left(\frac{\tau_{a,out}}{\tau_a} - 1 \right). \end{aligned} \quad (7)$$

The difference between the N_{S1} and N_{S2} expressions consists only in the last terms, $\mu \ln(\tau_{a,out}/\tau_a)$ versus $\mu[(\tau_{a,out}/\tau_a) - 1]$. Both terms increase monotonically with $\tau_{a,out}$. The value of $\tau_{a,out}$ is the same, regardless of how we evaluate the total entropy generation rate: there is one $\tau_{a,out}$ for each geometric configuration of the crossflow heat exchanger. We will show numerically that because of this feature the minimization of N_{S1} leads to the same optimal geometry as the minimization of N_{S2} . The minimized N_{S1} and N_{S2} values, however, are different as soon as $\tau_{a,out}$ differs from τ_a .

To minimize the entropy generation rate is equivalent to minimizing the pressure P_1 , or the compressor power that produces the \dot{m}_e stream. This equivalence is proclaimed by the Guoy-Stodola theorem [16,17].

In the EGM method the entropy generation calculation is complemented by the analysis of the heat flow and fluid flow through each component. This analysis accounts for the physical parameters and size constraints of the component. For the first component of our system—the engine compressor (a)—(1) in Fig. 1—these effects are embodied in the specified compressor efficiency

$$\eta_{c1} = \frac{T_{1,rev} - T_a}{T_1 - T_a}. \quad (8)$$

Noting that $T_{1,rev} = T_a(P_1/P_a)^b$, Eq. (5) becomes

$$\tau_1 = \tau_a + \frac{\tau_a}{\eta_{c1}} \left[\left(\frac{\tilde{P}_1}{\tilde{P}_a} \right)^b - 1 \right]. \quad (9)$$

Next, for the separate compressor (1)–(2) the definition of the isentropy efficiency η_{c2} and the first law analysis yield

$$\tau_2 = \tau_1 + \frac{\tau_1}{\eta_{c2}} \left[\left(\frac{\tilde{P}_2}{\tilde{P}_1} \right)^b - 1 \right] \quad (10)$$

$$w_c = \frac{\tau_1}{\eta_{c2}} \left[\left(\frac{\tilde{P}_2}{\tilde{P}_1} \right)^b - 1 \right]. \quad (11)$$

In Eq. (11) the compressor power input w_c is dimensionless, $w_c = \dot{W}_c / (\dot{m}_e c_{pe} T_4)$.

The heat transfer between the two streams in the crossflow heat exchanger is described by the effectiveness-NTU relation [28]

$$\varepsilon = 1 - \exp\{\mu N^{0.22} [\exp(-\mu^{-1} N^{0.78}) - 1]\}, \quad (12)$$

which is based on the assumption that $\dot{m}_e c_{pe}$ is the smaller of the two capacity rates (i.e., $\mu > 1$), and where N is the number of heat transfer units, $N = UA / (\dot{m}_e c_{pe})$. The definition of the effectiveness ε produces two relations between the inlet and outlet temperatures of the two streams,

$$\tau_2 - \tau_3 = \varepsilon (\tau_2 - \tau_{a,1}) \quad (13)$$

$$\tau_{a,2} - \tau_{a,1} = \frac{\varepsilon}{\mu} (\tau_2 - \tau_{a,1}). \quad (14)$$

Equations (12)–(14) hold for $\mu > 1$; the corresponding set for $\mu < 1$ is not listed, for the sake of brevity. The pressure drop along the hot side of the heat transfer surface, $\Delta \tilde{P}_e = \tilde{P}_2 - \tilde{P}_3$, is analyzed later in this section.

Downstream of the crossflow heat exchanger is the turbine (3)–(4): the definition of the efficiency η_t , and the first law analysis of the turbine yield

$$\tau_3 = 1 + \eta_t \tau_3 (1 - \bar{P}_3^{-b}) \quad (15)$$

$$w_t = \eta_t \tau_3 (1 - \bar{P}_3^{-b}). \quad (16)$$

The dimensionless turbine power output is defined as $w_t = \dot{W}_t / (\dot{m}_e c_{pe} T_4)$. Finally, since the turbine drives the separate compressor, $w_t = w_c$, the first-law analysis of the turbine and compressor (together) requires

$$\tau_2 - \tau_1 = \tau_3 - 1. \quad (17)$$

On the cold side of the system, we analyze the course followed by the ram air. This begins with the diffuser (a)–($a,1$), for which the η_d definition and the first law of thermodynamics require

$$\eta_d = \frac{T_{a,1rev} - T_a}{T_{a,1} - T_a} \quad (18)$$

$$c_{p,a}(T_{a,1} - T_a) = \frac{1}{2}(V_a^2 - V_{a,1}^2), \quad (19)$$

where $T_{a,1rev} = T_a(P_{a,1}/P_a)^b$. The dimensionless version of Eqs. (18, 19) is

$$\frac{\tau_{a,1} - 1}{\tau_a} = \frac{1}{\eta_d} \left[\left(\frac{\bar{P}_{a,1}}{\bar{P}_a} \right)^b - 1 \right] \quad (20)$$

$$\frac{\tau_{a,1} - 1}{\tau_a} = \frac{1}{2} (\bar{V}_a^2 - \bar{V}_{a,1}^2). \quad (21)$$

The dimensionless bulk velocity $\bar{V} = V / (c_{pa} T_a)^{1/2}$ is proportional to the Mach number $M = V / (\gamma_a R_a T_a)^{1/2}$, or $\bar{V} = M(\gamma_a - 1)^{1/2}$. Invoking the conservation of the mass flow rate \dot{m}_a in every cross-section A_c and the ideal gas model, namely $\dot{m}_a = \rho V A_c$ and $\rho = P / (RT)$, we write the Mach number as

$$M = \frac{\dot{m}_a}{P A_c} \left(\frac{R_a}{\gamma_a T} \right)^{1/2}. \quad (22)$$

In sum, when the geometry and operating conditions are specified, Eqs. (20), (21), and (22) pinpoint state ($a,1$), or $\bar{P}_{a,1}$ and $\tau_{a,1}$.

The heating process ($a,1$)–($a,2$) experienced by the \dot{m}_a stream is governed by the effectiveness-NTU relations (12)–(14). The pressure drop $\Delta \bar{P}_a = \bar{P}_{a,1} - \bar{P}_{a,2}$ is given by Eq. (27) later in this section.

Finally, the irreversible flow through the nozzle is described by the efficiency and first-law relations

$$\eta_n = \frac{T_{a,2} - T_{a,out}}{T_{a,2} - T_{a,out,rev}} \quad (23)$$

$$c_{p,a}(T_{a,2} - T_{a,out}) = \frac{1}{2}(V_{a,out}^2 - V_{a,2}^2). \quad (24)$$

Recognizing $T_{a,out,rev} = T_{a,2}(P_a/P_{a,2})^b$ and the nondimensional variables employed earlier, we can nondimensionalize Eqs. (23, 24) as

$$1 - \frac{\tau_{a,out}}{\tau_a} = \eta_n \left[1 - \left(\frac{\bar{P}_a}{\bar{P}_{a,2}} \right)^b \right] \quad (25)$$

$$\frac{\tau_{a,2}}{\tau_a} - \frac{\tau_{a,out}}{\tau_a} = \frac{1}{2} (\bar{V}_{a,out}^2 - \bar{V}_{a,2}^2). \quad (26)$$

For the pressure drops along the counterflow ($\Delta P_e, \Delta P_a$) we use the classical formulation [29]

$$\Delta P_i = \frac{1}{2} G_i^2 v_{i,in} \left[(K_{c,i} + 1 - \sigma_i^2) + 2 \left(\frac{v_{i,out}}{v_{i,in}} - 1 \right) + f_i \frac{A_i}{A_{c,i}} \frac{\bar{v}_i}{v_{i,in}} - (1 - \sigma_i^2 - K_{e,i}) \frac{v_{i,out}}{v_{i,in}} \right], \quad (i = e, a), \quad (27)$$

where

$$\bar{v}_i = \frac{1}{2}(v_{i,in} + v_{i,out}) \quad \sigma_{in} = \frac{A_{c,i}}{A_{f,i}}. \quad (28)$$

In these relations $G_i, v_i, A_i, f_i, \sigma_i, K_{c,i}, K_{e,i}, A_{c,i}$, and $A_{f,i}$, represent in order, the mass velocity ($G_i = \dot{m}_i / A_{c,i}$), the specific volume ($v_i = R_i T_i / P_i$), the total heat transfer area, the friction factor, the cross-section contraction ratio, the contraction loss coefficient, the enlargement loss coefficient, the flow cross-section and the stream cross-section before entering the duct. The friction factor is available as a function of the Reynolds number based on hydraulic diameter, $f_i = f_i(\text{Re}_i)$, either as empirical correlations for parallel-plate channels [30] or as tabulated data for finned surfaces [29].

The same heat exchanger sources provide the heat transfer coefficient information needed for evaluating the number of heat transfer units N . The flow of heat across the A_i surface overcomes three thermal resistances in series,

$$\frac{1}{N} = \frac{\dot{m}_e c_{pe}}{UA} = \dot{m}_e c_{pe} \left(\frac{1}{\eta_{0,i} h_e A_e} + \frac{t_w}{k_w A_w} + \frac{1}{\eta_{0,a} h_a A_a} \right). \quad (29)$$

In this expression $\eta_{0,i}, t_w, k_w$, and A_w are the fin efficiencies of the finned surfaces, the thickness of the wall penetrated by heat transfer, the wall thermal conductivity, and the average heat transfer surface, $A_w = (A_e + A_a) / 2$. The heat transfer coefficients (h_e, h_a) are available in dimensionless form, as the respective Stanton number versus the channel Reynolds number, $h_i / (c_{pi} G_i) = St_i(\text{Re}_i)$.

4 Parallel-Plate Heat Exchanger

The preceding analysis completes the model, and allows us to relate N_{S1} to the irreversibilities and physical sizes of all the components. The numerical minimization of the entropy generation rate can proceed, but first we must specify the type of the heat transfer surface built into the crossflow heat exchanger. This assumption is necessary in order to access the f_i and St_i information that is available in the heat exchanger literature.

In this optimization study we assumed the simplest and best documented surface type: parallel plates of spacings B_e and B_a , as shown in Fig. 3. For the laminar regime ($\text{Re}_{D_h} < 2300$) we used the friction factor and heat transfer coefficient correlations (e.g., [30]),

$$f_i = \frac{24}{\text{Re}_{D_{h,i}}} \quad \frac{h_i D_{h,i}}{k_i} = 8.235, \quad (30)$$

where $D_{h,i} = 2B_i$, $\text{Re}_{D_{h,i}} = G_i D_{h,i} / \mu_i$, and $i = e, a$. The correlations used for the turbulent regime were [30]

$$f_i = 0.079 \text{Re}_{D_{h,i}}^{-1/4} \quad (2300 < \text{Re}_{D_{h,i}} < 2 \times 10^4) \quad (31)$$

$$\frac{h_i D_{h,i}}{k_i} = \frac{(f_i/2)(\text{Re}_{D_{h,i}} - 10^3) \text{Pr}_i}{1 + 12.7(f_i/2)^{1/2} (\text{Pr}_i^{2/3} - 1)} \quad (2300 < \text{Re}_{D_{h,i}} < 5 \times 10^6). \quad (32)$$

The height H_{ea} of the elemental channel unit is defined as the height of the assembly composed of one engine-air passage and one ram-air passage,

$$H_{ea} = B_e + B_a + 2t_w. \quad (33)$$

If n is the number of elemental units in the stack, the height of the heat exchanger core is

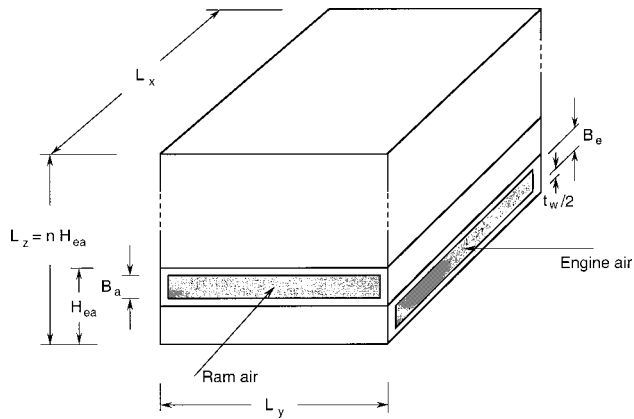


Fig. 3 The geometry of a crossflow heat exchanger core with parallel-plate channels

$$L_z = nH_{ea} \quad (34)$$

The total volume of the core is constrained, $V_t = L_x L_y L_z$, constant. The length scale $V_t^{1/3}$ is used for the purpose of nondimensionalizing all the lengths that characterize this geometry,

$$(\tilde{B}_e, \tilde{B}_a, \tilde{t}_w, \tilde{H}_{ea}, \tilde{L}_x, \tilde{L}_y, \tilde{L}_z) = (B_e, B_a, t_w, H_{ea}, L_x, L_y, L_z) / V_t^{1/3} \quad (35)$$

such that the volume constraint reads

$$\tilde{L}_x \tilde{L}_y \tilde{L}_z = 1 \quad (36)$$

Another constraint that we attach to the geometric optimization procedure is the total volume (or weight) of the wall material, $2nL_x L_y t_w$. This second constraint is best represented by the volume fraction $\phi (\ll 1)$ occupied by the wall material in the entire volume, $\phi = 2nL_x L_y t_w / V_t$, constant, or

$$\phi = 2n \frac{\tilde{t}_w}{\tilde{L}_z} = 2n \tilde{L}_x \tilde{L}_y \tilde{t}_w \quad (\text{constant}). \quad (37)$$

According to Fig. 3, the architecture of the heat exchanger core is determined completely if we specify six dimensions: L_x , L_y , L_z , B_e , B_a , and t_w . There are two constraints, Eqs. (36) and (37), and the reasonable assumption that the wall thickness is a specified parameter ($\tilde{t}_w \ll 1$) dictated by the availability of standard sizes of sheet metal. In conclusion, the geometric design of the core has three degrees of freedom.

5 Entropy Generation Minimization

The model described in Sections 3 and 4 allows the computation of the two entropy generation numbers, N_{S1} and N_{S2} , defined by Eqs. (4) and (7), respectively. This is possible once physical values (Table 1), a set of external parameters (M , \tilde{A}_{cd} , ϕ , and \tilde{P}_1) and the set of geometric parameters (L_y/L_x , L_z/L_x , and B_e/B_a), are chosen for the overall system. Equations (8)–(37) are then combined to form a nonlinear system of eleven nondimensional equations and eleven unknowns ($\tau_{a,1}$, $\tilde{P}_{a,1}$, $\tau_{a,2}$, $\tilde{P}_{a,2}$, τ_2 , \tilde{P}_2 , τ_3 , \tilde{P}_3 , ε , $\tilde{A}_{c,out}$, and $\tau_{a,out}$). This system was solved by functional iteration. A maximum tolerance of 10^{-6} was imposed on $\|R\|$, which is the residual norm of the resulting system of nonlinear equations. The numerical optimization was performed by varying the set of geometric parameters (L_y/L_x , L_z/L_x , and B_e/B_a), for each set of external parameters (M , \tilde{A}_{cd} , ϕ and \tilde{P}_1), and identifying the optimal set of geometric parameters such that N_{S1} and N_{S2} were minimum.

The critical part of this phase of the work was the identification of the degrees of freedom (the variables) that would permit the minimization of N_{S1} , i.e., the optimal selection of important geo-

Table 1 Physical values used as reference case in the numerical optimization of the overall system

$c_p = 1 \text{ kJ kg}^{-1} \text{ K}^{-1}$	$T_4 = 283.2 \text{ K}$
$k_w = 20.8 \text{ W m}^{-1} \text{ K}^{-1}$	$V_1 = 1 \text{ m}^3$
$\dot{m}_c = 0.7 \text{ kg s}^{-1}$	$\gamma = 1.4$
$P_a = 0.03 \text{ MPa}$	$\eta_{c1} = 0.9$
$P_4 = 0.1 \text{ MPa}$	$\eta_{c2} = 0.7$
$Pr = 0.72$	$\eta_d = 0.97$
$R = 287 \text{ J kg}^{-1} \text{ K}^{-1}$	$\eta_n = 0.95$
$t_w = 0.6 \text{ mm}$	$\eta_t = 0.8$
$T_a = 244.5 \text{ K}$	

metric features of the core. The first variable identified in this way was the plate spacing ratio B_e/B_a . Figure 4 shows that an optimal spacing ratio exists over a wide domain covered by other specified parameters of the larger installation, for example, the bleeding pressure \tilde{P}_1 (Fig. 4(a)), the cross-sectional area of the diffuser inlet $\tilde{A}_{cd} = A_{cd}/1\text{m}^2$ (Fig. 4(b)), and the Mach number M (Fig. 4(c)).

In the designs optimized in Fig. 4 the shape of the core and the number of elemental channels are fixed: $\tilde{L}_x = 5$, $\tilde{L}_y = 1$, $\tilde{L}_z = 0.2$, and $n = 10$. The other parameters that had to be specified are the reference values collected in Table 1, for example, $\tilde{t}_w = t_w/V_t^{1/3} = 0.6 \text{ mm}/1 \text{ m} = 0.0006$, hence $\phi = 0.06$.

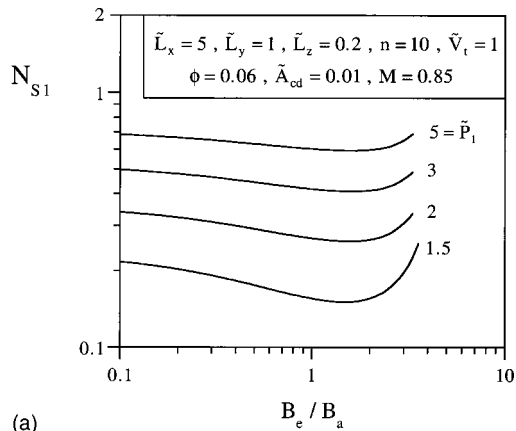
Figure 4 reveals a potentially cost-saving feature of the thermodynamic optimization: the optimized ratio B_e/B_a is relatively insensitive to changes in some of the specified system parameters (e.g., \tilde{P}_1 and M , Figs. 4(a) and 4(c)). The order of magnitude of B_e/B_a is 1. This lack of sensitivity lends robustness to the optimized design: we pursued the robustness feature in subsequent stages of this study. On the other hand, the optimal ratio B_e/B_a decreases as the diffuser inlet area \tilde{A}_{cd} increases (Fig. 4(b)). This trend is expected, because a larger \tilde{A}_{cd} captures a larger ram-air flow rate, which must be accommodated by a larger B_a spacing.

The optimization of the ratio B_e/B_a was built as the first (innermost) loop in the more complex numerical optimization routine that was developed ultimately for the entire installation. The next step in the search for additional geometric degrees of freedom that would permit the minimization of N_{S1} was the focus on the geometric aspect ratios of the core, L_z/L_x and L_y/L_x . We assigned fixed values to these two ratios, and repeated the optimization with respect to B_e/B_a . This search is summarized in Figs. 5(a,b), which show that the N_{S1} minimum with respect to B_e/B_a persists.

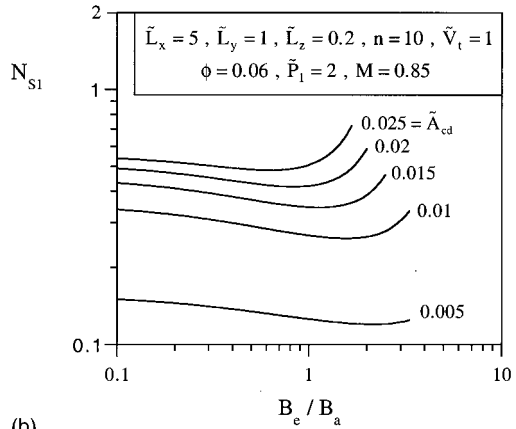
From this point on we pursued the geometric optimization of the core by varying three dimensionless numbers, the ratios B_e/B_a , L_y/L_x , and L_z/L_x . In Fig. 6 we verified that there exists a thermodynamic optimum with respect to the aspect ratio L_y/L_x . In this test we fixed B_e/B_a and L_z/L_x along with the other specified parameters ($M, \tilde{A}_{cd}, \tilde{P}_1, \phi$). The required number of elemental units in the core, n , decreases as L_y/L_x increases in Fig. 6. Discrete points are plotted on this figure, because we made calculations only for integer values of n .

A similar conclusion follows from Fig. 7, where L_z/L_x varies while B_e/B_a and L_y/L_x are held fixed. The necessary number of elemental units increases as L_z/L_x increases. An optimal ratio L_z/L_x exists such that the global entropy generation number N_{S1} is minimum.

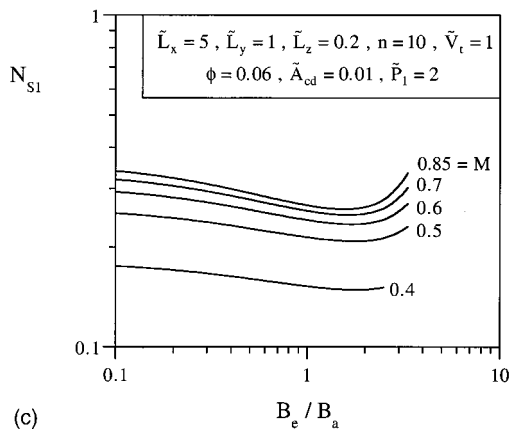
The bulk of the numerical work was centered on the minimization of N_{S1} with respect to all three geometric parameters, B_e/B_a ,



(a)



(b)

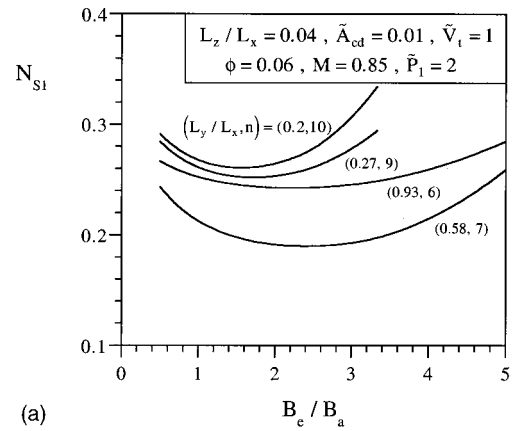


(c)

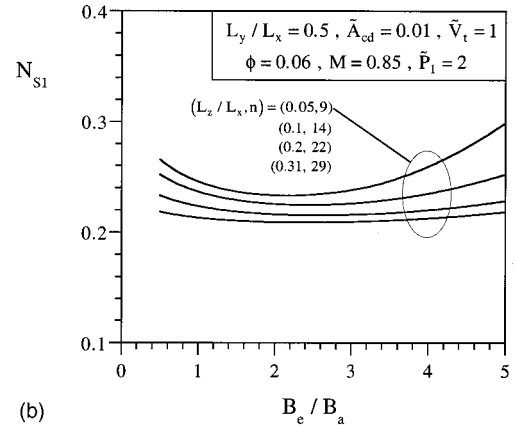
Fig. 4 The minimization of entropy generation rate with respect to the ratio of channel spacings (B_e/B_a), and the effect of varying \tilde{P}_1 , \tilde{A}_{cd} , and M

L_y/L_x , and L_z/L_x . The numerical procedure was organized into three nested loops, however, it was not executed blindly. Each intermediate optimum (e.g., with respect to B_e/B_a , L_y/L_x , or L_z/L_x) was verified to make sure that it represents a realistic geometry. Each step in the code was monitored. Examples of this intermediate testing are presented in Figs. 8(a,b), which summarize the results at the end of the two-way optimization, namely, the optimization with respect to B_e/B_a and L_y/L_x . The subscript “mm” indicates that $N_{S1,mm}$ was already minimized twice.

Figure 8(a) shows the effect of varying the third aspect ratio, L_z/L_x , and that $N_{S1,mm}$ can indeed be minimized for a third time. Figures 8(a,b) also report the corresponding geometric parameters



(a)



(b)

Fig. 5 The minimization of entropy generation rate with respect to the ratio of channel spacings (B_e/B_a) when the aspect ratios of the heat exchanger core are fixed ($L_y/L_x, L_z/L_x$)

at the end of the two-way optimization ($L_y/L_x, B_e/B_a, n$), and how they vary with the third geometric parameter (L_z/L_x).

The results of minimizing the global irreversibility N_{S1} with respect to the three geometric degrees of freedom are presented in Fig. 9. On the abscissa we varied one of the externally specified parameters, \tilde{P}_1 . The optimized architecture of the heat exchanger core is represented by the ratios $(B_e/B_a, L_y/L_x, L_z/L_x)_{opt3way}$. The figure also reports the required number of elemental units $n_{opt3way}$, and the minimized entropy generation rate $N_{S1,mmm}$.

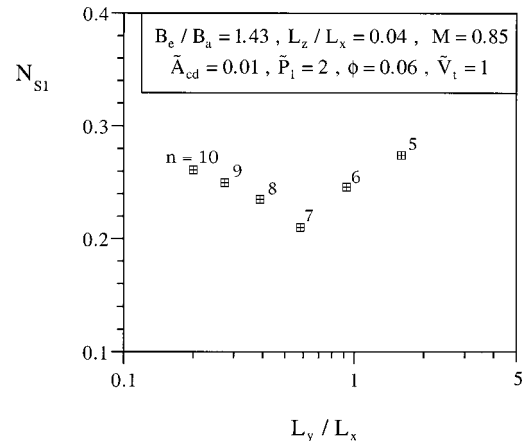


Fig. 6 The minimization of entropy generation rate with respect to the heat exchanger aspect ratio L_y/L_x

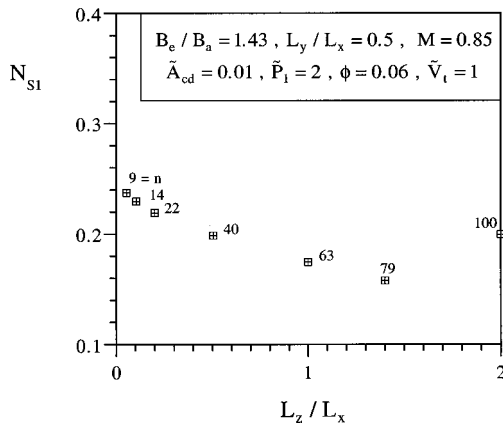


Fig. 7 The minimization of entropy generation rate with respect to the heat exchanger aspect ratio L_z/L_x

This bank of geometric results can be enlarged by repeating the procedure for finite ranges of other external parameters, M , \bar{A}_{cd} and ϕ .

An important test was conducted by repeating the entire three-way optimization by using the entropy generation number N_{S2} of Eq. (7). The results are nearly the same as in Fig. 9. The use of N_{S2} instead of N_{S1} makes no difference with respect to the resulting optimized architecture $(B_e/B_a, L_y/L_x, L_z/L_x)_{opt3way}$. For the purpose of deriving geometric form from thermodynamic optimization, it is sufficient to consider the global system upstream of the point of discharge into the ambient, $T_{a,out}$, Fig. 1. On the other hand, when the thermal mixing with the ambient is included

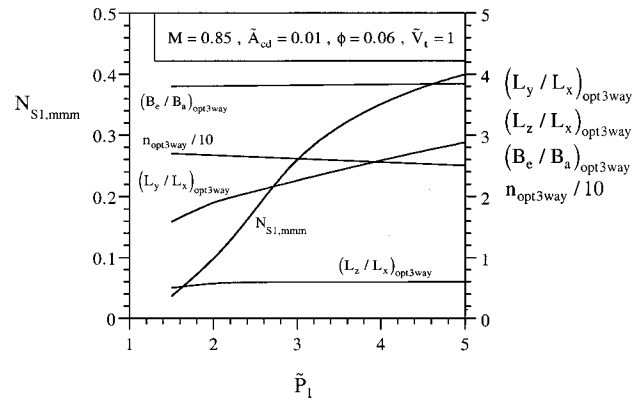


Fig. 9 The effect of \bar{P}_1 on the minimization of N_{S1} with respect to all three degrees of freedom, B_e/B_a , L_y/L_x , and L_z/L_x

in the calculation (N_{S2}), the minimized irreversibility ($N_{S2,mmm}$) is greater than when the mixing with the ambient is not accounted for ($N_{S1,mmm}$, Fig. 9). Similar conclusions are provided by Figs. 10–12, which show the effect of remaining external parameters (\bar{A}_{cd}, M, ϕ).

6 Discussion

Taken together, Figs. 8–12 document the three-way optimized architecture of the crossflow heat exchanger over a wide range of external parameters ($\bar{P}_1, \bar{A}_{cd}, M, \phi$). These results hold for the reference properties listed in Table 1, where the total volume was set at $V_t = 1 \text{ m}^3$. In a subsequent phase of this study we relaxed this

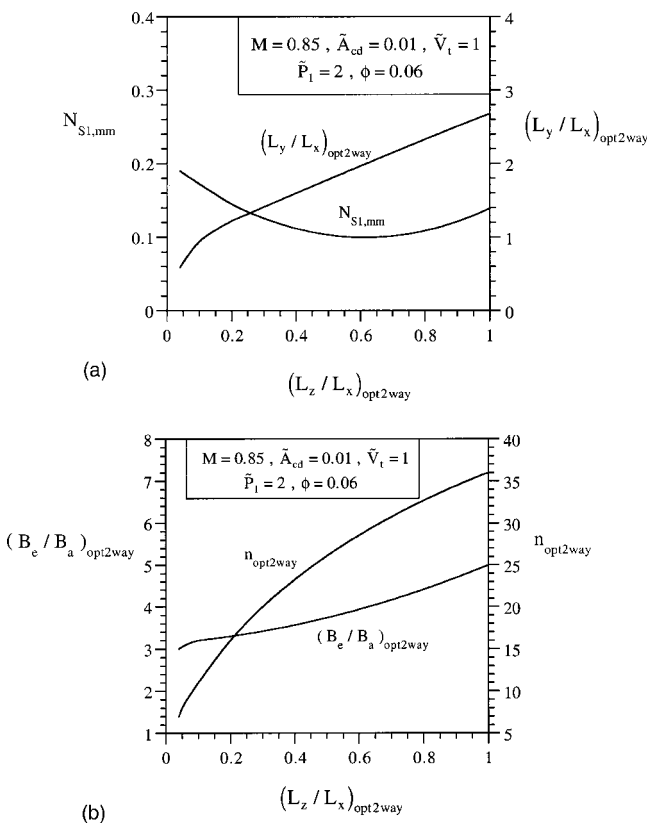


Fig. 8 Summary of results at the end of the minimization of N_{S1} with respect to two of the three degrees of freedom, B_e/B_a and L_y/L_x

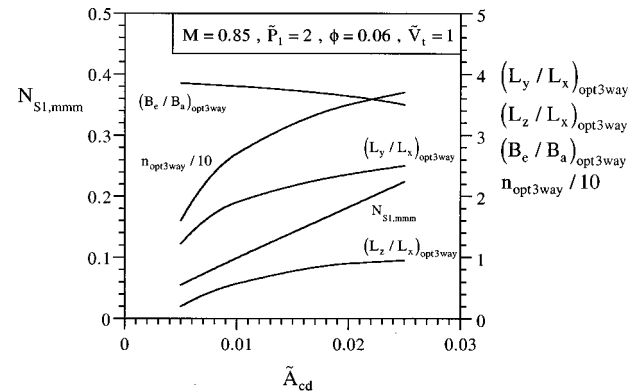


Fig. 10 The effect of \bar{A}_{cd} on the minimization of N_{S1} with respect to all three degrees of freedom, B_e/B_a , L_y/L_x and L_z/L_x

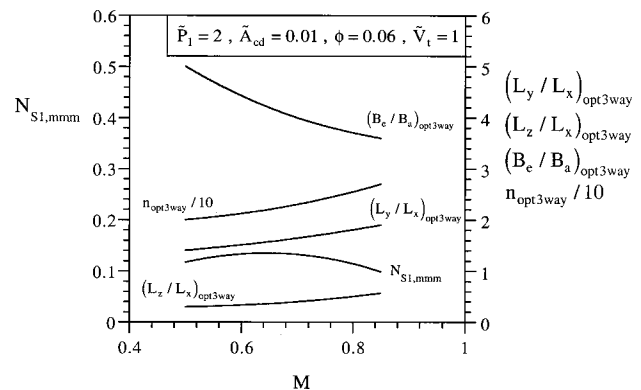


Fig. 11 The effect of M on the minimization of N_{S1} with respect to all three degrees of freedom, B_e/B_a , L_y/L_x , and L_z/L_x

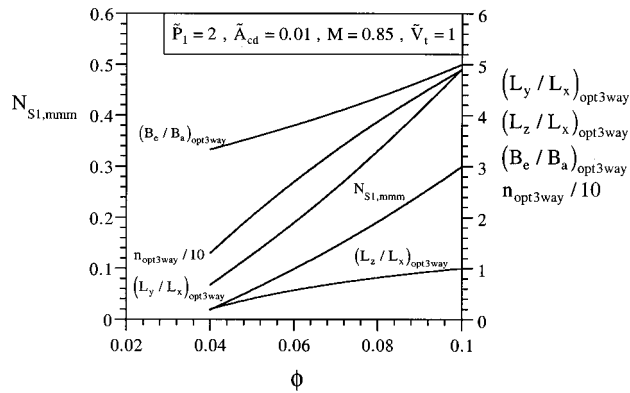


Fig. 12 The effect of ϕ on the minimization of N_{S1} with respect to all three degrees of freedom, B_e/B_a , L_y/L_x , and L_z/L_x

volume constraint, and varied V_t over the range 0.5–2 m³. This variation is indicated by the dimensionless volume

$$\tilde{V}_t = \frac{V_t}{1m^3} \quad (38)$$

indicated on the abscissas of Fig. 13. The optimized geometric features and the three-way minimized entropy generation rate depend on the total volume. The three-way minimized entropy generation rate of the entire system increases as \tilde{V}_t increases. Two dimensionless parameters of the optimized geometry ($L_z/L_x, n$) are insensitive to changes in \tilde{V}_t when $\tilde{V}_t > 1$.

To illustrate the improvement in heat exchanger performance provided by this optimization approach, an optimum heat exchanger geometry that was defined by it has been compared to a corresponding “typical industry” geometry (i.e., an alternate geometry that was defined by a design method used currently in the aerospace industry). Design requirements for this comparison were selected arbitrarily for a typical operating condition for the subject heat exchanger type and application. These requirements were specifically the mass flow rate, inlet temperature and pressure, and exit temperature and pressure on both sides of heat exchanger. A “typical industry” heat exchanger geometry that satisfies these requirements was then determined by applying the heat exchanger design algorithm (implemented in a computer program) that was developed in the Integrated Environmental Control System (ICES) project [31], a contracted effort sponsored by the Air Force. In addition to the design requirements listed above, five other conditions had to be specified to execute this algorithm: the separator plate spacings for both the engine and ram-air flow

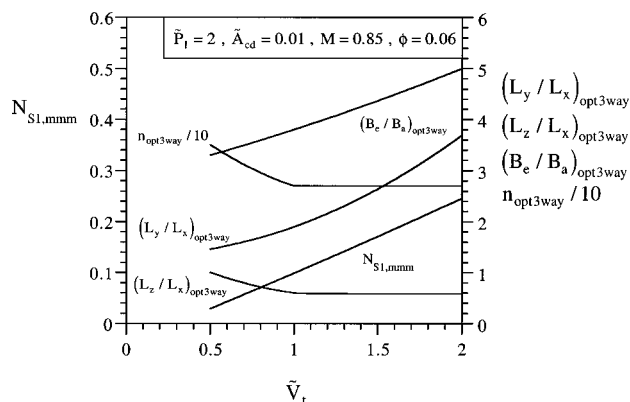


Fig. 13 The effect of the total volume on the minimization of N_{S1} with respect to all three degrees of freedom, B_e/B_a , L_y/L_x , and L_z/L_x

channels (B_e and B_a), the fin geometry for the heat transfer surfaces, the separator plate material, and the separator plate thickness (t_w). To be consistent with the optimization approach developed herein, smooth plates were selected as the heat transfer surfaces. Steel was selected as the separator plate material based on the required operating temperatures. Values for separator plate spacings (B_a and B_e) and separator plate thickness were set (fixed) the same as those found in typical cross-flow heat exchangers that are used for applications similar to the design requirements. The resulting “typical industry” heat exchanger geometry is shown in Fig. 14.

The industry approach produces the core dimensions listed on the left side of Table 2, where the total volume and solid-fraction volume are $\tilde{V}_t = 0.043$ and $\phi = 0.06$. The remaining external parameters are $M = 0.85$, $\tilde{A}_{cd} = 0.01$, $\tilde{P}_1 = 2$ and the values listed in Table 1. The right side of Table 2 shows the corresponding dimensions recommended by the optimization method described in this paper. Noteworthy are the bottom two lines, which show that the traditional design recommends a geometry that generates more than three times as much entropy as the configuration optimized in this paper. Again, this conclusion does not depend on whether the total entropy generation rate is calculated as N_{S1} or as N_{S2} . The two geometries are compared further in Fig. 14.

It is worth noting that, from the aircraft industry’s point of view, the results presented in this paper must be regarded as being of a preliminary nature. This is due to (1) the specific heat exchanger configuration that is optimized, and (2) the weight and volume constraints that are imposed in the optimization approach. The selected heat exchanger configuration has smooth plates for heat transfer surfaces, while cross-flow heat exchangers designed for aircraft applications typically have fins on these surfaces. These fins greatly increase the wetted area of the heat transfer surfaces, thereby improving the heat exchange effectiveness (i.e., heat transfer performance). The fins also structurally support and stabilize the plates that separate the flow channels (the walls that are bounded by the heat transfer surfaces). This allows the plates to be very thin, further improving the heat exchange effectiveness. The work presented in this paper will have to be extended to address finned heat transfer surfaces for it to be directly useful in industry applications. Similarly, the weight and volume constraints that are imposed arbitrarily on the heat exchanger in this optimization approach will have to be relaxed, in favor of determining the heat exchanger size that minimizes the aircraft’s take-off gross weight.

When completed, the results of this work will provide industry with a structured process for synthesizing the thermodynamic optimum geometry for a cross-flow heat exchanger directly from the physical laws. Eventually, with still further efforts in this direction, it may be possible to extend the EGM methodology to the point where it can provide this same capability for entire, complex thermodynamic systems. Such a capability would be of great benefit to industry, as described in [32].

We close with a comment on engineering thermodynamics, the status of which was reviewed in Section 1. In this paper we relied on entropy generation minimization (EGM) because it is the simplest, divorced from costs. We recognized up front (Section 1) the limitations and orientative value of the method. Thermoeconomics authors may illustrate the integrative approach by using thermoeconomics tools. This work should probably be done, because industry needs integrative and constructal design[1].

Although valuable for what it is and what it has to offer, thermoeconomics tends to obscure the thermodynamics portion of its foundation. Economics (costs) considerations creep without notice into thermodynamics, where they do not belong. Because of costs, we are tempted to think that some components are more important than others, or that the entropy generation in the heat exchanger does not have the same thermodynamics value as the entropy generation in the remaining components. This is improper. Entropy generation is entropy generation, and it is pure thermody-

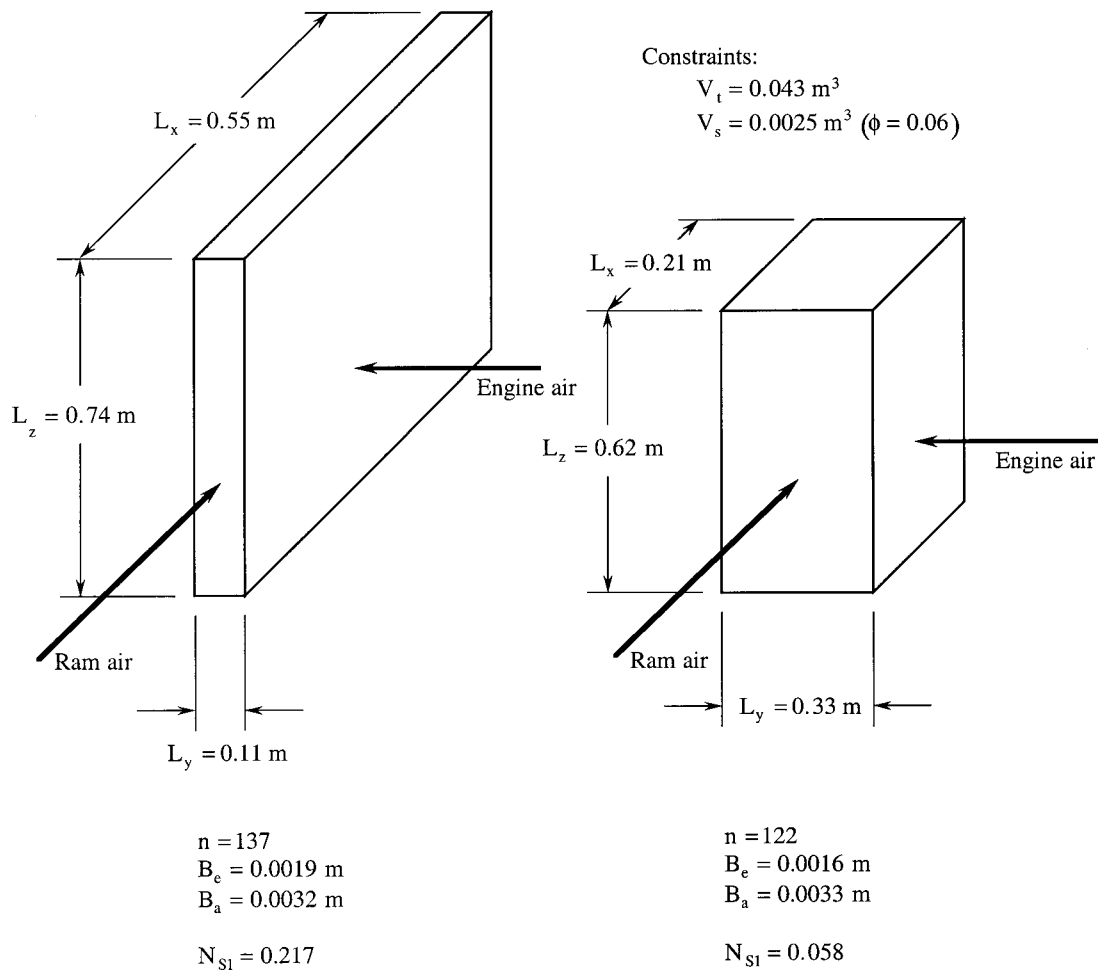


Fig. 14 The two geometries compared in Table 2: the traditional design versus the thermodynamically optimal geometry described in this paper.

Table 2 Comparison between a design produced by traditional methods in industry, and the geometric configuration optimized thermodynamically in this paper

	Traditional method	Entropy Generation Minimization
L_x	0.546 m	0.207 m
L_y	0.106 m	0.334 m
L_z	0.738 m	0.620 m
B_e	0.0019 m	0.0016 m
B_a	0.0032 m	0.0033 m
t_w	0.00015 m	0.00015 m
H_{ca}	0.0054 m	0.0051 m
n	137	122
ρ_{steel}	7800 kg/m ³	7800 kg/m ³
mass	19.4 kg	20 kg
V_t	0.0428 m ³	0.0428 m ³
ϕ	-0.06	-0.06
L_z/L_x	1.35	3
L_y/L_x	0.194	1.618
B_e/B_a	0.6	0.5
N_{S1}	0.217	0.058
N_{S2}	0.271	0.078

namics. It is the only—the universal—measure of imperfection in a thermodynamic sense, no matter where it occurs in the system. It is due to currents that overcome resistances. The road to maximum system performance at the global level is by balancing all the resistances together, i.e., by distributing the imperfection optimally through the space occupied by the system. This is how the flow system acquires its architecture [1].

Acknowledgment

This material is based upon work supported by the Air Force Office of Scientific Research under Contract No. F49620-98-C-0007. Any opinions, findings and conclusions or recommendations are those of the authors and do not necessarily reflect the views of the Air Force Office of Scientific Research. The authors thank Prof. G. Tsatsaronis for his insightful and constructive comments on the original version of the manuscript.

Nomenclature

- A = heat transfer area
- A_c = cross-sectional area
- A_f = stream cross-section before entering the duct
- b = exponent, R/c_p
- B = channel spacing
- c_p = specific heat at constant pressure
- D_h = hydraulic diameter
- f = friction factor
- G = mass velocity
- h = heat transfer coefficient

H_{ea} = thickness of elemental unit
 k = thermal conductivity
 $K_{c,e}$ = contraction and enlargement coefficients
 $L_{x,y,z}$ = lengths
 \dot{m} = mass flow rate
 M = Mach number, Eq. (22)
 n = number of elemental units
 N = number of heat transfer units
 N_S = entropy generation number, Eqs. (3), (4) and (7)
 P = pressure
 Pr = Prandtl number
 \dot{Q}_e = heat transfer rate
 R = ideal gas constant
 Re = Reynolds number
 \dot{S}_{gen} = entropy generation rate
 St = Stanton number
 t_w = wall thickness
 T = temperature
 U = overall heat transfer coefficient
 v = specific volume
 V = velocity
 V_t = total volume
 w = dimensionless power
 \dot{W} = power

Greek Symbols

γ = ratio of specific heats, c_p/c_v
 ΔP = pressure difference
 ε = effectiveness
 η = efficiency
 η_0 = fin efficiency
 μ = ratio of capacity rates, Eq. (3)
 σ = contraction ratio
 τ = dimensionless temperature, Eq. (2)
 ϕ = solid volume fraction

Subscripts

a = ram air
 c_1 = engine compressor
 c_2 = compressor, Fig. 1
 d = diffuser
 e = engine air
 in = inlet
 n = nozzle
 out = outlet
 rev = reversible
 t = turbine
 w = wall

Superscripts

(\sim) = dimensionless, Eqs. (2), (35) and (36)

References

- [1] Bejan, A., 2000, *Shape and Structure, from Engineering to Nature*, Cambridge University Press, Cambridge, UK.
- [2] Bejan, A., 1977, "The Concept of Irreversibility in Heat Exchanger Design: Counterflow Heat Exchangers for Gas-to-Gas Applications," *J. Heat Transfer*, **99**, pp. 374–380.
- [3] London, A. L., and Shah, R. K., 1983, "Costs and Irreversibilities in Heat Exchanger Design," *Heat Transfer Eng.*, **4**, pp. 59–73.
- [4] Sekulic, D. P., and Herman, C. V., 1986, "One Approach to Irreversibility Minimization in Compact Crossflow Heat Exchanger Design," *Int. Commun. Heat Mass Transfer*, **13**, pp. 23–32.
- [5] Sekulic, D. P., 1986, "Entropy Generation in a Heat Exchanger," *Heat Transfer Eng.*, **7**, pp. 83–88.
- [6] Poulidakos, D., 1980, "Fin Geometry for Minimum Entropy Generation Rate," M.S., thesis, University of Colorado, Boulder, Co.
- [7] Poulidakos, D., and Johnson, J. M., 1989, "Second Law Analysis of Combined Heat and Mass Transfer Phenomena in External Flow," *Energy*, **14**, pp. 67–73.
- [8] Krane, R. J., 1987, "A Second Law Analysis of the Optimum Design and Operation of Thermal Energy Storage Systems," *Int. J. Heat Mass Transf.*, **30**, pp. 43–57.
- [9] Witte, L. C., and Shamsundar, N. A., 1983, "A Thermodynamic Efficiency Concept for Heat Exchanger Devices," *J. Eng. Power*, **105**, pp. 199–203.
- [10] Witte, L. C., 1988, "The Influence of Availability Costs on Optimal Heat Exchanger Design," *J. Heat Transfer*, **110**, pp. 830–835.
- [11] Paoletti, S., Rispoli, F., and Sciubba, E., 1989, "Calculation of Exergetic Losses in Compact Heat Exchanger Passages," *ASME AES*, **10-2**, pp. 21–29.
- [12] Benedetti, P., and Sciubba, E., 1993, "Numerical Calculation of the Local Rate of Entropy Generation in the Flow Around a Heated Finned Tube," *ASME HTD*, **266**, pp. 81–91.
- [13] Sekulic, D. P., and Shah, R. K., 1995, "Thermal Design Theory of Three-Fluid Heat Exchangers," *Adv. Heat Transfer*, **26**, pp. 219–328.
- [14] Bejan, A., 1997, *Advanced Engineering Thermodynamics, Second Edition*, Wiley, New York.
- [15] Gambill, J. M., Wiese, D. E., Claeys, H. M., Matulich, D. S., and Weiss, C. F., 1993, "Integrated Aircraft Thermal Management and Power Generation," SAE Paper No. 932055, presented at the 23rd International Conference on Environmental Systems, Colorado Springs, CO, July 12–15.
- [16] Bejan, A., 1982, *Entropy Generation through Heat and Fluid Flow*, Wiley, New York.
- [17] Bejan, A., 1996, *Entropy Generation Minimization*, CRC Press, Boca Raton, FL.
- [18] Feidt, M., 1987, *Thermodynamique et Optimisation Énergétique des Systèmes et Procédés*, Technique et Documentation, Lavoisier, Paris.
- [19] Krane, R. J., ed., 1994, *Thermodynamics and the Design, Analysis, and Improvement of Energy Systems 1994*, AES-Vol. 33, ASME, New York.
- [20] Krane, R. J., ed., 1995, *Thermodynamics and the Design, Analysis, and Improvement of Energy Systems 1995*, AES-Vol. 35, ASME, New York.
- [21] Lazzaretto, A., and Tsatsaronis, G., 1997, "On the Quest for Objective Equations in Exergy Costing," *Proceedings of the ASME Advanced Energy Systems Division*, M. L. Ramalingam, J. L. Lage, V. C. Mei, and J. N. Chapman, eds., AES-Vol. 37, pp. 197–210.
- [22] Moran, M. J., 1982, *Availability Analysis: A Guide to Efficient Energy Use*, Prentice-Hall, Englewood Cliffs, NJ.
- [23] Moran, M. J., and Sciubba, E., 1994, *Exergetic Analysis: Principles and Practice*, *J. Eng. Gas Turbines Power*, **116**, pp. 285–290.
- [24] Richter, H. J., ed., 1993, *Thermodynamics and the Design, Analysis and Improvement of Energy Systems 1993*, HTD-Vol. 266, ASME, New York.
- [25] Stecco, S. S., and Moran, M. J., 1992, *Energy for the Transition Age*, Nova Science, New York.
- [26] Bejan, A., Tsatsaronis, G., and Moran, M., 1996, *Thermal Design and Optimization*, Wiley, New York.
- [27] Ahern, J. E., 1980, *The Exergy Method of Energy Systems Analysis*, Wiley, New York.
- [28] Incropera, F. P., and DeWitt, D. P., 1990, *Fundamentals of Heat and Mass Transfer*, 3rd ed., Wiley, New York.
- [29] Kays, W. M., and London, A. L., 1984, *Compact Heat Exchangers*, 3rd ed., McGraw-Hill, New York.
- [30] Bejan, A., 1993, *Heat Transfer*, Wiley, New York.
- [31] Dieckmann, R. R., Watson, A. C., and Glover, S. F., 1972, "Development of Integrated Control System Designs for Aircraft," Vol. I-ECS Design, Technical Report AFFDL-TR-72-9, McDonnell Douglas Corporation, St. Louis, MO, pp. 58–84.
- [32] Bejan, A., and Siems, D. L., 2001, "The Need for Exergy Analysis and Thermodynamic Optimization in Aircraft Development," *Exergy—An International Journal*, **1**, in press.

An Improved Design and Rating Analyses of Counter Flow Wet Cooling Towers

Jameel-ur-Rehman Khan

Syed M. Zubair¹
smzubair@kfupm.edu.sa

Mechanical Engineering Department,
King Fahd University of Petroleum & Minerals,
Dhahran 31261, Saudi Arabia

Cooling towers are one of the largest heat and mass transfer devices that are in common use. In this paper, we present a detail model of counter flow wet cooling towers. The authenticity of the model is checked by experimental data reported in the literature. The values of number of transfer units (NTU) and tower effectiveness (ϵ) obtained from the model were compared with the commonly described models. Appreciable difference in NTU and ϵ values is found if the resistance to heat transfer in the water film and non-unity of Lewis number is considered in the calculations. The results demonstrate that the errors in calculating the tower effectiveness could be as much as 15 percent when considering the effect of air-water interface temperature. A procedure for the use of the model in designing and rating analyses of cooling towers is demonstrated through example problems. The limiting performance of the cooling towers; that is effectiveness equal to one, is explained in terms of air-approach temperature. The model is also used for obtaining the maximum possible mass-flow rate ratio of water-to-air, for different operating conditions. [DOI: 10.1115/1.1376395]

Keywords: Cooling Towers, Direct Contact, Heat Transfer, Heat Exchangers, Modeling

Introduction

Cooling towers are widely used in most industrial power generation units, refrigeration and air conditioning plants, chemical, petrochemical, and petroleum industries to reject waste heat to the environment. In particular, steam power plants reject heat at about twice the rate at which electric power is generated. For a given water-cooling load, a wet cooling tower needs only about one-fourth the amount of contact surface when compared with that of a dry tower. It should be noted that dry towers (or air-cooled heat exchangers) are economically capable of cooling the water to within about 10°C of the ambient dry-bulb temperature [1]. Such temperature levels are often too high for cooling water requirements of most industrial processes. The water consumption rate of a wet cooling tower system is only about 5 percent that of a once-through system, making it the least expensive system to operate with purchased water supplies. Additionally, the amount of heated water discharged (blowdown) is very small, so that the ecological effect is reduced. Lastly, cooling towers can economically cool water to within 3 to 6°C of the ambient wet-bulb temperature [1–2].

The cooling towers, as shown in Fig. 1, generally consist of large chambers loosely filled with trays or decks of wooden boards as slats or of PVC material. The water to be cooled is pumped to the top of the tower, where it is distributed over the top deck by sprays or distributor troughs made of wood or PVC material. It then falls and splashes from deck-to-deck down through the tower. Air is permitted to pass through the tower horizontally due to wind currents or is drawn vertically upward (countercurrent) to the falling water. In the case of countercurrent towers the air motion may be due to the natural chimney effect of the warm moist air in the tower or may be caused by fans at the bottom (forced draft) or at the top (induced draft) of the tower.

A basic theory of cooling tower operation was first proposed by Walker et al. [3]. The practical use of basic differential equations, however, was first presented by Merkel [4], in which he combined

the equations for heat and water vapor transfer. He showed the utility of total heat or enthalpy difference as a driving force to allow for both sensible and latent heats. The basic postulations and approximations that are inherent in Merkel's theory are (1) the resistance for heat transfer in the liquid film is negligible, (2) the mass flow rate of water per unit of cross sectional area of the tower is constant, i.e., there is no loss of water due to evaporation, (3) the specific heat of air-stream mixture at constant pressure is same as that of the dry air, and (4) the Lewis number for humid air is unity. It is important to note that the formulation and imple-

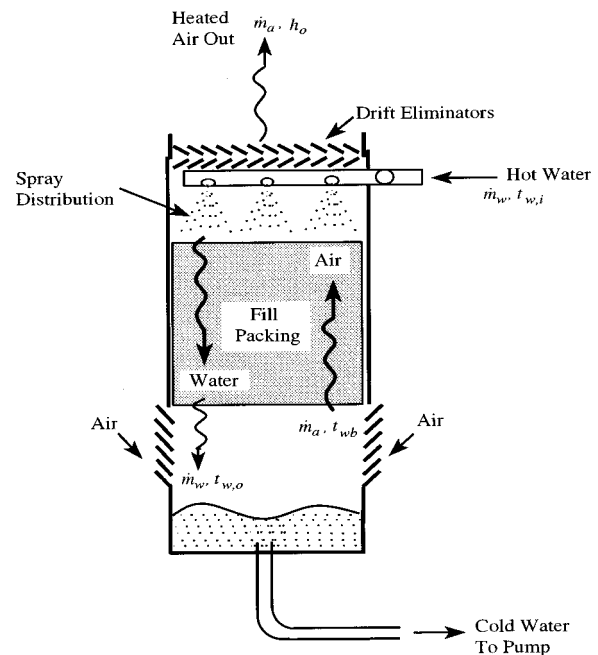


Fig. 1 Schematic of a wet counter flow cooling tower

¹Corresponding author.

Contributed by the Heat Transfer Division for publication in the JOURNAL OF HEAT TRANSFER. Manuscript received by the Heat Transfer Division January 11, 2000; revision received January 20, 2001. Associate Editor: V. P. Carey.

mentation of Merkel's theory in cooling tower design and rating is presented and discussed in most unit operations and process heat transfer textbooks.

Webb [5] performed a unified theoretical treatment for thermal analysis of cooling towers, evaporative condensers and evaporative fluid coolers. In this paper specific calculation procedures are outlined for sizing and rating each type of evaporative exchanger. In another paper Webb and Villacres [6] described three computer algorithms that have been developed to perform rating calculations of three evaporatively cooled heat exchangers. The algorithms are particularly useful for rating commercially available heat exchangers at off-design conditions. The heat and mass transfer characteristics of a particular heat exchanger is derived from the manufacturer's rating data at the design point.

Jaber and Webb [7] presented an analysis that shows how the theory of heat exchanger design may be applied to cooling towers. They demonstrated that the effectiveness (ϵ) and number of transfer units (NTU) definitions are in very good agreement with those used for the heat exchanger design, and are applicable to all cooling tower operating conditions. It should be noted that Jaber and Webb [7] did not consider heat-transfer resistance in the air-water interface and the effect of water evaporation on the air-process states, along the vertical length of the tower. The results are only applicable to Lewis number equal to one. Furthermore they employed Merkel's approximation of replacing the sum of, single-phase heat transfer from the water-air interface to the air and the mass transfer (evaporation of water) at the interface with the enthalpy as a driving potential. It is important to note that the accuracy of results obtained from such an assumption depends upon the method of calculating the moist air properties.

Braun et al. [8] presented effectiveness models for cooling towers and cooling coils. The models utilize existing effectiveness relationship developed for sensible heat exchangers with modified definitions for number of transfer units and the fluid capacitance rate ratio. Results of the models were compared with those of more detailed numerical solutions to the basic heat and mass transfer equations and experimental data. They also did not consider the effect of air-water interface temperature; however, they did consider the effect of water evaporation on the air process states along the vertical length of the tower. The results are only presented for Lewis number equal to unity.

Dessouky et al. [9] presented a solution for the steady-state counter-flow wet cooling tower with new definitions of tower effectiveness and number of transfer units. Their model is essentially a modified version of Jaber and Webb's model with the inclusion of Lewis number, which appears as a multiplication factor to the enthalpy driving potential. They did consider the effect of interface temperature and Lewis number, however, the effect of water evaporation on the air process states, along the vertical length is not considered. Furthermore they used an approximate equation for calculating the moist air enthalpy, which was obtained by curve fitting the tabulated thermodynamic properties of saturated air-water vapor mixture. It is important to note that the calculation of moist air properties should be accurate to obtain reliable results. The objective of this paper is to consider together the effects of Lewis number, the heat-transfer resistance in the air-water interface, and the effect of water evaporation on the air process states, along the vertical length of the tower. In this regard we have used reliable air-water thermodynamic property equations that are developed by Hyland and Wexler [10–11].

Mathematical Formulation

A schematic of a counterflow-cooling tower showing the important states is given in Fig. 2. The major assumptions that are used to derive the basic modeling equations may be summarized as [12–14]:

- heat and mass-transfer in a direction normal to the flows only
- negligible heat and mass transfer through the tower walls to the environment

- negligible heat transfer from the tower fans to air or water streams
- constant water and dry air specific heats
- constant heat and mass transfer coefficients throughout the tower
- constant value of Lewis number throughout the tower
- water lost by drift is negligible
- uniform temperature throughout the water stream at any cross section
- uniform cross-sectional area of the tower

From steady-state energy and mass balances on an incremental volume (refer to Fig. 2), the following differential equation may be written

$$\dot{m}_a dh = \dot{m}_w dh_{f,w} + \dot{m}_a dWh_{f,w} \quad (1)$$

We may also write the water energy balance in terms of the heat- and mass-transfer coefficients, h_c and h_D , respectively, as

$$\dot{m}_w dh_{f,w} = h_c A_V dV(t_w - t) + h_D A_V dV(W_{s,w} - W)h_{fg,w} \quad (2)$$

and the air side water-vapor mass balance as

$$\dot{m}_a dW = h_D A_V dV(W_{s,w} - W) \quad (3)$$

By substitution Lewis number as $Le = h_c / h_D c_{pa}$ in Eq. (2), we obtain

$$\dot{m}_w dh_{f,w} = h_D A_V dV [Le c_{pa} (t_w - t) + (W_{s,w} - W)h_{fg,w}] \quad (4)$$

It should be noted that we have defined Lewis number in Eq. (4), similar to the definition that is used by Braun et al. [8] and Threlkeld [13–14]; however, Jaber and Webb [7] and El-Dessouky et al. [9] have used $Le = Sc/Pr$, commonly used in heat and mass-transfer literature. In this regard, we prefer to stick to the notation of Threlkeld [13–14], that is considered as one of the standard references in the cooling tower literature. Combining Eqs. (1), (3), and (4), we get

$$\frac{dh}{dW} = Le c_{pa} \frac{(t_w - t)}{(W_{s,w} - W)} + h_{g,w} \quad (5)$$

Using the approximation of constant c_{pa} , we have

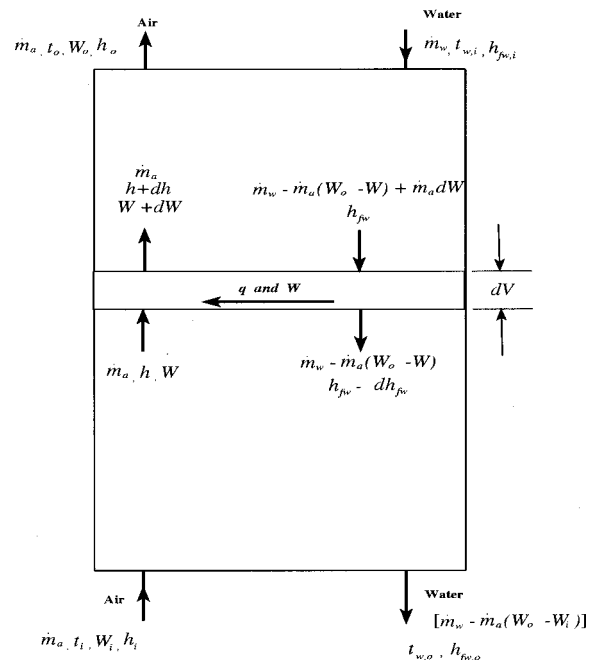


Fig. 2 Mass and energy balance of a wet counter flow cooling tower

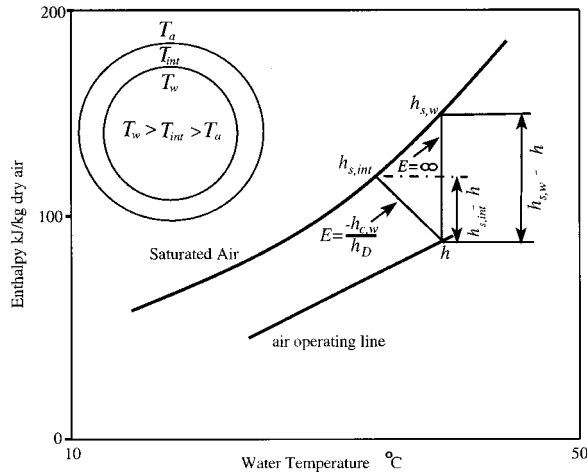


Fig. 3 Water operating line on enthalpy-temperature diagram indicating the effect of tie line ($E = -h_{c,w}/h_D$) on saturated moist air enthalpy

$$h_{s,w} - h = c_{pa}(t_w - t) + h_g^0(W_{s,w} - W) \quad (6)$$

Equation (5) may then be written as

$$\frac{dh}{dW} = Le \frac{(h_{s,w} - h)}{(W_{s,w} - W)} + (h_{g,w} - h_g^0)Le \quad (7)$$

It should be noted that Eq. (7) describes the condition line on the psychrometric chart for the changes in state for moist air passing through the tower. For given water temperatures ($t_{w,i}$, $t_{w,o}$), Lewis number (Le), inlet condition of air and mass flow rates, Eqs. (1) and (6) may be solved numerically for exit conditions of both the air and water stream. The solution is iterative with respect to the air humidity ratio and temperatures (W , t , and t_w). At each iteration, Eqs. (1)–(6) can be integrated numerically over the entire tower volume from the air inlet to outlet by a procedure similar to that described in references [12–14]. Initially inlet condition of air and the condition of saturated air in equilibrium with leaving water temperature are known. The quantity dh/dW is calculated by using Eq. (7). Then in the second step enthalpy of inlet air is increased by a small amount ($h_i + \Delta h$). The resulting incremental change in water temperature is calculated by the equation: $\Delta t_w = -(\dot{m}_a/\dot{m}_w c_w)(\Delta h - Wh_{f,w})$. Next, the state of saturated air in equilibrium with water temperature is calculated at this increased water temperature. The procedure is repeated until we get the water temperature equal to the water inlet temperature.

In deriving Eqs. (1)–(6), it was assumed that there is no resistance to heat flow in the interface between air and water. In other words, the interface temperature was assumed to be equal to the bulk water temperature. However, for heat transfer to take place between air and water, the temperature of the interface film should be less than the bulk water temperature, as shown in Fig. 3. In that case all the terms in Eqs. (1)–(6) with the subscripts (s,w) will be replaced by (s,int). Webb [5] assumed that t_w is nearly equal to ($t_{int} + 0.5$).

Figure 3 shows both enthalpies of the saturated air-water vapor mixture and tower operating line as a function of water temperature. Considering the short distance between $h_{s,w}$ and $h_{s,int}$ on the saturation curve as a straight line, following simple relationship can be easily deduced [9]

$$h_{s,w} - h = h_{s,w} - h_{s,int} + E(t_w - t_{int}), \quad (8)$$

where E is slope of the tie line and is constant for a given cooling tower. This slope is given by

$$E = -h_{c,w}/h_D \quad (9)$$

The above equation can be used for obtaining the interface temperature. However for large values of E the interface and bulk water temperature are equal.

Detail Model

A computer program is written for solving Eqs. (1)–(6) numerically. In this program properties of air-water vapor mixture and moist air are needed at each step of numerical calculation. These properties are obtained from the property equations given in Hyland and Wexler [10–11], which are also used by ASHRAE [2] in computing air-water vapor thermodynamic properties. The program gives the dry-bulb temperature, wet-bulb temperature of air, water temperature and humidity ratio of air at each step of numerical calculation starting from air-inlet to air-outlet values. If the value of ($h_D A_V$) is known, the required tower volume may be obtained by using [13–14]

$$V = \frac{\dot{m}_a}{h_D A_V} \int_{W_i}^{W_o} \frac{dW}{W_{s,w} - W} \quad (10)$$

The integral in the above equation is solved numerically. The number of transfer units of the tower are calculated by

$$NTU = h_D A_V V / \dot{m}_a = \int_{W_i}^{W_o} \frac{dW}{W_{s,w} - W} \quad (11)$$

The cooling tower effectiveness (ε) is defined as the ratio of actual energy to the maximum possible energy transfer.

$$\varepsilon = \frac{h_o - h_i}{h_{s,w,i} - h_i} \quad (12)$$

General correlations for heat and mass transfer of cooling towers in terms of physical characteristics do not exist. It is usually necessary to correlate the tower performance data for specific tower designs. Mass transfer data are typically correlated in the form [1]

$$\frac{h_D A_V V}{\dot{m}_w} = c \left(\frac{\dot{m}_w}{\dot{m}_a} \right)^n \quad (13)$$

where c and n are empirical constants specific to a particular tower design. Multiplying both sides of the above equation by (\dot{m}_w/\dot{m}_a) and considering the definition for NTU (refer to Eq. (11)) gives the empirical value of NTU as

$$NTU_{em} = c \left(\frac{\dot{m}_w}{\dot{m}_a} \right)^{n+1} \quad (14)$$

The coefficients c and n of the above equation were fit to the measurements of Simpson and Sherwood [15] for four different tower designs over a range of performance conditions by Braun et al. [8]. The experimental and empirical values were compared with the values obtained by our detail model, and the results are shown in Table 1. As can be seen from the Table, the calculated and empirical values of NTU are well within the acceptable limits. Also the wet-bulb temperature of outlet air ($t_{wb,o}$), calculated from the present model is compared with the experimental values reported in Simpson and Sherwood [15], the two values are very close to each other (within ± 0.6 percent). Therefore, the

Table 1 Experimental and calculated values of cooling tower parameters

$t_{w,i}$ (°C)	$t_{w,o}$ (°C)	$t_{wb,i}$ (°C)	$t_{wb,o}$ (°C)	\dot{m}_a (kg/s)	\dot{m}_w (kg/s)	NTU_{em}	NTU_{cal}	$t_{wb,o}^{cal}$ (°C)	$t_{wb,o}^{exp}$ (°C)
31.22	23.88	37.05	21.11	1.158	0.754	1.297	1.235	26.45	26.05
41.44	26.00	34.11	21.11	1.158	0.754	1.297	1.214	30.72	31.16
28.72	24.22	29.00	21.11	1.187	1.259	1.745	1.777	26.42	26.17
34.50	26.22	30.50	21.11	1.187	1.259	1.745	1.706	30.06	29.90
38.78	29.33	35.00	26.67	1.265	1.008	1.467	1.465	33.09	32.89
38.78	29.33	35.00	26.67	1.250	1.008	1.476	1.494	33.17	32.89

model developed in this paper can be used to either design or rate counter-current wet cooling towers. A classical problem of designing a cooling tower is to calculate the required tower volume (or NTU), given the type of packing, the wet bulb temperature of the entering air, water inlet temperature, water outlet temperature and mass flow rates of water and air. On the other hand, in a typical rating problem the exit cooled water temperature is obtained given volume of the tower (or NTU), water inlet temperature, inlet air dry-bulb temperature, inlet air wet bulb temperature and the mass flow rates of water and air. The heat and mass transfer coefficients h_c , $h_{c,w}$, and h_D , required for calculating Le and NTU can be determined experimentally. Webb [5] have reported experimental values of the above coefficients, as functions of Reynolds number and packing parameters. The designer of cooling towers should determine experimentally, the above coefficients based on the given packing geometry.

Design of Cooling Towers

Effect of Le and E . In the literature, Merkel's model is mostly used for design and rating calculations of cooling towers. However, the difference in values of NTU and ϵ predicted by Merkel's model and detail thermodynamic model is significant for different values of E and Le . Figure 4 is a plot between NTU and E for different values of Le . The plot is drawn for the following set of input data which is also used by Dessouky et al. [9]: $t_{w,i} = 35.0^\circ\text{C}$, $t_{w,o} = 30.0^\circ\text{C}$, $h_i = 76.6 \text{ kJ/kg}$, and $\dot{m}_w/\dot{m}_a = 1.00$. The figure shows that for $Le = 1.0$ both the detail model and the Dessouky's model are predicting about the same value of NTU . However for Le equal to 0.87 and 1.2, there is an appreciable difference between the two models. Figures 5(a) and 5(b) are plots between the effectiveness (ϵ) and the non-dimensional temperature ratio (R) defined as

$$R = \frac{t_{w,i} - t_{w,o}}{t_{w,i} - t_{wb,i}} \quad (15)$$

for different values of the mass flow rate ratio (\dot{m}_w/\dot{m}_a). The plot is generated for the following set of input conditions which are also considered in the experimental work of Simpson and Sherwood [15]: $t_{db,i} = 29.0^\circ\text{C}$, $t_{wb,i} = 21.11^\circ\text{C}$, $t_{w,i} = 28.72^\circ\text{C}$, $Le = 0.9$ and $h_D A_V = 3.025 \text{ kg/s}\cdot\text{m}^2$. In this figure, R is varied by varying the value of $t_{w,o}$ from $t_{w,i}$ to $t_{wb,i}$. It should be noted that as the value of $t_{w,o}$ decreases from $t_{w,i}$ to $t_{wb,i}$ the value of R increases from 0.0 to 1.0. The dashed lines in both the figures represent Dessouky's model. Figure 5(a) is drawn for $E = 11.1$, which is used by Baker and Shryock [16], while Fig. 5(b) is drawn with $E = \infty$ that corresponds to the interface temperature equal to

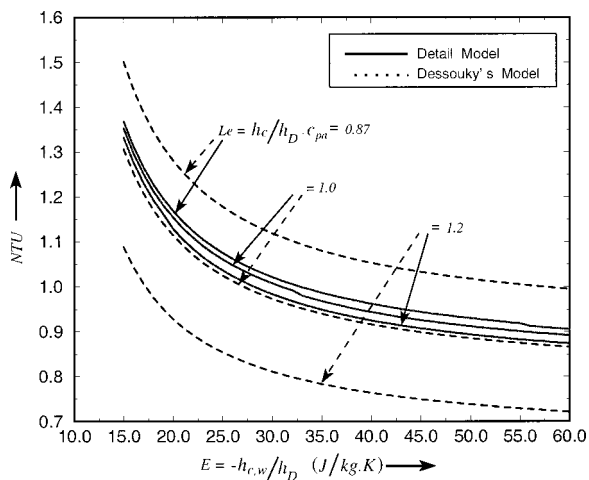


Fig. 4 Comparisons of NTU with slope of tie line $E = -h_{c,w}/h_D$ for different values of Lewis number Le

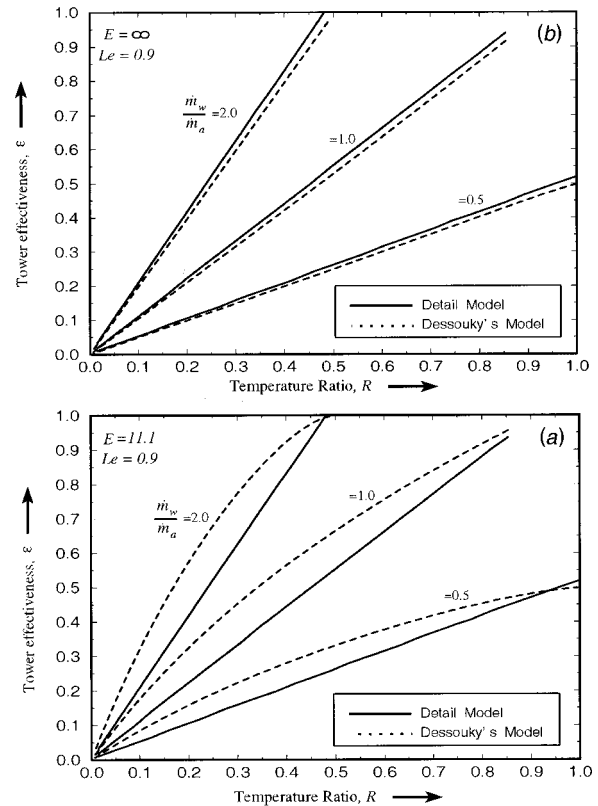


Fig. 5 Comparisons of effectiveness ϵ with temperature ratio R by varying the water-outlet temperature $t_{w,o}$ for different values of mass-flow rate ratios. Slope of the tie line $E = 11.1$ (Fig. 5(a)), and $E = \infty$ (Fig. 5(b)).

the bulk water temperature. Clearly for lower values of E , Dessouky's model and detail model predict different values of ϵ , however, for $E = \infty$, as expected, both the models predict same values of ϵ . Table 2 summarizes the values of NTU and ϵ for different values of Lewis number Le and E , obtained from detailed model, Braun's model, Dessouky's model and Jaber (or Merkel's) model. It should be noted that Jaber's model with $Le = 1.0$ is equivalent to Merkel's model. The values given in the table is obtained by using the input data also shown on the table. As can be seen from the table that some results are fairly close in comparison and others are quite different.

Effect of Water Outlet Temperature. Figure 6(a) is a plot between the effectiveness and non-dimensional temperature ratio R , for different values of the mass flow rate ratio (\dot{m}_w/\dot{m}_a). The input data used in this figure is same as that of Fig. 5. As expected, the figure shows that as the value of $t_{w,o}$ decreases, the effectiveness of the tower ϵ increases. This increase of ϵ with R is higher for larger mass flow rate ratios. Figure 6(b) is the corresponding plot between R and air-approach temperature that is defined as the temperature difference between the water inlet temperature and wet bulb temperature of outlet air ($t_{w,i} - t_{wb,o}$). It is important to note that this difference in temperature is a measure of the closeness to saturation condition of the cooling tower. For example, lower the temperature difference, the higher will be effectiveness and vice versa. When this temperature difference is equal to zero, the effectiveness of the tower is equal to 1.0. This figure clearly demonstrates the reason why for higher mass flow rate ratios, the effectiveness of the tower is approaching unity for values of R less than 1.0, as is demonstrated in the case of $\dot{m}_w/\dot{m}_a = 2.0$. However for $\dot{m}_w/\dot{m}_a = 0.5$, the tower never reaches the saturation point. Figure 7 shows the plot between NTU and R for the above set of input data. The figure shows that for

Table 2 Values of NTU and ϵ obtained from different models for various values of Le and E ,—design calculations*

Detail Model, $E=11.1$	$Le=0.8$	$Le=1.0$	$Le=1.2$
NTU	0.426	0.418	0.412
ϵ	0.643	0.643	0.643
Dessouky's Model, $E=11.1$	$Le=0.8$	$Le=1.0$	$Le=1.2$
NTU	3.703	2.962	2.469
ϵ	0.749	0.749	0.749
Detail Model, $E=60.0$	$Le=0.8$	$Le=1.0$	$Le=1.2$
NTU	1.178	1.183	1.186
ϵ	0.646	0.646	0.646
Dessouky's Model, $E=60.0$	$Le=0.8$	$Le=1.0$	$Le=1.2$
NTU	2.258	1.806	1.505
ϵ	0.645	0.645	0.645
Braun's Model, $E=\infty$	$Le=0.8$	$Le=1.0$	$Le=1.2$
NTU	1.745	1.773	1.792
ϵ	0.650	0.650	0.650
Jaber or Merkel's Model, $E=\infty$	$Le=1.0$		
NTU	1.847		
ϵ	0.650		

*Input data: $t_{w,i} = 28.72^\circ\text{C}$, $t_{w,o} = 24.22^\circ\text{C}$, $t_{a,b,i} = 29.00^\circ\text{C}$, $t_{wb,i} = 21.11^\circ\text{C}$
 $\dot{m}_a = 1.187 \text{ kg/s}$, $\dot{m}_w = 1.259 \text{ kg/s}$, and $h_D A_V = 3.02 \text{ kg/s}\cdot\text{m}^3$

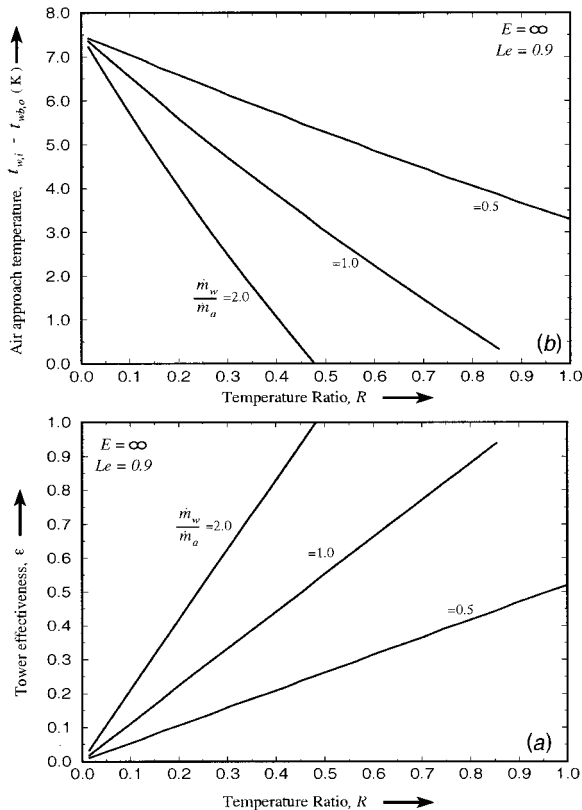


Fig. 6 Comparisons of effectiveness ϵ with temperature ratio R by varying water-outlet temperature $t_{w,o}$ (Fig. 6(a)), and air approach temperature ($t_{w,i} - t_{w,o}$) with R (Fig. 6(b)).

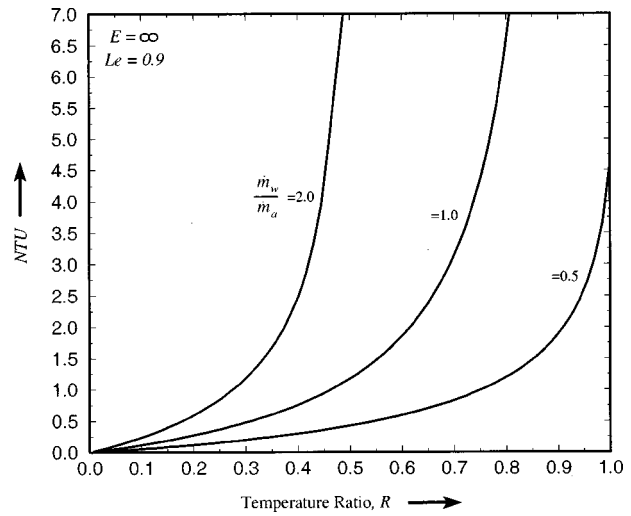


Fig. 7 Comparisons of NTU with temperature ratio R by varying water-outlet temperature $t_{w,o}$

$\dot{m}_w/\dot{m}_a = 2.0$, the increase in NTU is less for $R \leq 0.4$; however, beyond this point the value of NTU increases rapidly. This implies that to obtain lower values of $t_{w,o}$, a large volume of cooling tower is required. It should be noted that NTU represents the size of cooling towers. Also Fig. 6(a) shows that for every value of R , there is one value of \dot{m}_w/\dot{m}_a at which the effectiveness of the tower is equal to 1.0. This value of $(\dot{m}_w/\dot{m}_a)_{\max}$ is defined as the maximum possible value of mass flow rate ratio, any other value greater than this value will not increase the tower effectiveness. Figure 8 is the plot between $(\dot{m}_w/\dot{m}_a)_{\max}$ and R for the above set of input data. This figure shows that for lower values of R , the maximum mass flow rate ratio required to obtain $\epsilon = 1.0$ is very high. However, for $R \geq 0.1$, these values of mass flow rate ratio decrease rapidly. This can be explained from the fact that for a particular mass flow rate ratio, values of ϵ increase linearly with R , (refer Fig. 6(a)). It should also be noted that the values of $(\dot{m}_w/\dot{m}_a)_{\max}$ are independent of Le for all values of R . This can be explained due to the fact that ϵ of the tower depends on the inlet dry and wet bulb temperatures of air and the water inlet and outlet

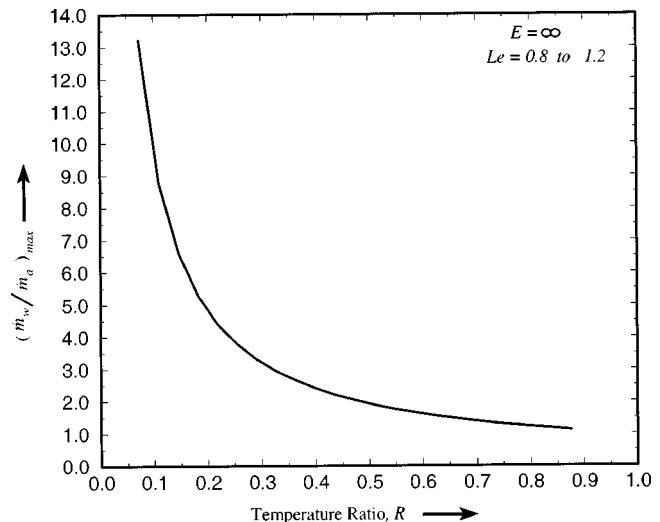


Fig. 8 Variations of maximum mass-flow rate ratio with temperature ratio R by varying the water-outlet temperature $t_{w,o}$

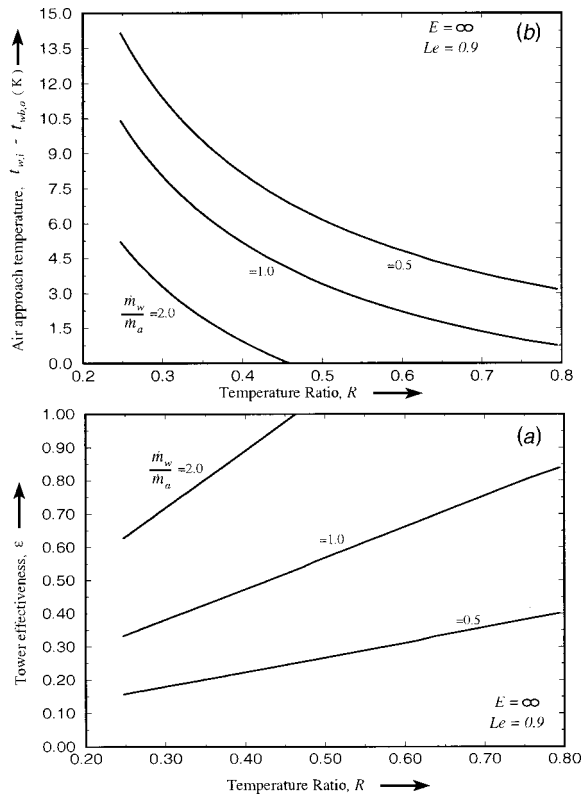


Fig. 9 Comparisons of effectiveness ε with temperature ratio R by varying air inlet wet-bulb temperature $t_{wb,i}$ (Fig. 9(a)), and air approach temperature ($t_{w,i} - t_{wb,o}$) with R (Fig. 9(b))

temperatures. Because these temperatures are input for designing cooling towers, the effectiveness will be constant and will not vary with Le .

Effect of Inlet Air Wet Bulb Temperature. Figure 9(a) is a plot between effectiveness and temperature ratio R for different values of (\dot{m}_w/\dot{m}_a) . These plots are generated for the following set of input data: $t_{db,i} = 29.0^\circ\text{C}$, $t_{w,o} = 24.22^\circ\text{C}$, $t_{w,i} = 28.72^\circ\text{C}$, and $h_D A_V = 3.025 \text{ kg/s}\cdot\text{m}^3$. We emphasize that inlet air wet bulb temperature ($t_{wb,i}$) is varied from 10.56°C to $t_{w,o}$ to produce these plots. In this case, as expected, the tower effectiveness increases with R and this increase is high for higher mass flow rates. On

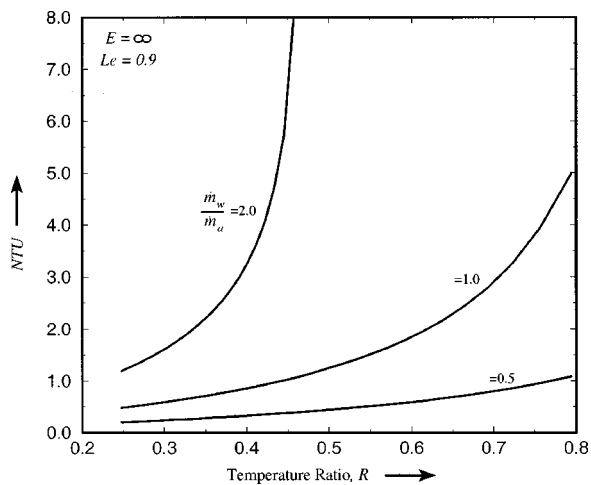


Fig. 10 Comparisons of NTU with temperature ratio R by varying air inlet wet-bulb temperature $t_{wb,i}$

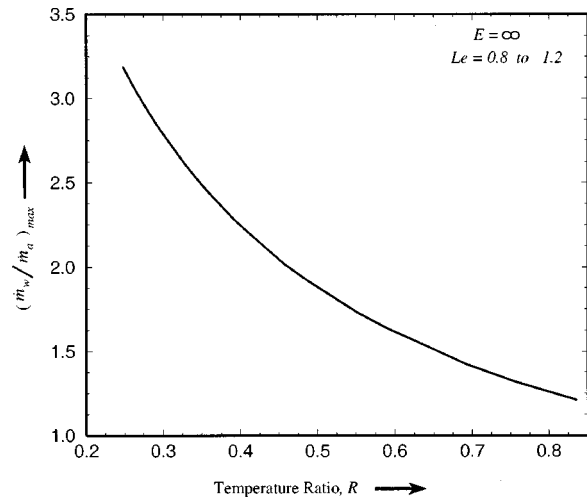


Fig. 11 Variations of maximum mass-flow rate ratio with temperature ratio R by varying the air inlet wet-bulb temperature $t_{wb,i}$

comparing Fig. 6(a) with Fig. 9(a), we note that for same mass flow rate ratios, the tower effectiveness increases rapidly with $t_{w,o}$. Figure 9(b) is the plot between $(t_{w,i} - t_{wb,o})$ and R . As explained earlier in Fig. 6, Fig. 9(b) demonstrates the reason why for higher mass flow rate ratio $\dot{m}_w/\dot{m}_a = 2.0$, the effectiveness of the tower is equal to unity for $R \geq 0.45$. This explains the behavior of Fig. 9(a). Figure 10 shows the plot between NTU and R , while Fig. 11 is the plot between $(\dot{m}_w/\dot{m}_a)_{\max}$ and R for the above set of input data. These figures show a behavior similar to those of Figs. 7–8, with only different numbers, indicating the influence of inlet air wet bulb temperature. Similar to Fig. 8, the values of $(\dot{m}_w/\dot{m}_a)_{\max}$ are independent of Le for all values of R due to the reasons discussed earlier.

Rating of Cooling Towers

Table 3 summarizes the values of $t_{w,o}$ and ε for different values of Lewis number Le and E , obtained from the detail model, Braun's model, Dessouky's model and Jaber (or Merkel's) model. As can be seen from this table that there is no appreciable difference in the water outlet temperatures predicted by various models.

Effect of Inlet Air Wet Bulb Temperature. Figure 12(a) is the plot between the tower effectiveness (ε) and inlet air wet bulb temperature ($t_{wb,i}$) for different values of mass flow rate ratios. This figure is generated for the following set of input data: $t_{db,i} = 29.0^\circ\text{C}$, $t_{w,i} = 28.72^\circ\text{C}$, $\dot{m}_a = 1.187 \text{ kg/s}$, $h_D A_V = 3.025 \text{ kg/s}\cdot\text{m}^3$, and $V = 0.697 \text{ m}^3$. Figure 12(b) is the corresponding plot between $(t_{w,i} - t_{wb,o})$ versus $t_{wb,i}$. In these plots, the values of $t_{wb,i}$ was varied from 11 to 27°C . It is interesting to note that for the values of $t_{wb,i}$ considered, the tower effectiveness remain almost constant and there is no appreciable change in $(t_{w,i} - t_{wb,o})$ with \dot{m}_w/\dot{m}_a , particularly at high values of $t_{wb,i}$. Figure 13 is the plot between water outlet temperature ($t_{w,o}$) and inlet air wet bulb temperature ($t_{wb,i}$) for the above set of input data. This figure shows that $t_{w,o}$ changes by about 12.0°C for the range of $t_{wb,i}$ considered in the figure, i.e., for the case of $\dot{m}_w/\dot{m}_a = 0.5$. However as the mass flow rate ratio increases, the increase in $t_{w,o}$ decreases, as can be seen for $\dot{m}_w/\dot{m}_a = 0.60$ and $= 0.75$ for which the increase in $t_{w,o}$ are 11 and 9°C , respectively.

Effect of Water Inlet Temperature. Figure 14(a) is the plot between the tower effectiveness (ε) and the water inlet temperature ($t_{w,i}$) for different values of mass flow rate ratios. This figure is generated for the following set of input data: $t_{db,i} = 29.0^\circ\text{C}$, $t_{wb,i} = 21.1^\circ\text{C}$, $\dot{m}_a = 1.187 \text{ kg/s}$, $h_D A_V = 3.025 \text{ kg/s}\cdot\text{m}^3$,

Table 3 Values of $t_{w,o}$ and ϵ obtained from different models for various values of Le and E ,—rating calculations*

Detail Model, $E=11.1$	$Le=0.8$	$Le=1.0$	$Le=1.2$
$t_{w,o}$	24.798°C	24.841°C	24.884°C
ϵ	0.567	0.560	0.557
Dessouky's Model, $E=11.1$	$Le=0.8$	$Le=1.0$	$Le=1.2$
$t_{w,o}$	25.182°C	24.799°C	24.506°C
ϵ	0.587	0.640	0.682
Detail Model, $E=60.0$	$Le=0.8$	$Le=1.0$	$Le=1.2$
$t_{w,o}$	24.305°C	24.340°C	24.357°C
ϵ	0.636	0.632	0.628
Dessouky's Model, $E=60.0$	$Le=0.8$	$Le=1.0$	$Le=1.2$
$t_{w,o}$	24.630°C	24.240°C	23.938°C
ϵ	0.597	0.640	0.682
Braun's Model, $E=\infty$	$Le=0.8$	$Le=1.0$	$Le=1.2$
$t_{w,o}$	24.197°C	24.220°C	24.236°C
ϵ	0.654	0.650	0.646
Jaber or Merkel's Model, $E=\infty$	$Le=1.0$		
$t_{w,o}$	24.119°C		
ϵ	0.641		

*Input data: $t_{w,i} = 28.72^\circ\text{C}$, $t_{db,i} = 29.00^\circ\text{C}$, $t_{wb,i} = 21.11^\circ\text{C}$, $NTU = 1.773$,

$\dot{m}_a = 1.187 \text{ kg/s}$, $\dot{m}_w = 1.259 \text{ kg/s}$, and $h_D A_p = 3.02 \text{ kg/s.m}^3$

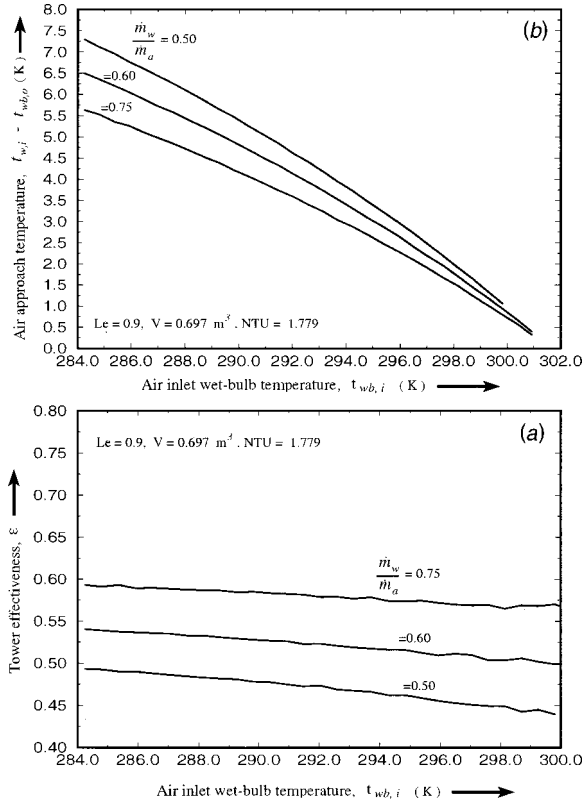


Fig. 12 Comparisons of effectiveness ϵ with inlet air wet bulb temperature $t_{wb,i}$ (Fig. 12(a)), and air approach temperature $(t_{w,i} - t_{wb,o})$ with R (Fig. 12(b))

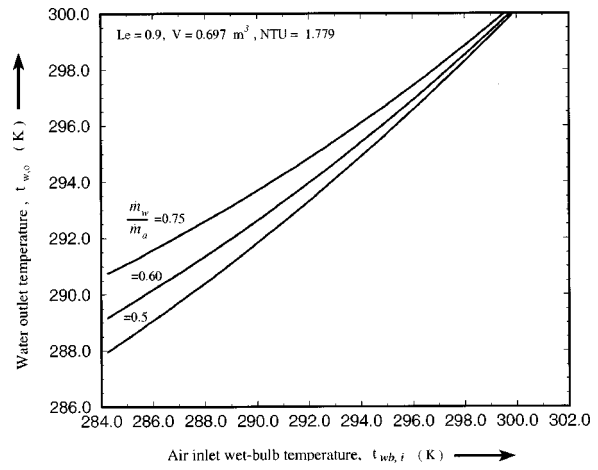


Fig. 13 Comparisons of water outlet temperature $t_{w,o}$ with inlet air wet bulb temperature $t_{wb,i}$

and $V=0.697 \text{ m}^3$. Figure 14(b) is the corresponding plot between water outlet temperature ($t_{w,o}$) and water inlet temperature ($t_{w,i}$). It should be noted that there is an appreciable change in effectiveness of the cooling tower for the range of $t_{w,i}$ considered, unlike Fig. 12(a) where there is no significant change in ϵ for the range of $t_{wb,i}$ considered. Thus, indicating that changes in water-inlet temperature has relatively more effect on ϵ of the cooling tower, compared to changes in $t_{wb,i}$ for the same tower configuration. Figure 14(b) shows that the change in $t_{w,o}$ for the range of $t_{w,i}$ considered, decreases with the decrease in mass-flow rate ratios. Also, for a particular mass flow rate ratio this change in $t_{w,o}$ is less

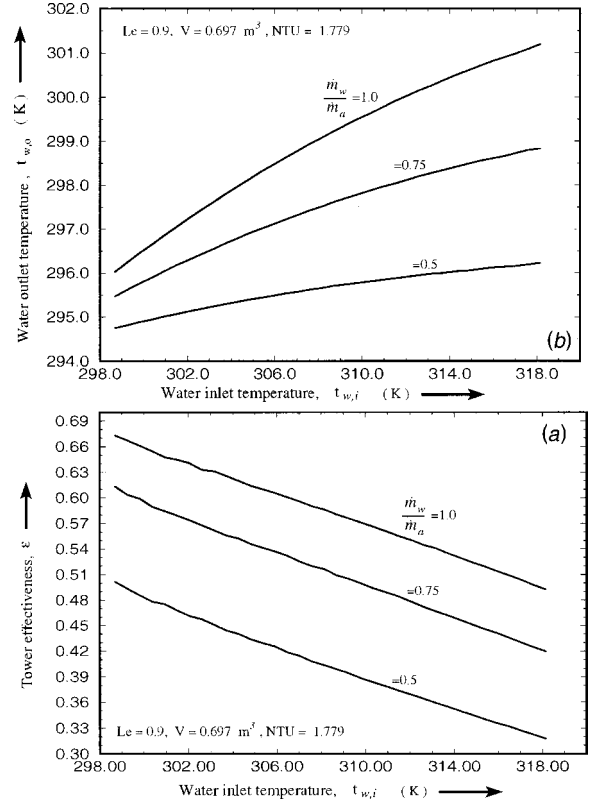


Fig. 14 Comparisons of effectiveness ϵ with water inlet temperature $t_{w,i}$ (Fig. 14(a)), and water outlet temperature $t_{w,o}$ with $t_{w,i}$ (Fig. 14(b)).

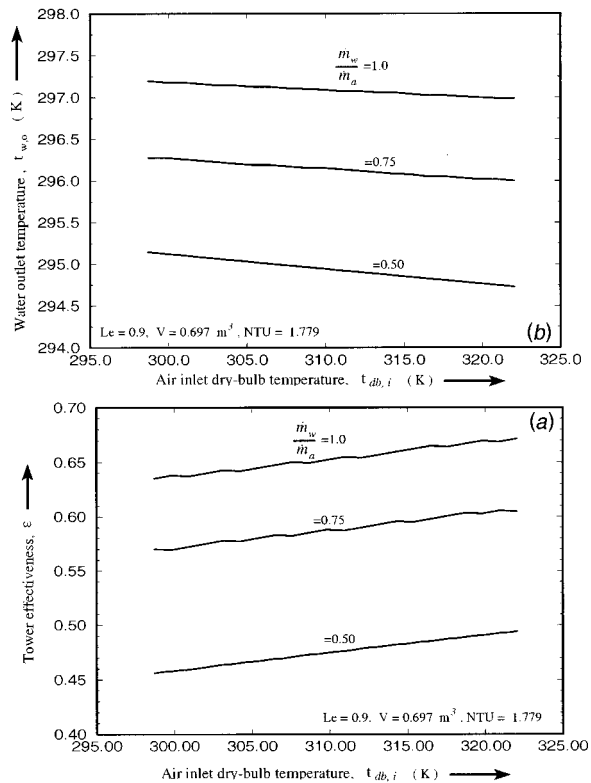


Fig. 15 Comparisons of effectiveness ϵ with inlet air dry bulb temperature $t_{db,i}$ (Fig. 15(a)), and water outlet temperature $t_{w,o}$ with $t_{db,i}$ (Fig. 15(b))

compared to the corresponding change shown in Fig. 13, implying that changes in $t_{wb,i}$ has relatively more effect on $t_{w,o}$, compared to changes in $t_{w,i}$ for the same tower.

Effect of Inlet Air Dry Bulb Temperature

Figure 15(a) is the plot between the tower effectiveness (ϵ) and inlet air dry-bulb temperature ($t_{db,i}$) for different values of mass flow rate ratios, while Fig. 15(b) is the plot between water outlet temperature ($t_{w,o}$) and inlet air dry-bulb temperature ($t_{db,i}$). These plots are drawn for the following set of input data: $t_{w,i} = 28.72^\circ\text{C}$, $t_{wb,i} = 21.1^\circ\text{C}$, $\dot{m}_a = 1.187 \text{ kg/s}$, $h_D A_V = 3.025 \text{ kg/s} \cdot \text{m}^3$, and $V = 0.697 \text{ m}^3$. These curves, as expected, demonstrate that there is a negligible effect of changes in inlet air dry bulb temperature on the performance of cooling towers, which is a typical characteristic of wet-cooling towers [1].

Conclusions

A more realistic detail model for the steady-state operation of a counter flow wet cooling tower is described with respect to example problems. In this model, we have considered the effect of water evaporation on the air process states, the resistance of heat transfer in the water film and the non-unity of the Lewis number. The data obtained from the application of the model showed that a substantial error can be made when the resistance to heat transfer in the water film is neglected and the Lewis number is considered to be unity. However, the magnitude of errors in calculating tower thermal parameters is a strong function of the ratio between the heat and mass transfer coefficients that are used in the calculations. The design and rating analyses of the wet cooling tower, which is considered in the experimental work of Simpson and Sherwood [15] are explained in more detail. The variation of tower effectiveness is investigated in terms of air approach tem-

perature. It is also demonstrated that the inlet air dry-bulb temperature has a negligible effect on the tower performance, which is typical of wet cooling tower.

Acknowledgments

The authors acknowledge the support provided by King Fahd University of Petroleum and Minerals for this research project.

Nomenclature

- A_V = surface area of water droplets per unit volume of the tower, m^2/m^3
- c_{pa} = specific heat at constant pressure of moist air, $\text{kJ}/\text{kg}_a \cdot \text{K}$
- c_w = specific heat of water, $\text{kJ}/\text{kg}_w \cdot \text{K}$
- E = slope of the "tie" line, $\text{kJ}/\text{kg}_w \cdot \text{K}$
- h = enthalpy of moist air, kJ/kg_a
- h_c = convective heat-transfer coefficient of air, $\text{kW}/\text{m}^2 \cdot \text{K}$
- $h_{c,w}$ = convective heat-transfer coefficient of water, $\text{kW}/\text{m}^2 \cdot \text{K}$
- h_D = convective mass-transfer coefficient, $\text{kg}_w/\text{m}^2 \cdot \text{s}$
- h_f = specific enthalpy of saturated liquid water, kJ/kg_w
- $h_{f,w}$ = specific enthalpy of water evaluated at t_w , kJ/kg_w
- h_g = specific enthalpy of saturated water vapor, kJ/kg_w
- h_g^0 = specific enthalpy of saturated water vapor evaluated at 0°C , kJ/kg_w
- $h_{fg,w}$ = change-of-phase enthalpy ($h_{fg,w} = h_{g,w} - h_{f,w}$), kJ/kg_w
- $h_{s,w}$ = enthalpy of saturated moist air evaluated at t_w , kJ/kg_a
- $h_{s,int}$ = enthalpy of saturated moist air evaluated at t_{int} , kJ/kg_a
- Le = Lewis number ($Le = h_c/h_D c_{p,a}$)
- \dot{m}_a = mass flow rate of dry air, kg_a/s
- \dot{m}_w = mass flow rate of water, kg_w/s
- NTU = number of transfer units
- Pr = Prandtl number
- R = dimensionless temperature range (refer to Eq. (15))
- Sc = Schmidt number
- t = dry-bulb temperature of moist air, $^\circ\text{C}$
- t_{int} = air-water interface temperature, $^\circ\text{C}$
- t_w = water temperature, $^\circ\text{C}$
- V = volume of tower, m^3
- W = humidity ratio of moist air, kg_w/kg_a
- $W_{s,w}$ = humidity ratio of saturated moist air evaluated at t_w , kg_w/kg_a
- ϵ = effectiveness

Subscripts

- a = moist air
- db = dry-bulb
- em = empirical
- g,w = vapor at water temperature
- i = inlet
- int = air-water interface
- max = maximum
- o = outlet
- s,w = saturated moist air at water temperature
- w = water
- w,i = water inlet
- w,o = water outlet
- wb,i = wet-bulb inlet
- wb,o = wet-bulb outlet

Superscripts

- cal = calculated
- exp = experimental

References

- [1] ASHRAE, 1983, *ASHRAE Equipment Guide*, chap. 3, American Society of Heating, Refrigerating, and Air-Conditioning Engineers, Inc., Atlanta, GA.
- [2] ASHRAE, 1989, *ASHRAE Handbook of Fundamentals*, American Society of Heating, Refrigerating, and Air-Conditioning Engineers, Inc., Atlanta, GA.
- [3] Walker, W. H., Lewis, W. K., McAdams, W. H., and Gilliland, E. R., 1923,

- Principles of Chemical Engineering*, 3rd ed., McGraw-Hill Inc., New York.
- [4] Merkel, F., 1925, "Verdunstungshuhlung," *Zeitschrift des Vereines Deutscher Ingenieure (V.D.I.)*, **70**, pp. 123–128.
- [5] Webb, R. L., 1984, "A Unified Theoretical Treatment for Thermal Analysis of Cooling Towers, Evaporative Condensers, and Fluid Coolers," *ASHRAE Trans.*, **90**, No. 2, pp. 398–415.
- [6] Webb, R. L., and Villacres, A., 1984, "Algorithms for Performance Simulation of Cooling Towers, Evaporative Condensers, and Fluid Coolers," *ASHRAE Trans.*, **90**, No. 2, pp. 416–458.
- [7] Jaber, H., and Webb, R. L., 1989, "Design of Cooling Towers by the Effectiveness-NTU Method," *ASME J. Heat Transfer*, **111**, No. 4, pp. 837–843.
- [8] Braun, J. E., Klein, S. A., and Mitchell, J. W., 1989, "Effectiveness Models for Cooling Towers and Cooling Coils," *ASHRAE Trans.*, **95**, No. 2, pp. 164–174.
- [9] El-Dessouky, H. T. A., Al-Haddad, A., and Al-Juwayhel, F., 1997, "A Modified Analysis of Counter flow Cooling Towers," *ASME J. Heat Transfer*, **119**, No. 3, pp. 617–626.
- [10] Hyland, R. W., and Wexler, A., 1983, "Formulations for the Thermodynamic Properties of the Saturated Phases of H₂O from 173.15 to 473.15 K," *ASHRAE Trans.*, **89**, No. 2, pp. 500–519.
- [11] Hyland, R. W., and Wexler, A., 1983, "Formulations for the Thermodynamic Properties of Dry Air from 173.15 to 473.15 K, and of Saturated Moist Air from 173.15 to 372.15 K, at Pressure to 5 MPa," *ASHRAE Trans.*, **89**, No. 2, pp. 520–535.
- [12] Myers, R. J., 1967, "The Effect of Dehumidification on the Air Side Heat Transfer Coefficient for a Finned-Tube Coil," M.Sc. thesis, University of Minnesota, Minneapolis, MN.
- [13] Threlkeld, J. L., 1972, *Thermal Environmental Engineering*, 2nd ed. Prentice-Hall Inc., New Jersey.
- [14] Kuehn, T. H., Ramsey, J. W., and Threlkeld, J. L. 1998, *Thermal Environmental Engineering*, 3rd ed. Prentice-Hall Inc., New Jersey.
- [15] Simpson, W. M., and Sherwood, T. K., 1946, "Performance of Small Mechanical Draft Cooling Towers," *Refrigerating Engineering*, **52**(6), pp. 525–543 and 574–576.
- [16] Baker, D. R., and Shryock, H. A., 1961, "A Comprehensive Approach to the Analysis of Cooling Tower Performance," *Trans. ASME*, **83**, pp. 339–349.

Heat Transfer Enhancement to the Drag-Reducing Flow of Surfactant Solution in Two-Dimensional Channel With Mesh-Screen Inserts at the Inlet

Peiwen Li

Industrial Technology Researcher
Mechanical Engineering Laboratory AIST, MITI,
Japan
The Energy Conservation Center, Japan

Yasuo Kawaguchi

Senior Researcher
Mechanical Engineering Laboratory AIST, MITI,
Japan
Namiki 1-2, Tsukuba, Ibaraki, Japan
e-mail: m4050@mel.go.jp

Hisashi Daisaka

Graduate Student
Keio University, Japan

Akira Yabe

Director of Research Planning Office
Mechanical Engineering Laboratory AIST, MITI,
Japan

Koichi Hishida

Professor
Keio University, Japan

Masanobu Maeda

Professor
Keio University, Japan

The heat transfer enhancement of drag-reducing flow of high Reynolds number in a two-dimensional channel by utilizing the characteristic of fluid was studied. As the networks of rod-like micelles in surfactant solution are responsible for suppressing the turbulence in drag-reducing flow, destruction of the structure of networks was considered to eliminate the drag reduction and prevent heat transfer deterioration. By inserting wire mesh in the channel against the flow, the drag-reducing function of the micellar structure in surfactant aqueous solution was successfully switched off. With the Reynolds number close to the first critical Reynolds number, the heat transfer coefficient in the region downstream of the mesh can be improved significantly, reaching the same level as that of water. The region with turbulent heat transfer downstream of the mesh becomes smaller as the concentration of surfactant in the solution increases. Three types of mesh of different wire diameter and opening space were evaluated for their effect in promoting heat transfer and the corresponding pressure loss due to blockage of the mesh. The turbulent intensities were measured downstream from the mesh by using a Laser Doppler Velocimetry (LDV) system. The results indicated that the success of heat transfer enhancement is due to the strong turbulence promoted by the mesh which destroys the network of rod-like micelles by applying high shear stress and thus relaxing the shear induced state (SIS). [DOI: 10.1115/1.1370518]

Keywords: Channel Flow, Enhancement, Fluids, Heat Transfer, Non-Newtonian

1 Introduction

Toms [1] and Mysels [2] independently identified that adding small amounts of polymers or surfactants can result in a significant reduction of the friction drag of turbulent flow. Due to such reduction of frictional drag of turbulent flow, the pumping power consumed for transporting fluid can be reduced significantly. The behavior of friction factor for various aqueous solutions of polymers and surfactants has been investigated extensively in the last fifty years [3–7]. Among various applications, the addition of drag-reducing additives to the circulating water of district heating and cooling (DHC) systems is a promising one. This is because the solution is enclosed in the circulation system and there is no loss of the additives, thus protecting the environment from contamination by the additives. In such cases, polymers are less useful due to serious and irrecoverable degradation of the drag reduction effect caused by mechanical stress at the circulation pump. Surfactants however, are less affected by mechanical forces to their drag reducing ability and have been widely accepted as drag-reducing additives in DHC systems [8–10].

Because of the suppression of turbulence in the drag-reducing flow, the heat transfer is also reduced significantly and even more seriously than that of friction factor, which thus adversely affects the performance of heat exchangers in DHC systems [11,12]. This is unacceptable because the serious reduction of heat transfer may lower the exergy efficiency of the district heating and cooling system even if there is conservation of energy from drag reduction [13]. However, there have not been sufficient studies on the heat

transfer enhancement mechanism of surfactant solution, and there is no generally accepted efficient way to enhance the heat transfer of drag-reducing surfactant solution. Therefore, the present experimental work attempted to find an effective way of enhancing the heat transfer for drag-reducing flow of surfactant solution.

Of the methods described in the literature to enhance the heat transfer of surfactant solution, the conventional way tried by Sato et al. [14] to modify the heat transfer surface works reasonably well, but with a large penalty of pressure loss. In industrial applications, minimal modification of the existing heat exchangers is important from economic considerations if surfactant additives are to be used in DHC systems. In this study, devices were set in front of the heat transfer section against the flow to destroy the micellar structures and so eliminate their drag-reducing effect and enhance heat transfer, since micellar structures in surfactant solution are responsible for the suppression of turbulence [15,16]. We selected a mesh as the device because of its simple geometry and low cost. In the work of Gasljevic and Matthys [17], a plug of laminated mesh was expected to flatten the velocity profiles in a pipe flow to achieve a higher heat transfer coefficient. Because of enormous pressure loss and limited heat transfer enhancement, they concluded that intensive local energy dissipation might not be a viable means of heat transfer augmentation in heat exchangers. However, the turbulence characteristic downstream of the plug was not discussed in their work. In view of the mechanism of turbulence suppression in drag-reducing flow, the production of turbulence should be an important issue in the study of heat transfer enhancement. Therefore, it is worth studying how the mesh size, surfactant concentration and Reynolds number affect the heat transfer enhancing effect as this has not been sufficiently investigated elsewhere. It is also important to know the turbulence quan-

Contributed by the Heat Transfer Division for publication in the JOURNAL OF HEAT TRANSFER. Manuscript received by the Heat Transfer Division October 26, 1999; revision received November 20, 2000. Associate Editor: S. S. Sadhal.

ties in the downstream region of the mesh plug to understand the mechanism of promoting turbulence in drag-reducing flow of surfactant solution.

It has been revealed that the observed low value of friction of drag-reducing flow is due to the suppression of turbulence and reduction of Reynolds' shear stress [5] in the flow by adding surfactant. Therefore, it is crucial to restore turbulence in the flow to enhance the heat transfer of drag-reducing flow. It has been often stated in the literature and is generally accepted that the rod-like (or worm-like) micelles' networks make the surfactant solution a viscoelastic fluid and cause the turbulence in the flow to be suppressed at high Reynolds number [18]. The rod-like micelles were reported [19–22] to exist at conditions above a critical micelle concentration (CMC) in surfactant solutions and to aggregate as networks or super structures under the shear induced state (SIS) [15,23]. Conversely, relaxation of the shear induced state (SIS) and destruction of the rod-like micelles' networks may be an efficient way to promote turbulence in the drag-reducing flow at high Reynolds number. The degradation of drag reduction at very high Reynolds number beyond a critical Reynolds number is a good example, in which the large wall shear stress over the critical wall shear stress is crucial, which is the threshold at which the shear induced state starts to relax. Nevertheless, because the surfactant micellar solution has a non-Newtonian feature, the special mechanism of suppressing turbulence by using surfactant additives in high Reynolds number flow should be considered when studying how to enhance the heat transfer of the drag-reducing flow.

When surfactant solution flows against the wire mesh, the fluid element passing through the opening may experience a short path with high shear stress, which can result in the destruction of the rod-like micelles' networks. Then, as the fluid temporarily becomes a Newtonian fluid, high Reynolds number flow naturally becomes turbulent flow and we can expect high heat transfer comparable to that of water without drag reducers. Three types of fine wire mesh were used in the present experimental investigation to destroy the micellar structure. The mesh plug is expected to promote turbulence downstream within a sufficiently long region, and therefore the heat transfer surface of existing heat exchangers need not be modified. In other words, one may treat the flow downstream of the mesh as normal turbulent flow within a certain region.

As the factors affecting the formation and destruction of the rod-like micelles' networks, the effects of surfactant concentration, mesh dimensions, the Reynolds number or velocity of the flow, the critical Reynolds number or critical wall shear stress, etc. on heat transfer are investigated. The turbulence quantities downstream of the mesh plug were also measured to provide important information about the variation of turbulent structures in order to clarify the heat transfer enhancing mechanism of drag-reducing surfactant solution of high Reynolds number. Even if the rod-like micelles may temporarily be broken up by mesh insertions, they still tend to aggregate as networks under SIS downstream of the mesh. This process may have a significant effect on the turbulence variation downstream of the mesh, therefore, measurement of turbulence quantities in the region downstream of the mesh is of significance for studying the formation of networks of the rod-like micelles.

Using three types of mesh, we set out to select the optimum one with the greatest heat transfer enhancement at minimum pressure loss caused by the mesh plug. Therefore, the pressure loss caused by the mesh plug was also investigated in the study.

Note that the critical Reynolds number for drag-reducing flow is an onset value such that when the flow Reynolds number exceeds it, the drag-reducing ability starts to degrade gradually till it completely disappears at a larger Reynolds number. A flow with Reynolds number not larger than the critical Reynolds number is called drag-reducing flow (DR flow). The Reynolds numbers investigated in this study are limited to those within the drag-

reducing region because we are interested in transportation of fluid under the condition of drag reduction and elimination of this condition in heat exchangers.

2 Experimental Apparatus and Procedure

A schematic view of the circulation system used in the present study is shown in Fig. 1. A tank with a volume of 2 m^3 served as the reservoir for the surfactant aqueous solution. Because the temperature of the surfactant solution influences the critical Reynolds number sensitively [24], a thermostat was installed to control the temperature of the solution in the tank through heating by an electric heater and cooling by tap water in a coil. To ensure uniformity of temperature in the tank, an agitator with rotating impeller was installed. The temperature fluctuation of surfactant solution in the tank was thus controlled to within 0.1°C around the set value.

The two-dimensional water channel was 6 meters in length, which was connected properly by three sections of 2 meters each. The flow cross-section was 500 mm in spanwise width and 40 mm in height (H). One section served as a heat transfer section. The channel walls were of 20 mm thickness and made of transparent acrylic resin except the heating surface, to allow the Laser Doppler Velocimetry (LDV) system to be used to measure the two-dimensional velocity components. A settling chamber equipped with a distributor and a quarter-circular contraction nozzle was used to provide a uniform velocity profile. A honeycomb rectifier of 150 mm length was installed at the entrance to remove large eddies. A collection chamber with a diffuser connected to the outlet of the channel was installed to avoid flow instability caused by flow separation at the channel outlet. The flow from the collection chamber flowed through an electro-magnetic flow meter and returned to the reservoir through plastic pipes. The resolution of the flow meter was $0.01 \text{ m}^3/\text{min}$. Pressure taps were set on the mid-line of the bottom wall.

The heating surface was 1.6 meters in length located 4.3 meters downstream from the entrance of the channel. A stainless steel film heater was attached to the inner side of the bottom wall. The electric current and voltage through the film heater were measured to calculate the uniform wall heat flux. Under the film heater, thermocouples were set on the mid-line of the channel span to measure the streamwise distribution of local temperature of the heating wall. Because the film thickness was $20 \mu\text{m}$, the temperature difference on the film's thickness was ignored. All the experiments were done at a room conditioning temperature of 30°C ,

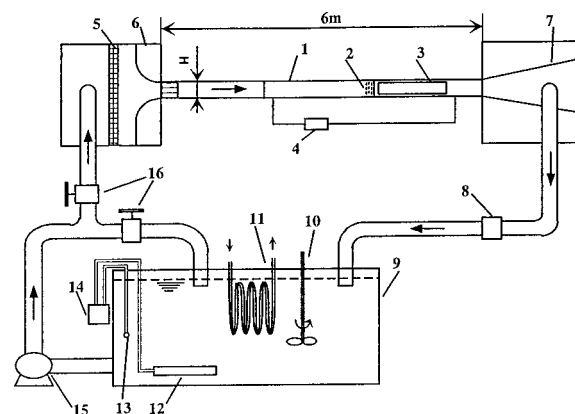


Fig. 1 Schematic of experiment facility (Notations: 1-2Dchannel; 2-mesh plug; 3-Optical window for LDV laser shoot; 4-Pressure transducer; 5-Filter; 6-Contractor; 7-Deffuser; 8-Flow meter; 9-Tank; 10-Agitator; 11-Cooling coil; 12-Heater; 13-Thermometer; 14-Thermostat; 15-Pump; 16-Valve)

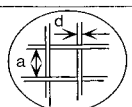
Table 1 The dimensions of wire mesh

Mesh type	Mesh code	opening width (mm)	Wire diameter (mm)	Opening rate (%)
A	16	1.3	0.2	76
B	50	0.33	0.2	35
C	150	0.098	0.07	33

Note:

$$R = \left(\frac{a}{a+d} \right)^2 \times 100$$

R: opening rate
a: opening width
d: diameter of wire



which was close to the inlet temperature of the test section. The maximum heat loss from channel wall to outside was estimated to be less than 0.5 percent.

The three types of wire mesh were commercially available, made of stainless steel and had dimensions as listed in Table 1. As schematically shown in Fig. 2, the mesh sheet was attached to a wire frame and arranged with its cells against the main flow. In case of including several sheets of mesh in one plug, the clearance between two sheets was 5 mm. The coordinate shown in Fig. 2 is adopted in the later discussions.

An LDV measurement system was installed on a mobile platform, which could be positioned streamwise arbitrarily to measure the two-dimensional velocity at different stations downstream from the mesh plug. The LDV system consisted of an argon-ion laser, standard DANTEC 55X optics system working in a two-color three-beam mode, front scattering system with two photomultipliers, and two counter-processors. The probe volume had a length of 1.3 mm and a beam waist diameter of 0.08 mm. A very small amount of polyethylene beads, 0.05 ppm with diameter of 5 μm and density of 950 kg/m³, was used as scattering particles for the laser. Typically, 8000 data were acquired at one spatial point in the measurement of velocity.

The pressure drop was measured with a high precision pressure transducer at a resolution of 0.1 Pa. With the measured pressure drop over a certain streamwise distance, *L*, the wall shear stress and Fanning friction factor are given by

$$\tau_w = \frac{\Delta PH}{2L} \quad (1)$$

$$f = \frac{\tau_w}{(1/2)\rho U_b^2} \quad (2)$$

One thermo-couple was set in the settling chamber to measure the inlet mean temperature of the flow. A data acquisition unit, IM DA 100-01E (Yokogawa Electric Co.), was connected to a personal computer that automatically converted the thermo-couple's output voltage into temperature. Temperatures were monitored to ensure that data in the steady state was being acquired. All the temperature readings were obtained and averaged over several minutes. The outlet fluid temperature was estimated from the heat balance between the electric power and temperature increment of the flow. The local heat transfer coefficient is defined as follows:

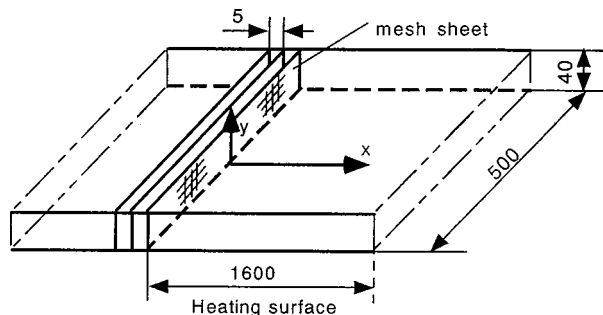


Fig. 2 Two-dimensional channel and mesh plug (unit:mm)

$$h = \frac{q_w}{(T_w - T_f)} \quad (3)$$

When the channel was asymmetrically heated, the Nusselt number may be slightly lower than that of the symmetrically heated channel. The effect of asymmetric heating decreases with an increasing Prandtl number. For water of asymmetric heating, Nusselt number was reported to be 10 percent lower than the symmetric heating case in the literature [25–27].

The properties of the surfactant solution are based on the mean temperature of the flow. It is a common practice to use the thermo-physical properties of solvent (here it is water) in data reduction for surfactant solutions. In the most application-oriented studies [11,17,28] such a treatment is convenient for comparing the friction and heat transfer results under the same situations of flow and heat flux between the solvent and the surfactant solution. On the other hand, the surfactant solution has viscoelastic characteristics and much remains to be done to clarify its rheological properties [20]. The surfactant solutions may show higher viscosity and large errors may arise if this is not taken into account in the pure theoretical analysis. The height of the channel, *H*, was adopted as the characteristic length for Reynolds number and Nusselt number.

The surfactant tested in our experiment was cetyltrimethyl ammonium chloride (CTAC), which belongs to the cationic group of surfactants and is less affected by calcium or sodium ions naturally existing in tap water. Its effective temperature in drag reduction ranges from 10°C to 45°C. Although we did not obtain data of the critical micelles concentration (CMC) of CTAC, the significant drag reduction shown at 25 ppm and 30°C in our experiments described later is the evidence that the CMC of CTAC at around 30°C is at least lower than 25 ppm. This is because the presence of rod-like micelles can cause a drag-reducing effect. The chemical formula of CTAC is C₁₆H₃₃N(CH₃)₃Cl with molecular weight of 320.00 g/mole. Local tap water was used as solvent in the test. The same weight concentration of sodium salicylate (NaSal; HOC₆H₄COONa, 160.10 g/mole) was added to the solution to provide organic ions. The organic counter-ions from the sodium salicylate greatly affect the CMC of that particular surfactant system material [20,21]. For simplicity, the composition of solution was indicated only by the surfactant concentration in this work, but the same mass concentration of NaSal was always included in the solution.

Uncertainties of the calculated results were estimated by using the root-sum-square method of Kline and McClintock [29]. By calibration of measuring instruments, the uncertainties of measured values for temperature, pressure drop, flow rate of water of surfactant solution, the voltage and resistance of the electric film heater were determined to be ±0.1°C, ±1.0 Pa, ±7.5 × 10⁻³ m³/min, ±1.4003 V, and ±0.01 Ω, respectively. The distance of the pressure taps, the length of the heating plate, channel height, and spanwise width have uncertainties of ±0.7 mm, ±0.7 mm, ±0.1 mm, and ±0.14 mm, respectively. The standard DANTEC LDV system was well calibrated and the uncertainties for mean velocities and velocity fluctuations were estimated to be ±0.2 percent and ±1.0 percent, respectively. We also checked the results of many measurements at one point with running conditions unchanged: the values of mean velocity, root mean square of velocity fluctuations and Reynolds stress all showed very reliable repeatability with deviations from average value of no larger than ±0.2 percent, ±1.0 percent, and ±1.4 percent, respectively. Then, the uncertainty analysis of the reduced results was conducted.

For convenience, the uncertainties of the experimental results that were calculated from measured values were expressed as percentages compared to the values of the results. The pressure drop measured for the mesh plug has uncertainty of less than ±0.5 percent. The bulk velocity and Reynolds number both have uncertainties of ±1.5 percent. Because of the small value of pressure drop of drag-reducing flow, the wall shear stress, τ_w , and fric-

tional factor, f , have uncertainties of ± 3.5 and ± 4.7 percent, respectively. All the above uncertainties of velocity, Reynolds number, wall shear stress and frictional factor are calculated under the Reynolds numbers of 2.0×10^4 . In most cases in the experiments, the Reynolds numbers were larger than 2.0×10^4 and therefore the above uncertainties will be smaller, however, at the minimum Reynolds number of 1.0×10^4 they may be as large as ± 3.0 percent, ± 3.0 percent, ± 8.1 percent, and ± 10.0 percent, respectively. The uncertainties of heat transfer coefficients are affected significantly by uncertainties of temperature and the heat flux. With the heat loss taken into consideration, the uncertainties of heat transfer coefficients are estimated to be less than ± 6 percent for drag-reducing flow. Because of small temperature differences between heating wall and bulk flow, the uncertainties of heat transfer coefficients for water can be ± 10.0 percent although we used larger heat flux than that for surfactant solution. When the heat transfer was effectively enhanced in drag-reducing flow, the local heat transfer coefficients close to that of water had uncertainties as high as ± 13.0 percent. The uncertainties of Nusselt numbers are essentially almost equal to the uncertainties of heat transfer coefficients. The surfactant concentrations have uncertainties of less than ± 0.5 percent.

3 Results and Discussion

3.1 Friction Behavior Without Plug. As a preliminary work, tests on the friction factors of the flow of solutions at different surfactant concentration were conducted at a constant bulk temperature of 30°C in a smooth channel to obtain fundamental data. The friction factors are shown in Fig. 3. For comparison, the friction factors given by Dean's equation [30] for two-dimensional turbulent flow of water with Reynolds number ranging from 6.0×10^3 to 6.0×10^5 are plotted in the figure by the solid line. Dean's equation is as follows:

$$f = 0.073 \text{Re}^{-0.25} \quad (\text{Dean's equation [30]}). \quad (4)$$

The dashed line in Fig. 3 shows the minimum friction factor for drag-reducing flow given by Virk's equation [31] indicating the maximum drag reduction asymptote as follows:

$$1/\sqrt{f} = 19 \log(\text{Re} \sqrt{f}) - 32.4 \quad (\text{Virk's equation [31]}). \quad (5)$$

With increasing surfactant concentration, the maximum drag reduction is shifted to higher Reynolds number. This indicates that corresponding to the large concentration, there is a large critical Reynolds number. It was pointed out by Ohlendorf et al. [20] that the length of rod-like micelles increases with increasing surfactant concentration. The critical Reynolds number is actually a threshold at which the network of rod-like micelles starts to disintegrate. In drag-reducing flow, rod-like micelles in the network align in the flow direction, therefore, the disassociation of the network of

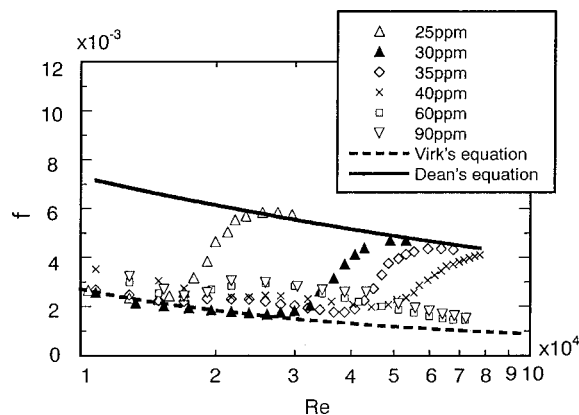


Fig. 3 Friction factors versus Reynolds number in smooth channel ($T_b=30^\circ\text{C}$)

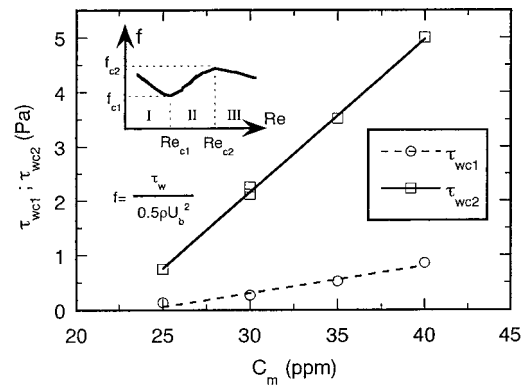


Fig. 4 Critical wall shear stress versus concentration of surfactant in smooth channel ($T_b=30^\circ\text{C}$) (region I ($\text{Re} < \text{Re}_{c1}$)—DR flow; region II ($\text{Re}_{c1} < \text{Re} < \text{Re}_{c2}$)—post DR flow; region III ($\text{Re} > \text{Re}_{c2}$)—turbulent flow)

rod-like micelles in the solutions with high concentration must occur at a high threshold of Reynolds number or, more correctly, wall shear stress.

Related to the critical Reynolds number is the critical wall shear stress. It was proved that the unique threshold for the disintegration of the aggregation of rod-like micelles as a network is wall shear stress, as evidenced by the dependency of the critical Reynolds number on the hydraulic diameter of flow duct reported by Ohlendorf et al. [20], Gasljevic and Matthys [32], Usui et al. [33], and our previous work [34]. The critical wall shear stress is shown in Fig. 4 for surfactant solution at several concentrations and temperature of 30°C .

In order to judge the wall shear stress necessary to turn drag-reducing flow to completely turbulent flow for surfactant solution of different concentrations, it is necessary to define another critical wall shear stress at which the friction factor of surfactant solution reaches that of water. For distinction as shown in Fig. 4, we name this critical wall shear stress as the "second critical wall shear stress," and the wall shear stress at which the drag-reducing flow starts to degrade as the "first critical wall shear stress." The second critical wall shear stress and the corresponding critical Reynolds number represents the point at which the flow completely loses its drag-reduction ability and becomes turbulent flow. Hereafter, we call the flow at Reynolds number smaller than the first critical Reynolds number as drag-reducing flow shown in Fig. 4 as region I, and that larger than the second critical Reynolds number as turbulent flow (region III). The flow at Reynolds number between the first critical Reynolds number and the second critical Reynolds number will be called post-drag-reducing flow (region II).

Both of the two critical wall shear stresses increase with the increment of surfactant concentration. However, the second critical wall shear stress increases at a larger gradient. Thus, the difference between the second critical wall shear stress and the first critical wall shear stress increases with the increment of surfactant concentration. It can be deduced that promoting turbulence in the flow with higher concentration of surfactant will be more difficult because both of its two critical shear stresses are higher than that of the solution with lower concentration of surfactant.

3.2 Heat Transfer

Channel Without Plug. In order to provide a basis for comparison of heat transfer coefficient in the later discussions of the heat transfer enhancement effect of the mesh, tests of heat transfer in a smooth channel were conducted. Figure 5 shows the results of mean Nusselt number versus Reynolds number for water and surfactant solutions with inlet temperature of 30°C in the channel without mesh. The heat transfer data from water flow agrees very

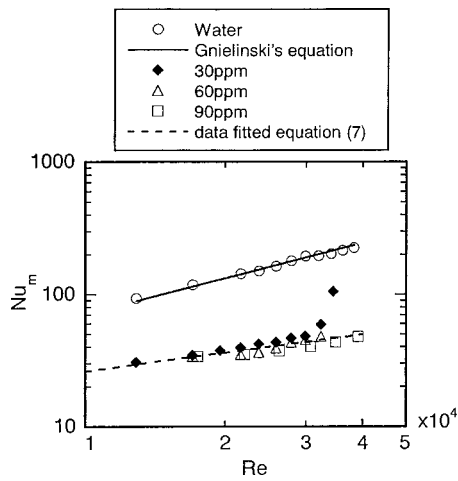


Fig. 5 Mean Nusselt number versus Reynolds number in smooth channel ($T_{in}=30^{\circ}\text{C}$)

well with the Gnielinski' equation [35], which is suitable for the heat transfer in the hydraulic fully developed and thermally developing region and the hydraulic diameter was used as the characteristic length for Nusselt number and Reynolds number in the equation.

$$\text{Nu}_{mD} = 0.012(\text{Re}_D^{0.87} - 280)\text{Pr}^{0.4} [1 + (D/L)^{2/3}] \quad (6)$$

(Gnielinski's equation [35]).

The heat transfer coefficients of drag-reducing surfactant solution are rather low compared to that of water flow at the same Reynolds numbers. Also, the Nusselt number of drag-reducing flow shows relatively weak increment with increasing Reynolds number, which reflects the suppression of turbulence and thus the nature of the flow is between laminar flow and turbulent flow [5]. Because of the same level of turbulence suppression under the three concentrations, i.e., 30 ppm, 60 ppm, and 90 ppm, their heat transfer reduction and Nusselt number are almost the same if the Reynolds numbers do not exceed their corresponding first critical Reynolds number. Due to the difference of the critical Reynolds number, the Nusselt number for case of 30 ppm shows a significant increase when the Reynolds number is above 3.0×10^4 , while the cases of 60 ppm and 90 ppm still keep a low Nusselt number. Putting those heat transfer data in the drag-reducing region together for concentrations from 30 ppm to 90 ppm, we obtained a correlation (see Eq. (7)) similar to that of Gnielinski's equation [35] for predicting the Nusselt number for the present results. 95 percent of the experimental values have deviations of less than 10 percent from the empirical equation proposed in this study for the tested solutions. The Reynolds number in Eq. (7) ranges from 1.5×10^4 to 4.0×10^4 . However, when Eq. (7) is used for solutions of surfactant concentration ranging from 30 ppm to 90 ppm, the Reynolds number must be limited to not larger than the first critical Reynolds number of the solutions respective to its concentration of surfactant. L in Eq. (7) is the length of the two-dimensional heating surface.

$$\text{Nu}_m = 0.28(\text{Re}^{0.42} - 6)\text{Pr}^{0.4} [1 + (D/L)^{2/3}] \quad (7)$$

The local Nusselt numbers for the solutions at three different concentrations are shown in Fig. 6. There is a minor increment of local Nusselt number for the 30 ppm case in comparison with other concentrations at the entrance region. Because the Reynolds number in Fig. 6 belongs to the drag-reducing region for any of the three concentrations, most of the local heat transfer coefficients show no significant difference from one another.

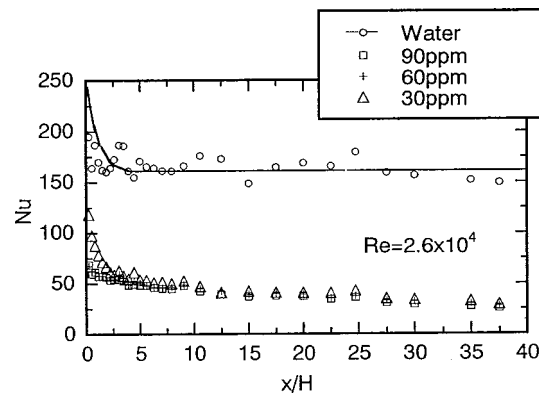


Fig. 6 Local Nusselt number of water and surfactant solution in smooth channel ($T_{in}=30^{\circ}\text{C}$)

Channel With Micellar Structure Destruction Device—Mesh Plug.

Three types of mesh plug were used in the experiment to destroy the micellar structure in order to promote turbulence in the channel. Their effects in promoting heat transfer will be discussed hereafter. Because the turbulent water flow already contains strong turbulence, the mesh plug has a minor enhancing effect on the heat transfer of water flow in the channel only at a very short distance from the entrance, as shown in Fig. 7. However, for surfactant solution at the concentration of 30 ppm and certain Reynolds number, there is a significant improvement of the heat transfer as seen in Fig. 8. Downstream of the mesh plug, the local heat transfer coefficient reaches almost the same value as that of water. When considering this different heat transfer enhancing effect to water and surfactant solution by the mesh, it is necessary to discuss the mechanism of heat transfer enhancement by mesh insertion for water and surfactant solution. The rod-like micelle has a diameter in the order of several nanometers, and its length may be several tens of times the diameter, which increases with increasing concentration [20]. In the work of Lu et al. [18], entangled rod-like micelles, or thread-like as they called it, were observed in the quiescent state and the shear thickening was visualized by Hu et al. [15] as evidence of the shear-induced structures of micelles in surfactant solution, which is often called network structures of rod-like micelles. The large suppression of turbulence in a turbulent flow at high Reynolds number is generally believed due to the suppression of small-scale turbulence eddies by the network structures of rod-like micelles. In the bursting and growth of these eddies, extensional motions dominate [15,16,18]. The result that heat transfer was enhanced downstream of the mesh strongly suggested that turbulence was recovered in

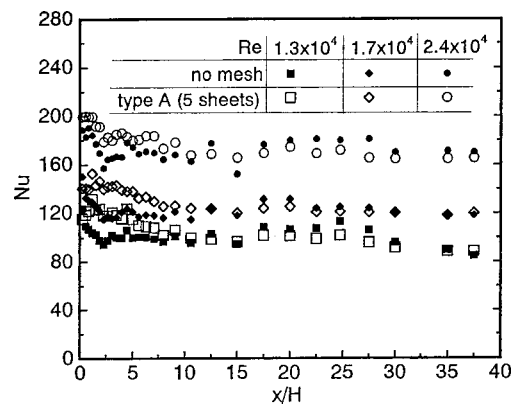


Fig. 7 Local Nusselt number of water flow downstream of mesh ($T_{in}=30^{\circ}\text{C}$)

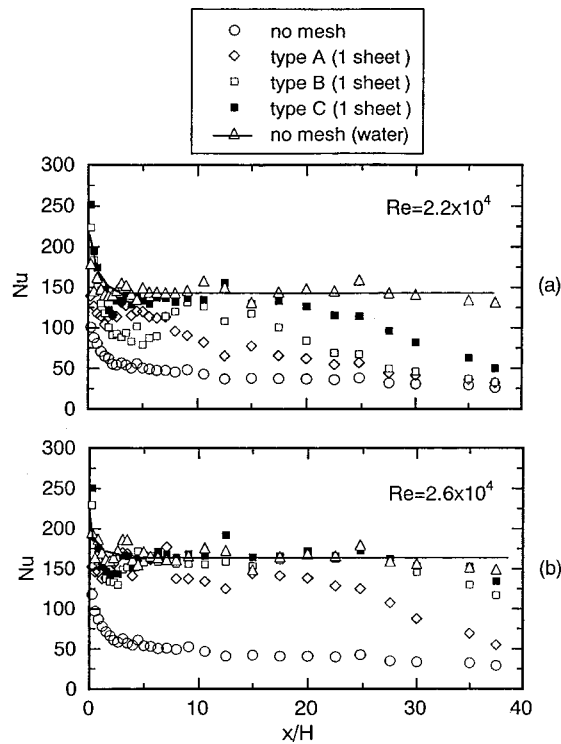


Fig. 8 Enhanced local Nusselt number by different types of mesh ($T_{in}=30^{\circ}\text{C}$; $C_m=30\text{ ppm}$)

this region; the results of turbulence measurements will be discussed later in this work. One may also deduce that the recovery of turbulence is due to the destruction of the micellar structure of the rod-like micelles. Mesh enforces high shear stress and has both possibilities to generate turbulence and destroy the network structures of micelles, but the later is more important for flow of surfactant solution in this case. It is a high shear stress rather than high shear rate which destroys the shear alignment of the micelles, i.e., destroys the network structure of the micelles [15,16].

Due to the strong tendency of the rod-like micelles to aggregate to form a network once the high shear stress is relieved, the flow far from the mesh plug tends to recover as drag-reducing flow because the high shear stress does not last for a long distance and thus there is a decrease of the heat transfer coefficient far downstream. Because the three types of mesh have different wire diameter and opening rate as listed in Table 1, they exert different magnitudes of destruction on the rod-like micelles' network. Thus the heat transfer recovery from the stage of turbulent to drag-reducing flow covers a different length of region. The plug of the A-type mesh has the minimum length of recovery region, while the C-type mesh has the maximum. At a larger Reynolds number, the heat transfer augmented region is enlarged and also demonstrates less difference among the three types of mesh in promoting turbulence in drag-reducing flow. The mesh sheets are supported by a mesh holder made of 2.0 mm wire. To examine the effects of the holder, heat transfer using the holder without mesh was also tested. Since there was no heat transfer improvement in this test, it is believed that the heat transfer was enhanced by the mesh through modification of the fluid or destruction of the micelles' structure.

Because the A-type mesh has a relatively larger opening rate which impedes the flow less and it effectively enhances heat transfer if the Reynolds number is large enough, plugs using several sheets of A-type mesh were devised. The heat transfer performance of surfactant solution with different number of mesh sheets in the plug is shown in Fig. 9. The different level of heat transfer enhancement reflects the different times of destruction to the mi-

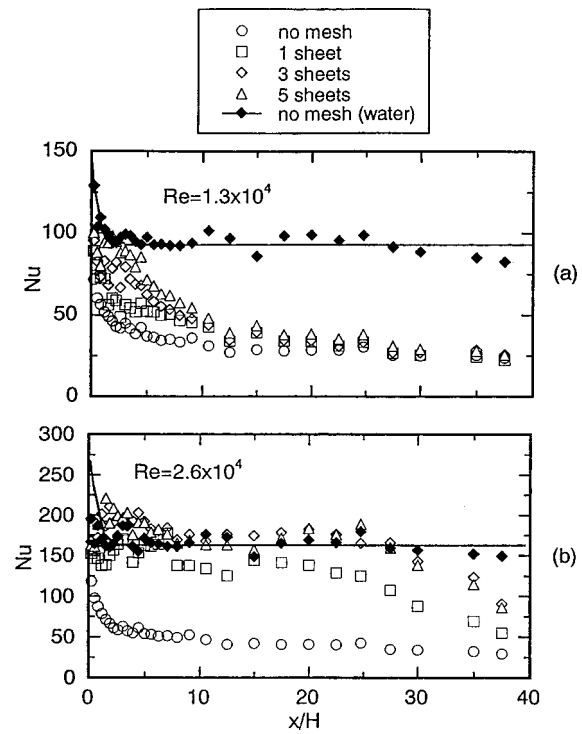


Fig. 9 Enhanced local Nusselt number with number of mesh sheet included in a plug ($T_{in}=30^{\circ}\text{C}$; $C_m=30\text{ ppm}$)

celles' structure by those mesh sheets in the plug. It is clear that the plug with more mesh sheets gives a better heat transfer enhancement. However, the Reynolds number of the surfactant flow is of primary importance; at a small Reynolds number the heat transfer enhancement by the mesh plug is limited even when 5 sheets are included in the plug. At a larger Reynolds number the plugs with 3 or 5 mesh sheets all gave satisfactory heat transfer enhancement.

In order to evaluate the overall performance of the mesh plug in enhancing the heat transfer of surfactant solution, Fig. 10 depicts the mean Nusselt number versus the Reynolds number at a surfactant concentration of 30 ppm. There is a clear trend that when the Reynolds number of the flow is closer to the critical Reynolds number, for instance larger than 2.2×10^4 , every type of mesh plug demonstrates a tremendous effect in enhancing the heat transfer. With Reynolds number between 2.4×10^4 to 3×10^4 , even one sheet of A-type mesh can promote the heat transfer coefficient to three times that of the smooth channel. This suggests that after temporary destruction, the formation of a new network of rod-like micelles is strongly affected by the velocity or Reynolds number of the flow. In other words, the promotion of turbulence by the mesh can only take effect above a certain level of kinetic energy of the flow itself. Therefore, an adequate Reynolds number or velocity has to be considered for improving the heat transfer performance by using a mesh plug in surfactant solution. In the works of Gasljevic and Matthys [17] on the heat transfer of pipe flow, the solution tested had a large concentration of surfactant. It can be deduced that the critical Reynolds number would be very high, but the Reynolds numbers they tested were relatively low and therefore the heat transfer enhancement effect by laminated mesh plug was very limited in their work.

Heat transfer tests for solutions at higher concentrations of surfactant were conducted in this study. Figures 11 and 12 show some of the results at several Reynolds numbers. Because the solution having a high concentration of surfactant have longer rod-like micelles which correspond to high critical Reynolds number or critical wall shear stress, destruction of the structure of the

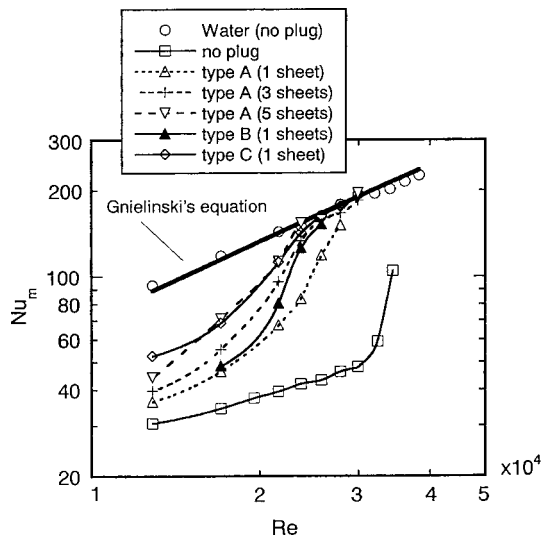


Fig. 10 Mean Nusselt number versus Reynolds number using different types of plug ($T_{in}=30^{\circ}\text{C}$; $C_m=30\text{ ppm}$)

rod-like micelles' network becomes more difficult, or in other words, the formation of the network structure of the rod-like micelles' downstream is much easier in such a case. This can be seen from the significant differences in the effectiveness of heat transfer enhancement by using a plug including 5 sheets of A-type mesh for the solution with surfactant concentration of 40 ppm and 60 ppm. The mesh plug actually has a very limited effect here in enhancing the heat transfer at the Reynolds numbers that other-

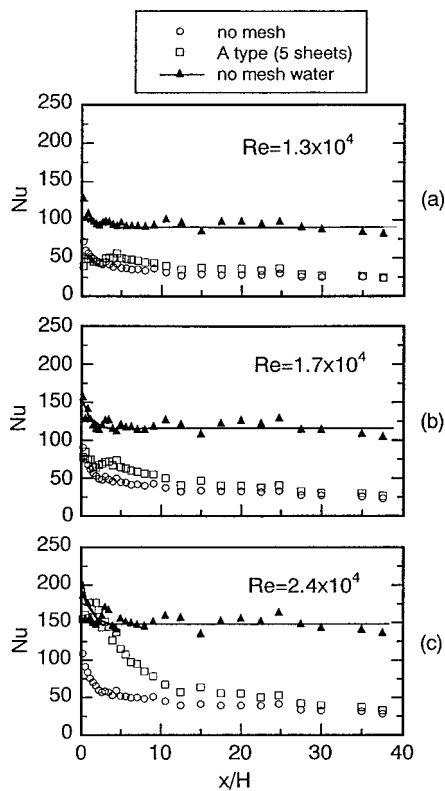


Fig. 11 Enhanced local Nusselt number with 5 sheets of A type mesh included in a plug ($T_{in}=30^{\circ}\text{C}$; $C_m=40\text{ ppm}$)

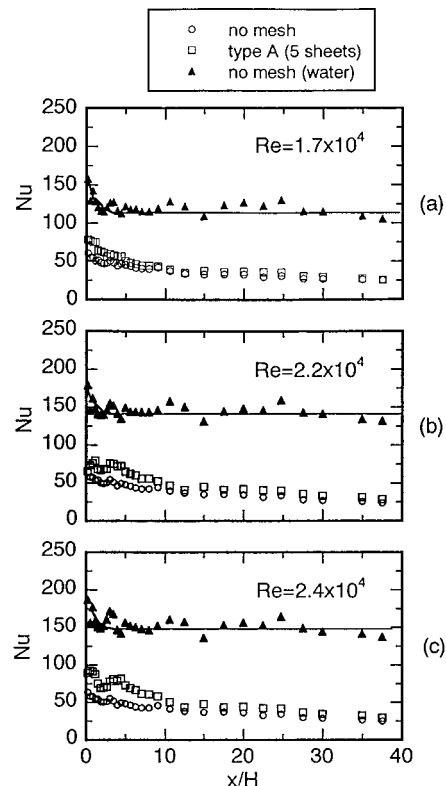


Fig. 12 Enhanced local Nusselt number with 5 sheets of A type mesh included in a plug ($T_{in}=30^{\circ}\text{C}$; $C_m=60\text{ ppm}$)

wise work well for the 30 ppm case. Nevertheless, it is possible to improve the effectiveness of heat transfer enhancement by the mesh plug by increasing the Reynolds number.

Based on the above results, the mechanism of mesh insertion to destroy the structures of rod-like micelles' network is discussed hereafter. The mesh wires apply impact and large shear stress to the flow of surfactant solution, and, thus, destroy the micelles' network. If partial similarity with solid destruction holds, there might be a threshold velocity for effective destruction of the micelles' network. For solution at high concentrations of surfactant, the rod-like micelles are longer, and the same effective destruction as that of low concentrations of surfactant can only be achieved by high flow speed or using more mesh wires. On the one hand, less destruction of the super structures of the rod-like micelles' network, like the case of one sheet of A-type mesh for the solution of 30 ppm surfactant, cannot produce enough turbulence. However, excessive destruction or impact on the super structure of the rod-like micelles' network, like the case of five sheets of A-type mesh in the 30 ppm surfactant solution, may not promote the turbulence proportional to that by one sheet of A-type mesh. This is because once the micellar structure is destroyed and turbulence is promoted, more mesh sheets are not necessary, and like that in water flow the mesh cannot be used to enhance heat transfer.

The turbulence may be promoted by one-time destruction of the rod-like micelles' network by a mesh with fine holes, however, several times of destruction by a mesh with large holes may have the same effect. Taking the mesh wire as an edge in cutting the flowing network of rod-like micelles, the ratio of the mesh's total wire length to flow area (including wire) is 1.33, 3.77, and 11.9 mm^{-1} , respectively for the three types of mesh, A, B, and C. The A-type and B-type meshes have the same wire diameter and three sheets of A-type mesh may have roughly the same edge-to-area ratio as that of one sheet of B-type mesh. This may help to explain the same level of heat transfer enhancement by one sheet of B-type and three sheets of A-type mesh as shown in Fig. 10. A

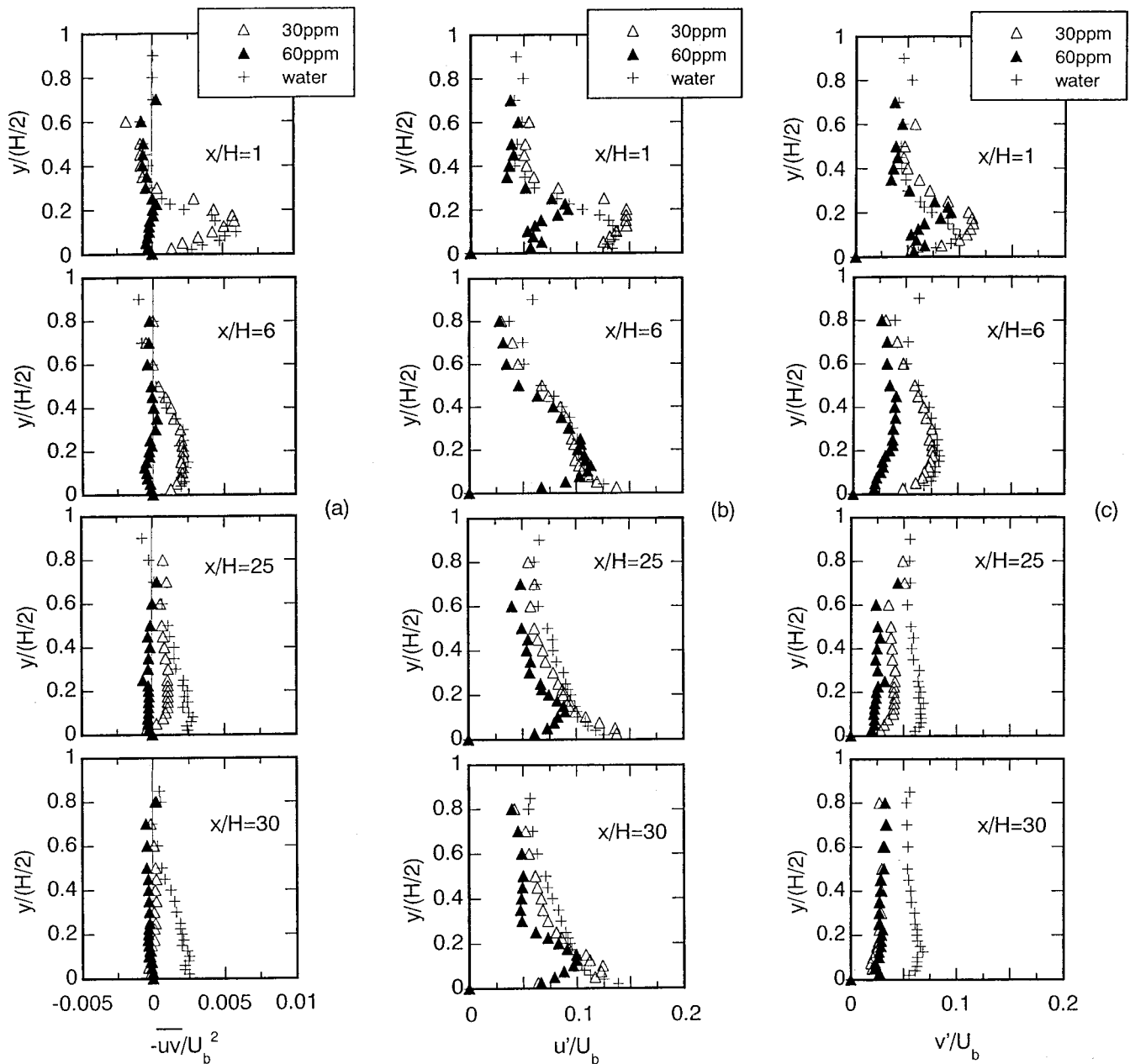


Fig. 13 Turbulent quantities of drag-reducing isothermal flow downstream of plug with 5 sheets of A-type mesh included ($T_b = 30^\circ\text{C}$; $\text{Re} = 2.2 \times 10^4$)

more detailed investigation of the proper mesh dimensions for better destruction of the micelles' networks to promote turbulence is a subject for further study.

3.3 Variation of Turbulence Intensities Downstream from Mesh Plug. The turbulence intensities of the flow downstream of the mesh plug were measured to obtain direct proof that strong turbulence was promoted when the heat transfer coefficient was enhanced. All the measurements of two-dimensional velocity for isothermal flow by LDV were conducted in the channel with a plug of 5 sheets of A-type mesh. Figure 13 shows the variation of three components of turbulence stress downstream from the plug. For comparison, the normalized turbulence properties of water, and the solutions with surfactant concentration of 30 ppm and 60 ppm are plotted together at four streamwise positions. The Reynolds number was 2.2×10^4 .

From the heat transfer results, it is known that the mesh plug cannot enhance the heat transfer of the solution with surfactant concentration of 60 ppm at Reynolds number of 2.2×10^4 . The very low turbulence intensities shown in Fig. 13 for the 60 ppm solution exhibit turbulence suppression and loss of turbulent diffusivity. This observation is the direct reason for the low heat transfer coefficients shown in the previous section. However, the solution at a surfactant concentration of 30 ppm shows almost the same intensity of turbulence as that of water downstream of the mesh. In the 30 ppm case, the shift of turbulence intensity from the stage of water-like to that of the case of the 60 ppm solution demonstrated that the flow recovers from turbulent flow to drag-reducing flow downstream. It is thus believed that the improvement of heat transfer coefficient resulted from the promoted turbulence in the flow. Because the rod-like micelles' networks are responsible for the suppression of turbulence in the surfactant so-

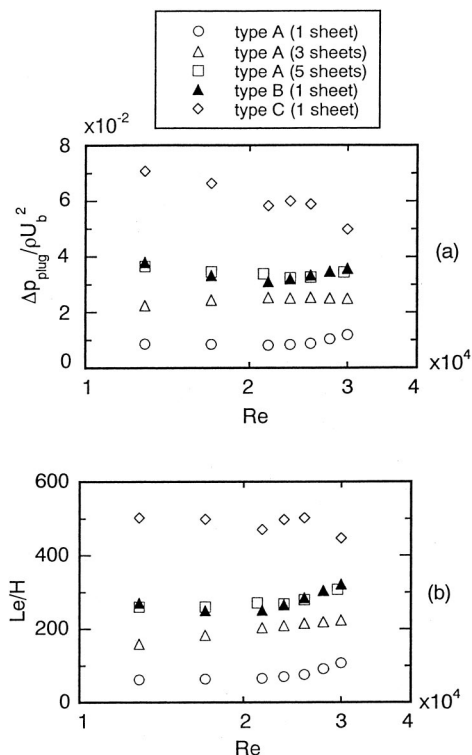


Fig. 14 Equivalent length of pressure loss resulted by mesh plug ($T_{in}=30^\circ\text{C}$; $C_m=30$ ppm)

lution, we deduce that after the destruction of the rod-like micelles' networks there will be no suppression and thus turbulence re-appears. However, if the high shear stress does not remain in the whole flow region, the rod-like micelles' networks can be reorganized under the shear induced state which allows the recovery of the drag reducing effect.

3.4 Pressure Drop by Mesh Plug. As well as the heat transfer enhancement, the mesh plug also results in pressure loss in the flow. It is desired to enhance the heat transfer at a low cost of pressure loss, otherwise the reduction of pressure drop obtained by the drag-reducing effect will be offset. In order to derive the value of pressure drop that resulted only from the plug, the pressure drop of surfactant solution over 4 meters of channel length including the mesh plug was tested, and the same measurement was conducted for a smooth channel without plug. The difference of the two pressure measurements was calculated and used to obtain the pressure drop that resulted from the mesh plug. Figure 14 shows the dimensionless pressure drop that resulted from the mesh plug versus Reynolds number for 30 ppm surfactant solution. It is seen that the A-type single mesh gives the minimum pressure drop. The plug including one sheet of B-type mesh resulted in the same pressure drop as that produced by 5 sheets of A-type mesh.

In order to estimate the pressure loss caused by the plug, an equivalent length (Le) of straight smooth channel with fully developed water flow was calculated for the convenience of estimating the pressure loss when using a mesh plug to enhance heat transfer in heat exchangers. With increasing Reynolds number, turbulence arises that results in the increase of Le as seen in Fig. 14.

3.5 Overall Evaluation of Heat Transfer Enhancement and Pressure Loss by Mesh Plug. To estimate the overall effectiveness of heat transfer enhancement using a mesh plug in surfactant solution, the mean heat transfer coefficient of surfactant solution by using a mesh was normalized by that of water flow as

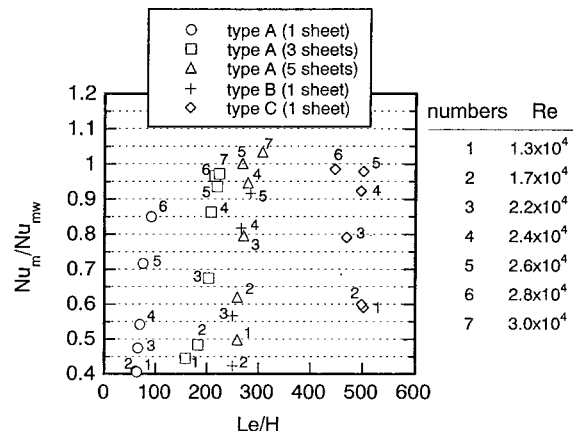


Fig. 15 Heat transfer enhancement versus pressure drop using mesh plug ($T_{in}=30^\circ\text{C}$; $C_m=30$ ppm)

shown in Fig. 15. The numbers attached to symbols in the figure represent different Reynolds number as seen from the legend column. The vertical axis represents the percentage of heat transfer coefficient of surfactant solution to that of water flow. The horizontal axis represents the pressure loss caused by the plug, which is the cost for the heat transfer enhancement.

At low Reynolds numbers the heat transfer enhancement effect is very limited as seen in the figure, but the effect increases with increasing Reynolds number. As an example, in order to improve the mean heat transfer coefficient to 85 percent of that of water flow at Reynolds number of 2.8×10^4 , one sheet of A-type mesh is enough, while to achieve 95 percent three sheets of A-type mesh may be appropriate. Overall, the A-type mesh is recommended in the present study for its good performance of heat transfer enhancement and low level of pressure loss.

Conclusions

The heat transfer and the mechanism of effective heat transfer enhancement for drag-reducing surfactant solution was studied, and the following conclusions were drawn.

1 As the result of preliminary experiments, the second critical Reynolds number or wall shear stress was adopted, which represents the upper limit of transition at which the drag-reducing flow completely changes into turbulent flow. The second critical wall shear stress is proportional to the concentration of surfactant in the solution. The difference between the second critical wall shear stress and the first critical wall shear stress increases with increasing concentration of surfactant in the solution, which indicates that to destroy the network of rod-like micelles for promoting turbulence high shear stress is needed for solutions with high concentration of surfactant. Within the range of concentrations tested, the heat transfer coefficients of drag-reducing flow are rather low and have no significant difference if the Reynolds number is lower than the corresponding critical Reynolds number. A correlation for Nusselt number against Reynolds number was obtained for the present two-dimensional channel, which is suitable for surfactant concentrations from 30 ppm to 90 ppm and Reynolds number lower than their respective critical Reynolds number.

2 The effectiveness of three types of wire mesh forming a plug for promoting turbulence in enhancing heat transfer was studied. In general, the Reynolds number and concentration of surfactant significantly affect the effectiveness of heat transfer enhancement by using the mesh. When the Reynolds number is close to the first critical Reynolds number, the mesh plug can promote the heat transfer coefficient of drag-reducing flow effectively. Therefore,

the mesh that is effective for enhancing heat transfer for a solution of low concentration may not be effective for a solution of high concentration under the same Reynolds number.

3 It is deduced that due to the destruction of the rod-like micelles' networks by the mesh plug there will be no suppression of turbulence in a certain region downstream of the mesh. Through measurement using LDV, the same level of turbulence intensities as that of water flow in surfactant solution was clarified in the case that heat transfer was enhanced significantly. If Reynolds number does not exceed the first critical Reynolds number, the turbulence gradually decreases further downstream of the mesh plug, which demonstrates that the flow recovers from turbulent to drag-reducing flow. The recovery region, however, has different length depending on the Reynolds number and concentration of surfactant.

4 An overall evaluation was conducted on the principle of effective heat transfer enhancement with low cost of pressure loss caused by the mesh plug. The A-type mesh was shown to be preferable. At a Reynolds number close to the critical Reynolds number for a surfactant concentration of 30 ppm, the A-type mesh plug promotes the mean heat transfer coefficient effectively on the present 1.6 meter long heating plate, while the pressure loss caused by the plug is relatively small.

Acknowledgment

The first author is grateful for the support of the industrial technology research program of the New Energy and Industrial Technology Development Organization (NEDO) of Japan.

Nomenclature

C_m	= mass concentration of surfactant and counter-ion material in solutions (ppm)
C_p	= specific heat (kJ/kg K)
D	= hydraulic diameter of the two-dimensional channel (m)
f	= fanning friction factor (with subscription of $c1$ corresponds to the first critical Reynolds number and $c2$ the second critical Reynolds number)
$\tau_w / (0.5\rho U_b^2)$	
h	= heat transfer coefficient (W/m ² K)
H	= channel height (m)
L	= length of heating section; distance between pressure taps (m)
Le	= equivalent length of smooth channel with fully developed water flow over which the pressure loss equals to that resulted by mesh plug, $Le = \Delta p_{\text{plug}} / \Delta p_{w-1m}$ (m)
$Nu; Nu_m; Nu_{mD}; Nu_{mw}$	= local Nusselt number; mean Nusselt number; mean Nusselt number using hydraulic diameter as characteristic length; mean Nusselt number of water without mesh plug
ppm	= part per million
ΔP	= pressure drop (Pa)
ΔP_{plug}	= pressure drop resulted by mesh-plug (Pa)
ΔP_{w-1m}	= pressure drop of fully developed water flow over one meter of smooth channel (Pa)
q_w	= wall heat flux (W/m ²)
Pr	= Prandtl number $\nu\rho C_p/\lambda$
$Re; Re_D$	= Reynolds number $U_b H/\nu; U_b D/\nu$ (with subscription of $c1$ corresponds to the first critical wall shear stress and $c2$ the second critical wall shear stress)
T_b	= temperature of bulk flow (°C)

T_f = mean temperature of flow in heat transfer section (°C)

T_{in} = inlet temperature of flow in heat transfer section (°C)

T_w = wall temperature (°C)

u' = root mean square of turbulent velocity fluctuation in streamwise direction (m/s)

v' = root mean square of turbulent velocity fluctuation in normal direction (m/s)

$-\overline{uv}$ = kinetic Reynolds shear stress (m²/s²)

U_b = bulk velocity (m/s)

x = streamwise distance from starting point of heating plate as shown in Fig. 2 (m)

y = distance in normal direction apart from heating wall as shown in Fig. 2 (m)

Greek Symbols

ρ = density of solvent (Kg/m³)

λ = thermal conductivity of solvent (W/m·K)

ν = kinematic viscosity of solvent (m²/s)

τ_w = wall shear stress (with subscription of $c1$ is the first critical wall shear stress, $c2$ the second critical wall shear stress) (Pa)

References

- [1] Toms, B. A., 1948, "Some Observations on the Flow of Linear Polymer Solutions Through Straight Tubes at Large Reynolds Numbers," *Proceedings of 1st Int. Congr. on Rheology*, 2, pp. 135–141.
- [2] Mysels, K. J., 1949, US Patent 2492173, December 27, 1949.
- [3] Gyr, A., and Bewersdorff, H. W., 1995, *Drag Reduction of Turbulent Flows by Additives*, Kluwer Academic Publishers, The Netherlands.
- [4] Berman, N. S., and Cooper, E. E., 1972, "Stability Studies in Pipe Flows Using Water and Dilute Polymer Solutions," *AIChE J.*, 18, pp. 312–320.
- [5] Kawaguchi, Y., Tawaraya, Y., Yabe, A., Hishida, K., and Maeda, M., 1996, "Turbulent Transport Mechanism in a Drag-reducing Flow with Surfactant Additive Investigated by Two Component LDV," *Proceedings of 8th International Symposium on Application of Laser Techniques to Fluid Mechanics*, pp. 29.4.1–29.4.7.
- [6] Toh, K. H., and Ghajar, A. J., 1988, "Heat Transfer in the Thermal Entrance Region for Viscoelastic Fluid in Turbulent Pipe Flows," *Int. J. Heat Mass Transf.*, 31, No. 6, pp. 1261–1267.
- [7] Inaba, H., and Haruki, N., 1996, "Drag Reduction and Heat Transfer Characteristics of Water Solution with Surfactant in a Straight Pipe," *Proceedings of the 3rd KSME-JSME Thermal Engineering Conference*, pp. 215–220.
- [8] Bewersdorff, H. W., and Ohlendorf, D., 1988, "The Behavior of Drag-Reducing Cationic Surfactant Solutions," *Colloid and Polymer Science*, 266, No. 10, pp. 941–953.
- [9] Bewersdorff, H. W., 1989, "Drag Reduction in Surfactant Solutions," *Proceedings of IUTAM Symposium, Structure of Turbulence and Drag Reduction*, edited by A. Gyr, Zurich/Switzerland, pp. 293–312.
- [10] Myska, J., and Zakin, J. L., 1996, "Comparison of Flow Behavior of Polymeric and Cationic Surfactant Drag-reducing Additives," *Fluid Engineering Division, Summer Meeting, FED-Vol. 237*, ASME, New York, pp. 165–168.
- [11] Pollert, J., Zakin, J. L., Myska, J., and Kratochvil, P., 1994, "Use of Friction Reducing Additives in District Heating System Field Test at Kladono-Krocehlavy, Czech Republic," *Proceedings of Int. District Heating and Cooling 1994 Conference*, pp. 141–156.
- [12] Steiff, A., and Klopper, K., 1996, "Application of Drag-Reducing Additives in District Heating Systems," *Fluid Engineering Division, Summer Meeting, FED-Vol. 237*, ASME, New York, pp. 235–242.
- [13] Li, P. W., Kawaguchi, Y., and Yabe, A., 2000, "Feasibility Study of New Heat Transportation System with Drag-Reducing Surfactant Additives," *Symposium on Energy Engineering in the 21st Century*, Hong Kong.
- [14] Sato, K., Mimatsu, J., and Kumada, M., 1998, "Drag Reduction and Heat Transfer Augmentation of Surfactant Additives in a Two-Dimensional Channel Flow," *Proceedings of the 35th Japan National Heat Transfer Symposium*, pp. 693–694.
- [15] Hu, Y., Boltenhagen, P., and Pine, D. J., 1998, "Shear Thickening in Low-concentration Solutions of Worm-like Micelles—I) Direct Visualization of Transient Behavior and Phase Transitions," *J. Rheol.*, 42(5), pp. 1185–1207.
- [16] Hu, Y. T., Boltenhagen, P., Matthys, E., and Pine, D. J., 1998, "Shear Thickening in Low-Concentration Solutions of Wormlike Micelles. II. Slip, Fracture, and Stability of the Shear-Induced Phase," *J. Rheol.*, 42(5), pp. 1209–1226.
- [17] Gasljevic, K., and Matthys, E. F., 1997, "Experimental Investigation of Thermal and Hydrodynamic Development Regions for Drag-Reducing Surfactant Solutions," *ASME Journal of Heat Transfer*, 119, pp. 80–88.
- [18] Lu, B., Li, X., Zakin, J. L., and Talmon, Y., 1997, "A Non-Viscoelastic Drag

- Reducing Cationic Surfactant System," *J. Non-Newtonian Fluid Mech.*, **71**, pp. 59–72.
- [19] Chaffey, C. E., and Porter, G. S., 1984, "Steady Shear Flow of Solutions of Rod-like Macromolecules," *J. Rheol.*, **28**, pp. 249–272.
- [20] Ohlendorf, D., Interthal, W., and Hoffmann, H., 1986, "Surfactant System for Drag Reduction: Physico-Chemical Properties and Rheological Behavior," *Rheol. Acta*, **25**, pp. 468–486.
- [21] Lindner, P., Bewersdorff, H. W., Hee, R., Sittart, P., Thiel, H., Langowski, J., and Oberthur, R., 1990, "Drag-Reducing Surfactant Solutions in Laminar and Turbulent Flow Investigated by Small-angle Neutron Scattering and Light Scattering," *Prog. Colloid Polym. Sci.*, **81**, pp. 107–112.
- [22] Usui, H., 1997, "Turbulent Control by Functional Fluids," *J. Jpn. Soc. Fluid Mech.*, **16**, pp. 105–109.
- [23] Hu, Y., and Matthys, E. F., 1995, "Characterization of Micellar Structure Dynamics for a Drag-reducing Surfactant Solution under Shear, Normal Stress Studies and Flow Geometry Effects," *Rheol. Acta*, **34**, pp. 450–4600.
- [24] Kawaguchi, Y., Daisaka, H., Yabe, A., Hishida, K., and Maeda, M., 1997, "Existence of Double Diffusivity Fluid Layers and Heat Transfer Characteristics in Drag-Reducing Channel Flow," *Proceedings of 2nd International Symposium on Turbulence Heat and Mass Transfer*, edited by K. Hanjalic and T. W. J. Peeters, Delft, pp. 157–166.
- [25] Barrow, H., 1961, "Convection Heat Transfer Coefficients for Turbulent Flow between Parallel Plates With Unequal Heat Fluxes," *Int. J. Heat Mass Transf.*, **1**, p. 306.
- [26] Hatton, A. P., and Quarmby, A., 1963, "The effect of Axially Varying and Unsymmetrical Boundary Conditions on Heat Transfer With Turbulent Flow Between Parallel Plates," *Int. J. Heat Mass Transf.*, **6**, p. 903.
- [27] Kostic, M., and Hartnett, J. P., 1986, "Heat Transfer to Water Flowing Turbulently through a Rectangular Duct With Asymmetric Heating," *Int. J. Heat Mass Transfer*, **29**, p. 1283.
- [28] Q, Y. Y., Kawaguchi, Y., Lin, Z. Q., Erwing, M., Christensen, R. N., and Zakin, J. L., 1999, "Enhance Heat Transfer in Drag Reducing Surfactant Solutions," *Proceedings of the 11th European Drag Reduction Working Meeting*, Prague, Czech Republic, p. 42.
- [29] Kline, S. J., and McClintok, F. A., 1953, "Describing Uncertainties in Single-Sample Experiments," *Mech. Eng. (Am. Soc. Mech. Eng.)*, **75**, pp. 3–8.
- [30] Dean, R. B., 1978, "Reynolds Number Dependence of Skin Friction and Other Bulk Flow Variables in Two-Dimensional Rectangular Duct Flow," *J. Fluids Eng.*, **100**, pp. 215–223.
- [31] Virk, P. S., 1975, "Drag Reduction Fundamentals," *AIChE J.*, **21**, No. 4, pp. 625–656.
- [32] Gasljevic, K., and Matthys, E. F., 1995, "On the Diameter Effect for Turbulent Flow of Drag-reducing Surfactant Solutions," *Developments and Applications of Non-Newtonian Flows*, FED-Vol. 231/MD-Vol. 66, ASME, New York, pp. 237–243.
- [33] Usui, H., Itoh, T., and Saeki, T., 1998, "On Pipe Diameter Effects in Surfactant Drag-reducing Pipe Flows," *Rheol. Acta*, **37**, pp. 122–128.
- [34] Li, P. W., Daisaka, H., Kawaguchi, Y., Yabe, A., Hishida, K., and Maeda, M., 1998, "Study on Heat Transfer of Surfactant Solution as Drag-reducing Flow," *Proc., of the 35th Japan National Heat Transfer Symposium*, **3**, pp. 691–692.
- [35] Gnielinski, V., 1976, "New Equations for Heat and Mass Transfer in Turbulent Pipe and Channel Flow," *Int. Chem. Eng.*, **16-2**, pp. 359–368.

Using Porous Fins for Heat Transfer Enhancement

S. Kiwan

Assistant Professor
e-mail: kiwan@just.edu.jo

M. A. Al-Nimr

Professor
e-mail: malnimr@just.edu.jo

Mechanical Engineering Department,
Jordan University of Science and Technology,
Irbid-Jordan

This work introduces a novel method that enhances the heat transfer from a given surface by using porous fins. The thermal performance of porous fins is estimated and compared with that of the conventional solid fins. It is found that using porous fin of porosity ϵ may enhance the performance of an equal size conventional solid fin and, as a result, save 100 ϵ percent of the fin material. The effect of different design and operating parameters on the porous fin thermal performance is investigated. Examples of these parameters are Ra number, Da number, and thermal conductivity ratio. It is found that more enhancement in the porous fin performance may be achieved as Ra increases especially at large Da numbers. Also, it is found that there is an optimum limit for the thermal conductivity ratio beyond which there is no further improvement in the fin performance.

[DOI: 10.1115/1.1371922]

Keywords: Conduction, Finned Surfaces, Heat Transfer, Natural Convection, Porous Media

Introduction

The fins industry has been seeking ways to reduce the size and cost of fins. This demand is often justified by the high cost of the high-thermal-conductivity metals that are employed in the manufacture of finned surfaces and by the cost associated with the weight of the fin especially in airplanes and motorcycles applications.

The reduction in the size and cost of fins is achieved by the enhancement of the heat transfer carried out by the fins. The enhancement of heat transfer from fins has become an important factor that has captured the interest of many researchers. Enhancement of heat transfer from fin can be accomplished through the following techniques: (1) increasing the surface area to volume ratio, (2) increasing the thermal conductivity of the fin, and (3) increasing the convective heat transfer coefficient between the surface of the solid fin and the surrounding fluid.

Regarding the first technique, large number of works have been conducted to find the optimum shape of fins [1–9]. This approach is based on splitting a certain dimension of the fins in an optimal way providing that the total volume of the fin material is fixed. For example, Duffin [1] has used variational calculus to find the optimum fin shape. The optimum profile shape of fins with temperature-dependent conductivity has been determined by Jany and Bejan [2]. The optimum dimensions for a plate fin with fixed volume and transversal laminar boundary layers have been determined by Bejan [3]. An overview of the fin optimum shaping issue has been presented by Snider and Kraus [4]. Poulidakos and Bejan [5] have shown that optimum fin shapes and dimensions can be determined also based on purely thermodynamic grounds. Under the unidirectional heat transfer assumption, fin optimization has been carried out by [6–7]. Also, the optimization process has been carried out by [8–9] under the effect of variable convection heat transfer coefficient.

In the present work we intend to use porous fins to enhance the fins thermal performance. Due to their larger effective surface area, porous fins have better thermal performance as compared to the performance of equal weight conventional solid ones.

In the literature, porous substrates of high thermal conductivity have been used to improve the thermal performance of different thermal systems [10–13]. As an example, porous substrates have been used to improve the performance of conventional and tube-

less solar collector [11,12] and to improve the performance of heat exchangers [10]. Porous fins can be manufactured using high thermal conductivity materials such as Aluminum, Copper, and Silver.

In the present work, the thermal performance of porous fins is investigated numerically and a comparison between their performance and that of the solid fins is conducted. In the analysis, the Brinkman-Forchheimer-extended Darcy model is adopted to simulate the fluid behavior inside the porous fins. This model is used to study the effect of several operating and design parameters on the thermal performance of the fin.

Analysis

Referring to Fig. 1, an array of porous fins are attached on a hot surface in order to enhance the heat transfer from the hot surface to the cold one. In order to facilitate the solution of the governing equations, several assumptions are adopted. These assumptions include: (1) the fins have infinite depth and the array ends effects are neglected; (2) laminar flow with no internal heat generation; (3) no viscous dissipation; (4) the porous medium is homogeneous, isotropic, and saturated with a single-phase fluid; (5) both the fluid and the solid matrix have constant physical properties; (6) the surface radiant exchanges are neglected; and (7) the solid matrix and the fluid are assumed to be at local thermal equilibrium with each other. The interactions between the porous medium and the clear fluid is simulated by the Darcy-Brinkman-Forchheimer formulation and the continuity of velocity and stresses at the interface [14]. Using the dimensionless parameters given in the nomenclature, the equations of continuity, motion and energy, for both porous and fluid domains, are reduced to the following non-dimensional equations, respectively

$$\frac{\partial U_1}{\partial X} + \frac{\partial V_1}{\partial Y} = 0 \quad (1)$$

$$U_1 \frac{\partial U_1}{\partial X} + V_1 \frac{\partial U_1}{\partial Y} = -\epsilon_1^2 \frac{\partial P_1}{\partial X} + \epsilon_1 \text{Pr}_2 \left[\frac{\partial^2 U_1}{\partial X^2} + \frac{\partial^2 U_1}{\partial Y^2} \right] - \frac{\epsilon_1^2 \text{Pr}_2}{\text{Da}} U_1 - \epsilon_1^2 A U_1 \sqrt{U_1^2 + V_1^2} + \epsilon_1^2 \text{Ra}_2 \text{Pr}_2 \theta_1 \quad (2)$$

$$U_1 \frac{\partial V_1}{\partial X} + V_1 \frac{\partial V_1}{\partial Y} = -\epsilon_1^2 \frac{\partial P_1}{\partial Y} + \epsilon_1 \text{Pr}_2 \left[\frac{\partial^2 V_1}{\partial X^2} + \frac{\partial^2 V_1}{\partial Y^2} \right] - \frac{\epsilon_1^2 \text{Pr}_2}{\text{Da}} V_1 - \epsilon_1^2 A V_1 \sqrt{U_1^2 + V_1^2} \quad (3)$$

Contributed by the Heat Transfer Division for publication in the JOURNAL OF HEAT TRANSFER. Manuscript received by the Heat Transfer Division January 20, 2000; revision received July 14, 2000. Associate Editor: A. Bejan.

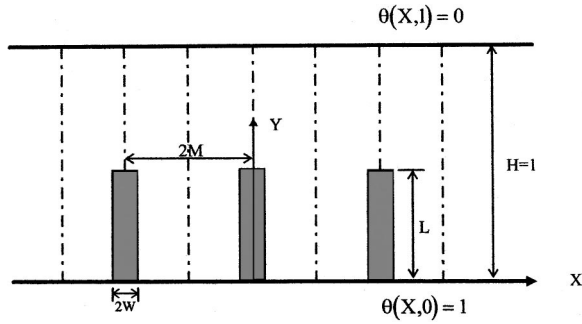


Fig. 1 Schematic diagram for the fins configuration

$$U_1 \frac{\partial \theta_1}{\partial X} + V_1 \frac{\partial \theta_1}{\partial Y} = \alpha_R \left[\frac{\partial^2 \theta_1}{\partial X^2} + \frac{\partial^2 \theta_1}{\partial Y^2} \right] \quad (4)$$

$$\frac{\partial U_2}{\partial X} + \frac{\partial V_2}{\partial Y} = 0 \quad (5)$$

$$U_2 \frac{\partial U_2}{\partial X} + V_2 \frac{\partial U_2}{\partial Y} = - \frac{\partial P_2}{\partial X} + \text{Pr}_2 \left[\frac{\partial^2 U_2}{\partial X^2} + \frac{\partial^2 U_2}{\partial Y^2} \right] + \text{Ra}_2 \text{Pr}_2 \theta_2 \quad (6)$$

$$U_2 \frac{\partial V_2}{\partial X} + V_2 \frac{\partial V_2}{\partial Y} = - \frac{\partial P_2}{\partial Y} + \text{Pr}_2 \left[\frac{\partial^2 V_2}{\partial X^2} + \frac{\partial^2 V_2}{\partial Y^2} \right] \quad (7)$$

$$U_2 \frac{\partial \theta_2}{\partial X} + V_2 \frac{\partial \theta_2}{\partial Y} = \left[\frac{\partial^2 \theta_2}{\partial X^2} + \frac{\partial^2 \theta_2}{\partial Y^2} \right] \quad (8)$$

and the governing equations of the conventional solid fin are reduced to the following conduction equation in the solid domain:

$$\frac{\partial^2 \theta_1}{\partial X^2} + \frac{\partial^2 \theta_1}{\partial Y^2} = 0, \quad (9)$$

where

$$\text{Da} = \frac{K_1}{h^2}, \quad A = \frac{F_1 h}{\sqrt{K_1}}, \quad \text{Ra}_2 = \frac{g \beta_2 \Delta T h^3}{\alpha_2 \nu_2},$$

$$\text{Pr}_2 = \frac{\nu_2}{\alpha_2}, \quad \Delta T = T_h - T_c, \quad \alpha_R = \frac{\alpha_1}{\alpha_2}.$$

In Eqs. (1)–(9), subscripts 1 and 2 refer to the porous and clear domains, respectively.

In the case under consideration, the momentum and energy equations assume the following boundary conditions:

At $Y=0$ and $W < X < M$

$$U_2 = 0, \quad V_2 = 0, \quad \theta_2 = 1.$$

At $Y=0$ and $0 < X < W$

$$U_1 = 0, \quad V_1 = 0, \quad \theta_1 = 1.$$

At $Y=H$ and any X

$$U_2 = 0, \quad V_2 = 0, \quad \theta_2 = 0.$$

At $X=0$ and any Y and at $X=M$ and any Y

$$\frac{\partial U_1}{\partial X} = \frac{\partial U_2}{\partial X} = \frac{\partial V_1}{\partial X} = \frac{\partial V_2}{\partial X} = \frac{\partial \theta_1}{\partial X} = \frac{\partial \theta_2}{\partial X} = 0.$$

At $X=W$ and $0 < Y < L$

$$U_1 = U_2, \quad V_1 = V_2, \quad \theta_1 = \theta_2,$$

$$\frac{\partial U_1}{\partial X} = \frac{\partial U_2}{\partial X}, \quad \frac{\partial V_1}{\partial X} = \frac{\partial V_2}{\partial X}, \quad k_R \frac{\partial \theta_1}{\partial X} = \frac{\partial \theta_2}{\partial X}.$$

At $Y=L$ and $0 < X < W$

$$U_1 = U_2, \quad V_1 = V_2, \quad \theta_1 = \theta_2,$$

$$\frac{\partial U_1}{\partial Y} = \frac{\partial U_2}{\partial Y}, \quad \frac{\partial V_1}{\partial Y} = \frac{\partial V_2}{\partial Y}, \quad k_R \frac{\partial \theta_1}{\partial Y} = \frac{\partial \theta_2}{\partial Y}.$$

For solid conventional fins, all boundary conditions are the same except: at $X=0$ and any Y

$$\frac{\partial U_2}{\partial X} = \frac{\partial V_2}{\partial X} = \frac{\partial \theta_1}{\partial X} = \frac{\partial \theta_2}{\partial X} = 0.$$

At $X=W$ and $0 < Y < L$

$$U_2 = V_2 = 0, \quad k_R \frac{\partial \theta_1}{\partial X} = \frac{\partial \theta_2}{\partial X}$$

At $Y=L$ and $0 < X < W$

$$U_2 = V_2 = 0, \quad k_R \frac{\partial \theta_1}{\partial Y} = \frac{\partial \theta_2}{\partial Y}$$

At $Y=0$ and $0 < X < W$

$$\theta_1 = 1,$$

where

$$k_R = \frac{k_1}{k_2}, \quad W = \frac{w}{h}, \quad H = \frac{h}{h} = 1, \quad L = \frac{l}{h}, \quad M = \frac{m}{h}.$$

Solution Methodology

The equations and boundary conditions described above are solved by using the finite element code FIDAP 7.06a [15]. The code solved for the velocity, pressure and temperature fields. A mixed pressure formulation is used (see [15] for more details).

The meshes used in the final runs are tested for mesh independent solution. Two criteria are considered in getting a mesh-independent solution; no significant change (less than 1 percent) in the solution fields and in the heat flux calculations. All meshes are graded to provide smaller elements near the boundaries, the interfaces between porous and clear domains and the surfaces of symmetry boundary conditions as shown in Fig. 2. This is done for accurate temperature predictions in order to resolve the steep velocity and temperature gradients there. All boundary elements are two-node linear, while all non-boundary elements are four-node, quadrilateral elements. Several mesh sizes ranging from 1000 up to 4500 elements were used to study the problem under consideration. It is found for all cases studied here that increasing the mesh size beyond 4000 elements resulted in less than flux calculations. Thus the solutions obtained using 4500-element mesh can be considered mesh independent solutions.

To validate the numerical scheme used in the present study, a comparison with relevant result is made. This comparison is carried out for the problem of natural convection heat transfer in a square cavity [16]. This case is close to the problem under consideration with no porous fin. The result of this comparison showed that the numerical model predictions for the velocity and temperature fields are accurate within 2 percent.

Thermal Performance of the Porous Fins

The improvement in the fin thermal performance can be evaluated in terms of the ratio q_p/q_s which is the ratio of the heat transfer carried out from the hot surface using porous fins to that carried out using solid conventional fin. It is clear from the dimensionless governing equations that the performance of the porous fin depends on the following dimensionless parameters:

$$\epsilon_1, \quad \text{Pr}_2, \quad \text{Da}, \quad A, \quad \text{Ra}_2, \quad \alpha_R, \quad k_R, \quad W, \quad M, \quad L.$$

Wherever we have to fix their values, the above parameters are assumed as

$$\text{Da} = 6 \times 10^{-6}, \quad L = 0.125, \quad \text{Ra}_2 = 1 \times 10^7,$$

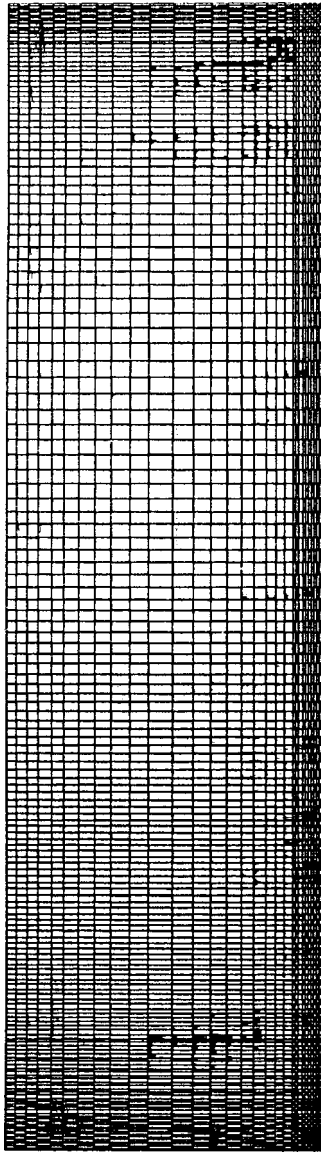


Fig. 2 Finite element mesh for the flow field

$$W=0.0125, \quad M=0.25, \quad k_R=4400, \quad Pr_2=0.71$$

$$\alpha_R=2.5, \quad A=1.0, \quad \epsilon=0.5.$$

Results and Discussion

The basic philosophy behind using porous fins is to increase the effective surface area through which heat is convected to the ambient fluid. As shown in Fig. 3, porous fins may be simulated by imagining that one single solid fin of fixed weight is divided to N slides of equal sizes and which have the same total weight as the original fin. Figure 4 shows the ratio of heat transfer carried out by the N slides to that carried out by the original fin as a function of number of slides N . The total heat transfer carried out by the N slides is estimated by multiplying the heat transfer carried out through one slide by N . It is clear from this figure that dividing the fin to slides increases the heat transfer dramatically. The same figure shows the material weight which can be saved if the remaining slides have to convect the same amount of heat carried out by the original single fin. As an example, if the original fin is divided to 5 slides, then 30 percent of these slides are sufficient to

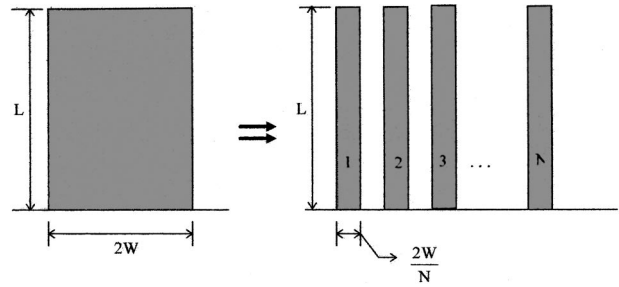


Fig. 3 Simple simulation for the porous fin

convect the same amount of heat carried out by the original fin. This implies that we may save 70 percent of the original fin total material.

The above simulation overestimates the benefit obtained from using porous fins since it assumes that the convective heat transfer coefficient within the pores of the porous fin has the same value as that at the outer surface of the solid fin. In reality, the convective heat transfer coefficient within the porous material is much lower than that at the outer surface of the solid fin.

Figure 5 shows a sample plot of the streamlines and isotherma in the computational domain. It is clear from Fig. (5a) that the fluid penetrates inside the porous fin. Figure 6 shows the effect of the thermal conductivity ratio k_1/k_2 on the heat transfer ratio q_p/q_s for different fin lengths. As predicted, increasing the thermal conductivity ratio has the effect of increasing the heat transfer ratio due to the increase in the effective thermal conductivity of the porous fin. However, there is an optimum value for k_1/k_2 beyond which there is no significant improvement in q_p/q_s . Increasing the fin effective thermal conductivity raises the fin temperature until all parts of the fin attain a maximum temperature which is the fin base temperature. At this limit, the fin convects the maximum possible heat and no further improvement in its performance can be achieved by increasing its effective thermal conductivity. Also, it is clear from this figure that using porous fins of porosity ϵ improves the fin performance by a certain percentage depends on the fin length and on other operating and design conditions. Improving the fin performance is not the main achievement obtained by using porous fins. The main achievements is the saving of 100 ϵ percent in the weight of the fin. As an example, if a porous fin of porosity 0.1 has improved the conventional solid fin performance by 10 percent, this implies that we may improve the conventional fin performance by about 22 percent $(=100((q_p/q_s)/(1-\epsilon)-1))$ percent) if the same weight of the conventional solid fin material is utilized in manufacturing porous fins each has the same volume as the conventional solid one.

Using porous fin increases the effective surface area of the fin through which the fin convects heat to the working fluid. Al-

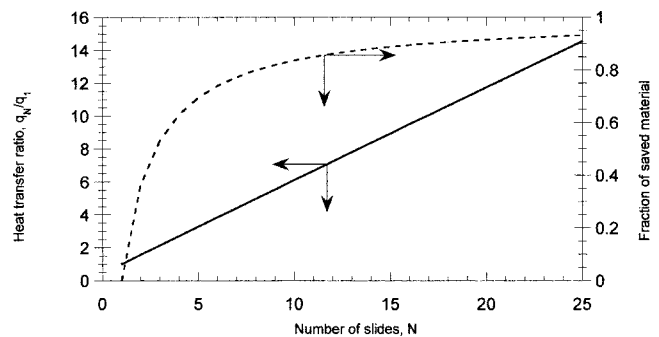


Fig. 4 Effect of slides number on the heat transfer ratio and on the fraction of saved material

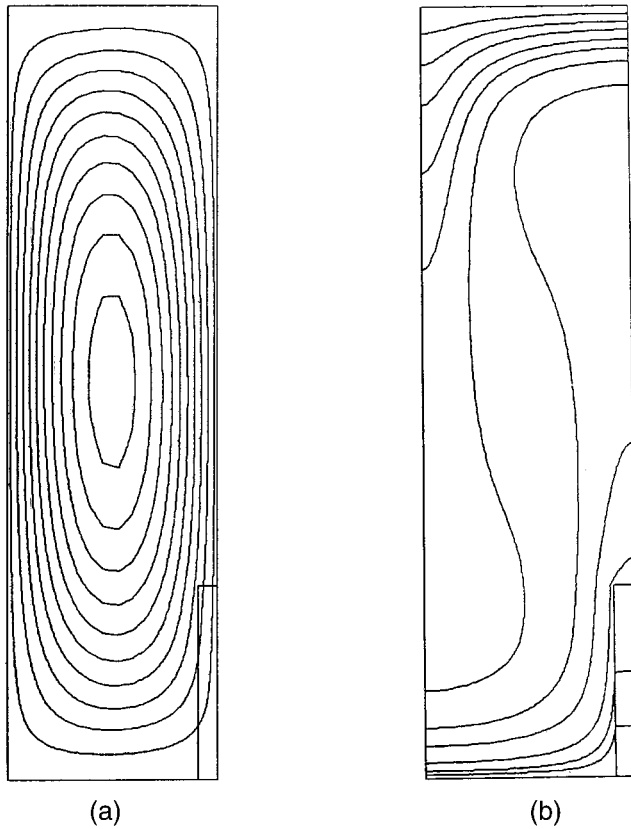


Fig. 5 Sample plot for the (a) streamlines and (b) isotherms in the flow field

though the effective thermal conductivity of the porous fin decreases, due to the removal of the solid material, the increase in the fin effective surface area overcomes this reduction.

Also, it is clear from Fig. 6 that increasing the fin length reduces the heat transfer ratio. Increasing the fin length causes more improvement in the solid fin performance as compared to the improvement in the porous fin performance. As the fin length increases, the temperature of the part very near the tip approaches the working fluid temperature. This implies that the driving force for natural convection decreases, and as a result, the fluid can not penetrate through the pores of the porous domain. Both porous and conventional fins can not benefit so much from the increase in the fin length. However, the reduction in the porous fin effective thermal conductivity, due to the removal of the solid material, makes the benefit obtained from increasing the porous fin length lower than that obtained from increasing the conventional solid fin length.

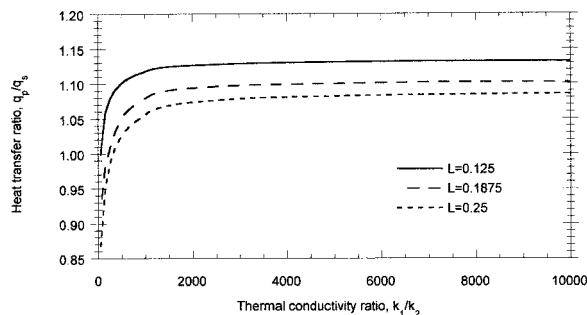


Fig. 6 Effect of thermal conductivity ratio on the heat transfer ratio for different fin lengths

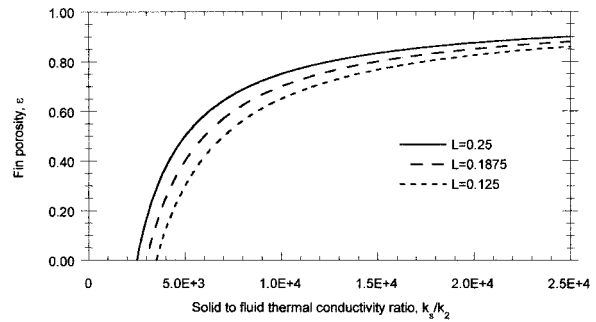


Fig. 7 Effect of solid to fluid thermal conductivity ratio on fin porosity

Another important observation may be drawn from Fig. 6 which is the fact that the optimum k_1/k_2 ratio ($= (k_1/k_2)_{opt}$), at which the porous fin attains its maximum performance, increases as the fin length increases. As mentioned previously, increasing the fin length causes less improvement in the porous fin performance compared to the improvement in the conventional fin performance.

A relation between the fin porosity, or the saving in the fin weight, and the solid to fluid thermal conductivity ratio, can be derived for each fin length. The optimum thermal conductivity ratio $(k_1/k_2)_{opt}$, which is found directly from Fig. 6, is given as:

$$\left(\frac{k_1}{k_2}\right)_{opt} = \epsilon + (1 - \epsilon) \frac{k_s}{k_2} \approx (1 - \epsilon) \frac{k_s}{k_2}$$

from which

$$\epsilon \approx 1 - \frac{\left(\frac{k_1}{k_2}\right)_{opt}}{\frac{k_s}{k_2}}$$

Figure 7 shows the variation in ϵ as a function of k_s/k_2 . As clear from this figure, and under a fixed fin performance, more saving in the fin weight can be achieved by using fins having large k_s/k_2 ratio. However, this saving reaches to an asymptotic level beyond which no further saving in the fin material is achieved. As the thermal conductivity of the solid material k_s increases, the temperature of the porous fin increases, and in the limit as $k_s/k_f \rightarrow \infty$, the fin attains temperatures very close to the fin base temperature. At this limit, the convected heat through the fin reaches to a maximum value and no further increase in this heat may be achieved regardless of the increase in the k_s/k_2 .

Figure 8 shows the effect of Ra number on the heat transfer ratio at different Da numbers. As predicted, increasing Ra number increases the heat transfer ratio q_p/q_s . Increasing Ra number improves the convective heat transfer coefficient between the fin and the working fluid. This improves the performance of both porous and solid fins. However, in porous fins the convective heat transfer coefficient interacts with the fin through a volumetric surface area which is much larger than the conventional fin surface area. As a result, any improvement in the convective heat transfer coefficient causes much more improvement in the porous fin performance as compared to the improvement in the conventional fin performance. Also, it is clear from the same figure that the effect of Ra number is more significant on fins having large Da number. As the permeability of the porous fin increases, i.e., increasing Da number, the working fluid ability to penetrate through the fin pores and to convect heat increases. Porous fins having small Da number behave as a solid fins due to their small permeability. As a result, the ratio q_p/q_s is very close to 1 for very small Da

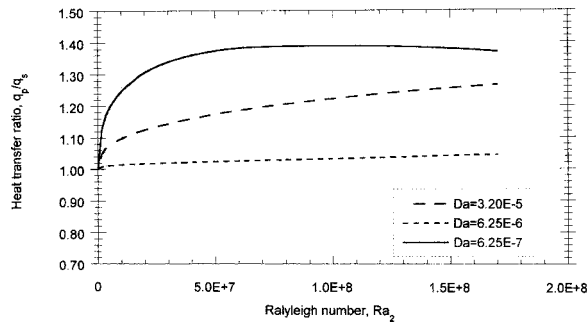


Fig. 8 Effect of Rayleigh number on the heat transfer ratio for different Darcy numbers

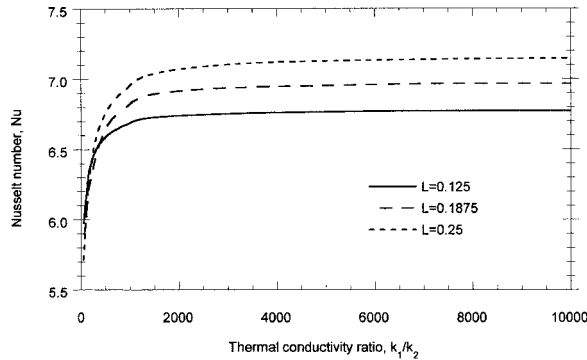


Fig. 9 Effect of thermal conductivity ratio on Nusselt number at different fin lengths

number and the effect of Ra number on this ratio is insignificant. Figure 9 shows the effect of the thermal conductivity ratio on Nu number which is defined as

$$Nu = \frac{2q_p''m}{\Delta Tk_2},$$

and which represents the dimensionless convective heat transfer coefficient between the hot surface, including the porous fins, and the cold surface. As predicted, Nu number increases as the thermal conductivity ratio increases. However, there is an optimum limit for k_1/k_2 beyond which there is no further improvement in Nu number. As mentioned previously, significant increase in the porous fin length causes insignificant improvement in the fin performance. As a result, it is necessary to increase the optimum ratio $(k_1/k_2)_{opt}$ to enable the fin to reach its maximum performance as the fin length increases.

Also, it is clear from the same figure that Nu number increases as the fin length increases. Increasing the fin length increases the heat transfer carried out from the fin and as a result, increases Nu number.

Conclusion

This work introduces a novel method that enhances the heat transfer from a given surface by using porous fins. The thermal performance of porous fins is estimated and compared with that of the conventional solid fins.

It is found that using porous fin of porosity ϵ may enhance the performance of an equal size conventional solid fin and, as a result, save 100 ϵ percent of the fin material. Also, it is found that more enhancement in the fin performance may be achieved as Ra number increases. As a result, any improvement in the convective heat transfer coefficient causes much more improvement in the

porous fin performance as compared to the improvement in the conventional fin performance. The effect of Ra number is more significant on fins having large Da number.

As predicted, Nu number increases as the thermal conductivity ratio increases. However, there is an optimum limit for the thermal conductivity ratio beyond which there is no further improvement in Nu number. Also, it is found that Nu number increases as the fin length increases.

Nomenclature

- A = dimensionless coefficient of the microscopic inertia term, $F_1 h / \sqrt{K_1}$
- c = specific heat
- Da = Darcy number, K_1 / h^2
- F_1 = Forchheimer coefficient, $1.8 / (180\epsilon^5)^{0.5}$
- g = gravity constant
- h = distance between the hot and the cold surfaces
- H = dimensionless Distance between the hot and the cold surfaces, $h/h = 1$
- k = thermal conductivity
- k_R = thermal conductivity ratio, k_1/k_2
- K_1 = permeability of the porous fin
- l = fin length
- L = dimensionless fin length, l/h
- m = half the spacing between the center lines of two adjacent fins
- M = half the dimensionless spacing between the center lines of two adjacent fins, m/h
- N = number of slides
- Nu = Nusselt number, $2q_p''m / \Delta Tk_2$
- p = pressure
- P = dimensionless pressure, $ph^2 / \rho_2 \alpha_2^2$
- Pr = Prandtl number, ν/α
- q = heat transfer
- q_1 = heat transfer from the original fin
- q_N = total heat transfer from the N slides
- q'' = heat flux per unit area
- q_R = heat transfer ratio, q_p/q_s
- r = radial coordinate
- Ra_2 = Rayleigh number of the clear domain, $g\beta_2\Delta Th^3/\alpha_2\nu_2$
- T = temperature at any point
- T_c = temperature of the cold surface
- T_h = temperature of the hot surface
- u = axial velocity
- U = dimensionless volume averaged axial velocity, uh/α_2
- v = transverse velocity
- V = dimensionless transverse velocity, vh/α_2
- w = half width of the fin
- W = dimensionless half width of the fin, w/h
- x = axial coordinate
- X = dimensionless axial coordinate, x/h
- y = transverse coordinate
- Y = dimensionless transverse coordinate, y/h

Greek Symbols

- α = thermal diffusivity
- β = coefficient of volumetric thermal expansion
- ΔT = temperature difference, $T_h - T_c$
- ϵ = porosity or void ratio
- θ = dimensionless temperature, $(T - T_c) / (T_h - T_c)$
- μ = dynamic viscosity
- ν = kinematic viscosity
- ρ = density

Subscripts

- 1 = porous domain properties
- 2 = clear or fluid domain properties
- c = cold
- h = hot

p = porous fin properties
 R = ratio
 s = solid fin properties

References

- [1] Duffin, R., 1959, "A Variational Problem Relating to Cooling Fins," *J. Math. Mech.*, **8**, pp. 47–56.
- [2] Jany, P., and Bejan, A., 1988, "Ernst Schmidt's Approach to Fin Optimization: An Extension to Fins with Variable Conductivity and the Design of Ducts for Fluid Flow," *Int. J. Heat Mass Transf.*, **31**, pp. 1635–1644.
- [3] Bejan, A., 1984, *Convection Heat Transfer*, John Wiley and Sons, New York.
- [4] Snider, A. D., and Kraus, A. D., 1986, "The Quest for the Optimum Longitudinal Fin Profile," *ASME HTD*, **64**, pp. 43–48.
- [5] Poulidakos, D., and Bejan, A., 1982, "Fin Geometry for Minimum Entropy Generation in Forced Convection," *ASME J. Heat Transfer*, **104**, pp. 616–623.
- [6] Irey, R. K., 1968, "Errors in the One-Dimensional Fin Solution," *ASME J. Heat Transfer*, **90**, pp. 175–176.
- [7] Lau, W., and Tan, C. W., 1973, "Errors in One-Dimensional Heat Transfer Analyses in Straight and Annular Fins," *ASME J. Heat Transfer*, **95**, pp. 549–551.
- [8] Stachiewicz, J. W., 1969, "Effect of Variation of Local Film Coefficient on Fin Performance," *ASME J. Heat Transfer*, **91**, pp. 21–26.
- [9] Look, D. C., Jr., 1988, "Two-Dimensional Fin Performance: Bi (Top Surface) $\geq Bi$ (Bottom Surface)," *ASME J. Heat Transfer*, **110**, pp. 780–782.
- [10] Alkam, M., and Al-Nimr, M. A., 1999, "Improving the Performance of Double-Pipe Heat Exchangers by Using Porous Substrates," *Int. J. Heat Mass Transf.*, **42**, pp. 3609–3618.
- [11] Al-Nimr, M. A., and Alkam, A., 1998, "A Modified Tubeless Solar Collector Partially Filled with Porous Substrate," *Renewable Energy*, **13**(2), pp. 165–173.
- [12] Alkam, M. K., and Al-Nimr, M. A., 1999, "Solar Collectors with Tubes Partially Filled with Porous Substrates," *ASME J. Sol. Energy Eng.*, **121**, pp. 20–24.
- [13] Al-Nimr, M. A., and Alkam, M., 1997, "Unsteady Non-Darcian Forced Convection Analysis in an Annulus Partially Filled with a Porous Material," *ASME J. Heat Transfer*, **119**, pp. 799–804.
- [14] Vafai, K., and Kim, S. J., 1995, "On the Limitations of the Brinkman-Forchheimer-Extended Darcy Equation," *Int. J. Heat Fluid Flow*, **16**, pp. 11–15.
- [15] Engelman, M. S., 1993, *Fidap Theoretical Manual-Revision 7*, 1st ed., Fluid Dynamics International, Inc., Evanston, IL.
- [16] del Vahl Davis, G., 1983, "Natural Convection in a Square Cavity—A Benchmark Solution," *Int. J. Numer. Methods Fluids*, **3**, pp. 249–264.

Precision Temperature Control of High-Throughput Fluid Flows: Theoretical and Experimental Analysis

Kevin M. Lawton

Steven R. Patterson
e-mail: spatters@unc.edu

Russell G. Keanini

Center for Precision Metrology,
Department of Mechanical Engineering and
Engineering Science,
University of North Carolina at Charlotte,
Charlotte, NC 28223

A precision method for attenuating temperature variations in a high-throughput control fluid stream is described and analyzed. In contrast to earlier investigations, the present study emphasizes heat transfer analysis of the constituent control device and derives theoretical descriptions of system responses to time-varying fluid temperatures. Experiments demonstrate that the technique provides: (1) frequency-dependent attenuation which is several orders of magnitude greater than that obtained via a perfect mixing volume; (2) attenuation, over two decades of disturbance frequency, that reduces in-flow temperature variations by factors ranging from 10 to $\approx 10^4$; (3) asymptotic attenuation greater than three orders of magnitude for spectral components having periods less than the device thermal equilibrium time; and (4) attenuation which is fully consistent with theoretical predictions. The model developed provides design criteria for tailoring system performance. In particular, it is shown that for a given control stream flow rate, the magnitude of maximal attenuation can be adjusted by varying the thermal resistance between the flow and attenuating medium, while the range of frequencies maximally attenuated can be adjusted by varying the product of thermal resistance and attenuating medium heat capacity. The analysis and design are general and should prove useful in the design and analysis of other high-throughput precision temperature control systems. [DOI: 10.1115/1.1375810]

Keywords: Control, Heat Transfer, Heat Exchangers

1 Introduction

Due to the inherent thermal sensitivity of materials and systems, precision experiments and instrumentation generally require precision temperature control. In some experiments, thermal effects can be the largest source of dimensional error and non-repeatability [1]. Likewise, thermal variability can limit the operation of various sensors and devices, e.g., laser interferometers, autocollimators, and capacitance probes [2]. Temperature stability, i.e., the maintenance of a given temperature to a given degree of precision, often constitutes a particularly challenging aspect of precision system design [3].

Precision temperature control near room temperature has received significant attention. One class of controllers uses resistive heaters to maintain a small enclosure near ambient. Due to the small size of these systems, high stability, on the order of $\pm 10 \mu\text{K}$ to $\pm 100 \mu\text{K}$ over hours, days or months of time can be achieved. Examples include $\pm 20 \mu\text{K}$ stability in standard cells over several months [4], $\pm 60 \mu\text{K}$ stability in laser diodes over approximately one hour [5], $\pm 10 \mu\text{K}$ stability in geophysical accelerometers over several days [6], and $\pm 100 \mu\text{K}$ stability in semiconductor lasers over tens of hours [7]. Resistance-based controllers providing milliKelvin stability have also been developed or proposed for use in thermometry [8], physical property measurement [9,10], strain measurement [9], and optical microscopy [11].

Another class of controllers uses fluids to heat or cool enclosures near room temperature. Since these controllers have both heating and cooling capabilities, they are particularly suited for use with heat-generating devices. Examples include an oil-cooled

vacuum chamber providing $\pm 15 \mu\text{K}$ control over tens of hours [12], precision temperature-controlled water baths providing $\pm 25 \mu\text{K}$ stability over tens of hours [13,14], and a stirred water bath providing $\pm 3.5 \mu\text{K}$ stability over tens of hours [15].

In contrast to resistance-based precision thermal control and precision thermal control in closed, non-circulating fluid systems, relatively little work has been reported on precision thermal control of flowing or recirculating control fluid streams. Lopez and Barron [16] used temperature-controlled forced air to achieve $\pm 0.1 \text{ K}$ control over liquid crystal samples. Ogasawara [14] used recirculating water to maintain a thermostatic water bath to within $\pm 25 \mu\text{K}$ of a set point. This approach had also been used to control plasma tube temperatures in lasers [17,18]. Sydenham and Collins [19], using recirculating water in a deep underground test facility (where the latter minimized background thermal variations), achieved $\pm 40 \mu\text{K}$ stability in a 10 m long steel standard over hundreds of hours.

This paper describes the theoretical models, design, construction, and performance of a ‘‘thermal gradient attenuator’’ low-pass filter. This device is a critical component for producing a high stability chilled water supply that can be used for precision temperature control. By attenuating higher frequency temperature oscillations in the control fluid, active heater controllers need only reject lower frequency disturbances to achieve precise temperature control.

This work extends previous investigations by developing a relatively simple approach capable of providing centiKelvin stability over hours and milliKelvin stability over minutes, within recirculating flows. Equally important, considerable attention is devoted to modeling system heat transfer and system dynamics.

Contributed by the Heat Transfer Division for publication in the JOURNAL OF HEAT TRANSFER. Manuscript received by the Heat Transfer Division June 27, 2000; revision received January 20, 2001. Associate Editor: D. A. Zumbrennen.

2 Thermal Gradient Attenuator—Justification for Need

A multi-purpose temperature-controlled chamber has been designed for use in precision metrology experiments. The chamber walls are channeled to allow flow of temperature-controlled chilled water, which in turn provides thermal control of the chamber interior. Although a heater controller is available to modulate the chilled water temperature, because of limited bandwidth it cannot reject the higher frequency temperature oscillations of the available chilled water supply (see Figs. 1 and 2). Since the desired level of temperature control is order 0.1 mK, the large short-term temperature deviations of the chilled water must be significantly attenuated before entering the heater control system.

In order to attenuate these higher frequency oscillations, a thermal gradient attenuator, shown schematically in Fig. 3, must be placed in the chilled water stream. As shown in Figs. 1 and 2, the spectrum for the entering chilled water stream contains significant spectral components over the range from 0.04 to 10 mHz, with peak rates of change of order 1 K/min. With dominant temporal variations occurring at relatively low frequencies, effective attenuation requires that the attenuator exhibit large attenuation at the relatively low frequency of 0.04 mHz.

For the purpose of analysis, the thermal gradient attenuator is modeled as three subsystems, each characterized by a dominant heat transfer mode and an associated dynamic. The core of the device is identified as the tube bank-attenuator subsystem since it consists of an array of uniformly distributed identical tubes that direct the flow of the control fluid past the attenuator medium. The entrance and exit volumes below and above the tube bank-attenuator are identified as the lower accumulator and upper accumulator subsystems. Subsystem and total device performance are characterized using transfer functions, which model the ratio of the output and input temperatures as functions of frequency.

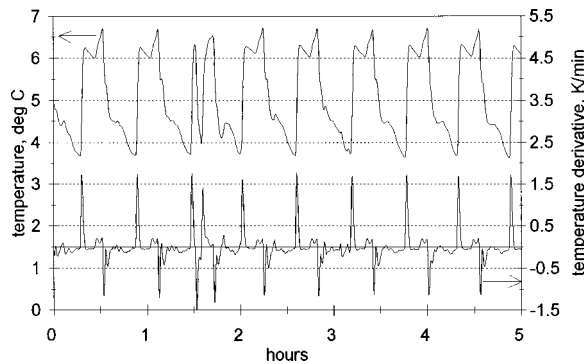


Fig. 1 Chilled water temperature and temperature derivative versus time, 1.9 l/min flow rate

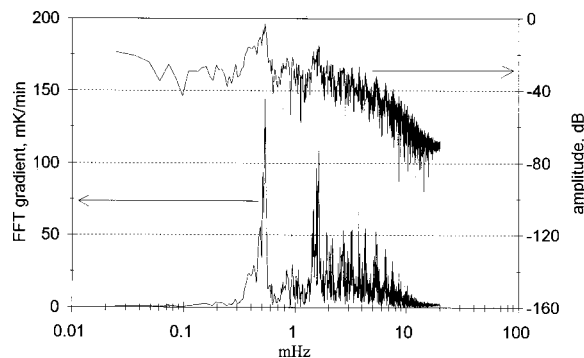


Fig. 2 Chilled water spectrum and average FFT gradients versus frequency; 1.9 l/min flow rate

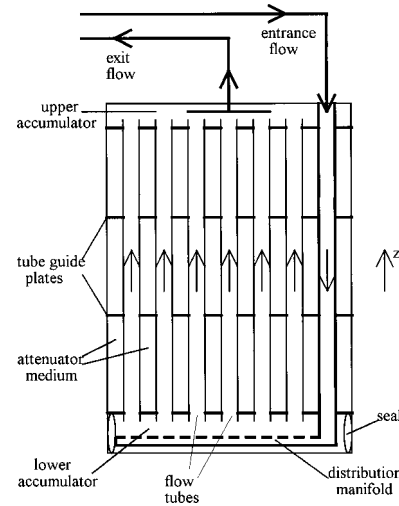


Fig. 3 Thermal gradient attenuator configuration

3 Lumped-Differential Model of the Tube Bank-Attenuator Subsystem

The model of the tube bank-attenuator sub-system is based on two radially-lumped, coupled differential equations which model the time and axially-dependent temperature variations within the flowing control fluid and the surrounding attenuating medium. The derivation of these equations proceeds in three steps: (1) assumptions relevant to the tube bank-attenuator are stated; (2) order of magnitude arguments are used to simplify the energy equation within the flow, the tube wall, and the surrounding attenuating medium; and (3) each simplified equation is radially integrated, leading to the lumped working equations. Neto and Cotta [20,21] have developed a lumped-differential analysis of double-pipe heat exchangers. The present formulation for a restricted class of heat exchanger leads to two relatively simple, integrable differential equations, while the more general approach in Neto and Cotta, which incorporates a generalized integral transform method [22], leads to a large system of coupled differential equations.

The class of heat exchangers modeled here is restricted by a set of assumptions relating to the geometry, thermal properties of the components, and the frequency range of the input disturbances. These assumptions can be related to a single tube and the surrounding attenuator medium. The length of the attenuator medium is taken to be much larger than the radial dimension, and the ratio of axial fluctuation length scale, \bar{w}/f , to radius, r , is sufficiently small that radial conduction dominates axial conduction. Thus,

$$\frac{\bar{w}/f}{r} \gg 1 \quad \text{so that} \quad \frac{\partial T}{\partial r} \gg \frac{\partial T}{\partial z} \quad (1)$$

and

$$r/L \ll 1. \quad (2)$$

It is also assumed that the attenuator medium is either a solid or a stagnant fluid where advection is negligible. In the latter case, it is assumed that the ratio of conductive to time-dependent temperature variations

$$\frac{\vec{u} \cdot \nabla T}{\partial T / \partial t} \approx \frac{u_s}{f \cdot L} \quad (3)$$

are small, where the velocity scale, $u_s = (g \cdot \beta \cdot L \cdot \Delta T)^{1/2}$, is determined by buoyancy.

Based on these assumptions, heat transfer, to first order, within the attenuator medium is governed by the equation

$$\frac{\partial T}{\partial t} = \alpha_a \frac{1}{r} \cdot \frac{\partial}{\partial r} \left(r \frac{\partial T}{\partial r} \right). \quad (4)$$

Similarly, conduction within the tube wall is governed by

$$\frac{\partial}{\partial r} \left(r \frac{\partial T}{\partial r} \right) = 0 \quad (5)$$

while within the fluid flow

$$\frac{\partial T}{\partial t} + w(r) \frac{\partial T}{\partial z} = \alpha_a \frac{1}{r} \cdot \frac{\partial}{\partial r} \left(r \frac{\partial T}{\partial r} \right), \quad (6)$$

where $w(r)$ is the fully-developed laminar flow velocity profile [23]. For tubes with sufficiently high aspect ratio and small Reynolds number, the entry length comprises a small fraction of the total length, and the above equation is a good approximation for the entire tube.

Equations (4) through (6) may be integrated radially to obtain respective lumped equations for the mean temperature in the attenuator, tube wall, and fluid flow regions

$$\frac{\partial \bar{T}_a}{\partial t} = \frac{\alpha_a}{(r_a - r_i)^2} \left(r_a \frac{\partial T}{\partial r} \Big|_{r_a} - r_i \frac{\partial T}{\partial r} \Big|_{r_i} \right) \quad (7)$$

$$r_f \frac{\partial T}{\partial r} \Big|_{r_f} = r_i \frac{\partial T}{\partial r} \Big|_{r_i} \quad (8)$$

$$\frac{\partial \bar{T}_f}{\partial t} + \frac{1}{r_f^2} \int_0^{r_f} r w(r) \frac{\partial T}{\partial z} dr = \frac{\alpha}{r_f} \frac{\partial T}{\partial r} \Big|_{r_f}, \quad (9)$$

where the mean temperatures are defined as

$$\bar{T}_a(z, t) = \frac{1}{r_a^2 - r_i^2} \int_{r_i}^{r_a} r \cdot T(r, z, t) \cdot dr \quad (10)$$

$$\bar{T}_f(z, t) = \frac{1}{r_f^2} \int_0^{r_f} r \cdot T(r, z, t) \cdot dr. \quad (11)$$

When the radial conduction time scale is much shorter than the disturbance and axial convection time scales, radial temperature gradients are quickly smoothed, and the integral in Eq. (9) may be approximated as

$$\int_0^{r_f} r w(r) \frac{\partial T}{\partial z} dr \approx r_f^2 \bar{w} \frac{\partial \bar{T}_f}{\partial z}, \quad (12)$$

where the radially averaged velocity is given by

$$\bar{w} = \frac{2}{r_f^2} \int_0^{r_f} r w(r) dr. \quad (13)$$

The integrated energy equation, Eq. (8), implies that at any instant, the local radial heat transfer rate, $q = q(z, t)$, is constant within the tube wall. By solving Eq. (5), it is readily shown that

$$q(z, t) = 2 \pi k_t L \frac{[T(r_f, z, t) - T(r_i, z, t)]}{\ln(r_i/r_f)} = \frac{[T(r_f, z, t) - T(r_i, z, t)]}{R_t} \equiv \frac{[T|_{r_f} - T|_{r_i}]}{R_t}, \quad (14)$$

where R_t is the total tube thermal resistance along its length, L . Similarly, heat transfer at the inner and outer tube boundaries are given as

$$q(z, t) = \frac{[\bar{T}_f - T|_{r_f}]}{R_f} = -r_f k_f L \frac{\partial T}{\partial r} \Big|_{r_f}, \quad (15)$$

where R_f is the fluid thermal resistance, and

$$q(z, t) = \frac{[T|_{r_i} - \bar{T}_a]}{R_a}, \quad (16)$$

where R_a is the attenuator thermal resistance. Given the following definition and equation

$$R \equiv R_f + R_t + R_a = \frac{[\bar{T}_f - T|_{r_f}]}{q} + \frac{[T|_{r_f} - T|_{r_i}]}{q} + \frac{[T|_{r_i} - \bar{T}_a]}{q} = \frac{[\bar{T}_f - \bar{T}_a]}{q} \quad (17)$$

and substituting Eqs. (13) and (15) into Eq. (9) yields

$$\frac{\partial \bar{T}_f}{\partial t} + \bar{w} \frac{\partial \bar{T}_f}{\partial z} = \frac{1}{\tau_f} (\bar{T}_a - \bar{T}_f), \quad (18)$$

where $\tau_f = RC_f$ is the fluid time constant. Similarly, Eq. (7) simplifies to

$$\frac{\partial \bar{T}_a}{\partial t} = \frac{1}{\tau_a} (\bar{T}_f - \bar{T}_a), \quad (19)$$

where $\tau_a = RC_a$, is the attenuator time constant.

4 Tube Bank-Attenuator Transfer Function

Neglecting heat transfer through the outer wall of the attenuator assembly, the transfer function of the entire tube bank-attenuator is the same as that of a single tube, given proper flow rate scaling. Thus, the transfer function of the entire tube bank follows from Eqs. (18) and (19). A more compact result follows by introducing the dimensionless space and time variables

$$\eta = z/(\bar{w} \tau_a) \quad \text{and} \quad \tau = t/\tau_a \quad (20)$$

and the dimensionless heat capacity ratio

$$\zeta = \tau_a/\tau_f = C_a/C_f. \quad (21)$$

Substitution of Eqs. (20) and (21) into Eqs. (18) and (19) yields

$$\frac{\partial \bar{T}_f}{\partial \tau} + \frac{\partial \bar{T}_f}{\partial \eta} = \zeta (\bar{T}_a - \bar{T}_f) \quad (22)$$

$$\frac{\partial \bar{T}_a}{\partial \tau} = (\bar{T}_f - \bar{T}_a). \quad (23)$$

Taking the Laplace transforms of Eqs. (22) and (23), with initial conditions equal to zero, yields

$$s \hat{T}_f + \frac{\partial \hat{T}_f}{\partial \eta} = \zeta (\hat{T}_a - \hat{T}_f) \quad (24)$$

$$s \hat{T}_a = (\hat{T}_f - \hat{T}_a), \quad (25)$$

where $s = 2i\pi f \tau_a$, and f is the frequency in Hz. Eliminating \hat{T}_a yields

$$\frac{\partial \hat{T}_f}{\partial \eta} + \frac{s}{s+1} (s + \zeta + 1) \hat{T}_f = 0. \quad (26)$$

This equation is readily solved to provide an expression for the fluid temperature as a function of dimensionless length and dimensionless frequency

$$\hat{T}_f(\eta, s) = \hat{T}_f(\eta=0, s) \cdot \exp \left[\frac{-s}{s+1} (s + \zeta + 1) \eta \right]. \quad (27)$$

Thus, the tube bank transfer function [24] is given by

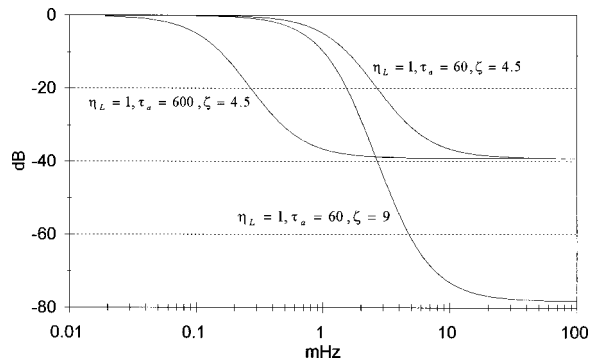


Fig. 4 Theoretical model transfer functions versus frequency

$$\begin{aligned} Trm_a(s) &= \frac{\hat{T}_f(\eta = \eta_L, s)}{\hat{T}_f(\eta = 0, s)} = \exp\left[\frac{-s}{s+1}(s+\zeta+1)\eta_L\right] \\ &= \exp\left[\frac{-s\cdot\zeta\cdot\eta_L}{s+1}\right] \cdot \exp[-s\cdot\eta_L], \end{aligned} \quad (28)$$

where the latter form separates the effect of transport delay, $\exp(-s\cdot\eta_L)$, from other effects in the attenuator. Since only the real part of the exponent affects the magnitude of the transfer function, the transfer function magnitude can be expressed in the form

$$Trm_a(s) = \exp\left[-\zeta\cdot\eta_L\cdot\text{Re}\left(\frac{s}{s+1}\right)\right]. \quad (29)$$

Figure 4 depicts the tube bank-attenuator transfer function for several values of η_L , ζ , and τ_a . For a given dimensionless length, η_L , the heat capacity ratio, ζ , determines the magnitude of the asymptotic attenuation. In addition, for a given η_L , the range of frequencies optimally attenuated increases as τ_a increases, so that attenuation extends to lower disturbance frequencies. In particular, the asymptotic attenuation is proportional to

$$\zeta\cdot\eta_L = \frac{C_a}{C_f} \frac{L}{2\bar{w}\tau_a} = \frac{1}{\dot{m}c_f R}, \quad (30)$$

which means that given a fluid with mass flow rate, \dot{m} , and specific heat, c_f , the total thermal resistance between the fluid flow and the attenuator medium determines the asymptotic attenuation. In terms of dimensional variables, the transfer function, Eq. (29), is

$$Trm_a(f) = \exp\left[-\frac{1}{\dot{m}c_f R} \cdot \text{Re}\left(\frac{2i\pi f\tau_a}{2i\pi f\tau_a + 1}\right)\right]. \quad (31)$$

This form more clearly shows the effect of τ_a in determining the frequency at which significant attenuation occurs. Given a thermal resistance to achieve an asymptotic attenuation requirement, the heat capacity of the attenuator, C_a , determines the attenuator time constant, which in turn determines the frequency range over which asymptotic attenuation is closely approached.

5 Tube Bank-Attenuator Configuration and Properties

In order to efficiently package a large heat capacity (to attenuate a wide range of frequencies), the attenuator medium should have large specific heat capacity (heat capacity per volume). Other considerations for the medium include cost and ease of distributing the material about the tubes in order to provide the desired thermal resistance for optimal attenuation. Water fulfills these requirements well since it is inexpensive and has a specific capacity

(4.2 MJ K⁻¹ m⁻³) which is higher than that of aluminum, steel, copper, and numerous other, more expensive materials.

The device configuration consists of an externally insulated 208 liter (55-gallon) drum, 947 nylon tubes (each 0.8 m long and 4.8 mm in diameter), and 4 acrylic spacer plates (Fig. 3). Chilled water enters the attenuator from the top, flows to the bottom where it is distributed to the tube bank through a lower accumulator, flows upward through the tubes into an upper accumulator, and then exits. Nylon was chosen as the tube material because of its low cost and suitable thermal resistance. The tubes are arranged in a hexagonal pattern with tube center spacing of approximately 16 mm. Thus, each tube is surrounded by an annulus of attenuator medium having an effective radius of approximately 8 mm. The tube aspect ratio condition of Eq. (2) is satisfied for this configuration since $r/L = O(10^{-2})$. Also, the radially lumped model is valid for frequencies below an upper frequency limit determined by the inverse of the radial diffusion time scale

$$f_1 \approx \frac{\alpha_a}{(r_m)^2} = O(10^{-2} \text{ Hz}), \quad (32)$$

where r_m is the radius encompassing half of the area of the attenuator medium.

Because the in-tube temperature variations are small relative to the dominant input temperature variations, the tube wall is approximately isothermal. Thus, the convection coefficient can be computed from the laminar, thermally fully developed flow condition [25]

$$h_f = \text{Nu} \frac{k_f}{D_f} = 3.66 \frac{k_f}{D_f}. \quad (33)$$

Given h_f , the fluid thermal resistance is

$$R_f = \frac{1}{h_f A_s}, \quad (34)$$

where A_s is the convection surface area. The validity of the assumption of thermally fully developed flow is supported by the fact that the thermal development length [23] for these parameters is approximately 2 percent of the tube length.

The attenuator thermal resistance, R_a , is based on the approximation of steady state conduction through a stationary fluid. From Eqs. (3) and (32), the ratio of the time derivative to radial diffusion terms is small, so that the temperature field is approximately steady within the attenuator medium. Thus, the effective attenuator thermal resistance is

$$R_a = \frac{\ln(r_m/r_t)}{2\pi k_a L}. \quad (35)$$

6 Accumulator and Total Transfer Functions

In order to complete the model of the entire device, the transfer functions of the upper and lower accumulators must be developed. Chilled water is distributed to the tube bank by the lower accumulator and collects prior to exiting in the upper accumulator. The lower accumulator feeds the tube bank through a perforated-tube distribution manifold containing numerous small holes (Fig. 3). The flow through each hole produces a small jet within the lower accumulator, which in turn, induces strong mixing. It is thus assumed that the lower accumulator functions as a perfectly mixed volume, with the corresponding lumped energy equation given by

$$\rho_f \frac{d\bar{T}_{la}}{dt} V_{la} = \dot{M}(T_{in}(t) - \bar{T}_{la}), \quad (36)$$

where \dot{M} is the total mass flow rate for all of the tubes, $T_{in}(t)$ is the time varying input temperature, V_{la} is the lower accumulator volume, and \bar{T}_{la} is the average lower accumulator temperature. Taking the Laplace transform yields the transfer function

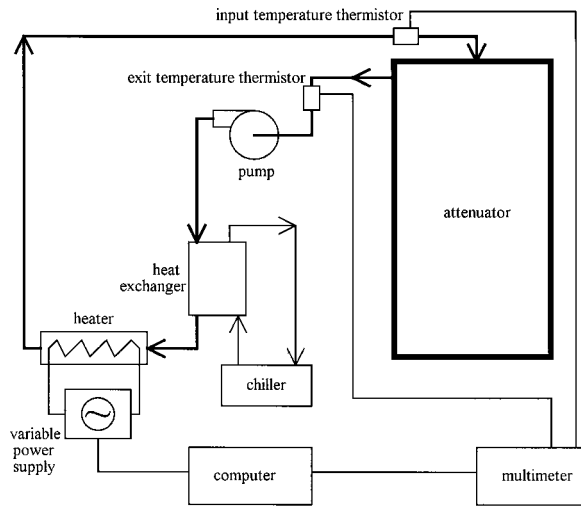


Fig. 5 Attenuator test setup

$$Tr_{la}(s) = \frac{1}{1 + \tau_m s}, \quad (37)$$

where $\tau_m = \rho_f V_{la} / \dot{M}$ is the characteristic residence time for the flow in the lower accumulator.

In contrast to the lower accumulator, mixing in the upper accumulator is relatively weak. In addition, since the length, L_{ua} , of the upper accumulator is much smaller than the radius, r_{ua} , axial conduction dominates the heat transfer. Considering the scales of each term in the associated energy equation, and assuming that the flow is essentially vertical and uniform across the upper accumulator, the governing equation is

$$\frac{dT_{ua}}{dt} + \bar{w}_{ua} \frac{dT_{ua}}{dz} = \alpha_f \frac{d^2 T_{ua}}{dz^2}, \quad (38)$$

where \bar{w}_{ua} is the uniform vertical velocity across the accumulator. Taking the Laplace transform of Eq. (38), the associated transfer function is

$$Tr_{ua}(s) = \exp(\lambda L_{ua}), \quad (39)$$

where $\lambda = (\bar{w}_{ua} - \sqrt{\bar{w}_{ua}^2 + 4\alpha_f^2}) / 2\alpha_f$. Given Eqs. (28), (37), and (39), the total transfer function of the entire attenuator device is

$$Tr_T(s) = Tr_{la}(s) \cdot Tr_a(s) \cdot Tr_{ua}(s). \quad (40)$$

7 Experimental Setup

An experimental setup for testing attenuator performance is shown in Fig. 5. A constant-displacement pump maintains a constant flow rate of water through the system. A cartridge heater, controlled through a computer-based data acquisition board and connected to a variable power supply, is used to impose single-frequency sinusoidal temperature variations on the flow. The computer also captures input and output temperatures from the thermal gradient attenuator using thermistors and a high-precision digital multimeter (via GPIB interface).

8 Transfer Function Results

Measured and theoretical transfer functions for the thermal gradient attenuator are shown in Fig. 6, where attenuation is shown for 18 imposed frequencies. The root mean squared (RMS) difference between measured and theoretical values is approximately 3 dB. Also shown for reference is a transfer function corresponding to a perfectly mixed attenuator volume and a transfer function corresponding to an attenuator dominated by axial conduction, where the total volume is equal to that of the experimental device.

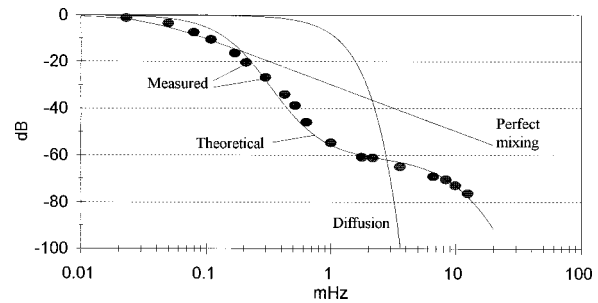


Fig. 6 Drum attenuator transfer functions versus frequency; measured, theoretical, perfect mixing, and diffusion for 2.5 l/min flow rate

In the region near 1 mHz, where time derivatives of temperature are largest (and are thus least conducive to precision thermal control), the attenuator provides in excess of 20 dB more attenuation than a perfect mixer. Likewise, in the lower portion of the frequency range, $f < 3$ mHz, the attenuator provides significantly more attenuation than does axial diffusion. Although axial diffusion provides more attenuation for $f > 3$ mHz, this occurs beyond the point where the attenuator has already provided 60 dB of attenuation.

Attenuator performance compares favorably with that obtained by Ogasawara [14]. Ogasawara's device consisted of a fluid-filled enclosure in which spiral baffles promoted mixing of water. He reported that the device reduced temperature variations by a factor of 3. By contrast, and as shown in Fig. 6, the thermal gradient attenuator provides attenuation on the order of 60 dB, corresponding to factor of reduction on the order of 10^3 . Interestingly, it appears that Ogasawara's device can be modeled as a perfectly mixed volume; indeed, the order of attenuation obtained by Ogasawara is consistent with the degree of attenuation associated with a perfect mixer.

Four additional sets of attenuation data are shown in Fig. 7, with standard measurement [26] and model uncertainties. Each data set, corresponding to a different chilled water flow rate, was obtained following a minor device modification (where a seal was installed to eliminate small leaks between the tube bank and the lower accumulator). Consistent with the results shown in Fig. 6, the measurements in Fig. 7 match theoretical predictions to within 5 dB RMS. The largest discrepancies appear at very low frequencies where chilled water input temperature variations are small and large attenuation is not needed. The theoretical envelopes representing model uncertainty are calculated via Eq. (40) using measured mean flow rates and mean attenuator water levels along

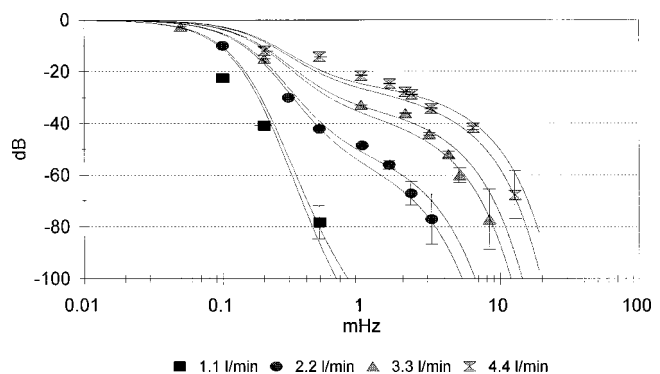


Fig. 7 Measured and theoretical transfer functions versus frequency, with uncertainty bars on measured points and uncertainty envelopes for theoretical curves, where envelopes reflect uncertainty in flow rates and accumulator water levels

with associated estimated uncertainties. Measurement uncertainty is estimated by first expressing the system transfer function as the ratio of the amplitudes of the output and input temperature variations

$$Tr(f) = \frac{T_{out}(f)}{T_{in}(f)}. \quad (41)$$

The uncertainty in the transfer function is then estimated by assuming that individual uncertainties are independent and normally distributed, so that [27]

$$\sigma_{Tr} = \left[\left(\frac{\partial Tr}{\partial T_{out}} \right)^2 \cdot \sigma_{T_{out}}^2 + \left(\frac{\partial Tr}{\partial T_{in}} \right)^2 \cdot \sigma_{T_{in}}^2 \right]^{1/2}, \quad (42)$$

where

$$\sigma_{T_{out}}^2 = \sigma_{T_{out}}^2(f) = (S_t \cdot \sigma_T)^2 + (T_{out}(f) \cdot \sigma_s)^2 \quad (43)$$

$$\sigma_{T_{in}}^2 = \sigma_{T_{in}}^2(f) = (S_t \cdot \sigma_T)^2 + (T_{in}(f) \cdot \sigma_s)^2 \quad (44)$$

and σ_T ($=0.25$ ohm) is the thermistor measurement uncertainty, S_t ($=1.77 \cdot 10^{-3}$ K/ohm) is the nominal thermistor sensitivity, and σ_s ($=5 \cdot 10^{-4}$ K/K) is the uncertainty of S_t .

9 Attenuation of Broadband Thermal Variations

The device performance was also tested with the inlet stream subject to broadband thermal disturbances. For this experiment, in-house chilled water serves as the control fluid stream, where the associated power spectrum in Fig. 2 shows that temperature variations are spectrally broadband. In addition, a sinusoidal (8.6 mHz) thermal variation was superimposed on the control fluid stream to provide additional higher frequency disturbance to fully test the attenuator performance (at 2.2 l/min flow rate). As shown in Fig. 8, the resultant in-stream temperature exhibits large amplitude (3.5 K peak to peak) variations and equally large (4 K/min) time rates of change.

Under these conditions, the device functions as a low-pass filter, where high frequency disturbances are suppressed to magnitudes below measurement sensitivity (for the 8.6 mHz variation), and transmitted low frequency disturbances are reduced in magnitude; see Fig. 9. The dominant variation in the output stream reflects the slow periodic oscillation of the input at approximately 3 cycles every 2 hours (≈ 0.4 mHz). The attenuation of approximately 2 orders of magnitude for this low frequency (Fig. 7) is consistent with the data in Figs. 8 and 9.

The most important result of Fig. 9 is the dramatic reduction in the short-term variations, or temperature derivative. Achieving temperature control better than milliKelvin levels without filtering the input stream in Fig. 8 would be very difficult because of the large and rapidly changing disturbances. After attenuation by the attenuator device, the short-term deviations are reduced by 3 or-

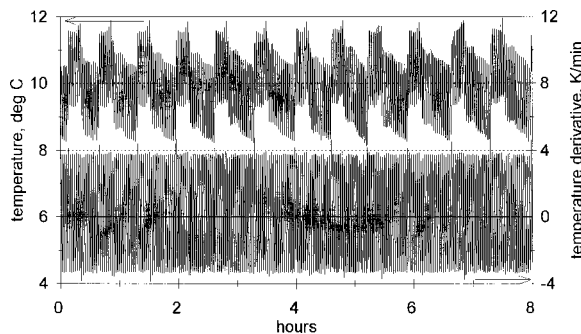


Fig. 8 Attenuator input temperature and temperature derivative versus time for an unfiltered chilled water stream with a superimposed 8.6 mHz sinusoid

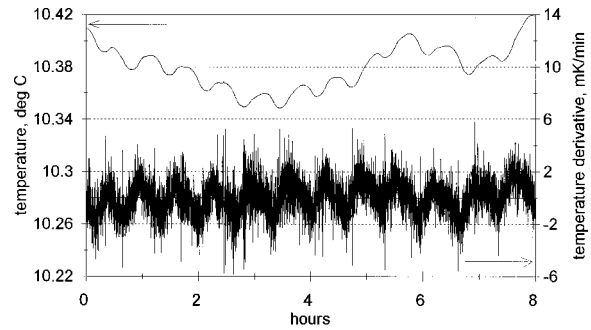


Fig. 9 Attenuator output temperature and temperature derivative versus time for the unfiltered chilled water stream with a superimposed 8.6 mHz sinusoid

ders of magnitude to order 1 mK/min, which is a suitably well behaved source for precision temperature control.

10 Summary and Conclusions

The analysis, design, and performance of a precision thermal gradient attenuator has been presented. For purposes of analysis, the system was decomposed into three subsystems: a lower accumulator where the control fluid collects and is passively mixed, a tube bank-attenuator where the control fluid exchanges heat with a surrounding, stagnant attenuation medium (here, water), and an upper accumulator where the control fluid again collects prior to exiting the device. Analytic expressions have been developed to describe the performance of each subsystem and the total system.

A set of experiments in which sinusoidal temperature disturbances are imposed on the control fluid stream, have been performed in order to evaluate device performance. Performance measured over a disturbance frequency range from 0.1 mHz to 10 mHz, and at four representative control stream flow rates, is well described by the analytic model. At all but the lowest frequencies, the system provides significantly greater attenuation than that produced by a perfectly mixed volume. In addition, a comparison with earlier work [14] shows that the present device provides frequency-dependent attenuation which is two, and, at higher frequencies, almost three orders of magnitude greater than the earlier device.

Finally, an experiment was performed to investigate the system performance under conditions where the control stream is subject to broadband thermal disturbances. In this case, the system functions as a low-pass filter/attenuator, effectively eliminating spectral components having periods shorter than the device thermal equilibration time, τ_d , and attenuating lower frequency components. Consistent with attenuation observed for spectrally pure disturbances, it is found that unfiltered temperature oscillations exhibit increasing attenuation with increasing spectral frequency.

The analytic model allows prediction of system response and provides simple criteria for designing system performance. The model shows that for fixed control stream flow rate, the magnitude of maximal attenuation can be tuned by adjusting the total thermal resistance between the stream and the attenuator medium. Given a thermal resistance that produces a desired maximal attenuation, the frequency range subject to maximal attenuation can be tuned by adjusting the attenuator heat capacity. The analysis and design are general and should prove useful in the design and analysis of other high-throughput precision temperature control systems.

Acknowledgment

This work was supported by the National Science Foundation, Grant No. DMI-9500390.

Nomenclature

α_a, α_f	= attenuator and fluid diffusivities
A_s	= convection surface area
β	= thermal expansion coefficient
C_a, C_f	= single tube attenuator and fluid total heat capacities
D_f	= fluid diameter
f	= frequency, Hz
f_l	= upper frequency limit determined by the inverse radial diffusion time scale
h_f	= fluid convection coefficient
k_a, k_f, k_t	= attenuator, fluid, and tube conductivities l/min
L	= attenuator tube length
L_{ua}	= upper accumulator length
\dot{m}	= mass flow rate of water through each tube
\dot{M}	= total mass flow rate of water through the attenuator device
η	= dimensionless axial coordinate
η_L	= dimensionless tube length
$O()$	= order of magnitude of the expression
ρ_f	= fluid density
r_a, r_f, r_t	= attenuator, fluid and tube outer radii
r_m	= radius encompassing half of the attenuator area
r_{ua}	= upper accumulator outer radius
R	= thermal resistance between the fluid flow and the lumped attenuator medium
R_a, R_f, R_t	= attenuator, fluid, and tube thermal resistances
s	= dimensionless Laplace transform variable
τ	= dimensionless time
τ_a, τ_f	= attenuator and fluid time constants
τ_m	= characteristic residence time for the flow in the lower accumulator
T	= temperature
\bar{T}_a, \bar{T}_f	= radially averaged mean attenuator and fluid temperatures
\hat{T}_a, \hat{T}_f	= Laplace transformed mean attenuator and fluid temperatures
T_{in}, T_{out}	= time varying input and output temperatures
\bar{T}_{la}	= lower accumulator average temperature
Tr	= transfer function
$Tr_a, Tr_{la}, Tr_{ua}, Tr_T$	= attenuator, lower accumulator, upper accumulator, and total transfer functions
Trm_a	= attenuator transform function magnitude
u_{β}	= buoyancy velocity scale
\mathbf{u}	= vector velocity field
V_{la}	= volume of lower accumulator
w	= axial velocity in the z -direction

\bar{w}	= average axial in-tube fluid velocity
\bar{w}_{ua}	= average axial velocity in the upper accumulator
ζ	= heat capacity ratio: attenuator to fluid

References

- [1] Bryan, J., 1990, "International Status of Thermal Error Research," *Annals of the CIRP*, **39**, pp. 645–656.
- [2] Slocum, A. H., 1992, *Precision Machine Design*, Prentice Hall, NJ, p. 96.
- [3] Smith, S. T., and Chetwynd, D. G., 1997, *Foundations of Ultraprecision Mechanism Design*, Gordon and Breach, Amsterdam, p. 84.
- [4] Cutkosky, R. D., and Field, B. F., 1974, "Standard Cell Enclosure with 20 μ K Stability," *IEEE Trans. Instrum. Meas.*, **23**, pp. 295–298.
- [5] Lee, H. S., Yang, S. H., and Chung, N. S., 1990, "Temperature Controller Using an Error Signal Modulation," *Rev. Sci. Instrum.*, **61**, pp. 1329–1331.
- [6] Dratler, J., 1974, "A Proportional Thermostat with 10 Microdegree Stability," *Rev. Sci. Instrum.*, **45**, pp. 1435–1444.
- [7] Esman, R. D., and Rode, D. L., 1983, "100 μ K Temperature Controller," *Rev. Sci. Instrum.*, **54**, pp. 1368–1370.
- [8] Cutkosky, R. D., and Davis, R. S., 1981, "Simple Control Circuit for Temperature Control and Other Bridge Applications," *Rev. Sci. Instrum.*, **52**, pp. 1403–1405.
- [9] Strem, R. B., Das, B. K., and Greer, S. C., 1981, "Digital Temperature Control and Measurement System," *Rev. Sci. Instrum.*, **52**, pp. 1705–1708.
- [10] Williams, G. I., and House, W. A., 1981, "Thermistor Controlled Water/Oil Bath for Precision Measurements in the Range 0–30 C," *J. Phys. E*, **14**, pp. 755–760.
- [11] Miller, R. J., and Gleeson, H. F., 1994, "A Computer Interfaced High-Stability Temperature Controller and Heating Stage for Optical Microscopy," *Measurement Science and Technology*, **14**, pp. 904–911.
- [12] Sarid, D., and Cannell, D. S., 1974, "A 15 Microdegree Temperature Controller," *Rev. Sci. Instrum.*, **45**, pp. 1082–1089.
- [13] Harvey, M. E., 1968, "Precision Temperature-Controlled Water Bath," *Rev. Sci. Instrum.*, **39**, pp. 13–18.
- [14] Ogasawara, H., 1986, "Method of Precision Temperature Control Using Flowing Water," *Rev. Sci. Instrum.*, **57**, pp. 3048–3052.
- [15] Priel, S., 1978, "Thermostat with a Stability of 3.5 μ K," *J. Phys. E*, **11**, pp. 27–30.
- [16] Iglesias, M. C. L., and Baron, M., 1990, "Temperature Control in Small Air-Heated Measuring Cells," *Rev. Sci. Instrum.*, **61**, pp. 2245–2246.
- [17] Ogasawara, H., and Nishimura, J., 1982, "Frequency Stabilization of Internal-Mirror He-Ne Lasers by a Flowing Water Method," *Appl. Opt.*, **21**, pp. 1156–1157.
- [18] Ogasawara, H., and Nishimura, J., 1983, "Frequency Stabilization of Internal-Mirror He-Ne Lasers," *Appl. Opt.*, **22**, pp. 655–657.
- [19] Sydenham, P. H., and Collins, G. C., 1975, "Thermistor Controller with Microkelvin Stability," *J. Phys. E*, **8**, pp. 311–315.
- [20] Neto, F. S., and Cotta, R. M., 1992, "Counterflow Double-Pipe Heat Exchanger Analysis Using a Mixed Lumped-Differential Formulation," *Int. J. Heat Mass Transf.*, **35**, pp. 1723–1731.
- [21] Neto, F. S., and Cotta, R. M., 1993, "Dynamic Analysis of Double-Pipe Heat Exchangers Subjected to Periodic Inlet Temperature Disturbances," *Wärme und Stoffübertragung*, **18**, pp. 497–503.
- [22] Ozisik, M. N., and Murray, R. L., 1974, "On the Solution of Linear Diffusion Problems With Variable Boundary Conditions," *ASME J. Heat Transfer*, **96**, pp. 48–51.
- [23] Incropera, F., and DeWitt, D., 1990, *Introduction to Heat Transfer*, Wiley, New York, p. 432.
- [24] Dorf, R. C., and Bishop, R. H., 1995, *Modern Control Systems*, Addison-Wesley, New York, p. 394.
- [25] Bejan, A., 1984, *Convection Heat Transfer*, Wiley, New York, p. 298.
- [26] International Organization for Standardization, 1993, *Guide to the Expression of Uncertainty in Measurements*, Geneva.
- [27] Beckwith, T. G., Marangoni, R. D., and Lienhard, J. H., 1993, *Mechanical Measurements*, Addison-Wesley, New York, p. 82.

This section contains shorter technical papers. These shorter papers will be subjected to the same review process as that for full papers.

Detailed Heat Transfer Coefficient Distributions on a Large-Scale Gas Turbine Blade Tip

Shuye Teng

Je-Chin Han

e-mail: jchan@mengr.tamu.edu

G. M. S. Azad

Turbine Heat Transfer Laboratory,
Department of Mechanical Engineering,
Texas A&M University,
College Station, TX 77843-3123

Measurements of detailed heat transfer coefficient distributions on a turbine blade tip were performed in a large-scale, low-speed wind tunnel facility. Tests were made on a five-blade linear cascade. The low-speed wind tunnel is designed to accommodate the 107.49 deg turn of the blade cascade. The mainstream Reynolds number based on cascade exit velocity was 5.3×10^5 . Upstream unsteady wakes were simulated using a spoke-wheel type wake generator. The wake Strouhal number was kept at 0 or 0.1. The central blade had a variable tip gap clearance. Measurements were made at three different tip gap clearances of about 1.1 percent, 2.1 percent, and 3 percent of the blade span. Static pressure distributions were measured in the blade mid-span and on the shroud surface. Detailed heat transfer coefficient distributions were measured on the blade tip surface using a transient liquid crystal technique. Results show that reduced tip clearance leads to reduced heat transfer coefficient over the blade tip surface. Results also show that reduced tip clearance tends to weaken the unsteady wake effect on blade tip heat transfer.

[DOI: 10.1115/1.1373655]

Keywords: Forced Convection, Heat Transfer, Measurement Techniques, Turbines, Unsteady, Wakes

Introduction

Turbine blades are exposed to high thermal loads associated with high temperature gases from the combustor. Blade tips are one of the most susceptible regions to burnout due to this high thermal load. They are exposed to hot gases on all sides (including pressure side, suction side, and blade tip), typically difficult to

cool, and subjected to potential damage. Therefore, blade tip is recognized as a critical area in turbine blade design. Blade tip failure is primarily caused by the hot leakage flow through the tip gap. The leakage flow accelerates due to pressure difference between the pressure and the suction sides of a blade. This tip leakage flow is undesirable because it might lead to cracking and oxidation along the pressure side tip corner from mid-chord to trailing edge. Blade tip clearance also has a significant influence on turbine efficiency, thus, the designers improve efficiency by either reducing the tip clearance gap if possible or implementing a more effective tip leakage sealing mechanisms. Whatever design choice is selected for a particular turbine blade tip, accurate measurement of detailed flow field and heat transfer in the blade tip region is extremely important. Reliable experimental data are also important for computational model development and efficient cooling system design.

Some studies have focused on the blade tip leakage flow for aerodynamic purposes and studied the effects of blade tip leakage flow on blade performance. Studies by Bindon and Morphus [1] and Bindon [2] have contributed to the general understanding of tip-gap flow patterns. Bindon made pressure and flow field measurements on an axial turbine blade tip in a linear cascade under low-speed conditions. He suggested that the pressure side near tip flow rolls over the tip due to strong active pressure gradient across the tip. The leakage flow has a sink-like character on the pressure side and a source-like character on the suction side near the tip. The tip leakage flow has a significant effect on the blade tip heat transfer, the pressure side near-tip region heat transfer, and the suction side near-tip heat transfer. Moore et al. [3] studied the flow and heat transfer in turbine tip gaps. Yamamoto [4] made flow measurements between adjacent blades in the passage using a five-hole pitot probe. Yaras et al. [5] studied the effect of simulated rotation on tip leakage and found a significant reduction in the gap mass flow rate due to rotation. Sjolander and Cao [6] studied the flow field in an idealized turbine tip gap. Kaiser and Bindon [7] investigated a quantitative analysis of the effects of tip clearance, tip geometry, and multiple stages on turbine stage efficiency in a rotating turbine rig environment.

The earliest study on simulated two-dimensional rectangular tip heat transfer is done by Mayle and Metzger [8]. They studied heat transfer to a simulated tip with and without a rotating shroud. Results showed that the effect of moving wall is negligible over the entire range of parameters considered in the study. The pressure-driven flow through the tip gap mainly influences the blade tip heat transfer. The experiments that neglected the effect of blade rotation may be used to assess the blade tip heat transfer as long as the flow conditions are similar. Metzger and Rued [9] presented heat transfer and flow results in the near tip region of the pressure surface using a two-dimensional rectangular tip simulation and a sink flow. This model simulated a sink flow similar to the sink like characteristics of the blade tip gap on the pressure side. Rued and Metzger [10] presented heat transfer and flow results in the near tip region of the suction surface using a two-dimensional rectangular tip simulation and a source flow. This model simulated a blade suction surface with a gap feeding a source flow similar to the flow exiting the tip gap on the suction

Contributed by the Heat Transfer Division for publication in the JOURNAL OF HEAT TRANSFER. Manuscript received by the Heat Transfer Division June 27, 2000; revision received December 5, 2000. Associate Editor: M. Hunt.

surface of an airfoil. There are some other studies on squealer or grooved blade tip heat transfer because turbine blade tips are typically grooved chordwise to reduce tip flow and heat transfer. The groove acts as a labyrinth seal to increase flow resistance and thus reduce leakage flow that in turn reduces heat transfer. Chyu et al. [11] and Metzger et al. [12] studied heat transfer on grooved two-dimensional rectangular tip model.

With the development of efficient numerical codes, some researchers carried out numerical investigations to predict blade tip heat transfer and flow field. Metzger et al. [13] provided a numerical model to estimate tip and shroud heat transfer. Ameri and Steinthorsson [14,15] predicted rotor blade tip and shroud heat transfer for a SSME (Space Shuttle Main Engine) turbine. Ameri et al. [16] predicted flow and heat transfer on the tip of a GE-E³ first stage rotor blade for both a smooth tip and recessed tip. Ameri et al. [17] also predicted the effects of tip clearance and casing recess on heat transfer and stage efficiency for several squealer blade tip geometries. Most recently, Ameri and Bunker [18] performed a computational study to investigate detailed heat transfer distributions on blade tip surfaces for a large power generation turbine. They compared and validated their model with the experimental data of Bunker et al. [19] obtained for the same geometry.

There are comparatively limited data in the open literature on blade tip heat transfer in a cascade environment. Metzger et al. [13] used several heat flux sensors and measured local tip heat fluxes on the flat tips at two different tip gaps in a rotating turbine rig. Yang and Diller [20] reported local heat transfer coefficient at a single location on a turbine blade model with a recessed cavity in a stationary linear cascade. Bunker et al. [19] studied the heat transfer and flow on the first stage blade tip of a power generation gas turbine. The blade tip geometry is that of a flat tip with a recessed shroud casing and a nominal tip clearance of approximately 1 percent of the blade span. Tip surface heat transfer is presented for sharp-edge and radius-edge tips, three clearances, and two freestream approach turbulence levels. This study provided nearly full surface information on heat transfer coefficients in a non-rotating cascade environment with appropriate pressure distribution on the blade tip and shroud model. Azad et al. [21,22] studied the flow and heat transfer on the first stage blade tip of an aircraft gas turbine (GE E³ blade). The effects of tip-gap clearance and free-stream turbulence level on the detailed heat transfer coefficient distributions under engine representative flow conditions were obtained for both the plane and squealer tips using a transient liquid crystal technique. They found that the overall heat transfer coefficients on the squealer tip are lower than that on the plane tip under the same conditions.

The present study used a transient liquid crystal technique to measure the detailed heat transfer coefficient distributions on a gas turbine blade tip. Tests were performed on a five-blade linear cascade in a large-scale, low-speed wind tunnel facility. The blade configuration produced a velocity distribution typical of an aircraft gas turbine blade. Pressure measurements were made in the blade mid-span area as well as on the shroud surface, which is opposite the blade tip surface. Heat transfer measurements were made on the blade tip surface for a tip gap clearance of 1.1 percent, 2.1 percent, and 3 percent of the blade span (25.4 cm), respectively, under both steady and unsteady flow conditions.

Experimental Apparatus

Figure 1 shows the schematic of the test section and the camera location. The test apparatus consisted of a low speed wind tunnel with an inlet nozzle, a linear turbine blade cascade with the test blade in the center, and a suction type blower. The wind tunnel was designed to accommodate the 107.49 deg turn of the blade cascade. The cascade inlet mean velocity was about 20 m/s. The mean velocity increased 2.5 times from the inlet of the cascade to the exit. The inlet Mach number is 0.072. The peak Mach number is 0.144 at $X/SL=0.45$. A spoked wheel type wake generator,

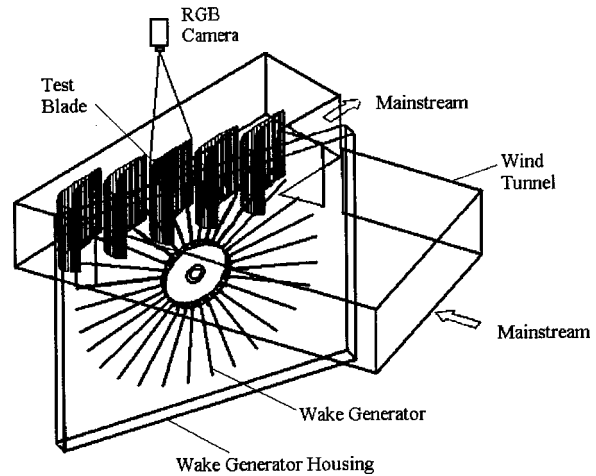


Fig. 1 Five blade cascade with the tip of the central blade coated with liquid crystal and viewed by a RGB camera

similar to the one used by Ou et al. [23], simulated the upstream unsteady wake. The wake generator had 32 rods, each 0.63 cm in diameter, to simulate the trailing edge of an upstream vane. The wake Strouhal number was adjusted by controlling the rod rotation speed (N). The blade configuration, scaled up five times, produced a velocity distribution typical of an advanced high-pressure aircraft turbine blade row. The unsteady wakes are actually velocity deficiencies caused by the blockage of the mainstream flow by the rotating rods. The ensemble-averaged turbulence intensity profiles at the cascade inlet (Du et al. [24]) show that intensity could be as high as 20 percent inside the wake, but the time mean averaged turbulence intensity was about 10.4 percent for a wake Strouhal number (S) of 0.1. For cases without the unsteady wake effect, the time mean averaged turbulence is about 0.7 percent.

Figure 2 presents a schematic view of the blade tip heat transfer setup. The cascade had five blades, each with an axial chord length of 17 cm and a radial span of 25.4 cm. The blade spacing was 17.01 cm at the cascade inlet and the throat-to-blade span ratio was 0.2. The central blade was the test blade with variable tip gap clearances. The neighborhood blades did not have tip gap clearance. The test blade was made of non-conductive material (RENSHAPE) to satisfy the semi-infinite solid assumption used in the transient liquid crystal technique. It is a non-conductive insulating material, similar to wood. The maximum blade thickness at 50 percent span is 4.80 cm. The tip of the central test blade was coated with a thin layer of liquid crystal for detailed heat transfer measurement.

Figure 3 shows the pressure tap locations on the test blade and the shroud opposite the test blade. The tap holes had an outer and inner diameter of 1.65 mm and 0.83 mm, respectively. One set of tap holes was located in the mid-span (50 percent of the blade span) of the test blade. The pressure taps were placed on both the pressure and suction surfaces. Pressure taps were also placed on the shroud surface, as shown in Fig. 3, to measure the pressure distribution on the shroud surface, which is a good indicator of the tip surface pressure. A total of 48 pressure taps were used to measure the shroud surface pressure. One subset of pressure taps was located around the tip perimeter and along the central camber line, and a second subset of taps was located 10 mm outside the tip edge. All these pressure taps were located on the shroud surface opposite the tip surface. No pressure taps were placed on the tip surface. These pressure distributions were useful in estimating the tip leakage flow. Pressures were measured by an inclined manometer.

Figure 4 presents the heater instrumentation for the blade tip

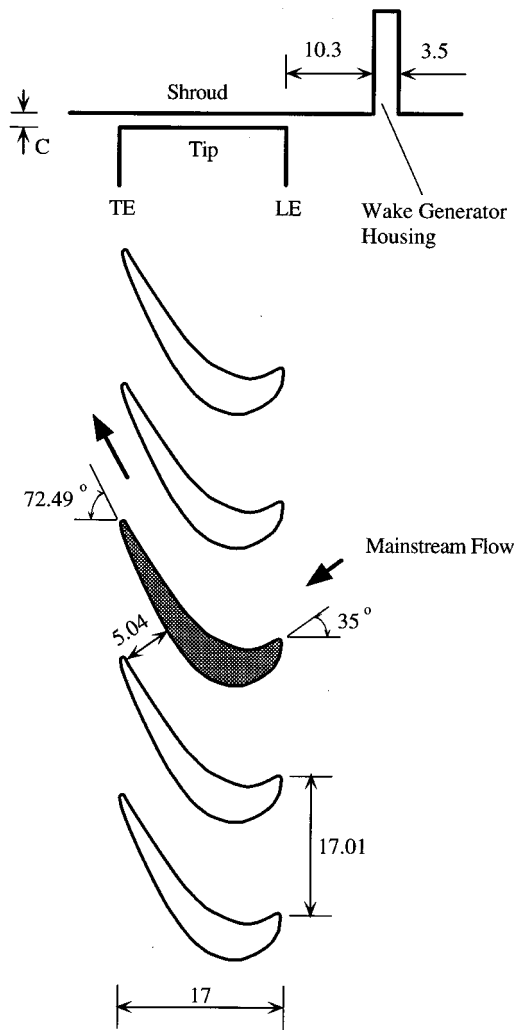


Fig. 2 Schematic view of blade tip heat transfer setup (unit: cm)

heat transfer experiment. The inside of the top 1/4 portion of the blade was hollow for heater instrumentation. The blade tip portion had a thickness of 0.64 cm, which was thick enough to meet the one-dimensional semi-infinite model assumption used in the transient liquid crystal method. The blade tip was heated underneath by a copper plate with a heating wire. Heating wire was uniformly distributed over one side of a 0.1 cm thick copper plate. The other side of the copper plate was tightly glued to the underside of the blade tip portion. This ensured the uniform heating of the blade tip region. However, there was no heating wire in the trailing edge portion because the blade was too thin there. The blade shell had a thickness of 0.48 cm. The inside surface of the blade shell was instrumented with a thin foil heater. The foil had a thickness of 0.0038 cm. During the test, the blade shell was heated to a temperature as high as the blade tip to prevent heat conduction from the edge of the blade tip to the rest of the blade. After both the heating wire and the foil heater had been instrumented, the top hollow portion was filled with fiber glass insulation material. The top portion was then glued together with the rest of the blade model. The span of this test blade was 24.64 cm. This test blade will provide a up to 3 percent tip clearance from the shroud. The four blades for flow guidance (as shown in Fig. 2) have a span of 25.4 cm and there is no tip clearance between the guide blades and the shroud. The test blade was fastened to the bottom endwall with screws. Different hard rubber gaskets of desired thickness were placed between the test blade bottom and the endwall to

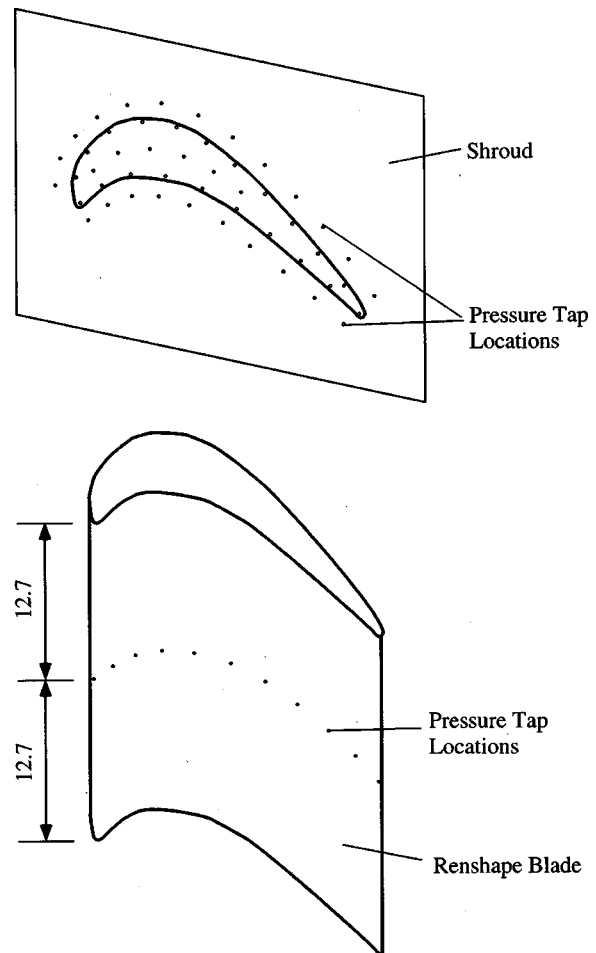


Fig. 3 Pressure tap locations on blade and shroud (unit: cm)

create tip gaps of the desired heights. The 1.1 percent, 2.1 percent, and 3.1 percent tip gaps are defined according to the span of the guide blades.

Before the heat transfer experiment, the initial temperatures, T_i , were obtained by placing 36 thermocouples on the tip surface.

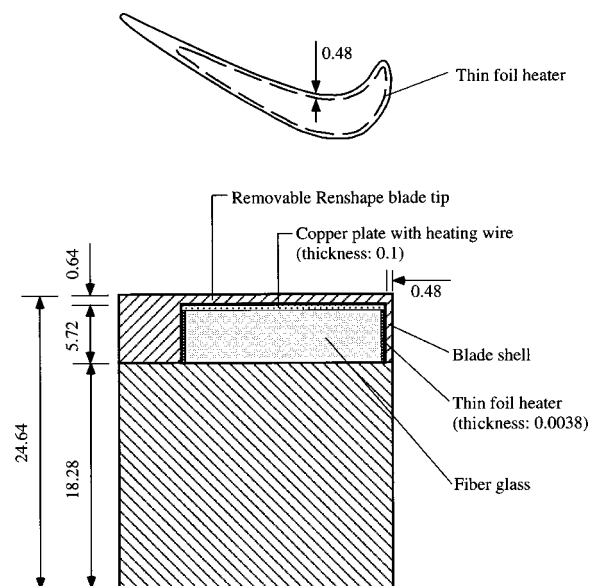


Fig. 4 Blade tip heater instrumentation (unit: cm)

One set of thermocouples was located along the tip perimeter and another along the central camber line. These temperatures were then interpolated to get an initial temperature map over the whole tip surface. The uniformity of the surface temperature with heating was within $\pm 2^\circ\text{C}$. An interpolation scheme was used to further reduce the temperature non-uniformity in the initial surface temperature to within $\pm 0.2^\circ\text{C}$. In the heat transfer experiment, all thermocouples were taken away. The whole blade tip surface was coated with a thin layer of liquid crystal (Hallcrest, Type BM/R32C5W/C17-10). Color to temperature calibration was done on a copper bar coated with liquid crystal as suggested by Vedula and Metzger [25]. The primary color display of liquid crystal is from an initial colorless stage to red, green, blue, and then colorless again. The color change temperatures to red, green, and blue are 31.6°C , 32.7°C , and 37.2°C , respectively. The coating was a light spray of several μm thickness. Ireland and Jones [26] showed the response time for the liquid crystals to be only a few milliseconds. The duration of the transient test is much longer than the response time of the liquid crystal. The test blade tip surface was heated uniformly by the copper plate with uniformly distributed heating wire. The blade surface temperature was monitored during heating using two embedded thermocouples placed near the top portion of both the suction and pressure sides. In the present study, the blade surface was preheated to a temperature above the liquid crystal blue color (37.2°C). The liquid crystal color change time was measured using a high precision image processing system. The system consisted of a RGB (Red, Green, and Blue) camera connected to a color frame grabber board in the PC and a color video monitor. The composite signal from the camera was split into red, green, and blue components before passing on to the color frame grabber board inside the PC. An image processing software was used to measure the time of color change of liquid crystals. Details on the image processing system were presented by Teng et al. [27]. The suction blower was started before the transient test. It took about 5 s for the flow to reach a full cascade inlet speed of 25 m/s. The velocity quickly increases from 15 m/s to 25 m/s in the last second of that 5 s. The image system began to take data 5 s after the start of the blower. Several surface temperature points were taken once more after the suction blower had started for 5 ± 1 seconds to calibrate the initial temperature distribution. The blade surface was heated to a very high temperature so that it would take long time to be cooled down to the temperature where the liquid crystal changes color. The transient test took an average of 60 to 90 s. So the uncertainty caused by the accelerating of the mainstream flow at the very beginning of the transient tests was controlled to be within 8.3 percent.

Flow Condition in the Cascade and Pressure Measurements

Figure 5 presents the surface static pressure distribution measured at the midspan portion of a pressure tap instrumented blade. Pressure distribution was measured using a Dwyer manometer (Model No. 424). The uncertainty is respectively ± 0.01 and ± 0.1 inches of water when ΔP is less or larger than 2 inches of water. The static pressure is presented in terms of P_o/P , which is the ratio of the total pressure (P_o) and the local static pressure (P). Due to the suction wind tunnel, the local static pressure (P) is lower than the atmospheric pressure (P_o). A higher value of P_o/P corresponds to a lower static pressure, while a lower value corresponds to a higher static pressure. The static pressure on the suction side decreases to about $X/SL=0.45$ and then increases slightly to the exit. The static pressure on the pressure side is only slightly less than the total pressure in the region from the leading edge to $X/PL=0.4$. After $X/PL=0.4$, the static pressure of the pressure side begins to decrease all the way to the exit. From Fig. 5 we see that, at 50 percent of the blade span, the maximum static pressure difference between the pressure and suction sides occurs at about $X/SL=X/PL=0.4$.

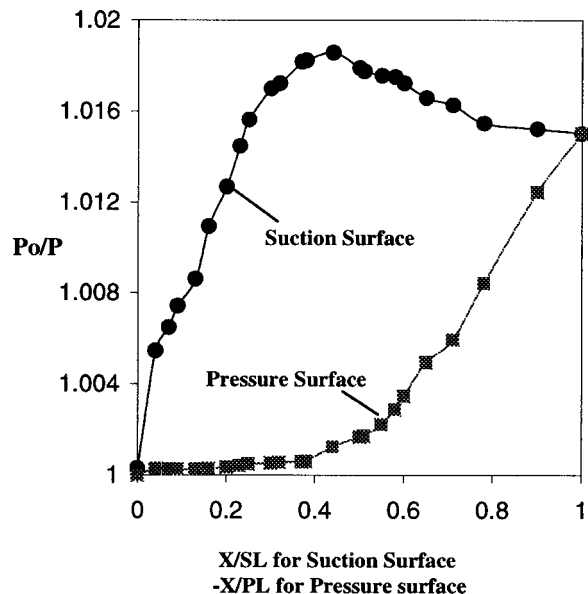


Fig. 5 Static pressure distribution (total pressure/local static pressure) at the blade mid-span portion

Figure 6 presents the static pressure distributions in terms of P_o/P on the shroud surface opposite the blade tip surface for the three different tip gaps: 1.1 percent, 2.1 percent, and 3 percent. Pressure measurements were not made on the blade tip surface.

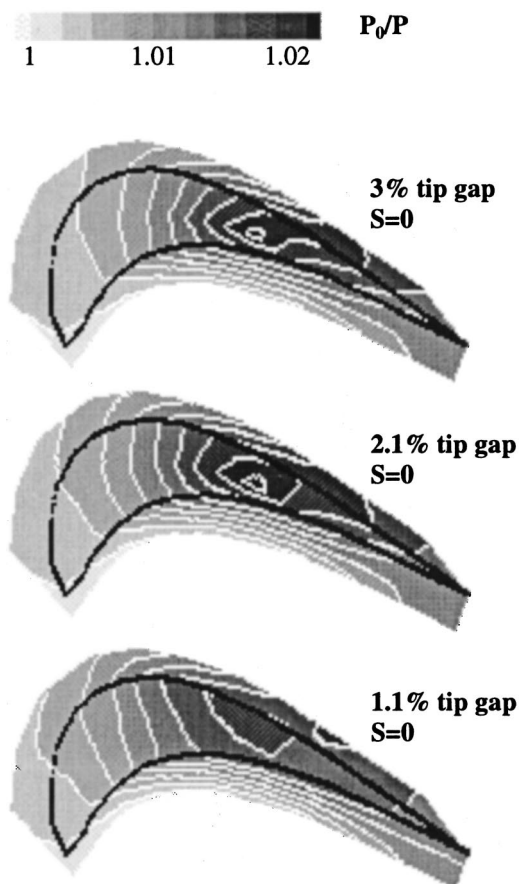


Fig. 6 Static pressure distributions on the shroud surface opposite to the blade tip surface for three different tip gaps

Here, again, a higher value of P_o/P corresponds to a lower static pressure, while a lower value corresponds to a higher static pressure. The contour plot in Fig. 6 helps explain the heat transfer results on the tip surface. The blade shape black curve indicates the blade location under the shroud. The P_o/P distributions clearly demonstrate the tip leakage flow path. The lower P_o/P value (the higher static pressure) near the pressure side leading edge portion indicates where the leakage flow enters the tip gap, while the higher P_o/P value (the lower static pressure) at the suction side near the trailing edge portion indicates that the leakage flow exits the tip gap through this location. The lowest static pressure spot is located at about half chord length and in the center of the blade tip surface. In the leakage flow path, a separation vortex is generated as the incoming flow separates off the inner edge of the pressure side rim and exits near the suction side trailing edge. Sjolander and Cao [6] observed this separation vortex and Ameri et al. [16] also predicted this phenomenon. Due to this separation vortex, the heat transfer rate increases in this region as will be shown in the heat transfer results. Figure 6 shows that, for the smallest tip gap (1.1 percent), the pressure gradient was slightly increased in the front tip portion and greatly reduced in the central portion, which caused the leakage flow to shift slightly forward and be weakened on the central tip surface.

Heat Transfer Data Analysis

A transient liquid crystal technique is used to measure the detailed heat transfer coefficients on the blade tip surface. The technique is similar to the one described by Teng et al. [27]. A one-dimensional transient conduction into a semi-infinite solid with convective boundary condition was assumed. The solution for surface temperature was obtained as

$$\frac{T_w - T_i}{T_m - T_i} = \left[1 - \exp\left(\frac{h^2 \alpha t}{k^2}\right) \operatorname{erfc}\left(\frac{h \sqrt{\alpha t}}{k}\right) \right] \quad (1)$$

where T_w is the wall temperature when liquid crystals change to red from green (32.7°C) at time t , T_i is the initial surface temperature, T_m is the oncoming mainstream flow total temperature, and α and k are the thermal diffusivity and conductivity of the insulation blade material, respectively. The heat transfer coefficient was obtained from Eq. (1). Please note that here the oncoming mainstream flow total temperature T_m (instead of the local bulk flow temperature inside the tip flow passage) is used as a reference temperature to calculate h . The local heat transfer rate is $q = h(T_w - T_m)$. The experimental uncertainty in the measurement of the local heat transfer coefficient, based on Kline and McClintock's [28] methodology, is about ± 8.3 percent. The uncertainty in the region of blade tip edge could be higher due to two-dimensional conduction effect.

Heat Transfer Measurements

Experiments are performed at a cascade exit Reynolds number of 5.3×10^5 . The corresponding flow velocity at the cascade exit is 50 m/s. For the 3 tip gaps, tests were run for no rod, no wake effect cases ($\bar{T}u = 0.7$ percent) and cases with wake Strouhal number of 0.1 ($\bar{T}u = 10.4$ percent).

Figure 7 presents the detailed Nusselt number distributions for the 3 tip gaps under the no wake effect condition. The general experimental trends observed are consistent with the findings of previous investigations. However, the local surface heat transfer distributions are varied among studies because the blade shapes and flow conditions are different. In Fig. 7, regions of high and low heat transfer coefficients are shown very clearly in the detailed distribution contour. The magnitude of the Nusselt number varies from about 200 to over 1000. There is no data for the trailing edge portion (about 25 percent of the chord length) due to the difficulty in instrumenting heating wire in this area.

Figure 7(b) shows the tip local heat transfer contour plots for a typical tip clearance gap of 5.4 mm (2.1 percent of the blade

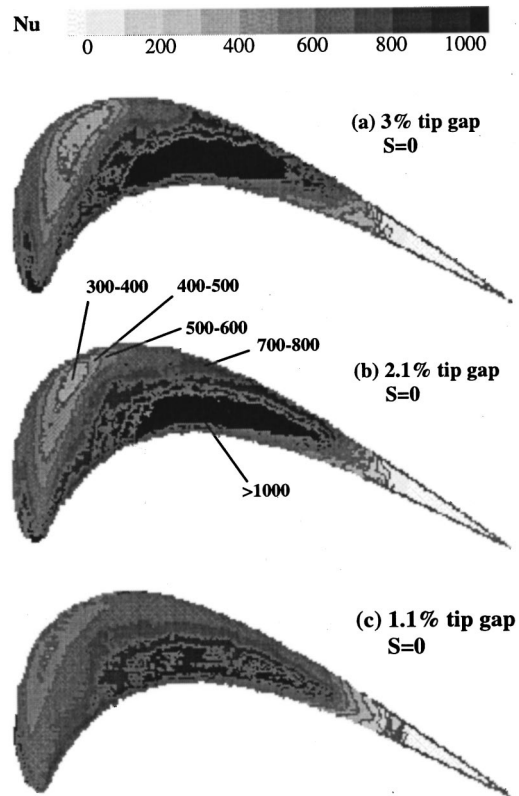


Fig. 7 Detailed Nusselt number distributions without unsteady wake effect ($S=0$)

span). The tip leakage originates from the pressure side near the leading edge, sweeps across from pressure to suction side over the central part of the tip surface, and then exits through the suction side. This area of tip leakage flow corresponds to a high heat transfer coefficient region as shown in Fig. 7(b). The heat transfer coefficient along this tip leakage flow path is higher toward the pressure side than the suction side. This happens because of the flow entrance effect. The leakage flow enters through the pressure side and exits through the suction side. A separation vortex is generated at the pressure side as the incoming flow separates from the inner edge of the pressure side rim and exits near the trailing edge of the blade. The lower heat transfer coefficient toward the suction side may be the result of a boundary layer that develops at the pressure side edge and grows toward the suction side. In addition, although the static pressure of the suction surface is lower than that of the pressure surface, it is higher than the lowest static pressure spot in the central blade region. After the leakage flow passes the lowest pressure spot, it actually encounters an adverse pressure gradient and is forced to change its original flow direction from towards the suction surface to towards the trailing edge. This could also contribute to the comparatively lower heat transfer coefficient in the tip region toward the suction side. In Fig. 7(b), we also notice a triangular region of significantly low heat transfer coefficients between the leading edge and the front suction surface. An explanation for this occurrence can be seen in Fig. 6, the static pressure distribution plot. The pressure gradient is small from the leading edge to $X/C_x = 0.2$, where this low heat transfer triangular region exists, while the pressure gradient is doubled from $X/C_x = 0.2$ to 0.4, where the leakage flow goes through and accelerates. Figure 7(b) also shows a thin high heat transfer trace starting from the leading edge portion and lasts for a short distance along the suction side edge, this is because of a pressure gradient which exists at the leading edge portion. This pressure gradient drives another small leakage flow over the other side of the low heat transfer triangular region.

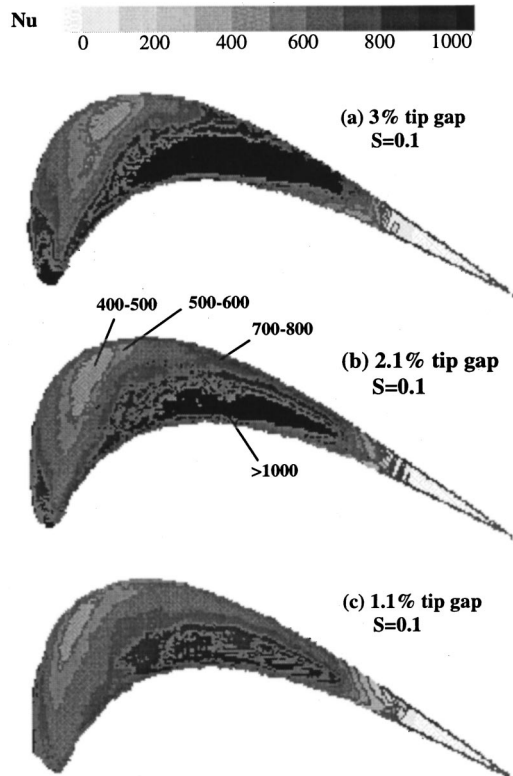


Fig. 8 Detailed Nusselt number distributions without unsteady wake effect ($S=0.1$)

Figure 7(a) and 7(c) present the tip local heat transfer contour plots for another two typical tip clearance gaps of 7.62 mm and 2.86 mm (3 percent and 1.1 percent of the guide blade span), respectively. These figures show that the tip gap has a great effect on tip heat transfer coefficient distribution. A wider tip gap results in an overall higher heat transfer coefficient distribution, while a narrower tip gap results in an overall lower heat transfer coefficient distribution. This is because a wider tip gap allows more leakage flow, while a narrower tip gap increases the flow resistance and decreases the leakage flow. Tip gaps also have an effect on the leakage flow path direction. The narrower tip gap results in the forward shifting of the leakage flow towards the leading edge. The low heat transfer triangular region is reduced and the heat transfer coefficient in this region increases. In Fig. 6 it is observed that, for the smallest tip gap, the pressure gradient is slightly increased in the front tip portion and greatly reduced in the central portion, which causes the leakage flow to shift slightly forward and be weakened on the central tip surface. The other small leakage flow over the suction side edge and leading edge portion is also weakened with a decreased tip gap.

Figure 8 presents the detailed Nusselt number distributions for the 3 tip gaps with unsteady wake effect. Unsteady wake results in an overall, though slightly, increased heat transfer coefficient distribution for the wider tip gap 3 percent. For the tip gap of 2.1 percent, the high heat transfer area in the mid-chord region is slightly reduced due to the unsteady wake effect, which results in slightly lower averaged Nusselt numbers in that region than the case without unsteady wake effect. Unsteady wake does not show much effect on the smallest tip gap of 1.1 percent. This is because the small tip gap has the effect of preventing the unsteady wake from getting into the tip gap and enhancing the tip surface heat transfer. Unsteady wake has the greatest effect on the tip gap of 3 percent: the pressure driven leakage flows are disturbed and the heat transfer coefficient in the low heat transfer triangular region is increased.

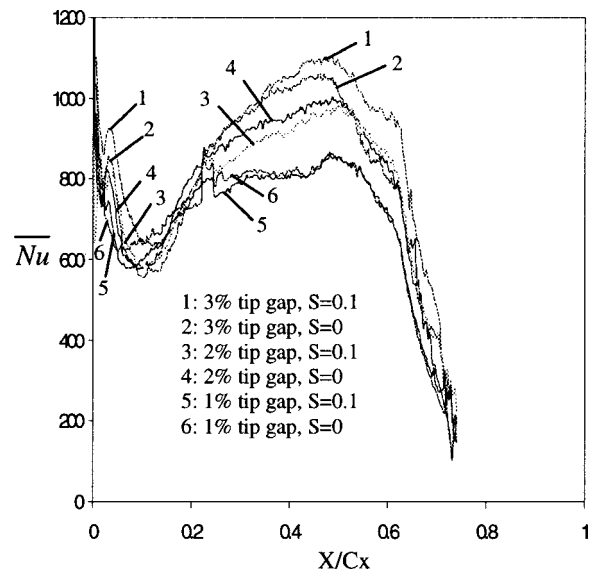


Fig. 9 Blade tip averaged Nusselt number distribution based on local blade thickness

Figure 9 presents the averaged Nusselt number (\bar{Nu}) along the blade tip width direction for the three different tip gaps. It shows that, since the leading edge region has a very high heat transfer coefficient, the averaged Nusselt number decreases at first from $X/C_x=0$ to 0.1. It then increases along the chord length and decreases towards the trailing edge. The highest averaged Nusselt number is shown to be at around $X/C_x=0.5$ for all six cases studied. Differences mainly exist in the mid-chord region from $X/C_x=0.2$ to $X/C_x=0.6$. The largest tip gap, 3 percent, has the highest averaged Nusselt number in comparison to the other two tip gaps. Unsteady wake effect slightly enhances the averaged Nusselt number for the tip gap of 3 percent, but diminishes with a decrease of tip gaps.

Conclusions

Heat transfer coefficients and static pressure distributions on a turbine blade tip were measured in a large-scale low-speed wind tunnel facility. Tests were performed on a five-blade linear cascade. The mainstream Reynolds number based on cascade exit velocity was 5.3×10^5 . The blade was a large-scale two-dimensional model of an aircraft turbine blade. The blade configuration was scaled up to five times and produced a velocity distribution typical of a turbine blade row. Measurements were made at three different tip gap clearances of about 1.1 percent, 2.1 percent, and 3 percent of the blade span. The wake Strouhal number was kept at 0 or 0.1. Detailed heat transfer coefficient distributions were measured using a transient liquid crystal technique. The conclusions based on the experimental results are:

1 The detailed heat transfer measurements combined with the pressure distribution measurements provide comprehensive information and a better understanding of local heat transfer behavior on blade tip surface.

2 A major pressure-driven leakage flow exists between the pressure and suction surfaces in the mid-chord region, which results in a critical region of very high heat transfer coefficients. A minor pressure-driven leakage flow also exists from the leading edge portion and lasts for a short distance along the suction side edge.

3 A triangular region of low heat transfer exists between the leading edge and the front suction surface.

4 Because of the entrance effect on the pressure side tip surface as well as the adverse pressure gradient on the suction side tip

surface in the mid-chord region, a higher heat transfer coefficient exists on the tip surface toward the pressure side as opposed to the suction side.

5 Larger tip gaps result in a higher overall heat transfer coefficient, while smaller tip gaps result in a lower overall heat transfer coefficient. Decreased tip gaps slightly push the tip leakage flow towards the leading edge suction side.

6 Unsteady wake effect slightly enhances the averaged Nusselt number for a tip gap of 3 percent, but diminishes with the decrease of tip gaps.

7 Comparison with previous studies shows that local heat transfer coefficients are sensitive to the blade tip geometry and flow conditions.

The observations and conclusions made out of this work are still limited in the sense that the test was conducted with stationary blades. Cautions need to be taken in extending the findings to rotating systems. In addition, the tests were run in a low speed wind tunnel and there is a difference to the real Mach number distribution of the engine design. Local flow field measurements in the clearance gap region may be needed for a more complete characterization/description of the heat transfer results.

Acknowledgment

This paper is prepared with the support of the NASA Lewis Research Center under grant number NAG3-2002. The NASA technical team is Mr. Robert Boyle and Dr. Raymond Gaugler. This work was also supported by the Texas Higher Education Coordinating Board—Advanced Technology Program under grant number 999903-165. Their support is greatly appreciated.

Nomenclature

- C = tip clearance gap (mm)
 C = blade chord length (23.2 cm, distance between the blade leading edge and trailing edge)
 C_x = blade axial chord length (17 cm)
 d = wake generator rod section diameter (mm)
 h = local blade tip heat transfer coefficient ($\text{W}/\text{m}^2 \cdot ^\circ\text{C}$)
 \bar{h} = averaged blade tip heat transfer coefficient along blade tip width direction
 k = thermal conductivity of blade material ($0.159 \text{ W}/\text{m} \cdot ^\circ\text{C}$)
 k_{air} = thermal conductivity of mainstream air
 LE = leading edge of the blade
 n = number of rods on wake generator
 N = speed of rotating rods
 Nu = local blade tip Nusselt number based on axial chord, hC_x/k_{air}
 \bar{Nu} = averaged blade tip Nusselt number, $\bar{h}C_x/k_{\text{air}}$
 P = local static pressure
 P_0 = total pressure at the inlet (atmospheric pressure)
 PL = streamwise length on the pressure surface (25.6 cm)
 q = local blade tip surface heat transfer rate
 Re = Reynolds number based on exit velocity and axial chord, V_2C_x/ν
 S = wake Strouhal number, $2\pi Ndn/(60V_1)$
 SL = streamwise length on the suction surface (33.1 cm)
 t = liquid crystal color change time
 TE = trailing edge of the blade
 T_i = initial temperature of blade surface
 T_m = mainstream total temperature
 $\bar{T}u$ = free stream mean turbulence intensity at the inlet
 T_w = liquid crystal color change from green to red
 V_1 = cascade inlet velocity
 V_2 = cascade exit velocity
 X = streamwise distance from blade leading edge (Fig. 5), also the distance along chord length (Fig. 9)

- α = thermal diffusivity of blade material
 $(0.135 \times 10^{-6} \text{ m}^2/\text{s})$
 ν = kinematic viscosity of cascade inlet mainstream air

References

- [1] Bindon, J. P., and Morphis, G., 1988, "The Effect of Relative Motion, Blade Edge Radius and Gap Size on the Blade Tip Pressure Distribution in An Annular Turbine Cascade With Clearance," ASME Paper 88-GT-256.
- [2] Bindon, J. P., 1989, "The Measurement and Formation of Tip Clearance Loss," ASME J. Turbomach., **111**, pp. 258–263.
- [3] Moore, J., Moore, J. G., Henry, G. S., and Chaudhury, U., 1989, "Flow and Heat Transfer in Turbine Tip Gaps," ASME J. Turbomach., **111**, pp. 301–309.
- [4] Yamamoto, A., 1989, "Endwall Flow/Loss Mechanisms in a Linear Turbine Cascade With Blade Tip Clearance," ASME J. Turbomach., **111**, pp. 264–275.
- [5] Yaras, M. I., and Sjolander, S. A., 1991, "Effects of Simulated Rotation on Tip Leakage in a Planar Cascade of Turbine Blades: Part I—Tip Gap Flow," ASME Paper 91-GT-127.
- [6] Sjolander, S. A., and Cao, D., 1995, "Measurements of the Flow in an Idealized Turbine Tip Gap," ASME J. Turbomach., **117**, pp. 578–584.
- [7] Kaiser, I., and Bindon, J. P., 1997, "The Effect of Tip Clearance on the Development of Loss Behind a Rotor and a Subsequent Nozzle," ASME Paper 97-GT-53.
- [8] Mayle, R. E., and Metzger, D. E., 1982, "Heat Transfer at the Tip of An Unshrouded Turbine Blade," *Proc. Seventh Int. Heat Transfer Conf.*, Hemisphere Pub., New York, pp. 87–92.
- [9] Metzger, D. E., and Rued, K., 1989, "The Influence of Turbine Clearance Gap Leakage on Passage Velocity and Heat Transfer Near Blade Tips: Part I—Sink Flow Effects on Blade Pressure Side," ASME J. Turbomach., **111**, pp. 284–292.
- [10] Rued, K., and Metzger, D. E., 1989, "The Influence of Turbine Clearance Gap Leakage on Passage Velocity and Heat Transfer Near Blade Tips: Part II—Source Flow Effects on Blade Suction Side," ASME J. Turbomach., **111**, pp. 293–300.
- [11] Chyu, M. K., Moon, H. K., and Metzger, D. E., 1989, "Heat Transfer in the Tip Region of Grooved Turbine Blades," ASME J. Turbomach., **111**, pp. 131–138.
- [12] Metzger, D. E., Bunker, R. S., and Chyu, M. K., 1989, "Cavity Heat Transfer on a Transverse Grooved Wall in a Narrow Flow Channel," ASME J. Heat Transfer, **111**, pp. 73–79.
- [13] Metzger, D. E., Dunn, M. G., and Hah, C., 1991, "Turbine Tip and Shroud Heat Transfer," ASME J. Turbomach., **113**, pp. 502–507.
- [14] Ameri, A. A., and Steinhilsson, E., 1995, "Prediction of Unshrouded Rotor Blade Tip Heat Transfer," ASME Paper 95-GT-142.
- [15] Ameri, A. A., and Steinhilsson, E., 1996, "Analysis of Gas Turbine Rotor Blade Tip and Shroud Heat Transfer," ASME Paper 96-GT-189.
- [16] Ameri, A. A., Steinhilsson, E., and Rigby, L. D., 1997, "Effect of Squealer Tip on Rotor Heat Transfer and Efficiency," ASME Paper 97-GT-128.
- [17] Ameri, A. A., Steinhilsson, E., and Rigby, L. D., 1998, "Effect of Tip Clearance and Casing Recess on Heat Transfer and Stage Efficiency in Axial Turbines," ASME Paper 98-GT-369.
- [18] Ameri, A. A., and Bunker, R. S., 1999, "Heat Transfer and Flow on the First Stage Blade Tip of a Power Generation Gas Turbine: Part 2—Simulation Results," ASME Paper 99-GT-283.
- [19] Bunker, R. S., Bailly, J. C., and Ameri, A. A., 1999, "Heat Transfer and Flow on the First Stage Blade Tip of a Power Generation Gas Turbine: Part 1—Experimental Results," ASME Paper 99-GT-169.
- [20] Yang, T. T., and Diller, T. E., 1995, "Heat Transfer and Flow for a Grooved Turbine Blade Tip in a Transonic Cascade," ASME Paper 95-WA/HT-29.
- [21] Azad, G. M. S., Han, J. C., Teng, S., and Boyle, R., 2000, "Heat Transfer and Pressure Distributions on a Gas Turbine Blade Tip," ASME J. Turbomach., **122**, pp. 717–724.
- [22] Azad, G. M. S., Han, J. C., and Boyle, R., 2000, "Heat Transfer and Pressure Distributions on the Squealer Tip of a Gas Turbine Blade," ASME J. Turbomach., **122**, pp. 725–732.
- [23] Ou, S., Han, J. C., Mehendale, A. G., and Lee, C. P., 1994, "Unsteady Wake Over a Linear Turbine Blade Cascade with air and CO₂ Film Injection: Part I—Effect on Heat Transfer Coefficients," ASME J. Turbomach., **116**, pp. 721–729.
- [24] Du, H., Han, J. C., and Ekkard, S. V., 1998, "Effect of Unsteady Wake on Detailed Heat Transfer Coefficient and Film Effectiveness Distributions for a Gas Turbine Blade," ASME J. Turbomach., **120**, pp. 808–817.
- [25] Vedula, R. J., and Metzger, D. E., 1991, "A Method for the Simultaneous Determination of Local Effectiveness and Heat Transfer Distributions in Three-Temperature Convection Situations," ASME Paper No. 91-GT-345.
- [26] Ireland, P. T., and Jones, T. V., 1987, "The Response Time of a Surface Thermometer Employing Encapsulated Thermochromic Liquid Crystals," *J. Phys. E*, **10**, pp. 1195–1199.
- [27] Teng, S., Sohn, D. K., and Han, J. C., 1999, "Unsteady Wake Effect of Film Temperature and Effectiveness Distributions for a Gas Turbine Blade," ASME J. Turbomach., **122**, pp. 340–347.
- [28] Kline, S. J., and McClintock, F. A., 1953, "Describing Uncertainties in Single Sample Experiments," *Mech. Eng. (Am. Soc. Mech. Eng.)*, **75**, pp. 3–8.

Transport Phenomena of Developing Laminar Mixed Convection in Inclined Rectangular Ducts With Wall Transpiration

Wei-Mon Yan

e-mail: wmyan@huaan.hfu.edu.tw

Department of Mechanical Engineering, Huaan University, Shih Ting, Taipei, TAIWAN 22305, ROC

Pei-Yuan Tzeng

Department of Aeronautical Engineering, Chung Cheng Institute of Technology, Taoyuan, TAIWAN 33509, ROC

A numerical calculation has been carried out to investigate the mixed convection heat transfer in inclined rectangular ducts with wall transpiration. The vorticity-velocity method is employed to solve the governing equations. The present paper particularly addresses the effects of the independent parameters, namely, mixed convection parameter Δ , modified Rayleigh number Ra^ , wall Reynolds number Re_w , and aspect ratio γ . The predicted results show that either wall injection or wall suction has a considerable impact on the flow structure and heat transfer performance. Additionally, it was found that for injection case ($Re_w < 0$), the Nusselt number Nu is retarded with an increase in the wall Reynolds number Re_w , but the trend is reverse for the suction flow ($Re_w > 0$). [DOI: 10.1115/1.1374439]*

Keywords: Heat Transfer, Laminar, Mixed Convection, Three-Dimensional

Introduction

The heat transfer and fluid flow in porous-walled passages have received great attention in the past decades due to their wide applications. The porous-walled ducts are used in the transpiration cooling of high temperature thermal systems, gas-turbine blades, combustion chambers, exhaust nozzles, porous-walled flow reactors and solar energy collectors. Mixed convection heat transfer influenced by thermal buoyancy force has received much attention. But the effects of wall transpiration on mixed convection heat transfer in inclined ducts have not been widely studied although they are always encountered in many practical situations. For vertical ducts, the gravity force acts in the main flow direction, and there is no secondary flow in the cross section. For horizontal ducts, the combined buoyancy forces are normal to the main flow direction and they induce secondary flows in the cross plane. For inclined ducts, however, buoyancy forces act in both main flow and the cross-stream directions.

Numerical and experimental studies of fully-developed mixed convection heat transfer in inclined ducts have been examined by many investigators [1–3]. However, the assumption of fully-developed flow can only be established if the duct is very long. A numerical solution for the problem of mixed convection heat transfer in the entrance region of inclined rectangular ducts was studied by Morcos and Abou-Ellail [4]. Cheng and Yuen [5] presented a series of photographs of developing secondary flow patterns in the thermal entrance region of inclined tubes for laminar

mixed convection flow. Morcos et al. [6] performed an experimental study on laminar mixed convection heat transfer in the entrance region of inclined rectangular ducts. A numerical study of combined forced and free convection for laminar flow in the entrance region of isothermal, inclined tubes was carried out by Choudhury and Patankar [7]. Their results revealed that the buoyancy effects have a considerable influence on the fluid flow and heat transfer characteristics.

The heat transfer in porous tube in the region of fully developed flow has received considerable attention. Olson and Eckert [8] investigated experimentally the effects of injection on mixing length and eddy diffusivity of turbulent flow. Their results showed the normalized friction factors agreed with those measured in external flow and the normalized velocity defect profiles with injection agreed with those for flow without injection. The studies of heat transfer in porous tube in the developing region are available in the literature [9–12]. Yuan and Finkelstein [9] presented some entrance region heat transfer results that were restricted to asymptotically small values of the wall injection. Pederson and Kinney [10] extended the work of Kinney [13] to the thermal entrance region in a porous channel for various thermal boundary conditions. Raithby [11] solved the energy equation by the Fourier methods. He also obtained a number of asymptotic expressions of the solution of strong injection. The experimental results of Hirata et al. [12] revealed that the flow becomes fully developed up to the tube center at the axial location greater than 13 times of tube diameter. They also proposed a simple expression of defect law for velocity distribution in the core region.

The fluid flow and heat transfer in rectangular duct with porous walls has received attention recently. Hwang et al. [14] presented a numerical forced convection heat transfer and fluid flow in the entrance region of a square duct. Cheng and Hwang [15] conducted an experimental study to investigate the same problem. They found that the wall transpiration has a significant effect on the heat transfer and fluid flow in the entrance region of porous duct, but the buoyancy effect still remains untreated. Very recently, the mixed convection heat transfer in a horizontal rectangular duct with wall transpiration was investigated by Lee and Yan [16]. They showed that the buoyancy effect has a significant impact on the characteristics of flow structure and heat transfer performance. The objective of this work is to examine the wall transpiration effects on mixed convection in inclined ducts.

Analysis

Consideration is given to a steady laminar upward flow in the entrance region of a rectangular duct inclined at angle δ to the horizontal, as shown in Fig. 1. The u , v , and w are the velocity components in the x , y , and z directions, respectively. The fluid enters the channel with a uniform velocity w_o and a constant inlet temperature T_o . The porous-duct walls are maintained at a constant temperature T_w . In addition, the porous wall may be subjected to a suction or blowing velocity v_{in} . The temperature of the injected or suctioned fluid is the same as that of the duct wall.

The flow is assumed to be steady and have constant thermophysical properties except for the density change with temperature that leads to the buoyancy terms in the momentum equations. Boussinesq approximation is invoked for the consideration of buoyancy. With the above assumptions, the present problem can be formulated by the following equations [16]:

$$\partial^2 U / \partial X^2 + \partial^2 U / \partial Y^2 = \partial \xi / \partial Y - \partial^2 W / \partial X \partial Z \quad (1)$$

$$\partial^2 V / \partial X^2 + \partial^2 V / \partial Y^2 = -\partial \xi / \partial X - \partial^2 W / \partial Y \partial Z \quad (2)$$

$$\begin{aligned} U \partial \xi / \partial X + V \partial \xi / \partial Y + W \partial \xi / \partial Z + \xi (\partial U / \partial X + \partial V / \partial Y) \\ + (\partial W / \partial Y \cdot \partial U / \partial Z - \partial W / \partial X \cdot \partial V / \partial Z) \\ = \partial^2 \xi / \partial X^2 + \partial^2 \xi / \partial Y^2 - (Ra^* / Pr) \cdot \partial \theta / \partial X \end{aligned} \quad (3)$$

Contributed by the Heat Transfer Division for publication in the JOURNAL OF HEAT TRANSFER. Manuscript received by the Heat Transfer Division May 23, 2000; revision received January 20, 2001. Associate Editor: F. Cheung.

$$U \partial W / \partial X + V \partial W / \partial Y + W \partial W / \partial Z = -d\bar{P}/dZ + \partial^2 W / \partial X^2 + \partial^2 W / \partial Y^2 + \Delta / \text{Pr} \theta \quad (4)$$

$$U \partial \theta / \partial X + V \partial \theta / \partial Y + W \partial \theta / \partial Z = (\partial^2 \theta / \partial X^2 + \partial^2 \theta / \partial Y^2) / \text{Pr}. \quad (5)$$

In writing the above equations, the axial diffusion terms of the momentum equations and the energy equation are neglected due to the assumptions of high Reynolds and Peclet numbers [16–18]. In nondimensionalizing the governing equations, the following dimensionless variables are introduced:

$$\begin{aligned} X &= x/D_e & Y &= y/D_e \\ Z &= z/(\text{Re} D_e) & Z^* &= Z/\text{Pr} \\ U &= uD_e/\nu & V &= vD_e/\nu \\ W &= w/w_o & \bar{P} &= \bar{p}/(\rho w_o^2) \\ \theta &= (T - T_o)/(T_w - T_o) & \text{Gr} &= g\beta(T_w - T_o)D_e^3/\nu^2 \\ \text{Re}_w &= v_{in}D_e/\nu & \text{Ra} &= \text{PrGr} \\ \Delta &= (\text{Ra}/\text{Re})\sin\delta & \text{Ra}^* &= \text{Ra} \cdot \cos\delta \\ \text{Pr} &= \nu/\alpha & \gamma &= a/b. \end{aligned} \quad (6)$$

An additional constraint which is used to deduce the axial pressure gradient in axial momentum equation is that global mass conservation at any axial location must be satisfied. This constraint is expressed as

$$\bar{W} = 1 - \text{Re}_w(1 + \gamma)^2/\gamma \cdot Z, \quad (7)$$

where Re_w is the wall Reynolds number based on the injection or suction velocity v_{in} . For injection case, the Re_w is negative, while for suction case the Re_w is positive.

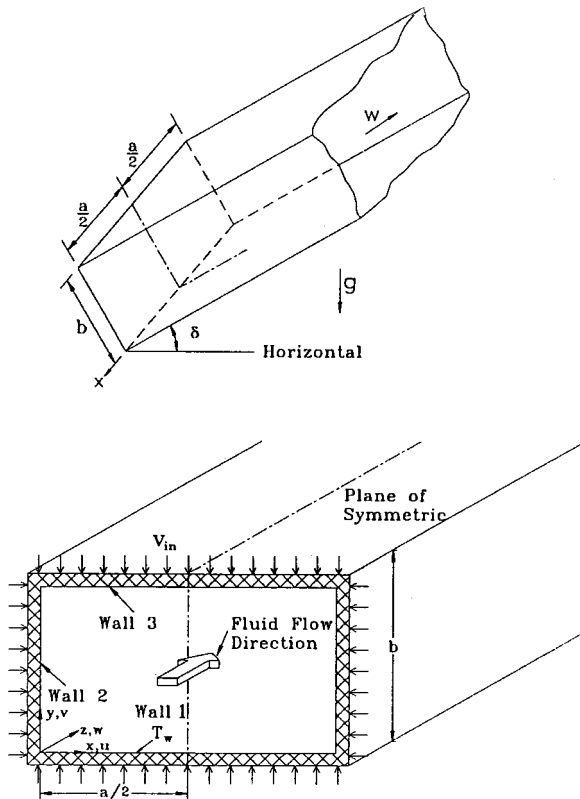


Fig. 1 Physical configuration and coordinate system

The boundary conditions for this problem are given by the following:

at the entrance, $Z=0$:

$$W=1, \quad U=V=\xi=0, \quad \theta=0 \quad (8a)$$

on the wall 1, $Y=0$:

$$W=0, \quad U=0, \quad V=\text{Re}_w, \quad \theta=1 \quad (8b)$$

on the wall 2, $X=0$:

$$W=0, \quad U=\text{Re}_w, \quad V=0, \quad \theta=1 \quad (8c)$$

on the wall 3, $Y=(1+\gamma)/(2\gamma)$:

$$W=0, \quad U=0, \quad V=-\text{Re}_w, \quad \theta=1 \quad (8d)$$

and on the symmetric plane, $X=(1+\gamma)/4$:

$$U = \partial V / \partial X = \partial W / \partial X = \partial \theta / \partial X = 0. \quad (8e)$$

In this work, there are one geometry parameter, γ , and four flow/thermal parameters, Δ , Ra^* , Re_w , and Pr . Δ is a mixed convection parameter defined by Eq. (6) that contains the ratio of the Rayleigh number Ra to the Reynolds number Re , modified by an inclination angle factor $\sin\delta$. For positive Δ , the thermal buoyancy aids the main flow, vice versa for negative Δ . Ra^* is a modified Rayleigh number given by Eq. (6). It is seen that with the introduction of the independent parameters Δ and Ra^* , the inclination angle from the horizontal direction δ does not appear explicitly in the formulation. Moreover, from Eq. (6), it is obvious that as

$$\delta \rightarrow 0: \quad \sin\delta \rightarrow 0, \quad \text{Ra}^* \rightarrow \text{Ra}, \quad \Delta \rightarrow 0 \quad (9)$$

and Eqs. (1)–(5) become the governing equations for mixed convection in a horizontal rectangular duct. Also, as

$$\delta \rightarrow \pi/2: \quad \sin\delta \rightarrow 1, \quad \text{Ra}^* \rightarrow 0, \quad \Delta \rightarrow \text{Ra}/\text{Re} \quad (10)$$

and the buoyancy term in the axial momentum equation (4) becomes

$$\delta \rightarrow \pi/2: \quad (\Delta/\text{Pr}) \cdot \theta \rightarrow (\text{Gr}/\text{Re}) \cdot \theta, \quad (11)$$

which is the correct buoyancy parameter for laminar mixed convection in the axial momentum equation in a vertical duct. Thus, it is clear that the introduction of Δ and Ra^* as independent parameters has not only reduced the number of governing parameters of the problem but has permitted a compact formulation in which all inclination angles, including the limiting cases of horizontal and vertical rectangular ducts, can be recovered. To reduce the computational efforts, the Prandtl number $\text{Pr}=0.7$ for air is used in this work. Effects of the rest four parameters are investigated. Δ was set to be 100 and -100 and Ra^* was taken between 0 and 10^5 . The wall Reynolds number Re_w ranges from 1.5 to -2 with aspect ratio γ being 2, 1, and 0.5.

After the velocity and temperature fields are obtained, the computations of the local friction factor and Nusselt number are of practical interest. Following the usual definitions, the expression for the product of peripherally averaged friction factor and Reynolds number, $f \text{Re}$, and Nusselt number, Nu , can be written based on the axial velocity gradient and temperature gradient on the duct walls,

$$f \text{Re} = -2(\overline{\partial W / \partial n}) \quad (12)$$

$$\text{Nu} = \overline{(\partial \theta / \partial n)} / (1 - \theta_b), \quad (13)$$

where the overbar represents average around the perimeter. θ_b is the bulk fluid temperature.

Solution Method

The governing equations are numerically solved by the vorticity-velocity method for three-dimensional parabolic flow [17]. Details of the solution procedure have been described elsewhere [16], and not repeated herein.

To ensure the independence of the numerical results, a grid-dependence test was performed before the main course of the computations. The grids were uniformly arranged in the cross-sectional plane but nonuniformly distributed in the axial direction for the uneven variations of W and θ at the region near the inlet. It was found in the separate numerical runs that, for a typical case with $Re_w = -1$, $Ra^* = 5 \times 10^4$, $\Delta = 100$, and $\gamma = 1$, the deviations in Nu and fRe calculated with $I \times J = 25 \times 50$ and 40×80 ($\Delta Z^* = 1 \times 10^{-5} \sim 5 \times 10^{-4}$) are always less than 2 percent. Furthermore, the deviations in Nu and fRe calculated on the grids of using $I \times J(\Delta Z^*) = 25 \times 50(2 \times 10^{-6} \sim 5 \times 10^{-4})$, and $25 \times 50(1 \times 10^{-5} \sim 5 \times 10^{-4})$ are estimated to be within 1 percent. In addition, the computations involving $I \times J = 50 \times 50$ ($\gamma = 2$) and 100×25 ($\gamma = 0.5$) grids are also used and found to be sufficiently accurate to describe the mixed convection heat transfer in inclined rectangular ducts. As an additional verification of the computational procedure, the hydrodynamically developing flow was computed without buoyancy effects. The results were compared with those of Shah and London [18]. The apparent friction factor was found to agree within 2 percent at all axial locations. Besides, the limiting results of forced convection in an one-porous-wall square duct with various injected rates were obtained and compared with those of Cheng and Hwang [15]. Excellent agreement was found. These program tests confirm the accuracy and convergence of the present numerical solution.

Results and Discussion

The effects of mixed convection parameter Δ and modified Rayleigh number Ra^* on the axial variations of fRe and Nu at $Re_w = -1$ and $\gamma = 1$ are presented in Fig. 2. From the defining equations of Ra^* and Δ (Eq. (6)), it is seen that holding Δ fixed while increasing Ra^* is like decreasing the inclination angle δ and simultaneously increasing the Rayleigh number Ra . Alternatively, the same effect can be obtained at a fixed inclination angle δ by increasing Ra and Re simultaneously such that the value of Δ remains the same. In any case, the effect of increasing Ra^* at a fixed Δ is to increase the combined buoyancy effects. In Fig. 2, the effect of Ra^* is practically negligible when $Ra^* \leq 10^3$. A monotonic decrease in Nu near the inlet is caused by the entrance effect. The onset of buoyancy effect occurs at some axial location from the inlet depending mainly upon the value of Ra^* . A minimum local Nu will not appear unless the entrance effect is balanced out by the buoyancy effects. After reaching the local minimum point, the variation of local Nu generally shows an increase to a maximum local Nu . At large downstream distance, the local Nu gradually approaches the asymptotic value given by the Graetz solution. Comparing the solid and dashed lines indicates that, at a fixed Ra^* , larger fRe and Nu are noted for a system with a positive buoyancy parameter Δ due to the aiding buoyancy force for $\Delta > 0$. It is worth noting in Fig. 2(a) that the effects of Ra^* on the fRe is relatively insignificant for the system with a positive Δ .

Figure 3 presents the wall Reynolds number Re_w on the axial variations of the circumferentially averaged friction factor fRe and Nusselt number Nu . Relative to the result of impermeable duct system ($Re_w = 0$), the effects of wall transpiration on the local fRe is slight near the inlet. The decay of fRe with Z^* is due to

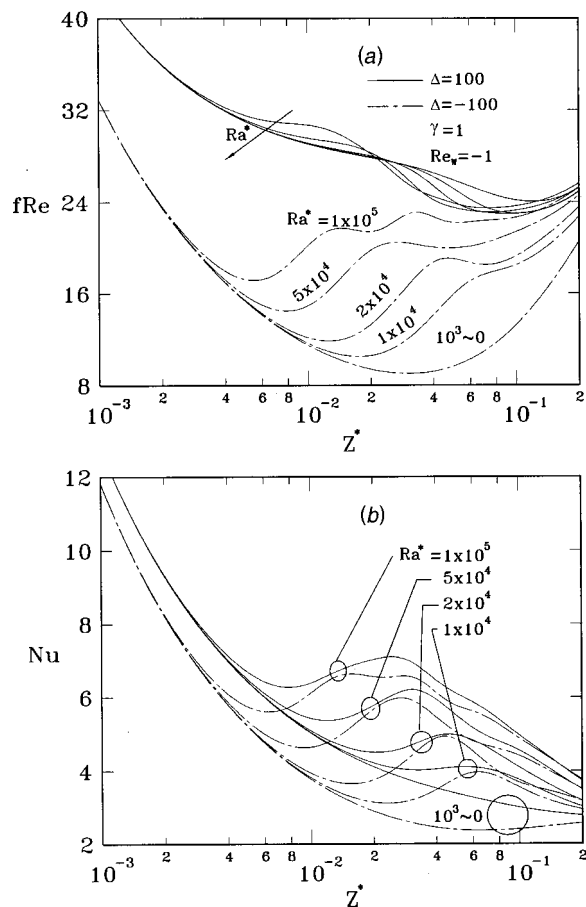


Fig. 2 The axial variations of the fRe and Nu for $Re_w = -1$ and $\gamma = 1$ with Δ and Ra^* as parameters

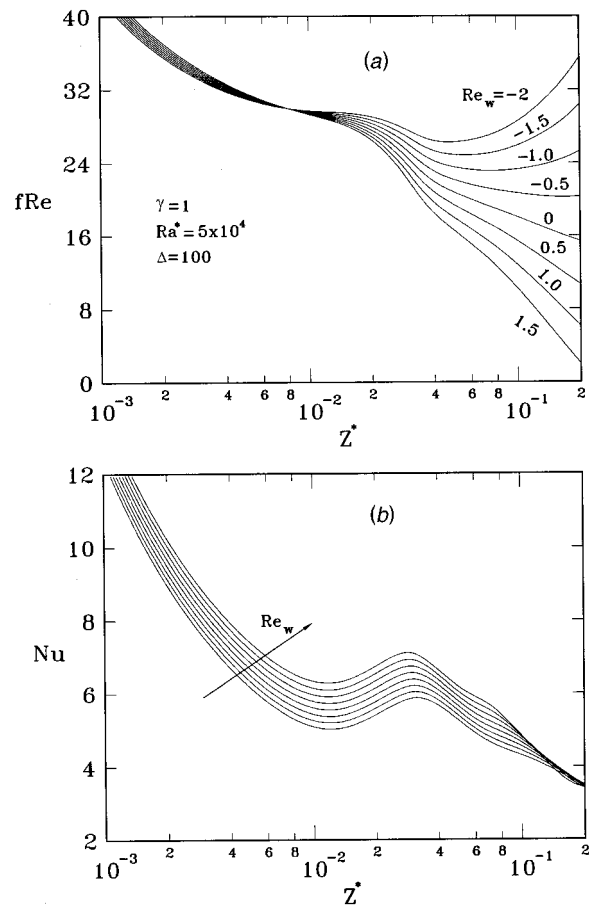


Fig. 3 Effects of wall Reynolds number Re_w on the axial variations of the fRe and Nu for $Ra^* = 5 \times 10^4$, $\Delta = 100$ and $\gamma = 1$

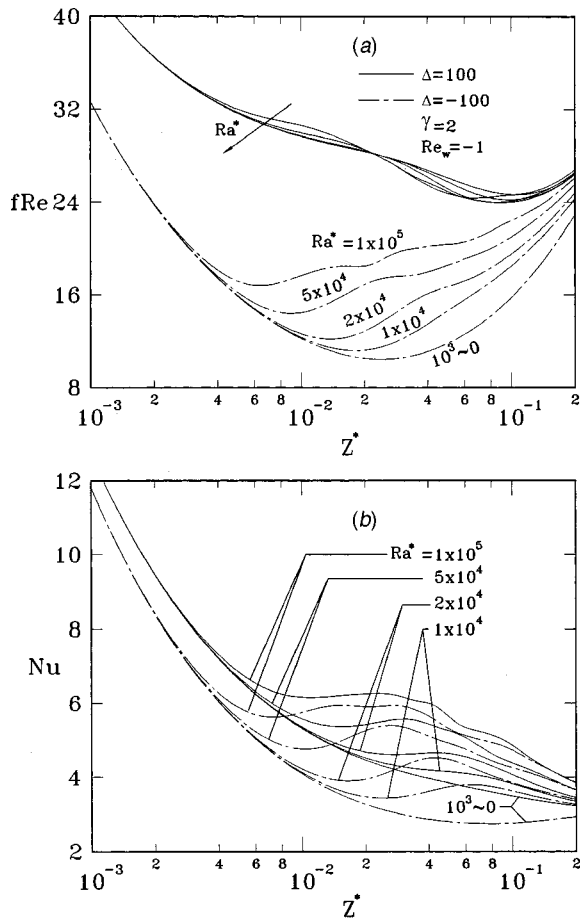


Fig. 4 The axial variations of the fRe and Nu for $Re_w = -1$ and $\gamma = 2$ with Δ and Ra^* as parameters

the entrance effect. In addition, a slightly larger (smaller) fRe is noted for a system with a suction (blowing) case. At about $Z^* = 8 \times 10^{-3}$, the curves for all blowing and suction cases converge. But after this location, the fRe increases with increasing axial location for the case of fluid injection ($Re_w < 0$), and the enhancement in fRe due to the wall injection effects increases with an increase in the injection rate. This can be explained by the steeper axial velocity gradient near the duct walls for the stronger injection rate. The mass extraction ($Re_w > 0$) will decelerate the main stream velocity. Hence the velocity gradient at the duct wall diminishes. This is projected in Fig. 3(a) that the fRe decreases with increasing suction rate Re_w . It is also found in Fig. 3(b) that a smaller Nu results for a system with a greater injection rate ($Re_w < 0$). This is owing to the fact that the wall injection increases the thermal boundary layer thickness and stimulates the fully developed temperature profiles being formed. That is, the temperature difference of the heated wall and the bulk fluid temperature is smaller for injection flow ($Re_w < 0$). Hence the Nusselt number is smaller for a higher negative Re_w . On the contrary, the temperature difference is increased by the fluid extraction in the case of suction flow ($Re_w > 0$). Hence a higher Nu is obtained with greater suction rate.

The effects of the aspect ratio of a rectangular duct on the flow and heat transfer results are of practical interest. The local fRe and Nu for the aspect ratios $\gamma = 2$ and 0.5 are shown in Figs. 4 and 5 with mixed convection parameter Δ and modified Rayleigh number Ra^* as parameters. In Figs. 4 and 5, the lowest curve can be regarded as a limiting case for purely forced convection. Comparing Figs. 2, 4, and 5, it is found that the general behaviors of the fRe and Nu for aspect ratios $\gamma = 2$ and 0.5 are quite similar to

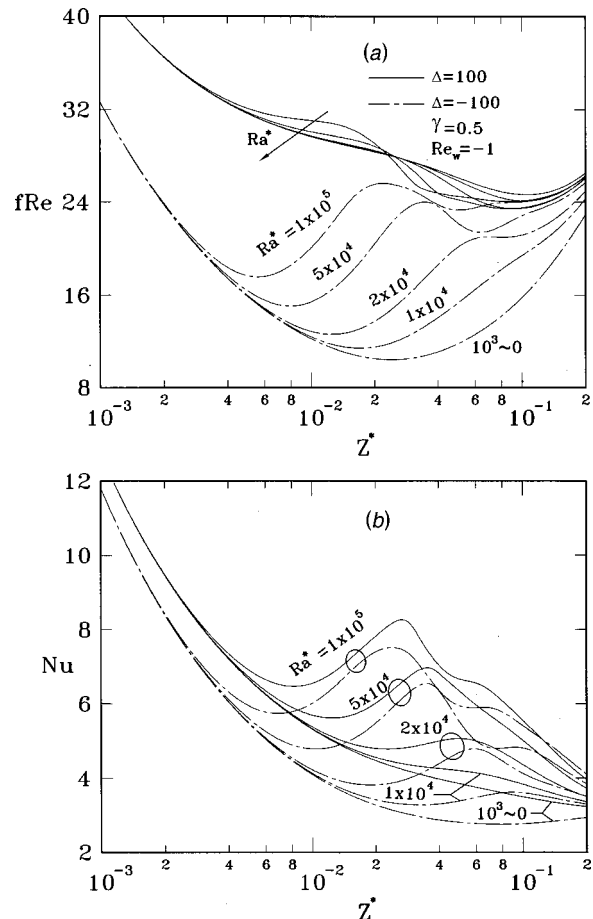


Fig. 5 The axial variations of the fRe and Nu for $Re_w = -1$ and $\gamma = 0.5$ with Δ and Ra^* as parameters

those of $\gamma = 1$. However, the results show that the Nu for aspect ratio $\gamma = 0.5$ (narrow and tall channel) is superior to that for $\gamma = 2$ (thin and flat channel). This is because that the relatively longer vertical side wall has a stronger buoyancy effect on the flow and heat transfer for a channel with a smaller γ . Additionally, in the absence of buoyancy, the Nusselt number would not depend on the aspect ratio, with $\gamma = 0.5$ and 2 yielding one curve.

Conclusion

The mixed convection heat transfer in inclined rectangular ducts with wall transpiration was numerically investigated by using a vorticity-velocity method. The effects of the mixed convection parameter Δ , modified Rayleigh number Ra^* , wall Reynolds number Re_w , and aspect ratio γ on the momentum and heat transfer were examined in detail. What follows is brief summary of the major results.

- 1 Within the range of parameters under investigation, the buoyancy effects are practically negligible when $Ra^* \leq 1 \times 10^3$.
- 2 For injection case ($Re_w < 0$), the Nusselt number Nu is retarded with an increase in the wall Reynolds number Re_w , but the trend is reverse for the suction flow ($Re_w > 0$).
- 3 The variations of the local Nusselt number are characterized by a decay near the inlet in which the forced-convection entrance effect dominates; but the decay is attenuated by the onset of buoyancy-driven secondary flows.
- 4 A stronger buoyancy effect is noted for a system with a smaller γ ($\gamma = 0.5$).

Acknowledgment

The financial support of this research by the National Science Council under the contract NSC 87-2212-E-211-006 is greatly appreciated.

Nomenclature

- a, b = width and height of a rectangular duct, respectively
 D_e = equivalent hydraulic diameter, $2ab/(a+b)$, m
 I, J = number of finite difference divisions in the X and Y directions, respectively
 n = dimensionless outward normal direction to the wall
 Ra^* = modified Rayleigh number, $Racos \delta$
 Re_w = wall Reynolds number, $v_{in}D_e/\nu$
 v_{in} = magnitude of fluid velocity injected or suctioned through the porous walls
 X, Y, Z = dimensionless rectangular coordinate, $X=x/D_e$, $Y=y/D_e$, $Z=z/(Re D_e)$
 Z^* = dimensionless z -direction coordinate, $z/(Pr Re D_e) = Z/Pr$

Greek Symbols

- δ = duct inclination angle
 Δ = mixed convection parameter, $(Ra/Re)\sin \delta$
 γ = aspect ratio of a rectangular duct, a/b
 ξ = dimensionless vorticity in axial direction

Subscripts

- b = bulk fluid quantity
 o = value at inlet
 w = value at wall

Superscripts

- $-$ = average value

References

- [1] Cheng, K. C., and Hong, S. W., 1972, "Effect of Tube Inclination on Laminar Convection in Uniformly Heated Tubes for Flat-Plate Solar Collectors," *Sol. Energy*, **13**, pp. 363–371.
- [2] Sabbagh, J. A., Aziz, A., El-Aring, A. S., and Hamad, G., 1976, "Combined Free and Forced Convection Heat Transfer in Inclined Circular Tubes," *ASME J. Heat Transfer*, **98**, pp. 322–324.
- [3] Abdelmeguid, A. M., and Spalding, D. B., 1979, "Turbulent Flow and Heat Transfer in Pipes With Buoyancy Effects," *J. Fluid Mech.*, **94**, Part 2, pp. 383–400.
- [4] Morcos, E. M., and Abou-Ellail, M. M. M., 1983, "Buoyancy Effects in the Entrance Region of an Inclined Multirectangular Channel Solar Collector," *ASME J. Sol. Energy Eng.*, **105**, pp. 157–162.
- [5] Cheng, K. C., and Yuen, F. P., 1985, "Flow Visualization Studies on Secondary Flow Pattern for Mixed Convection in the Entrance Region of Isothermally Heated Inclined Pipes, Fundamentals of Forced and Mixed Convection," *ASME HTD*, **42**, pp. 121–130.
- [6] Morcos, S. M., Hilal, M. M., Kamel, M. M., and Soliman, M. S., 1986, "Experimental Investigation of Mixed Laminar Convection in the Entrance Region of Inclined Rectangular Channels," *ASME J. Heat Transfer*, **108**, pp. 574–579.
- [7] Choudhury, D., and Patankar, S. V., 1988, "Combined Forced and Free Laminar Convection in the Entrance Region of an Inclined Isothermal Tube," *ASME J. Heat Transfer*, **110**, pp. 901–909.
- [8] Olson, R. M., and Eckert, E. R. G., 1966, "Experimental Studies of Turbulent Flow in a Porous Circular Tube With Uniform Fluid Injection Through the Tube Wall," *ASME J. Appl. Mech.*, **33**, pp. 7–17.
- [9] Yuan, S. W., and Finkelstein, A. B., 1958, "Heat Transfer in Laminar Pipe Flow With Uniform Coolant Injection," *Jet Propul.*, **28**, pp. 178–181.
- [10] Pederson, R. J., and Kinney, R. B., 1971, "Entrance-Region Heat Transfer for Laminar Flow in Porous Tubes," *Int. J. Heat Mass Transf.*, **14**, pp. 159–161.
- [11] Raithby, G. D., 1971, "Laminar Heat Transfer in the Thermal Entrance of Circular Tubes and Two-Dimensional Rectangular Ducts With Wall Suction and Injection," *Int. J. Heat Mass Transf.*, **14**, pp. 224–243.
- [12] Hirata, Y. S., Hirata, Y. S., and Ito, R., 1982, "Experimental Study of Flow Development in a Porous Tube With Injection or Suction," *J. Chem. Eng. Jpn.*, **15**, pp. 455–451.
- [13] Kinney, R. B., 1968, "Fully Development Frictional and Heat Transfer Characteristics of Laminar Flow in Porous Tubes," *Int. J. Heat Mass Transf.*, **11**, pp. 1393–1401.
- [14] Hwang, G. J., Cheng, Y. C., and Ng, M. L., 1993, "Developing Laminar Flow and Heat Transfer in a Square Duct With One-Walled Injection and Suction," *Int. J. Heat Mass Transf.*, **36**, pp. 2429–2440.

- [15] Cheng, Y. C., and Hwang, G. J., 1995, "Experimental Study of Laminar Flow and Heat Transfer in a One-Porous-Wall Square Duct With Wall Injection," *Int. J. Heat Mass Transf.*, **38**, pp. 3475–3484.
- [16] Lee, K. T., and Yan, W. M., 1998, "Mixed Convection Heat Transfer in Horizontal Rectangular Ducts With Wall Transpiration Effects," *Int. J. Heat Mass Transf.*, **41**, pp. 411–423.
- [17] Ramakrishna, K., Rubin, S. G., and Khosla, P. K., 1982, "Laminar Natural Convection Along Vertical Square Ducts," *Numer. Heat Transfer*, **5**, pp. 59–79.
- [18] Shah, R. A., and London, A. L., 1978, *Laminar Flow Forced Convection in Ducts*, Splt. 1 to Adv. Heat Transfer, Academic Press, New York, pp. 196–222.

Clouds Over Soot Evaporation: Errors in Modeling Laser-Induced Incandescence of Soot

G. J. Smallwood

Senior Research Officer

e-mail: greg.smallwood@nrc.ca

D. R. Snelling

Principal Research Officer

F. Liu

Associate Research Officer

Ö. L. Gülder

Senior Research Officer,

Group Leader

Combustion Research Group,
Institute for Chemical Process & Environmental
Technology,
National Research Council Canada,
1200 Montreal Road, Ottawa,
Ontario, Canada K1A 0R6

The ambiguity and incorrect treatment of the evaporation term among some LII models in the literature are discussed. This study does not suggest that the correct formulation presented for the evaporation model is adequate, or that it reflects the soot evaporation process under intense evaporation. The emphasis is that the current evaporation model must be used correctly in the evaluation of the LII model against experimental data. Numerical results are presented to demonstrate the significance of the molecular weight associated with the heat of evaporation and the thermal velocity of carbon vapor on the results obtained with the evaporation model. Other errors frequently repeated in the literature are also identified. [DOI: 10.1115/1.1370507]

Introduction

Laser-induced incandescence (LII) has experienced rapid development as a powerful diagnostic tool for spatially and temporally resolved measurements of soot volume fraction and primary particle size in various applications such as diffusion flames and diesel engine exhaust. The LII technique is based on the detection

Contributed by the Heat Transfer Division for publication in the *Journal of Heat Transfer*. Manuscript received by the Heat Transfer Division April 3, 2000; revision received December 7, 2000. Associate Editor: R. Skocypec.

and analysis of the incandescence signals of the enhanced thermal radiation from soot particles subjected to an intense laser pulse. Development of the mathematical model describing the heat and mass transfer processes of LII is not only essential in understanding some aspects of experimental results but it is also useful to improve the capabilities of the technique.

The first effort to model the nanoscale heat and mass transfer processes of soot in LII was made by Eckbreth [1]. Subsequent improvement and application of this model have been presented by Melton [2], Dasch [3], Tait and Greenhalgh [4], Hofeldt [5], and recently by Mewes and Seitzman [6], Snelling et al. [7], McManus et al. [8], Will et al. [9], Snelling et al. [10], and Schraml et al. [11]. Given the assumptions of the current LII model [10], it is not surprising to see some discrepancies between the model predicted and the experimental soot temperatures [11]. The discrepancies found in the study of Schraml et al. are partially attributed to their incorrect treatment of the evaporation heat loss term. Further research and evaluation of the LII model are clearly required. Nevertheless, the usefulness of the current LII model has been demonstrated in several studies [5,8–11]. Central to the LII process is soot evaporation, which reduces the soot particle size and provides an effective cooling mechanism that limits the further rise of soot particle temperature. An adequate treatment of the evaporation term is the key to the success of an LII model to predict the time-resolved soot particle size, soot temperature, and the excitation curve. Unfortunately, significant differences exist in the treatment of the vaporization heat loss term among the LII models found in the literature. Our research revealed that the ambiguity, confusion, and incorrect treatment of the soot evaporation term originated in the first LII modeling paper by Eckbreth [1]. The incorrect formulation has been widely spread in the growing community of LII modeling [2,4,9], although the correct formulation of the soot evaporation model was given by Dasch [3] and Hofeldt [5]. The present paper is motivated by the pressing need to clarify the confusion and incorrect treatment of the soot evaporation model among some researchers working on LII modeling. The objectives of this study are (1) to clarify the confusion surrounding the soot evaporation model and establish the correct formulation in order to prevent further use of the incorrect one, and (2) to numerically evaluate the impact of using the incorrect soot evaporation model.

Evaporation Models

A detailed description of the LII model employed in this study has been given by Snelling et al. [10] and therefore is not repeated here. The energy balance equation is given here for the convenience of the reader.

$$C_a q - \frac{2k_a(T - T_g)\pi d_p^2}{(d_p + G\lambda_{MFP})} + \frac{\Delta H_v(T)}{M_v(T)} \frac{dM}{dt} + q_{rad} = \frac{1}{6} \pi d_p^3 \rho_s c_s \frac{dT}{dt} \quad (1)$$

The terms in Eq. (1) represent, in order, the laser energy absorption by soot particle, heat conduction loss from the soot particle to the surrounding gas in the transition regime, heat loss due to soot evaporation, heat loss through the mechanism of thermal radiation, and finally the rate of soot particle internal energy change. The absorbed laser energy is determined by the laser intensity q , and the absorption cross section $C_a = (\pi^2 d_p^3 E(m))/\lambda$, where d_p is the diameter of the primary particles, $E(m)$ is a refractive index dependent function, and λ is the wavelength of the laser. The parameters in the conduction term include: k_a , the heat conduction coefficient of air; T , the soot temperature; T_g , the gas temperature; d_p , the diameter of the primary particles; G , a geometry-dependent heat transfer factor; and λ_{MFP} , the mean free path. The parameters in the evaporation term are: $\Delta H_v(T)$, the particle temperature dependent heat of evaporation of graphite; $M_v(T)$, the particle temperature dependent molecular weight of soot vapor; M , the mass of soot particle; and t is time. q_{rad} is the heat loss term due to radiation. Additional parameters presented in the internal energy term are: ρ_s , the density of soot; and c_s , the specific heat of soot.

To illustrate the differences in the treatment of the evaporation heat loss term between the present LII model and the models presented and/or employed by others, these evaporation models are compared in Table 1, where β is the evaporation coefficient, $P_v(T)$ is the particle temperature dependent vapor pressure of soot, and R is the universal gas constant.

Except for a minor difference in the introduction of the evaporation coefficient β between Model I and Models II and III, two important differences are observed. First, Model I employs a different molecular weight associated with the heat of vaporization from Models II and III: Model I uses the molecular weight of the soot vapor (M_v) while Models II and III use the molecular weight of the solid carbon (M_s). Secondly, a factor of π is missing from the denominator of the term inside the square root in Model II. It is not clear which expression was used in the studies of Will et al. [9] and Schraml et al. [11] since formulation for dM/dt was not given in their papers. Here we assume that Model III employs the same dM/dt formulation as Model I.

It is understandable to easily make incorrect use of the molecular weight associated with the heat of vaporization if careful thought is not given to the physical situation of soot (assuming graphite) evaporation. It is well known that multiple species of carbon coexist in the vapor with C_3 as the most abundant species based on the thermodynamic equilibrium calculations of Leider et al. [12]. In addition, the heat of evaporation, ΔH_v , is the energy required to evaporate unit mole solid carbon into multiple gaseous carbon species. Therefore, the mean molecular weight of the vapor should be used, not the molecular weight of the solid carbon, so that the heat of evaporation is consistent with the molecular weight. Certainly, it would be correct to use the molecular weight of solid carbon if only a single species (C_1) exists in the vapor, or if ΔH_v corresponding to C_1 only is used. A temperature

Table 1 Comparison of the evaporation models in the literature

Model I	Model II	Model III
Present study Dasch ^a [3] Hofeldt [5]	Eckbreth [1] Melton [2] Tait and Greenhalgh ^b [4]	Will et al. ^c [9] Schraml et al. ^c [11]
$-\frac{\Delta H_v}{M_v} \pi d_p^2 \beta P_v(T) \sqrt{\frac{M_v}{2\pi RT}}$	$-\frac{\Delta H_v}{M_s} \pi d_p^2 P_v(T) \sqrt{\frac{M_v}{2RT}}$	$\frac{\Delta H_v}{M_s} \frac{dM}{dt}$

^aDasch [3] did not use the evaporation coefficient β .

^bThe square root term was given as $\sqrt{\frac{M_v}{2} RT}$, which is likely to be a typo.

^cWill et al. [9] and Schraml et al. [11] did not present their expressions for dM/dt .

dependent mean molecular weight is used in the numerical model, rising from 24 at 2000 K to 36 at 3600 K to 48 at 4700 K. Thus the error in using C_1 , with a molecular weight of 12, increases from overestimating the enthalpy loss from soot mass evaporation by a factor of 2 at 2000 K to a factor of 4 at 4700 K.

As for the second difference associated with the thermal velocity of vapor between Model I and Model II, it is emphasized here that the expression of Model I is correct. A detailed derivation of the mass flux of vapor that crosses unit area toward one side was given by Kennard [13] and is written as

$$\Phi = P_v \sqrt{\frac{M_v}{2\pi RT}} \quad (2)$$

Application of Eq. (2) to calculate the evaporation heat loss term leads to the expression of Model I given in Table 1. The rationale of introducing an evaporation coefficient, β , has been discussed by Kennard [13]. The evaporation heat loss term of Model II given in Table 1 implies that the mass flux of vapor would read

$$\Phi' = P_v \sqrt{\frac{M_v}{2RT}} \quad (3)$$

resulting in a predicted enthalpy loss that is 1.8 times too high. The combination of the inconsistent use of molecular weights and the incorrect formulation for the mass flux of vapor presented in Model II produces an overall predicted enthalpy loss that ranges from 3.6 times too high at 2000 K to 7.2 times too high at 4700 K.

Such overestimations of the enthalpy losses are anticipated to cause the particle temperatures to be much cooler and the evaporated mass loss to be much less with Models II and III in comparison with Model I.

In addition to the confusion and incorrect treatment regarding the evaporation term of the LII models in the literature, it is also worth pointing out that Melton [2] gave an incorrect expression for the thermal conductivity of air, which has been previously identified [6]. According to Melton, the thermal conductivity of air was calculated as $K_a = 5.83 \times 10^{-5} (T/273)^{0.82} \text{ W cm}^{-1} \text{ K}^{-1}$ based on the expression given by Tsederberg [14]. It was noticed by Mewes and Seitzman [6] that this expression yields air thermal conductivity that is only about one fourth of well-established values. After consulting the expression given by Tsederberg, it was realized that Melton [2] neglected to convert calorie to joule in the expression shown above, thus accounting for the discrepancy. In addition, the analytical expression for the thermal conductivity of air given in Tsederberg is applicable only up to 1273 K. Therefore, neither the expression given in Melton nor the expression given in Tsederberg should be employed in LII modeling since temperatures in a flame are well above the upper temperature limit of the expression given in Tsederberg. On the other hand, one should be aware that use of the thermal conductivity of air in modeling the heat conduction term is only an approximation, since the local thermal conductivity of combustion gas varies significantly in a flame and in the exhaust gases due to variations in the composition.

Furthermore, there is a typographical error in Melton [2] in the sign of the exponent for the heat of vaporization of carbon, which should have read $7.78 \times 10^{+5} \text{ J/mol}$.

Results and Discussion

Characteristics of the excitation laser were given in detail in Snelling et al. [10]. Briefly, the wavelength of the laser is 532 nm and it has a typical Q-switched temporal profile of 7 ns FWHM duration. The spatial profile of the laser intensity is top-hat (uniform). The primary soot particle size assumed in the calculations is 32 nm. Unless otherwise stated, the evaporation coefficient β is assumed to be 1.0. $E(m)$ based on the refractive index of soot due to Lee and Tien [15] (0.176 at 532 nm) was used in all the calculations. The numerical solver uses an adaptive fourth-order Runge-Kutta algorithm that optimizes the step size to minimize the truncation error. The numerical results discussed below were obtained using a time step of 0.25 ns. Investigations were performed to ensure that this time step was sufficiently small to achieve results independent of the time step, with maximum deviation of less than 0.1 percent. Effects of using the three different evaporation models given in Table 1 on the model predictions were investigated.

The physical properties used in the present calculations are specified as follows. The local gas temperature $T_g = 1800 \text{ K}$, a typical value found in flames. The corresponding values of k_a , G , and λ_{MFP} are 0.12 W/m K, 22.064, and 0.5665 μm , respectively. The soot density and specific heat are taken at the values of local gas temperature, i.e., $\rho_s = 2.2 \text{ g/cm}^3$ [12] and $c_s = 2.1 \text{ J/g K}$ [16] since they only vary mildly with temperature. Properties related to the soot evaporation rate are obtained from the equilibrium calculations of Leider et al. [12] and are given as fifth-order polynomial expressions as $P_v = \exp(\sum_{i=0}^5 p_i T^i) \text{ atm}$, $M_v = \sum_{i=0}^5 m_i T^i \text{ kg/mole}$, and $\Delta H_v = \sum_{i=0}^5 h_i T^i \text{ J/K mole}$. The fitting coefficients are given in Table 2.

When conducting numerical calculations of soot particle size and temperature using the present LII model, it is worth pointing out that there are uncertainties in the predictions due to uncertainties associated with the thermal properties of soot such as the absorption function $E(m)$, the mean molecular weight of soot vapor M_v , the heat of vaporization ΔH_v , the vapor pressure P_v , and input parameters for the heat conduction rate. Based on our best knowledge it was estimated that uncertainties of these properties are well within 30 percent. The effects of the uncertainty in these properties on the numerical predictions were investigated by perturbing the values of the properties discussed above by ± 30 percent using Model I at a laser fluence of 0.725 J/cm². At this laser fluence, there is significant soot vaporization and properties associated with the heat conduction loss have almost no effect on the solution during and shortly after the laser pulse (the laser pulse duration is 30 ns). Effects of uncertainty of $E(m)$, M_v , ΔH_v , and P_v on the predictions are shown in Fig. 1. Uncertainties in $E(m)$, M_v , and ΔH_v have a significant effect on particle size but have less impact on particle temperature, Figs. 1(a), (b), and (c). Variation of the vapor pressure by 30 percent has a modest effect on the particle temperature and minimal effect on particle size, Fig. 1(d). Overall, the uncertainty in the predicted particle temperature and particle size is about 2 percent and 20 percent, respectively.

Effects on the History of Soot Particle Size and Temperature. Calculations were carried out using the three different

Table 2 Fitting coefficients for the vapor pressure, mean molecular weight, and the heat of vaporization

i	p_i	m_i	h_i
0	-122.96	0.017179	205398
1	0.090558	6.8654e-7	736.60
2	-2.7637e-5	2.9962e-9	-0.40713
3	4.1754e-9	-8.5954e-13	1.1992e-4
4	-2.4875e-13	1.0486e-16	-1.7946e-8
5	0.0	0.0	1.0717e-12

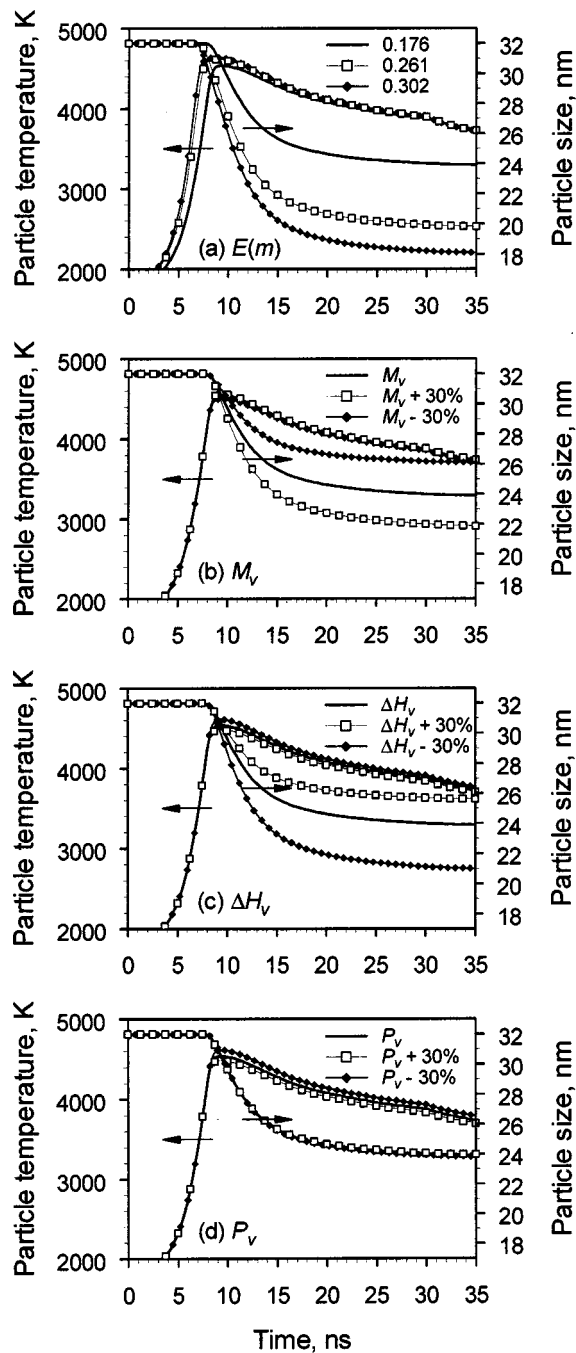


Fig. 1 Uncertainty analysis for specified thermal properties of soot: (a) refractive index dependent function; (b) mean molecular weight of soot vapor; (c) heat of vaporization; and (d) vapor pressure.

evaporation models shown in Table 1 for a laser peak fluence of 0.725 J/cm^2 , which is equivalent to a laser pulse energy of 6 mJ for the spatial profile. These results are compared in Fig. 2. Model I predicts that significant soot evaporation occurs under the computational conditions with the particle size reduced by about 26 percent. In contrast, Models II and III predict that the reduction in particle size is only about 8 percent. It is also interesting to observe that Model II predicts the particle size that is only very slightly lower than that from Model III. A slightly smaller particle size starting at the end of laser pulse is noticed as a result of using Melton's K_a since heat conduction loss is underestimated. Use of

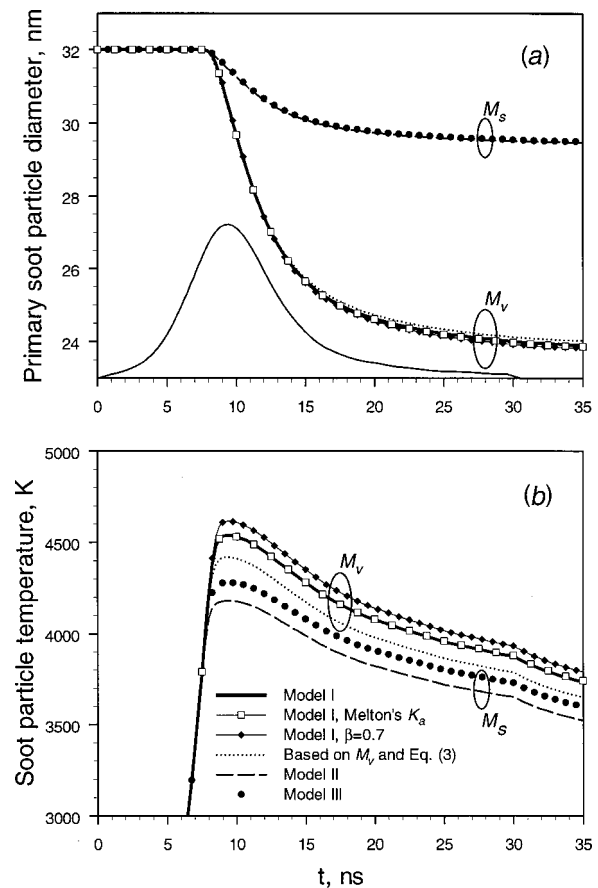


Fig. 2 Effects of some evaporation model parameters and the thermal conductivity on the predicted soot particle size (a) and temperature (b). The temporal profile of the laser intensity is shown for reference.

the incorrect K_a affects the soot temperature only near the end of the laser pulse (30 ns), Fig. 2(b), when heat conduction becomes important. Although not demonstrated in Fig. 2, use of Melton's K_a results in an incorrect prediction of the temperature decay at longer times. Results obtained with Model I using $\beta=0.7$ are also shown in the figure to demonstrate the effect of the evaporation coefficient. To present a thorough picture about the effect of the molecular weight (either M_s or M_v) and the thermal velocity of carbon vapor, equivalent to the mass flux expressions given in Eqs. (2) and (3), results based on M_v and Eq. (3) are also shown in Fig. 2.

Results shown in Fig. 2(a) reveal that it is very crucial to employ a molecular weight consistent with the heat of evaporation for the prediction of the soot particle size, while missing a factor of π in the thermal velocity of soot vapor has only slight effect on the particle size (see difference of results between Model II and Model III). Model I employing the incorrect thermal conductivity results in a slightly bigger particle size at the end of the soot evaporation.

Effects of different evaporation models and the evaporation coefficient on the predicted soot temperature are shown in Fig. 2(b). Model I predicts that the peak soot temperature is about 4530 K, while Models II and Model III predict about 4177 and 4277 K respectively. The reduced evaporation coefficient, $\beta=0.7$, reduces the mass loss rate during the first 10 ns of the laser pulse, which can be observed from the slightly slower decreases of soot particle size, Fig. 2(a). This reduced mass loss in turn reduces the heat loss through evaporation, resulting in a higher peak soot particle temperature, Fig. 2(b). At later times, this increased maximum

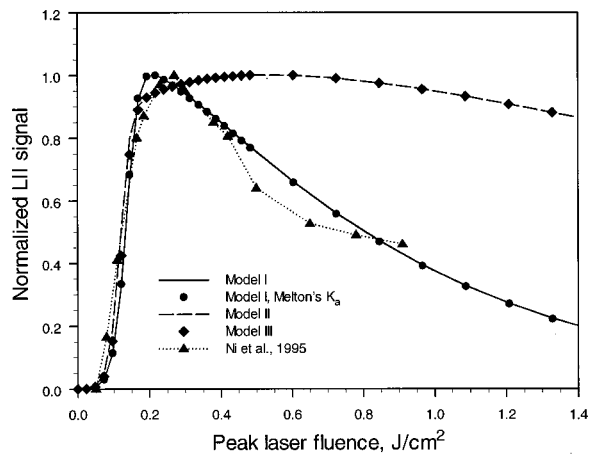


Fig. 3 Variation of the predicted and the experimental normalized prompt LII signals with laser fluence

temperature increases the mass loss rate due to the strong dependence of the vapor pressure on temperature, resulting in a slightly smaller final soot particle size.

It is evident from the results shown in Fig. 2 that the inconsistent use of M_s in the evaporation heat loss term, $\Delta H_v/M_s$, has a far more significant impact on the performance of the model than use of an incorrect expression for the thermal velocity or an inadequate evaporation coefficient. It is interesting to observe from the results shown in Fig. 2(a) that parameters that directly alter the mass loss rate of the soot particle, such as the evaporation coefficient β and the thermal velocity, ultimately have an insignificant effect on the soot particle size. Instead, they have a greater effect on the soot temperature. Parameters that directly affect the heat loss rate, such as the molecular weight associated with the heat of evaporation, have far more impact on the results, in particular the soot particle size. The complex interaction of these parameters is due in part to their strong temperature dependencies. The results are indeed a manifestation of the physics of LII: soot temperature is the driving force of soot particle evaporation.

Effects on Excitation Curve. The predicted normalized LII signal at 400 nm (collected at 20 ns after the start of the laser pulse for a gate width 18 ns) are compared in Fig. 3 with the experimental data of Ni et al. [17]. The excitation curve predicted by Model I agrees qualitatively well to the experimental curve, while Models II and III fail to capture the correct shape of the excitation curve.

Conclusions

Numerical results obtained using different evaporation models are presented and compared to demonstrate the importance of the evaporation model to the overall performance of the LII model. The following conclusions are reached based on the numerical results of this study:

1 Use of a molecular weight consistent with the heat of evaporation is crucial to the overall performance of the LII model. When a correct molecular weight based on the carbon vapor is

used, the LII model predicts the excitation curve for prompt LII signal collected at a fixed duration in qualitative agreement with experimental observation.

2 The incorrect use of the molecular weight for solid carbon associated with the heat of evaporation drastically affects the results of the model prediction. It results in lower soot temperature and significantly less soot evaporation. It also fails to predict the correct shape of the excitation curve.

3 The incorrect expression for the thermal velocity of carbon vapor affects the model results significantly less than the effect of the incorrect molecular weight.

The present study by no means attempts to claim that the correct formulation presented for the state-of-the-art evaporation model is adequate and truly reflects the soot evaporation process under intense evaporation. The emphasis of this work is that the current evaporation model must be used correctly in the evaluation of the LII model against experimental data.

References

- [1] Eckbreth, A. C., 1977, "Effects of Laser-Modulated Particulate Incandescence on Raman Scattering Diagnostics," *J. Appl. Phys.*, **48**, pp. 4473–4479.
- [2] Melton, L. A., 1984, "Soot Diagnostics Based on Laser Heating," *Appl. Opt.*, **23**, pp. 2201–2208.
- [3] Dasch, C. J., 1984, "New Soot Diagnostics in Flames Based on Laser Vaporization of Soot," *Twentieth Symposium (International) on Combustion*, The Combustion Institute, pp. 1231–1237.
- [4] Tait, N. P., and Greenhalgh, D. A., 1993, "PLIF Imaging of Fuel Fraction in Practical Devices and LII Imaging of Soot," *Berichte der Bunsengesellschaft fuer Physikalische Chemie*, **97**, pp. 1619–1625.
- [5] Hofeldt, D. L., 1993, "Real-Time Soot Concentration Measurement Technique for Engine Exhaust Streams," Society of Automotive Engineers, SAE Paper No. 930079.
- [6] Mewes, B., and Seitzman, J. M., 1997, "Soot Volume Fraction and Particle Size Measurements with Laser-Induced Incandescence," *Appl. Opt.*, **36**, pp. 709–717.
- [7] Snelling, D. R., Smallwood, G. J., Campbell, I. G., Medlock, J. E., and Gülder, Ö. L., 1997, "Development and Application of Laser-Induced Incandescence (LII) as a Diagnostic for Soot Particulate Measurements," *Advanced Non-Intrusive Instrumentation for Propulsion Engines*, AGARD Conference Proceedings 598, pp. 23-21 to 23-29.
- [8] McManus, K. R., Frank, J. H., Allen, M. G., and Rawlins, W. T., 1998, "Characterization of Laser-Heated Soot Particles Using Optical Pyrometry," AIAA Paper No. 98-0159.
- [9] Will, S., Schraml, S., Bader, K., and Leipertz, A., 1998, "Performance Characteristics of Soot Primary Particle Size Measurements by Time-Resolved Laser-Induced Incandescence," *Appl. Opt.*, **37**, pp. 5647–5658.
- [10] Snelling, D. R., Liu, F., Smallwood, G. J., and Gülder, Ö. L., 2000, "Evaluation of the Nanoscale Heat and Mass Transfer Model of the Laser-Induced Incandescence: Prediction of the Excitation Intensity," *Thirty Fourth National Heat Transfer Conference*, NHTC2000-12132.
- [11] Schraml, S., Dankers, S., Bader, K., Will, S., and Leipertz, A., 2000, "Soot Temperature Measurements and Implications for Time-Resolved Laser-Induced Incandescence (Tire-LII)," *Combust. Flame*, **120**, pp. 439–450.
- [12] Leider, H. R., Krikorian, O. H., and Young, D. A., 1973, "Thermodynamic Properties of Carbon up to the Critical Point," *Carbon*, **11**, pp. 555–563.
- [13] Kennard, E. H., 1938, *Kinetic Theory of Gases*, McGraw Hill Book Company, New York, pp. 63–69.
- [14] Tseederburg, N. V., 1965, *Thermal Conductivity of Gases and Liquids*, The M.I.T Press, Cambridge, MA, p. 89.
- [15] Lee, S. C., and Tien, C. L., 1981, "Optical Constants of Soot in Hydrocarbon Flames," *Eighteenth Symposium (International) on Combustion*, The Combustion Institute, pp. 1159–1166.
- [16] Chase, M. W., Jr., Davies, C. A., Downey, J. R., Jr., Frurip, D. J., McDonald, R. A., and Syverud, A. N., 1985, "JANAF Thermochemical Tables," Third Edition, *Journal of Physical and Chemical Reference Data*, **14**, Suppl. 1.
- [17] Ni, T., Pinson, J. A., Gupta, S., and Santoro, R. J., 1995, "Two-Dimensional Imaging of Soot Volume Fraction by the Use of Laser-Induced Incandescence," *Appl. Opt.*, **34**, pp. 7083–7091.